Determining Material Properties Using Impact Wave Propagation Method



Yongchao Huang

Kellogg College

University of Oxford

A thesis submitted for the degree of

Doctor of Philosophy

Trinity Term 2017

Determining material properties using impact wave propagation method

Yongchao Huang, Kellogg College, University of Oxford

Mechanically testing soft materials to identify dynamic material properties remains challenging in both theory and practice. Commonly used methods, the SHPB technique for example, have very limited capacity. One of the shortcomings is the impedance mismatch between bar and specimen: conventionally metal rods are employed, which generates a weak transmitted signal; also, the stress equilibrium assumption, on which traditional time domain analysis was built, is likely to be violated due to low wave speed in soft samples. Using low-impedance polymer bars is one of the promising solutions: it removes the obstacle of the weak signal. However, the problem of stress equilibrium is not yet resolved, and complexity increased: as viscosity is introduced, material behaviours become both time and frequency dependent. Therefore, applying polymeric bars in impact settings calls for rebuilding the analytical framework and testing it in simulation and experimental environments.

This work aims to answer the question: how material properties can be retrieved from an impact test? To realise this, three independent and integrated impact techniques were developed: the single rod direct impact method, the interface impact method, and the 3-rod impact method (modified SHPB). In each case, the frequency-dependent mechanical properties are derived from measurements of stress waves as they propagate in the system. The techniques were designed in a consecutive manner, but each can be used on its own. The first two techniques were fully deployed here, with complete theoretical, simulation and experimental investigations; the last technique was theoretically described, with some experimental phenomenon presented. Frequency domain analysis (*FFT*) was mainly adopted, important issues such as wave propagation, mechanical models, signal processing, dispersion, noise sensitivity, error analysis *etc.*, were demonstrated throughout the journey. It is for the first time a comprehensive investigation of the single rod technique was performed combining previous and extended work; while the interface technique was brand new. The integrated framework demonstrates the robustness, accuracy, and effectiveness of utilizing wave propagation approach to identify dynamic material properties; and with proper calibration, these established works can be applied to a broad range of polymeric system-based equilibrium-free impact tests.

CONTENTS

Abstract 2

Contents 3

Acknowledgement 10

Publications 11

Notations 12

Chapter 1 Introduction 15

1.1 Background 15

1.1.1 Soft materials and viscoelasticity 15

1.1.2 SHPB and typical material mechanical testing techniques 16

1.2 Objectives and challenges 18

1.3 Research roadmap 19

Chapter 2 Identifying viscoelastic material properties by measuring wave propagation in a single rod impact test: Theoretical Basis 23

2.1 Introduction 23

2.2 Theoretical background 26

2.3 Constitutive model-independent analysis 27

2.3.1 Wave equation for elastic and viscoelastic materials 27

2.3.2 Time domain solution to the 1D wave equation 30

2.3.3 Frequency domain solution to the 1D wave equation 32

2.3.4 Relating the propagation coefficient $\gamma(\omega)$ to complex modulus $E^*(\omega)$ 33

2.4 Model-dependent analysis 35

2.4.1 Maxwell Model 35

2.4.2 Voigt Model 38

2.4.3 S.L.S Maxwell model 39

2.4.3.1 Generalized models 39

2.4.3.2 The single term S.L.S Maxwell model 41

2.4.3.3 The generalized S.L.S Maxwell model 44

2.4.4 Summary of model-dependent analysis 47

Chapter 3 Determining viscoelastic material properties by measuring wave propagation in a single rod impact test: Experimental Investigations Part I—Setting the scene and Data processing.....49
3.1 Principles of Single Rod Test Analysis.....49
3.2 Single Rod Test Design.....52
3.2.1 Overview.....52
3.2.2 The measurement system.....54
3.2.3 Experimental aim and scheme.....55
3.3 Typical data analysis process.....58
3.3.1 Preliminary considerations.....58
3.3.2 Effects of impactor and drop height.....59
3.3.3 Data analysis process.....64
3.3.3.1 Background.....64
3.3.3.2 Pulse selection.....64
3.3.3.3 Zero Padding.....69
3.3.3.4 Time domain attenuation estimate.....71
3.3.3.5 Window function effects.....71
3.3.3.6 Construction of experimental FFT results.....74
3.3.3.7 Correction of geometric dispersion.....78
Chapter 4: Determining viscoelastic material properties by measuring wave propagation in a single rod impact test: Experimental Investigations Part II-Results Interpretation.....92
4.1 Results from Titanium.....92
4.2 Results from Magnesium.....97
4.3 Results from PMMA.....99
4.3.1 Data analysis and results.....99
4.3.2 Discussion.....101
4.3.2.1 Periodic oscillations 101
4.3.2.2 Impactor effect and ‘useful frequency range’.....102
4.3.2.3 Temperature effect.....107
4.3.2.4 Velocity measurement results.....110
4.3.2.5 Middle & edge Vibrometer results.....114

4.3.2.6 Gage effects....116
4.3.2.7 Sensitivity of modulus calculation to the propagation coefficient: analytical and numerical analysis....118
4.4 Summary of single rod impact tests....118
4.5 Results from DMA....120
4.5.1 The Time-Temperature-Superposition (TTS) principle....121
4.5.2 DMA Experimental setup....122
4.5.3 DMA results interpretation....123
4.5.4 Comparison of DMA and single rod impact test results....124
Chapter 5: Determining viscoelastic material properties by measuring wave propagation in a single rod impact test: Simulation Verification....127
5.1 Overview....127
5.2 Elastic simulations....129
5.2.1 Manually designed acceleration input....129
5.2.1.1 Input profiles....129
5.2.1.2 Simulation results....130
5.2.2 Experiment-based velocity input....132
5.2.2.1 Input profiles....132
5.2.2.2 Simulation results....133
5.3 Viscoelastic modelling....137
5.3.1 Model definition....138
5.3.1.1 Numerical fitting of experimental moduli to derive PRONY constants....138
5.3.2 Simulation results and discussions....141
5.3.2.1 Data processing and general results....141
5.3.2.2 Strain gauge size effect....144
5.3.3 Noise study....145
5.3.3.1 Noise classification and measurement....145
5.3.3.2 Case study: applying artificial and experimental noises to simulation signal....149
5.3.4 Comparison of the viscoelastic simulation-based and experiment-based results....160
5.4 Single rod simulation summary....161

Summary of the single rod impact technique (Chapter 2-5) 163
Chapter 6: Mechanical wave behaviours at 2-medium & 2-rod interface: Theoretical basis.....164
6.1 Introduction.....164
6.2 Analytical description of the interface impact phenomenon..... 164
6.2.1 Time domain analysis.....164
6.2.1.1 General time domain expressions..... 164
6.2.1.2 Boundary conditions at the interface: introducing the time domain TC & RC..... 168
6.2.1.3 Deriving time domain TC & RC: Introduction..... 171
6.2.1.4 Model-independent analysis (general material-general material) 171
6.2.1.5 Model-dependent analysis.....175
6.2.2 Frequency domain analysis.....182
Chapter 7: Simulations of mechanical wave behaviours at two-medium interfaces..... 192
7.1 Simulation scheme.....192
7.2 General model descriptions.....193
7.3 Data processing procedure.....195
7.3.1 Dispersion correction of interface signals.....197
7.3.1.1 The pre-cancellation method.....198
7.3.1.2 The revised BCs method.....199
7.3.2 Some mathematical issues in solving the interface equations.....200
7.4 Ti-Ti 2-medium interface.....207
7.4.1 Model descriptions.....207
7.4.2 Comparison of dispersive and dispersion corrected results.....207
7.4.3 Error analysis.....211
7.4.3.1 Uniformity of cross-sectional deformation.....211
7.4.3.2 Sensitivity of the interface analysis technique to distance..... 211
7.4.4 Applying single rod theory to analyse the 2 medium Ti-Ti signals.....214
7.5 Ti-Mg 2-medium interface.....216
7.6 Ti-PMMA 2-medium interface.....219
7.6.1 Error analysis.....219
7.6.1.1 Uniformity of cross-sectional deformation.....219

7.6.1.2 Sensitivity of the interface analysis technique to errors in x_{IR} and x_T 224
7.6.2 Noise study.....226
7.6.2.1 Generating of noise.....226
7.6.2.2 Effect of noise on material property derivation.....228
7.7 PMMA-Mg 2-medium interface.....231
7.8 Summary of 2-medium interface simulations.....234
Chapter 8: Simulations of mechanical wave behaviours at 2-rod interfaces…….....236
8.1 Ti-Ti 2-rod interface.....236
8.1.1 Model description.....236
8.1.2 Simulation outputs.....237
8.1.3 Data analysis.....238
8.1.4 Error analysis: sensitivities of interface equations to noises contained in transmission and reflection coefficients.....244
8.1.5 Using single rod theory to analyse 2 rod signals.....248
8.2 Ti-Mg 2-rod interface.....249
8.2.1 Model description.....249
8.2.2 Simulation outputs and results.....249
8.3 Ti-PMMA 2-rod interface.....251
8.4 PMMA-Mg 2-rod interface.....254
8.5 Error analysis.....257
8.5.1 Effect of non-normal incidence.....257
8.5.2 Misalignment investigations.....258
8.5.2.1 Neutral axis offset (NA. Offset) 260
8.5.2.2 Rotation of transmission rod.....268
8.5.2.3 General non-parallel faces.....274
Chapter 9: Mechanical wave behaviours at 2-medium & 2-rod interfaces: Experimental Implementations.....281
9.1 Experimental descriptions.....281
9.1.1 Overview and experimental setup.....281
9.2 The ‘perfect’ interface.....284

9.2.1 1200 mm long and 12.7 mm diameter Ti Rod.....284
9.2.1.1 Rod Geometry and 'single rod' analysis.....284
9.2.1.2 Interface analysis – pre-requisite data.....286
9.2.1.3 Interface analysis – pulse selection.....288
9.2.1.4 Interface analysis – effect of bending waves.....290
9.2.1.5 Interface Technique – 'virtual interface' location.....291
9.2.2 1500 mm long 13 mm diameter PMMA Rod.....292
9.2.2.1 Rod geometry and instrumentation.....292
9.2.2.2 The single rod method.....293
9.2.2.3 Interface method.....294
9.2.3 Further discussion of errors in the interface analysis method (PMMA rod as an example) 296
9.2.3.1 Shift of time domain signal.....296
9.2.3.2 Errors in $x_{I,R}$ and x_T.....297
9.3 Real interface tests.....299
9.3.1 Experimental scheme.....299
9.3.2 600 mmØ12.7 mm Ti-600 mmØ12.7 mm Ti.....300
9.3.2.1 Rod Geometry and interface contacts.....300
9.3.2.2 'Single rod' analysis.....301
9.3.2.3 Interface method.....301
9.3.3 1000 mmØ13mm PMMA-500 mmØ13 mm PMMA.....304
9.3.3.1 Rod geometry and interface contacts.....304
9.3.3.2 The single rod method.....305
9.3.3.3 The interface method.....306
9.3.4 600 mmØ12.7 mm Ti-500 mmØ13 mm PMMA.....309
9.3.4.1 Rod geometry and instrumentation.....309
9.3.4.2 The interface method.....310
9.3.5 1000 mmØ13mm PMMA-600 mmØ12.7 mm Ti.....312
9.3.5.1 Rod geometry and instrumentation.....312
9.3.5.2 The interface method.....312

9.4 Summary of interface experiments 314
9.5 Summary of the interface impact technique.....316
Chapter 10: Preliminary work on wave propagation in a 3-rod system.....321
10.1 Introduction.....321
10.2 Theoretical basis.....322
10.2.1 Long specimen assembly.....322
10.2.2 General treatment.....325
10.3 Conclusions.....329
Chapter 11: Conclusions and future work 331
11.1 Summaries.....331
11.1.1 All-in-one summaries.....331
11.1.1.1 The single rod impact technique.....331
11.1.1.2 The interface impact technique.....333
11.1.1.3 General comments.....334
11.1.2 Summaries by chapter.....336
11.2 Future work.....339
11.2.1 Further investigation of multiple-interface wave propagation theories.....339
REFERENCES 343

ACKNOWLEDGEMENT

This research project was funded by the Air Force Office of Scientific Research, Air Force Material Command, USAF, under grant number FA8655-12-1-2015. The author thanks S Fuller, J Foley and JL Jordan of AFOSR, M Snyder and R Pollak of EOARD, Chinese foundations for valuable support. The full research work was completed during 2013-2016, thesis written up and revised thereafter.

I am grateful for the supervision from my supervisor Prof. Clive R Siviour who guided me throughout the research process. His literate revision makes the thesis a logically human-readable one; the time he dedicated, including numerous holidays and weekends, is greatly appreciated. He sacrificed a lot to make things otherwise impossible, I am fortunate to work with and learn from him. I miss the mini table, the whiteboard, the messy drafts, and the elasticity book in his office.

I also acknowledge the help and support from friends at Oxford. To name some of them: Dr. Robert Paynter, Yoon, Laure, James, Heather, Jianan, Mahdi, Beth Mortimer, Amanda, Hisham, Richard Duffin, and the professors in the solid mechanics group. Thank Prof. C. Bacon for inspiring me a lot in the initial stage of single rod signal processing; my thanks also go to the lovely people at Kellogg, Magdalen colleges and OMI where I had an enjoyable journey.

Last but not least, I would like to thank my dad, a hero with a heart full of soul, with whom the old good days will be heavily missed. His spirits inspire me all the time, I wish he enjoys a happy life in heaven. I am also deeply indebted to my mother, my sisters, and family members, their love, dedication and tolerance are very much appreciated. I would also like to express my gratitude to my girlfriend who has been absent for the past years, to love or to be loved, it's still a hidden Markov learning problem. I myself deserves the praise for being concentrated and persistent, thanks Yong.

Due to space limit, readers could find details of equation derivation, some parallel and exploratory work, which amounts to some 500 pages in a digital version on Yong's website (referred to as the "*web version"* in all later context).

Yongchao Huang, Jan 2013 – Feb 2017, Oxford

PUBLICATIONS

Journal articles (in preparation)

Huang, Y., Siviour, C.R., Single rod impact technique: A review.

Huang, Y., Siviour, C.R., Wave behaviour at interface: Theories and simulations.

Huang, Y., Siviour, C.R., Wave behaviour at interface: Experimental investigations.

Huang, Y., Siviour, C.R., Application of frequency domain analysis in deriving material mechanical properties: A review.

Huang, Y., Siviour, C.R., Dispersion correction in impact tests.

Conferences

Huang, Y., Siviour, C.R., 2015. Single rod impact tests: Analytical, experimental, and modelling investigation, Proceedings of 11th International Conference on the Mechanical and Physical Behaviour of Materials under Dynamic Loading, 94, p.01052.

Huang, Y., Siviour, C.R., 2014. Wave propagation in viscoelastic materials and its application to SHPB tests. 16th International Conference on Experimental Mechanics. Cambridge.

Other scientific reports appeared on workshops and seminars.

NOTATIONS

The representations of common symbols and abbreviations are generalized as follows. Some symbols are redefined with respect to the contents of each chapter.

ε: *strain*

ε_I, ε_T, ε_R: *strain induced by incident, transmitted, reflected waves*

σ: *stress*

σ_I, σ_T, σ_R: *stress induced by incident, transmitted, reflected waves*

F: normal force

x: coordinate

x_I, x_T, x_R: *x coor by incident, transmitted, reflected waves*

ρ: *density*

ν: *Poisson's ratio*

μ, λ: *Lamé's constants*

$\boldsymbol{\lambda}$: *wavelength*

a: bar radius

R: radius of gyration

L: length

γ: *wave propagation coefficient*

α: *wave attenuation/damping coefficient*

f: frequency

κ: *wave number*

c: wave speed

c_L: *1D longitudinal wave speed*

δ: *partial differentiation*

Φ: *diameter*

θ: *phase angle*

ω: *angular frequency*

T: temperature

E: complex modulus*

E': storage modulus

E'': storage modulus

Δ*: volume expansion*

u: displacement

v: velocity

a: acceleration

t: time

i: imaginary unit

$\tilde{P}$, $\tilde{N}$*: Fourier transforms of the strains at origin*

define the Fourier transforms of the strains at $x = 0$ *due to the waves traveling in the directions of increasing and decreasing* x*, respectively,*

°C: Celsius degree

S: cross-sectional area

TC: transmission coefficient, a ratio of the transmitted wave to incident wave

RC: reflection coefficient, a ratio of the reflected wave to incident wave

RT: reflection-to-transmission coefficient, a ratio of the reflected wave to transmitted wave

Z: characteristic impedance

$\tilde{\varepsilon}$, $\tilde{u}$, $\tilde{\dot{u}}$, $\tilde{F}$, $\tilde{\sigma}$, $\tilde{a}$*: Fourier transforms of strain, displacement, velocity, force, stress and acceleration*

U: measured Oscilloscope voltage

Δf*: frequency resolution*

v_R*: Rayleigh velocity*

k: spring Hookean constant

E_0*: instantaneous modulus*

τ*: relaxation time*

$\bar{g}_1^p$, $\bar{k}_1^p$, τ_1^G, τ_1^K*: PRONY constants*

$\tilde{\varepsilon}^{1D}$, $\tilde{\varepsilon}^{3D}$: *one-dimensional, three-dimensional strains*

f_l, f_h: *low, high frequency limits*

δ: *variable variation*

Pa, GPa: pascal, gigapascal

α_T, α_v: *translational, vertical shifting factor*

T_{ref}: *reference temperature*

T_g: *glass transition temperature*

G_0, G_s, G_l: *instantaneous, storage, loss shear modulus*

χ^2: *square error function*

SNR: signal-to-noise ratio

SNR_{dB}: *SNR expressed in deciBels*

P: signal power

I: moment of inertia

DMA: dynamic mechanical analysis

SHPB: split Hopkinson pressure bar

Chapter 1: Introduction

1.1 Background

1.1.1 Soft materials and viscoelasticity

Materials with low strength, modulus, and mechanical impedance are classified as soft materials. These include elastomers, polymers, foams, gels and biological tissues, and cover wide range of engineering applications. For example, due to their damping and force regulating properties, rubbers have long been used in shock-absorbing and crash-resistant components, to reduce effects of vibration and impact in automotive and aerospace engineering; rubber-based composites, with the capacity of energy dissipation, have been applied in seismic engineering for decades; in the arena of sports, polymers are used as materials for tennis rackets, golf shafts, mountain bike frames, *etc.* Further, elastomeric coatings are used to minimize fragmentation from vehicles and buildings that experience explosive or ballistic loading [1]. Therefore, understanding the mechanical response of soft materials to high strain rate deformation is of engineering interest.

Soft materials can exhibit time-, frequency-, and temperature-dependent, responses when subjected to external forces. These dependencies are large, when compared to other structural materials such as metals, making the dynamic behaviour of polymers, in particular, complicated. Viscoelasticity is a common property of soft materials, which must be understood for proper utilization [2]. Viscoelasticity can be classified into two types: linear viscoelasticity and nonlinear viscoelasticity. If a material is subjected to deformations or stresses small enough, *i.e.* within the linear viscoelastic region (LVR), its rheological functions do not depend on the magnitude of the deformation or stress, and the response conforms to the Boltzmann superposition principle. In this thesis, all work, if not specially indicated, is within the context of linear viscoelasticity.

A wide range of materials possess the property of viscoelasticity, *e.g.* rubber [3], polyethylene elastomers [4], PMMA [5], and foams [6]. Many metals and alloys are observed to exhibit viscoelasticity over a wide range of frequencies [7, 8]. Moreover, most, if not all, biological materials are viscoelastic to a greater or lesser extent [9-11]. In polymers, the degree of viscoelasticity is

strongly dependent upon the test temperature and the deformation rate, as well as such structural variables such as degree of crystallinity, crosslinking, and molecular mass [12]. Research into the viscoelastic response of polymers has undergone extensive development over the past decades [13]. There are basically two methodologies to investigate the phenomenon: the mechanical and molecular approaches. The classical mechanical approach has proven to be very successful in treating a large number of problems [13], and was employed in this research.

1.1.2 SHPB and typical material mechanical testing techniques

A number of mechanical testing techniques have been developed to characterize dynamic material behaviours and obtain intrinsic material properties from low to high strain rates: these include classic tension, compression and torsion tests (*e.g.* servo-hydraulic machines for quasi-static 10^{-5}-10^{-1} s^{-1} and intermediate strain rates 10^{-1}-10 s^{-1}), drop weights (10-10^{3} s^{-1}), the SHPB (10^{2}-10^{4} s^{-1}), and Taylor (10^{3}-10^{5} s^{-1}) and Plate (>10^{5} s^{-1}) impact tests [14, 15]. By observing sample behaviour, some of these techniques directly yield material properties such as modulus, whist others present stress-strain curves. Conventional high rate testing methods such as the split Hopkinson pressure bar (SHPB) have very limited capacity for soft materials due to preconditions of the testing methods (*e.g.* static stress equilibrium in specimens in an SHPB test). Effective techniques for characterizing metals and stiff polymers at high strain rates are difficult to apply to very soft materials, and the measurements are of particularly poor quality at small deformations.

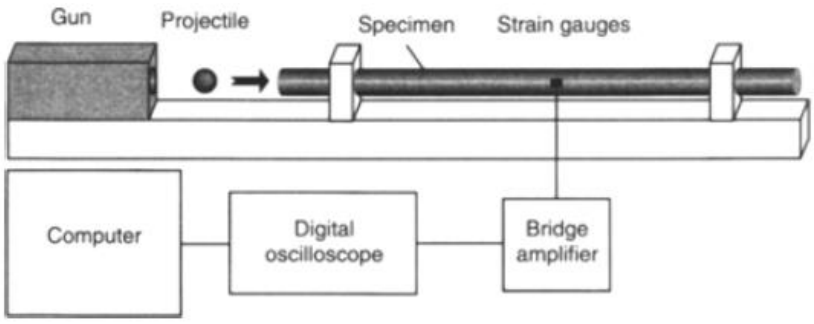


Figure. 1-1 A single rod direct impact method by C. Bacon [18]

Direct impact tests on a single long rod (*Fig. 1-1*), as performed by Kolsky [16], Pritz [17], Bacon [18], and more recently Hillstrom [19] and Benatar [20], are effective in deriving material properties such as modulus and Poisson's ratio. The experimental setup is simple and convenient: a long rod is

used as the specimen and a small amplitude stress wave is excited. The monitored quantities can be displacement, strain, particle velocity, *etc*. From the measured waves, propagation characteristics such as damping and wave speed can be obtained, and based on these, the frequency-dependent material properties, in particular the complex modulus, can be derived. Instead of directly measuring the material stress-strain response under various loading conditions, this approach provides a different way to look at the frequency-dependent material properties.

In parallel, techniques that use oscillatory loading to probe response at small strains have been developed, including Dynamic Mechanical Analysis (DMA); however, these cannot be applied at high strain rates. Some properties can be extrapolated through time-temperature superposition (TTS), but this cannot be relied on without validation, especially in biomaterials and composites, for which it is relatively untested. Another limit in high rate research is the paucity of real-time diagnostics to visualize and quantify structural deformation. High speed cameras can operate above 1 million images per second; however, microsocopy and tomography are not fast enough. Any strategy for understanding soft materials, especially composites, must overcome these limitations.

Probably the best-established high rate apparatus is the split-Hopkinson (or Kolsky) bar (SHPB, *Fig. 1-2*), widely employed for over fifty years to characterise common engineering materials [14, 15, 20, 21, 22]. The specimen is sandwiched between two slender rods, stress waves are produced by impacting the input bar with a projectile, and detected by strain gauges on both rods. During the wave propagation at the bar-specimen interface, some of the wave is reflected and some transmitted. Wave profiles detected are used to calculate strain, force and velocity in the bars, and they can be shifted to the bar-specimen interface to characterize specimen mechanical response.

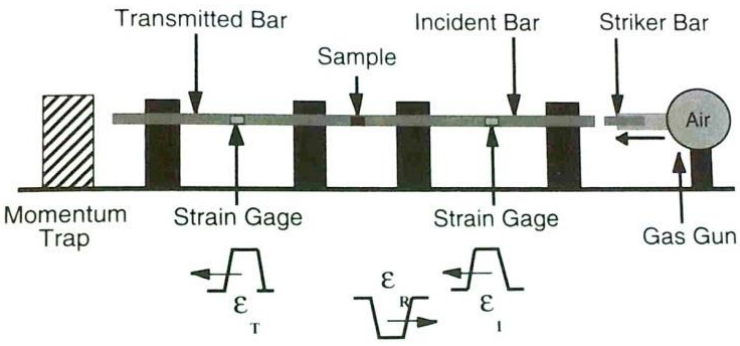


Figure. 1-2 Schematic of a SHPB setup [14]

The conventional SHPB technique has very limited capacity in testing soft materials: firstly, the low mechanical impedances of soft materials lead to low wave speed and increase delays in attaining stress equilibrium, violating the key assumption in conventional SHPB signal analysis. Secondly, when it comes to testing soft materials, the impedance mismatch between bar and specimen results in weak transmission signals with low signal-to-noise ratios [23]. Thirdly, it is impossible to obtain material modulus because the sample typically yields before it achieves stress equilibrium, instead it produces post-yield stress-strain curves for each loading rate, and repeated work is required to investigate material behaviours under various rates. Fortunately, these issues can be overcome by improving the current experimental and analysis methods. For example, the problem of weak transmission signal can be resolved by utilizing sensitive sensors (*e.g.* piezoelectric gauges [24]) or low-impedance bars (*e.g.* hollow metal bars or viscoelastic bars [6, 25]). However, the non-equilibrium testing method, which relaxes the static stress-equilibrium assumption, together with the use of frequency domain analysis methods, gives the potential to obtain dynamic material modulus.

1.2 Objectives and challenges

The general purpose of this research is to investigate the mechanical behaviour of soft materials under high strain rate loading, and to develop applicable techniques for testing low-impedance materials. Specifically, I aim to modify the conventional SHPB setup for non-testing soft materials using polymer bars, within the framework of which long specimens and non-equilibrium tests can be accommodated with common sensing approaches such as gages. The modified SHPB setup (Fig. 1-3) uses low impedance bars, and the non-equilibrium characteristic which allows long specimen to be used and accuracy to be guaranteed even small deformation is yielded. The goal was decomposed into a 3-phase task: examining wave behaviours in a single rod, at interfaces, and in a multiple rod system. Notably, each phase has the ability to retrieve materials properties independently, which meets the two purposes mentioned above.

Viscoelastic bars were increasingly employed in Hopkinson tests [18, 22, 26]. However, occasions involving viscoelasticity (both bar and specimen) is still a challenge in practice. Firstly, discrepancies

between theory and practice exist due to effects such as multimode deformation approximation [27], experimental imperfection, noise inference, *etc*. Secondly, wave propagation in multiple rod system brings in complexity. In SHPB tests, transmission and reflection occur at both input bar-specimen and specimen-output bar interfaces, and the intensity depends on both material impedances, as well as the contact conditions. Traditional time domain analysis loses its advantage as all viscoelastic properties are frequency-dependent, and the prerequisite knowledge of the rods is needed before they are used in an SHPB setup. Thirdly, when performing SHPB experiments on viscoelastic materials, the assumption of stress equilibrium fails; instead, research into non-equilibrium analysis method, which hasn't been explored much, is desired. Due to the frequency-dependent nature of viscoelasticity, non-equilibrium analysis is normally performed in the frequency domain. Systematically reformulating frequency domain relations (*e.g.* constitutive, boundary conditions), and tackling the critical issues (*e.g.* quantifying upper and lower frequency bounds) are some of the issues to be addressed in the current research.

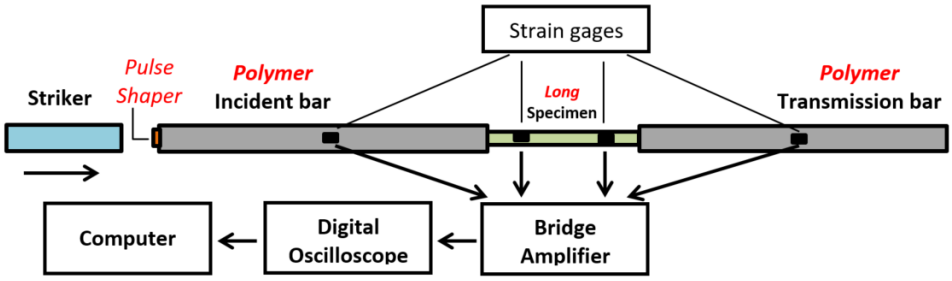


Figure. 1-3 A non-equilibrium SHPB test setup using polymeric bars (gages on specimen are not necessary)

1.3 Research roadmap

This thesis sequentially presents the 3-stage research, with Chapters 2 to 5 describing the single rod impact method, and 6 to 9 summarizing the interface method. Chapter 10 gives insights into wave propagation in a 3-rod system, and Chapter 11 summaries the current work and looks into future potential improvements.

Chapters 2, 3, 4, 5 feature research interpreting wave propagation in a single rod. Chapter 2 provides the theoretical basis, in which wave equations were built and time and frequency domain solutions

were found. Particularly, wave propagation in a single rod was characterized by the wave propagation coefficient γ, which consists of the damping coefficient α and wavenumber κ (Eq. (2.19)); the dispersion free relation (Eq. (2.27)) serves as the basis for recovering material properties from the propagation coefficient. As an application of the single rod theories, 3 mechanical models (Maxwell, Voigt, S.L.S Maxwell), together with the elastic one, were examined (Table. 2-2).

Experiments were then conducted in which the single rod theories were applied in processing the experimental data. Chapter 3 first illustrates the principles for single rod data analysis, including calculation of the propagation coefficient γ. Also illustrated in Chapter 3 are the single rod experimental design, the typical data processing procedure and some critical issues (*e.g.* pulse selection and frequency limits) encountered. The effects of geometric dispersion and correction methods have also been treated in detail. Results from single rod tests on 3 rods (Ti, Mg and PMMA) are presented in Chapter 4. As elastic material properties were known before experiments were carried out, I started by analysing the elastic case to validate the single rod analysis method—the results from Ti and Mg showed good agreements with theoretical calculations. The results from PMMA tested the effectiveness of the pendulum-based single rod impact technique in detecting the temperature-dependent viscoelastic behaviours: the proposed single rod impact method and the corresponding analysis methodology are powerful to capture the variations of mechanical material properties induced by temperature change as small as 2 $°C$. Furthermore, results from other reliable techniques, such as Laser Doppler Velocimetry (LDV) and DMA methods in Chapter 4, provided support evidence validating the single rod technique. In addition, by employing various simulations in Chapter 6, the validity of the analysis methodology was further confirmed. Typical issues addressed in the simulation section include: numerical fitting of experimental data to build the Prony model for viscoelastic behaviour with multiple relaxations, the strain gage effect and comparison with experimental result to check the linearity of strain gage measurements. Also presented is the noise study, in which different noise levels have been tested on the simulation models, either by numerical approach or by introducing misalignments in model setup, to evaluate the sensitivity of the single rod analysis methodology to errors, showing the method's robustness.

Chapters 6~10 give a full description of the interface impact technique. The theories and methodologies derived here are brand new (although some contents such as the boundary conditions are already known). The basic problem that the interface analysis answers is, given 2 rods in contact and the material properties of one rod, how can we figure out the properties of the other one? The theoretical basis is provided in Chapter 6, in which the problem has been treated in both time and frequency domains: in the time domain, emphasis was on validating the expressions of the derived transmission and reflection coefficients, and 4 model-dependent cases (*e.g.* Elastic-Elastic, Elastic-Maxwell, Elastic-Voigt, Elastic-S.L.S Maxwell) were analysed; frequency domain analysis has the capacity of using these coefficients to resolve for the unknown material properties of the target rod. Simulation verifications were introduced in Chapter 8. 4 cases of interfaces (*i.e.* Ti-Ti, Ti-Mg, Ti-PMMA and PMMA-Mg) were modelled: firstly, 'perfect' interfaces were modelled using single rods consisting of 2 media. Effective dispersion correction strategies, the complexity of numerical computing of the boundary condition equations (BCs), the effect of errors contained in travel distance, errors in timing, and noise were investigated. It is found that results derived from the interface analysis method can be vulnerably disturbed by noise, which may limit its application; the 'real' interfaces are modelled in Chapter 9, in which the same 4 cases were employed. The capacity of the 2 BC equations (representing force and velocity equilibrium respectively) to resolve for the unknown transmission rod properties was compared in the Ti-Ti case; error analysis showed that misalignments (central axis offset, rotation, and non-parallelism) can lead to errors, mainly due to the occurrence of a bending wave. This again supports the statement that this technique is quite susceptible to errors.

Interface experiments are presented in Chapter 9. Firstly, 'perfect' interfaces were assumed in single Ti and PMMMA rod tests: similar to the 2-media simulations, the data were analysed using both interface and single rod methods—they generated consistent results, which gives confidence in the interface analysis technique with ideal BC assumptions. The effect of pulse selection was discussed in the Ti case; errors contained in timing and travel distance were researched in the PMMA case. Analysis of the 4 'real' interface cases, *i.e.* Ti-Ti, PMMA-PMMA, Ti-PMMA, PMMA-Ti, again confirmed the high sensitivity of the interface analysis technique to disturbances.

Chapter 10 presents some preliminary work on wave propagation in a 3-rod system, which contains two genres of theories and five cases of experimental trials. The first set of theory assumes a long specimen to be used in a Hopkinson setup, while the second represents a more general type. They both yield wave propagation characteristics (transmission coefficient and reflection coefficient) as functions of material properties (modulus and impedance). Exploratory experiments performed coincide with the theoretical frame work but haven't been analysed, yet further research on wave propagation in multiple rod system is in need.

Chapter 2: Identifying viscoelastic material properties by measuring wave propagation in a single rod impact test: Theoretical Basis

The following four chapters present a complete description of the single rod impact technique, from which wave propagation characteristics, *i.e.* the propagation coefficient γ and wave speed c, can be obtained and used to identify complex modulus as a function of frequency. To accomplish this, firstly, a comprehensive analytical study of wave propagation in a slender rod was performed, this consists of both model-dependent and model-independent studies; then, experiments were performed in which elastic Titanium and Magnesium rods, and a viscoelastic Polymethyl Methacrylate (PMMA) rod were tested, and data analysed based on the theoretical principles. Subsequently, FE-simulations, constructed using experimental material properties to assemble analytical models representing Titanium and PMMA, were run to verify the analysis method and to avoid undesired experimental or analytical errors. These simulations also facilitate assessment of effects of dispersion, noise, pulse selection *etc*. Consistency is seen among analytical, experimental and simulation work, confirming the validity of the method. This is the most complete description of the single rod technique, and the first to explore, systematically and in detail, effects of experimental configuration and to validate the DMA and laser Vibrometer data.

2.1 Introduction

Frequency-dependent and temperature-dependent mechanical properties of polymers, in particular the complex modulus, wave speed and relaxation times, are of interest in many engineering applications. Polymer components often experience small-amplitude loading within the frequency range of 100 Hz to 10 kHz at room temperature, for which the wave propagation-based testing methods are well suited for the determination of complex modulus [27-32], Poisson's ratio [31, 33], and phase velocity [18, 29, 30, 33, 34]. Of the available techniques, impact tests on a single rod are probably the simplest approach to determine these mechanical properties within this frequency range. Experimental work (*e.g.* [16, 18, 34, 35]) on this topic has been performed over several decades, while simulation-based approaches have also emerged in recent years (*e.g.* [21]).

Single rod impact tests, in which a stress wave is induced into a rod and the mechanical response, is measured as a function of time and position, have been investigated over decades. Kolsky experimentally investigated stress wave propagation along three polymer rods: polystyrene, polythene and PMMA, and accurately predicted the propagating pulse shapes using experimentally-determined complex modulus and damping properties [16]. Lundberg and Blanc performed impact tests on a slender cylindrical Nylon 6 rod and derived the material mechanical properties by using a two-measurement-point method [30]. Bacon carried out impact tests on PMMA and aluminium alloy rods using a spring gun and measured the propagation coefficient [18]. Hillstrom *et al.* performed single bar impact tests on polymethyl methacrylate (PMMA) and polypropylene (PP) at room temperature, compared the results of 2 excitations, *i.e.* hammer impact by pendulum and bullet by air gun, and improved the quality of the existing complex modulus identification method by increasing the number of strain measurement sections and making use of non-uniform strain gauge distributions [32]. Benatar *et al.* used an air gun to fire PMMA projectiles to generate compressive stress waves in a commercial PMMA rod, and by measuring the surface strain in the middle of the rod, calculated the phase velocity and attenuation coefficient [33]. Mousavi *et al.* identified the complex moduli and Poisson's ratio of PMMA and PP by conducting axial and torsional impact tests on rods [31]. Ahonsi *et al*. reported an investigation on deriving the propagation coefficient of a polymer rod by impact simulations [21]. These works, either based on 1D, 3D (Love's theory [36], P-C equation [37, 38]) or simplified 3D theories [27, 29] of wave propagation, normally measure the strain, ε, displacement, u, or particle velocity, $\dot{u}$, as functions of time to calculate the frequency-dependent propagation coefficient $\gamma(\omega)$. By employing relations described further below (such as Eq. (2.29)), engineering quantities of interest, *i.e.* the complex modulus, $E^*(\omega)$, and the wave velocity, $c(\omega)$, can then be derived. Hence, all of the studies above conform to the same basic principle but vary in experimental design, using, for example, different specimen materials and lengths, gauge positions, measurement quantities, *etc*. Generally, most of the experiments were performed on rods with diameters 6.4 – 40 mm, and lengths from 0.7 to 2 m; strain gauges with small physical dimensions were commonly used to make the measurements. The key features of these studies are summarized in Table. 2-1.

Table 2-1 A review of some previous single rod impact tests

	Measured wave type	Excitation	Tested materials and rod geometry	Measured quantities	Measurement methods	Boundary conditions	temperatures	Valid frequency range achieved
Korsky (1956) [16]	longitudinal compressive	Explosive detonation	polystyrene (Ø12.50 × 500 *mm*), PMMA (Ø12.50 × 400 *mm*), Polythene (Ø12.50 × 200 *mm*)	Displacement	A condenser microphone mounted at the free end	Suspended by long threads, free non-impact end	15 °C	unknown
Lundberg and Blanc (1988) [30]	longitudinal compressive	A pendulum steel hammer (Ø10 × 21 *mm*), with a spherical impact end, drop heights vary from 7.5-50 mm	Nylon 6 (Ø10 × 600 *mm*, Ø10 × 1493 *mm*)	Strain & particle velocity	2 pairs of diametrically opposite strain gauges on middle surface to measure strain pulses; an inductive velocity transducer mounted at the non-impact end to measure the particle velocity pulses	Suspended horizontally, free non-impact end	20 – 22 °C	20 Hz-20 kHz
Bacon (1998) [17]	longitudinal compressive	Spherical steel/PMMA projectiles (Ø10) pushed by spring gun	PMMA (Ø16 × 1500 *mm*, Ø40 × 1850 *mm*), Aluminium (Ø16 × 1500 *mm*)	Strain	1 pair of strain gauges mounted on surface to measure strain pulses	Supported by ball bearings and axially movable, free non-impact end	Unknown	Up to 20 kHz
Hillstrom *et al* (2000) [32]	longitudinal compressive	Axially impacted by a pendulum steel hammer (Ø10 × 20 *mm*) with spherical impact end, a lead bullet (with length ~6 mm) fired by an air gun	Polypropylene (Ø16.60 × 2000 *mm*), PMMA (Ø16.00 × 2000 *mm*)	Strain	Diametrically opposite strain gauges at 3 or 5 positions on bar surface	Suspended horizontally with thin wires, free non-impact end	21.8 – 22.2 °C	Lower: 0.1-0.4 kHz Upper: 11/14 kHz
Benatar *et al* (2003) [33]	longitudinal compressive	Pendulum cylinders with the same diameter as the tested rod and 1 cm in length, fired by an air gun	PMMA (Ø12 × 700 *mm*, Ø6.4 × 700 *mm*),	Strain	Axial small resistance strain gauges bonded at distances of 10 cm, circumferential gauge at 35 cm from the impacted end	Horizontally supported by PTFE bushings, free non-impact end	Unknown	Up to 65 kHz for the Ø6.4 mm PMMA rod; up to 55 kHz for Ø12 mm
Mousavi *et al* (2004) [31]	longitudinal compressive (Shear tests not summarized)	Lead bullets with mass 0.54 g fired by an air gun; cylinders with the same diameter as the tested rod, 8 and 10 cm in length, fired by an air gun	Polypropylene (Ø10 × 1000 *mm*, Ø20 × 2000 *mm*), PMMA (Ø10 × 1000 *mm*, Ø20 × 2000 *mm*)	Strain	Diametrically opposite strain gauge pairs mounted in axial and circumferential directions at 5 non-uniformly distributed sections	Suspended horizontally by thin wires, free non-impact end	Room temperature	1-40 kHz for Ø10 mm PMMA, 1-15 kHz for Ø10 mm PMMA; 1-15 kHz for Ø10 mm and Ø20 mm PP
Ahonsi *et al* (2012) [21]	longitudinal compressive	Steel bearing ball (Ø6 *mm*); PMMA bar (Ø20 × 350 *mm*)	PMMA bars (Ø20 × 1000 *mm*, Ø20 × 2000 *mm*)	Strain	Strain values extracted either at the mid-length of the bar, or at 3 equidistant gauge stations	free non-impact end	Unknown	Up to 70 kHz for phase velocity evaluation, and up to 40 kHz for attenuation coefficient; up to 10-15 kHz with noise

Based on these previous efforts, in the current project a portable pendulum setup that can hold a rod geometry of about 1.0 m long by 12.7 mm diameter, was designed for experimental trials, and its ability to effectively determine the mechanical properties of PMMA in the frequency range of 2000 – 30,000 Hz was addressed.

2.2 Theoretical background

A number of theories have been developed to describe wave propagation in 1D/3D elastic/viscoelastic solids. Of these, the Pochhammer-Chree (P-C) [37, 38] equation gives an exact solution to the relevant wave equations for stress waves propagating in a circular rod of infinite length and finite diameter; however, it cannot be solved directly. A number of simplifications of the P-C equation are available for rods with various cross-sections and for different frequency ranges. For example, Love's theory takes into account the lateral deformation during wave propagation in solids, although its accuracy is limited to low frequency waves [36]. Zhao and Gary generalized a 3D solution for longitudinal wave propagation in any infinite linear viscoelastic cylindrical bar [29], whilst Benatar *et al.* simplified the Pochhammer frequency equation for low and intermediate loss viscoelastic materials [33]. A good approximation to the P-C equation is the four-mode theory [27] which involves higher deformation modes and can be solved directly. The difference between these wave propagation theories lies in whether they use a 1D or 3D analysis, and how the cross-sectional deformation is treated if it is a 3D analysis. In a 1D analysis, only axial movement (*i.e.* 1 DOF) is present and it further assumes that the deformed and undeformed planes remain parallel to each other [27]. The 1D deformation assumptions can be satisfied in a 'slender' bar, with a small diameter (*e.g.* 10 times [16]) compared to the wavelength of the wave components propagating in it.

3D solutions of course capture more accurately the true wave behaviour as they employ various displacement fields to describe different deformation modes through the cross-section. In the following theoretical analysis, some basic equations used in the 1D and Love's 3D analysis are explored, these will then be applied in later experimental and simulation data analysis.

There are two problems to be solved when dealing with wave propagation analysis: firstly, to establish a governing wave equation which represents the 1D/3D wave motions in the

elastic/viscoelastic solid; secondly, to employ reasonable 1D/3D displacement or strain fields to solve this wave equation. The difference between 1D and 3D analyses is incorporated in both the wave equation and the corresponding solutions. Both of them may contain some material property information such as the density, ρ, Poisson's ratio, v, and Lamé's constants, μ and λ; some bar geometry information such as the bar radius, a, or the radius of gyration, R; as well as some wave propagation characteristics such as the frequency-dependent propagation coefficient, γ. An integrated equation containing all the above information can be obtained by substituting the assumed solution into the designed wave equation; the wave propagation coefficient, as a function of the frequency-dependent material properties (*e.g.* the complex dynamic modulus E^*) can either be numerically or analytically resolved depending on the complexity of the resulting equation. How to incorporate the 3D effects into the analysis remains the key point in various 3D theories; this description starts with the relatively simple 1D derivation and then moves to Love's 3D theory.

2.3 Constitutive model-independent analysis

2.3.1 Wave equation for elastic and viscoelastic materials

A detailed description of wave propagation in an isotropic elastic medium can be found in various well-written literature sources concerning the theory of elasticity, *e.g.* Kolsky's [39], Love's [36] and Timoshenko's [40] books. The equations governing small amplitude motion of a segment in a 3D body can be deduced from the equations of equilibrium

$$(\lambda+\mu)\left(\frac{\partial\Delta}{\partial x},\frac{\partial\Delta}{\partial y},\frac{\partial\Delta}{\partial z}\right)+\mu\nabla^2(u,v,w)=\rho\left(\frac{\partial^2u}{\partial t^2},\frac{\partial^2v}{\partial t^2},\frac{\partial^2w}{\partial t^2}\right) \tag{2.1}$$

where $\Delta=\frac{\partial u}{\partial x}+\frac{\partial v}{\partial y}+\frac{\partial w}{\partial z}$ is the volume expansion, the vector (u,v,w) represents the three components of displacement in the x, y and z directions, and ∇^2 represents the operation

$$\nabla^2=\frac{\partial^2}{\partial x^2}+\frac{\partial^2}{\partial y^2}+\frac{\partial^2}{\partial z^2} \quad . \tag{2.2}$$

Eq. (2.1) represents the general wave equation of both dilatation (longitudinal) and distortion (transverse) waves propagating in an isotropic elastic medium, it holds regardless of the stress-strain relations. Note that in deriving Eq. (2.1) body forces (*e.g.* gravity) are absent.

By assuming that either the volume expansion, Δ, is zero, or that no rotation accompanies the

deformation, a wave propagating in a solid can be classified as distortional/equivoluminal or irrotational/dilatational; each assumption simplifies the governing wave equation (2.1). In a 3D solid, waves propagating at a long distance from the point of disturbance can be considered as plane waves, and can be further sorted as longitudinal waves, with particle motion parallel to the direction of wave propagation, and transverse waves, with particle motion perpendicular to this direction (parallel to the wave front). Longitudinal waves, such as compression and tension waves, belong to the group of dilatational waves while transverse waves, such as shear waves, are distortional waves. As the waves examined in the current research are all longitudinal waves, only these were discussed in the following analysis.

The wave equation of dilatation waves can be simplified as

$$(\lambda + 2\mu)\nabla^2(u, v, w) = \rho\left(\frac{\partial^2 u}{\partial t^2}, \frac{\partial^2 v}{\partial t^2}, \frac{\partial^2 w}{\partial t^2}\right) \tag{2.3}$$

when it comes to longitudinal waves, Eq. (2.3) can be further simplified, as $v = w = 0$,

$$(\lambda + 2\mu)\frac{\partial^2 u}{\partial x^2} = \rho\frac{\partial^2 u}{\partial t^2} \tag{2.4}$$

from which the phase speed $c_{dilatation}$ can be deduced

$$c_{dilatation} = \sqrt{\frac{\lambda+2\mu}{\rho}} = \sqrt{\frac{E(1-\upsilon)}{(1+\upsilon)(1-2\upsilon)\rho}} \quad . \tag{2.5}$$

In an isotropic solid, the following relations stand

$$\lambda = \frac{E\upsilon}{(1+\upsilon)(1-2\upsilon)}, \mu = \frac{E}{2(1+\upsilon)} \quad . \tag{2.6}$$

It can thus be seen that the 3D effect, revealed by the Poisson's ratio, affects the propagation speed. it is noted that if the material exhibits no sideways expansion ($v = 0$), the wave speed reduces to the following equation, which is the same as the wavespeed in a geometry which allows 1D stress wave propagation (*i.e.* slender rod, as derived below)

$$c_L = \sqrt{\frac{E}{\rho}} \quad . \tag{2.7}$$

Now we will look at the 1D elastic case, firstly without considering the Poisson effect, *i.e.* in a rod with infinitesimal diameter, or a rod made from a material with $v = 0$. The 1D wave equation can be derived either by making use of Eq. (2.4), or simply by use of Newton's Second law to obtain

$$\frac{\partial \sigma}{\partial x} = \rho \frac{\partial^2 u}{\partial t^2}. \tag{2.8}$$

This equation involves only the inertia force and represents the equilibrium equation in a small segment of the bar; it is valid for both elastic and viscoelastic materials.

In discussing the propagation of waves in an elastic medium, it is of advantage to use differential equations in terms of displacements [40], the solutions of which are harmonic motions at different frequencies from which any arbitrary waveform can be constructed as a Fourier series. It is thus necessary to express Eq. (2.8) in terms of displacement by using an appropriate constitutive law and the compatibility/continuity equation.

The compatibility equation applied to any material is

$$\varepsilon = \frac{\partial u}{\partial x} \ \ or \ \frac{\partial v}{\partial x} = \frac{\partial \varepsilon}{\partial t} \tag{2.9}$$

whilst, for the elastic case, we have the constitutive relation

$$\sigma = E\varepsilon. \tag{2.10}$$

Combining Eq. (2.8), (2.9) and (2.10) gives

$$\rho \frac{\partial^2 u}{\partial t^2} = E \frac{\partial^2 u}{\partial x^2} \tag{2.11}$$

or in a more common form

$$\frac{\partial^2 u}{\partial t^2} = c_L^2 \frac{\partial^2 u}{\partial x^2}. \tag{2.12}$$

This ((2.11) or (2.12)) is called the 1D wave equation for elastic materials. It is a hyperbolic partial differential equation that concerns the time and spatial variation of the displacement. From the derivation process it is thus seen that, Eq. (2.12) is actually an approximation to the general wave equation assuming each slice of the rod is in simple tension/compression corresponding to the axial strain $\frac{\partial u}{\partial x}$ (Eq. (2.9)), and all other stress and strain components are negligible [40]. Both Eq. (1.7) and Eq. (1.11) can be extended to viscoelastic cases by introducing frequency-dependent modulus.

The wave equation (Eq. (2.11)) is a linear differential equation and thus adheres to the superposition principle: the displacement caused by multiple waves is the sum of the displacements that would have been caused by each wave individually. Therefore, the behaviour of a complex wave can be

analysed breaking it into components using techniques such as the Fourier transform. This is also in line with our previous analysis: for each single frequency wave component, the dynamic modulus and wave speed are fixed, the material thus behaves like an elastic one. However, when viscoelastic constitutive (*i.e.* stress-strain) relations, other than the elastic relation Eq. (2.10), are introduced, wave equations are of higher order, and different viscoelastic mechanical models can lead to different degrees of complexity, this will later be discussed in the model-dependent section. In the following process for deriving the solution, the 1D solution comes in a uniform form that can be applied to both elastic and viscoelastic materials, in the viscoelastic case this can be achieved simply by replacing E with the complex modulus $E^* = E' + iE''$, where E' is known as the storage modulus, and E'' as the loss modulus.

In reality, not even the slenderest rod is truly one dimensional. When 3D effects are to be considered, the wave equation can be revised. For example, in order to consider the 3D effects induced by radial inertia, Aleyaasin *et al.* [34] modified the governing equation by adding an extra inertia term, broadly corresponding to the radial acceleration of the particles in the rod owing to Poisson's effect as the wave propagates. However, there are various ways to approximate the Poisson effect depending on the cross-sectional modes of oscillation [27]. Most of the theories below are based on the assumption of 1D longitudinal wave propagation, with corrections for radial inertia where required. The further assumption that the wavefront is planar is also made; whilst in the experiments waves were generated by ball impacts, at a suitable distance, verified by simulation as *e.g.* 50 mm for metal rod and 100 mm for PMMA rod, they become uniform over the cross-section and can be considered plane/longitudinal waves according to Saint-Venant's principle as well as Timoshenko [40].

2.3.2 Time domain solution to the 1D wave equation

The wave equation for 1D longitudinal wave propagation in isotropic elastic solids has now been derived. The second challenge, as suggested before, is to find an appropriate displacement solution to Eq. (2.12). As can be seen from Eq. (2.12), the solution of the 1D wave equation of an isotropic elastic media describes the disturbances propagating at a fixed speed c_L.

The general solution to Eq. (12) can be represented in the form [39, 40]

$$u(x,t) = f(x+ct) + g(x-ct). \tag{2.13}$$

This general solution represents two waves traveling along the *x* axis (the longitudinal axis of the rod) in two opposite directions with the constant velocity $c = c_{1D-dilatation}$. An explicit specific form, assuming a frequency-dependent harmonic motion of each particle in the solid, has been widely used [16, 40]

$$u(x,t) = Ae^{i(\omega t \pm f_1 x)} = Ae^{\pm \alpha x} e^{i(\omega t \pm \kappa x)} \tag{2.14}$$

in which

$$f_1 = \kappa - i\alpha \quad (\alpha \geq 0) \tag{2.15}$$

$$|\kappa(\omega)| = \frac{2\pi}{\lambda(\omega)} = \frac{\omega}{c(\omega)}. \tag{2.16}$$

As a function of both time and location, $u(x,t)$ represents a propagating wave. The time-dependent character is described by the angular velocity, ω, while the space character by the spatial velocity, κ. For viscoelastic materials, the damping characteristic depends on propagation distance and thus is included in the term $e^{\pm \alpha x}$.

Some general points can be made about this equation. Firstly, it should be noted that Eq. (2.14) is a general solution for 1D wave propagation in both elastic and viscoelastic solids. In this solution, $\alpha(\omega)$ (unit: m^{-1}) is an attenuation/damping coefficient, which accounts for the frequency-dependent wave amplitude attenuation owing to viscoelastic behaviour of the material. It is a positive even function [30, 32], and is zero for perfectly elastic materials. $\kappa(\omega)$ (unit: rad m^{-1}) is the angular wavenumber, also called the spatial frequency of a wave; it is an odd function, positive for $\omega > 0$ [32, 41]. In addition, Lundberg *et al*. [30, 32] pointed out that $\kappa(\omega)$ should be continuous and monotonically increasing, which leads to $\kappa(\omega = 0) = 0$. $c(\omega)$ (unit: m s^{-1}) is the phase velocity of the propagating wave, it is a positive even function [30], bounded and monotonically increasing for $\omega > 0$. Finally, $\lambda(\omega)$ is the wavelength of the frequency component ω. It is continuous and monotonically decreasing for $\omega > 0$; and $\lambda(\omega) \to \infty$ when $\omega \to 0$ [32].

It should be noted that more complex wave profiles, in which the particles do not exhibit simple harmonic motion, are multi-frequency combinations of the above equation, represented most simply by a Fourier series. The solution, therefore, lends itself to analysis in the frequency domain.

2.3.3 Frequency domain solution to the 1D wave equation

Frequency analysis is an appropriate signal processing methodology when looking at frequency-dependent wave behaviours. In this case, we will now introduce another strain-based general solution to the wave equation (2.12) in frequency domain.

Firstly, Eq. (2.14) is revised by considering the difference in the amplitudes of the waves propagating in positive and negative x directions

$$u(x,t) = A\mathrm{e}^{i(\omega t - f_1 x)} + B\mathrm{e}^{i(\omega t + f_1 x)} \tag{2.17}$$

differentiating Eq. (2.17) with regard to x gives the time domain strain

$$\varepsilon(x,t) = \frac{\partial u(x,t)}{\partial x} = -if_1 A e^{i(\omega t - f_1 x)} + if_1 B\mathrm{e}^{\mathrm{i}(\omega \mathrm{t} + \mathrm{f}_1 \mathrm{x})} \tag{2.18a}$$

performing a Fourier Transform on Eq. (2.18a) leads to a general frequency domain solution

$$\tilde{\varepsilon}(x,\omega) = \tilde{P}(\omega)e^{-if_1 x} + \tilde{N}(\omega)e^{if_1 x}. \tag{2.18b}$$

Here, the functions $\tilde{P}(\omega)$ and $\tilde{N}(\omega)$ define the Fourier transforms of the strains at $x = 0$ due to the waves traveling in the directions of increasing and decreasing x, respectively, these functions depend on boundary conditions [42], and the so-called propagation coefficient $\gamma(\omega)$ is defined

$$\gamma(\omega) = if_1 = i(\kappa - i\alpha) = \alpha(\omega) + i\kappa(\omega) \tag{2.19}$$

then the general expression of strain in the frequency domain can be written as [18, 21, 30, 42]

$$\tilde{\varepsilon}(x,\omega) = \tilde{P}(\omega)e^{-\gamma x} + \tilde{N}(\omega)e^{\gamma x}. \tag{2.20a}$$

The corresponding frequency domain expressions of displacement, particle velocity, force, acceleration can be deduced based on the strain. Some of these results are given in the literature (*e.g.* [18]); here a simplified derivation process is presented due to space limit, for more details please refer to the *web version* of this thesis.

In the time domain, we have

$$\varepsilon(x,t) = \frac{\partial u(x,t)}{\partial x}$$

which gives

$$u(x,t) = \int \varepsilon(x,t)dx$$

applying Fourier Transform yields

$$\tilde{u}(x,\omega) = -\frac{1}{\gamma}[\tilde{P}(\omega)e^{-\gamma x} - \tilde{N}(\omega)e^{\gamma x}]. \tag{2.20b}$$

Similarly, we have

$$\tilde{\ddot{u}}(x,\omega) = i\omega\tilde{u}(x,\omega) = i\omega\int\tilde{\varepsilon}dx = -\frac{i\omega}{\gamma}[\tilde{P}(\omega)e^{-\gamma x} - \tilde{N}(\omega)e^{\gamma x}] \tag{2.20c}$$

$$\tilde{a}(x,\omega) = -\omega^2\tilde{u}(x,\omega) = -\omega^2\int\tilde{\varepsilon}dx = \frac{\omega^2}{\gamma}[\tilde{P}(\omega)e^{-\gamma x} - \tilde{N}(\omega)e^{\gamma x}] \tag{2.20d}$$

$$\tilde{\sigma}(x,\omega) = \frac{\tilde{F}}{A} = -\frac{\rho\omega^2}{\gamma^2}[\tilde{P}(\omega)e^{-\gamma x} + \tilde{N}(\omega)e^{\gamma x}] \tag{2.20e}$$

$$\tilde{F}(x,\omega) = \rho A i\omega\int\tilde{u}(x,\omega)dx = -\frac{\rho A\omega^2}{\gamma^2}[\tilde{P}(\omega)e^{-\gamma x} + \tilde{N}(\omega)e^{\gamma x}] \tag{2.20f}$$

Note that in deriving above formulas, the following Fourier Transform property has been used: $FT\left(\frac{d^n x(t)}{dt^n}\right) = (i2\pi f)^n X(f)$.

2.3.4 Relating the propagation coefficient $\gamma(\omega)$ to complex modulus $E^*(\omega)$

In practice, the engineering property of interest is often the material modulus, it is thus of use to express the complex modulus $E^*(\omega)$ or compliance $J^*(\omega)$ as functions of the propagation coefficient $\gamma(\omega)$, and eventually as functions of material constants such as the density and the model constants (if a mechanical model is to be used), as well as the applied frequency. The results can be found elsewhere, *e.g.* Lundberg [30], but the detailed derivation process is presented here. To start with, the complex modulus can be written as

$$E^*(\omega) = E'(\omega) + iE''(\omega), tan\delta = \frac{E''(\omega)}{E'(\omega)} \tag{2.21}$$

in which the real part $E'(\omega)$ is termed the 'storage modulus' while the imaginary part $E''(\omega)$ is the 'loss modulus'. $E'(\omega)$ is a positive even function and $E''(\omega)$ is an odd function, positive for $\omega > 0$ [41]. The storage modulus $E'(\omega)$ is the elastic component and related to a material's stiffness. The loss modulus $E''(\omega)$ is the viscous part and related to a material's ability to dissipate energy through molecular motion. The ratio $tan\delta$ is termed the loss factor [43], which quantifies the phase difference between the elastic and viscous parts.

As the equilibrium equation Eq. (2.8) and the compatibility/continuity equation Eq. (2.9) also hold for linear viscoelastic materials if the complex modulus is used, combining both gives

$$\frac{\partial^2\sigma(x,t)}{\partial x^2} = \rho\frac{\partial^2\varepsilon(x,t)}{\partial t^2} \tag{2.22}$$

applying Fourier transform to the above wave equation yields

$$\frac{\partial^2}{\partial x^2}\tilde{\sigma}(x,\omega) = -\rho\omega^2\tilde{\varepsilon}(x,\omega). \tag{2.23}$$

For linear viscoelastic materials we have

$$\tilde{\sigma}(x,\omega) = E^*(\omega)\tilde{\varepsilon}(x,\omega) \tag{2.24}$$

combination of Eq. (2.23) and Eq. (2.24) gives

$$E^*(\omega)\frac{\partial^2}{\partial x^2}\tilde{\varepsilon}(x,\omega) = -\rho\omega^2\tilde{\varepsilon}(x,\omega) \tag{2.25}$$

or in a more regular form

$$\frac{\partial^2}{\partial x^2}\tilde{\varepsilon}(x,\omega) - \frac{-\rho\omega^2}{E^*(\omega)}\tilde{\varepsilon}(x,\omega) = 0. \tag{2.26}$$

Substituting the frequency domain strain solution Eq. (2.20a) into the above equation gives

$$\gamma^2(\omega) = \frac{-\rho\omega^2}{E^*(\omega)} \tag{2.27}$$

substituting Eq. (2.19) and Eq. (2.21) into Eq. (2.27) gives

$$\begin{aligned} \kappa^2 - \alpha^2 &= \frac{\rho\omega^2 E'(\omega)}{E'^2(\omega) + E''^2(\omega)} \\ 2\kappa\alpha &= \frac{\rho\omega^2 E''(\omega)}{E'^2(\omega) + E''^2(\omega)} \end{aligned} \tag{2.28}$$

from which the complex modulus $E^*(\omega)$ can be expressed as a function of κ and α

$$E'(\omega) = \frac{\rho\omega^2(\kappa^2-\alpha^2)}{(\kappa^2+\alpha^2)^2}, \quad E''(\omega) = \frac{\rho\omega^2(2\kappa\alpha)}{(\kappa^2+\alpha^2)^2}, \quad tan\delta = \frac{2}{\frac{\kappa}{\alpha}-\frac{\alpha}{\kappa}} \tag{2.29a}$$

or inversely, the propagation coefficient as functions of the modulus

$$\alpha^2 = \frac{\rho\omega^2}{2}\times\frac{\sqrt{E'^2+E''^2}-E'}{E'^2+E''^2}, \quad \kappa^2 = \frac{\rho\omega^2}{2}\times\frac{\sqrt{E'^2+E''^2}+E'}{E'^2+E''^2}, \; c = \frac{\omega}{\kappa} \tag{2.29b}$$

In fact, as the propagation coefficients (κ, α), the complex modulus E^* and the compliance J^* are all functions of material constants (ρ, k, τ), they are in essence correlated to each other.

Note that the above propagation coefficient-modulus/compliance relation (Eq. (2.29)) can also be derived in time domain. This was shown when discussing the dispersion effects later.

2.4 Model-dependent analysis

Mechanical analogue based study provides an intuitive approach to describing material behaviours, which has been proven to be very successful in treating a large number of material modelling problems [44]. Mechanical models, consisting of components such as springs and dashpots, and varying in numbers and arrangement, are employed to approximate the response of solids and fluids to applied loading. They are mechanically valid but in fact fictitious, as they do not represent the real microstructures. Those used to describe elastic, plastic, hyperelastic or viscoplastic response are out of the scope of the current research, but some basic, and highly relevant, mechanical linear viscoelastic (LVE) models were discussed here.

Hookean springs which represent elasticity, and Newtonian dashpots that account for viscosity are commonly assembled in different formats to constitute various linear viscoelastic mechanical models. The elastic springs give an instantaneous response upon loading according to Hooke's law $\sigma = k\varepsilon$, while the viscous dashpots follow a strain rate dependent stress-strain relation $\sigma = \eta\dot{\varepsilon}$ (the Newton equation). Different combinations of these two functional components, with different model constants, number, or arrangements, result in mechanical models that give different rate dependent viscoelastic responses. Among these combinations, the most basic two, which form the basis of other models, are the Maxwell and Voigt models. They were introduced first before moving on to the widely used Maxwell Standard Linear Solid (S.L.S Maxwell) model.

2.4.1 Maxwell Model

The Maxwell component is commonly used to describe relaxation behaviours. It consists of a dashpot (with viscosity η) and a spring (with elastic modulus k) acting in series (Fig. 2-1).

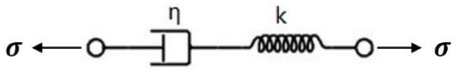


Figure 2-1. Maxwell model

The constitutive equation of a Maxwell material can be derived from the stress and strain relations

$$\begin{aligned} \sigma &= \sigma_s = \sigma_d \\ \varepsilon &= \varepsilon_s + \varepsilon_d \end{aligned} \tag{2.30}$$

in which σ, ε are the total stress and strain, the subscripts s and d denote spring and dashpot respectively. Solving Eq. (2.30) yields the constitutive equation for Maxwell materials:

$$k\dot{\varepsilon} = \dot{\sigma} + \frac{1}{\tau}\sigma \tag{2.31}$$

where η is the dashpot viscosity and $\tau = \frac{\eta}{k}$ is a characteristic time given by the ratio of the viscosity of the dashpot to the elasticity of the spring; for the Maxwell model this is termed the relaxation time, and later for the Voigt model the retardation time [16]. Note that the Maxwell model reduces to a purely elastic model if the dashpot becomes a rigid body, *i.e.* $\tau = \frac{\eta}{k} = \infty$.

A combination of the equilibrium equation (2.8), the compatibility equation (2.9), and the extra constitutive equation (2.31) gives the wave equation in terms of displacement

$$\rho\frac{\partial^3 u}{\partial t^3} - k\frac{\partial^3 u}{\partial x^2 \partial t} + \frac{\rho}{\tau}\frac{\partial^2 u}{\partial t^2} = 0. \tag{2.32a}$$

Again, solving the above wave equation by making use of the harmonic displacement solution Eq. (2.14) gives the propagation coefficient for a Maxwell material [39]

$$\begin{aligned} \kappa^2 &= \frac{\rho\omega^2}{2k}\left[\left(1 + \frac{1}{\omega^2\tau^2}\right)^{\frac{1}{2}} + 1\right] \\ \alpha^2 &= \frac{\rho\omega^2}{2k}\left[\left(1 + \frac{1}{\omega^2\tau^2}\right)^{\frac{1}{2}} - 1\right] \end{aligned} \tag{2.33}$$

the expressions of κ and α can be also obtained in frequency domain. Rewrite Eq. (2.32) in terms of strain

$$\rho\frac{\partial^2 \varepsilon}{\partial t^2} - k\frac{\partial^2 \varepsilon}{\partial x^2} + \frac{\rho}{\tau}\frac{\partial \varepsilon}{\partial \mathrm{t}} = 0. \tag{2.32b}$$

Fourier transform of the above strain-based wave equation yields

$$-\omega^2\rho\tilde{\varepsilon} - k\frac{\partial^2 \tilde{\varepsilon}}{\partial x^2} + i\omega\frac{\rho}{\tau}\tilde{\varepsilon} = 0.$$

Substituting the frequency domain strain general solution $\tilde{\varepsilon}(x,\omega) = \tilde{P}(\omega)e^{-\gamma x} + \tilde{N}(\omega)e^{\gamma x}$ (Eq. (2.20a)) into the above equation will give the same results as Eq. (2.33). This in turn verifies that the time domain displacement general solution $u(x,t) = Ae^{i\omega t}e^{\pm\gamma x}$ and the frequency domain strain general solution share the same propagation coefficient γ, as can be intuitively seen in Eq. (2.20a) and Eq. (2.20b).

It can be seen from Eq. (2.33) that both the wavenumber, κ, and attenuation coefficient, α, are determined by material property constants ρ, k and η (thus τ), as well as by input frequency, ω. They are both material property-dependent and frequency-dependent.

We now have derived the relation between model-specific parameters (k, τ) and wave propagation characteristics (α, κ) in Eq. (2.33), it could be submitted into the relation between wave propagation and modulus (Eq. (2.29a)) to yield a relation between the model parameters and modulus directly. However, repeated mathematics work is boring, here we adopted another approach. By substituting any arbitrary input, either $\varepsilon = \varepsilon_0 \cos\omega t$, $\varepsilon = \varepsilon_0 \sin\omega t$, or $\varepsilon = \varepsilon_0 e^{i\omega t}$, into the constitutive equation, Eq. (2.31), a resulting stress can be derived, and from the steady response a complex modulus can be identified. For example, if a sinusoidal excitation $\varepsilon = \varepsilon_0 e^{i\omega t}$ was input into the Maxwell system, substituting $\varepsilon(t) = \varepsilon_0 e^{i\omega t}$ yields the stress response

$$\sigma(t) = Ce^{-\frac{t}{\tau}} + \left(\frac{k\omega^2\tau^2}{1+\omega^2\tau^2} + i\frac{k\omega\tau}{1+\omega^2\tau^2}\right)\varepsilon_0 e^{i\omega t}.$$

Note that a constant C appears after integration, it can be determined by using the boundary condition $\sigma(t=0) = k\varepsilon(t=0) = k\varepsilon_0$, which gives

$$C = \frac{1-i\omega\tau}{1+\omega^2\tau^2} k\varepsilon_0$$

thus the stress corresponding to the input strain $\varepsilon = \varepsilon_0 e^{i\omega t}$ can be written as

$$\sigma(t) = \frac{1-i\omega\tau}{1+\omega^2\tau^2} k\varepsilon_0 e^{-\frac{t}{\tau}} + \left(\frac{k\omega^2\tau^2}{1+\omega^2\tau^2} + i\frac{k\omega\tau}{1+\omega^2\tau^2}\right)\varepsilon_0 e^{i\omega t}$$

as the first term $\frac{1-i\omega\tau}{1+\omega^2\tau^2} k\varepsilon_0 e^{-\frac{t}{\tau}}$ decays with time, the steady-state stress response is

$$\sigma(t) = \left(\frac{k\omega^2\tau^2}{1+\omega^2\tau^2} + i\frac{k\omega\tau}{1+\omega^2\tau^2}\right)\varepsilon_0 e^{i\omega t}$$

from which the dynamic modulus E^* can be derived

$$E^* = \frac{\sigma(t)}{\varepsilon(t)} = \frac{k\omega^2\tau^2}{1+\omega^2\tau^2} + i\frac{k\omega\tau}{1+\omega^2\tau^2}$$

in which

$$\begin{aligned} E' &= \frac{k\omega^2\tau^2}{1+\omega^2\tau^2} \\ E'' &= \frac{k\omega\tau}{1+\omega^2\tau^2} \end{aligned} \tag{2.34}$$

similarly, employing any stress input allows us to find the complex compliance

$$J^* = J' + iJ'' = \frac{1}{k} - i\frac{1}{\omega\tau k}. \tag{2.35}$$

Physically, the modulus of a material depends on the mechanical model that represents this material, thus the modulus can be alternatively obtained using the constitutive equation. For example, Fourier transform of Eq. (2.31) yields

$$k \times i\omega\tilde{\varepsilon}(\omega) = i\omega\tilde{\sigma}(\omega) + \frac{1}{\tau}\tilde{\sigma}(\omega)$$

which gives

$$\frac{\tilde{\sigma}(\omega)}{\tilde{\varepsilon}(\omega)} = \frac{i\omega k}{\frac{1}{\tau}+i\omega} = \frac{k\omega^2\tau^2}{1+\omega^2\tau^2} + i\frac{k\omega\tau}{1+\omega^2\tau^2}$$

which is the same as Eq. (2.34).

The Maxwell model works reasonable well as a representation of stress relaxation because it describes a real exponential stress decay. But it is inadequate for describing creep: the creep strain it predicts increases linearly with time while for real viscoelastic polymers show time-dependent decreasing creep strain rate.

2.4.2 Voigt Model

The Voigt component is more suitable for characterizing creep behaviour. It consists of a dashpot (with viscosity η) and a spring (with elastic modulus k) acting in parallel (Fig. 2-2).

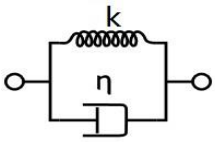


Figure 2-2. Voigt model

The constitutive equation of the Voigt model is

$$\sigma = k\varepsilon + \eta\frac{d\varepsilon}{dt}. \tag{2.36}$$

The Voigt model reduces to a purely elastic model if the dashpot becomes an infinite soft body, *i.e.* the retardation time $\tau = \frac{\eta}{k} = 0$. Similar to the Maxwell model, the wave equation for a wave propagating in a Voigt material can be derived by making use of the equilibrium equation Eq. (2.8), the compatibility equation (2.9), and the above constitutive equation Eq. (2.36)

$$\frac{\partial^2 u}{\partial t^2} - \frac{\eta}{\rho}\frac{\partial^3 u}{\partial x^2 \partial t} - \frac{k}{\rho}\frac{\partial^2 u}{\partial x^2} = 0. \tag{2.37}$$

Substituting the harmonic displacement solution Eq. (2.14) into the above equation gives the propagation coefficients for a material represented by this model

$$\begin{cases} \kappa^2 = \dfrac{\rho\omega^2}{2k(1+\omega^2\tau^2)}\left[(1+\omega^2\tau^2)^{\frac{1}{2}}+1\right] \\ \alpha^2 = \dfrac{\rho\omega^2}{2k(1+\omega^2\tau^2)}\left[(1+\omega^2\tau^2)^{\frac{1}{2}}-1\right] \end{cases} \tag{2.38}$$

Here, $\tau = \frac{\eta}{k}$ is termed the retardation time, and is a characteristic time constant of the Voigt model. Again, we can see the propagation coefficients κ and α are both material property-dependent and frequency-dependent.

The complex modulus $E^*(\omega)$ and compliance $J^*(\omega)$ of Voigt materials can be written as

$$\begin{aligned} E^*(\omega) &= E' + iE'' = k + i\eta\omega \\ J^*(\omega) &= J' + iJ'' = \frac{k}{k^2+\eta^2\omega^2} - i\frac{\eta\omega}{k^2+\eta^2\omega^2}. \end{aligned} \tag{2.39}$$

The Voigt model is a better representation than the Maxwell model for characterizing viscoelastic creep behaviour, because a time-dependent decreasing strain rate is described. However, it is unsuccessful in describing stress relaxation as, after the initial transient, constant stress was calculated from a constant strain excitation.

It has thus been shown that both of these simple models are insufficient for fully characterizing viscoelastic materials: even over a very limited frequency range it is impossible to fit the observed behaviour of a polymer to the dispersion curves obtained from such two element models. A simple three element model, *i.e.* the standard linear solid model as introduced below, can give a better approximation to the behaviour of a real viscoelastic solid [16].

2.4.3 S.L.S Maxwell model

2.4.3.1 Generalized models

A viscoelastic rheological model usually comes in the form of either the generalized Maxwell model or the generalized Voigt chain, as shown in Fig. 2-3 [45]. The generalized Maxwell model consists of an isolated Hookean spring, an isolated Newtonian dashpot, and multiple sub-Maxwell components in parallel. The absence of the isolated spring results in a fluid-type behaviour while the absence of the isolated dashpot ensures an instantaneous response [45]. The generalized Voigt chain

is constructed by a chain of Voigt components acting in series; the isolated spring may be omitted if a fluid-type response is expected [45]. These two forms are in essence equivalent [46], and can yield the same material response if some mutual model constants adjusted.

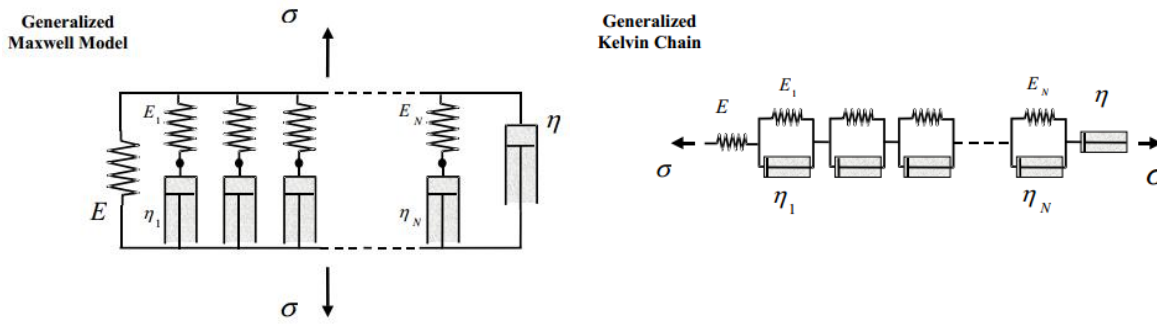


Figure 2-3. Generalized viscoelastic models [45]

In general, a linear viscoelastic constitutive equation can be used to describe the above two systems [45]:

$$p_0\sigma + p_1\dot{\sigma} + p_2\ddot{\sigma} + p_3\dddot{\sigma} + \cdots = q_0\varepsilon + q_1\dot{\varepsilon} + q_2\ddot{\varepsilon} + q_3\dddot{\varepsilon} + \cdots \tag{2.40}$$

or in a more general form

$$\boldsymbol{P}\sigma = \boldsymbol{Q}\varepsilon \tag{2.41}$$

where $\boldsymbol{P}$ and $\boldsymbol{Q}$ are the linear differential operators

$$\boldsymbol{P} = \sum_{i=0}^{n} p_i \frac{\partial^i}{\partial t^i}, \qquad \boldsymbol{Q} = \sum_{i=0}^{n} q_i \frac{\partial^i}{\partial t^i}. \tag{2.42}$$

As mentioned above, if the isolated dashpot in the generalized Maxwell model or the generalized Voigt chain is omitted, then these two models are reduced to characterize the mechanical behaviour of solids. The former is commonly termed the S.L.S Maxwell model, and the latter the S.L.S Voigt model. In fact, it has been shown that these two reduced generalized models are in essence the same in the sense that they can used to capture the same material behaviour but with different model constants [46]. As the S.L.S Maxwell is more commonly used either in open publications or commercial software such as ABAQUS, it is the one illustrated here.

The generalized Standard Linear Solid in Maxwell form (S.L.S Maxwell) is a popular model conventionally used by researchers [21, 26, 46] as it results in good fitting of viscoelastic behaviours. It has been widely implemented in commercial finite element software to simulate the mechanical

behaviour of viscoelastic materials. It possesses several different names, *e.g.* the PRONY model in ABAQUS [47] and the Wiechert model [43]. Similar models, *e.g.* the Parallel Network (PN) model, formed by incorporating some non-linear functional components in the S.L.S Maxwell model, have also been developed to predict non-linear viscoplastic behaviour [48].

The approximation accuracy of the S.L.S Maxwell depends on an appropriate choice of the number of the sub-Maxwell terms and the model constants adopted. Here, the single term S.L.S model (so-called 1-term PRONY model or the three-element model) will first be considered as it remains as the simplest S.L.S model, the conclusions can then be generalised to a multiple-term S.L.S model.

2.4.3.2 The single term S.L.S Maxwell model

The single term S.L.S Maxwell model consists of an auxiliary spring acting in parallel with a Maxwell model (Fig. 2-4).

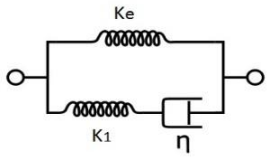


Figure. 2-4 Single term S.L.S Maxwell model

The constitutive equation, correlating the stress and strain via model constants, can be written as

$$(k_1 + k_e)\frac{d\varepsilon}{dt} = \frac{d\sigma}{dt} + \frac{1}{\tau}\sigma - \frac{k_e}{\tau}\varepsilon. \tag{2.43}$$

Here k_e is the long-term modulus (material stiffness exhibited when loading frequency tends to infinity), k_1 is the elastic constant of the sub-Maxwell component and $\tau = \frac{\eta}{k_1}$ is again the characteristic relaxation time of the model. The constitutive equation involves only stress, strain and their first derivatives with respect to time.

The wave equation can be derived in the same way as that of the Maxwell and Voigt models

$$\rho\frac{\partial^3 u}{\partial t^3} + \frac{\rho}{\tau}\frac{\partial^2 u}{\partial t^2} = (k_1 + k_e)\frac{\partial^3 u}{\partial x^2 \partial t} + \frac{k_e}{\tau}\frac{\partial^2 u}{\partial x^2}. \tag{2.44}$$

In view of the above wave equation, some typical mechanical behaviours of the S.L.S Maxwell materials can be observed.

a) Stress relaxation

In the case of stress relaxation, a constant strain ε_0 is input into the S.L.S Maxwell system, the resulting stress σ is $\sigma = k_e\varepsilon_0 + Ce^{-\frac{t}{\tau}}$. Applying initial condition $\sigma_{t=0} = (k_1 + k_e)\varepsilon_0$ gives $C = k_1\varepsilon_0$, which gives $\sigma(t) = (k_e + k_1 e^{-\frac{t}{\tau}})\varepsilon_0$. It is convenient to define the relaxation modulus as

$$E_{rel}(t) = \frac{\sigma(t)}{\varepsilon_0} = k_e + k_1 e^{-\frac{t}{\tau}}. \tag{2.45}$$

As an example, the time-dependent relaxation modulus of a single term S.L.S Maxwell material, with constants $k_e = 3$ GPa, $k_1 = 6$ GPa, $\tau = 5$ us, is shown graphically in Fig. 2-5. David [43] gave a physical explanation of the relaxation behaviour of this single term model: *The Standard Linear Solid is a three-parameter model capable of describing the general features of viscoelastic relaxation: k_e and k_1 are chosen to fit the glassy and rubbery moduli, and τ is chosen to place the relaxation in the correct time interval*. This can be equally explained as

$$\begin{gathered} k_e = E_r, k_1 = E_g - E_r; \\ \tau = t \;@\; \left\{E_{rel} = \left[E_r + \frac{1}{e}(E_g - E_r)\right]\right\}. \end{gathered} \tag{2.46}$$

b) Creep

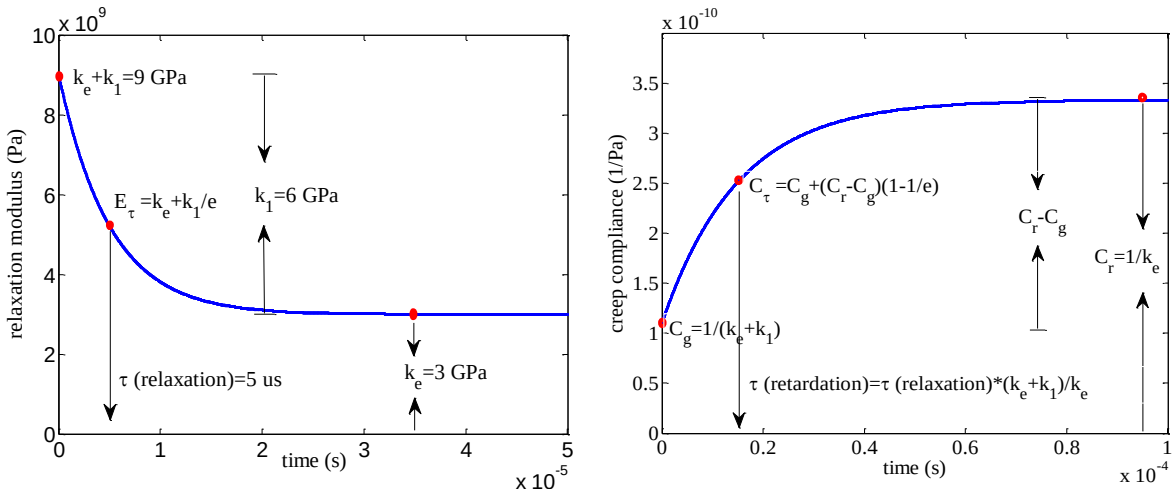


Figure 2-5. Relaxation modulus (left) and Creep compliance (right) of a single term S.L.S Maxwell model ($k_e = 3$ GPa, $k_1 = 6$ GPa, $\tau = 5$ us)

In the case of creep, a constant stress σ_0 is input into the system, the resulting strain response is

$$\varepsilon(t) = \frac{1}{k_e + k_1} + \left(\frac{1}{k_e} - \frac{1}{k_e + k_1}\right)\left(1 - e^{-\frac{k_e t}{(k_e + k_1)\tau}}\right)\sigma_0$$

the creep compliance can be computed as

$$C_{crp}(t) = \frac{\varepsilon(t)}{\sigma_0} = C_g + (C_r - C_g)(1 - e^{-\frac{t}{\tau_c}}) \tag{2.47a}$$

in which

$$C_g = \frac{1}{k_e + k_1}, C_r = \frac{1}{k_e}, \tau_c = \tau\left(\frac{k_e + k_1}{k_e}\right) \tag{2.47b}$$

C_g is the glassy compliance and C_r the rubbery compliance [43]. The characteristic time for creep τ_c (the retardation time) is longer than the characteristic time for relaxation τ, by a factor equal to the ratio of the glassy to the rubbery modulus [43].

An example of the time-dependent creep compliance is graphically shown in Fig. 2-5.

c) Wave propagation coefficients

In the same way as Maxwell and Voigt models, the propagation coefficient of the single term S.L.S Maxwell model can be derived as

$$\begin{aligned}
\kappa^2(\omega) &= \frac{\rho\omega^2}{2k_e}\left\{\frac{\sqrt{\left[\omega^2\tau^2\left(1+\frac{k_1}{k_e}\right)+1\right]^2 + \omega^2\tau^2\frac{{k_1}^2}{{k_e}^2}}}{\omega^2\tau^2\left(1+\frac{k_1}{k_e}\right)^2+1} + \frac{\omega^2\tau^2\left(1+\frac{k_1}{k_e}\right)+1}{\omega^2\tau^2\left(1+\frac{k_1}{k_e}\right)^2+1}\right\} \\
\alpha^2(\omega) &= \frac{\rho\omega^2}{2k_e}\left\{\frac{\sqrt{\left[\omega^2\tau^2\left(1+\frac{k_1}{k_e}\right)+1\right]^2 + \omega^2\tau^2\frac{{k_1}^2}{{k_e}^2}}}{\omega^2\tau^2\left(1+\frac{k_1}{k_e}\right)^2+1} - \frac{\omega^2\tau^2\left(1+\frac{k_1}{k_e}\right)+1}{\omega^2\tau^2\left(1+\frac{k_1}{k_e}\right)^2+1}\right\}
\end{aligned} \tag{2.48}$$

Note that Eq. (2.48) is consistent with the results derived by Aleyaasin *et al* [34] but with a slightly different appearance.

d) Complex modulus and compliance

The complex modulus and compliance of S.L.S Maxwell materials can be written as

$$\begin{aligned}
E^*(\omega) &= k_e + \frac{k_1\omega^2\tau^2}{1+\omega^2\tau^2} + i\frac{k_1\omega\tau}{1+\omega^2\tau^2} \\
J^* &= \frac{(1+\omega^2\tau^2)k_e + \omega^2\tau^2k_1}{k_e^2 + \omega^2\tau^2(k_1+k_e)^2} - i\frac{\omega\tau k_1}{k_e^2 + \omega^2\tau^2(k_1+k_e)^2}
\end{aligned} \tag{2.49}$$

2.4.3.3 The generalized S.L.S Maxwell model

More complex S.L.S Maxwell models can be constructed by adding more sub-Maxwell terms, and the resulting model is called the generalized S.L.S Maxwell model (Fig. 2-6), which is calibrated to have a distribution of relaxation times to fit the real material response. As long as sufficient relaxation times are included, the S.L.S Maxwell model is capable of describing a broad range of material responses [49]. It is reported that between 5 and 10 Maxwell elements are usually sufficient to fit experimental data [50]. The analysis of the generalized S.L.S Maxwell solid is similar to that of the single-term model, except that the constitutive equation (and thus the solution) becomes more complicated as more high-order differential terms are involved. A high-order differential equation has been described to analysing the generalized model (Eq. (2.40) ~ (2.42)); this can be applied to the S.L.S Maxwell model, which is a specific case when the isolated dashpot is omitted from the generalized model. Here an alternative approach employed by Danton [51] was introduced.

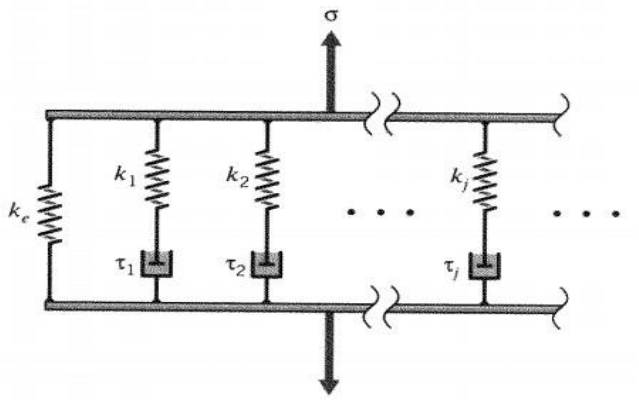


Figure 2-6. Generalized S.L.S Maxwell Model/Prony Model/Wiechert Model [43]

For a single Maxwell element i we have the constitutive equation Eq. (2.31), which can be re-written to be in the form

$$\sigma_i = \frac{\tau_i k_i \partial_t}{1 + \tau_i \partial_t} \varepsilon_i \tag{2.50}$$

with $\sigma_0 = k_e \varepsilon_0$ for the isolated spring. In these equations, σ_i and ε_i represent the stress and strain experienced by the i^{th} Maxwell element respectively; k_e is the modulus of the isolated spring and k_i the modulus of the i^{th} Maxwell element; ∂_t denotes the derivative with respect to t and can be handled as an algebraic entity.

The strain in all the elements remain the same ($\varepsilon_i = \varepsilon$); the total stress yielded by the whole parallel model is

$$\sigma = \sum \sigma_i = [k_e + \sum_{i=1}^{n} \frac{\tau_i k_i \partial_t}{1+\tau_i \partial_t}]\varepsilon \tag{2.51a}$$

multiplying the minimum common multiple of the denominators gives

$$\left[\prod_{j=1}^{n}(1+\tau_j\partial_t)\right]\sigma = k_e\left[\prod_{j=1}^{n}(1+\tau_j\partial_t)\right]\varepsilon + \left[\sum_{i=1}^{n}\tau_i k_i \partial_t \prod_{j=1,j\neq i}^{n}(1+\tau_j\partial_t)\right]\varepsilon. \tag{2.51b}$$

The above constitutive equation is again shown to be in the form of Eq. (2.41). Danton gave some comments on the above equations [51]: (1) The stress and strain have the same highest derivative order, no matter whether the isolated spring exists or not. This indicates the generalized Maxwell model can always exhibit an instantaneous response; (2) This model can represent a fluid if the arrangement has one Maxwell component without spring, *i.e.* an isolated dashpot appears. This has also been discussed in the section of generalized models [45].

a) Stress relaxation

Because the S.L.S Maxwell model is arranged in parallel, its relaxation function is the sum of the relaxation functions of each Maxwell unit [51]

$$E_{rel}(t) = k_e + \sum_j k_j e^{-\frac{t}{\tau_j}} \tag{2.52a}$$

this finite sum is called a discrete relaxation spectrum. As the number of Maxwell units increases to infinity, the summation becomes an integral, and a relaxation spectrum appears

$$E_{rel}(t) = k_e + \int_0^{+\infty} k(\tau) e^{-\frac{t}{\tau}} d\tau \tag{2.52b}$$

we can thus find

$$E_{rel}(t=0) = k_e + \sum_j k_j,\ E_{rel}(t\to\infty) = k_e$$

thus $E_\infty = k_e$ is defined as the long-term modulus while $E_0 = k_e + \sum_j k_j$ is the instantaneous modulus. By defining these two moduli, Eq. (2.52a) can be rewritten as

$$E_{rel}(t) = E_0 - \sum_j k_j (1 - e^{-\frac{t}{\tau_j}}). \tag{2.52c}$$

Similarly, for shear modulus and bulk modulus we have:

$$G_{rel}(t) = G_0 - \sum_j G_j(1 - e^{-\frac{t}{\tau_j}}) \tag{2.53a}$$

$$K_{rel}(t) = K_0 - \sum_j K_j(1 - e^{-\frac{t}{\tau_j}}) \tag{2.54a}$$

in which

$$G_0 = G_\infty + \sum_j G_j, \quad K_0 = K_\infty + \sum_j K_j$$

are the instantaneous shear and bulk modulus respectively. G_∞ and K_∞ are the long-term moduli.

dividing Eq. (2.53a) and (2.54a) by the corresponding instantaneous moduli E_0 and K_0, we define

$$\bar{g}_i^P = \frac{G_j}{G_0}, \bar{k}_i^P = \frac{K_j}{K_0}$$

$$g_R(t) = \frac{G_{rel}(t)}{G_0}, k_R(t) = \frac{K_{rel}(t)}{K_0}.$$

Eq. (2.53a) and Eq. (2.54a) can be rewritten as

$$g_R(t) = 1 - \sum_j \bar{g}_i^P(1 - e^{-\frac{t}{\tau_j}}) \tag{2.53b}$$

$$k_{rel}(t) = 1 - \sum_j \bar{k}_i^P(1 - e^{-\frac{t}{\tau_j}}). \tag{2.54b}$$

Eq. (2.53b) and Eq. (2.54b) are used to define the PRONY viscoelastic materials in *ABAQUS*.

b) Stress response to constant strain rate $\dot{\varepsilon}$

Imagine that a strain with constant strain rate, *i.e.* $\varepsilon = \dot{\varepsilon}t$ is applied to the S.L.S Maxwell model, the response can be obtained by using the Boltzman superposition integral

$$\sigma(t) = \sum_j \sigma_j(t) = \sum_j E_{rel}(t - \xi_j)\Delta\varepsilon_j = \int_{-\infty}^{t} E_{rel}(t - \xi)d\varepsilon = \int_{-\infty}^{t} E_{rel}(t - \xi)\frac{d\varepsilon}{d\xi}d\xi$$

$$= \int_{-\infty}^{t} E_{rel}(t - \xi)\dot{\varepsilon}d\xi = \int_{-\infty}^{t}(k_e + \sum_j k_j e^{-\frac{(t-\xi)}{\tau_j}})\dot{\varepsilon}d\xi = k_e\dot{\varepsilon}t + \sum_j k_j\dot{\varepsilon}\tau_j(1 - e^{-\frac{t}{\tau_j}}).$$

c) Complex modulus

The frequency-dependent complex Young's modulus can be derived by transforming Eq. (2.52a) into the frequency domain using Fourier transform

$$E'(\omega) = k_e + \sum_j \frac{k_j\omega^2{\tau_j}^2}{1+\omega^2{\tau_j}^2}$$
$$E''(\omega) = \sum_j \frac{k_j\omega\tau_j}{1+\omega^2{\tau_j}^2} \tag{2.55}$$

or equivalently [52]

$$E^*(\omega) = k_e + \sum_{j=1}^{n} \frac{k_j\omega^2\tau_j^2}{1+\omega^2\tau_j^2} + i\sum_{j=1}^{n} \frac{k_j\omega\tau_j}{1+\omega^2\tau_j^2} = k_e + \sum_{j=1}^{n} k_j(1 - \frac{1}{1+i\omega\tau_j})$$

similarly, the shear and bulk moduli can be derived by making use of Eq. (2.53a) and Eq. (2.54a)

$$\begin{aligned} G'(\omega) &= G_0\left(1-\sum_j \bar{g}_i^P\right)+G_0\sum_j \frac{\bar{g}_i^P\omega^2{\tau_j}^2}{1+\omega^2{\tau_j}^2} \\ G''(\omega) &= G_0\sum_j \frac{\bar{g}_i^P\omega\tau_j}{1+\omega^2{\tau_j}^2} \end{aligned} \tag{2.56}$$

$$\begin{aligned} K'(\omega) &= K_0\left(1-\sum_j \bar{k}_i^P\right)+K_0\sum_j \frac{\bar{k}_i^P\omega^2{\tau_j}^2}{1+\omega^2{\tau_j}^2} \\ K''(\omega) &= K_0\sum_j \frac{\bar{k}_i^P\omega\tau_j}{1+\omega^2{\tau_j}^2} \end{aligned}. \tag{2.57}$$

Eq. (2.56) and Eq. (2.57) are used in ABAQUS to define PRONY shear and bulk behaviours.

2.4.4 Summary of model-dependent analysis

We now have three sets of quantities at hand to describe material mechanical behaviours: the propagation coefficient (α, κ, c), the complex modulus $(E', E'', tan\delta)$ and the model-dependent constants (k_i, τ). Of course, these are mutually interrelated, as shown in Fig. 2-7; for each specific model, the relations are shown in Table. 2-2. Hence, the next stage in the research is to identify one set of parameters from which the others can be derived. This gives us the freedom to choose methods ease of measurement. For example, in experiments we measure wave propagation (any of force, stress, strain, displacement, acceleration, velocity), then model-free modulus can be calculated via relation ① in Fig. 2; then via relation ② we can use the modulus calculated to fit an approximate mechanical model which can be defined in simulation, and by monitoring wave propagation in simulations, we again have the wave propagation characteristics. The iterative cycle integrates analytical, experimental, and simulation verifications.

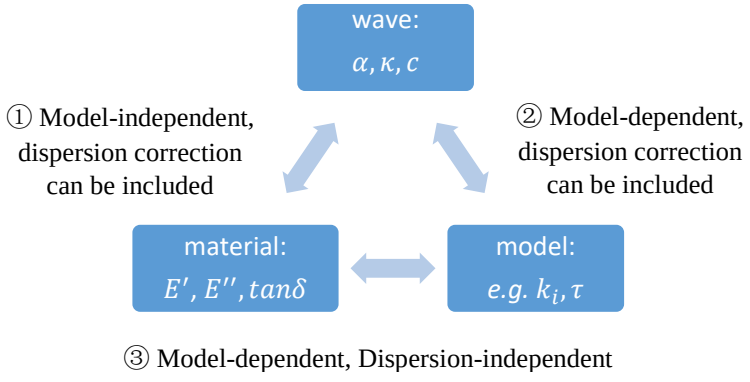
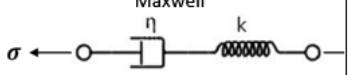
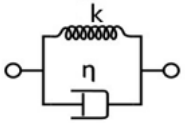
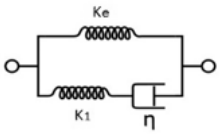
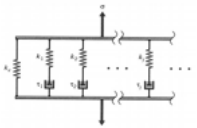


Figure. 2-7 Relationships between different characterization quantities

Table. 2-2 Summary of model-dependent analysis

Models		Maxwell 	Voigt 	SLS Maxwell	
				Single-term 	Multiple-term 
Constitutive equation		$k\dot{\varepsilon} = \dot{\sigma} + \frac{1}{\tau}\sigma$	$\sigma = k\varepsilon + \eta\frac{d\varepsilon}{dt}$	$(k_1 + k_e)\frac{d\varepsilon}{dt} = \frac{d\sigma}{dt} + \frac{1}{\tau}\sigma - \frac{k_e}{\tau}\varepsilon$	$\left[\prod_{j=1}^{n}(1+\tau_j\partial_t)\right]\sigma = k_e\left[\prod_{j=1}^{n}(1+\tau_j\partial_t)\right]\varepsilon + \left[\sum_{i=1}^{n}\tau_i k_i\partial_t \prod_{j=1,j\neq i}^{n}(1+\tau_j\partial_t)\right]\varepsilon$
1D wave equation		$\rho\frac{\partial^3 u}{\partial t^3} - k\frac{\partial^3 u}{\partial x^2\partial t} + \frac{\rho}{\tau}\frac{\partial^2 u}{\partial t^2} = 0$	$\frac{\partial^2 u}{\partial t^2} - \frac{\eta}{\rho}\frac{\partial^3 u}{\partial x^2\partial t} - \frac{k}{\rho}\frac{\partial^2 u}{\partial x^2} = 0$	$\rho\frac{\partial^3 u}{\partial t^3} + \frac{\rho}{\tau}\frac{\partial^2 u}{\partial t^2} = (k_1 + k_e)\frac{\partial^3 u}{\partial x^2\partial t} + \frac{k_e}{\tau}\frac{\partial^2 u}{\partial x^2}$	x
Mechanical	E^*	$E' = \frac{k\omega^2\tau^2}{1+\omega^2\tau^2}$, $E'' = \frac{k\omega\tau}{1+\omega^2\tau^2}$, $\tan\delta = \frac{1}{\omega\tau}$	$E' = k$, $E'' = \eta\omega$, $\tan\delta = \frac{\eta\omega}{k}$	$E' = k_e + \frac{k_1\omega^2\tau^2}{1+\omega^2\tau^2}$, $E'' = \frac{k_1\omega\tau}{1+\omega^2\tau^2}$, $\tan\delta = \frac{k_1\omega\tau}{k_e + (k_e+k_1)\omega^2\tau^2}$	$E' = k_e + \sum_j \frac{k_j\omega^2\tau_j^2}{1+\omega^2\tau_j^2}$, $E'' = \sum_j \frac{k_j\omega\tau_j}{1+\omega^2\tau_j^2}$,
	J^*	$J' = \frac{1}{k}$, $J'' = -\frac{1}{\omega\tau k}$	$J' = \frac{k}{k^2+\eta^2\omega^2}$, $J'' = \frac{-\eta\omega}{k^2+\eta^2\omega^2}$	$J' = \frac{(1+\omega^2\tau^2)k_0+\omega^2\tau^2 k_1}{k_e^2+\omega^2\tau^2(k_1+k_e)^2}$, $J'' = -\frac{\omega\tau k_1}{k_e^2+\omega^2\tau^2(k_1+k_e)^2}$	x
Wave propagation characteristics	α^2	$\frac{\rho\omega^2}{2k}\left[\left(1+\frac{1}{\omega^2\tau^2}\right)^{\frac{1}{2}} - 1\right]$	$\frac{\rho\omega^2}{2k(1+\omega^2\tau^2)}\left[(1+\omega^2\tau^2)^{\frac{1}{2}} - 1\right]$	$\frac{\rho\omega^2}{2k_e}\left\{\frac{\sqrt{\left[\omega^2\tau^2\left(1+\frac{k_1}{k_e}\right)+1\right]^2 + \omega^2\tau^2\frac{k_1^2}{k_e^2}} - \left[\omega^2\tau^2\left(1+\frac{k_1}{k_e}\right)+1\right]}{\omega^2\tau^2\left(1+\frac{k_1}{k_e}\right)^2+1}\right\}$	x
	κ^2	$\frac{\rho\omega^2}{2k}\left[\left(1+\frac{1}{\omega^2\tau^2}\right)^{\frac{1}{2}} + 1\right]$	$\frac{\rho\omega^2}{2k(1+\omega^2\tau^2)}\left[(1+\omega^2\tau^2)^{\frac{1}{2}} + 1\right]$	$\frac{\rho\omega^2}{2k_e}\left\{\frac{\sqrt{\left[\omega^2\tau^2\left(1+\frac{k_1}{k_e}\right)+1\right]^2 + \omega^2\tau^2\frac{k_1^2}{k_e^2}} + \left[\omega^2\tau^2\left(1+\frac{k_1}{k_e}\right)+1\right]}{\omega^2\tau^2\left(1+\frac{k_1}{k_e}\right)^2+1}\right\}$	x

Chapter 3: Determining viscoelastic material properties by measuring wave propagation in a single rod impact test: Experimental Investigations Part I—Setting the scene and Data processing

In the following two chapters, the principles behind the single rod method to identify material modulus are illustrated, some considerations in designing the single rod test discussed, then pendulum experiments, designed based on these considerations, performed to measure the wave propagation characteristics (the propagation coefficient) in elastic (Titanium, Magnesium) and viscoelastic (PMMA) rods. Then, the propagation coefficient is used to recover material moduli; at the same time, data from DMA tests are described as a comparison method for PMMA properties. A typical data processing procedure is presented with some critical issues such as pulse selection, dispersion correction and experimental settings demonstrated using the Ti case as an example, whilst the effect of temperature on material response is demonstrated for the PMMA case.

3.1 Principles of Single Rod Test Analysis

Before moving on to look at analysis of experimental or simulation data, the overall principles are illustrated. The analysis is based on Eq. (2.29a), which shows how the dynamic modulus $E^*(\omega)$ of a material can be recovered from the propagation coefficient $\gamma(\omega)$, a characteristic quantity that can be calculated from measurements of waves propagating in slender rods. An impact on one end of the rod is used to generate a wave that travels back and forth. Theoretically, the waves can be measured using any one of the 6 quantities: displacement, particle velocity, strain, acceleration, force and stress. Ideally, these values can be monitored at any location along the rod. However, the optimal measurement location depends on the target measurement quantity and equipment. For surface strain measurement for example, considering wave overlapping at the strain gauge station, the optimal measurement location for a single rod may be halfway along its length; whilst for a Laser Doppler Vibrometer (LDV) it is more convenient to monitor the particle velocity at one end.

Here the focus is on strain measurement; LDV-based particle velocity measurement was introduced later as a comparison when characterizing PMMA. In the experiments reported here, the test rods are instrumented with strain gauges at a single gauge station/section: multiple measurements are

obtained by making use of the reflection of the wave at the bar ends. This method only deals with 2 pulses, which makes it quite simple compared to the multiple section measurement method that involves matrix calculation and optimisation to identify material modulus [31]. Furthermore, it avoids the necessity of building a very long rod, as pulses reflect with a π phase shift but no amplitude change at the rod ends. Finally, if the gauges are linear, no calibration is required because all the calculations use either strain ratios or times of arrival. The particle velocity measurement works similarly, except that the Vibrometer is used to perform measurements at one end of the rod, where the particle velocity is double that elsewhere.

The general principles behind identification of material properties using the single bar impact can be found in several places in the literature, *e.g.* Bacon [18], Ahonsi [21], Benatar [33], *etc*. These principles are generalized and extended here; frequency domain analysis is used as it facilitates the observation of frequency-dependent material properties. Note that 'frequency' is more often used term in viscoelastic analysis while 'strain rate' is favoured in interpreting elastic properties. Empirically, they can be related to each other using the rough approximation $\dot{\varepsilon} = \frac{f}{4}$.

Consider a wave propagating in a single direction, the increasing x direction for example, the general frequency expressions of strain Eq. (2.20a), displacement Eq. (2.20b), particle velocity Eq. (2.20c), force Eq. (2.20d), stress Eq. (2.20e) and acceleration Eq. (2.20f) can be simplified

$$\tilde{\varepsilon}(x,\omega) = \tilde{P}(\omega)e^{-\gamma(\omega)x} = \tilde{P}(\omega)e^{-\alpha(\omega)x}e^{-i\kappa(\omega)x}$$

$$\tilde{u}(x,\omega) = -\frac{1}{\gamma(\omega)}\tilde{P}(\omega)e^{-\gamma(\omega)x} = -\frac{1}{\gamma(\omega)}\tilde{P}(\omega)e^{-\alpha(\omega)x}e^{-i\kappa(\omega)x}$$

$$\tilde{\dot{u}}(x,\omega) = -\frac{i\omega}{\gamma(\omega)}\tilde{P}(\omega)e^{-\gamma(\omega)x} = -\frac{i\omega}{\gamma(\omega)}\tilde{P}(\omega)e^{-\alpha(\omega)x}e^{-i\kappa(\omega)x}$$

$$\tilde{F}(x,\omega) = -\frac{\rho A\omega^2}{\gamma^2(\omega)}\tilde{P}(\omega)e^{-\gamma(\omega)x} = -\frac{\rho A\omega^2}{\gamma^2(\omega)}\tilde{P}(\omega)e^{-\alpha(\omega)x}e^{-i\kappa(\omega)x}$$

$$\tilde{\sigma}(x,\omega) = -\frac{\rho\omega^2}{\gamma^2(\omega)}\tilde{P}(\omega)e^{-\gamma(\omega)x} = -\frac{\rho\omega^2}{\gamma^2(\omega)}\tilde{P}(\omega)e^{-\alpha(\omega)x}e^{-i\kappa(\omega)x}$$

$$\tilde{a}(x,\omega) = \frac{\omega^2}{\gamma(\omega)}\tilde{P}(\omega)e^{-\gamma(\omega)x} = \frac{\omega^2}{\gamma(\omega)}\tilde{P}(\omega)e^{-\alpha(\omega)x}e^{-i\kappa(\omega)x}.$$

In these equations, the factor of $e^{-\alpha(\omega)x}$ represents the frequency-dependent amplitude attenuation, and $e^{-i\kappa(\omega)x}$ indicates the frequency-dependent phase change. Hence, if one of these quantities is

measured at two locations (these two locations could be identical, as is the case in our later single gauge station measurement experiments), x_1 and x_2, we have

$$\frac{\tilde{\varepsilon}(x_1,\omega)}{\tilde{\varepsilon}(x_2,\omega)} = \frac{\tilde{u}(x_1,\omega)}{\tilde{u}(x_2,\omega)} = \frac{\tilde{\dot{u}}(x_1,\omega)}{\tilde{\dot{u}}(x_2,\omega)} = \frac{\tilde{F}(x_1,\omega)}{\tilde{F}(x_2,\omega)} = \frac{\tilde{\sigma}(x_1,\omega)}{\tilde{\sigma}(x_2,\omega)} = \frac{\tilde{a}(x_1,\omega)}{\tilde{a}(x_2,\omega)} = e^{-\gamma(\omega)(x_1-x_2)} = e^{-\alpha(\omega)(x_1-x_2)}e^{-i\kappa(\omega)(x_1-x_2)}. \tag{3.1}$$

The attenuation coefficient can thus be calculated from the amplitude of the ratios while the wavenumber can be obtained from the phases (in following analysis, only strain representations are used, the other 5 quantities have the same form)

$$\begin{cases} \alpha = -\dfrac{\ln\left|\dfrac{\tilde{\varepsilon}(x_1,\omega)}{\tilde{\varepsilon}(x_2,\omega)}\right|}{x_1 - x_2} \\ \kappa = -\dfrac{angle\left[\dfrac{\tilde{\varepsilon}(x_1,\omega)}{\tilde{\varepsilon}(x_2,\omega)}\right]}{x_1 - x_2} \\ c(\omega) = \dfrac{\omega}{\kappa(\omega)} \end{cases} \tag{3.2a}$$

Here, the numerator accounts for the natural logarithm of the ratio of the Fourier transform, while the denominator $x_1 - x_2$ gives the travel distance over which the variation happens. We see that the attenuation coefficient α and wavenumber κ may both be frequency-dependent.

A more direct method to work out the propagation coefficient $\gamma(\omega)$ from equation (3.1) is

$$\gamma(\omega) = -\frac{ln\dfrac{\tilde{\varepsilon}(x_1,\omega)}{\tilde{\varepsilon}(x_2,\omega)}}{x_1 - x_2} \tag{3.2b}$$

and according to Eq. (2.19), we know $\alpha = real(\gamma), \kappa = imaginary(\gamma)$.

However, a data processing issue associated with wavenumber calculation arises here. As phase is generally calculated in the range from 0 to 2π, the wavenumbers $\kappa(\omega)$ calculated directly from Eq. (3.2a) or Eq. (3.2b) will be non-continuous in a step-increasing form, thus corrections are needed in order to make it continuous and monotonically increasing. A numerical procedure known as 'unwrapping', in which multiples of $\pm 2\pi$ are added when steps appear, *i.e.* when absolute jumps between consecutive elements are larger than π radians, was used by Bacon [18] while using Eq. (3.2a) to resolve κ. When dealing with real data, it is convenient to use the MATLAB function 'unwrap' to perform the phase correction

$$\kappa = -\frac{unwrap\left\{angle\left[\frac{\tilde{\varepsilon}(x_1,\omega)}{\tilde{\varepsilon}(x_2,\omega)}\right]\right\}}{x_1 - x_2}$$

It is thus obvious that the two sub-coefficients of the propagation coefficient $\gamma(\omega)$, *i.e.* the attenuation coefficient $\alpha(\omega)$ and the wavenumber $\kappa(\omega)$, can be calculated from ratios of the any of the 6 quantities: strain $\tilde{\varepsilon}(x,\omega)$, displacement $\tilde{u}(x,\omega)$, particle velocity $\tilde{\dot{u}}(x,\omega)$, force $\tilde{F}(x,\omega)$, stress $\tilde{\sigma}(x,\omega)$ and acceleration $\tilde{a}(x,\omega)$. In these trials, strain measurement was adopted in all tests while velocity measurement was only conducted in PMMA (T = 23.4 ℃) for comparison purpose.

The equations described so far make the assumption that the wave propagation is in a state of uniaxial stress, *i.e.* 1D wave propagation. In real rods, the coefficients experimentally determined by Eq. (3.2) contain both viscoelastic and geometric dispersion effects. Geometric dispersion affects only the phase of the Fourier components of the wave, not their magnitude, and thus causes inaccuracies in wavenumber calculation. Before the 'real' propagation coefficient, induced only by the intrinsic viscoelasticity, can be derived, dispersion correction should be applied to exclude this geometric effect when it is significant. For this, additional information, *e.g.* an estimate of the material modulus E and Poisson's ratio ν, is needed; this was discussed later.

After the propagation coefficient $\gamma(\omega)$ has been calculated, this is substituted into Eq. (2.29a) to yield the target modulus. Looking at the whole derivation process, it is seen that it is essential to have the prerequisite knowledge of material density ρ (Eq. (2.29a)), and to accurately determine the travel distance $x_1 - x_2$ (Eq. 3.2). Inaccuracy in these prerequisite info brings in errors. The following section presents a single worked example of an experiment on a 1.3 m long, 13 mm diameter PMMA rod at 17.5 °C to illustrate the whole data analysis process in detail. Key points such as appropriate impactor and pulse selection, strain amplitude, and some numerical problems, were addressed.

3.2 Single Rod Test Design

3.2.1 Overview

In a similar manner to previous research by Bacon [18], experiments have been performed using a pendulum impact apparatus to generate a stress wave in a single, instrumented rod. There are two

considerations in the design of the single bar impact tests: bar dimension and number of measurement stations. The bar diameter is ideally as small as possible to yield 1D wave propagation, although 3D effects can be accounted for in the analysis using the dispersion correction described later. In these tests, diameters of 12.7 mm for Ti and Mg, and 13 mm for PMMA were used. More considerations are involved in selecting the bar length. As stated above, if a boundary condition (*e.g.* free end) is used, one measurement station can be used to determine the material dynamic properties, provided that there is no wave overlapping at the measurement station [32]; otherwise, the maximum frequency at which material properties can be determined will be affected [21]. It is thus desirable that a long bar is used to avoid wave overlap, so that no extra effort is needed to recover the isolated incident and reflected pulses by using wave separation techniques. However, by comparing the propagation coefficients derived from 1 m and 2 m bar simulations, Ahonsi *et al* [21] conclude that increasing the bar length reduces the frequency range over which the propagation coefficient can be determined accurately. This is due to the fast attenuation of high frequency components, which results in small signal-to-noise ratios and thus lower accuracies in data analysis. A rod length of 1000 mm was adopted in the current research.

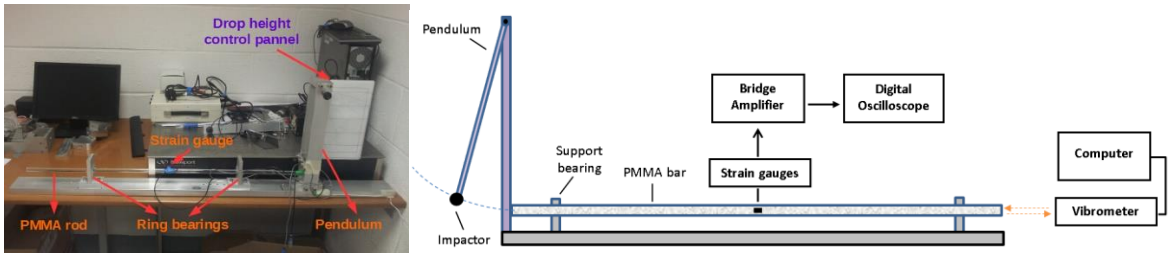


Figure. 3-1 Schematic and real single rod impact experimental setup: (left) experimental apparatus, (right) simplified schematic representation

The portable pendulum setup used for the experiments is shown in Fig. 3-1. With a geometry of about 1.5 × 0.1 × 0.5 m (L×W×H), it can accommodate a 1 m long rod with diameter up to 14 mm. The base is made of aluminium and the pendulum arm has a length of about 300 mm. In this study, three rods were tested: a Titanium rod with a geometry of 12.7 mm diameter × 1000 mm long, a Magnesium rod (12.7 × 1000 mm) and a PMMA rod (13 × 1000 mm). The Titanium rod is Ti6Al4V with a density of 4417 kg m^{-3} and Young's modulus of around 110 GPa; The Magnesium rod has a

density of 1799 kg m^{-3} and estimated elastic Young's modulus of around 45 GPa; The commercial PMMA (also known under the trade name 'Perspex') used here is an amorphous thermoplastic with a density of 1186 kg m^{-3}, and estimated instantaneous Young's modulus of around 5.4 GPa. Rods were held by two polymer ring bearings and are free to move axially. A small concern arises here as energy might be dissipated by the friction at the bearing supports during wave propagation, some authors use thin wires to horizontally support the rods instead.

3.2.2 The measurement system

Strain histories were measured using resistance strain gauges. Two pairs of axially mounted strain gauges were attached to the surface at the centre of the bar so that the gauges were spaced at 90° intervals around the bar. Each gauge has a resistance of 120 Ω and length of 3 mm. A modified half bridge was used (Fig. 3-2), in which the two opposite gauges were connected in series and together constitute one leg of the half bridge; the other two legs of the bridge were built-in constant resistors of 240 Ω. This configuration ensures that any contributions due to accidental bending (*e.g.* imperfect impact and eccentricity) are eliminated [30, 32]. Note that, the bridge should be initially balanced before undergoing any deformation, and no circumferential gauges were used to measure the Poisson's ratio here.

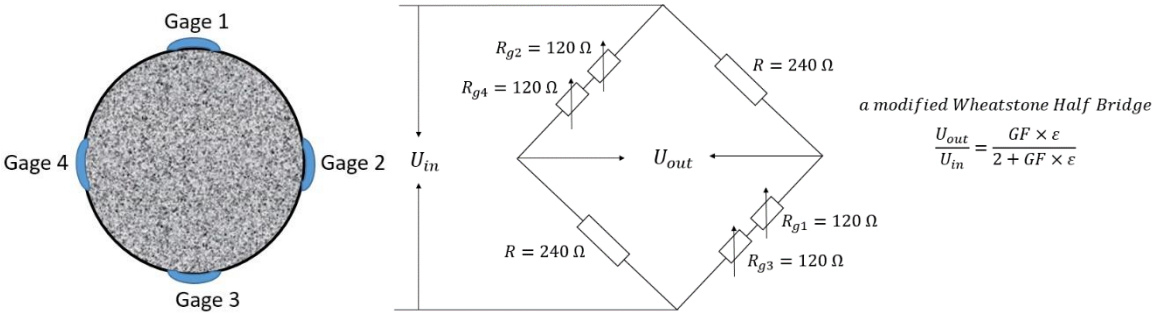


Figure. 3-2 Gauge layout and the Wheatstone half bridge

Strain signals were then directed to an FE-H379-TA amplifier and finally captured by a 4-channel Tektronics digital oscilloscope. The vertical (*i.e.* voltage) scale of the oscilloscope was set so that the pulses filled the screen, ensuring maximum amplitude resolution and minimising the effects of digitisation as much as possible. Amplitude accuracy can also be improved by using the high-resolution mode which is effectively the same as 10-bit digitisation. The horizontal scale was set to

be 0.1 s, during which 100k data points were recoded with a sampling rate of 1 MHz. The time interval between 2 subsequent adjacent pulses, PMMA rod for example, is approximately 1 m / 2117 m s^{-1} = 472 μs, so the 0.1 s timescale allows a large number of pulses to be recorded: in practice, the upper limit on the number of pulses which can be used is determined by how quickly they attenuate. Usually, it was found that the first six pulses are enough for data analysis.

Using the modified half bridge, real strain can be related to the measured voltages as follows:

$$U_{oscilloscope} = Amplification \times \frac{GF \times \varepsilon}{2 + GF \times \varepsilon} \times U_{in}. \quad (3.3)$$

In the current experiments the gage factors *GF* were 2.11 for the gauges used on the Ti rod and 2.10 for those on the PMMA rod, whilst for the amplifiers settings used, $Amplification = 10\,V/4.3\,mv = 2326$ and the supply voltage $U_{in} = 6.02$. Note that, the term $GF\varepsilon$ in the denominator is rather small as strain is normally in the order of 10^{-6} to 10^{-3}, thus in all subsequent calculations this non-linear term was ignored.

A vibrometer was used in the 23.4 ℃ PMMA tests to measure particle velocities at the non-impact end. The reasons for introducing the velocity measurement are: firstly, unlike strain gages which have the 'gage effect', laser dot has a small measurement area; secondly, it serves as a comparison for the strain-based method. Particle velocity signals were recorded separately.

3.2.3 Experimental aim and scheme

Using this apparatus, experiments were performed to investigate a number of different aspects of the technique: a) Impactor type and hence wave profile; b) Strain amplitude; c) Temperature; d) critical issues such as appropriate pulse section, denoising, centering, FFT, and the lower and higher frequency limits that can be achieved; e) Dispersion Correction; f) Validation with vibrometer; g) verification using DMA tests. A detailed experimental scheme is presented in Table. 3-1. Note that the maximum real strains achieved in all these tests are within the allowance of a normal linear viscoelastic region (LVR), *i.e.* 0.1 %.

Impactor selection is an important issue. In Hopkinson bar testing, impactors are normally made of the same materials as the rods, because the mechanical impendence match between the impactor and

the rod ensures maximum energy transfer. In order to investigate the impactor effect, impactors with different materials (PMMA, steel and aluminium), shapes (cylinder and balls), diameters and lengths, were employed. In principle spherical balls can generate pulses with higher frequency components compared to cylindrical projectiles (as commonly used in SHPB tests), and the impactor diameter or length should be as small as possible to avoid wave superposition, as during wave propagation both the viscoelastic and geometric dispersion effects lead to an extension of pulse duration [18]. Taking these into consideration, an impactor selection process was designed, this was illustrated in the data analysis process.

Temperature was controlled in the PMMA experiments. Temperature dependent behaviours, as a result of changes in molecular mobility, are commonly seen in thermoplastics. All previous work using this technique (Table. 2-1) was either conducted at constant temperature or in an environment that ensures that temperature varies in a very small range. In this work, the ability of the single rod impact technique to capture the mechanical property variations of PMMA under small temperature changes was investigated by performing experiments at 17.5, 19.5, 23.4 and 27 °C. The temperatures indicated were measured on the surface of a separate rod of identical material as the test rod, and in the tested temperature range the PMMA material remains in its glassy state (within LVR).

Table. 3-1 Experimental scheme

Specimen tested	T	Impactors used	Quantity measured	Location & No. of measurement stations	Wave travel distance between 2 adjacent pulses	Max strain ($\times 10^{-3}$)
Ø12.70 × 1000 mm Ti rod	22.6 °C	All 8 impactors	Strain	Middle surface (1)	1 m	PMMA Ball: 0.00171% For Ø12.50 mmPMMA ball; Al ball: 0.00633% For Ø12.34 mmAluminium ball;
Ø12.70 × 1000 mm Mg rod	21.8 °C	Ø12.50 mm PMMA ball $h = 28\ cm$ & Ø12.34 mm Aluminium ball $h = 27\ cm$	Strain	Middle surface (1)	1 m	0.00367% For Ø12.50 mmPMMA ball; 0.01066% For Ø12.34 mmAluminium ball;
Ø13.00 × 1000 mm PMMA rod	17.5 °C	All 8 impactors	Strain	Middle surface (1)	1 m	0.0148% For Ø12.50 mmPMMA ball; 0.0261% For Ø12.34 mmAluminium ball;
Ø13.00 × 1000 mm PMMA rod	19.5 °C	All 8 impactors	Strain	Middle surface (1)	1 m	0.0147 % For Ø12.50 mmPMMA ball; 0.0261% For Ø12.34 mmAluminium ball;
Ø13.00 × 1000 mm PMMA rod	23.4 °C	Ø12.50 mm PMMA ball $h = 30\ cm$ & Ø12.34 mm Aluminium ball $h = 27\ cm$	Strain & Particle velocity	Middle (1) & End surface (1)	1 m for strain pulses, 2 m for particle velocity pulses	0.0147 % For Ø12.50 mmPMMA ball; 0.0272% For Ø12.34 mmAluminium ball;
Ø13.00 × 1000 mm PMMA rod	27 °C	All 8 impactors	Strain	Middle surface (1)	1 m	0.0149 % For Ø12.50 mmPMMA ball; 0.0266% For Ø12.34 mmAluminium ball;

1. All rods have free ends;
2. In all tests, there are 4 strain gages installed at each station, sampling rate is 1 MHz, and data length 100k in all tests. Frequency range achieved varies depending on a number of factors discussed later;

3.3 Typical data analysis process

3.3.1 Preliminary considerations

A schematic diagram of typical strain and particle velocity recordings captured in the PMMA rod test are shown in Fig. 3-3.

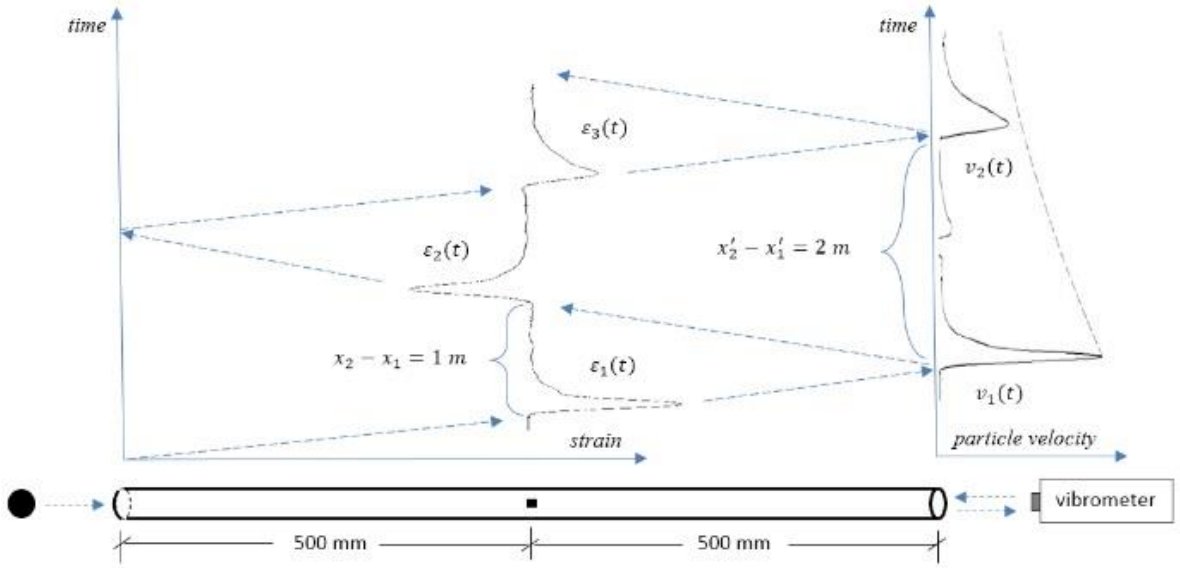


Figure 3-3. Typical signals from pendulum impact tests

The data analysis scheme in the PMMA case is shown in Fig. 3-4. Analysis has been performed on the signals produced by spherical impactors, 12.5 mm diameter PMMA and 12.34 mm diameter aluminium over a number of drop heights at four temperatures. For each temperature, the final results are an average of those from all the drop heights, and for each drop height, two tests were conducted in the same conditions. For each test, the results were calculated based on an average of two calculations using different pulses, as described later.

Before proceeding to the viscoelastic PMMA case, the titanium and magnesium cases were first analysed: as the material properties of these elastic rods were commonly known, the results can serve as a verification of the technique. Here, only the effects of impactor type and drop height were considered. In this section, examples were presented to illustrate the detailed data analysis process. The commercial software MATLAB was employed as a tool to process the experimentally collected signals. The overall aim of performing data analysis is to derive the frequency-dependent viscoelastic material properties, however, before starting signal processing, there are 2 basic problems which

must be addressed with regard to the time domain signals: under what conditions, *e.g.* impactor types and drop heights, is there no wave superposition; and how to appropriately select each pulse in that condition? The first problem deals with the impactor and strain amplitude effects while the second concerns pulse selection.

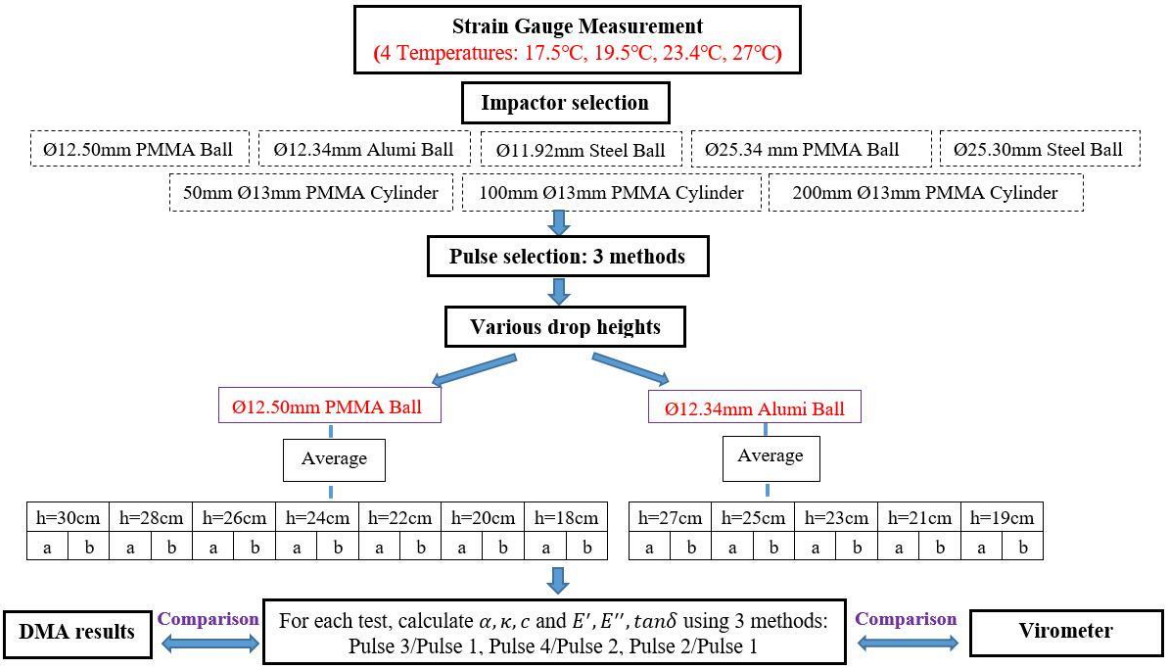


Figure. 3-4a Data analysis scheme for the $1m$ $\emptyset 13$ mm PMMA rod

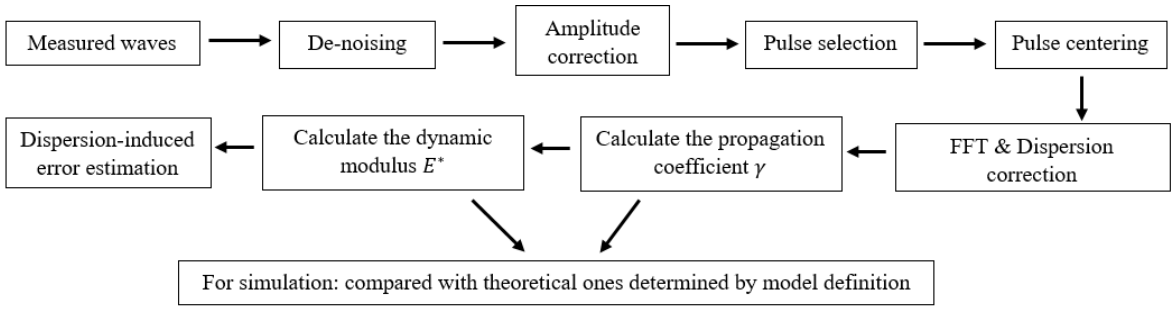


Figure. 3-4b A typical signal processing procedure

3.3.2 Effects of impactor and drop height

It is expected that the impactor affects the pulses generated in two related aspects: the impactor shape (ball or cylinder) affects the highest frequencies contained in a pulse, through the rise time, while the size (ball diameter or cylinder length) has influence on the pulse duration. The impactor speed (drop height), which dominates the strain amplitude generated, also has an effect on the pulse

duration in viscoelastic rods, but another purpose of employing different drop heights is to examine whether the same mechanical response is obtained for different strain amplitudes.

Theoretically, whatever impactors are used, the analysis should give the same material properties. In reality, however, different impactor shapes generate pulses which contain different frequency components, and different impactor lengths will give different wave durations, which introduce wave superposition and also affect the spectrum of frequencies in the pulse. In fact, the impactor issue belongs to a broader topic of excitations, which covers the effects of impactors (materials, shapes, lengths, *etc*) and excitation methodologies (air gun, pendulum, *etc*) on the 'useful frequency range' that can be achieved in an impact test. As a pendulum excitation method was adopted in all tests, only the impactor effect is discussed here. Eight impactors of different materials (and thus mechanical impedance) and different sizes were employed (Table. 3-2). If pulse extension induced by dispersion or viscoelasticity is not considered, the pulse duration can be estimated as

$$\text{Pulse duration} \approx \frac{2\times impactor\ diameter\ or\ length}{wave\ speed\ in\ impactor} \tag{3.4}$$

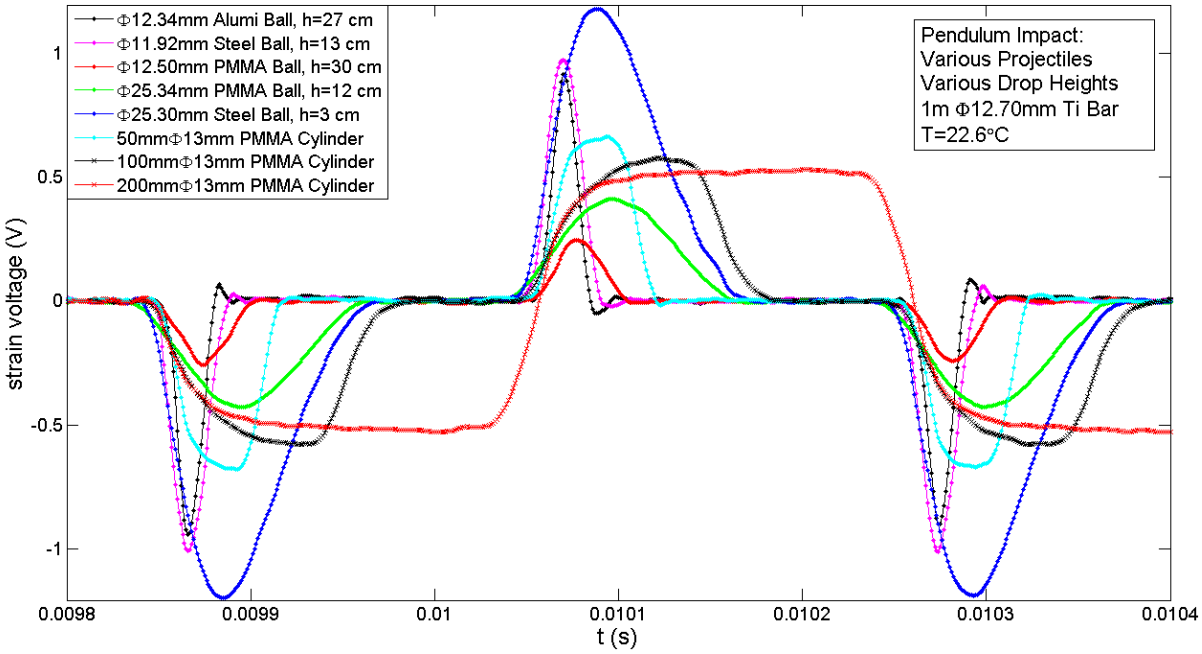
given the geometries and properties of the impactors listed in Table. 3-2, this is estimated to vary from about 5 to 190 μs.

Table. 3-2 Impactors and drop heights

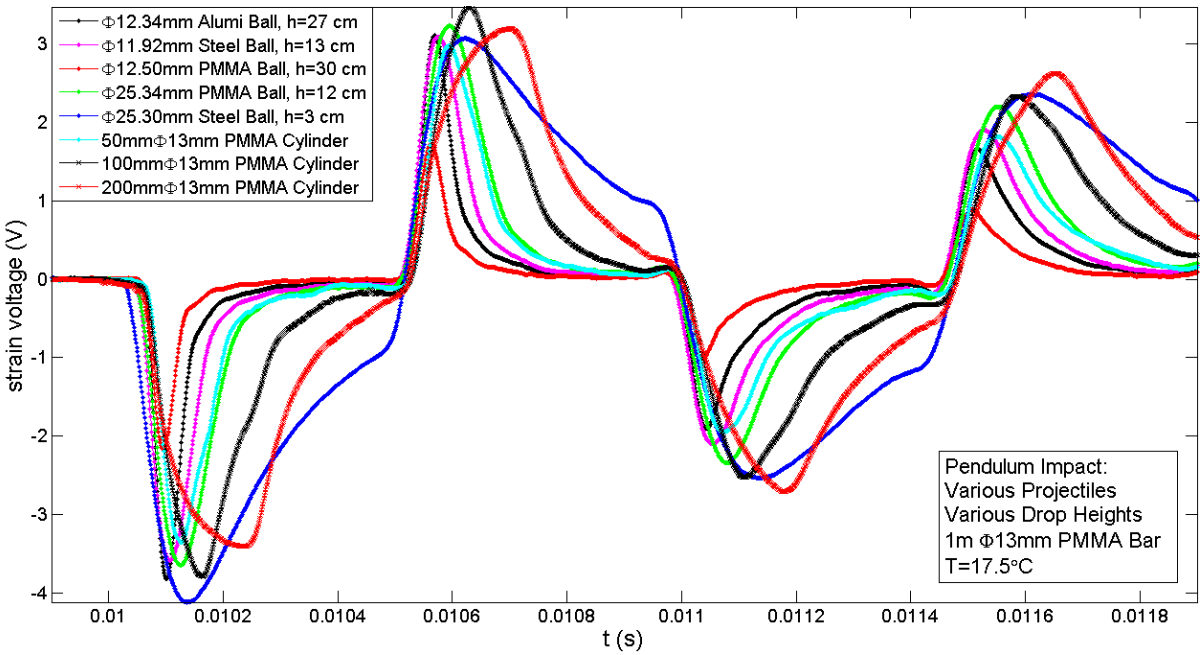
Impactors	Ø12.50 mm PMMA ball	Ø25.34 mm PMMA ball	Ø11.92 mm Steel ball	Ø25.30 mm Steel ball
Excitation method	Pendulum	Pendulum	Pendulum	Pendulum
Drop heights	$30, 28, 26, 24, 22, 20, 18$	$12, 10, 8, 6, 4\ cm$	$13, 11, 9, 7, 5\ cm$	$3, 2, 1\ cm$
Impactors	Ø12.34 mm Aluminium ball	Ø12.90 × 49.88 mm PMMA Cylinder	Ø13.00 × 100.09 mm PMMA Cylinder	Ø13.00 × 200 mm PMMA Cylinder
Excitation method	Pendulum	By hand	By hand	By hand
Drop heights	$27, 25, 23, 21, 19\ cm$	-	-	-

Signals generated by the eight impactors (at the highest drop heights) are shown in Fig. 3-5. These data show that: a) spherical balls generate harmonic-like pulses with sharp rising time while cylinders produce trapezoidal pulses with a relatively gentle rising wave front, this is consistent with Bacon's conclusion that cylindrical impactors normally give a lower frequency range [18]; b) due to the

mechanical impedance mismatch between impactor and rod materials, impacts on the PMMA rod yield larger strain amplitudes; c) extended tails can be seen in PMMA signals, mainly due to viscoelastic effects, while the Titanium rod shows elastic behaviour; d) the spherical PMMA and Aluminium might give better results in terms of avoiding wave superposition. In all the following analyses, only these two impactors were used.



(a) 1000 Ø 12.7 mm Ti rod, $T = 22.6$ ℃



(b) 1000 Ø 13 mm PMMA rod, T = 17.5 ℃

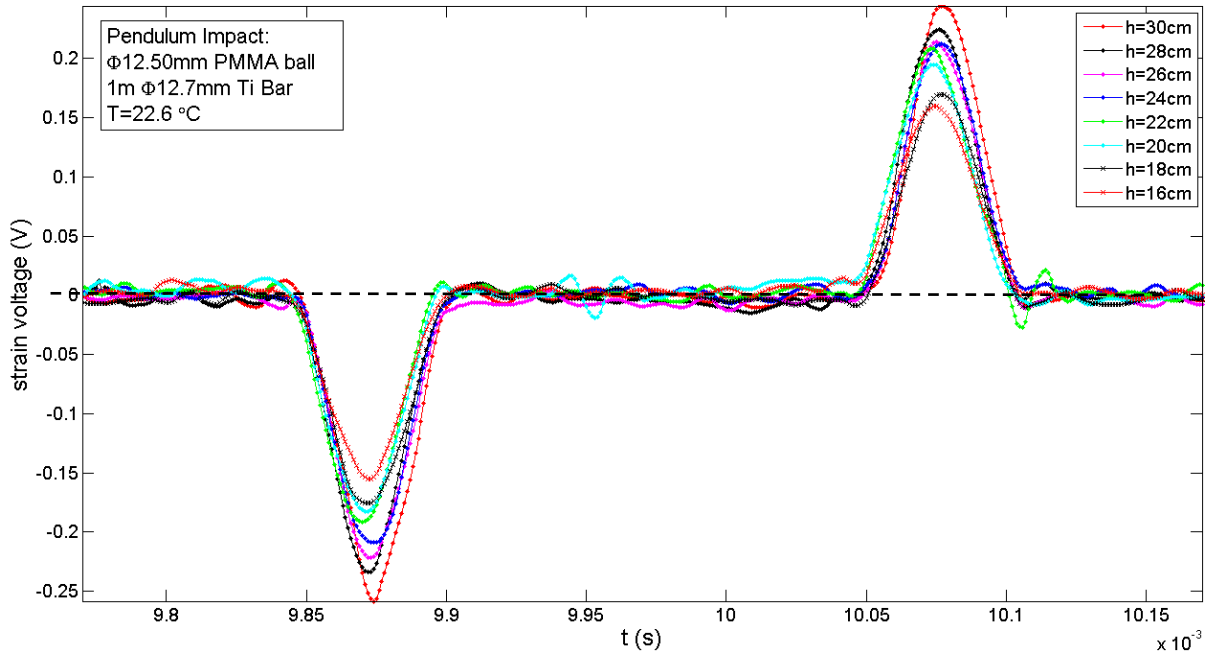
Figure. 3-5 Strain pulses generated by 8 impactors

Further experiments were performed using the spherical PMMA impactor in which different drop heights were employed to generate various impact speeds and thus strain amplitudes (Fig. 3-6). In these cases, drop height has an effect on the wave duration, especially for the viscoelastic PMMA rod, as shown in the inset in Fig.3-6. This means that a longer time is needed for larger amplitude pulses to recover than for smaller amplitude pulses. This phenomenon is reasonable as linear viscoelastic behaviours conform to the Boltzmann superposition principle in which the strain is associated with the loading history. Hence, Eq. (3.4) only gives the shortest wave duration generated by elastic impactors at the impact end; if viscoelastic and dispersion effects are present, the pulse duration can extend considerably and depends on the maximum strain amplitude. However, all the drop heights employed here do not produce severely overlapped pulses that are visibly unacceptable, thus all the pulses are considered valid for the next stage of the analysis.

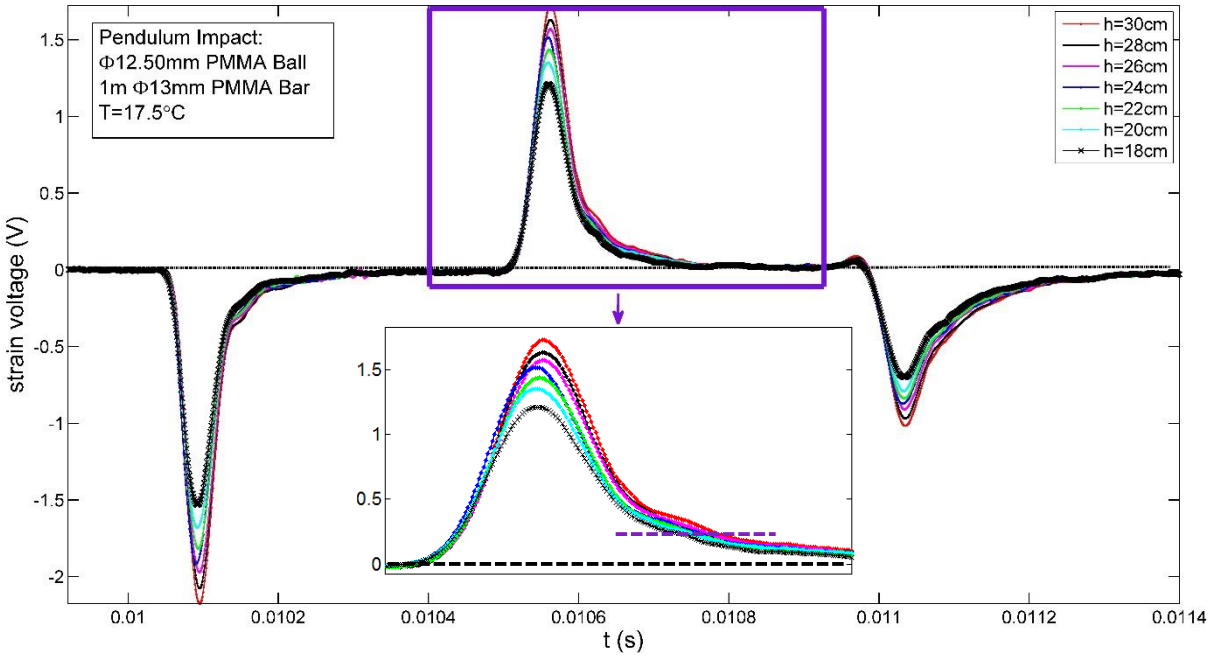
As drop height determines the strain amplitude generated, it is important to confirm that all tests performed remain within the Linear Viscoelastic Region (LVR); as linear viscoelasticity was assumed in all the previous derivations and is a prerequisite for all the analysis (see [32]). Within the LVR, the material's response is independent of the magnitude of the deformation [53]; beyond this, it is both time and strain-dependent [54]. As a general rule of thumb, solids are linear at strains less than 0.1% [53] or 0.5% [46]. However, the real LVR depends on the type of material, and is commonly established by testing samples under incremental strains. In these experiments, Table. 3-1, with the largest drop heights adopted (h=30 cm for the PMMA ball and 27 cm for the Aluminium ball), the corresponding maximum strains are within 0.1%. Furthermore, by examining the results obtained from different drop heights later, it is verified that the PMMA rod was linear in all the tests: the material parameters obtained are independent of drop-height and impactor type.

In addition, a closer examination of Fig. 3-6 reveals that strain pulses in Titanium rod could return to zero level while the ones in PMMA rod did not reach zero even after a long period. These long 'tails' in PMMA rod were also observed in later viscoelastic simulation strain recordings. A high signal-to-noise ratio is preferred in the analysis. As high frequency components attenuate quickly, a valid 'signal-to-noise ratio' at high frequencies determines the highest frequency (*i.e.* 'the

valid/useful upper frequency') that can be analysed. Consistently in this analysis it is observed that the FFT magnitude of those frequency components beyond 20 kHz is very low, which results in a low signal-to-noise ratio and causes the evaluation of the propagation coefficient to be inaccurate and oscillatory. In principle, one may expect the signal-to-noise ratio to be improved by employing larger drop height giving larger strain amplitudes and thus larger signals.



(a) 1000 Ø 12.7 mm Ti rod, Ø12.50 mm PMMA ball, $T = 22.6$ ℃



(b) 1000 Ø 13 mm PMMA rod, Ø12.50 mm PMMA ball, $T = 17.5$ ℃

Figure. 3-6 Strain pulses generated by 8 drop heights

With a given impactor, an averaging technique was used to analyse the data at different drop heights. This helps remove experimental errors and minimize the truncation effect because the pulse duration selected in each drop height case is not necessarily the same. This explains the difference between single test results and averaged results, as we will see later: the single test results oscillate more than the means.

3.3.3 Data analysis process

3.3.3.1 Background

Data analysis was performed in the Fourier Domain in order to establish frequency dependent properties. As experimentally collected signals are discrete and aperiodic, the Discrete Fourier Transform (DFT), more precisely the Fast Fourier Transform (FFT), was used. The following section clarifies how the FFT results were derived, and addresses some critical steps in the FFT calculations, *e.g.* the effects of window function, pulse centering, *etc*.

In the following section, an example data set from the 13 mm diameter PMMA rod impacted with the 12.5 mm diameter PMMA sphere at a height of 30 cm and temperature of 17.5 °C was used to illustrate the whole data analysis process in detail. Analysis code was written in the commercial software MATLAB. The aim of performing this analysis is to derive the frequency-dependent viscoelastic material properties, including material damping characteristics such as the propagation coefficient and hence loss modulus, and the wave propagation properties such as the wave speed, and thus the storage modulus. Assuming that the experiment has been designed so that there is no overlap between pulses, the first challenge is pulse selection.

3.3.3.2 Pulse selection

An experimental signal is shown in Fig. 3-7(a). Although PMMA has less damping capacity than other polymers, such as Polypropylene (PP [31, 32]), the amplitude still decays rapidly, and is similar to the noise after a distance of 19.5 m (20 round trips). Considering the signal-to-noise ratio and the increasing duration of the wave, leading to wave superposition, only the first 6 pulses were considered and only the first 4 averaged to yield the final results.

The raw signal in Fig. 3-7(a) was first de-noised using the MATLAB automatic wavelet-based de-noising function *wden*. Caution should be taken when choosing appropriate numerical de-noising functions because some of them may modify the pulse phase. The zero level of the pulse was then corrected, so that the mean strain amplitude before the first perturbation was zero.

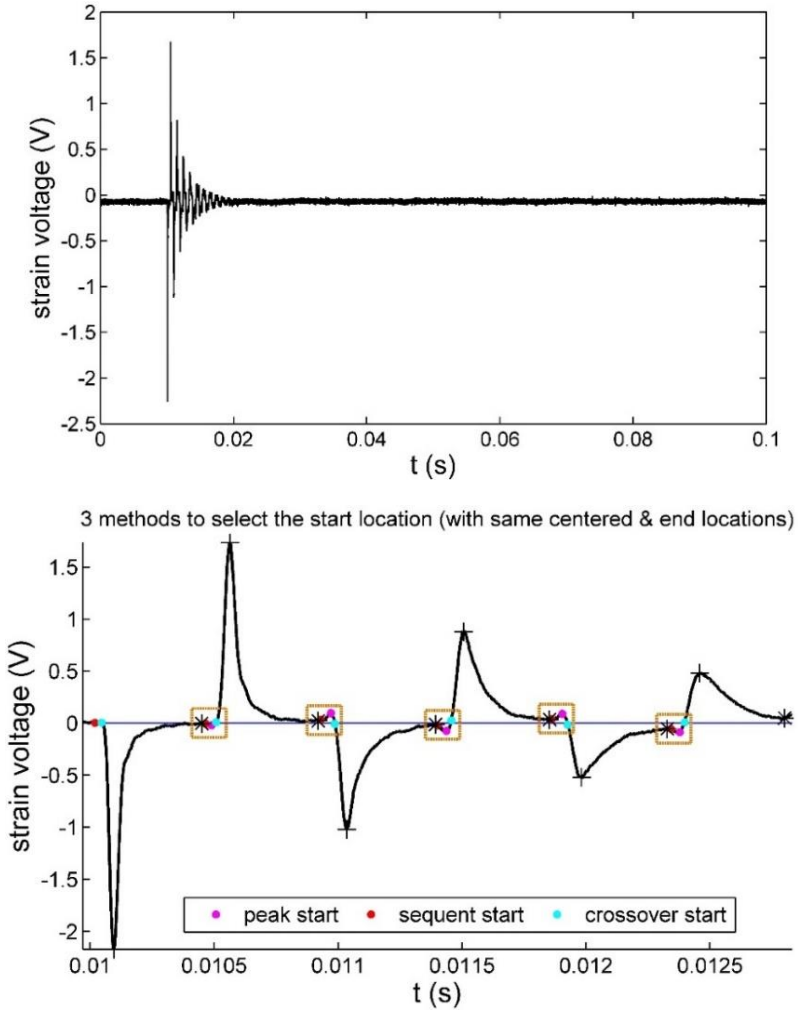


Figure. 3-7 Typical strain signal from PMMA (17.5 ℃). Top: (a) Raw signal, whole record length. Bottom: (b) Pulse selection (start points: red, magenta, cyan dots; end points: black stars; peaks: black squares).

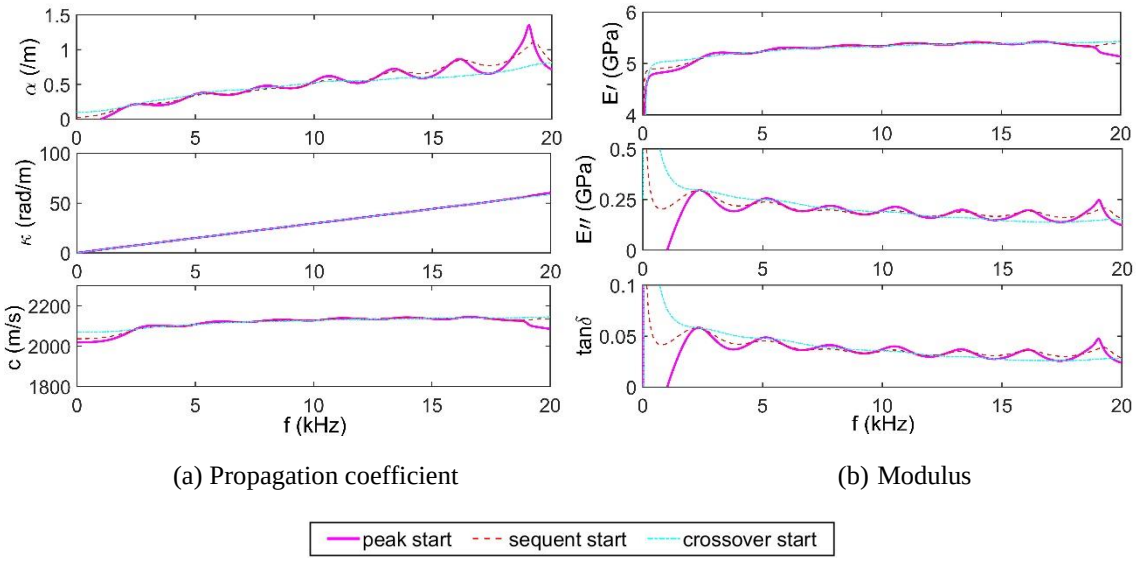
Fig. 3-7(b) shows the first six pulses of the signal. As expected, due to a combination of geometric and material dispersion the pulse length extends significantly during propagation; in this case most of the lengthening is a result of the viscoelastic nature of the bar material. For the later pulses, this causes partial overlapping of the tail of each pulse with the start of the subsequent one. Appropriate choice of the start and end points of each pulse should satisfy the expectation that the pulse selected contains all its own frequency components without overlapping with others.

Table. 3-3 Pulse details in Figure. 3-7(b)

Pulse No. / Selection method	1			2			3		
	Start time	End time	Duration	Start time	End time	Duration	Start time	End time	Duration
sequential start	0.01002	0.01045	430 us	0.01047	0.01092	450 us	0.01093	0.01139	460 us
warping peak start	0.01002	0.01045	430 us	0.01049	0.01092	430 us	0.01097	0.01139	420 us
zero crossover start	0.01005	0.01045	400 us	0.01051	0.01092	410 us	0.01099	0.01139	400 us
	4			5			6		
sequential start	0.0114	0.01185	450 us	0.0114	0.01185	450 us	0.0114	0.01185	450 us
warping peak start	0.01144	0.01185	410 us	0.01144	0.01185	410 us	0.01144	0.01185	410 us
zero crossover start	0.01146	0.01185	390 us	0.01146	0.01185	390 us	0.01146	0.01185	390 us

In addition to the overlapping, an abnormal ‘warping’ (indicated inside the brown rectangle) is observed at the junction of two adjacent pulses; it was shown later that this is not observed in the simulation signals (Chapter 5). This is thought to be caused either by the non-linearity of the PMMA bar or the strain gauge. It is thus natural to choose the end point of each pulse somewhere before the warping position. Determining the start point (except that of the first pulse), however, is more difficult as any position after the end point of the last pulse seems reasonable. Placing the start point too early means the selection may contain some information from the previous pulse; on the other hand, too late a start point will cause the loss of information from the pulse itself. In this study, three different methods, as shown in Fig. 3-7(b) and Table. 3-3, for choosing the start point have been considered: a sequential start point (red dots) following the end point of last pulse; the warping peak start point (magenta dots); and the zero crossover start point (cyan dots). Results derived using these 3 selection methods (with the same end point) were shown in Fig. 3-8 (the detailed derivation process was introduced later). It is found that different pulse selection methods lead to slightly different results, with the sequential and peak start methods giving larger attenuation coefficient, loss modulus, and loss factor values at high frequencies than the zero crossover start method. This is likely to be induced by the aforementioned reason: some information might be missing with the zero crossover start method. Despite this disadvantage, the zero crossover start method does yield more stable

results, as oscillations can be seen on the peak start and sequential start curves at a frequency interval of 2700 ~2900 Hz. These oscillations are believed to be induced by the window function effect: a rectangular window, with width associated with the selected pulse duration, is effectively applied to each pulse during signal processing, which results in an oscillating *sinc* function in the frequency domain after the Fourier transform. The frequency of the *sinc* function is determined by the window width, described further below (Fig. 3-11); for example, a window width equal to the pulse durations τ selected in Fig. 3-7(b), 390~470 μs, results in a sinc function with an oscillation on a frequency interval $\Delta f = \frac{1}{\tau} = 2130\sim2570\,Hz$. This is similar to the oscillation interval in propagation coefficient and modulus results. The window function, which was discussed later, is unavoidable in signal processing; but its effects can be alleviated by proper window function selection.



(a) Propagation coefficient (b) Modulus

Figure. 3-8 Results obtained using 3 pulse selection methods (17.5 ℃, no dispersion correction)

Hence, the reason the 'zero crossover start' method yields more stable results is that using this pulse selection method, all the 6 pulses selected possess almost the same duration (Table. 3-3), which helps cancel the window function effect to some extent when deriving the ratios of different pulses (Eq. 3.2(a)). The other selection methods give different pulse durations and thus the numerators and denominators of the ratios have different *sinc* function periods, leading to oscillating propagation coefficient and modulus results.

Another advantage of using the 'zero crossover start' method is that it can help reduce the energy leakage induced by a sudden truncation at the end of each pulse. All the pulses selected have been processed in a way such that they were first subtracted by the start value to ensure a zero start point, however because of the viscoelastic behaviour of the bar material they do not end at zero amplitude unless they have relaxed for a long enough period. Fig. 3-7(b) shows that the truncation effect becomes more significant in pulses that have travelled a long distance and evidently extended their lengths. In this sense, an appropriate choice of the start point is important because the start value, subtracted from all the other values in the pulse, will have an effect on the truncated value and thus the oscillating frequency interval. Using the 'zero crossover start' method minimizes this effect.

It should be noted that the 'oscillations' seen in Fig. 3-8 should be distinguished from the 'irregularities' indicated by Hillstrom [32]. In his research he noted that irregular results commonly occur at certain 'critical frequencies' defined by the condition that the distances between the measurement stations become integral multiples of a half wavelength. It was shown that these 'critical frequencies' were calculated to be 525 n Hz (for integer n). The oscillations here, however, are believed to be induced by a truncation of the time domain signal because the tails have no definite ends [55]. It is indicated by Welch *et al* [52] that, a discontinuity in time domain results in oscillations throughout the frequency data and the oscillation intensity depends on the truncation degree. Truncation of the signal also causes a loss of low frequency data even when the signal level is small. The oscillations caused by truncation can be reduced by averaging results obtained by using different truncation length [52]. Mousavi *et al.* found the oscillation phenomenon in testing PP using an aluminium rods SHPB setup [55], the oscillations in their modulus results are induced by the truncation of the time domain signals, which possess overlapping. The method they proposed for truncation correction can effectively reduce the oscillations in modulus results but it can only applied in processing the SHPB signals. They also suggested that, the truncation errors can be reduced by using longer bars or multi-point strain measurement for separation of waves.

It should also be noted that although there is deviation between the methods at frequencies below 2 kHz, it was shown later that these results are not reliable owing to the pulse length. Also excluded are those outside 20 kHz as very little energy is contained at these frequencies.

3.3.3.3 Zero Padding

After the pulses have been selected, there are two further challenges. Firstly, due to the extension of the pulse duration during propagation, the selected pulses may have different lengths; this will lead to difficulties in the later calculations, as the frequency resolution Δf_{min} in the FFT is

$$\Delta f_{min} = \frac{f_s}{N} = \frac{f_s}{signal\ duration \times f_s} = \frac{1}{signal\ duration}. \tag{3.5}$$

where $f_s = 1$ MHz is the sampling rate. Note that here 'pulse duration' to define the length of the pulse selected in the previous step while the term 'signal duration' refers to the length of the whole signal. It is thus seen that it is highly desirable for the lengths of all the pulses to be the same, so that the FFTs are sampled at the same frequency points (*i.e.* a uniform sampling rate) and the propagation coefficients can be calculated at each of these points using the ratios in Eq. (3.2a).

The other challenge is that the FFT of each selected pulse gives only information (especially phase) regarding the Fourier components of the selected pulse. To derive the propagation coefficient, however, *global* phase information is needed (Eq. (3.2a)): the attenuation coefficient is given by the magnitude ratio while the wavenumber issued by considering the phase difference between two traveling pulses. Mathematically, the phase of a pulse is associated with its location in the time domain, which is why non-phase-change functions must be used in de-noising.

In order to preserve the original relative global phase information from the raw signals, and to ensure a uniform frequency resolution for all the FFTs, a process called 'zero padding' was performed: the selected pulses are kept in their original position and padded with zeros, both before and afterwards as required, until each pulse becomes the same length as the whole recorded signal (in this case 0.1 s). Thus, after zero padding, every pulse is a separate signal which possesses the same 'signal length' (and thus the same $\Delta f_{min} = 10\,Hz$) regardless of the variable pulse durations selected in the previous step.

In addition, during the zero-padding process, compressive pulses with negative strain values were inverted. This simulates an infinite rod in which the wave is tensile and recorded at multiple equidistant strain gauge stations. It was noted later, however, that the best results were obtained by comparing either pairs of compressive pulses or tensile pulses, not compression to tension.

In order to obtain FFT information at any frequency, it is tempting to pad more to make the signal length as long as possible and improve frequency resolution Δf_{min}. This is correct in the sense that it gives continuous FFT values rather than discrete ones. However, mathematical investigation verifies that only the original signal provides 'real' and 'useful' information about the pulse itself, padding the original signal with zeros doesn't give extra information. The fact that spectral lines become denser after zero padding doesn't necessarily infer an improvement of the 'effective' minimum frequency resolution Δf_{min}; instead there is an interpolation between the non-padded FFT values, whilst the FFTs of both the non-zero-padded and the zero-padded signals share the same values at any given frequency. Hence it is meaningless to pad extra zeros, apart from those required for comparison between pulses as described above. Otherwise, one can expect to obtain information at any frequency just by measuring 1 set of data from experiment and then padding it with infinite zeros. To illustrate this point, an example of the Gaussian pulse (which is of similar shape to our experimentally collected pulses) and its FFTs (with and without zero padding) is shown in Fig. 3-9.

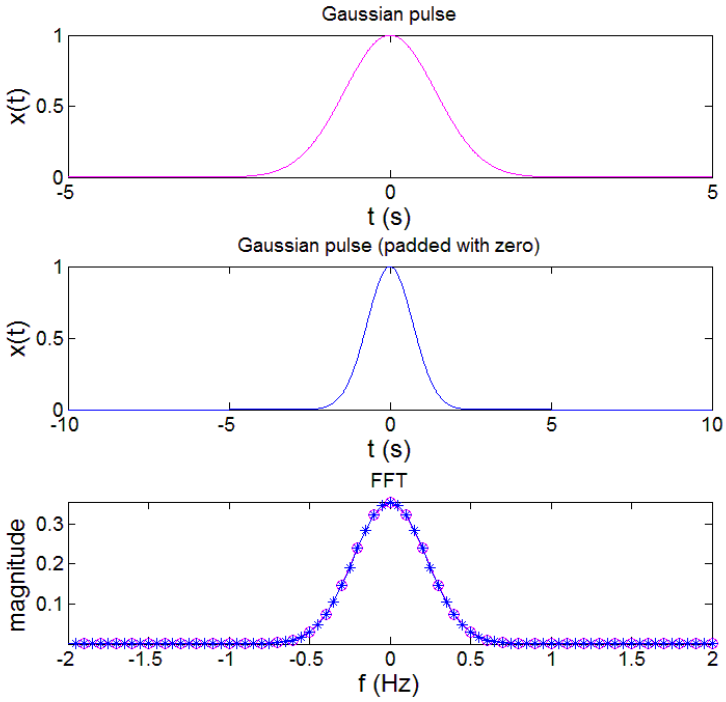


Figure. 3-9 Gaussian pulse and corresponding Fourier transforms

(Without zero padding: magenta lines & hollow circles; with zero padding: blue lines & stars)

3.3.3.4 Time domain attenuation estimate

Before moving to the frequency domain analysis, a rough estimate of the amplitude attenuation in the time domain was obtained roughly assuming a form of exponential magnitude decay

$$\frac{Max.\varepsilon_{i+1}}{Max.\varepsilon_i} = e^{-\alpha(x_{i+1}-x_i)}. \tag{3.6}$$

An example is given in Fig. 3-10, in which the strain amplitude was estimated to attenuate at a rate of $\alpha = 0.289\ m^{-1}$. It is noted, however, that time domain analysis gives no frequency information.

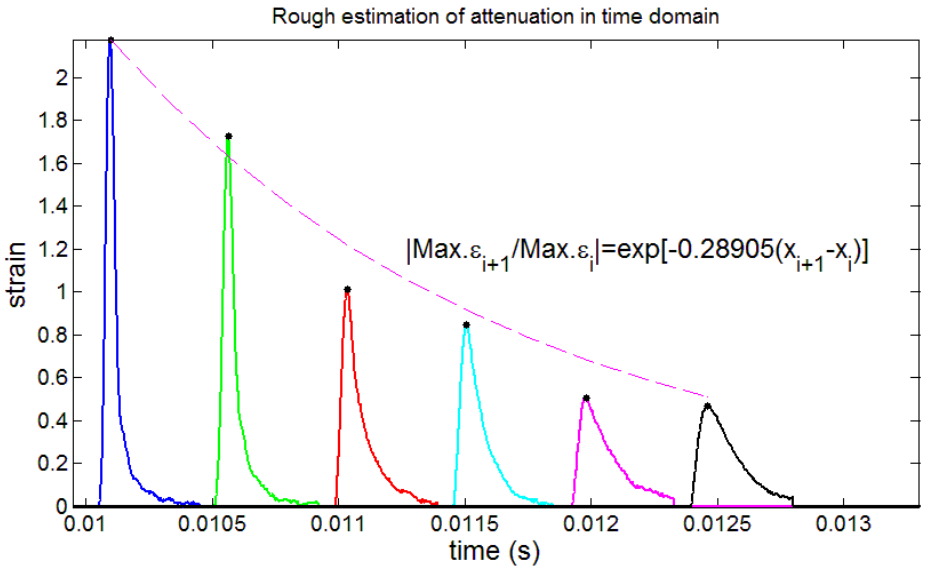


Figure. 3-10 A rough estimate of time domain attenuation ($T = 17.5\ ℃$)

3.3.3.5 Window function effects

In practice the signals processed have finite length; mathematically this behaves as though extracted from an infinite periodic signal, equivalent to multiplying the infinite signal by a rectangular window in time domain. Multiplication in time domain is equivalent to convolution in frequency domain (the convolution theorem): the FFT of a signal with finite length is actually a convolution of the FFT of the equivalent infinite periodic signal and the FFT of the rectangular window. If we were indeed dealing with a sample of an infinite periodic signal, various techniques could be applied to reduce the adverse window effects. However, in this case, since the whole pulse is measured, it is enough to be aware of the key features of the FFT and their implications for experimental design and interpretation.

In the time domain, a unit rectangular window $\sqcap(t/\tau)$ can be defined as

$$w(t) = \begin{cases} 1 & (|t| \le \tau/2) \\ 0 & (|t| > \tau/2) \end{cases} \tag{3.7}$$

in which τ is the window width. Its Fourier transform can be expressed as

$$W(f) = \frac{sin(\pi f \tau)}{\pi f}. \tag{3.8}$$

Imagine there is an infinite-duration signal $x(t)(-\infty < t < +\infty)$, the corresponding time domain truncated signal, which is exactly what is collected from experiments, is thus

$$x_T(t) = x(t) \times w(t)$$

in which the subscript T denotes truncation.

According to the convolution theorem, the Fourier transform of $x_T(t)$ is

$$X_T(f) = X(f) * W(f).$$

As the FFT of the rectangular window has unlimited bandwidth, as a result, although the frequency components contained in the original signal might be limited, the resulting FFT of a finite-length signal could be of unlimited bandwidth. This leads to spectral leakage (or 'energy leakage') at unwanted frequencies near the frequencies contained in the original signal.

The example presented in Fig. 3-11 helps illustrate the window function effect. Ideally, the FFT of an infinite-length cosine signal is a real Dirac function at frequencies f_0 and $-f_0$. If the infinite-length signal was truncated, energy leakage appears at frequencies nearby. Therefore, the spectral leakage will lead to a magnitude decrease at the frequencies expected.

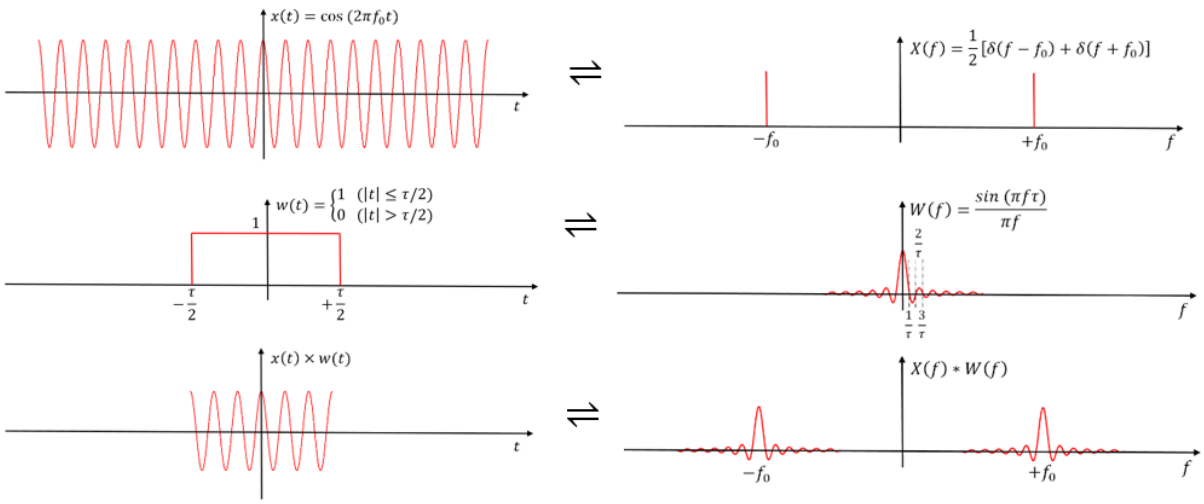


Figure. 3-11 Window function effect

In Fig. 3-12, windows with 3 different lengths (10, 5, 2.5 periods) are employed to generate signals with different lengths. It can be seen that a long enough window (such as 10 periods here) does help reduce spectral leakage and give accurate magnitudes as expected. Furthermore, non-integral period truncation may also lead to spectral leakage. Also shown in Fig. 3-12 is a comparison of the FFTs of the non-zero-padded and zero-padded signals. In both cases energy leakage is observed, and the statement that zero padding is equivalent to an interpolation of FFT is verified.

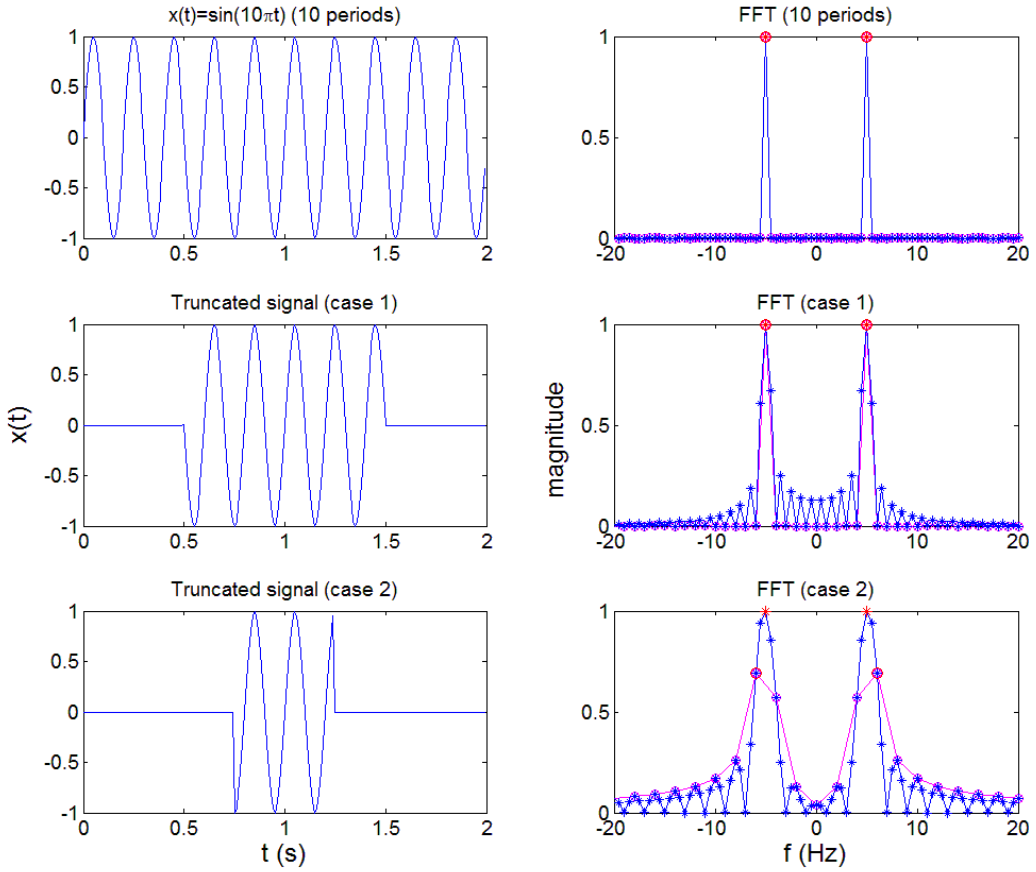


Figure. 3-12 Effects of window width on spectral leakage

(Without zero padding: magenta lines & hollow circles; with zero padding: blue lines & stars)

The window function effect is inevitable because only finite-length signals can be obtained in real experiments; thus a unity rectangular window, with its length equal to the pulse length selected, was automatically multiplied during Fourier transform. However, the effect can be reduced by manually choosing appropriate window types and lengths: measuring the signal over a long period, *i.e.* a wide enough window, or measuring a complete single pulse but artificially duplicating it to make a long-

duration signal; or choosing an appropriate window function that balances the main and side lobe magnitudes (*i.e.* minimize energy leakage), and the bandwidth (frequency resolution). Power-law windows (power-law functions of time), trigonometric windows (sine or cosine functions of time), and exponential windows (exponential functions of time) are the 3 commonly used window types. An ideal window function should have a narrow main lobe which gives relatively accurate magnitude and ensures a good frequency resolution, with quickly attenuated side lodes which yield less spectral leakage at the same time. However, in reality what happens is that a window function which focuses more on revealing the real magnitude normally possesses lower frequency resolution, and vice versa. For example, Hamming window (one of the trigonometric windows) can effectively reduce energy leakage as its side lobes attenuate quickly, but the frequency resolution is poor due to its wide main lode. How to choose an appropriate window is out of this thesis's vision and only the rectangular pulse $\sqcap(t/\tau)$ has been automatically multiplied in signal processing.

Ahonsi *et al.* [21] indicated that using Laplace transform rather than Fourier transform can help reduce the window function effects, an exponential window was multiplied to their signals before performing FFT, which is equivalent to doing Laplace transform and it effectively alleviated the inaccuracy in propagation coefficient at some critical frequencies induced by the window function.

3.3.3.6 Construction of experimental FFT results

After pulse selection and zero padding, each pulse inherits both its magnitude and position from the raw signal. These zero-padded signals are now ready for discrete Fourier transform (DFT) using the Matlab function *fft*. However, in order to obtain the best possible results, these pulses were first individually shifted to their signal centers--a process called 'pulse centering' which is essential to improve the signal-to-noise ratio at high frequencies.

Here I again use a Gaussian pulse to approximate the experimental signal and analytically illustrate the construction of the FFT curves (Fig. 3-13). As raw experimental pulses (Fig. 3-7(a)) are not normally located in the signal centre, to approximate the raw signal, the origin located Gaussian pulse is first shifted to $t=t_0$, which can be mathematically constructed by convoluting the centered Gaussian pulse with the shifted Dirac function $\delta(t-t_0)$ in the time domain. According to the

convolution theorem, the corresponding Fourier transform of the shifted Gaussian pulse is thus the product of their individual FFTs in frequency domain, which generates an oscillatory outline characteristic. For simplicity of analytical analysis, Fig. 3-13 assumes a continuous time domain signal (*i.e.* infinite sampling rate) of infinite duration; however, in practice data are always discrete and finite. This means that the final FFT values are also discrete, and the final oscillatory FFT values depend on both the signal itself as well as the Dirac function: the FFT of the Dirac function is continuous, while those of the experimental signal have a frequency resolution of Δf_{min}; by multiplication, the Dirac function FFTs are sampled with the frequency interval Δf_{min}, and the final FFT values are their products at the sampling points.

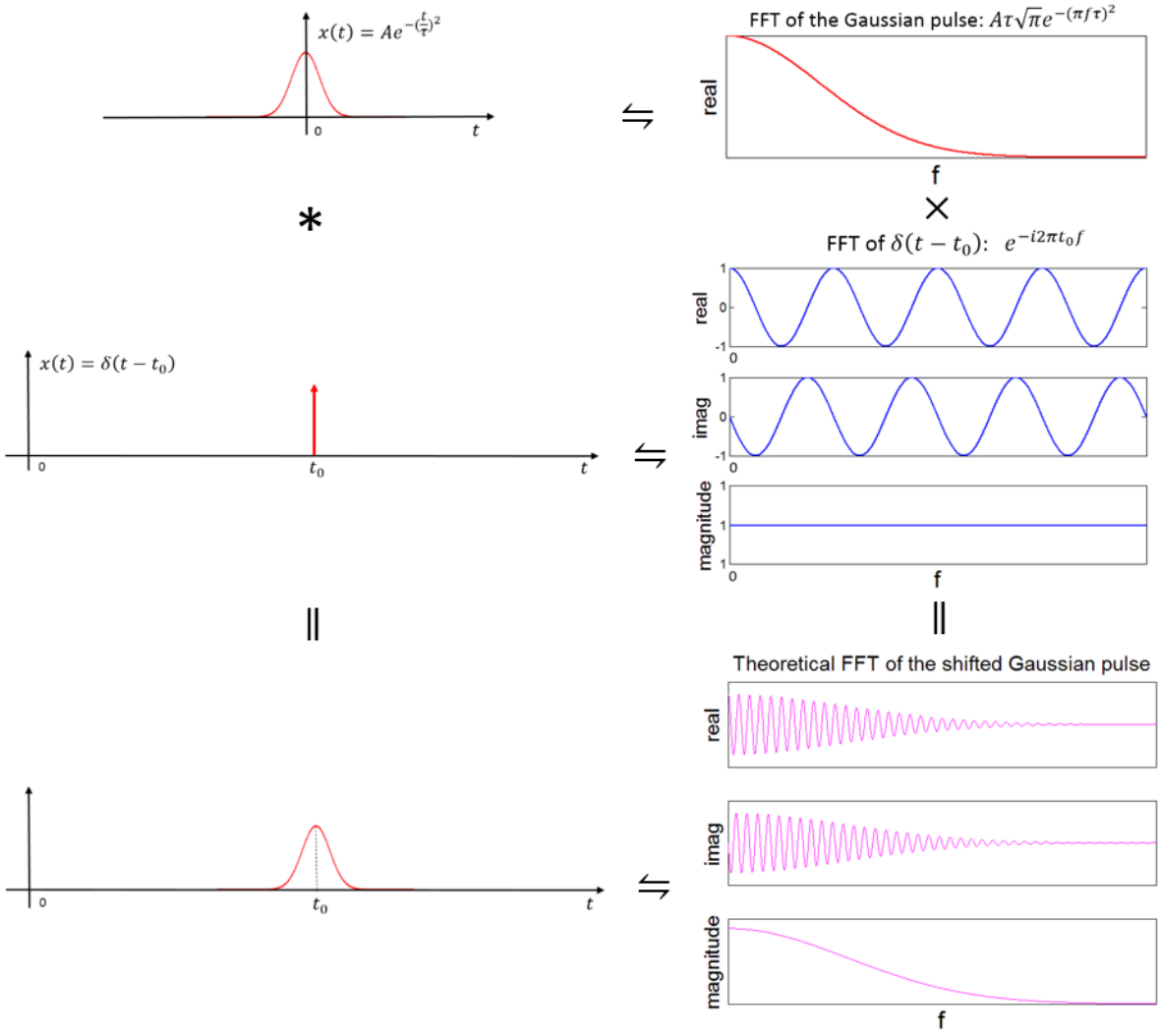


Figure. 3-13 Theoretical Fourier transform of a shifted Gaussian pulse with infinite length

Fig. 3-14(a) gives an example of the FFT of a set of raw experimental data. Theoretically, the highest frequency that can be achieved by FFT is

$$f_{h-FFT} = \frac{f_s}{2} = \frac{10^6}{2} = 5 \times 10^5\ Hz \tag{3.9}$$

where f_s is the sampling rate determined by the raw data (*1* MHz in this case).

The minimum frequency resolution Δf_{min} achieved is

$$\Delta f_{min} = \frac{f_s}{N} = \frac{f_s}{signal\ duration \times f_s} = \frac{1}{signal\ duration} = \frac{1}{0.1} = 10\ Hz \tag{3.10}$$

thus, it is seen that the minimum frequency resolution Δf_{min} is fixed and determined by the signal duration (which is the same for all the signals after zero padding). Increasing the sampling rate can help increase the highest frequency achieved in FFT, but only increasing the signal duration will help increase the minimum frequency resolution.

In order to maximise the usable data, we would ideally like to produce as large as possible FFT values to improve the signal-to-noise ratios even at high frequency. This can be realised if every one of these samples lies on a peak in the oscillating function (*i.e.* only these peaks of the Dirac function FFT are sampled). This is achieved in practice by fixing the oscillation of the FFT of the Dirac function to match Δf_{min}: a process called 'centering' before FFT. By observing the theoretical FFT derivation process, it is seen that the interaction between the minimum frequency resolution Δf_{min} of the signal itself and the oscillation $\frac{1}{t_0}$ of the shifted Dirac function $\delta(t - t_0)$ plays a key role in determining the final FFT values. As the minimum frequency resolution Δf_{min} is fixed by experimental settings, only the oscillation of the Dirac function, is adjustable. Since this oscillation occurs with peaks spaced at $\frac{1}{t_0}$, for a shift of t_0 in the time signal, the criterion is equivalent to saying that the pulse must be centred in the time signal, since this will give peaks at $\frac{1}{t_0} = \frac{2}{signal\ duration} = 2\Delta f_{min}$, and hence all the peaks (positive and negative) were sampled in the FFT, giving the envelope of the continuous Fourier Transform of the underlying pulse.

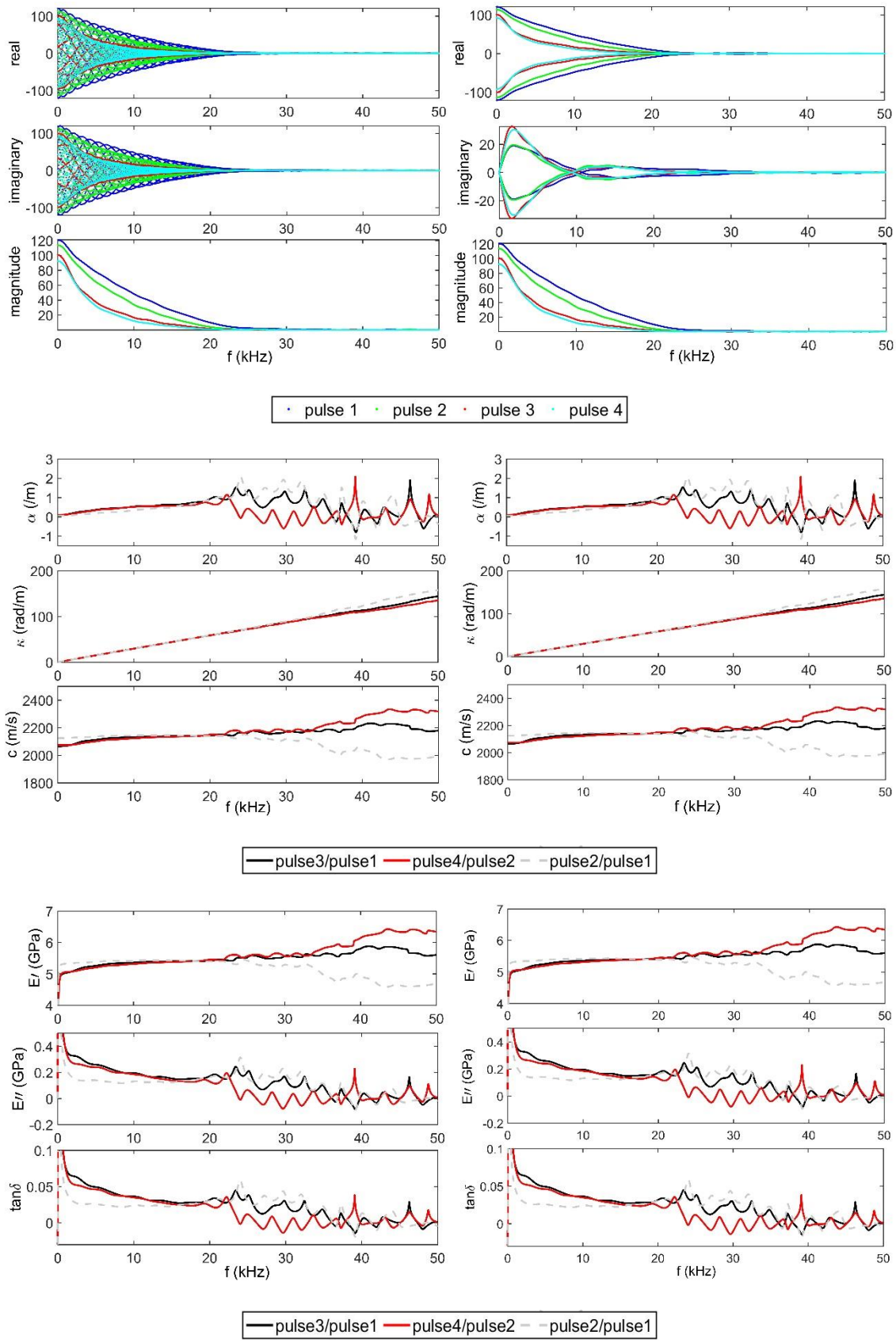


Figure. 3-14 FFT, propagation coefficient, and modulus results of an experimental signal (17.5 ℃). Top: (a) FFT (left: without centering, right: with centering). Middle: (b) Propagation coefficient (left: without centering, right: with centering). Bottom: (c) Modulus (left: without centering, right: with centering)

A comparison between the centered and non-centered signal FFTs is presented in Fig. 3-14(a). As centering a pulse corresponds to modifying its phase by multiplying a $e^{i\Delta\varphi}$ in FFT, it changes the real and imaginary parts of the FFT, but maintains the same magnitude. Therefore, centering a pulse does not extend the highest frequency identifiable for the attenuation coefficient, but it may help when calculating the wavenumber and thus the wave speed using Eq. (3.2a), and further the modulus using Eq. (2.29a). Note that the original relative position information was partially removed after shifting these pulses to the same signal centre. The lost phase information must be compensated when calculating the wavenumber using Eq. (3.2a).

Unfortunately, although there is clear improvement in the FFT values in Fig. 3-14(a) as expected, there is little difference when deriving the propagation coefficient and modulus in Fig. 3-14 (b) and (c). However, the necessity of performing centering still exists: when calculating the wavenumber using the ratio $\tilde{\varepsilon}(x_1,\omega)/\tilde{\varepsilon}(x_2,\omega)$, without centering, errors might be generated due to small number division at high frequencies especially in the presence of noise, centering helps maximize both the real and imaginary parts of $\tilde{\varepsilon}(x_1,\omega)$ and $\tilde{\varepsilon}(x_2,\omega)$, which increases the SNR for each pulse; however, still the original magnitudes and compensated phase information of the raw signals were used to derive material properties. This explains why the results in Fig. 3-14(b) look pretty much the same, but in some extreme cases, they might deviate from each other as some errors, induced by the small number division and the low SNR of each signal, may be contained in the non-centered signals. Note that, no dispersion correction has been performed in both cases.

3.3.3.7 Correction of geometric dispersion

Theoretical basis

Geometric dispersion of stress waves in slender rods occurs even in purely elastic materials. It is caused by radial inertia in the bar material, and becomes significant when the diameter of the rod is of the same order as the wavelength or larger [18, 39, 56]. Due to dispersion, waves are distorted during propagation because different frequencies travel at different speeds. As high frequency components possess shorter wavelength, they tend to disperse more and travel at a lower velocity than those at lower frequency [16]. Effectively, this renders invalid 1D assumption made in deriving

the wave equation. Davies [35] has shown that a pulse wavelength must be at least 10 times the diameter of the rod to avoid appreciable dispersion. Otherwise, the effects of geometric dispersion may need to be removed in order to accurately obtain the underlying material response.

It is of use to discuss how the dispersion affects the analysis results. Kolsky [16] shows that the high frequency oscillations seen in experimental signals are due to high frequency components travelling at a lower phase velocity than those of low frequency, and assigns this to the effect of lateral inertia. These are often described as Pochhammer-Chree oscillations. Gorham [56] also assumes the frequency-dependent phase velocity $c_n(\omega)$ was induced by lateral inertia in his dispersion correction trials. Zhao and Gary [29], however, show that in viscoelastic materials, the geometric dispersion affect not only affect the phase velocity but also the attenuation coefficient, such that that the 1D analysis underestimates the damping coefficient and overestimates the phase velocity. They proposed a 3D analysis [29] which gives more accurate results. Bacon [18] concludes that there is either an increasing or decreasing phase velocity with increasing frequency depending on the relative importance of the geometric and viscoelastic effects. This is consistent with Kolsky's note that the geometric effect is in the opposite sense to that produced by the polymer properties, which would result in the phase velocity increasing with frequency [16].

Theoretically, the dispersion effect can be corrected directly using the Pochhammer frequency equation, however, the parameters in this equation become complex when it comes to viscoelastic materials, which makes it very difficult or even impossible to solve. In addition, pre-determined material constants such as the viscoelastic Proni series are required in order to effectively perform the correction. Benatar *et al.* [33] formulated corrections for geometric dispersion for both the attenuation coefficient and phase velocity by assuming an approximate Poisson's ratio in a simplified Pochhammer frequency equation, and showed that the frequency-dependent viscoelastic properties can be accurately determined up to 55 kHz for a 12 mm PMMA rod. Both numerical and empirical methods have been proposed by Zhao and Gary and Gorham *et al*. (Zhao and Gary [13], Gorham [56]) for dispersion correction. The numerical correction method adopted by Gorham [56] is based on the observation that the dispersion is caused by the frequency dependence of phase velocity on geometry, and thus a geometry dependent phase shift was applied after performing FFT on the

dispersed frequency components. This helps correct the derived wavenumber and thus the phase velocity, however, Zhao and Gary stated that this may be wrong, as the effect of geometric dispersion on the damping coefficient is not included, and accordingly a simple correction method was proposed based on the assumption that the Poisson's ratio is a real constant.

The requirement that the wavelength $\lambda(\omega)$ should be at least 10 times larger than the rod diameter d [35], leads to the following relations

$$f \leq f_{h-1D} = \frac{c}{10 \times rod\ diameter},\ |\kappa(\omega)| \leq \frac{0.2\pi}{d},\ c(\omega) \geq \frac{5\omega d}{\pi}. \tag{3.11}$$

In the PMMA rod impact experiments performed in the current study, the rod diameter is 13 mm and the shortest wavelength at which appreciable energy travels is about 105 mm, at a frequency of 20,000 Hz, which is almost 8 times the diameter; we expect slight dispersion frequencies over 16 kHz. Benatar *et al.* [33] also found that the usable frequency range for determining the phase velocity and attenuation for a 12 mm rod is about 20 kHz.

In addition, based on a 3D solution for cylindrical rod, Zhao and Gary proposed an empirical critical frequency f_c up to which the 1D analysis can be used with less than 5% error

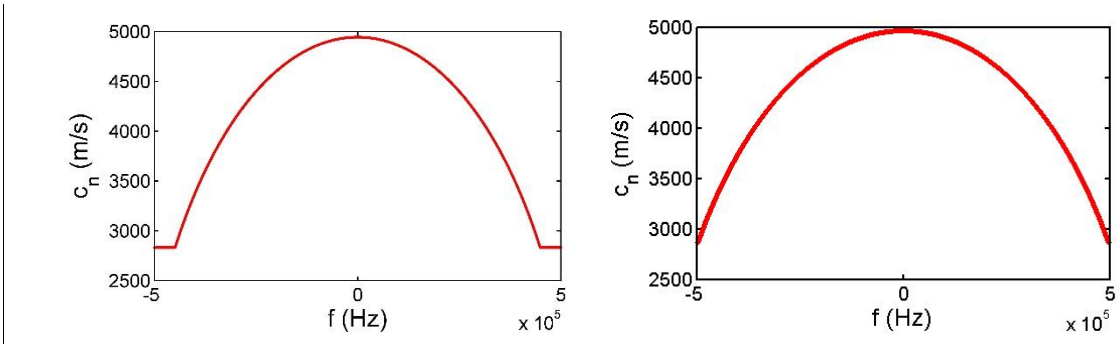
$$f_c = \frac{c_L}{4d} \tag{3.12}$$

in the PMMA case, this upper critical frequency is calculated to be ~40,000 Hz.

Because these calculations indicate that geometric dispersion may affect the highest frequencies in the current study, the phase shift method proposed by Gorham [56] has been employed to process both the experimental and simulation data.

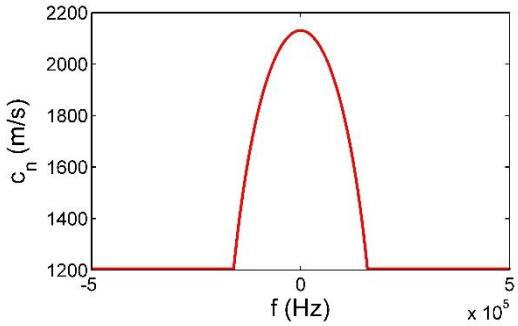
The quality of phase correction depends on the dispersive wave speed profile adopted. As stated before, there are a number of wave theories to describe the wave propagation even in perfectly elastic bars, and different theories lead to different wave speed profiles. Bancroft [57] numerically solved the Pochhammer-Chree frequency equation and derived the velocity profile as functions of the Poisson's ratio and the ratio of the diameter of the bar to the wavelength. Gorham [56] interpolated Bancroft's tabulated data to numerically correct the dispersion effect. Anderson [27] compared different phase velocity profiles derived using a series of approximated Pochhammer-Chree frequency equations of different orders. As all these velocity calculation methods give similar values

for frequencies up to 20,000 Hz; for simplicity, here a dispersive wave speed profile, which is based on Love's theory, was adopted in dispersion phase correction when processing Ti, Magnesium and PMMA rod data (Fig. 3-15). The initial information (diameter, instantaneous modulus, density, Poisson's ratio) used in generating the dispersive wave speed profile was either collected from measurements or estimated based on existing knowledge. Note that, although only positive frequencies are used to calculate material properties, as Fourier components are symmetric, if it is required to reconstruct the original pulse with the dispersion removed, negative frequencies in the FFT must be retained, hence the dispersion profile also contains these frequencies.



(a) Ø12.70 mm Ti rod ($\rho = 4500$ kg/m^3, $E = 110\ GPa, \upsilon = 0.32$)

(b) Ø12.70 mm Mg rod ($\rho = 1799$ kg/m^3 , E=44.5 GP$a, \upsilon = 0.29$)



(c) Ø13.00 mm PMMA rod ($\rho = 1180$ kg/m^3, E=5.36 GP$a, \upsilon = 0.38$)

Figure. 3-15 Love-based dispersive wave velocity profiles for dispersion correction

Here the detailed process for deriving the velocity profile was presented. We start by revising the governing equation of axial motion [36]

$$\frac{\partial^2 u}{\partial x^2} + \frac{\upsilon^2 \rho J}{EA}\frac{\partial^4 u}{\partial x^2 \partial t^2} = \frac{1}{E/\rho}\frac{\partial^2 u}{\partial t^2} \qquad \text{(Love's theory)} \qquad (3.13a)$$

$$\frac{\partial \sigma}{\partial x} = \rho \frac{\partial^2 u}{\partial t^2} - \rho \upsilon^2 R^2 \frac{\partial^4 u}{\partial x^2 \partial t^2} \qquad \text{(Aleyaasin [34]).} \qquad (3.13b)$$

where υ and J are Poisson's ratio and second polar moment of area, respectively. Compared to the 1D equation, a radial inertia term has thus been inserted in the equations. Whilst Love's equation was originally intended for elastic materials it can be used for viscoelastic rods by using the complex modulus E^* instead of E [27]. The Aleyaasin equation is based on the 'equivalent mass method', and as it is simply a modified expression of Newton's second law, it is independent of mechanical mode. The two equations are equivalent.

Substituting the general solution Eq. (2.14) into Eq. (3.13) yields an updated relation between the propagation coefficient $\gamma(\omega)$ and the modulus [28, 32, 34]

$$E^*(\omega) = \frac{-\rho\omega^2}{\gamma^2(\omega)} \times [1 - \gamma^2(\omega)\upsilon^2 R^2] = \frac{-\rho\omega^2}{\gamma^2(\omega)} + \rho\omega^2\upsilon^2 R^2 \tag{3.14a}$$

$$\gamma^2(\omega) = \frac{-\rho\omega^2}{E^*(\omega) - \frac{\rho\omega^2\upsilon^2 a^2}{2}} = \frac{-\rho\omega^2}{E^*(\omega) - \rho\omega^2\upsilon^2 R^2} \tag{3.14b}$$

where υ is the frequency-dependent Poisson's ratio, a is the bar radius and R the radius of gyration of the solid circular cross-section,

$$\mathrm{R} = \frac{a}{\sqrt{2}}.$$

Eq. (3.14a) and Eq. (3.14b) are the equations that govern the relationship between the dispersed/undispersed wave propagation coefficient and undispersed/dispersed modulus. A comparison between the 1D relation Eq. (2.27) and the 3D relation Eq. (3.14a) reveals that, the 3D dispersion effect is associated with material density, Poisson's ratio, lateral sample size and frequency; the intrinsic material modulus can be obtained either by substituting the 1D propagation coefficient γ into Eq. (2.27), or by substituting the 3D γ into Eq. (3.14a).

If a dispersive propagation γ^{3D} is substituted into Eq. (3.14a), the intrinsic material modulus $E^*(\omega)$ can be derived. As the intrinsic modulus $E^*(\omega)$ and the 1D propagation coefficient γ^{1D} conform to Eq. (2.27), the relationship between the 1D and 3D propagation coefficient can be yielded:

$$\gamma^{1D^2} = \frac{-\rho\omega^2}{\frac{-\rho\omega^2}{\gamma^{3D^2}(\omega)} \times [1 - \gamma^{3D^2}(\omega)\upsilon^2 R^2]} = \frac{\gamma^{3D^2}}{1 - \gamma^{3D^2}(\omega)\upsilon^2 R^2}. \tag{3.15}$$

Based on Eq. (3.14b), in purely elastic materials the following inertia-induced dispersive velocity can be derived

$$c(\omega) = \frac{\omega}{\kappa(\omega)} = \sqrt{\frac{E}{\rho} - \frac{\omega^2 \upsilon^2 a^2}{2}} \tag{3.16}$$

Further,

$$c(\omega) = \frac{c_L}{\sqrt{1+2\pi^2 \upsilon^2 \frac{a^2}{\lambda^2}}} \tag{3.17}$$

where E is the frequency-independent material modulus and c_L is the 1D classical elastic wave speed defined in Eq. (2.7).

At low frequency (*e.g.* $f \leq 20\ kHz$), this dispersive wave speed profile is quite close to that used by Bancroft [57]. As expected, the phase velocity tends towards c_0 at low frequencies [56]; however, it becomes imaginary as frequency increases, which is not correct. In this study, as the Rayleigh wave velocity acts as the limiting velocity for a bar [27, 56], those speeds below the Rayleigh value are replaced with the Rayleigh velocity. Although this introduces a sharp inflection point this lies far beyond the frequency range of interest for the current research (0-20,000Hz): normally, little information is carried by the signal in this limiting velocity region.

When dealing with experimental/simulation data, an estimate of the elastic modulus E, which corresponds to the classical wave speed c_0, must be given in order to determine the dispersive wave speed profile. Also, to accurately determine the profile, the density and Poisson's ratio must be known. The quality of dispersion correction can be checked by examining the degree of distortion during wave propagation.

It should be noted that there are also a number of Rayleigh velocity computation methods available. Here an approximation method employed by Pichugin [58] was adopted to approximate the Rayleigh velocity

$$v_R \approx \left[\frac{256}{293} + \upsilon\left(\frac{60}{307} - \upsilon\left(\frac{4}{125} + \upsilon\left(\frac{5}{84} + \frac{4}{237}\upsilon\right)\right)\right)\right] \times \sqrt{\frac{\mu}{\rho}} \tag{3.18}$$

where μ is the shear modulus. This approximation gives a relative error below 0.05% for $-1 < \upsilon < 1/2$.

Model-dependent geometric dispersion correction

Based on Eq. (3.14), the relation between the propagation coefficient and modulus (Eq. (2.27)) can be updated taking the inertia effect into account

$$E'(\omega)=\frac{\rho\omega^2(\kappa^2-\alpha^2)}{(\kappa^2+\alpha^2)^2}+\rho\omega^2\upsilon^2R^2,\quad E''(\omega)=\frac{\rho\omega^2(2\kappa\alpha)}{(\kappa^2+\alpha^2)^2},\ tan\delta=\frac{2}{\frac{\kappa}{\alpha}-\frac{\alpha}{\kappa}+\frac{(\kappa^2+\alpha^2)^2\nu^2R^2}{\kappa\alpha}}. \tag{3.19a}$$

$$\alpha^2=\frac{\rho\omega^2}{2}*\frac{\sqrt{[E'(\omega)-\rho\omega^2\upsilon^2R^2]^2+E''^2}-[E'(\omega)-\rho\omega^2\upsilon^2R^2]}{[E'(\omega)-\rho\omega^2\upsilon^2R^2]^2+E''^2},$$

$$\kappa^2=\frac{\rho\omega^2}{2}*\frac{\sqrt{[E'(\omega)-\rho\omega^2\upsilon^2R^2]^2+E''^2}+[E'(\omega)-\rho\omega^2\upsilon^2R^2]}{[E'(\omega)-\rho\omega^2\upsilon^2R^2]^2+E''^2}, \tag{3.19b}$$

$$c=\frac{\omega}{\kappa}.$$

Again, Eq. (3.19a) and Eq. (3.19b) are the relationships between the dispersed/undispersed modulus and the undispersed/dispersed propagation coefficient considering 3D effects. Note that, if the dispersed propagation coefficient (α^{3D},κ^{3D}) is substituted into Eq. (3.19a), the intrinsic modulus $E^*(\omega)$ will result; similarly, substituting the dispersed modulus $E^{3D*}(\omega)$ into Eq. (3.19b) will yield the real intrinsic propagation coefficient.

As an analytical illustration, a simple 1-term S.L.S Maxwell model is employed to numerically demonstrate the difference between the corrected and uncorrected results. The wave equation represented by the S.L.S Maxwell model can be obtained by making use of the equilibrium equation (2.8), the compatibility equation (2.10), and the constitutive equation (2.44) [34]

$$\rho\upsilon^2R^2\frac{\partial^5u}{\partial x^2\partial t^3}+\frac{\rho}{\tau}\upsilon^2R^2\frac{\partial^4u}{\partial x^2\partial t^2}+(k_1+k_e)\frac{\partial^3u}{\partial x^2\partial t}-\rho\frac{\partial^3u}{\partial t^3}-\frac{\rho}{\tau}\frac{\partial^2u}{\partial t^2}+\frac{k_e}{\tau}\frac{\partial^2u}{\partial x^2}=0. \tag{3.20}$$

Substituting $u(x,t)=Ae^{i(\omega t\pm f_1x)}$ and $f_1=\kappa-i\alpha$ into the above wave equation gives the expressions of the corrected κ and α [34]

$$\kappa(\omega)^2=\frac{\rho\omega^2}{2k_e}\left\{\sqrt{\frac{1+\omega^2\tau^2}{\omega^2\tau^2\left[\left(1+\frac{k_1}{k_e}\right)-\frac{\rho\upsilon^2R^2\omega^2}{k_e}\right]^2+(1-\frac{\rho\upsilon^2R^2\omega^2}{k_e})^2}}+\frac{\omega^2\tau^2\left[\left(1+\frac{k_1}{k_e}\right)-\frac{\rho\upsilon^2R^2\omega^2}{k_e}\right]+\left(1-\frac{\rho\upsilon^2R^2\omega^2}{k_e}\right)}{\omega^2\tau^2\left[\left(1+\frac{k_1}{k_e}\right)-\frac{\rho\upsilon^2R^2\omega^2}{k_e}\right]^2+\left(1-\frac{\rho\upsilon^2R^2\omega^2}{k_e}\right)^2}\right\}$$

$$\alpha(\omega)^2=\frac{\rho\omega^2}{2k_e}\left\{\sqrt{\frac{1+\omega^2\tau^2}{\omega^2\tau^2\left[\left(1+\frac{k_1}{k_e}\right)-\frac{\rho\upsilon^2R^2\omega^2}{k_e}\right]^2+(1-\frac{\rho\upsilon^2R^2\omega^2}{k_e})^2}}-\frac{\omega^2\tau^2\left[\left(1+\frac{k_1}{k_e}\right)-\frac{\rho\upsilon^2R^2\omega^2}{k_e}\right]+\left(1-\frac{\rho\upsilon^2R^2\omega^2}{k_e}\right)}{\omega^2\tau^2\left[\left(1+\frac{k_1}{k_e}\right)-\frac{\rho\upsilon^2R^2\omega^2}{k_e}\right]^2+\left(1-\frac{\rho\upsilon^2R^2\omega^2}{k_e}\right)^2}\right\}. \tag{3.21}$$

A summary of the analytical S.L.S Maxwell propagation coefficient and modulus considering and without considering the inertia induced 3D effect was presented in Table. 3-4. It is seen that the geometric dispersion generally leads to an increase in attenuation coefficient and wavenumber, and a drop in phase speed. It has been analytically verified that, either substituting the 1D propagation coefficient expression (Eq. (2.48)) into the 1D relation Eq. (2.27), or substituting the 3D dispersed propagation coefficient (Eq. (3.21)) into the 3D relation (Eq. (3.19a)) leads to the same intrinsic material modulus in the right column of Table. 3-4—these represent the two options to cancel the geometric dispersion effect: either remove dispersion from signals to produce dispersion-excluded propagation coefficient first, and then follow a standard 1D calculation using Eq. (2.27); or without any pre-cancellation but use the revised propagation coefficient-modulus relations (Eq. (3.19a)). Both methods are effective and equivalent and can yield real intrinsic material modulus. The first method is defined as the 'forehead cancellation method' which was employed in processing both the experimental and simulation data; in this section a known model is employed to analytically illustrate the second method, as follows.

The 1D and 3D analytical $c(w)$ and $\alpha(\omega)$ curves for waves propagating in a rod made from a material described by a 1-term Prony model, which represents a circular PMMA rod, are presented in Fig. 3-16 with the following material properties, which have been derived by fitting the experimental results obtained later.

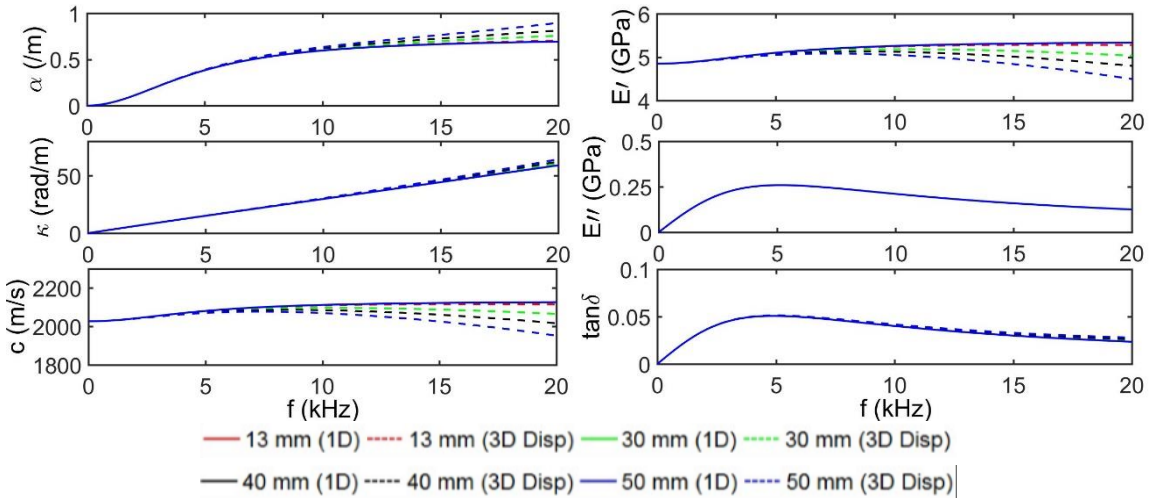
$E_0 = k_e + k_1 = 5.367$ GPa, $\bar{g}_1^p = \bar{k}_1^p = 0.09651$, $\tau_1^G = \tau_1^K = 30.88$ μs

$k_e = E_0\left(1 - \bar{g}_1^p\right) = 4.849\ GPa,$ $k_1 = E_0\bar{g}_1^p = 0.5179$ GPa

$\rho = 1180\frac{\text{kg}}{\text{m}^3}$, Poisson's ratio $\upsilon = 0.38$, $d = 0.013$ m, $R = \frac{0.013}{2\sqrt{2}} = 0.004596$ m

In Fig. 3-16, the 3D 'nominal' propagation coefficient was calculated using Eq. (3.21), while the resulting 'nominal' modulus was calculated still using the 1D relation Eq. (2.29a), which generates errors. It is observed from the figure that, with a rod diameter of 13 mm, small differences can again be seen in the attenuation and velocity values for frequencies up to 20 kHz, this is because the dispersion term $\frac{\rho\upsilon^2\mathrm{R}^2\omega^2}{\mathrm{k_e}}$ in Eq. (3.21) is small. Appreciable changes can only be seen in the

propagation coefficient for diameters 30, 40 and 50 mm, and it becomes more critical for larger diameters and higher frequencies. Specifically, geometric dispersion leads to an increase in *both* attenuation coefficient and wavenumber, and a decrease in phase velocity for high frequency components. This indicates that high frequencies will travel at a lower wave speed, which is seen as 'high frequency oscillation tails' and results in an extension in the duration of the wave as it propagates. Fig. 3-16(b) shows that, by using the 3D theories by Aleyaasin [34] and Love [36], the inertia induced dispersion effect can be accurately cancelled and the intrinsic material modulus be recovered. Therefore, in all the following data analysis process, the first dispersion correction method, based on these theories, was adopted.



(a) propagation coefficient (b) modulus

Figure 3-16. 1-term S.L.S Maxwell model-based propagation coefficient and modulus: $d = 13, 30, 40, 50\ mm$

Table. 3-4 A comparison of the 1D and 3D analytical S.L.S Maxwell propagation coefficient and modulus

	$[E'(\omega), E''(\omega), tan\delta(\omega)]$ & $[\alpha(\omega), \kappa(\omega), c(\omega)]$ (model-independent)	$[\alpha(\omega), \kappa(\omega), c(\omega)]$ & $[k_e, k_1, \tau]$ (S.L.S Maxwell materials)	$[E'(\omega), E''(\omega), tan\delta(\omega)]$ & $[k_e, k_1, \tau]$ (S.L.S Maxwell materials)
1D	$\begin{cases} E'(\omega) = \frac{\rho\omega^2(\kappa^2-\alpha^2)}{(\kappa^2+\alpha^2)^2} \\ E''(\omega) = \frac{\rho\omega^2(2\kappa\alpha)}{(\kappa^2+\alpha^2)^2} \\ tan\delta(\omega) = \frac{2}{\frac{\kappa}{\alpha}-\frac{\alpha}{\kappa}} \end{cases}$ $\begin{cases} \alpha^2(\omega) = \frac{\rho\omega^2}{2} * \frac{\sqrt{E'^2+E''^2}-E'}{E'^2+E''^2} \\ \kappa^2(\omega) = \frac{\rho\omega^2}{2} * \frac{\sqrt{E'^2+E''^2}+E'}{E'^2+E''^2} \\ c(\omega) = \frac{\omega}{\kappa(\omega)} \end{cases}$	$\begin{cases} \alpha^2(\omega) = \frac{\rho\omega^2}{2k_e}\left\{\sqrt{\frac{1+\omega^2\tau^2}{\omega^2\tau^2\left(1+\frac{k_1}{k_e}\right)^2+1}} - \frac{\omega^2\tau^2\left(1+\frac{k_1}{k_e}\right)+1}{\omega^2\tau^2\left(1+\frac{k_1}{k_e}\right)^2+1}\right\} \\ \kappa^2(\omega) = \frac{\rho\omega^2}{2k_e}\left\{\sqrt{\frac{1+\omega^2\tau^2}{\omega^2\tau^2\left(1+\frac{k_1}{k_e}\right)^2+1}} + \frac{\omega^2\tau^2\left(1+\frac{k_1}{k_e}\right)+1}{\omega^2\tau^2\left(1+\frac{k_1}{k_e}\right)^2+1}\right\} \\ c(\omega) = \frac{\omega}{\kappa(\omega)} \end{cases}$	$\begin{cases} E'(\omega) = k_e + \frac{k_1\omega^2\tau^2}{1+\omega^2\tau^2} \\ E''(\omega) = \frac{k_1\omega\tau}{1+\omega^2\tau^2} \\ \tan\delta(\omega) = \frac{k_1\omega\tau}{k_e+(k_e+k_1)\omega^2\tau^2} \end{cases}$
3D	$\begin{cases} E'(\omega) = \frac{\rho\omega^2(\kappa^2-\alpha^2)}{(\kappa^2+\alpha^2)^2} + \rho\omega^2 v^2R^2 \\ E''(\omega) = \frac{\rho\omega^2(2\kappa\alpha)}{(\kappa^2+\alpha^2)^2} \\ tan\delta(\omega) = \frac{2}{\frac{\kappa}{\alpha}-\frac{\alpha}{\kappa}+\frac{(\kappa^2+\alpha^2)^2v^2R^2}{\kappa\alpha}} \end{cases}$ $\begin{cases} \alpha^2(\omega) = \frac{\rho\omega^2}{2} * \frac{\sqrt{(E'-\rho\omega^2v^2R^2)^2+E''^2}-(E'-\rho\omega^2v^2R^2)}{(E'-\rho\omega^2v^2R^2)^2+E''^2} \\ \kappa^2(\omega) = \frac{\rho\omega^2}{2} * \frac{\sqrt{(E'-\rho\omega^2v^2R^2)^2+E''^2}+(E'-\rho\omega^2v^2R^2)}{(E'-\rho\omega^2v^2R^2)^2+E''^2} \\ c(\omega) = \frac{\omega}{\kappa(\omega)} \end{cases}$	$\begin{cases} \alpha^2(\omega) = \frac{\rho\omega^2}{2k_e}\left\{\sqrt{\frac{1+\omega^2\tau^2}{\omega^2\tau^2\left[\left(1+\frac{k_1}{k_e}\right)-\frac{\rho v^2R^2\omega^2}{k_e}\right]^2+(1-\frac{\rho v^2R^2\omega^2}{k_e})^2}} - \frac{\omega^2\tau^2\left[\left(1+\frac{k_1}{k_e}\right)-\frac{\rho v^2R^2\omega^2}{k_e}\right]+\left(1-\frac{\rho v^2R^2\omega^2}{k_e}\right)}{\omega^2\tau^2\left[\left(1+\frac{k_1}{k_e}\right)-\frac{\rho v^2R^2\omega^2}{k_e}\right]^2+\left(1-\frac{\rho v^2R^2\omega^2}{k_e}\right)^2}\right\} \\ \kappa^2(\omega) = \frac{\rho\omega^2}{2k_e}\left\{\sqrt{\frac{1+\omega^2\tau^2}{\omega^2\tau^2\left[\left(1+\frac{k_1}{k_e}\right)-\frac{\rho v^2R^2\omega^2}{k_e}\right]^2+(1-\frac{\rho v^2R^2\omega^2}{k_e})^2}} + \frac{\omega^2\tau^2\left[\left(1+\frac{k_1}{k_e}\right)-\frac{\rho v^2R^2\omega^2}{k_e}\right]+\left(1-\frac{\rho v^2R^2\omega^2}{k_e}\right)}{\omega^2\tau^2\left[\left(1+\frac{k_1}{k_e}\right)-\frac{\rho v^2R^2\omega^2}{k_e}\right]^2+\left(1-\frac{\rho v^2R^2\omega^2}{k_e}\right)^2}\right\} \\ c(\omega) = \frac{\omega}{\kappa(\omega)} \end{cases}$	

Application to data analysis

As described above, when processing experimental data, there are basically two methods to deal with the dispersion effect. The first is the 'forehead cancellation method', performing dispersion cancellation on the signals in the FFT stage (before α and κ are calculated) to yield the 1D α and κ first, then substituting the dispersion-excluded α and κ values into Eq. (2.27) to calculate the real intrinsic modulus. In cancelling the dispersion effects for the raw signals, the simple dispersive wave speed profile described above was used for correcting the frequency-dependent phase only; the alternative approach is directly substituting the uncorrected 3D α and κ into the revised propagation coefficient-modulus equations (Eq. (3.14) or Eq. (3.19a)) from which the real modulus can also be evaluated. The 'forehead cancellation method' is more realisable in practice while the second method is model-oriented, it can only be applied once the model is known (*e.g.* in simulations) and the corresponding explicit relations (Eq. (3.14) or Eq. (3.19a)) have been revised accordingly. Also, distinction lies in their effects: the 'forehead cancellation method' (as adopted by Gorham [56]) just corrects the phase (thus the wavenumber, speed and modulus), while the second method (as adopted by Alyaasin [34]) corrects both attenuation and phase. However, they do share something in common: the second method adopts the Love/ Alyaasin based equations (Eq. (3.13)) to obtain the modified propagation coefficient-modulus relations (Eq. (3.19)); while the dispersive wave profiles (Eq. (3.16)) adopted in the 'forehead cancellation method' is also originated from the Love/Alyaasin motion equations (Eq. (3.13)).

To implement the 'forehead cancellation method', dispersion effects can be cancelled by multiplying a phase correction term $e^{-i\omega\Delta l(\frac{1}{c_L}-\frac{1}{c(\omega)})}$ to the Fourier transforms of a wave propagating over the relative travel distance $\Delta l = L$. This correction assumes that the geometric dispersion only causes phase change, and not attenuation. Gorham [56] also indicated that, by multiplying a positive term $e^{+i\omega\Delta l(\frac{1}{c_L}-\frac{1}{c(\omega)})}$ to the frequency domain signal, the dispersion effect is added. It should be noted here that, as ratios $\frac{\tilde{\varepsilon}_{i+1}^{1D}}{\tilde{\varepsilon}_i^{1D}}$ were used to work out the propagation coefficient, only the relative difference in

phase matters, the travel distance Δl was used. In fact, if we consider cancelling the absolute dispersion effect over the travel routine of the waves, we have

$$\frac{\tilde{\varepsilon}_{i+1}^{1D}}{\tilde{\varepsilon}_{i}^{1D}} = \frac{\tilde{\varepsilon}_{i+1}^{3D} \times e^{+i\omega[\frac{L}{2}+iL](\frac{1}{c_L}-\frac{1}{c(\omega)})}}{\tilde{\varepsilon}_{i}^{3D} \times e^{+i\omega[\frac{L}{2}+(i-1)L](\frac{1}{c_L}-\frac{1}{c(\omega)})}} = \frac{\tilde{\varepsilon}_{i+1}^{3D}}{\tilde{\varepsilon}_{i}^{3D}} \times e^{+i\omega L(\frac{1}{c_L}-\frac{1}{c(\omega)})} \tag{3.22}$$

As an illustration, dispersion correction was here applied to data from one of the experiments on PMMA described later. The material constants used in the correction are: E =5.357 GPa, ρ=1180 kg/m^3, υ=0.38, a=13 mm.

The density and diameter were experimentally measured, while the modulus at the frequency of 20,000 Hz was chosen as the elastic modulus E, and Poisson's ratio was estimated as a constant 0.38 for PMMA in the valid frequency range. A comparison between uncorrected and corrected experimental results is shown in Fig. 3-17. It can be seen that, by using the phase correction-only method, no evident difference can be seen for frequencies below 10 kHz; storage modulus and phase velocity increase a bit between 10 kHz and 20 kHz. Hillstrom [32] has also concluded that there is no necessity for dispersion correction for frequencies up to 14 kHz, unless excitations producing pulses with high frequency components can be achieved. Also, as the method only correct the phase change induced by dispersion, it doesn't modify the damping parts, *i.e.* the attenuation coefficient and the loss modulus, as expected.

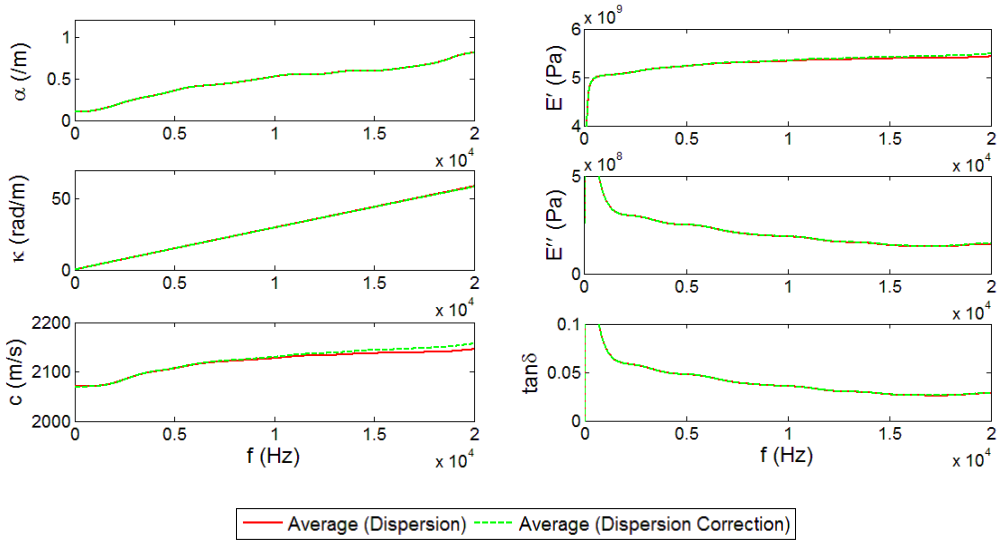
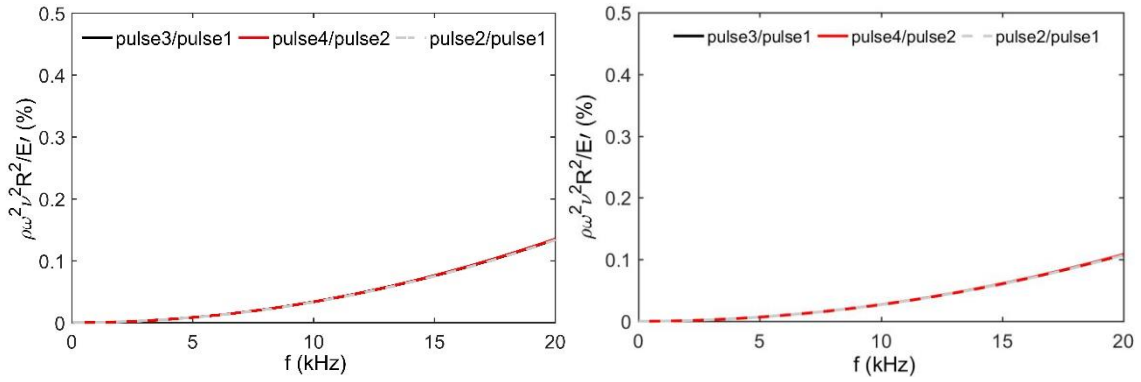


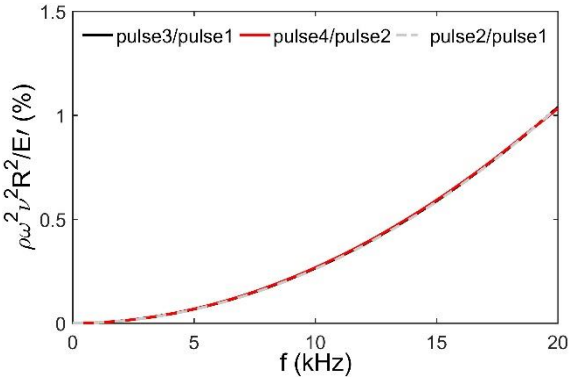
Figure. 3-17 uncorrected and corrected experimental propagation coefficient and modulus

All dispersion corrections in later analysis were done using the method proposed by Gorham [56], with the Love/Alyaasin theory-based dispersive wave speed profiles in Fig. 3-15. To evaluate the relative weight of the geometric dispersion term to the real material storage modulus (Eq. (3.14)), a ratio of the inertia-induced dispersion term $\rho\omega^2\upsilon^2R^2$ to the dispersion-excluded storage modulus E' was explicitly shown in Fig. 3-18. It can be seen that that, for both elastic rods (*i.e.* Ti and Mg) the theoretical dispersion term is rather small (less than 0.15% and 1.5% of the storage modulus value at 20,000 Hz respectively); while the ratio is a little bigger for PMMA, as the constants (density, Poisson's ratio, and radius of gyration) changes. However, with these rod settings, the dispersion correction terms are rather small for all three rods, which again explains the tiny difference between the dispersed and corrected results in Fig. 3-16 and Fig. 3-17.



(a) Ø12.70 mm Ti rod ($\rho = 4500\ \frac{kg}{m^3}, E = 110\ GPa, \upsilon = 0.32$)

(b) Ø12.70 mm Mg rod ($\rho = 1798.74$ kg/m^3, E=44.5 GP$a, \upsilon = 0.29$)



(c) Ø13.00 mm PMMA rod ($\rho = 1180$ kg/m^3, E=5.36 GP$a, \upsilon = 0.38$)

Figure. 3-18 Relative weight of the inertia-induced dispersion term to storage modulus (dispersion correction using Love-based dispersive wave velocity profiles in Fig. 3-15)

In practice, dispersion correction can be done during the centering process by shifting different frequency components with different time increments based on the dispersive wave speed profiles, this is realised by first shifting all the components in a pulse to the signal center by assuming an elastic wave speed c_L in time domain, the dispersion-induced phase change after traveling for a distance L was considered by multiplying $e^{-i\omega L(\frac{1}{c_L}-\frac{1}{c_{n(\omega)}})}$ after FFT. This helps cancel the dispersion effect and intrinsic material properties can be derived using Eq. (2.29a).

Chapter 4: Determining viscoelastic material properties by measuring wave propagation in a single rod impact test: Experimental Investigations Part II-Results Interpretation

As introduced in the previous chapter, three rods were used in pendulum impact experiments: Titanium, Magnesium, and PMMA. The first two have elastic properties, while the PMMA rod exhibits linear viscoelastic material behaviour. In an ideal elastic case there is no wave attenuation, and all the equations applicable to viscoelastic characterisation hold for elastic behaviours, with $\alpha = 0$. These include the general time and frequency domain representations of a propagating wave (Eq. (2.14) and Eq. (2.20)); the 1D and 3D relations between propagation coefficient and modulus (Eq. (2.27) and Eq. (3.14)); the model-based relations of material constants and propagation coefficient (*e.g.* Eq. (2.48) and Eq. (3.21)); as well as the methodologies used to calculate the propagation coefficient (Eq. (3.2)). Therefore, the same process was employed to analyse the elastic and viscoelastic signals, *i.e.* de-noising, amplitude correction, pulse selection, zero padding, centering, dispersion correction and FFT. In this section, the Titanium and Magnesium data are presented, followed by a more detailed description of the viscoelastic data. As comparison to the PMMA case, results from three Dynamic Mechanical Analysis (DMA) tests are scaled to the same frequency range using the Time-Temperature-Superposition (TTS) principle, despite some dispersions, both techniques yield consistent results on the same scale, which again demonstrates the effectiveness of the single rod impact technique.

4.1 Results from Titanium

Fig. 4-1 shows a typical signal collected from one of the 12.7 mm diameter, 1000 mm long Titanium rod at 22.6 °C. Although we expect little energy loss during wave propagation in this material, there is a peak amplitude drop due to geometric dispersion; in addition, some energy may be dissipated at the supports.

Fig. 4-2 shows the selected and shifted signals, and subsequent data analysis processes with and without dispersion correction. When applying the dispersion correction, the dispersive wave speed profile in Fig. 3-15(a), with constants $\rho = 4500$ kg/m^3, $E = 110$ GPa, $\upsilon = 0.32$, was applied. The density was measured, whilst the elastic modulus E and the Poisson's ratio υ are estimated from the

literature. A small change in the pulse shape is observed. Firstly, an amplitude drop of 6.1% was recorded in the un-corrected signals after the pulse travels over a distance of 5 m (Pulse 1 to Pulse 6), after dispersion correction this was reduced to 2.4%. However, this does not imply that the magnitudes are increased. In fact, Gorham's correction method just modifies the phase of each Fourier component (the real and imaginary parts), which may lead to an increase of total amplitude after superposition. Secondly, all 6 pulses are expected to strictly have the same shape and to overlap after centering and dispersion correction, the inconsistencies in Fig. 4-2(a) are probably induced by noise during wave propagation and manual errors in centering (*e.g.* improper peak selection). Errors in estimating the elastic modulus E and the Poisson's ratio υ when generating the dispersive wave speed profile can also affect the correction precision.

Fig. 4-2(c) shows the dependence of amplitude and phase on frequency and distance. In an elastic rod, the wavenumber, κ, is expected to increase linearly with frequency, f, because the wave speed, c, is independent of f, this requires angle $\left[\frac{\tilde{\varepsilon}_i}{\tilde{\varepsilon}_1}\right]$ to increase linearly with both frequency and travel distance, $x_i - x_1$, and thus the angle $\left[\frac{\tilde{\varepsilon}_i}{\tilde{\varepsilon}_1}\right], f, (x_i - x_1)$ surface is flat, which is consistent with the results shown in Fig. 4-2(c). Regarding the development of $\ln\left|\frac{\tilde{\varepsilon}_i}{\tilde{\varepsilon}_1}\right|$, which is expected to be zero for an elastic rod (as indicated by Eq. (3.2a)), there is increased noise at high frequencies and shorter travel distances.

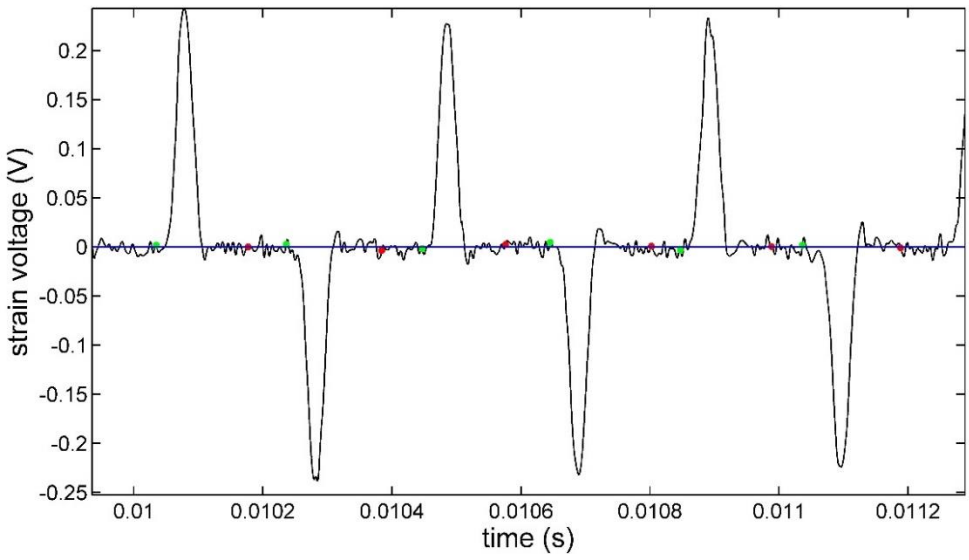
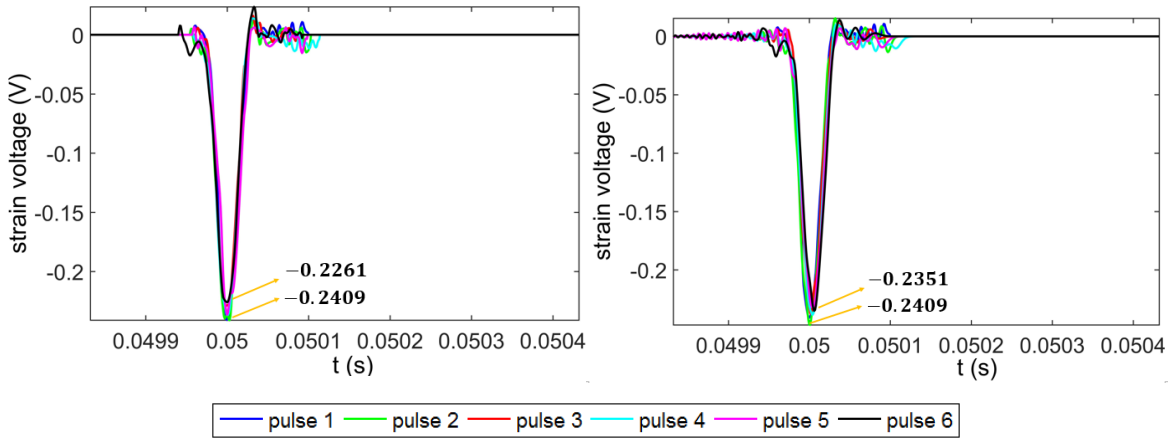
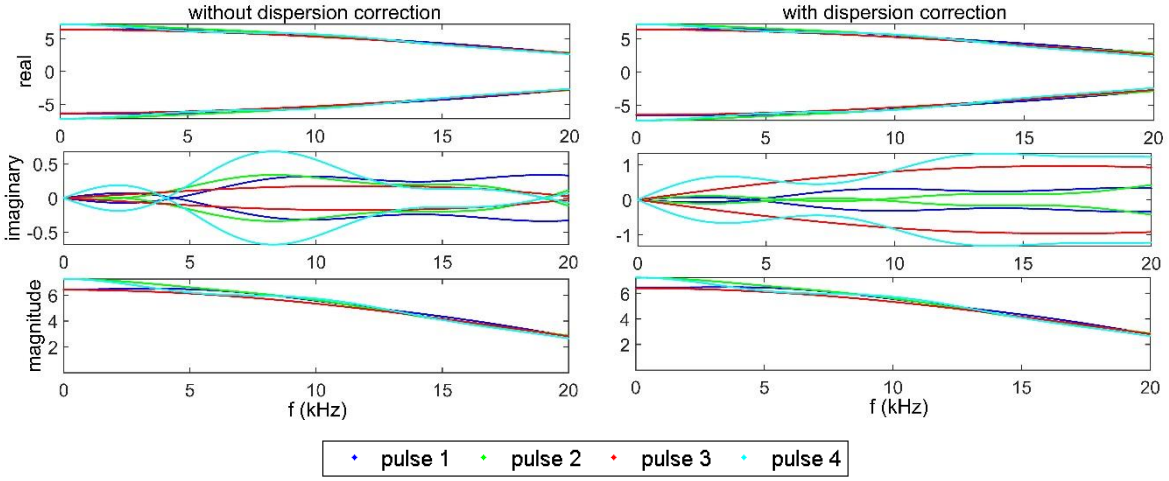


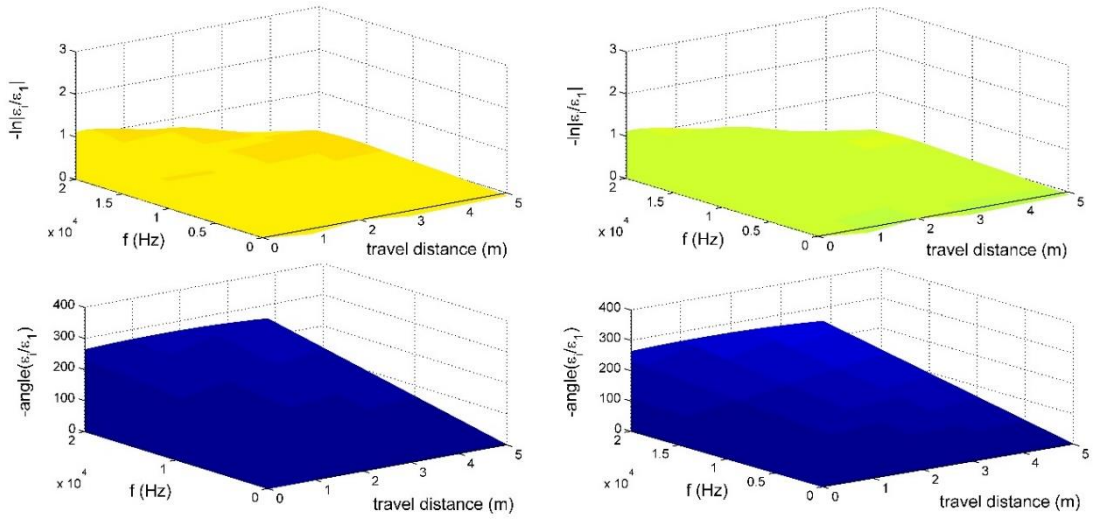
Figure. 4-1 A typical signal collected in Titanium rod impact tests (Pulses 2-7, 12.7 mm diameter, 1000 mm long Ti rod at 22.6 °C)



(a) Dispersion correction



(b) FFT



(c) $\ln\left|\frac{\tilde{\varepsilon}_i}{\tilde{\varepsilon}_1}\right|$ and $\text{angle}\left[\frac{\tilde{\varepsilon}_i}{\tilde{\varepsilon}_1}\right]$ as functions of the relative travel distance $x_i - x_1$ (see Eq. (3.2a))

Figure. 4-2 Centered pulses, corresponding FFTs and their ratios before (left) and after (right) dispersion correction (12.7 mm diameter, 1000 mm Ti rod, 12.5 mm PMMA ball at 22.6 °C)

The resulting propagation coefficient and modulus are shown in Fig. 4-3. Titanium has a density of $4500\ \mathrm{kg/m^3}$ and theoretical Young's modulus of about $110\ \mathrm{GPa}$, which yields an approximate wave speed $c_L = 4950\ \mathrm{m/s}$. Experimental results in Fig. 4-3 are quite close to these theoretical values within a frequency range of $5{\sim}30$ kHz. This is the 'useful frequency range' within which the elastic material properties can be effectively identified by this single rod impact configuration. In this case, the theoretical Titanium results can serve as a reference for determining the useful frequency range: its attenuation coefficient α, loss modulus E'', and loss factor $tan\delta$ should be strictly zero, as the strain amplitude doesn't exceed the elastic limit (see Table. 3-1). Furthermore, these data show how quickly, and in what manner, errors occur outside the useful range. In particular, we see that *E''* is not as good an indicator of the data quality as is α, whilst κ is not as good an indicator as *c*, or *E'*. This is because of the nature of the calculations, for example the calculation effectively uses as an input the deviation of κ from a straight line, so errors are magnified.

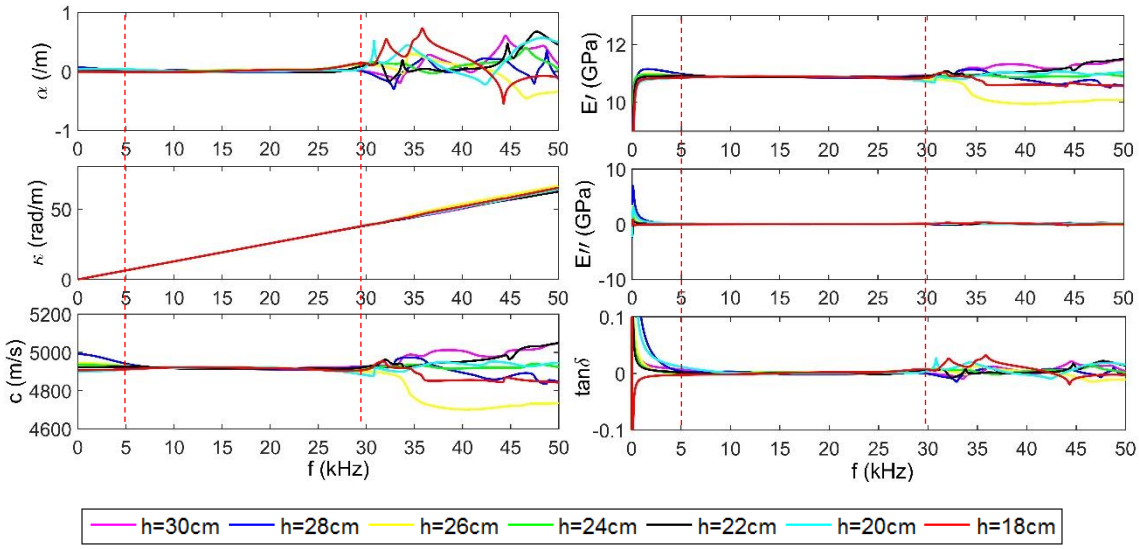
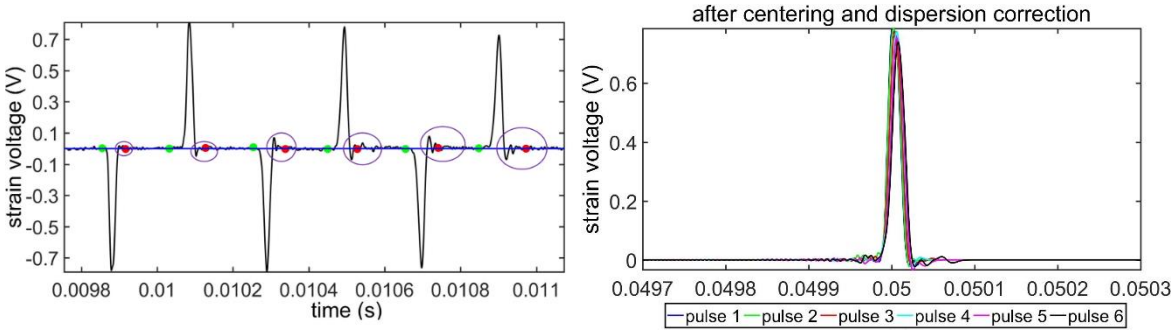


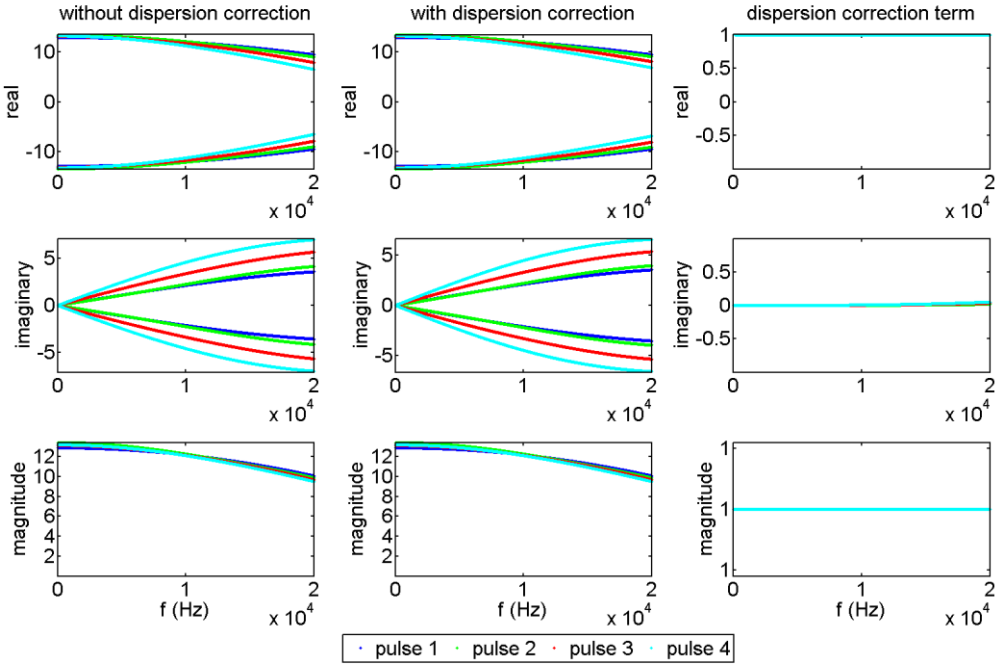
Figure. 4-3 Derived propagation coefficient and modulus from Titanium rod impact tests (based on Fig. 4-2)

For the purpose of confirmation, an extra Titanium rod impact test, using the same rod geometry but performed at $T = 21.8\ ℃$ with an aluminium ball impactor, was analysed in Fig. 4-4 and Fig. 4-5. Two balls, *i.e.* a 12.34 mm aluminium ball and a 12.5 mm PMMA ball, were used. For each ball, 2 heights (18 cm and 28 cm) were employed, and for each height two tests were repeated in the same condition. When processing the experimental data obtained from the same impactor, an average of Pulse 3/Pulse 1+Pulse 4/Pulse 2 has been adopted, and they were further averaged over 2 tests, 2

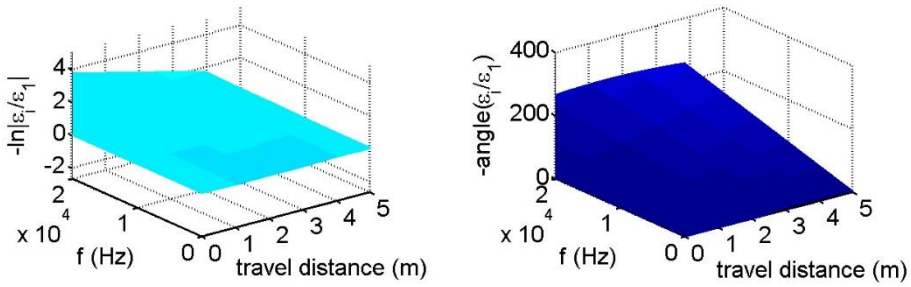
heights and 2 balls, which finally leads to the results in Fig. 4-5. The averaging technique helps remove experimental errors as well as the pulse selection error, it also produces smoother curves than those from a single test.



(a) A typical signal collected in Titanium rod impact tests (Pulses 1-6)



(b) FFT



(c) $\ln\left|\frac{\tilde{\varepsilon}_i}{\tilde{\varepsilon}_1}\right|$ and $angle\left[\frac{\tilde{\varepsilon}_i}{\tilde{\varepsilon}_1}\right]$ as functions of the relative travel distance $x_i - x_1$, (See Eq. (3.2a)

Figure. 4-4 Time domain signals, corresponding FFTs and their ratios after dispersion correction (12.7 mm diameter, 1000 mm Ti rod, 12.34 mm Aluminium ball at 21.8 °C)

It is seen in Fig. 4-4 that dispersion induced oscillations at the rear of the pulses become significant as travel distance increases. Fig. 4-5 shows that material properties can be determined up to ~ 25 kHz using a PMMA ball while an aluminium ball achieves ~60 kHz. The difference in the upper frequency limit is due to the different frequency components generated with different impactors. Overall, these data give confidence in the technique, the analytical calculations and the application to experimental data.

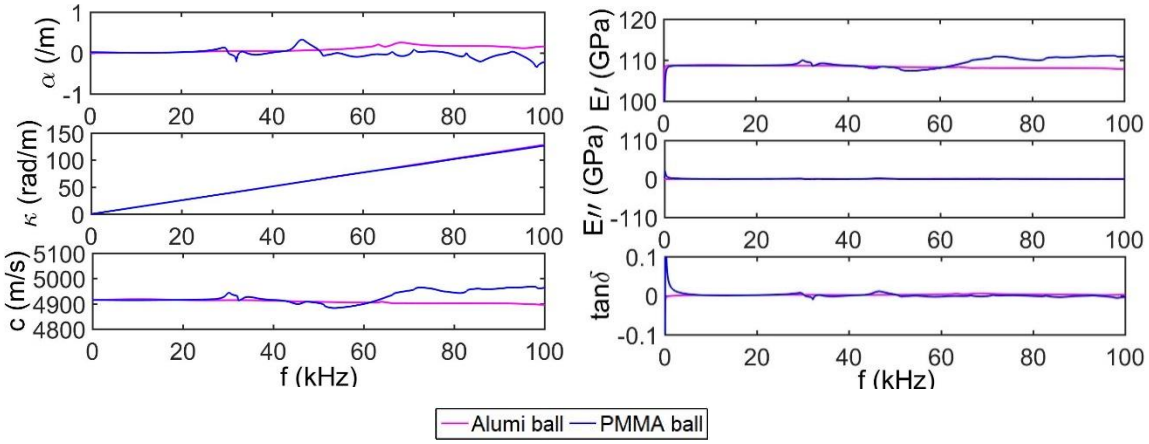
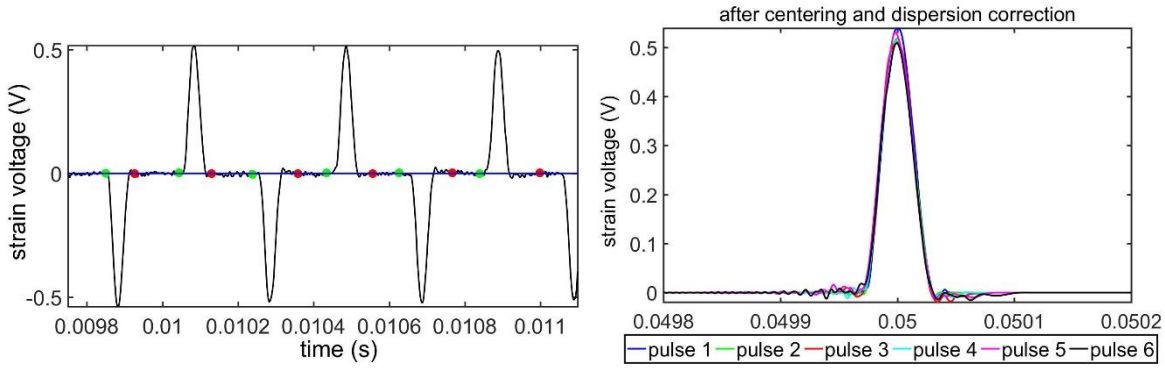


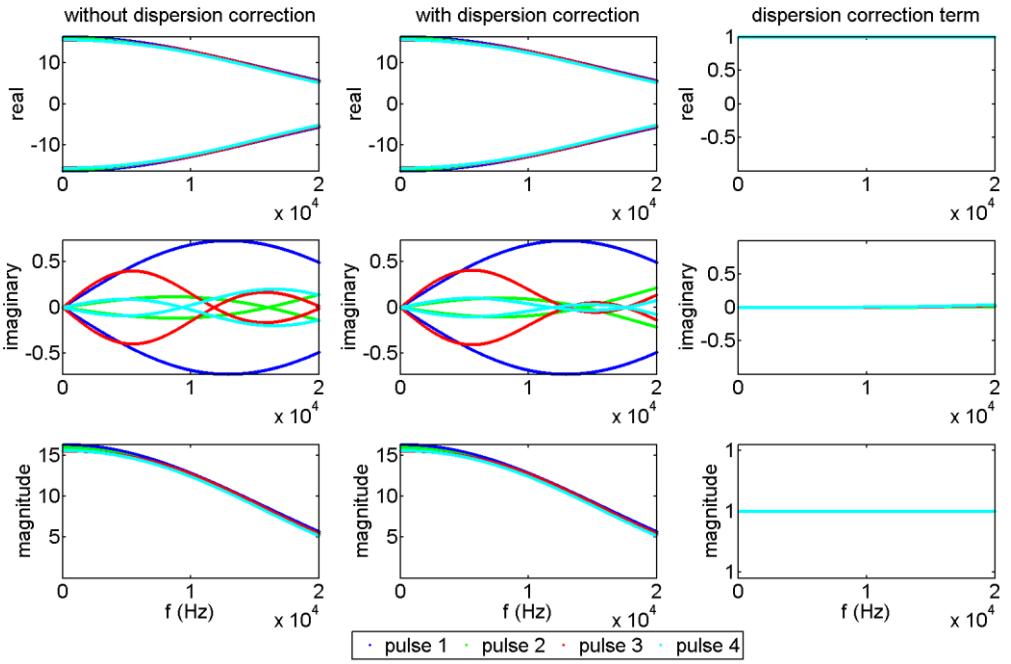
Figure. 4-5 Derived propagation coefficient and modulus from Titanium rod impact tests (based on Fig. 4-4)

4.2 Results from Magnesium

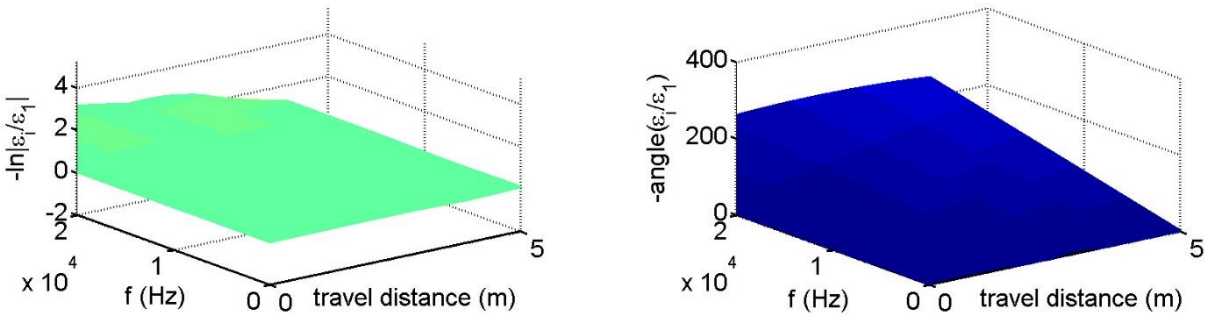
Signals collected from a $\emptyset 12.7 \times 1000$ mm Magnesium rod impact test are presented in Fig. 4-6. The same signal processing methodology was applied, in which the dispersive wave speed profile (Fig. 3-15(b)) has been adopted. Results yielded in Fig. 4-6(d) are in accordance with expectations, *i.e.* the attenuation coefficient, loss modulus and loss factor being zero for a metal bar within the elastic region, wave speed being around 5000 m/s, and storage modulus being around 45 GPa.



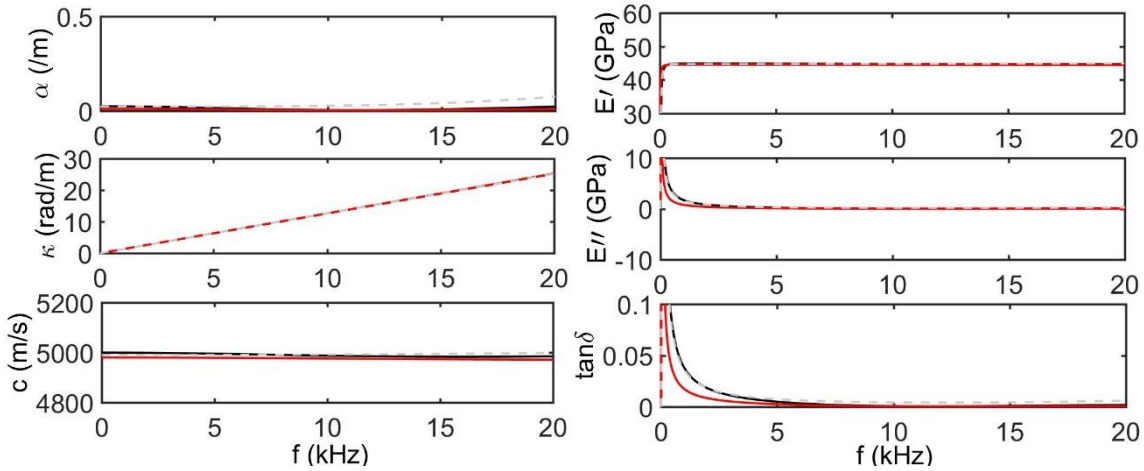
(a) Time domain signal (Pulse 1-6)



(b) FFT



(c) $\ln\left|\frac{\tilde{\varepsilon}_i}{\tilde{\varepsilon}_1}\right|$ and $angle\left[\frac{\tilde{\varepsilon}_i}{\tilde{\varepsilon}_1}\right]$ as functions of the relative travel distance $x_i - x_1$, (See Eq. (3.2a)



(d) Derived propagation coefficient and modulus

Figure. 4-6 Data analysis process and results (12.7 mm diameter, 1000 mm Mg alloy rods, 12.5 mm PMMA ball at 21.8 °C)

4.3 Results from PMMA

4.3.1 Data analysis and results

A typical raw PMMA impact signal is shown in Fig. 4-7; the sequentially attenuated strain amplitudes are presented in Table. 4-1. The strain at the impact end at the moment of impact is larger than the first strain peak (0.015 %), however, within the limiting strain (0.1%) of the LVR.

An example of the data analysis process is shown in Fig. 4-8. High frequency oscillations can be seen in the tail of each pulse (Fig. 4-7(a) and (b)), the tail is due to the viscoelastic effect; the oscillations, however, are attributed to geometric dispersion and are removed by modifying the phase of each frequency component (this has also been observed by Gorham [56]). Some high frequency oscillations then appear ahead of the wave front, this seems reasonable because, without geometric dispersion, high frequencies naturally travel faster than low frequencies due to viscoelastic effects. In the following sections, these data was discussed in detail.

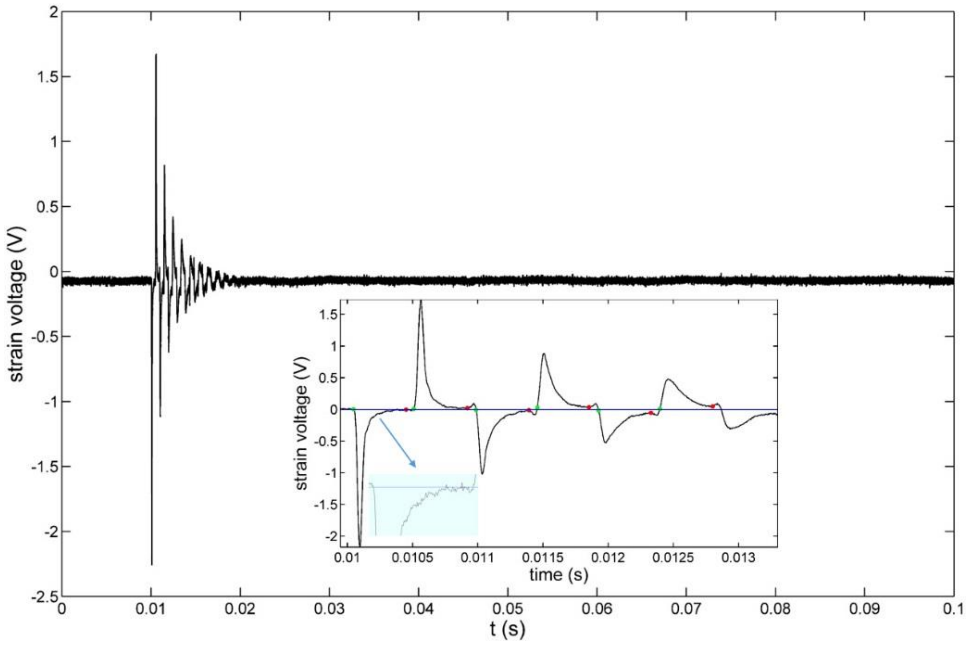
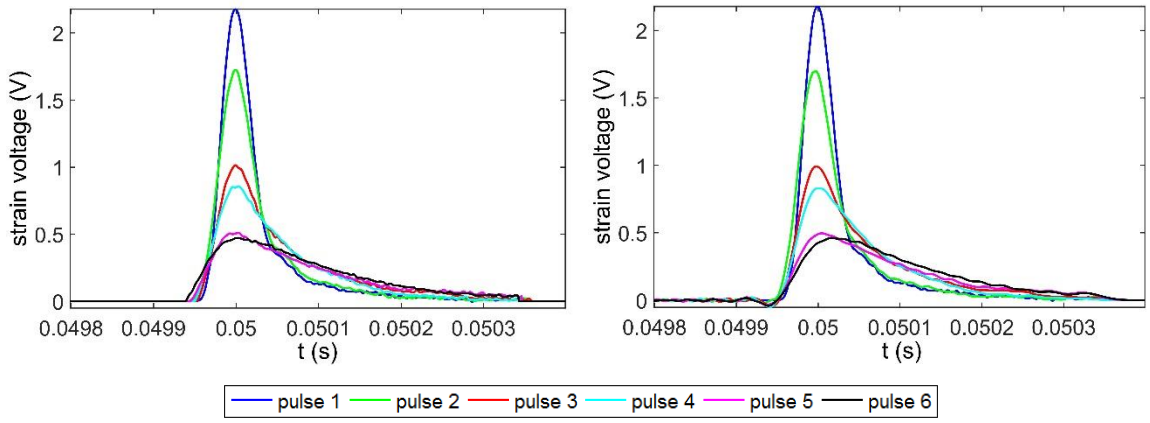


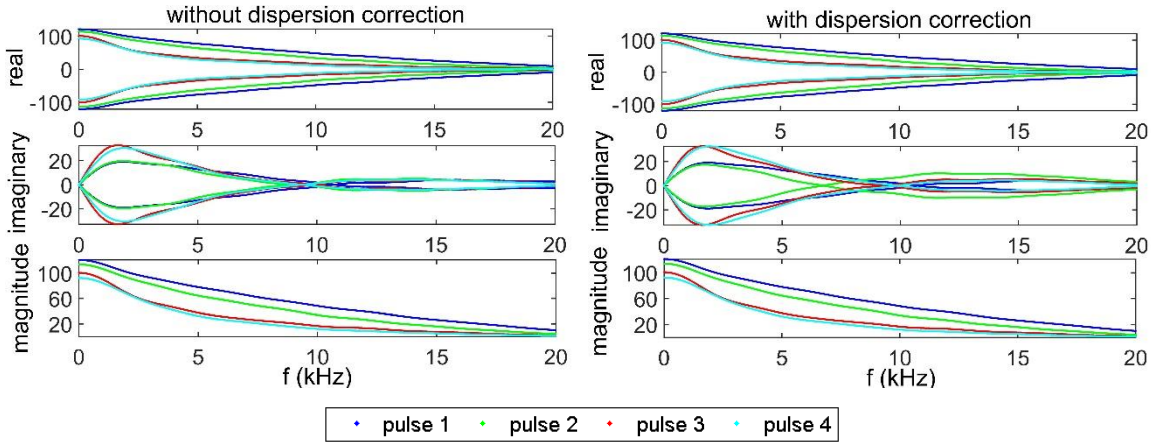
Figure. 4-7 A typical signal collected in PMMA rod impact tests

Table. 4-1 Strain amplitudes of the first 6 pulses after dispersion correction (13 mm diameter, 1000 mm PMMA rod at 17.5 °C)

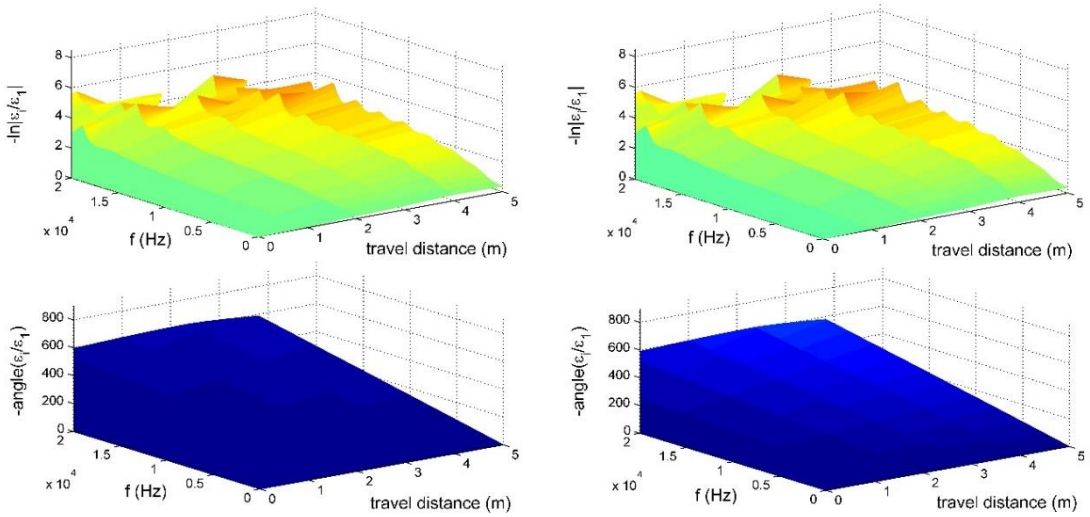
Pulse No. (i)	1	2	3	4	5	6
Peak strain voltage (V)	2.177	1.697	0.9912	0.8321	0.4962	0.4627
Real strain	0.0148%	0.0116%	0.0068%	0.0057%	0.0034%	0.0032%
$(\varepsilon_{max})_i/(\varepsilon_{max})_1$	100%	77.95%	45.53%	38.22%	22.79%	21.25%



(a) Centering (left) and dispersion correction (right)



(b) FFT



(c) $\ln\left|\frac{\tilde{\varepsilon}_i}{\tilde{\varepsilon}_1}\right|$ and $angle\left[\frac{\tilde{\varepsilon}_i}{\tilde{\varepsilon}_1}\right]$ as functions of the relative travel distance $x_i - x_1$, (See Eq. (3.2a)

Figure. 4-8 Centered pulses, corresponding FFTs and their ratios before (left) and after (right) dispersion correction (13 mm diameter, 1000 mm PMMA rod, 12.5 mm PMMA ball at 17.5 °C)

4.3.2 Discussion

4.3.2.1 Periodic oscillations

Firstly, we observe that the $angle\left[\frac{\tilde{\varepsilon}_i}{\tilde{\varepsilon}_1}\right]$-$f$-$(x_i - x_1)$ surface is no longer flat, as wave speed c becomes a nonlinear function of frequency f. As the attenuation coefficient is not constant for a PMMA rod (it increases non-linearly with frequency f), at a given frequency, $\ln\left|\frac{\tilde{\varepsilon}_i}{\tilde{\varepsilon}_1}\right|$ should increases linearly with increasing $x_i - x_1$ to keep the ratio $\ln\left|\frac{\tilde{\varepsilon}_i}{\tilde{\varepsilon}_1}\right| /(x_i - x_1)$ constant; whilst, for a fixed travel distance $x_i - x_1$, $\ln\left|\frac{\tilde{\varepsilon}_i}{\tilde{\varepsilon}_1}\right|$ should increases non-linearly with frequency f. This leads to a non-planar $\ln\left|\frac{\tilde{\varepsilon}_i}{\tilde{\varepsilon}_1}\right| - f - (x_i - x_1)$ surface in Fig. 4-8(c), with periodic oscillations appearing at some frequencies with spacing $\sim 2500\ Hz$. These oscillations are not obvious in the FFT magnitudes in Fig. 4-8(b), but their ratios show evident oscillations even though a proper pulse selection method (the 'zero crossover start points') has been adopted. This phenomenon has been seen in most of the experimental data analysis such as Fig. 3-8, and in the Titanium rod impact simulations presented later. As discussed in the 'Pulse selection' section, these oscillations are believed to be caused by the window function (the *sinc* function) effect which is unavoidable but can be alleviated by properly selecting each pulse to have the same duration and taking an average of the results derived by Pulse 3/Pulse 1 and Pulse 4/Pulse 2. These periodic oscillations don't necessarily belong to a group of 'irregularities' that found by Hillstrom [32]

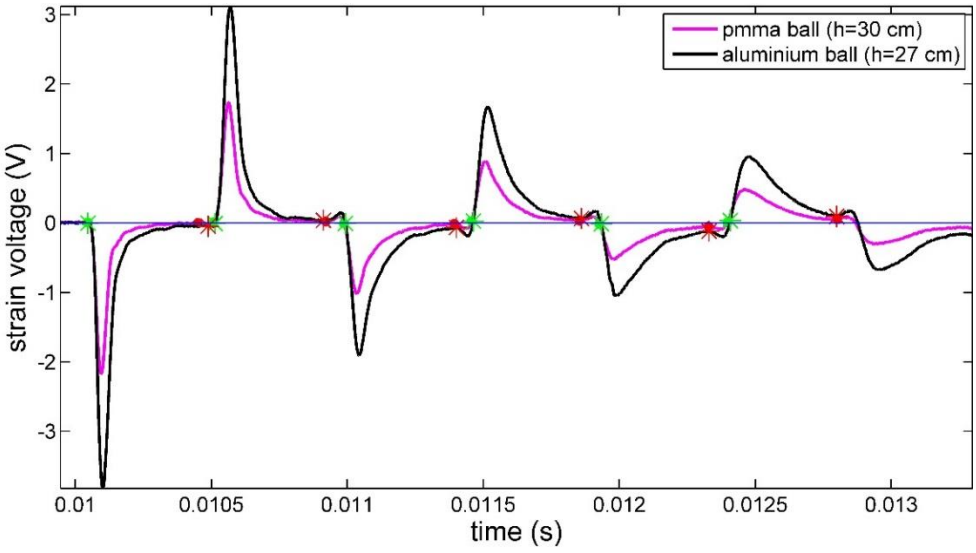
$$f_{cr} = \frac{c}{\lambda} = \frac{c}{2\times gauge\ distance/n} = \frac{2100}{2\times 2/n} = 525n\ Hz \text{ (n being any positive integer).} \quad (4.1)$$

Rather they are associated with the pulse selection and truncation. In SHPB research, by analysing both experimental and simulation signals in frequency domain, Welch *et al.* [52] found that the oscillations in the recovered complex modulus are induced by the truncation of signal in time domain, and they suggested this can be avoided either by averaging the results with different truncation lengths, using a longer rod, or using multi-point strain measurement method along with wave separation technique.

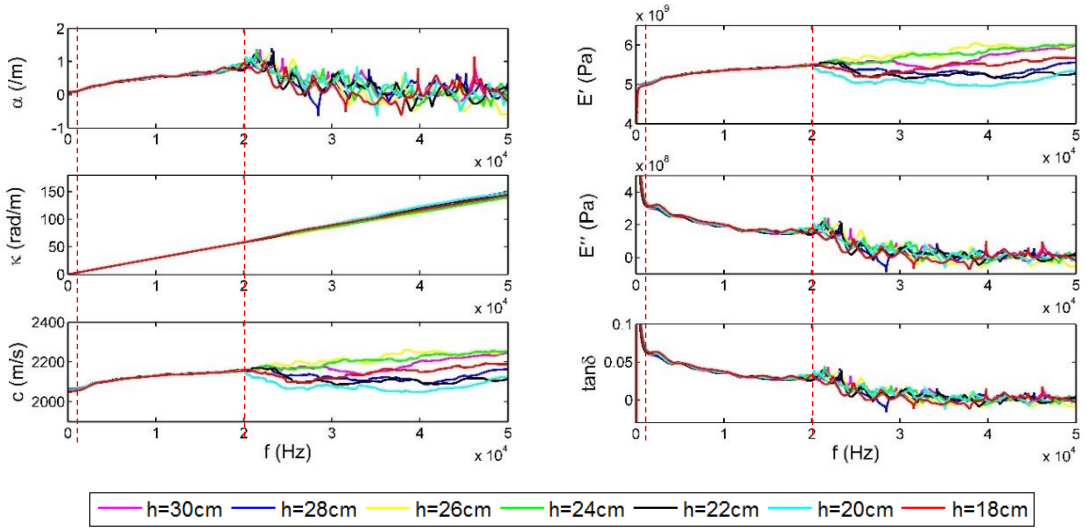
4.3.2.2 Impactor effect and 'useful frequency range'

A comparison of the signals generated by the PMMA and Aluminium impactors is made in Fig. 4-9(a). Considerable extension of pulse length can be seen in both cases; as the Aluminium ball possesses larger mechanical impedance than PMMA ball, the strain amplitude produced is larger even using a smaller drop height. Both balls give nearly the same 'useful frequency range', 2 ~ 20 kHz during which small variations in wave speed c and moduli are observed; the attenuation coefficient, α, increases nonlinearly with frequency but is less than 1 m^{-1}, the wavenumber, κ, appears to show an almost linear increase with increasing frequency; however, wave speed, c, exhibits a non-linear increase within this range. Comparing Fig. 4-9(c) and (d) leads to the conclusion that taking the mean of the results derived from different drop heights (thus different pulse lengths) can smooth the curves.

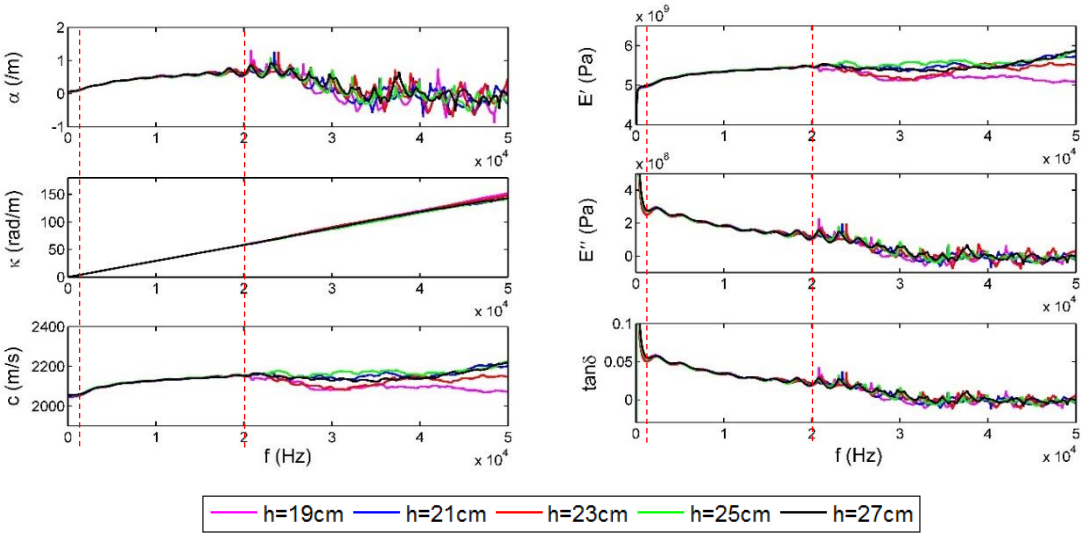
The results derived from both balls are almost the same up to 15 kHz, above which oscillations appear on the aluminium-based attenuation coefficient, α, loss modulus, E'', and loss factor, $\tan\delta$, curves, which makes these values derived from the aluminium ball slightly smaller than those from the PMMA ball. 'Oscillations' seem to be more severe with the aluminium ball signals due to the higher strain amplitude produced, which results in a more difficult pulse selection in terms of avoiding wave overlapping and thus a more significant window function effect.



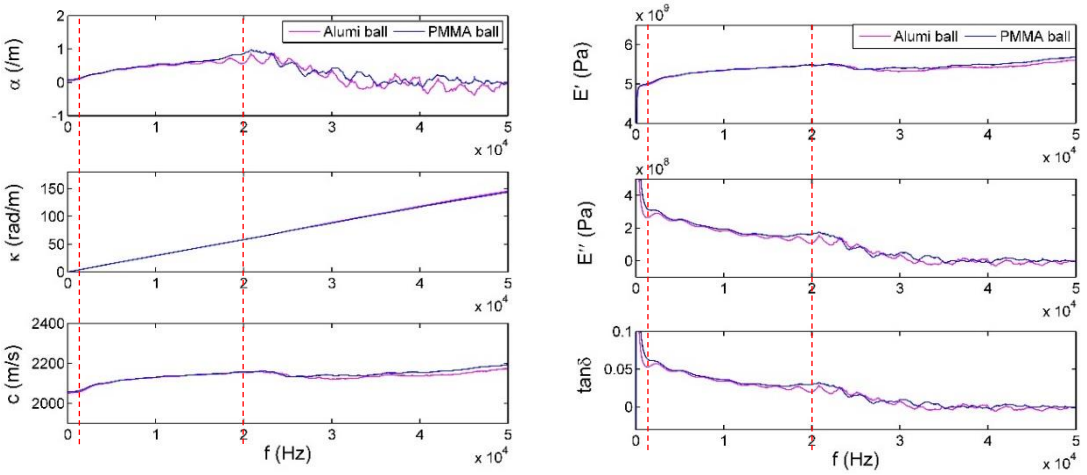
(a) Generated strain signals



(b) Propagation coefficient and modulus (PMMA ball)



(c)Propagation coefficient and modulus (Aluminium ball)



(d) Comparison of the average results of all drop heights

Figure. 4-9 Comparison of the signals and results from 12.5 mm PMMA and 12.34 mm Aluminium balls on a 13 mm diameter, 1000 mm long PMMA rod at 17.5 °C.

By comparing Fig. 4-3 and Fig. 4-9, it is observed that different frequency ranges have been achieved for Titanium and PMMA rods. A 'useful frequency range' is proposed to describe the range that can be effectively identified in an impact test: it has lower and upper limits and is normally narrower than estimated (*e.g.* Eq. (3.9) and Eq. (3.12)) [32]. The range achieved with the PMMA rod impact setup is about 2~20 kHz, by inspection, which is much narrower than that for the Titanium rod under almost the same testing conditions. The difference is believed to be mainly caused by the mechanical impedances of the rod materials leading to different frequency components. However, there are other factors that affect the useful frequency range; here, a discussion of lower and upper useful frequency limits is given based on relevant literature.

(a) Lower frequency bound

Hillstrom *et al.* [32] pointed out that a lower valid frequency limit exists because only frequency components with wavelength shorter than the distance between adjunct measurement sections are free from overlapping. For the current experiments, this limit is estimated to be

$$\begin{aligned} f_{l-Ti} &\approx \frac{c}{gauge\ distance} = \frac{4944\ m/s}{1\ m} = 4.9\ \text{kHz} \\ f_{l-PMMA} &\approx \frac{c}{gauge\ distance} = \frac{2100\ m/s}{1\ m} = 2.1\ \text{kHz} \end{aligned} . \tag{4.2}$$

In SHPB-based research to identify the complex modulus for low-impedance materials, Welch and Stromme [52] found that the capability of frequency domain analysis is limited by the lower useful frequency that can be achieved, either from experimental or simulation signals. The lower useful frequency is affected by factors such as the truncation effect, noise, and discretization. Truncation of the signal generally leads to a loss of low frequency information, it is thus desirable to extract the longest possible signal during pulse selection; this can be achieved by using longer rod, rod with lower wave speed, or multi-point strain measurements [52]. In most cases, the lower useful frequency is the inverse of the signal duration, as the minimum frequency resolution that can be achieved in FFT is exactly the inverse of the duration of the analysed signal. To increase the lower useful frequency, Welch and Stromme suggested that high bit-depth digitization be used, longer signals recorded and truncated, and averaging techniques implemented to reduce the undesirable effects of truncation and noise.

(b) Upper frequency bound

The upper useful frequency is limited by both experimental and numerical factors. Numerical limitations can be induced by the data processing methodologies. Most simply, as a sampling rate of 1 MHz was used in all these experiments, the highest frequency that can be achieved after FFT is 0.5 MHz (Eq. (3.9)). Further, Ahonsi *et al.* [21] found that if waves measured at a single gauge station are to be separated during data processing, the time at which the strain history is split into forward and backward waves can have a significant effect on the maximum frequency at which the propagation coefficient can be determined. Experimental factors include material properties, which determine the frequency components that can be conveyed in a specific rod, rod diameter, to meet the requirements of 1D wave propagation theory, strain magnitude and noise, to achieve large signal-to-noise ratio at high frequencies, and strain gauge length, which limits the shortest wavelength that can be measured.

Rod material properties affect the frequency components that can be generated and conveyed. A comparison between Titanium (Fig. 4-3) and PMMA (Fig. 4-9) results shows that, with the same impactor and almost the same rod diameter, the upper frequency limit in Titanium is higher (30 kHz) than in PMMA (20 kHz). This is associated with the interaction between impactor and rod, as well as rod material properties. Rod diameter is important: if no dispersion correction techniques are applied, one must use the 1-D wave assumption (see Eq. (3.11) and Eq. (3.12), numerical investigation in Fig. 3-16 and experimental in Fig. 3-17), and the wavelength must be at least 10 times the diameter of the rod. This gives an upper frequency limit, *e.g.* for PMMA (Eq. (3.11))

$$f_{h-1D} = \frac{c}{10 \times rod\ diameter} = \frac{2100\,\frac{m}{s}}{10 \times 0.013\ mm} \approx 16\ \text{kHz}.$$

In the data above, dispersion is observed above 16 kHz (Fig. 3-16 and Fig. 3-17) in the 13 mm diameter PMMA rod experiments. The upper valid frequency limit seen in the literature is similar, for example, 11-14 kHz with a PMMA bar diameter of 16 mm in Hillstrom's research [32], 40 kHz and 15 kHz for 10 mm and 20 mm diameter PMMA rods respectively by Mousavi [31]. Welch and Stromme [52] reported a 1D assumption upper frequency of 10-20 kHz in 15 mm diameter rod. In addition, after investigating the effect of rod diameter on complex modulus calculation from SHPB

signals, Zhao and Gary [29] proposed an empirical critical frequency $f_c = c_L/4d$ up to which the 1D analysis can be used within 5% error (Eq. (3.12)). For the current, this is ~40 kHz. However, dispersion correction may extend the upper useful frequency.

The highest frequency is also affected by the signal-to-noise ratio (SNR), determined by the strain magnitude and noise level. Strain magnitude is determined by several factors including impactor type, impact speed and rod length. Different impactor types produce pulses containing different frequency components, and different excitations, *e.g.* air gun rather than pendulum, can achieve better identifiable strain magnitudes at high frequencies [32]. Increasing rod length, however, has an inverse effect on the upper useful frequency [21]: increasing the bar length reduces the strain magnitude and decreases the frequency range over which the propagation coefficient can be determined accurately. This conflicts with the use of a longer bar to avoid wave overlapping. Strain magnitude is affected by the window function effect (Fig. 3-12) and centering (Fig. 3-14(a)): an appropriate choice of window function can give higher magnitudes at the cost of lower frequency resolution, whilst centering the pulse maximises the FFT values and might extend the upper frequency limit to some extent. Increasing drop height can help improve strain magnitude and SNR, but is limited for viscoelastic materials by the need to remain in the linear region, and the tail at the end of each pulse. Ahonsi *et al.* [21] found that the inclusion of 1% mean amplitude random noise could reduce the upper frequency limit from 40 kHz to 10-15 kHz.

Another experimental factor that could limit the upper useful frequency is the 'gauge effect': the gauge averages strain along its length to produce a single value: only components with wavelength at least 2 times the strain gauge length can be measured accurately. This leads to a maximum frequency that is significantly higher than the limits observed

$$f_{max} = \frac{c}{2\times strain\ gauge\ length} = \frac{2100}{2\times 0.005} = 0.21\ MHz\ . \tag{4.3}$$

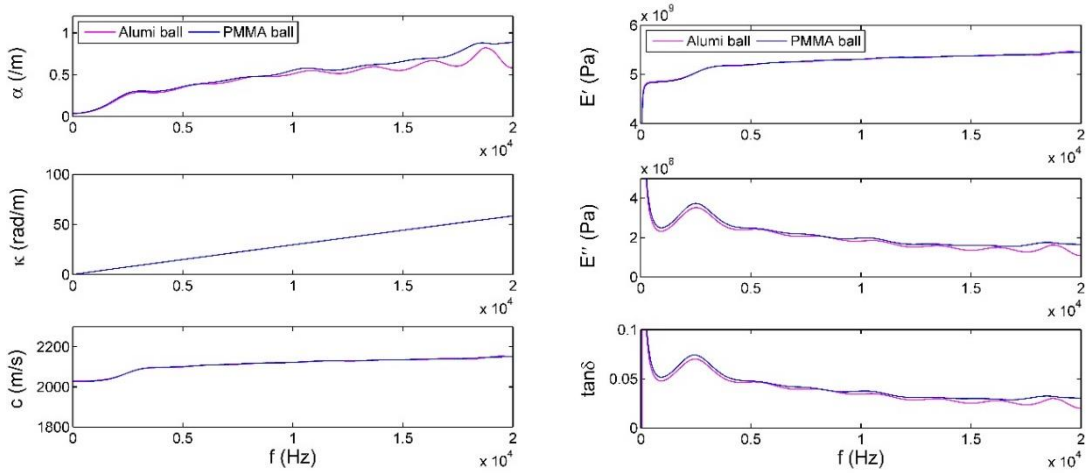
Other measures to extend the useful frequency range include measuring quantities other than strain (though no visible improvement was seen when comparing results derived from measured particle velocity and strain recordings in the PMMA rod impact tests presented later), and determining complex modulus in other modes such as shear [32].

4.3.2.3 Temperature effect

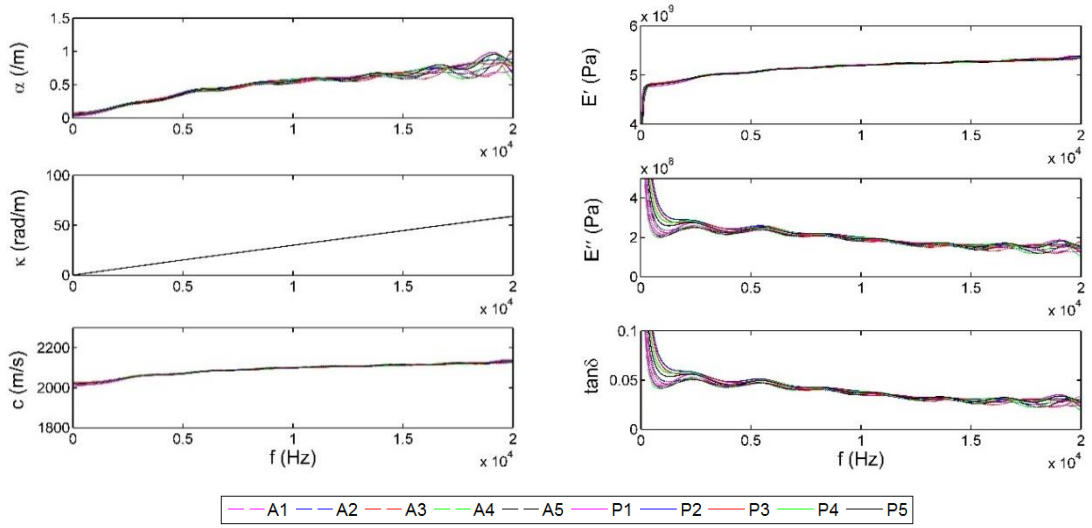
Average results of all drop heights at 3 further temperatures (19.5, 23.4 and 27 °C) within the 'useful frequency range' of 2~20 kHz are shown in Fig. 4-10(a)-(c), and a comparison of the 4 temperatures in Fig. 4-10(d). Table. 4-2 compares the variations of the temperature-dependent material properties within this range, these comparisons are also shown in Fig. 4-11. Note that the results at 19.5, 23.4 and 27 °C are averaged from all the drop heights, while those of at 23.4 °C are presenting at a fixed drop height (27 cm for the Aluminium ball and 20 cm for the PMMA ball) but repeated 5 times: Fig. 4-10(d) adopts an average of the 5 repetitions.

Fig. 4-10(d) and Fig. 4-11 reflect the temperature-dependent mechanical behaviours of the PMMA. It can be seen from these figures that: the attenuation coefficient, α, generally increases with increasing temperature, T, while the wave speed, c, and storage modulus, E', show clear decreases. Less obvious is the consistent increase of wavenumber, κ, loss modulus, E' , and loss factor, $\tan\delta$ with temperature, as these variations are too small within the temperature range studied. This trend is consistent with what we expect: as temperature increases, more space and energy become available for molecules to move around, thus they are more active at high temperatures than low temperatures leading to lower modulus. Accordingly, internal friction increases as well due to molecular movement, which makes energy loss larger as a result. Evidence from a temperature scan in later DMA experiments can also support the statement that, considering the general frequency components contained in these PMMA rod impact tests (1 kHz-20 kHz), the temperature range applied in these tests is located just before the secondary (β) transition temperature; during this temperature range, increasing the temperature will lead to an increase in loss modulus, E'', and loss factor, $\tan\delta$, but a drop in storage modulus, E'.

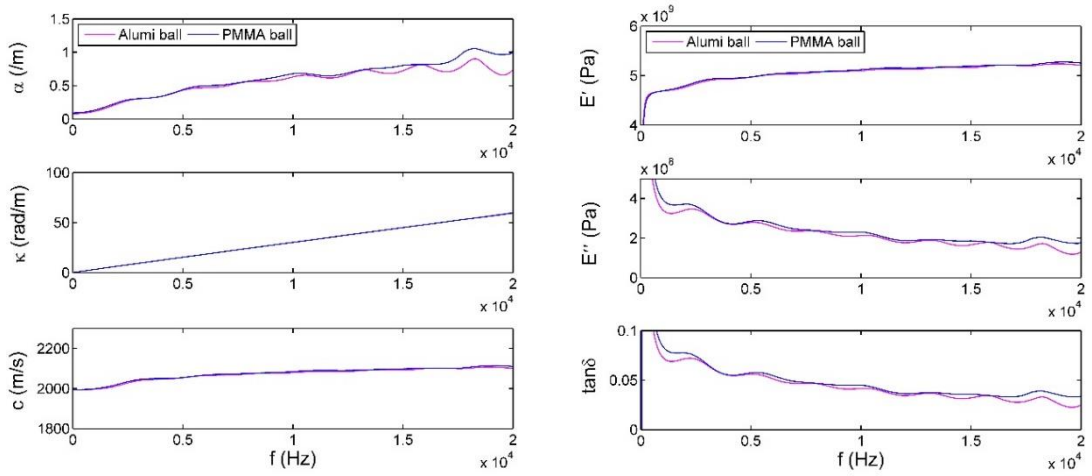
In addition, the sensitivity of this single rod impact technique was tested. Although the differences among these 4 temperatures (2 ℃, 3.9 ℃ and 3.6 ℃ respectively) are quite small, results show that this single rod impact technique was able to capture the variations in mechanical behaviours of this PMMA rod configuration. Further, as visibly shown on the wave speed, c, and storage modulus, E', curves, the difference of the results between 17.5 and 19.5 °C is slightly smaller than others, which is consistent with the smaller temperature interval between both.



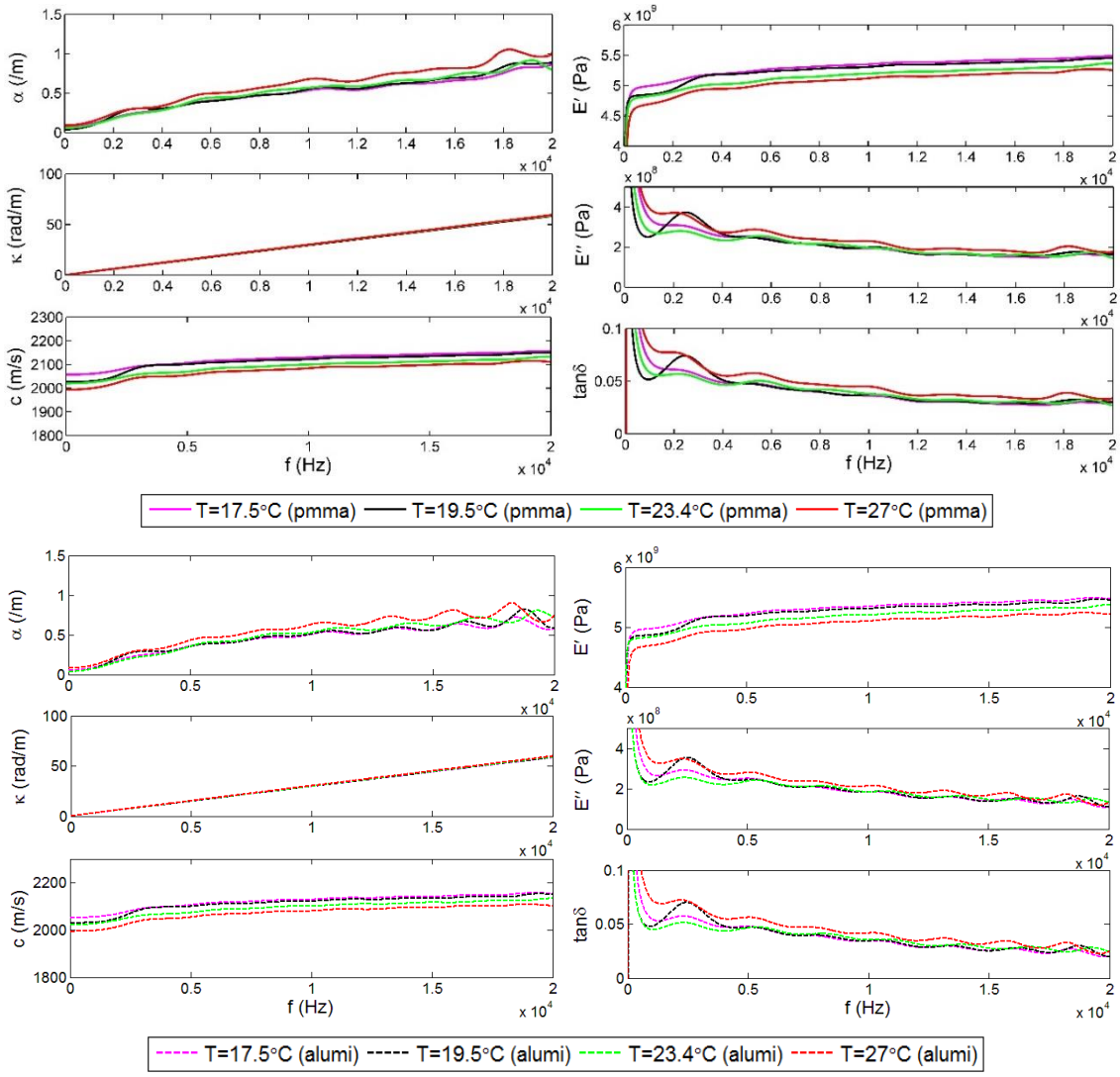
(a) 19.5 °C



(b) 23.4 °C (A: 'Aluminium ball', P: 'PMMA ball')



(c) 27 °C



(d) Overall comparison of average results

Figure. 4-10 Propagation coefficient and modulus derived by strain measurements at 4 temperatures on a 13 mm diameter 1000 mm long PMMA rod using 2 different balls.

Table. 4-2 Temperature dependent material properties by strain measurement (2 kHz~20 kHz)

T	ball	α (1/m)	κ (rad/s)	c (m/s)	E' (GPa)	E'' (GPa)	$tan\delta$
17.5 ℃	PMMA	0.185-0.86	6.06-58.3	2070-2160	5.1- 5.5	0.15-0.31	0.027-0.061
	Aluminium	0.17-0.72	6.07-58.3	2070-2160	5.0- 5.5	0.11-0.29	0.020-0.057
19.5 ℃	PMMA	0.215-0.89	6.13-58.4	2050-2150	4.9- 5.5	0.16-0.37	0.029-0.074
	Aluminium	0.20-0.825	6.13- 58.5	2050-2150	4.9-5.5	0.11-0.35	0.020-0.070
23.4 ℃	PMMA	0.17-0.92	6.16-58.91	2039-2133	4.9-5.4	0.15-0.28	0.027-0.057
	Aluminium	0.16-0.81	6.15-58.90	2041-2133	4.9-5.4	0.13-0.25	0.024-0.051
27 ℃	PMMA	0.24-1.06	6.22-59.56	2019-2115	4.8-5.3	0.17-0.37	0.033-0.078
	Aluminium	0.22-0.90	6.24-59.80	2013-2107	4.8-5.2	0.12-0.35	0.023-0.072

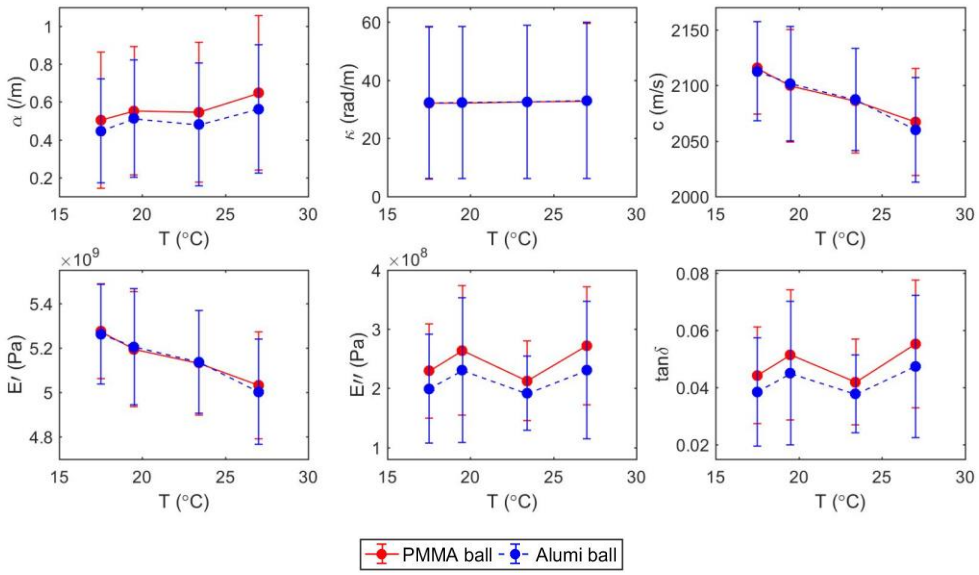


Figure. 4-11 Temperature dependent material properties (using data from Table. 4-2)

4.3.2.4 Velocity measurement results

Particle velocity measurements were performed on experiments at 23.4 °C using a laser Doppler Vibrometer (LDV). Whilst the strain gauges give surface measurements averaged axially over the gauge length, the LDV can monitor movements at different points on the cross-section, although only on the end of the rod removing the strain gauge effect on the upper frequency limit (the LDV limit is 1 MHz). The small measurement area also facilitates consideration of possible non-planar wavefronts by comparing results from different radii.

Fig. 4-12 shows a strain signal and a particle velocity signal measured in the same PMMA experiment. In a purely elastic material, strain, ε, and particle velocity, $\dot{u}$, can be linked as

$$\dot{u} = c\varepsilon. \tag{4.4}$$

For the PMMA here the real strain of the first pulse after cancelling amplification is

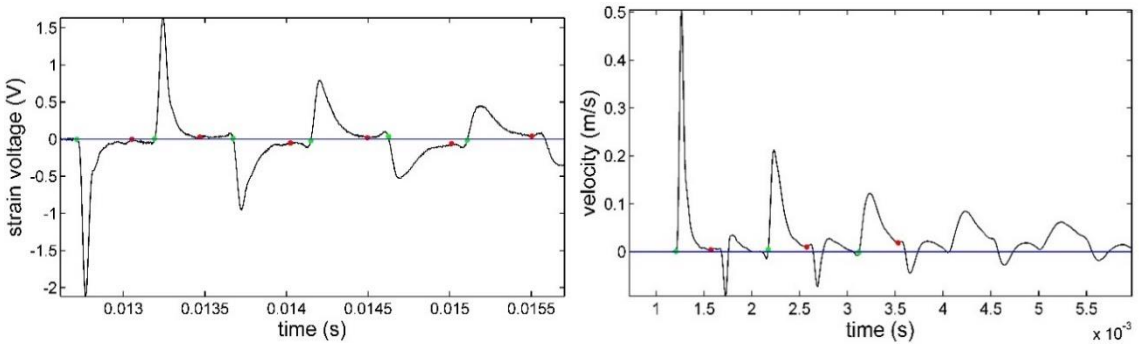
$$\varepsilon_{1st} = \frac{2\times strain\ voltage}{Amplification\times Gauge\ Factor\times Power\ Supply\ Voltage} = \frac{2\times 2.116\ V}{2325.58\times 2.10\times 6.0\ V} \approx 0.0144\%. \tag{4.5}$$

Therefore, assuming a wave speed of 2100 m/s, the corresponding particle velocity is estimated as

$$\dot{u}_{1st} = 2\times c\varepsilon_{1st} = 2\times 2100\frac{m}{s}\times 0.0144\% \approx 0.6\ m/s.$$

Note that the particle velocity is doubled at the free end. This is consistent with the LDV recordings in Fig. 4-12(b), allowing for some attenuation between the gauge station and rod end.

Two typical signals, produced by the PMMA ball and Aluminium ball respectively, are shown in Fig. 4-13. All particle velocity signals in the rod should be of the same sign (here positive when particles move towards the LDV), because, at the end of the rod, particles in both compressive and tensile waves move in the same direction. However, unexpected disturbances with opposite sign were seen in both recordings, abnormal warping is also found in the tail of each pulse.



(a)strain (b)velocity

Figure. 4-12 Typical signals collected in a PMMA rod impact test (13 mm diameter, 1000 mm PMMA rod, 12.5 mm PMMA ball, h = 20 cm, 23.4 °C)

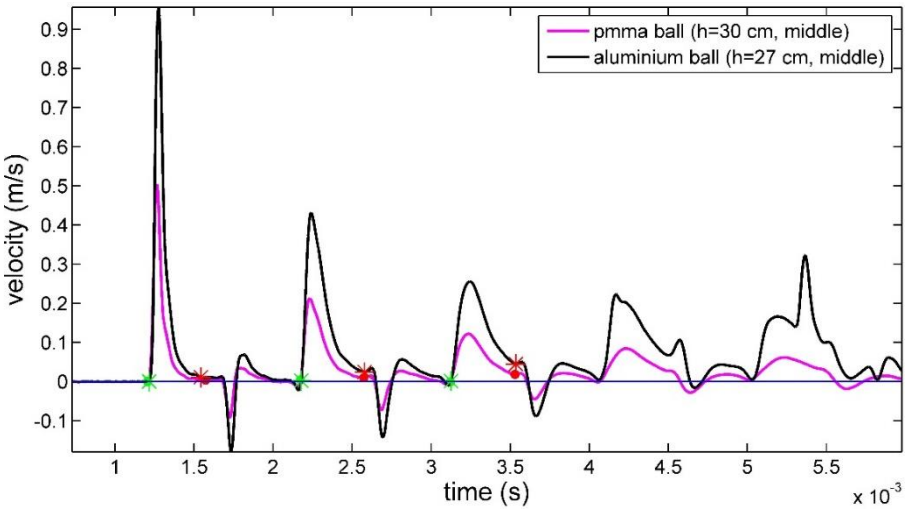
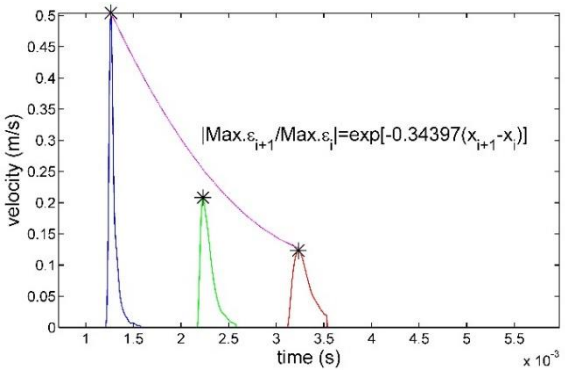


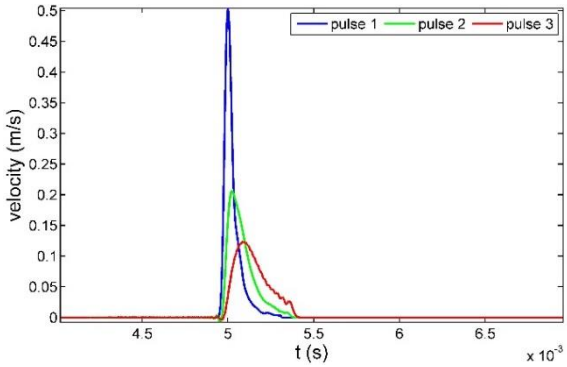
Figure. 4-13 Comparison of the velocity signals at Location 1 (middle), generated by the 12.5 mm PMMA and 12.34 mm Aluminium balls on the 13 mm diameter, 1000 mm long PMMA rod at 23.4 °C (green dots and stars represent pulse start, red dots and stars represent pulse end)

If the 'reasonable' pulses are extracted, with the start point of each pulse being determined using the 'zero crossover start' method and the end point selected just ahead of the unexpected warping, the particle velocity-based propagation coefficient and modulus can be calculated using a similar data analysis process as the strain signals. The detailed velocity data analysis process is shown in Fig. 4-14(a)-(d), featuring a PMMA ball impact signal. One significant difference in processing the velocity

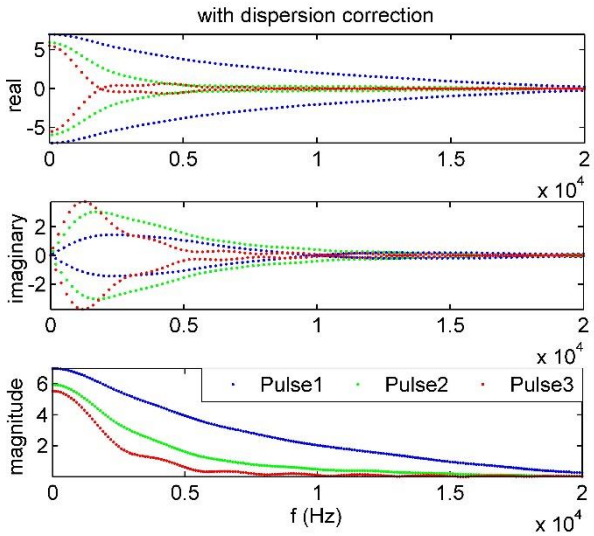
signals lies in the travel distance used when calculating the propagation coefficient in Eq. (3.2a) because the travel distance between every two adjacent velocity pulses is 2 m. While the first 6 pulses (first 7 pulses for Ti rod signals) are all considered 'valid' (here valid means no severe wave overlapping is observed), and an average of the first 4 pulses (Pulse 3/Pulse 1 and Pulse 4/Pulse 2) was adopted in calculating strain-based results, only the first 3 velocity pulses were selected, and results based on the first 2 pulses (Pulse 2/Pulse 1) were finally used in velocity-based analysis: hence the two analyses were performed using the same stress waves.



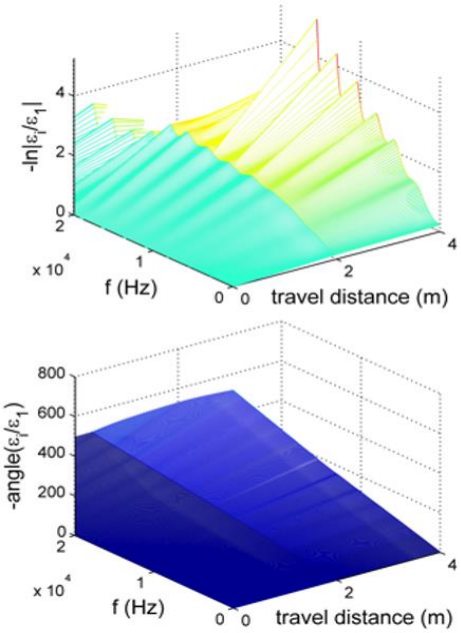
(a) a rough estimate of time domain attenuation



(b) centering and dispersion correction



(c) FFT



(d) $\ln\left|\frac{\tilde{\varepsilon}_i}{\tilde{\varepsilon}_1}\right|$ and $angle\left[\frac{\tilde{\varepsilon}_i}{\tilde{\varepsilon}_1}\right]$ as functions of $x_i - x_1$

Figure. 4-14 Data processing of particle velocity signals from the 13 mm diameter, 1000 mm long PMMA rod at 23.4 °C

A comparison of the propagation coefficient and modulus derived at 5 radially distributed locations by both ball impacts is made in Fig. 4-15. The useful frequency range achieved by velocity measurements is again 2~20 kHz, no improvement is seen compared to strain measurements. However, note that the strain-based results yielded by the Aluminium ball (Fig. 4-10(b)) seem to be more concentrated while those velocity-based Aluminium ball results (Fig. 4-15) tend to be more deviated outside the 'useful frequency range'. Fig. 4-16 shows a comparison of the results derived by the two measurement methods. Both methods give almost the same storage modulus E', but the velocity-based calculation gives a slightly larger attenuation coefficient, α, loss modulus, E'', and loss factor, $\tan\delta$. The difference in wavenumber, κ, is not visible in Fig. 4-16, but it leads to obvious variation in wave speed c at low frequencies (2-10 kHz); the sensitivity of wave speed to wave number was discussed later. Generally, the differences in the results derived by these two methods are believed to be caused by the 'strain gauge length effect' which induces inaccurate strain measurement over the gauge length, or non-linearity in the strain gauges. Both issues were examined in the simulation work.

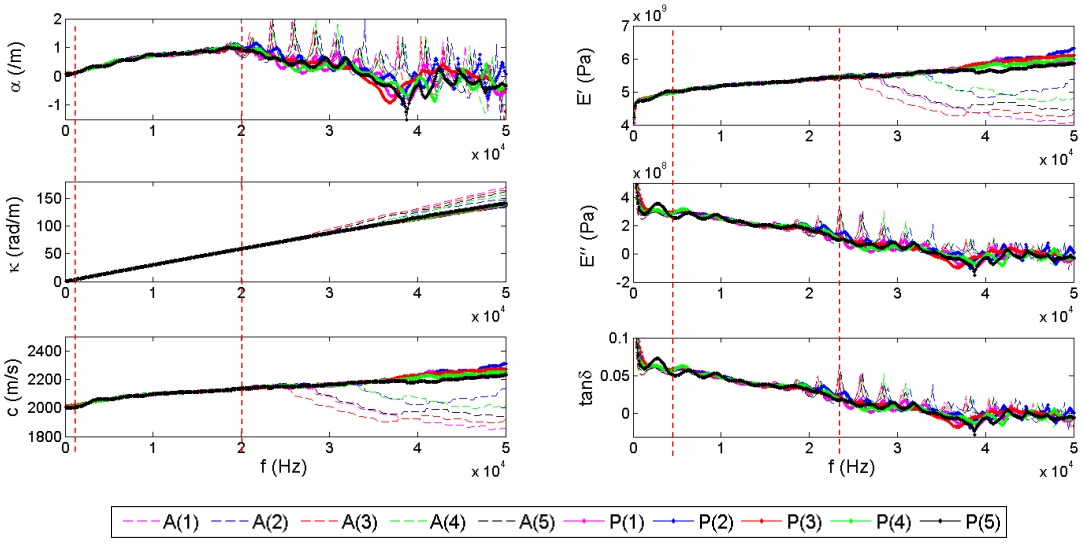


Figure. 4-15 Propagation coefficient and modulus derived by velocity measurements (A: 'Aluminium ball', P: 'PMMA ball') (13 mm diameter, 1000 mm long PMMA rod at 23.4 °C)

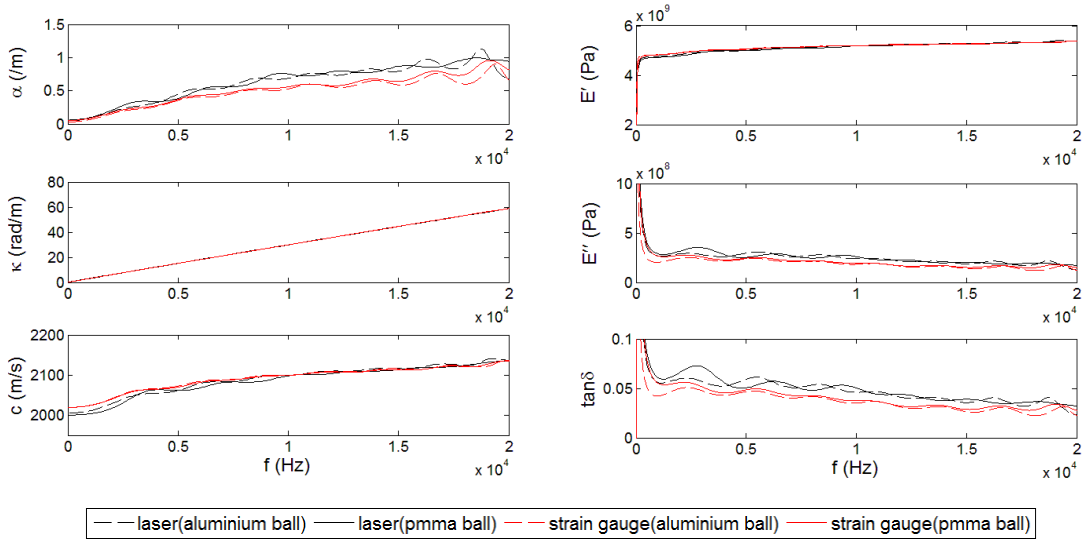


Figure. 4-16 Comparison of strain gauge-based and LDV-based results

4.3.2.5 Middle & edge Vibrometer results

When the PMMA rod is impacted by a spherical impactor, the contact surface in the middle is quite small; the impact might be treated as a concentrated loading which leads to a non-uniform distribution of deformation across the impact surface. However, as per the Saint-Venant's principle, the difference vanishes as wave travels over large distance from the impact end. The LDV enables the velocity measurement over a small area, here velocity signals at 5 locations uniformly distributed along the radius were monitored by a laser beam (Fig. 4-17). As only 1 location can be monitored by the LDV, a series of experiments was performed under identical impact conditions.

As an example, the recorded velocity waves in the middle and on the surface of the PMMA rod and their resulting propagation coefficient and modulus are shown in Fig. 4-18. No evident difference can be found in the corresponding amplitudes and results within the frequency range of interest (2 kHz~20 kHz) because these pulses have travelled over a distance of multiples of 1 m, which is large compared to the largest cross-sectional dimension (*i.e.* the 13 mm diameter), thus it is expected that a uniform deformation has been achieved across the section. A more general comparison of the results derived from the 5 location measurements, Fig. 4-19 further demonstrates this identity along the radius direction. Note that, the same start and end locations have also been used when processing the middle and edge signals on the same cross-section.

One may also expect no significant difference between the waves propagating on the axis and surface at the strain gauge station, as they have been travelled 0.5 m after being generated at the impact end. The same conclusion on the middle and edge signals were drawn from later simulations, which further validates the validity of the surface-based strain gauge measurements.

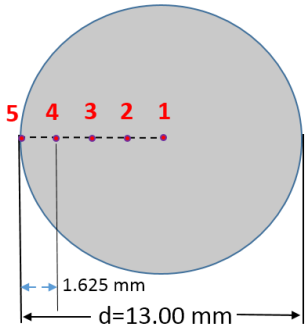
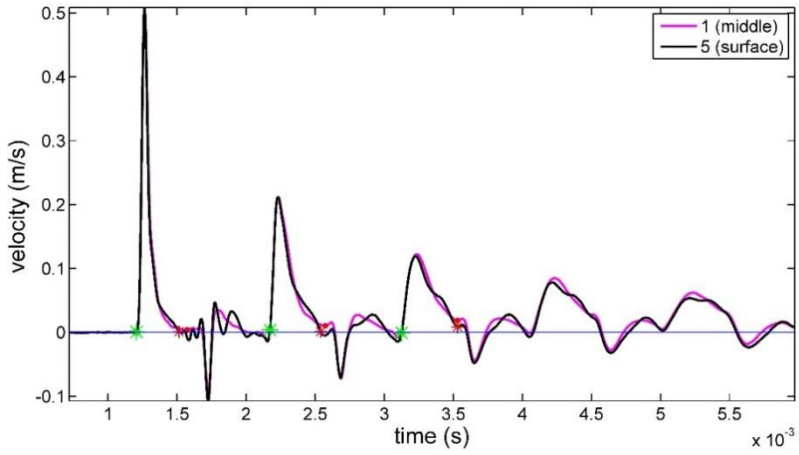
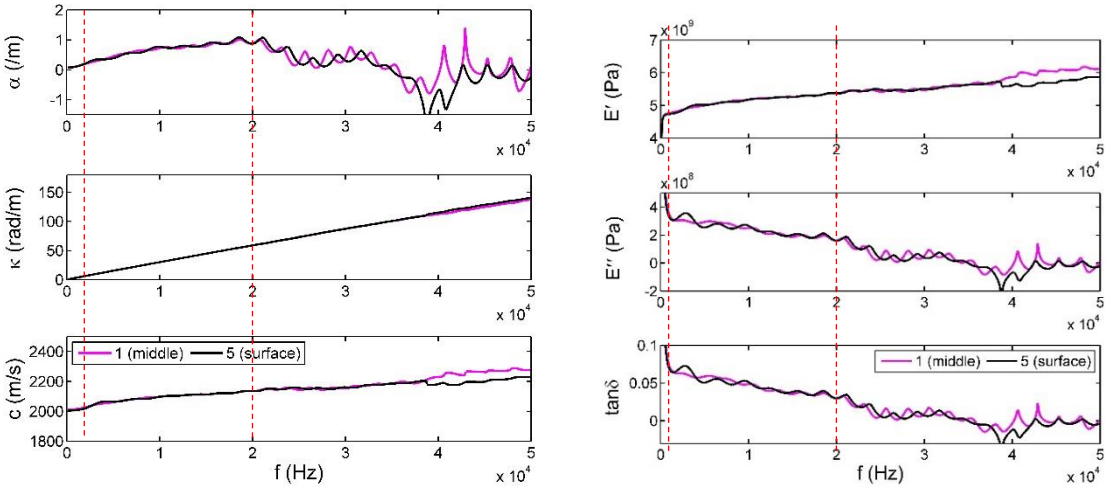


Figure. 4-17 Five LDV particle velocity measurement locations



(a) time domain signals



(b) propagation coefficient and modulus

Figure. 4-18 Comparison of Location 1 (middle) and 5 (surface) signals and results

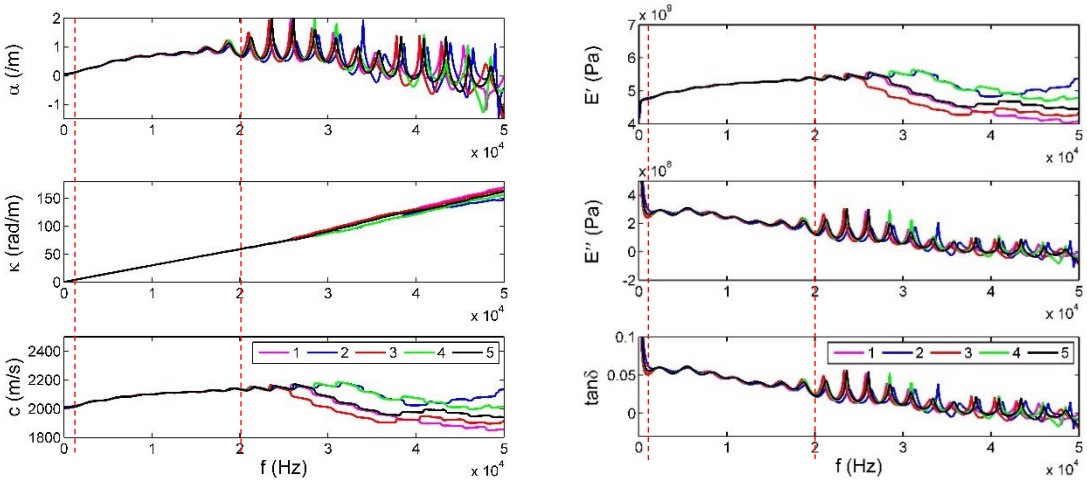


Figure. 4-19 Comparison of Location 1 - 5 results

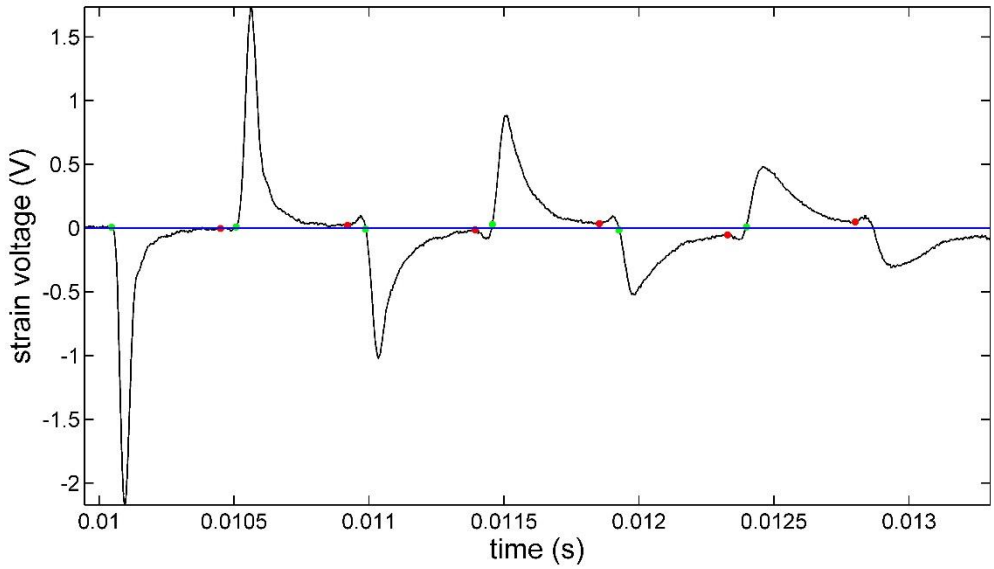
4.3.2.6 Gauge effects

During the data analysis process, two interesting observations were made which warrant further investigation. Firstly, in the experimental data analysis, a pair of opposite sign pulses (*i.e.* one compression and one tension) yields different results to a pair of pulses of the same sign, this phenomenon will later be shown not to occur when analysing simulation data, and therefore questions the linearity of the strain gauge. Secondly, small differences can still be seen while comparing the strain-based and particle velocity-based results (Fig. 4-16). These issues are thought to be associated with the gage itself and termed the 'gauge effects'.

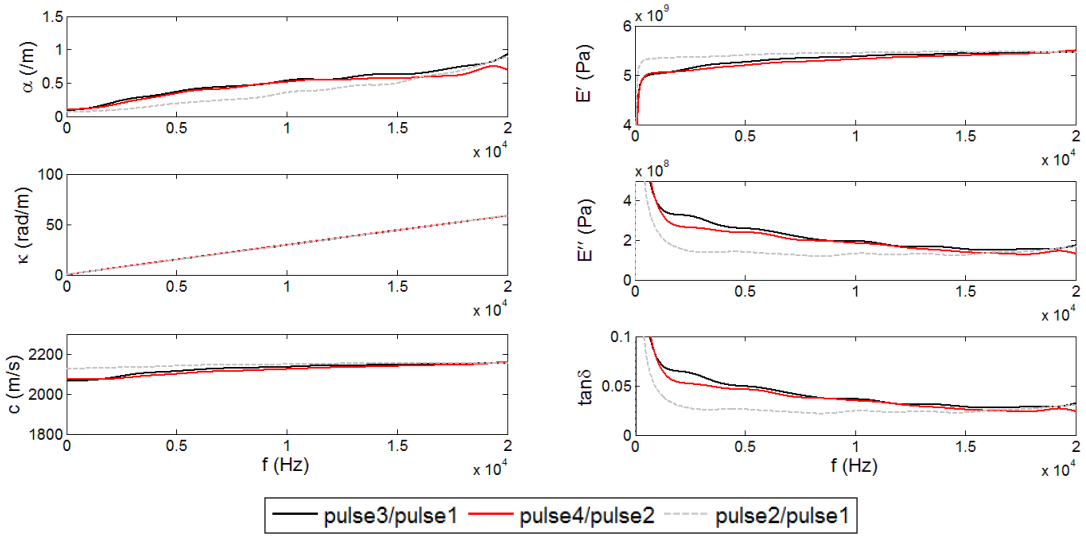
The general purpose of performing these impact tests is to derive material properties such as modulus by measuring propagating waves in the rod. The question arises at the initial stage of data analysis of which 2 pulses are to be used to calculate the ratio in Eq. (3.2a). As observed in Fig. 4-7, in a PMMA rod impact test nearly 20 pulses are contained in a signal. Excluding those that have travelled over 6 round trips and have significantly distorted shapes that lead to visible wave superposition, the first 6 pulses have been selected using the aforementioned 'zero crossover start point' (Fig. 4-7 and Fig. 4-20(a)). Theoretically any 2 pulses can be chosen to calculate the ratio in Eq. (3.2a) and thus there are 15 different combinations. After several trials, it was found that the first 4 pulses possess minimum overlap and thus were used in composing the final results.

Although number of pulses is narrowed there are still 6 combinations. However, it has been found that using ratios of the pulses with the same sign (*i.e.* both in compression or tension) give similar

results while using those with opposite sign (*i.e.* one in compression and the other in tension) will lead to significant deviation. The deviations are graphically shown in Fig. 4-20(b), in which three methods have been adopted: Pulse 3/Pulse 1, Pulse 4/Pulse 2, and Pulse 2/Pulse 1, representing compressive, tensile and mixed ratios. All the pulses have been zero amplitude corrected before being processed: each pulse starts but not necessarily ends at zero. Furthermore, the compressive pulses were inverted before the ratios were calculated. From Fig. 4-20 we see that P 3/P 1 and P 4/P 2 lead to results that are quite close to each other while P 2/P 1 gives smaller α, E'', $tan\delta$, and larger c and E' at frequencies below 15 kHz.



(a) Selection of Pulse 1-6 (green dot: start point; red dot: end point)



(b) Propagation coefficient and modulus derived by 3 methods (with dispersion correction)

Figure. 4-20 A PMMA ball impact signal and corresponding results (13 mm diameter, 1000 mm long PMMA rod at 17.5 °C)

The deviations in the results given by P 3/P 1 (or P 4/ 2) and P 2/P 1 may also be caused by inaccuracy in the location of the strain gauge, *i.e.* the strain gauge is not exactly located in the middle of the rod. The results given by P 3/P 1 and P 4/P 2 are quite similar because no matter where the gauge is, the travel distance in both cases is 2 m, the gauge location only affects the results yielded by P 2/P 1. To reduce these effects, all the final propagation coefficient and modulus results presented are normally based on an average of P 3/P 1 plus P 4/P 2.

4.3.2.7 Sensitivity of modulus calculation to the propagation coefficient: analytical and numerical analysis

From previous sections it is seen that the observed propagation coefficient $\gamma(\omega)$ can vary due to factors such as different impactors, pulse selection, measurement methodologies and the gage effect. The resulting modulus and wave speed recovered based on $\gamma(\omega)$ (*e.g.* Eq. 2.29(a)) will vary accordingly. The sensitivity analysis of wave speed and moduli to the propagation coefficient, based on Eq. 2.29(a), was included in the *web version* due to limit page number.

4.4 Summary of single rod impact tests

Experiments were performed on three rods: the 12.7 mm diameter 1000 mm length Ti rod at 21.8 ℃ and 22.6 ℃, the 12.7 mm 1000 mm length Mg rod at 21.8 ℃, the 13 mm diameter 1000 mm length PMMA rod at four temperatures (17.5, 19.5, 23.4 and 27 °C). These experiments demonstrate the single rod impact technique's capacity to measure wave propagation characteristics (attenuation coefficient, wavenumber, and wave speed) within the 'useful frequency range'; material mechanical properties such as the complex modulus and loss factor (which are of engineering interest) were then recovered from the wave propagation coefficients. Specifically, the known moduli of a Titanium alloy (Ti6Al4V) rod and a Magnesium rod were successfully identified within 5~30 kHz; the good agreements between the theoretical and experimental wave speed and moduli verify the validity of this single rod impact technique. It was seen later that, the PMMA moduli identified by this technique agrees reasonably with DMA results within 2~20 kHz. Experiments at different temperatures show that the technique is capable of detecting the mechanical changes induced by temperature variations as small as 2°C.

Some critical issues associated with the data analysis process were also discussed. These include the impactor effect, the drop height (strain amplitude) effect, the window function effect, pulse selection effect, zero padding, center shifting, useful frequency range. Other interesting topics, such as temperature effect of the viscoelastic PMMA material, comparison of strain and velocity measurement methodologies, uniformity of sectional deformations (by LDV method), wave propagation analysis methods which questions the 'gage effect' (finite gage length and linearity of strain gauge measurement), and sensitivity analysis of the calculation methods were explored. The following conclusions can be drawn:

(1) One station measurement is convenient in terms of simplifying the data analysis process, the rod tested should have an appropriate diameter considering 3D effects such as the inertia effect, and a proper length balancing between avoiding wave overlapping and achieving relatively large strain amplitudes (high SNR) for the propagating pulses. Smaller spherical balls are recommended to generate pulses that have shorter durations and contain higher frequencies.

(2) Deformation becomes uniform across rod section at locations suitably remote from the impact end, thus surface measurement is valid at these locations;

(3) Different strain amplitudes, produced by different drop heights, yield almost the same material properties, which indicates that, within the linear viscoelastic region (LVR), the response of PMMA to impact loading is only time and frequency dependent. If the material deforms outside LVR, however, it is expected that the response was strain dependent as well [54].

(4) The window function effect is unavoidable, but can be alleviated either by appropriately choosing the window function or by proper pulse selection.

(5) Zero padding helps locate each pulse while centering helps sample the maximum FFT values to achieve high SNRs, but it doesn't necessarily contribute to the improvement of the upper frequency limit;

(6) The 'useful frequency range' is limited by a number of experimental and numerical factors, typically being $5\sim30$ kHz for the $1000\,mm$ Ti and Mg rods, and $2\sim20$ kHz for the $1000\,mm$ PMMA rod. Employing more efficient excitations, *e.g.* air gun other than pendulum, might improve the signal-to-noise ratio at low and high frequencies [32], but measuring velocity other than strain

doesn't necessarily extend the 'useful frequency range' in our trials. Testing materials in torsion might be of help to extend the frequency range [32].

(7) This technique is capable of capturing the mechanical property variations induced by temperature change as small as 2 ℃.

(8) Strain gauge measurements might not be linear during a single rod impact test, thus pulses with the same sign are recommended to be used in these calculations.

(9) The 'irregularities' and 'critical frequencies' are not seen in our results, and oscillations are believed to be induced by the window function effect. Non-uniform distributed multiple gauge station measurement is claimed to be effective in avoiding irregular results [32].

The author is gratefully indebted to Prof. Bacon for his kind direction in the data processing stage; however, this work differs from his in following aspects: 1) three rods have been tested: Titanium, Magnesium, and PMMA; 2) impactor effect (shape, size, material) was investigated. Various impactors, *e.g.* balls with different materials and diameters, and cylinders with different lengths, were employed to select the most appropriate impactor for this pendulum test; 3) strain amplitude effect was investigated. Each impactor was dropped at various heights to generate a number of strain amplitudes; 4) temperature effect was investigated in the PMMA case. Four temperatures:17.5 ℃, 19.5 ℃, 23.4 ℃, and 27 ℃ were tested, the changes in PMMA mechanical material properties were examined; 5) some critical issues during data processing such as the effect of pulse section, centering, and the frequency limits that can be achieved by using this technique were discussed; 6) geometric dispersion correction was performed and discussed; 7) DMA tests were introduced as comparison in the PMMA case; 8) simulations were performed to verify the effectiveness of this technique, and to further investigate some critical issues such as the 'gage effect'.

4.5 Results from DMA

Dynamic Mechanical Analysis (DMA) was introduced as a comparison to the single rod method. DMA is a standard method for measuring mechanical properties of polymers as a function of frequency (or time) and temperature [59] and provides an easy, reliable and effective measurement

of dynamic behaviour. Unfortunately, the highest frequency that can be directly achieved is limited (normally ~100 Hz); however, in polymers, the effective range can be greatly extended by using the well-established Time-Temperature-Superposition (TTS) principle. In this research, three DMA tests were performed on PMMA specimens (shims) and the frequency-dependent complex modulus obtained at a fixed temperature using TTS. The moduli, together with the implied propagation coefficient, Eq. (2.29b), are compared to those from single rod impact tests.

PMMA material properties have been reported to be highly temperature dependent. For example, due to its large thermal expansion coefficient, the density varies from 1195 kg m^{-3} at 0 °C to 1150 kg m^{-3} at the glass transition temperature, which for atactic PMMA is T_g = 105 °C. The T_g values of commercial PMMA range from 85 to 165 °C due to the vast number of commercial compositions, which are copolymers with co-monomers other than methyl methacrylate. It burns at 460 °C. While it is hard, stiff and 'solid-like' at low temperature, it becomes soft and 'fluid-like' above the glass transition; a 'leathery' state is found between these. The mechanical behaviour is also frequency-dependent: at longer times or low frequencies, the polymer exhibits a more liquid like response while at shorter times or higher frequencies, it behaves more like a rigid, glassy solid [44], the similarity with temperature dependence leads to the well-established TTS principle.

4.5.1 The Time-Temperature-Superposition (TTS) principle

Mechanical properties of a viscoelastic material are both time and temperature dependent. For a given temperature, the time-dependent material response can in principle be measured directly in the laboratory, but it is unrealistically time-consuming to obtain long-term behaviour, and short time behaviour is difficult or impossible to measure because of instrumentation limits and structural resonance. The time-scale of laboratory DMA tests is typically limited to several decades [60] (*e.g.* 4 decades from 0.01 to 100 or 200 Hz [61, 62]), the relaxation curve, however, usually extends over many decades of time. Mechanical behaviours outside this range can be predicted by the TTS principle, which states that the time/frequency-dependent and temperature-dependent material behaviours can be mathematically interchanged, *i.e.* the material properties measured at high temperature and short times are actually the same as those obtained at lower temperature but longer

time periods. In other words, material behaviours can be accelerated at higher temperatures and there is a direct equivalence between time/frequency and temperature [63]. The TTS principle implies that as material property functions keep the same shape at different temperatures and can be shifted along the time/frequency axis to form a master curve at a constant temperature. This principle was established by Williams, Landel, and Ferry [62], and can also be applied to pressure-dependent material behaviours. The TTS principle is also referred to by various names such as the reduced variable method, thermo-rheological simplicity, or time-temperature reducibility. One basic assumption of the TTS is that the material should be linear viscoelastic under the deformations of interest, and should exhibit thermologically simple behaviours: the evolution of time- and temperature-dependent material properties should share the same kind of law [62].

Using the TTS principle, the time/frequency scale achieved in a laboratory experiment can be extended over many decades. By testing a specimen with the normal instrument frequencies at a range of temperatures, a set of time/frequency-dependent modulus $E^*(t)$ or $E^*(f)$ segments can be obtained (each segment is an isothermal frequency scan), these segments can be shifted along the logarithmic time/frequency scale using a set of proper temperature-dependent shifting factors α to construct a smoothing master curve at an arbitrary reference temperature T_{ref}; this master curve, either in an extended time or frequency scale, represents the material behaviour at T_{ref}. An example of the master curve in Fig. 4-21.

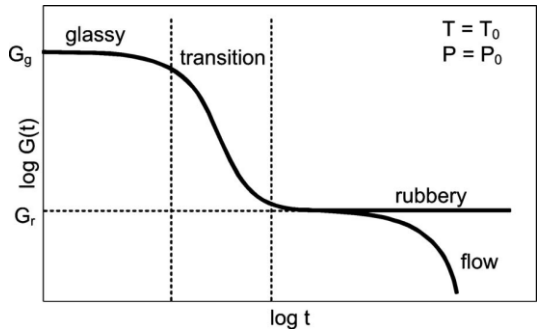


Figure. 4-21 An example of the shear modulus master curve showing the 4 states of a polymer [64]

4.5.2 DMA Experimental setup

A TA Q800 DMA machine was employed to perform tensile DMA experiments on the PMMA. A specimen aspect ratio (thickness/length) less than 1/8 is required for a tension test. In these

experiments, a PMMA sample size of 1×5×30 mm was used. After clamping, the actual sample height, *i.e.* the effective sample length between the upper and lower clamps, is automatically measured by the machine. In order to use the TTS principle, the maximum strain value was controlled to be within 0.1% (LVR strain limit) and frequencies 1, 5, 10, 25 and 50 Hz were scanned. The test temperature was ramped from -120 to 270 ℃ at 2 ℃/min. Ideally, an isothermal frequency sweep should be used; in practice, the temperature difference during a frequency scan cycle is fewer than 2 ℃.

4.5.3 DMA results interpretation

3 tests were performed under the same conditions as described above. A sample of the raw data reported by are shown in Fig. 4-22. Three distinct regions were observed in the modulus-temperature curve; during each region the PMMA material exhibits different mechanical behaviours: at low temperatures, the material is stiff, brittle, behaves like a glass, this region is called the glassy region. A small secondary transition, called the β transition, appears in this region. As the temperature increases, the polymer undergoes the main transition (α transition) from a 'glassy' state to a 'rubbery' state, this is characterized by a significant drop in stiffness. The modulus is approximately independent of temperature for a while before it enters a flow region. The data quality is generally good below the rubbery region, except that some storage modulus data are missing and irregularities appear in loss modulus during the primary transition region with the 1Hz measurement. The measurement of loss modulus becomes unstable when the material enters the rubbery region and starts melting, and this has been considered as the main cause of the failure in constructing the long term/small frequency part of the mater curve later.

Following the TTS principle, 3 approaches of computing the shifting factor α_T have been examined: manual shifting, the WLF approach, the Arrhenius method. Due to the limit of maxima thesis page number, the details were not presented here, interested readers are advised to refer to the full *web version*. The master curves obtained at two temperatures ($T_{ref} = 19.5$ ℃ and 23.4 ℃) are presented in Fig. 4-23. It is seen that different approaches of calculating α_T lead to different time/frequency scales. Despite the differences, the three methods give moduli that are almost the same in the

time/frequency range of interest (*i.e.* 10^{-2}~10^{8} Hz or equivalently 10^{-8}~10^{2} s). This is to some extent due to the fact that only in the α transition region are the modulus values sensitive to the α_T values. This is supported by the evidence that the shifting factor changes rather strongly with temperature as temperatures approaches the glass transition [60]. Note that, potential error sources existing throughout the DMA analysis cycle were included in the *web version*.

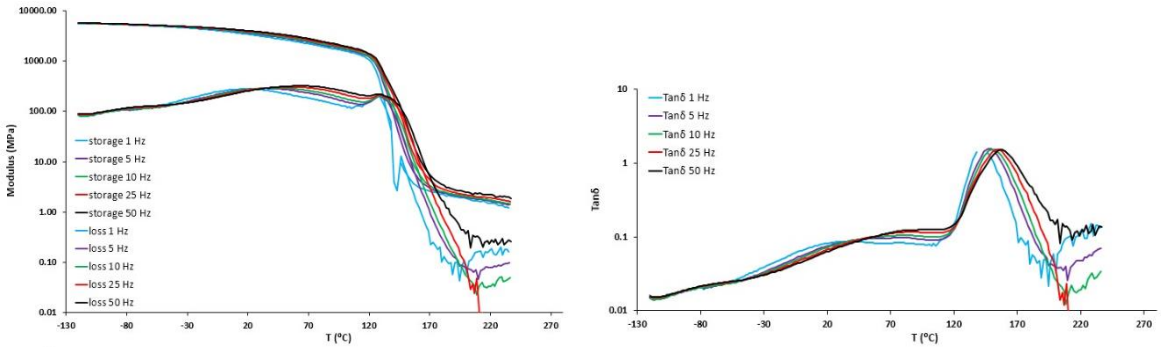


Figure. 4-22 DMA reported data (Test 1)

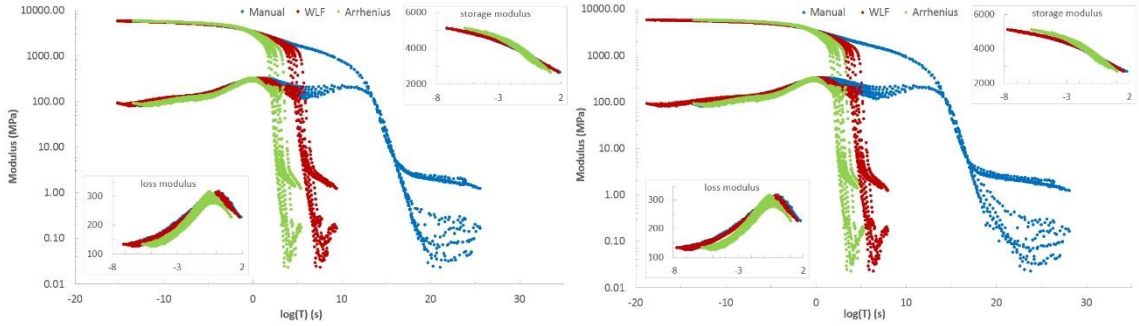


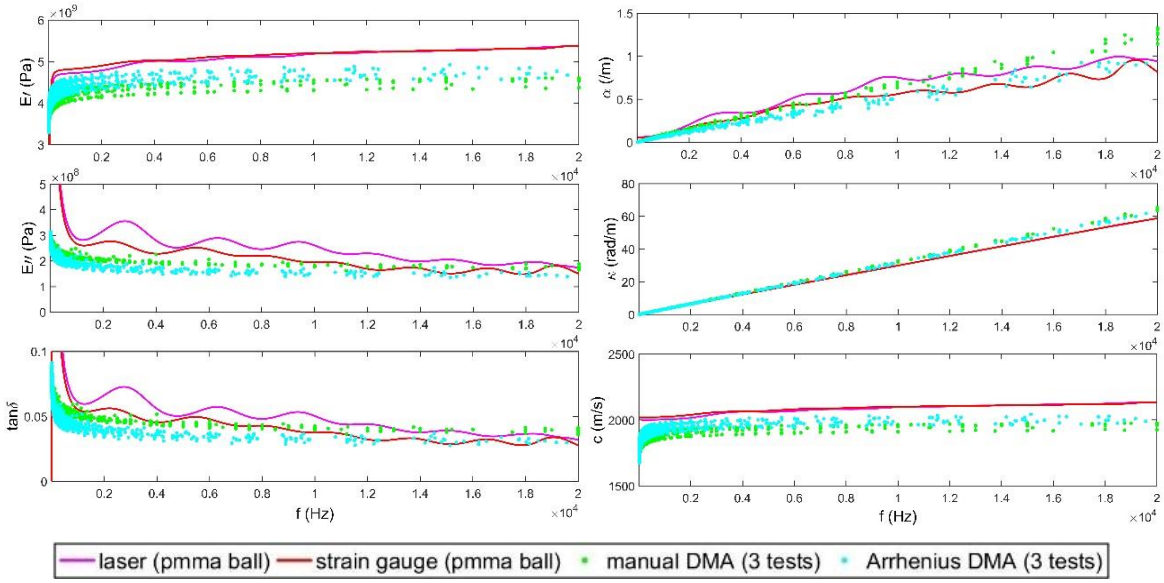
Figure. 4-23 Comparison of the mater curves obtained by 3 methods (Test 1, left: $T_{ref} = 19.5$ ℃; right: $T_{ref} = 23.4$ ℃)

4.5.4 Comparison of DMA and single rod impact test results

Comparisons of the results obtained by the two techniques (DMA and single rod impact test) at 23.4 and 19.5 ℃ are shown in Fig. 4-24. For single rod impact tests, the results using the two measurement methods (strain gauge and laser) but only the PMMA ball were presented; for DMA tests, only the manual and Arrhenius-based results were used. The techniques measure different quantities: the impact test measures the propagating waves in the rod, from which the propagation coefficient was first calculated and based on this the modulus can be derived (Eq. (2.29a)); the DMA reports the modulus, based on which the propagation coefficient was derived (Eq. (2.29b)).

A small gap is observed when comparing the modulus: the storage modulus derived by the single rod impact tests seem to be larger than that of the DMA tests all across the frequency range of interest (2 ~20 kHz), while the loss modulus and loss factor of the single rod impact tests are bigger at low frequencies. The storage modulus derived by the single rod impact tests are from 4.8 to 5.4 GPa, and from the DMA 4.1 to 4.9 GPa. Thus the single rod impact reports the material to be stiffer than the DMA results. Furthermore, the single rod impact storage modulus increases with increasing frequency while this trend is less obvious in the DMA-based storage modulus; the single rod impact results has a more finer frequency resolution (10 Hz) and thus seem to be more continuous, the DMA results show more deviation because the frequency interval is not constant and modulus can be only told at a set of discrete frequencies after shifting.

The attenuation coefficients obtained are similar at low and medium frequencies, but at high frequencies, approaching 20 kHz, the DMA-based coefficients are larger, this can be caused by the inefficient cancellation of the dispersion effect when processing the single rod impact data. More evident variations are seen in the wavenumber values, which leads to the relatively large variation in wave speed. The wave speed obtained by the single rod impact tests is in the range of 2017~2136 m/s and increases with frequency. The speeds based on the DMA moduli are 1883 ~2043 m/s and the increase with frequency is again not observed.



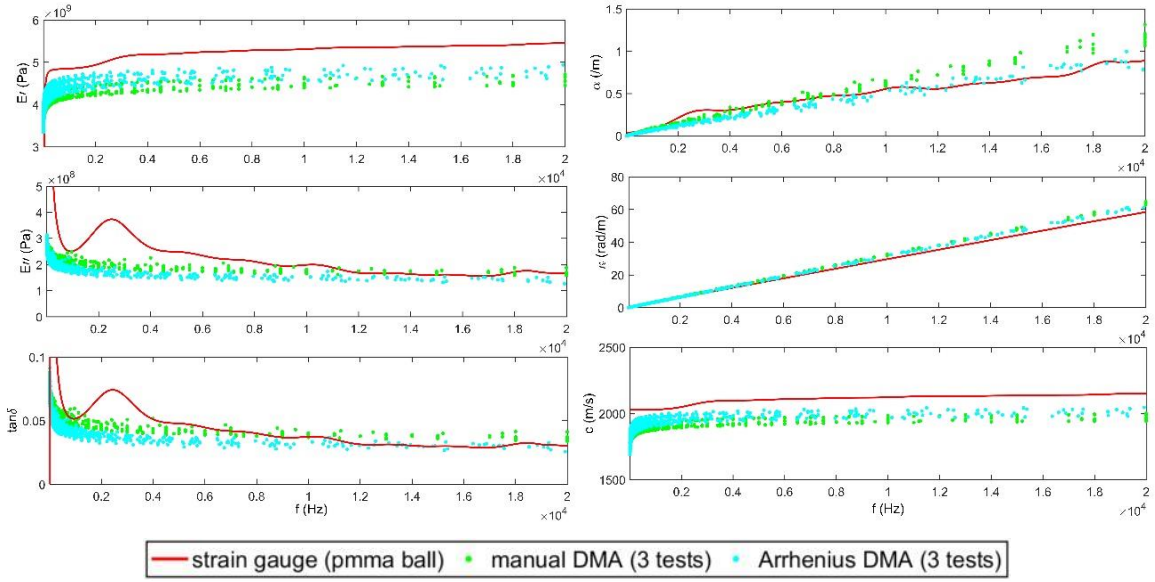


Figure. 4-24 Comparison of the results derived by single rod impact and DMA. Top 23.4 °C, bottom 19.5 °C (Left: modulus and loss factor; Right: propagation coefficient and wave speed)

Chapter 5: Determining viscoelastic material properties by measuring wave propagation in a single rod impact test: Simulation verification

5.1 Overview

Finite element (FE) simulation can serve as comparison or supplement to experiments. While the models adopted in FE simulations are simplified and thus might not fully describe real behaviour, the advantages over experiments are obvious: it is convenient to change the model boundary conditions, or geometry, and to extract data at a wide range of locations, which might be impossible or time-consuming to accomplish in practice. It is also more straightforward to methodically change material, model or analysis parameters. Finally, because the input material data are known, by recovering the given material parameters, the validity of both the analytical calculations and the analysis routines (as coded in MATLAB) can be confirmed.

In these trials, the commercial FE software ABAQUS was used to perform 2 sets of simulations: on purely elastic and viscoelastic rods. The elastic material was used to investigate the significance of geometric dispersion, to compare the signals along axis and on surface of the rod to verify the validity of the strain gauge measurement, and to examine the validity of the data analysis by comparing the simulation results with analytical calculations. Viscoelastic simulations were extensively analysed to give an understanding of issues which arose in experimental analysis, *e.g.* the useful frequency range and comparison of strain-based and velocity-based results.

In order to achieve this, the same analysis method, *i.e.* geometric dispersion correction and propagation coefficient and modulus derivation (*e.g.* Eq. (2.29) and Eq. (3.2)), were employed throughout the experimental and simulation data analysis. A progressive simulation programme was designed: firstly, the simulated rod was given elastic properties, but with modulus and density similar to PMMA; then, the rod was given viscoelastic properties. From the elastic simulations, the proposed data analysis method was verified to be effective in confirming zero damping and recovering the elastic modulus. For the viscoelastic simulations, two comparisons were made: firstly, with a known model definition, the results derived from simulation outputs are comparable to the corresponding analytically predicted values, confirming the validity of the data analysis method; secondly, using

experimentally measured material properties and velocity profile, the viscoelastic simulation results were found to be comparable to those derived from experiments.

A cylindrical rod with the geometry of 2 m length and 13 mm diameter was used in all simulations. The material properties were: mass density $\rho = 1180\,\mathrm{kg/m^3}$, Poisson's ratio $\nu = 0.38$, and instantaneous modulus $E_{inst} = 5.367$ GPa. Some common model settings are listed in Table. 5-1. The mesh size was approximately 1 mm, giving 402201 nodes, and 360000 linear hexahedral elements of type C3D8R, and field outputs were requested approximately every microsecond. The load was applied in two dynamic explicit steps: in the 'loading' step, the acceleration or velocity impulse was applied uniformly across the input end. Once the load had finished, a second 'ringing' step started, with free boundary conditions, in which the wave could oscillate freely in the bar. The bar length of 2 m is longer than in the experiment, but ensured that there was no wave overlap. For elastic cases, 4 manually designed acceleration profiles and a real experimental velocity profile have been defined in the boundary conditions. For the viscoelastic simulation, only the real experimental velocity input was used. Although in an ideal case the impact impulse should be generated using a separate impactor (like the balls and cylinders used in the experiments), it is reasonable to equivalently apply the designed impulse in the boundary conditions and distribute it uniformly across the whole impact section. The simplification of adding the loading impulse is made based on Saint Venant's principle, which states that the deformation across the cross-section becomes uniform at distances greater than the largest cross-sectional dimension from the loading end. This has been verified (at much larger distances) by the Vibrometer results (Fig. 4-18(a)).

Table. 5-1 Universal model definition and settings used in all simulations (SI Units: $\mathrm{m, kg, kg/m^3, Pa, m/s^2}$)

Geometry & Mass Density	Elastic		Meshing	Loading	Field output requests
	Instantaneous modulus E_{inst}	Poisson's ratio ν			
2ø0.013 1180	5.37e+009	0.38	Mesh size$\approx 1 \times 10^{-3}$, 402201 nodes, 360000 linear hexahedral elements of type C3D8R	2 dynamic, explicit steps: 1. Load acceleration/velocity impulse profile that defined in *Amplitudes* uniformly across the cross-section using *BCs*, time period=impulse duration; 2. Reserve 0.006 s to allow wave propagates freely in the rod before the simulation ends.	Every 1E-6 units of approx. time at requested sets

5.2 Elastic simulations

As well as confirming that the simulation is performing correctly (for example, that there are no damping factors in ABAQUS which may affect the results) elastic simulations were performed to understand the significance of geometric dispersion. The rod model is shown in Fig. 5-1a, in which 2 nodes on the non-impact end, and 8 elements in the centre, 4 distributed in the middle and 4 on the edge surface, are labelled. Strain values were taken from the elements while velocity signals were monitored at the nodes; these measurements match the experiments. For the first set of simulations (manually designed acceleration input), only surface signals (*i.e.* velocity at Node 6 and strain in Element 260001) were analysed. For the second set of simulations (real experiment-based velocity input), both those from the middle (velocity at Node 4 and strain in Element 235001) and edge (velocity at Node 6 and strain in Element 260001) were analysed, and a comparison of the strain analysis between Element 235001 and Element 260001 was presented. Note that due to the use of a second 'ringing' step allows a free boundary condition: a compressive strain pulse was reflected as tensile pulse, while particle velocity is doubled at the free ends.

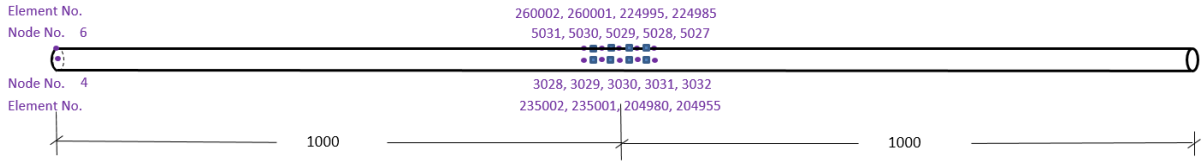


Figure. 5-1a An schematic of the simulation rod

5.2.1 Manually designed acceleration input

5.2.1.1 Input profiles

Both acceleration and velocity inputs were tested (Fig. 5-1b). This acceleration profile was initially designed to approximate the velocity derived from experiments. In the first set of simulations, the input acceleration was manually designed as

$$a(t) = A\omega sin\omega t$$

which results in a corresponding velocity profile

$$v(t) = A - Acos\omega t\ .$$

Four frequencies were applied, *i.e.*2, 5, 10 and 20 kHz, to examine the frequency dependence of the dispersion effect. In all cases the loading lasted for one period. The velocity amplitude 2A is set to

be 0.5 m/s; similar to that in the experiment and also within the linear viscoelastic region. Note that although the accelerations are sinusoidal, the pulses are finite so each contains a wide range of frequencies due to the truncation effects (see previous chapters).

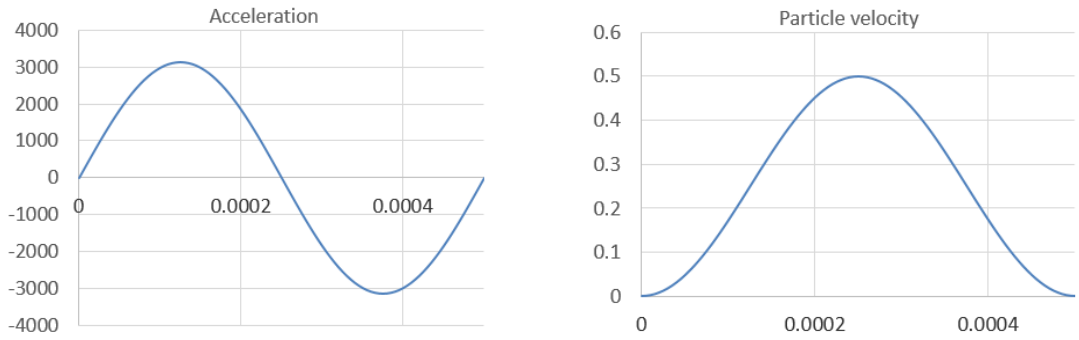
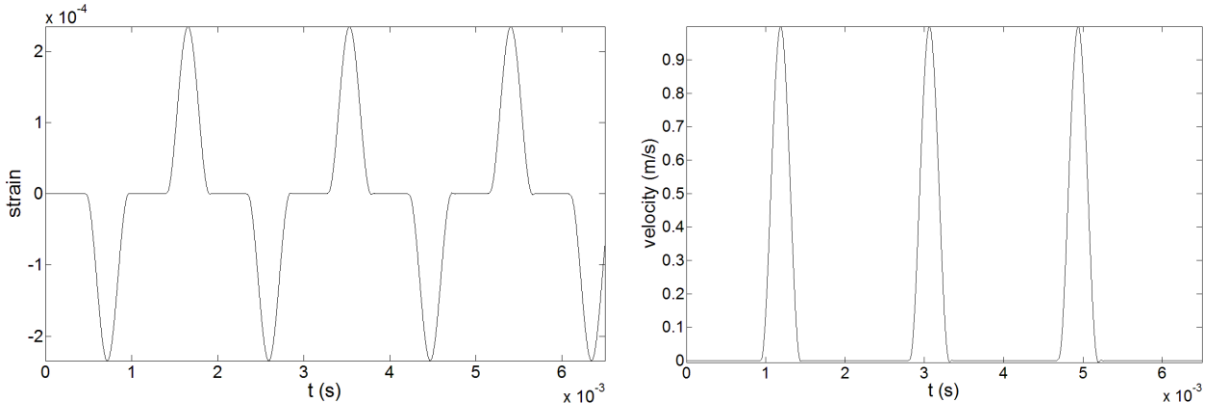


Figure. 5-1b Simulation employed input profiles: left acceleration, right velocity (2 kHz)

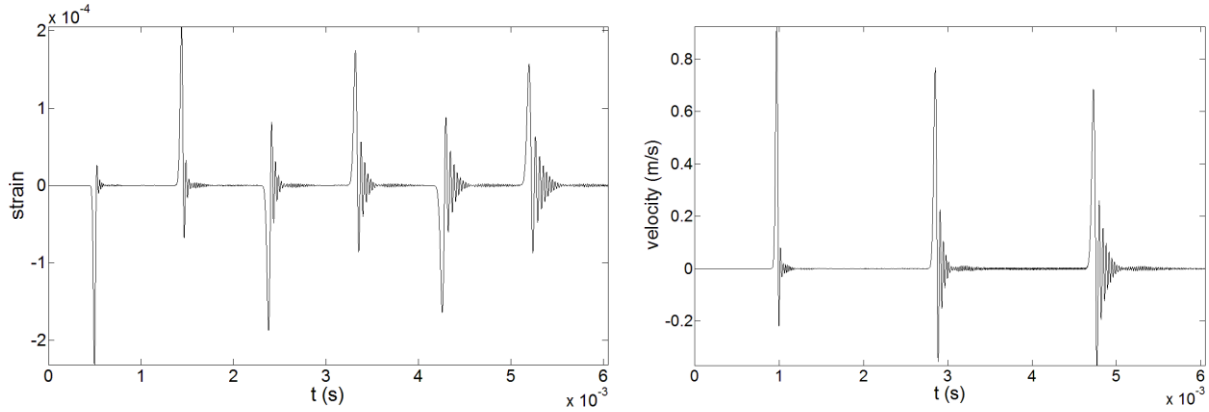
5.2.1.2 Simulation results

As an example, simulation outputs of the 2 and 20 kHz cases are shown in Fig. 5-1c and 5-1d respectively. As the frequency increases, the effects of geometric dispersion become apparent. The 2 kHz and 5 kHz inputs generally do not exhibit visible dispersion, while decreases in amplitude, oscillations in the tail and an extension in wave duration can be seen in the 10 kHz and 20 kHz cases, all of which are a result of geometric dispersion. With the knowledge that high frequencies disperse more than low frequencies, the difference in the time domain signals reflects the different weights of frequency components in each case: the 2 kHz and 5 kHz inputs may not contain as much high frequency energy as the 10 kHz and 20 kHz inputs. This confirms that dispersion correction is essential in the latter 2 cases to yield accurate results.



(a) Center edge strain history (Element 260001) (b)Free end edge velocity history (Node 6)

Figure. 5-1c Simulation outputs (acceleration input, 2 kHz)



(a) Center edge strain history (Element 260001) (b)Free end edge velocity history (Node 6)

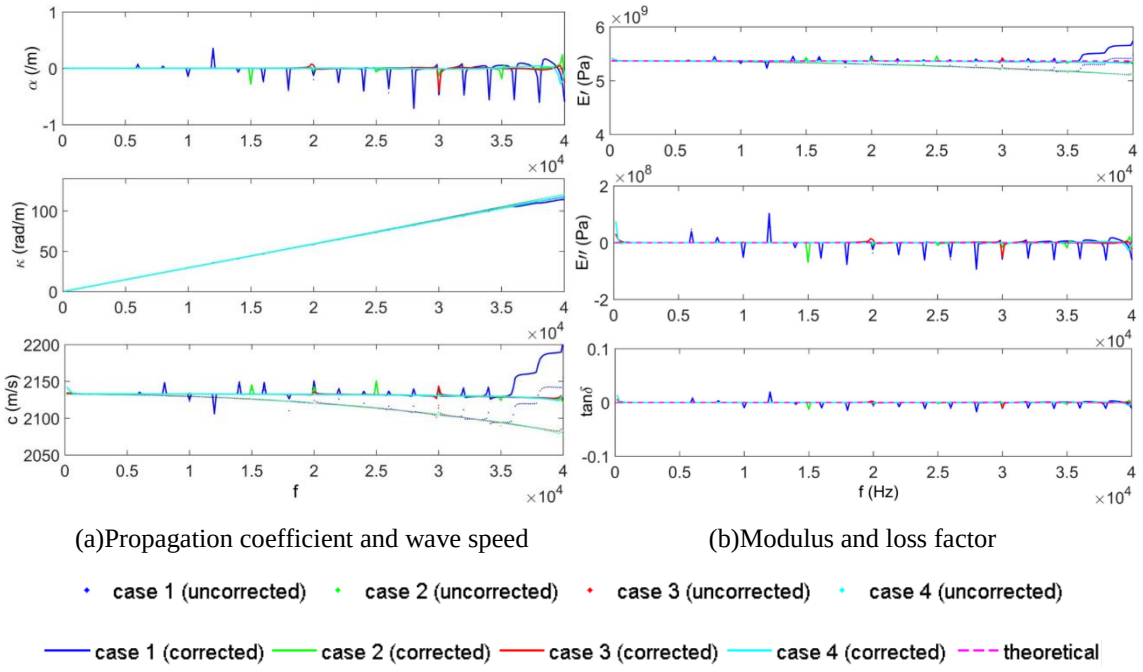
Figure. 5-1d Simulation outputs (acceleration input, 20 kHz)

The same data processing method as adopted in analysing the experimental data, and described above, has been employed here. A comparison of the velocity-based results (Node 6) of all 4 cases, with and without dispersion correction, is made in Fig. 5-2: the propagation coefficient and modulus derived should be the same. The results in Fig. 5-2 generally show good agreement, except for spikes at a frequency interval of 1/duration; these are expected to be introduced by the window function (the *sinc* function) effect which leads to small FFT values at these frequencies. The spikes in α are also reflected in E'' and $\tan\delta$ due to the close relation between these values. The storage modulus E', however, is less affected as it mainly depends on the wavenumber κ.

Ignoring the spikes in all cases, Fig. 5-2 shows that the dispersion correction plays a vital role in extending the 'useful frequency range': without dispersion correction the upper frequency is ~10 kHz while after dispersion correction this has been extended to ~35 kHz. As observed before (Fig. 3-17), the phase-only modification dispersion correction changes only the wavenumber, κ, wave speed, c, and the storage modulus, E'.

The 2 kHz simulation results show large deviation above 35 kHz; this may be due to insufficient frequency components in the input profile. However, it is noted that the increased dispersion at higher frequencies is not accompanied by a welcome increase in the upper frequency limit: all the cases in Fig. 5-2, whether dispersion corrected or not, show almost the same high frequency limit up to which the simulation-based moduli agree well with the input values. This might be due to the

small magnitudes that high frequencies possess in case 3 and 4. Similar to experimental results, the lower frequency limit indicated by the wave speed, modulus and loss factor is about 600-700 Hz.



(a)Propagation coefficient and wave speed (b)Modulus and loss factor

Figure. 5.-2 Acceleration input simulation results

5.2.2 Experiment-based velocity input

5.2.2.1 Input profiles

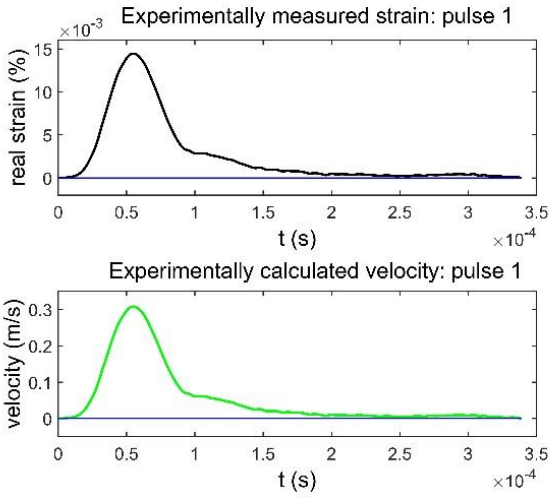


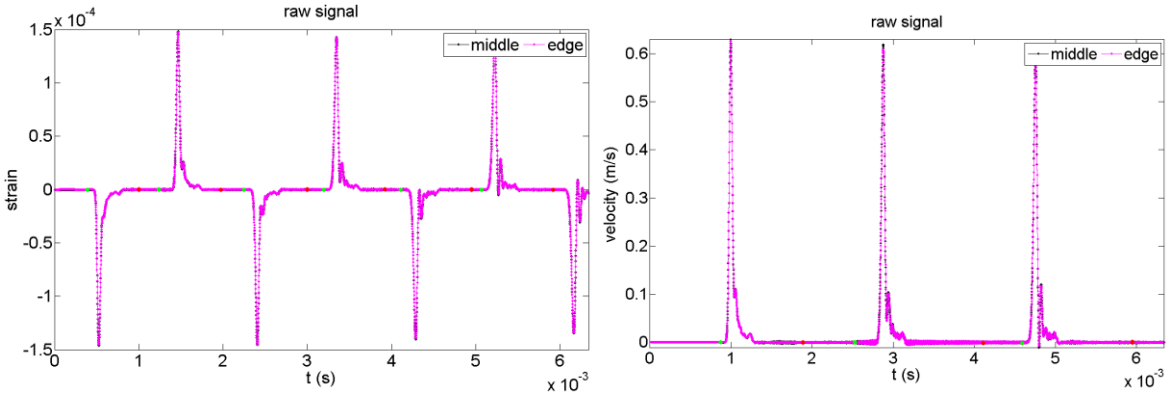
Figure. 5-3 Real experiment-based strain and velocity signals
($\emptyset 13.00 \times 1000\ mm$ PMMA rod, $T = 23.4\ ℃$)

In this simulation, the FE model remained the same but a real experimental velocity input was used. An experimental pulse, captured in one of the room temperature single rod impact tests, was used to calculate the real strain using Eq. (4.5), and the resulting velocity was obtained employing the elastic

relationship $\dot{u} = c\varepsilon$, which is reasonably accurate because the wave speed c, although frequency dependent, does not vary significantly within the frequency range of interest and thus can be considered constant ($c = \sqrt{\frac{E_{inst}}{\rho}} = 2133\ m/s$). The real strain and the approximate velocity profiles are shown in Fig. 5-3. The velocity input was defined in the simulation boundary conditions and distributed uniformly across the 'impact' section of the simulated rod.

5.2.2.2 Simulation results

Typical signals from an ABAQUS simulation are shown in Fig. 5-4. For this simulation, strain data were obtained from elements in the centre of the bar, both in the middle (Element 235001) of the bar and on the surface (Element 260001), and velocity data were obtained at one end, again from the middle (Node 4) and edge (Node 6). The time domain signals in Fig. 5-4 do not display an observable difference between the middle and edge signals. However, significant geometric dispersion, indicated by a drop of amplitude and oscillations in the tail, is seen during wave propagation in both strain and velocity signals, which means with this PMMA geometry and velocity profile, it is necessary to perform dispersion correction during the data analysis.



(a)Strain at Element 235001 (middle) and 260001 (edge) (b)Velocity at Node 4 (middle) and 6 (edge)

Figure. 5-4 Middle and edge strain and velocity signals (green dot: start point; red dot: end point)

The data analysis here is identical to the experimental procedure. Similarly, four comparisons have been made here: between the center and edge results (Element 235001 *vs* 260001), the raw and dispersion corrected results, a comparison of the strain-based and velocity-based results, and a self-comparison of the simulation-based and model defined modulus. The analysis was explained using the strain signal from Element 2350001 (Fig. 5-4(a)).

Fourier transforms of the centered pulses, with and without dispersion correction, are shown in Fig. 5-5. The dispersive wave speed profile adopted here is the same as that used in processing experimental data (Fig. 3-15(c)). The effect of the dispersion correction on the phase of the waves is clear (both the real and imaginary parts are aligned after the correction), whilst, as expected, the magnitudes do not change. The success of the dispersion correction is further confirmed by the perfect overlapping of the re-constructed pulses after dispersion correction when comparing the time domain signals before and after correction in Fig. 5-6, this is achieved by removing the dispersion-induced variations of wave speed in different frequencies, as discussed in previous section (Eq. (3.17)).

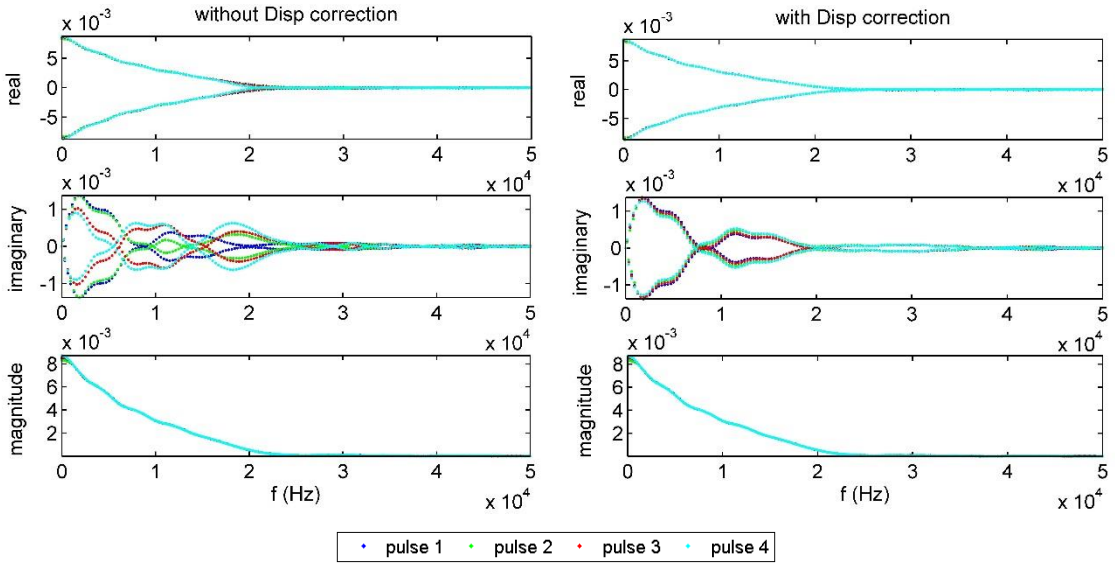


Figure. 5-5 Fourier transform of the 4 strain pulses captured at Element 2350001 (after centering)

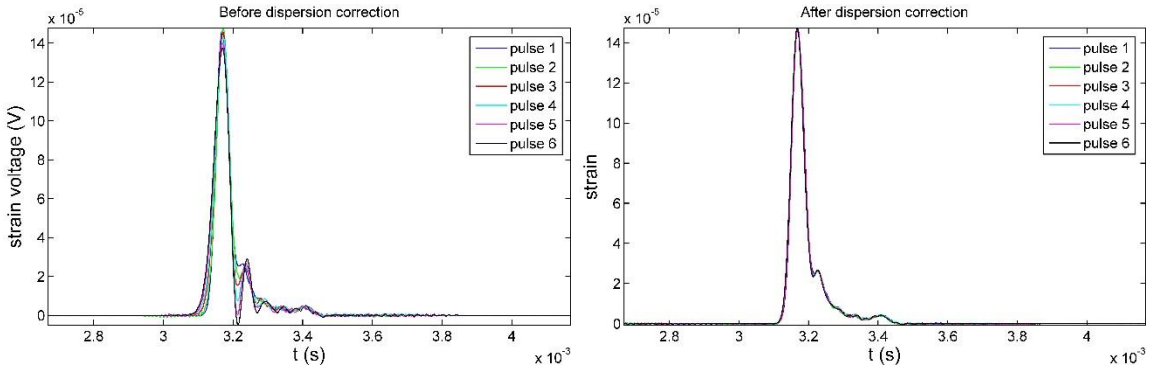


Figure. 5-6 Centered strain pulses from Element 2350001 recordings

Similar to earlier presentations of the experimental results (Fig. (4-2c)), Fig. 5-7 shows three dimensional representations of the evolution of the wave (in Fourier domain) as it propagates in the

bar, after dispersion correction and as functions of frequency and travel distance. The $\ln\left|\frac{\tilde{\varepsilon}_i}{\tilde{\varepsilon}_1}\right| - f - (x_i - x_1)$ plot represents the reduction in amplitude due to viscoelastic effects in the bar and for this elastic simulation $\ln\left|\frac{\tilde{\varepsilon}_i}{\tilde{\varepsilon}_1}\right|$ is zero within the useful frequency range; at high frequencies, however, magnitudes are small and noise appears. There are also periodic oscillations due to the window effect. In the minus $angle\left[\frac{\tilde{\varepsilon}_i}{\tilde{\varepsilon}_1}\right] - f - (x_i - x_1)$ plot, linear increase is observed with both increasing frequency and position, because the wavenumber κ increases linearly with frequency f in an elastic medium as a result of the frequency-independent wave speed c.

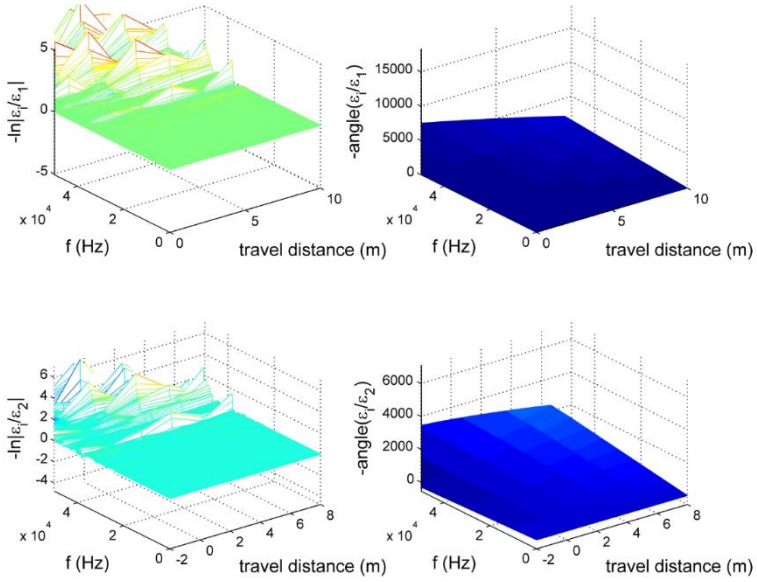
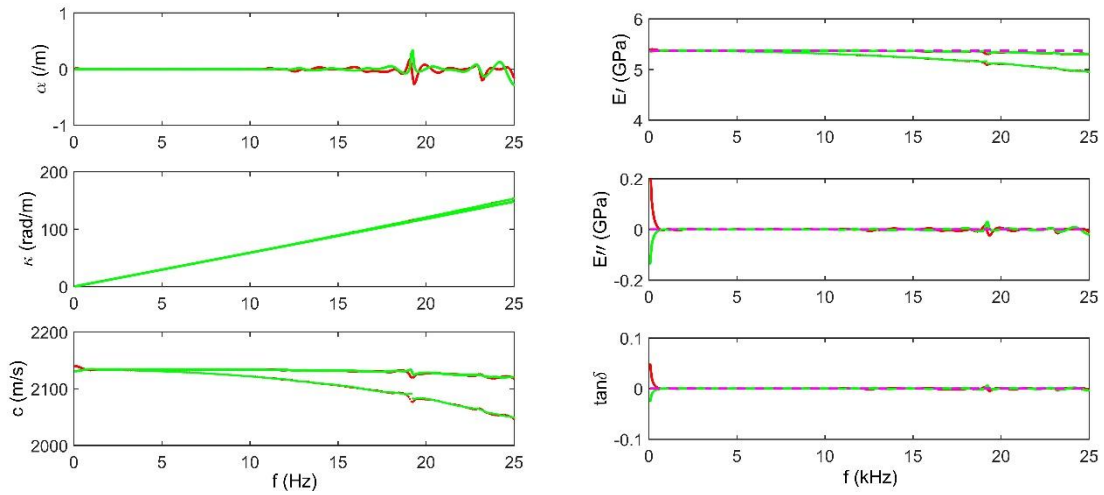


Figure. 5-7 3D dispersion corrected Fourier plots (Element 235001)

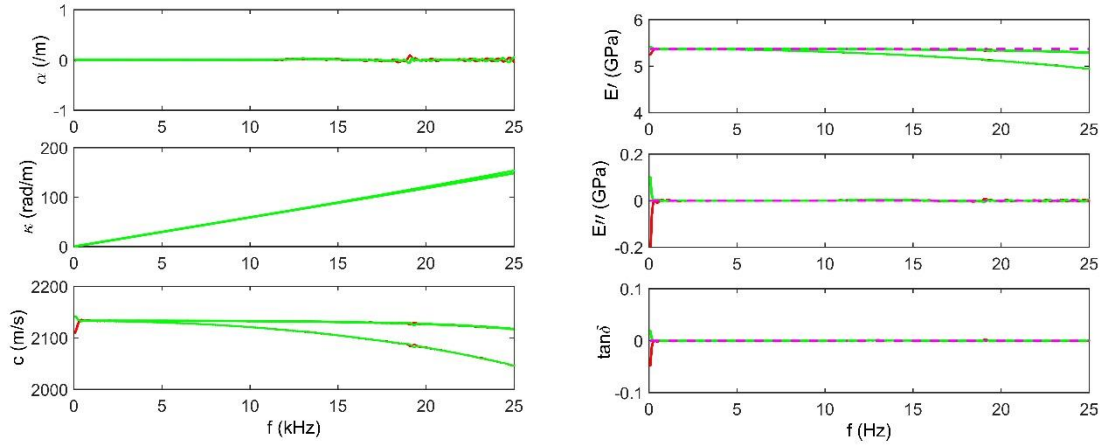
The strain-based and velocity-based results derived based on the middle and edge signals are shown in Fig. 5-8. The same start and end locations have been used within each cross-section, removing the effect of pulse selection. There are four comparisons in Fig. 5-8: the results with and without dispersion correction, the middle and edge results, the strain-based and velocity-based results, and the output and model definition.

The necessity of performing dispersion correction is confirmed in both figures. Theoretically, by removing the geometric effect (which yields a perfect 'slender' rod), both the wave speed and storage modulus should be exactly constant and frequency-independent in an elastic medium. Without dispersion correction, the wave speed and storage modulus begin decreasing above 10 kHz. After

dispersion correction, both quantities can be recovered up to 40 kHz. For the loss modulus and loss factor, dispersion correction moves the upper frequency limit from 15 to 40 kHz.



(a)Strain-based results (Element 235001 and 260001)



(b)Velocity-based results (Node 4 and 6)



Figure. 5-8 Comparison of middle and edge strain-based and velocity-based results

It is also observed that the middle and edge (surface) results are almost the same, consistent with the time domain signals shown in Fig. 5-4. This further confirms the experimental observations (Fig. 4-18 and Fig. 4-19): with this geometry configuration and at a measurement location reasonably far from the impact end, there is no significant difference between central and edge signals.

A comparison of the strain-based and velocity-based results reveals that both the strain and velocity recordings give similar results within the frequency range 1-50 kHz, the velocity-based results are generally more stable at high frequencies, this may be a result of noise in the strain calculations in ABAQUS. The comparison demonstrates that both variables can serve as the data source for using

the frequency domain analysis technique (Eq. (3.2a)), and it also confirms the stability of the data analysis method in deriving frequency-dependent material properties.

A comparison of the results from this 'experimental' input pulse and those from the manually designed sinusoidal functions is made in Fig. 5-9. Ignoring the results of Case 1 (2000 Hz manual acceleration input) which deviate after 35 kHz, and excluding the periodic spikes that are induced by the window function, it was found that the two sets of data give almost the same results in the frequency range 1 kHz-40 kHz. This again confirms the reliability of this analysis technique.

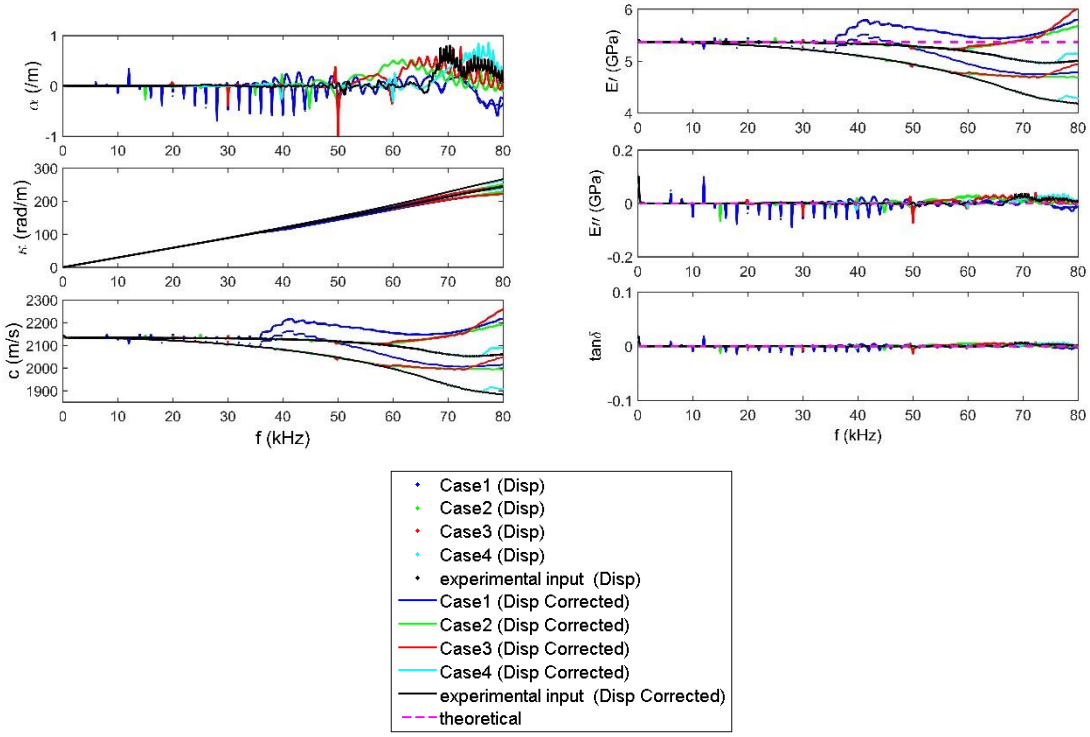


Figure. 5-9 Comparison of elastic simulation results: upper propagation coefficient, lower modulus (velocity-based, edge Node 6)

5.3 Viscoela0stic modelling

Linear viscoelastic material behaviours were defined using a PRONY model (the same as the SLS model), whose constants were obtained by fitting the material modulus curves derived from experimental single rod impact tests, and the experimental velocity input profile from the same experiment at $T = 23.4$ ℃ was employed (the same profile as Fig. 5-3). The resulting simulation results will be compared to both the analytical (self-comparison) and experimental ones.

5.3.1 Model definition

Viscoelastic behaviours were modelled using the time domain PRONY model in conjunction with the isotropic linear elasticity model in ABAQUS/Explicit (considering the impact loading nature of our tests, explicit analysis was employed). Viscoelasticity can be either defined in time or frequency domain and they share the same features: 1) they assume that the shear (deviatoric) and bulk (volumetric) behaviours are independent in multiaxial stress; 2) they can be used for small and large strain problems; 3) they can be used in conjunction with linear elastic behaviour. The difference lies in their applicability in ABAQUS/Explicit: time domain viscoelasticity is active in an explicit dynamic analysis while frequency domain viscoelasticity is not. As explicit analysis is needed to simulate the single rod impact phenomenon, time domain viscoelasticity was employed.

ABAQUS offers 4 alternative ways to define time domain viscoelasticity: direct specification of the PRONYPRONY series parameters, inclusion of creep test data, inclusion of relaxation test data, and inclusion of frequency-dependent data obtained from sinusoidal oscillation experiments. Abaqus/CAE can automatically evaluate the time domain viscoelastic response, and create response curves using the specified coefficients or test data [47].

5.3.1.1 Numerical fitting of experimental moduli to derive PRONY constants

The PRONY model, equivalently the S.L.S Maxwell model, is a parallel network model (Fig. 2-3) which combines a series of Hookean springs and Newtonian dashpots to approximate viscoelastic mechanical behaviours. It is capable of describing the broadband behaviour of viscoelastic materials by employing a large number of terms [65]. As real materials show broad relaxations it is common to employ multiple-term S.L.S Maxwell model to achieve a broad relaxation spectrum [27].

The model is characterized by the dimensionless shear and bulk moduli, $\bar{g}_i$ and $\bar{k}_i$, as well as the corresponding characteristic times τ_i (as described in Chapter 2)

$$\bar{g}_i^p = \frac{G_i}{G_0},\ \bar{k}_i^p = \frac{K_i}{K_0}$$

in which G_i and K_i represent the elastic shear and bulk moduli of each PRONY term while G_0 and K_0 are the instantaneous moduliThe shear and bulk moduli can of course be linked to the dynamic Young's modulus as follows

$$G = \frac{E}{2(1+\nu)},\ K = \frac{E}{3(1-2\nu)}$$

Numerically fitting the frequency-dependent dynamic modulus curves obtained from the single rod impact tests ($T = 23.4$ ℃, strain gage measured recordings) was a critical issue here, the challenge of obtaining a reasonable set of $\bar{g}_i^p$, $\bar{k}_i^p$ and τ_i to give a relatively precise fitting of frequency-dependent material functions (*e.g.* Young's modulus, shear modulus and bulk modulus) is widely recognised in the literature. With a PRONY series representation, experiment-based modulus curves can be either fitted in the time domain [65, 66], or in a Laplace-transform domain [67]. Several fitting methodologies can be found, for example, the collocation method [68, 69], the least-squares method [49], the multidata method [67], and the interconversion method [69]. In these trials, a least-squares method was used to fit the experiment-based shear and bulk modulus curves, from which 2 groups of PRONY constants ($\bar{g}_i^p$ and $\bar{k}_i^p$), can be obtained, although of course they are related to each other. Here the shear modulus is used as an example.

Using the shear modulus formula Eq. (2.56) [47], experimental data was fit within the frequency range 2-20 kHz; the Trust-Region-Reflective Algorithm and the nonlinear curve fitting function 'lsqcurvefit' in Matlab were employed. A scaled (weighted) least square residual, the weighted square error function χ^2, was iteratively evaluated to access the fitting quality

$$\chi^2 = \sum_{i=1}^{M}[(\frac{G_s}{\bar{G}_s} - \frac{\bar{G}_s}{\bar{G}_s})_i^2 + (\frac{G_l}{\bar{G}_l} - \frac{\bar{G}_l}{\bar{G}_l})_i^2] = \sum_{i=1}^{M}[(\frac{G_s}{\bar{G}_s} - 1)_i^2 + (\frac{G_l}{\bar{G}_l} - 1)_i^2]$$

where M is the number of frequencies at which the moduli are fitted, $\bar{G}_s$ and $\bar{G}_l$ are the experiment-based shear moduli.

The fitting results from 1-4 term PRONY models (which are most commonly used in viscoelastic characterisation) are presented in Table. 5-2 and Fig. 5-10. In these trials, the same initial values, based on *a priori* from experience, have been adopted for all models. Generally, as a result of the weighted least-squares fitting method, storage modulus data are fitted better than loss modulus. The 2-term model gives good results over most of the frequency regions but deviates slightly at low frequencies. From Table. 5-2 we can see that separate fittings of shear and bulk modulus lead to the same results as expected because they are both calculated from the same set of complex moduli. The

different constants reported by shear and bulk behaviours in the 4-term fitting case is probably due to the limit of iterations; also, with the number of PRONY terms increases, multiple solutions exist.

Table. 5-2 4-term PRONY model fitting scheme (2-20 kHz)

	PRONY constants	1-term	2-term	3-term	4-term
Initial values	Shear behaviour $(\bar{g}_i^p, \tau_i)$	(0.01, 1e-6)	(0.01, 1e-6); (0.01,1e-6)	(0.01, 1e-6); (0.01,1e-6); (0.01,1e-6)	(0.01, 1e-6); (0.01,1e-6); (0.01,1e-6); (0.01,1e-6)
	Bulk behaviour $(\bar{k}_i^p, \tau_i)$				
Fitting results	Shear behaviour $(\bar{g}_i^p, \tau_i)$	(0.097, 30.88e-6)	(0.092,52.92e-6); (0.031,5.88e-6)	(1,2659.05e-6); (0.059,32.78e-6); (0.029,3.98e-6)	(0.156,816.52e-6); (0.153,816.46e-6); (0.059,32.77e-6); (0.029,4e-6)
	Bulk behaviour $(\bar{k}_i^p, \tau_i)$	(0.097, 30.88e-6)	(0.092,52.92e-6); (0.031,5.88e-6)	(1, 2659.19e-6); (0.059, 32.78e-6); (0.029,3.98e-6)	(0.131,677.53e-6); (0.126,677.18e-6); (0.059,32.81e-6); (0.029,4e-6);
Resnorm		23.7	4.8	3.5	3.5

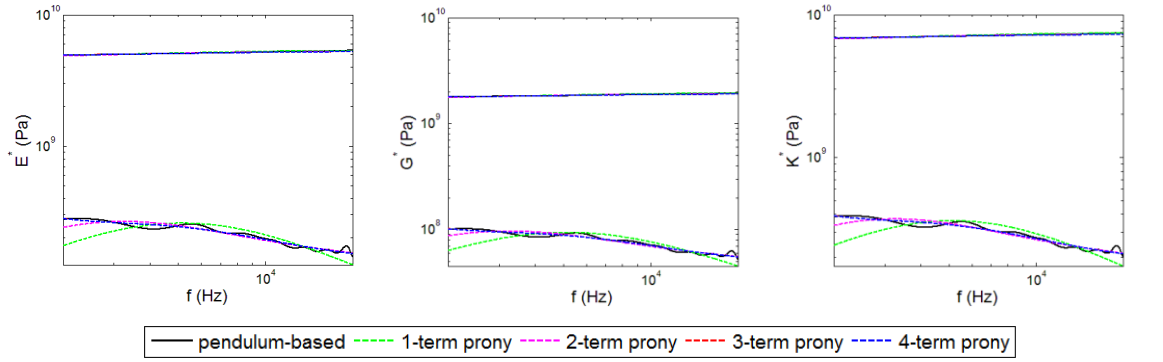


Figure. 5-10 1-4 term PRONY model fitting results (Modulus data source: $\emptyset 13.00 \times 1000\ mm$ PMMA rod, $T = 23.4$ °C, strain gage based, fitting frequency range: 2-20 kHz)

Although more terms may give more precise capture of the measured material behaviour, the 3-term and 4-term models do not improve the fitting quality significantly, and it is unlikely that all experimental data is clean and reflective of real material response, thus the 2-term simple PRONY model was used for subsequent simulations trials. The sensitivity of the fitting result to the initial values given was also examined using different initial values (details see full *web version*). When directly specifying PRONY constants in ABAQUS (Table. 5-3), if the instantaneous material behaviour is defined by linear elasticity, the bulk and shear behaviours can be defined independently,

which means these behaviours are not coupled and the constants ($\bar{g}_i, \bar{k}_i, \tau_i$) used to the behaviours do not have to be the same [47]. However, in this case they are exactly the same as they are all calculated from the same dynamic modulus.

Table. 5-3 Fitted PRONY model constants (T = 23.4 ℃)

$\bar{g}_i^p = \frac{k_i}{k_e + \sum k_i}$	$\bar{k}_i^p = \frac{k_i}{k_e + \sum k_i}$	τ_i (s)
0.031	0	5.88e-6
0.092	0	52.92e-6
0	0.031	5.88e-6
0	0.092	52.92e-6

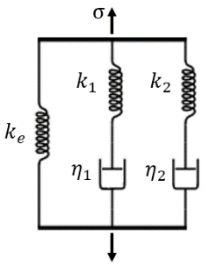


Figure. 5-11 A 2-term SLS Maxwell model

The SLS Maxwell model that represents the fitting results is shown in Fig. 5-11, in which

E_{inst} = 5.37GPa, $k_e = E_{inst} \times \left(1 - \bar{g}_1^P - \bar{g}_2^P\right)$ = 4.70 GPa

$k_1 = E_{inst} \times \bar{g}_1^P$ = 0.168 GPa, $\eta_1 = k_1 \times \tau_1$ = 990 Pa · s

$k_2 = E_{inst} \times \bar{g}_2^P$ = 0.494 GPa, $\eta_2 = k_2 \times \tau_2$ = 26200 Pa · s.

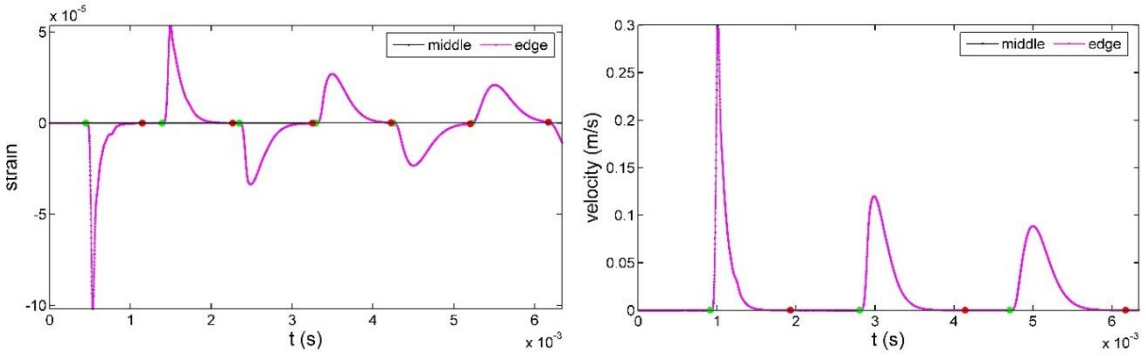
5.3.2 Simulation results and discussions

5.3.2.1 Data processing and general results

Typical signals collected in the central elements and at the non-impact end nodes are shown in Fig. 5-12. Similar to the elastic simulations (Fig. 5-4) and experiments (Fig. 4-18a), no visible difference is observed between the time domain signals in the centre and edge of the bar. Due to the viscoelastic effect, significant attenuation of amplitude is observed. Furthermore, evident extension of the pulse causes overlapping to appear in the strain data from the 3rd pulse onwards; thus we can expect that only the first 3 pulses can yield reliable results and that the velocity pulses which show no visible wave superposition may give better results. In fact, unless specially indicated, all the strain-based and velocity-based results are derived by using P 2/P 1.

There are several distinct differences between the experiment-based and simulation-based signals: firstly, the abnormal warping which has been observed in experimental recordings at the junction of two adjacent pulses (Fig. 3-7(b) and Fig. 4-13) is not seen in both the simulation-based signals, these abnormal warping is thought to be caused by the non-linearity of the PMMA bar or the strain gauge,

which is not modelled in the simulation. Secondly, the unexpected disturbances that has been seen in velocity measurements (Fig. 4-12(b) and Fig. (4-13)) do not appear in the simulations. Further, the noise level is much lower in both simulation-based strain and velocity recordings. As a, the pulses in Fig. 5-12 return to zero before the next pulse, avoiding the difficulty of careful pulse.

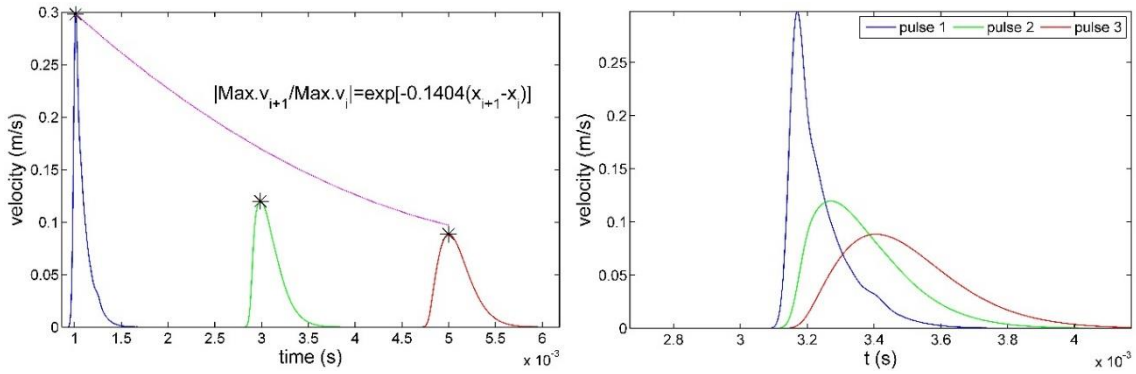


(a) Strain histories (Element 235001 and 260001) (b) Velocity histories (Node 4 and 6)

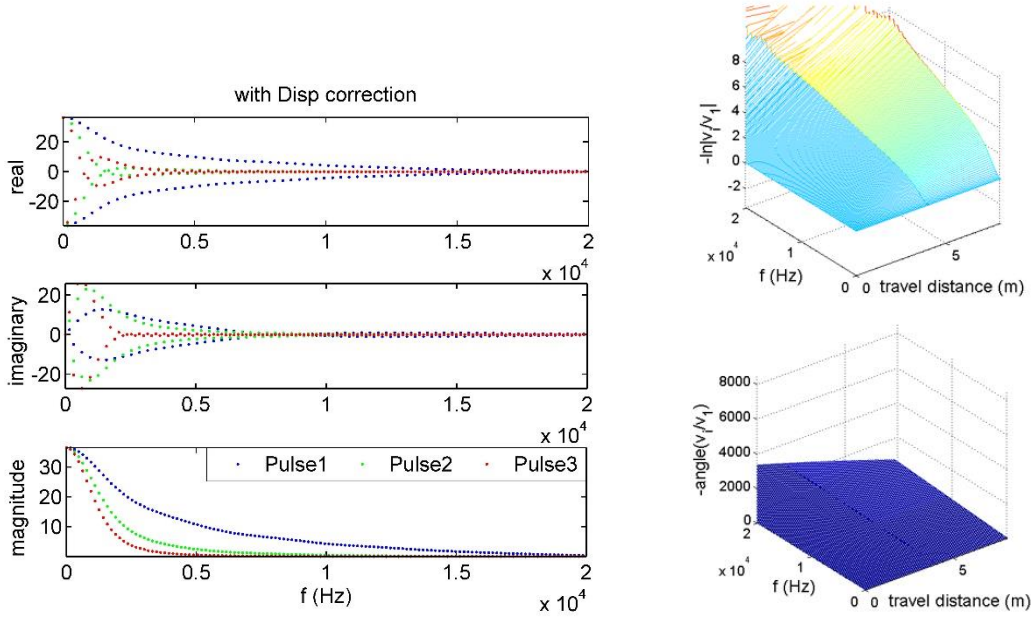
Figure 5-12. Middle and edge raw strain and velocity signals (green dot: start location; red dot: end location)

As the strain-based derivation process was been shown elastic simulations, the velocity signals recorded at Node 6 (free end edge node) are now used. A rough estimate of the attenuation can be calculated in the time domain, Fig. 5-13(a), whilst frequency-dependent magnitude attenuation can be found in Fig. 5-13(c). The dispersive wave speed profile used before (Fig. 3-15(c)) for both the experimental and elastic simulation data was adopted here.

After removing the geometric effect and centering, a difference in the phases is seen in Fig. 5-13(c), this is due to the viscoelastic effect (Fig. 5-13(b)). A linear relationship between $\ln\left|\frac{\tilde{\varepsilon}_i}{\tilde{\varepsilon}_1}\right|$ and the travel distance $x_i - x_1$ (α depends only on *f*) and a non-linear relationship between $\ln\left|\frac{\tilde{\varepsilon}_i}{\tilde{\varepsilon}_1}\right|$ and f lead to a non-planar $\ln\left|\frac{\tilde{\varepsilon}_i}{\tilde{\varepsilon}_1}\right|$ vs f vs$(x_i - x_1)$ surface in Fig. 5-13(d). In addition, the periodic oscillations, seen in our experimental (Fig. 4-8(c)) and elastic simulation signals (Fig. 5-7), appear here (Fig. 5-13(d)). The $angle\left[\frac{\tilde{\varepsilon}_i}{\tilde{\varepsilon}_1}\right]$-$f$-$(x_i - x_1)$ surface is also non-linear: wave speed c is now a nonlinear function of frequency f.



(a) A rough estimate of time domain attenuation (b) Centering and dispersion correction

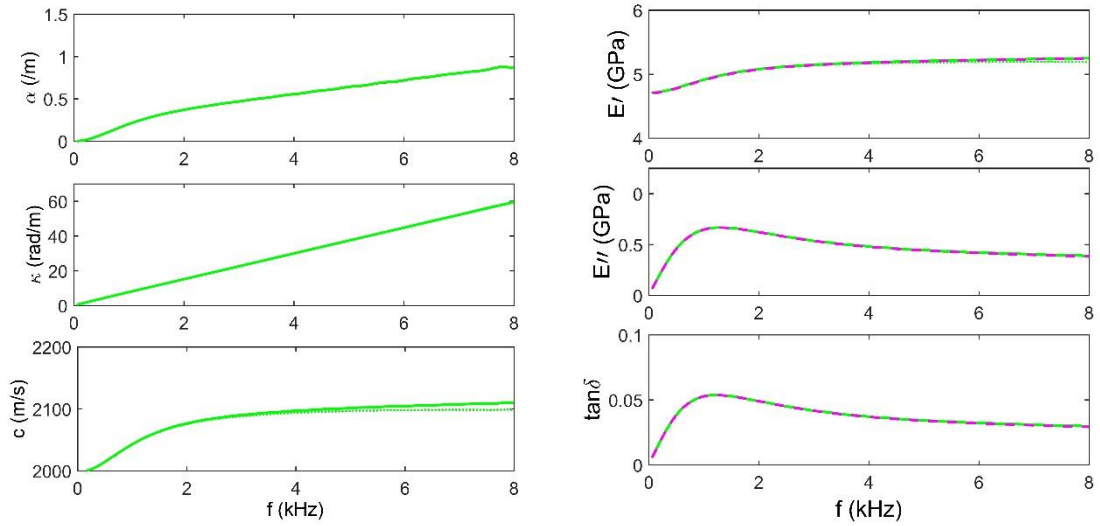


(c)FFT (d) $\ln\left|\frac{\tilde{v}_i}{\tilde{v}_1}\right|$ and $angle\left[\frac{\tilde{v}_i}{\tilde{v}_1}\right]$ as functions of $x_i - x_1$

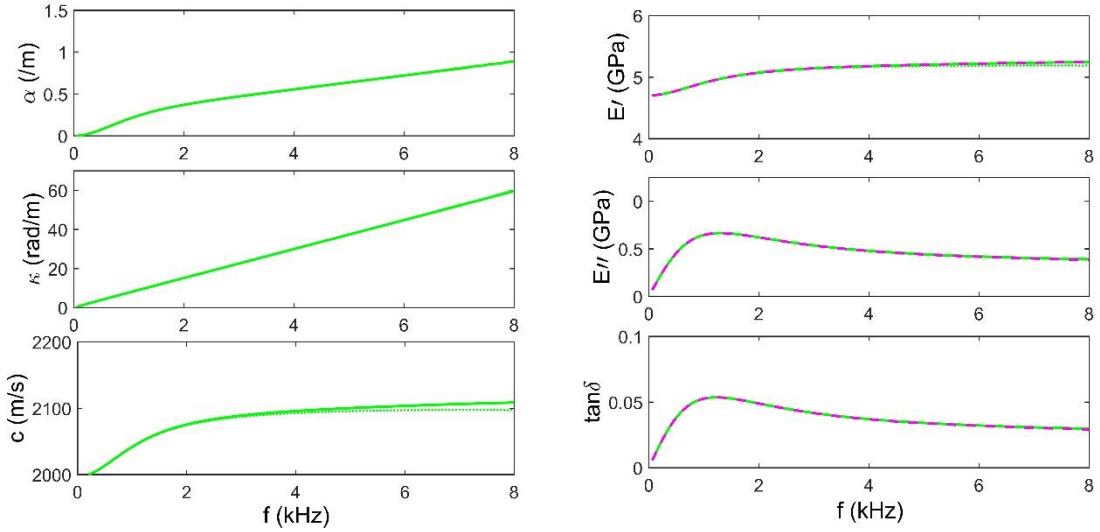
Figure. 5-13 Data processing of simulation-based particle velocity signals

Similar to Fig. 5-8, four comparisons were made in Fig. 5-14: with and without dispersion correction, middle and edge results, strain- and velocity-based, theoretical and simulation-based. The dispersion effect (Eq. (3.17)) causes a significant drop in wave speed and storage modulus above 10 kHz compared to the corresponding theoretically predicted values, geometric dispersion corrections is essential to derive intrinsic material properties at high frequencies. The middle-based and edge-based results, show no difference, consistent with the time domain signals in Fig. 5-12 and the single rod impact test results (Fig. 4-18 and Fig. 4-19). Good agreement between strain-based and velocity-based results can be seen by comparing Figure. 5-14(a) and (b): different variables can be employed (Eq. 3.2(a)) and all lead to the same material properties. Note that the lower useful frequency limit,

which was 2 kHz in experiments (*e.g.* Fig. 4-9) and 600-1000 Hz in the elastic simulation (*e.g.* Fig. 5-8), is not observed in the viscoelastic simulation analysis.



(a)Strain-based results (Element 235001 and 260001, Pulse2/Pulse 1)



(b)Velocity-based results (Node 4 and 6, Pulse2/Pulse 1)

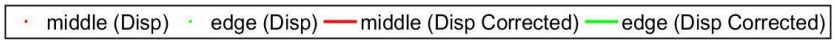


Figure. 5-14 Comparison of middle and edge strain-based and velocity-based results

5.3.2.2 Strain gauge size effect

As discussed in the experimental data processing section, the strain gauge has a finite length over which the strains it experiences are averaged. This may be a cause of the discrepancy between the laser-based and strain gauge-based results (Fig. 4-16), the other being the linearity of the strain gauge measurement. Ideally, the strain signals would be measured at a spot rather than over a finite length.

Simulation facilitates extracting strain values over regions of different sizes, based on which the effect of strain gauge size can be evaluated. Strain signals were extracted at 1 surface element (Element 260001) and 4 elements (Elements 224985, 224995, 260001, 260002). Each element has a length of 1 mm, and an average of strain values in the 4 elements was taken to be an analogue of a real strain measurement with a gauge length of 4 mm. Fig. 5-15 shows the results; although the difference is visible, it is rather small in the frequency range of interest. This is reasonable because the shortest wavelength appears at the highest frequency of interest (20 kHz), with a wavelength of about 100 mm: the effect of taking an average over 4 mm is negligible.

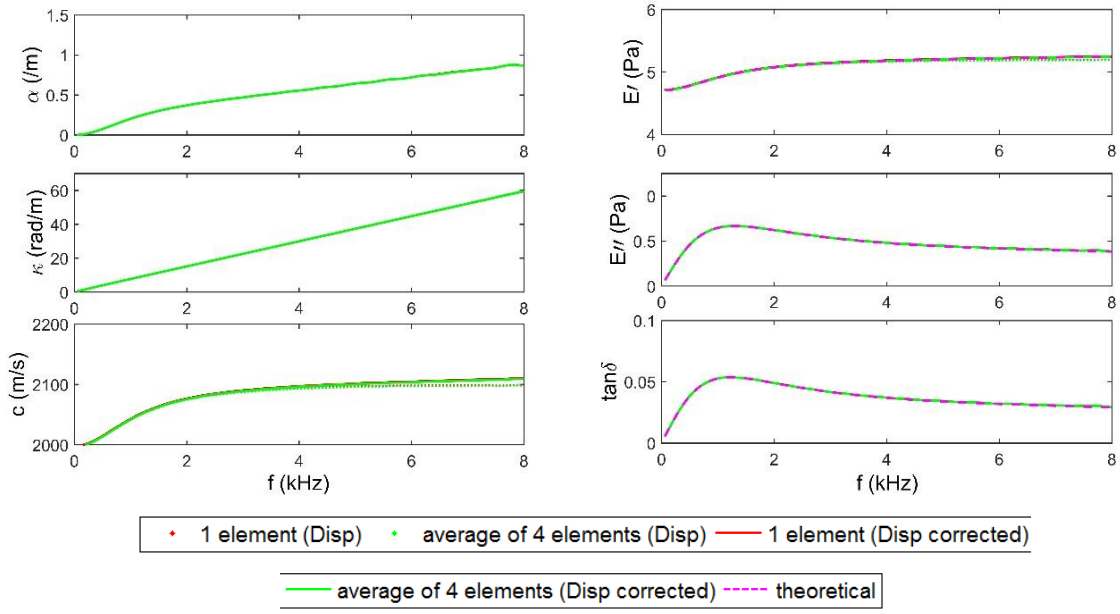


Figure. 5-15 A comparison of the 1-element and 4-element results (Pulse2/Pulse 1)

5.3.3 Noise study

5.3.3.1 Noise classification and measurement

Noise is an unwanted, and generally unknown random signal that results in either experimental or numerical errors and carry no useful information [70]. The classification of noise belongs to the subject of signal processing. Mathematically it can be classified into 2 types: additive noise can be added to the intended signal while multiplicative noise is introduced by multiplying the signal. In engineering and mathematics, especially in system and control theory and stochastic analysis, a multiplicative random term in the stochastic differential equation that the noise enters depends on the state of the system, while an additive random term does not [71].

In addition, multiplicative noise comes only with the intended/desired signal, it diminishes when the signal decreases in magnitude. Additive noise, however, is normally considered as system background noise, and it exists regardless of the appearance of the signal. Typical multiplicative noise is the speckle noise that commonly observed in image processing [72]. Typical additive noises include white noise (a random signal with a constant, uniformly distributed power spectral density), Gaussian noise (the noise amplitudes are Gaussian-distributed), additive white Gaussian noise (AWGN, an additive noise which has a uniform PSD across the frequency band and its amplitudes conform to Gaussian distribution), *etc*. Among the additive noises, AWGN is a basic model used to mimic the effect of many random processes that occur in nature [73]. A number of wideband noises that come from many natural sources, such as thermal noise and shot noise, can be considered as AWGN because the summation of these random process tends to have the normal/Gaussian distribution as per the central limit theorem of probability theory.

The relative importance of signal to noise can be measured by the signal-to-noise ratio (SNR), which is a ratio of noise power to signal power and often expressed in decibels (dB) in electrical signal processing [70, 74]. If the signal and the noise are measured across the same impedance, then the SNR can be obtained by calculating the square of the amplitude ratio [74]

$$SNR = \frac{P_{signal}}{P_{noise}} = (\frac{A_{signal}}{A_{noise}})^2 \tag{5.1a}$$

where A is the root mean square (RMS) amplitude (for example, RMS voltage). Sometimes an average amplitude square is also used, *e.g.* some functions in commercial numerical software, to compute the power (or energy) of a signal: $P_{signal} = A_{signal}^2/N$ (N is the data length). It can be seen from Eq. (5.1a) that, these 2 approaches of calculating the powers lead to the same SNR value.

Normally, the signal and noise powers are expressed on a logarithmic decibel scale (dBw or dBm):

$$P_{signal,dB} = 10log_{10}(P_{signal}), P_{noise,dB} = 10log_{10}(P_{noise}) .$$

Similarly, if SNR is expressed in deciBels

$$SNR_{dB} = 10log_{10}(SNR) .$$

Then

$$SNR_{dB} = 10log_{10}\left(\frac{P_{signal}}{P_{noise}}\right) = P_{signal,dB} - P_{noise,dB} \tag{5.1b}$$

alternatively,

$$SNR_{dB} = 10log_{10}(\frac{A_{signal}}{A_{noise}})^2 = 2(A_{signal,dB} - A_{noise,dB})\,. \tag{5.2}$$

It is the author's intention that the concept of SNR can be either defined in time or frequency domain. Both definitions are based on a power (or energy) ratio as defined in Eq. (5.1). The amplitude used in Eq. (5.1) can be either time domain amplitude or frequency domain magnitude, and the power (or energy) the corresponding square of either quantity. The most commonly used, of course, is the time domain SNR. While a uniform frequency domain $\widetilde{SNR}$, actually indicates an amplification of the original signal, as will be seen later.

(1) Time domain SNR

By definition, the power (or energy) of a time domain signal is the square of signal amplitude. Thus the time domain SNR can be calculated as

$$SNR = \frac{\sum_{i=1}^{N} x_i^2 /N}{\sum_{i=1}^{N} x_i'^2 /N} = \frac{\sum_{i=1}^{N} x_i^2}{\sum_{i=1}^{N} x_i'^2} \tag{5.3a}$$

$$SNR_{dB} = 10log_{10}\frac{\sum_{i=1}^{N} x_i^2 /N}{\sum_{i=1}^{N} x_i'^2 /N} = 10log_{10}\frac{\sum_{i=1}^{N} x_i^2}{\sum_{i=1}^{N} x_i'^2} \tag{5.3b}$$

in which x_i is the time domain amplitude of a clean signal, and x_i' of the noise.

It is seen from the definition that, the time domain SNR only requires the total energy ratio of the signal to noise, it doesn't contain energy distribution information. Therefore, if a clean signal is known, in a trial to derive a noise that controlled only by the time domain SNR, the derived noise can come in various forms. In fact, a time domain signal is normally characterized by its mean and variance, and in many noise study cases the noise encountered belongs to a category of the Gaussian white noise which has zero mean and unity variance that equals the time domain power of the noise signal. Thus controlling the time domain SNR is in fact controlling the signal variance, and as different signals can share the same variance, the noise deduced can be in different forms. It is thus essential to address that, a time domain SNR is not enough to exactly define a noise because the unclear allocation of noise distribution yields different distribution forms even with the same desired

SNR. Despite its failure in determining the distribution of the noise, the time domain SNR is a useful but rough indicator for evaluating the relative importance of signal to noise power.

In later trials, the time domain SNR was further divided into 2 types: the global SNR which defines the noise intensity in terms of the whole signal power, and the local SNR that controls the noise level with regard to an individual pulse contained in a series of signals.

(2) Frequency domain $\widetilde{SNR}$

As discussed before, the time domain SNR contains no detailed information about the noise distribution. The concept of frequency domain is thus put forward to allocate the noise across the whole frequency spectrum. It is defined as the Power Spectrum Density (PSD) of the signal to that of noise. PSD can be normally used to evaluate the energy of a single frequency, thus the frequency domain $\widetilde{SNR}$ can be defined as

$$\widetilde{SNR}(f) = \frac{PSD_{signal}(f)}{PSD_{noise}(f)} = \frac{Mag^2_{signal}(f)}{Mag^2_{noise}(f)} \tag{5.4a}$$

$$\widetilde{SNR}_{dB}(f) = 10log_{10}\left[\frac{PSD_{signal}(f)}{PSD_{noise}(f)}\right] = PSD_{dB,signal}(f) - PSD_{dB,noise}(f)$$
$$= 20log_{10}\left[\frac{Mag_{signal}(f)}{Mag_{noise}(f)}\right] = 2[Mag_{dB,signal}(f) - Mag_{dB,noise}(f)] \tag{5.4b}$$

where the FFT magnitude is the square root of the sum of the real and imaginary squares.

The difference between the time and frequency domain SNRs lies in their definitions: the time domain SNR gives a rough evaluation of the ratio of the total signal power to noise power while the frequency domain $\widetilde{SNR}$ defines a PSD ratio for every frequency. In a particular case where all the frequency components share the same constant frequency domain $\widetilde{SNR}$, due to the linearity property of Fourier Transform, the corresponding noise can be derived by amplifying the time domain clean signal by $\frac{1}{\sqrt{\widetilde{SNR}}}$. For example, if a time domain noise, with amplitude $x_i' = \frac{1}{m}x_i$, is to be generated, then in frequency domain we have

$$\frac{FFT_{signal}(f)}{FFT_{noise}(f)} = \frac{Real_{signal}(f) + Imag_{signal}(f)}{Real_{noise}(f) + Imag_{noise}(f)} = m \tag{5.5}$$

which is equivalent to

$$\begin{cases} Real_{signal}(f) = m \times Real_{noise}(f) \\ Imag_{signal}(f) = m \times Imag_{noise}(f) \end{cases}.$$

According to the definition of the frequency domain $\widetilde{SNR}$ (Eq. (5.4a)) we have

$$\widetilde{SNR}(f) = \frac{Mag^2_{signal}(f)}{Mag^2_{noise}(f)} = \frac{Real^2_{signal}(f)+Imag^2_{signal}(f)}{Real^2_{signal}(f)+Imag^2_{signal}(f)} = m^2 . \quad (5.6)$$

However, it should be noted that a uniform $\widetilde{SNR}$ across all the frequencies doesn't guarantee the resulting noise is an amplification of the corresponding clean signal in time domain, as it can be seen from Eq. (5.6) that an $\widetilde{SNR}$ of m^2 doesn't require a linear amplification of both the real and imaginary parts. Thus the amplification of the time domain signal, which amplifies both the real and imaginary parts at the same time, is just approach to achieve a uniform frequency domain $\widetilde{SNR}$.

5.3.3.2 Case study: applying artificial and experimental noises to simulation signal

Noise test scheme

The nature of the noise problem is that when the signal magnitudes are not large enough compared to that of the noise, the signal becomes weakly identifiable and thus the SNR becomes small and the results may be quite sensitive to the presence of noise. SNR plays a key role in signal processing. If a longer recording time is used, the signal magnitude will drop as a result, whilst the noise level is the same, leading to a reduction of the SNR [52]. Multi-point strain measurement can help improve the SNR as it allows higher strain magnitudes to be monitored [52]. By controlling the shape and length of the incident pulse, for example by using different types of excitations and pulse shapers, it may be possible to allocate more energy for the low and high frequency regions.

Computer-based simulation approximates perfect impact conditions of relatively small noise. The raw simulation signal may contain small numerical errors, and in all previous analysis wavelet-based de-noising method was applied in the pre-data processing stage. However, this noise is small and the raw simulation signal can be considered as a 'clean' signal to which noise can be added.

To start, a general case is used as an example, in which an additive white Gaussian noise (AWGN) was generated and added to a 'clean' experimental signal. Some general characteristics such as amplitude distribution of AWGN, the relation between time and frequency domain SNR, the PSD

distribution of the signals before and after noise addition, and the efficiencies of 3 common de-noising methodologies are discussed. Then some specific cases are used to examine the effects of noise on material properties derivation by adopting 2 different levels.

A general case: generating noise using time domain SNR

Gaussian white noise was produced by using the MATLAB function 'randn' based on a time domain SNR. Firstly, the time domain power of the signal X (with amplitude x_i) was calculated

$$P_{signal} = \frac{\sum_{i=1}^{N} x_i^2}{N}$$

in which $N = length(X)$. Then the time domain power of the noise X' (with amplitude x_i') was estimated by introducing SNR

$$P_{noise} = \frac{\sum_{i=1}^{N} x_i'^2}{N} = \frac{P_{signal}}{10^{\frac{SNR_{dB}}{10}}}$$

Note that as the mean of the AWGN noise $\bar{x'}$ is zero, its variance δ_{noise} equals its power

$$\delta_{noise}^2 = \frac{\sum_{i=1}^{N}(x_i' - \bar{x}')^2}{N} = P_{noise}\ .$$

By generating a normally distributed random noise X'' (with zero mean and unity variance and power), the objective noise X', with an updated variance δ_{noise} and power P_{noise} which corresponds to a certain SNR, can be obtained:

$$X' = \sqrt{P_{noise}}X'' = \sqrt{\frac{\frac{\sum_{i=1}^{N} x_i^2}{N}}{10^{\frac{SNR_{dB}}{10}}}}X''\ . \tag{5.7}$$

By checking the noise generation process, it can be seen that the SNR was included in the δ_{noise} term, which corresponds to an average variance over the time domain. This implies that generating a noise in time domain based on the time domain SNR may not guarantee a constant $\widetilde{SNR}$ for every component in frequency domain, which further indicates that defining a SNR by using PSD in frequency domain might be more reasonable to realise a uniform SNR over the whole frequency band. This point was verified later by examining Eq. (5.1a) throughout the frequency band, from which it was addressed that, if SNR is controlled by the summations of time domain amplitudes of both signal and noise, the frequency domain PSD-based SNR is not necessarily the same as the time

domain one. In fact, if noise is generated using the time domain SNR, the resulting frequency domain $\widetilde{SNR}$ (*e.g.* the Welch PSD ratio based on Eq. (5.4)) is not constant over the whole frequency band (Fig. 5-16(c)), it is larger or approximately the same as the designed value only in the frequency region where the PSD of the desired signal is large. In other regions, i.e. where small PSDs were observed, however, the PSD-based SNR_{dB} is mostly less than zero, which indicates signal is too small compared with noise.

During signal processing, the SNR can be controlled in 2 ways: either using a global/whole SNR or using a local/individual SNR. The first refers to the case in which the SNR is calculated based on the whole signal collected, while the later one corresponds to computing the SNR individually for each pulse. The global SNR seem to be more practical because it is closer to that observed in practice, a global SNR is the ratio of the sum of the whole energy in all 6 pulses to that of the noise over the whole monitoring period. The global additive noise can be used to simulate the background Gaussian noise which is independent of the desired signals.

A general case study was performed using the strain recording in Fig. 5-12(a), extracted at the edge element 260001 in the viscoelastic simulation with experimental velocity input. The clean strain signal and its corresponding Power Spectral Density (PSD) estimate (via Welch's method [75]) are shown in Fig. 5-16(a), also shown are the resulting noise and noisy signal. The global time domain SNR_{dB} was set to be 10 dB, which means that the sum of the square of the signal amplitudes is 10 times that of the noise based on Eq. (5.3b). A closer look at the original signal PSD (Fig. 5-16(a)) reveals that, the PSD generally keeps decreasing from low to high frequencies in the frequency interval $0\sim25$ kHz, with the PSDs at 20 kHz and 25 kHz being around -180 and -200 respectively. Those above 25 kHz are almost constantly below -200. It is thus concluded that, the singnal may not carry any information about frequencies above 25 kHz, and the differnce between 20 kHz and 25 kHz, is 100 times according to Eq. (5.3b).

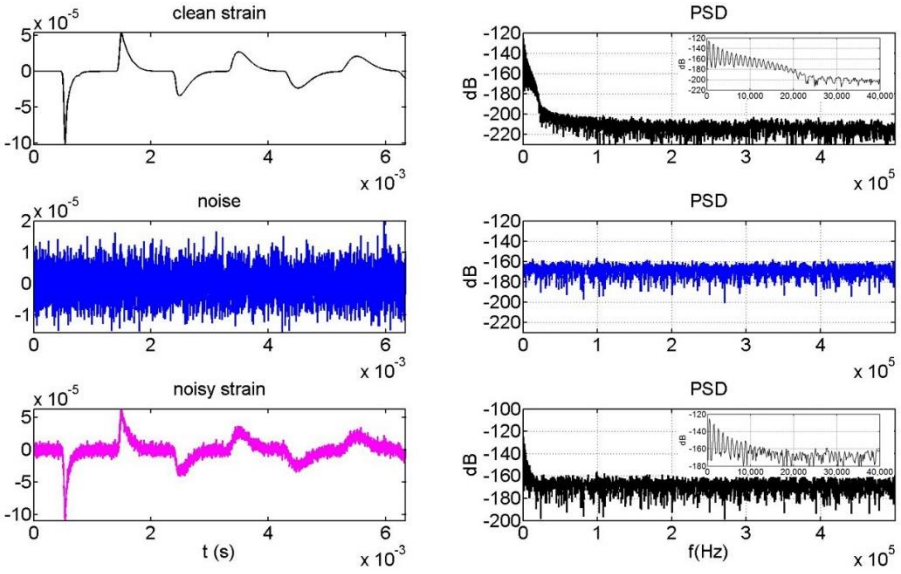
The additive Guassian white noise has the same length *N* as the clean strain signal, and it was generated according to Eq. (5.7). It is found that the PSD of the Gaussian white noise conforms to a uniform distribution across the frequency band (Fig. 5-16(a)), as indicated by the definition itself.

After sorting the random amplitudes, it is found that the distribution of amplitude obeys to the standard normal distribution with zero mean and unity variance (Fig. 5-16(b)). While the global time domain SNR_{dB} was used here, the resulting frequency domain $\widetilde{SNR}_{dB}$ was evaluated in Fig. 5-16(c) using Eq. (5.4b), in which the PSD was computed by Welch's method. It is seen that, the resulting frequency domain $\widetilde{SNR}_{dB}$ varies from -80 to 50 over the whole frequency band, which deviates a lot from the desired constant time domain SNR_{dB}. This indicates that a uniform SNR_{dB} in time domain doesn't necessarily guarantee a uniform $\widetilde{SNR}_{dB}$ in frequency domain across the whole frequency band, which again calls for the necessity of using a frequency domain $\widetilde{SNR}_{dB}$ if frequency characteristics are of interest in the future. The special case, i.e. a uniform $\widetilde{SNR}_{dB}$ in frequency domain, is equivalent to an amplification of the time domain signal as discussed before.

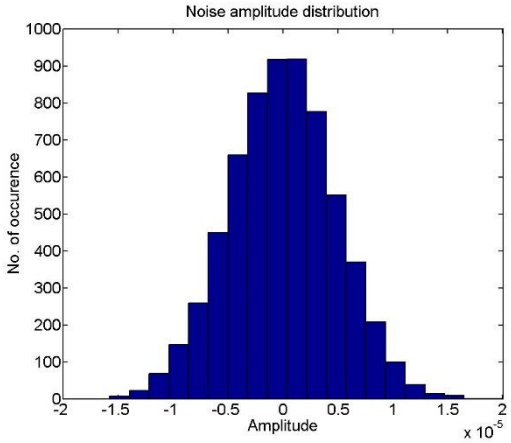
The resulting noisy signal and its PSD was shown in Fig. 5-16(a).Within a frequency range of $0\sim25$ kHz, which is believed to be the 'valid' frequency band that the original signal possesses, the origianl clean signal is either weakened or strengthened after adding the noise, which leads to the inregular variations in the noisy signal PSD. An improvement in PSD can be observed outside the 'valid' frequency range as noise dominates in this region.

As a preliminary attempt, 3 noise cancellation methodologies were introduced and compared here. The fisrt de-noising strategy is the wavelet-based de-noising methodology. The MATLAB built-in function 'wden' performs an automatic de-noising process of a 1D signal using wavelets. The noisy signal was decomposited using 'sym5' wavelets at level 2 with the soft minimax thresholding method. The second one, the Butterworth de-noising method, is fulfilled using the MATLAB function 'butter' and 'filtfilt'. Here, 'butter' designs an Nth order Butterworth filter and returns the filter coefficients which were then input into 'filtfilt' to filter the noisy signal. Here N=30 and a cut-off frequency of 100 kHz were set. The third method employs a cubical smoothing algorithm with five-point approximation (5-point cubical smoothing method). Fixed constant coefficients were used in the algorithm, and each data point of the resulting signal was computed arithmetically based on an 'average' of 5 noisy data nearby, no frequency analysis was involved.

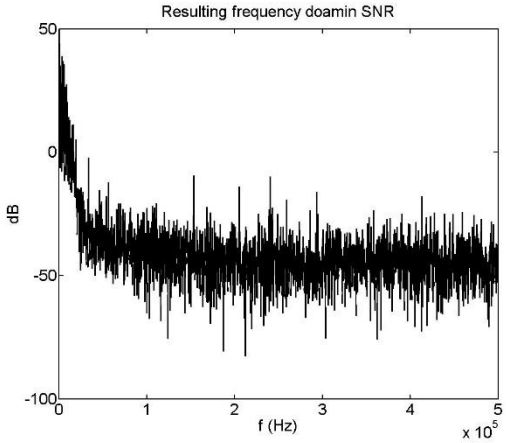
The clean, noisy and de-noised signals are shown in Fig. 5-16(d). It is seen that these 3 methods have different efficiencies in dealing with the noise, with the Butterworth filtering method being most effective, the wavelet one second and the 5-point cubical smoothing method the last in terms of cancelling high frequency noise components. Once the cut-off frequency was set, the Butterworth filter strictly acts as a low-pass digital filter. However, an estimation of the 'valid' frequency band has to be performed before using the Butterworth method to locate the cut-off frequency, this can normally achieved by performing spectral analysis, and it cannot remove noise frequencies mixing with the clean signal. The 2-level wavelet de-noising method can gently recognize the relatively high frequencies (*e.g.* > 20 kHz) but failed to separate the clean signal and noise in the low frequency region. The performance of the 5-point cubical smoothing method is even worse; it removes noises in certain band and cannot identify those in the 'valid' signal region. It should be noted that while the constants in the 5-point cubical smoothing formula are fixed, those in the first 2 methods can be adjusted. For example, the cut-off frequency in the Butterworth method can be user-defined, and the wavelet types and decomposition levels in the wavelet-based method can be modified to make the de-noising process more effective, for example, differences can be seen in the high frequency region (*e.g.* > 2 kHz) when the decomposition tree level is less than 4; however, no big difference can be seen when it is larger than 4, and for those < 2 kHz, whatever level is used, no evident difference can be seen. Also, some of the de-noising methodologies might modify the frequency phase as well. It is not the purpose here to discuss the de-noising methodologies in detail, readers can find these strategies, and even more effective methods, in the signal processing literature. More emphasis here was put on the sensitivity of the propagation coefficient and modulus to noise by analysing the noise signal without a de-noising process. And in all the previous trials, the 'wden' function has been gently adopted to de-noise the raw signals (either generated from simulation of experiments) without extra phase shift.



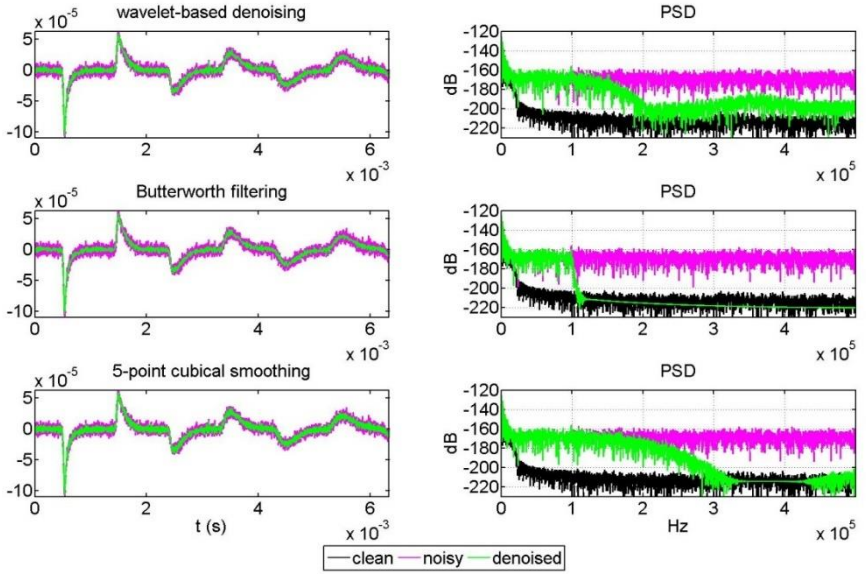
(a) PSDs of the clean, noise and noisy signals.



(b) Amplitude distribution of the Gaussian white noise



(c) Frequency domain $\widetilde{SNR}_{dB}$



(d) Comparison of different de-noising methods

Figure. 5-16 A experiment-based simulation signal noise study ($SNR_{dB} = 10\ dB$)

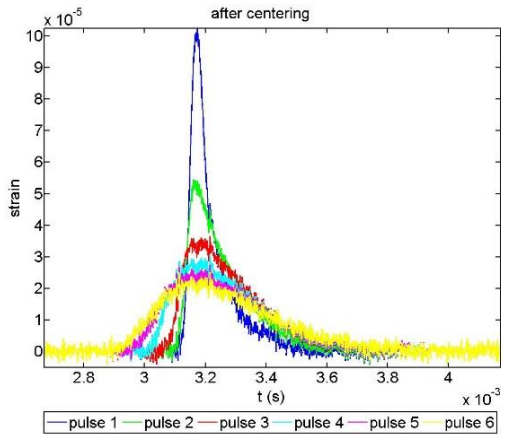
Effects of noise on material property derivation

In this section, both artificially generated noise, the additive white Gaussian noises (AWGN), and experimentally collected noise were modulated using time domain SNR; they were then added to the simulation strain signal (Fig. 5-12(a) or Fig. 5-16(a)), and the resulting material properties were compared with those generated by the clean signals and those theoretically predicted (Fig. 5-14(a)). In all the artificial noise trials, the same raw Gaussian white noise, which was generated by the MATLAB function 'randn' with zero mean and unity variance, was used and modulated (which means they all share the same time domain distribution characteristics except for their powers).

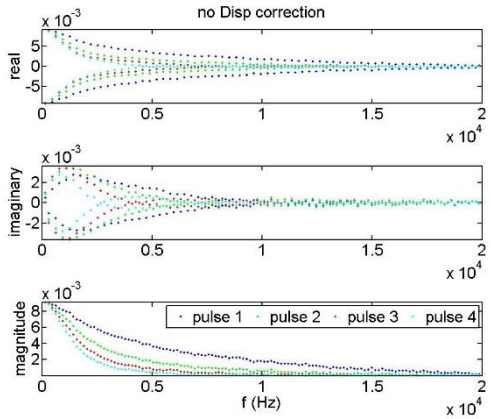
(1) Gaussian white noise

The noises adopted here were set either globally or locally at 2 levels: $SNR_{dB} = 10$ and $SNR_{dB} = 20$. $SNR_{dB} = 10$ represents that the summation of the square of the signal amplitudes are 10 times that of the noise, while a SNR_{dB} of 20 indicates 100 times. In the following discussions, the case $SNR_{dB} = 20$ will be analysed in detail, other three cases were presented in the *web version*.

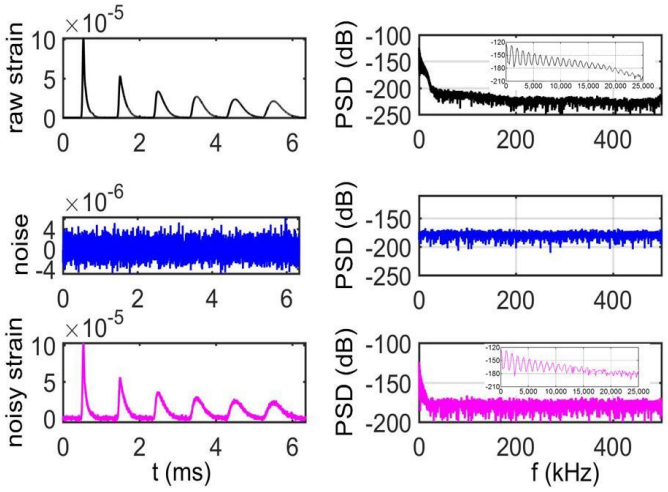
Six strain pulses were first extracted from the raw clean simulation signals (Fig. 5-12(a) or Fig. 5-16(a)). The noise was generated with a global time domain SNR_{dB} of 20 based on Eq. (5.7). The time domain noisy pulses are shown in Fig. 5-17a (a): as AWGN noise was added to all pulses, those with smaller amplitudes become noisier after addition. Noise also results in spikes in the Fourier transforms (Fig. 5-17a (b)), spectral analysis (Fig. 5-17a (c)) reveals that the noise doesn't affect the PSD much within the frequency range $0\sim10$ kHz. However, it modifies the PSDs of high frequency components as their magnitudes are small.



(a) 6 noisy pulses after centering

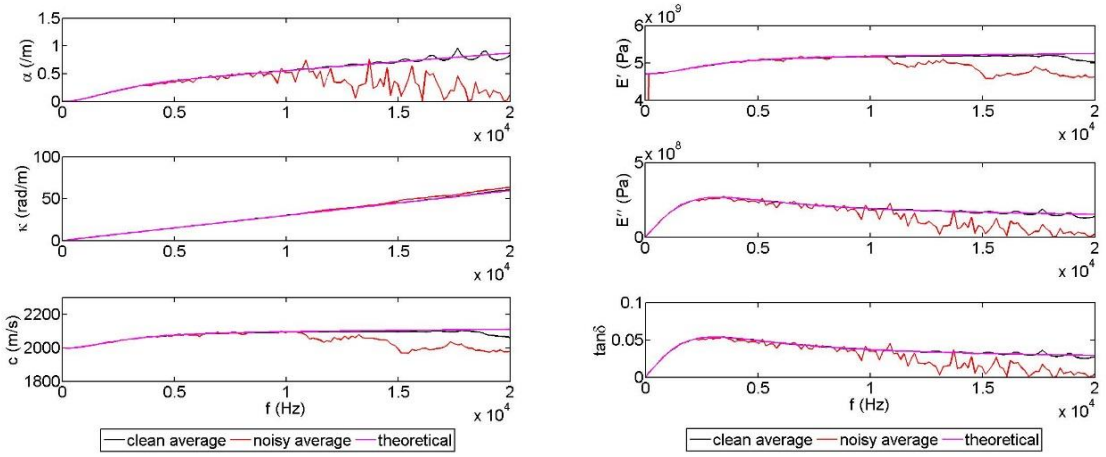


(b) FFTs of the first 4 noisy pulses

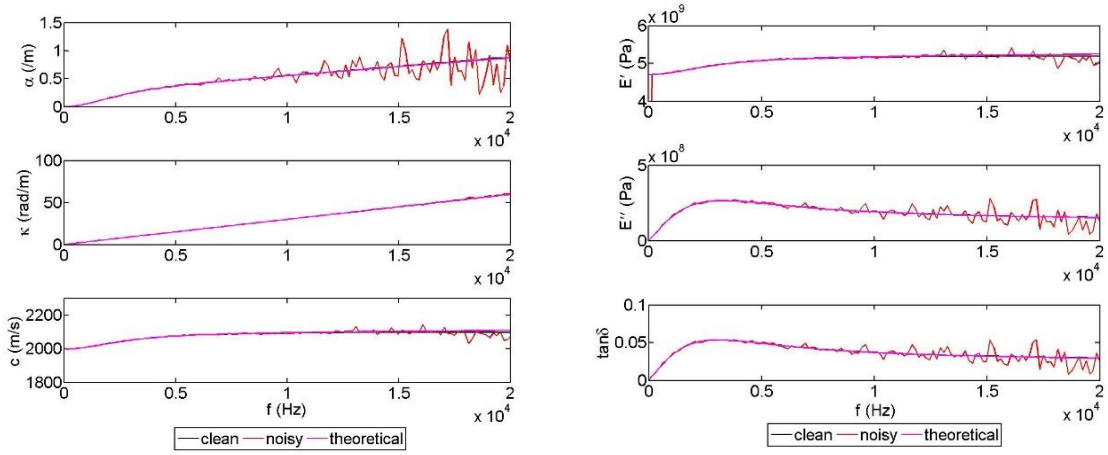


(c)Welch PSDs

Figure. 5-17a Time & frequency domain analysis of the clean and noisy signals (global $SNR_{dB} = 20$)



(a) Comparison of the results derived using (Pulse 3/Pulse 1+Pulse 4/Pulse 2)/2



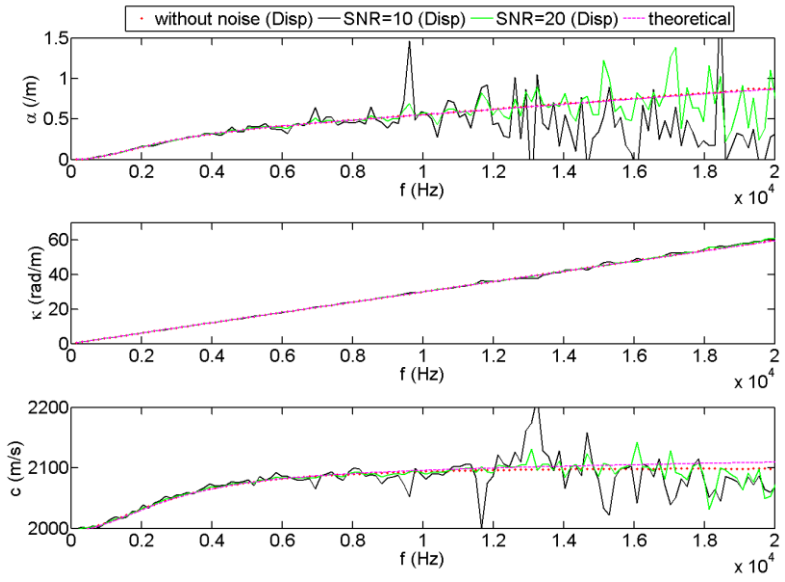
(b) Comparison of the results derived using Pulse 2/Pulse 1

Figure. 5-18a Resulting material properties from the noisy signals (global $SNR_{dB} = 20$)

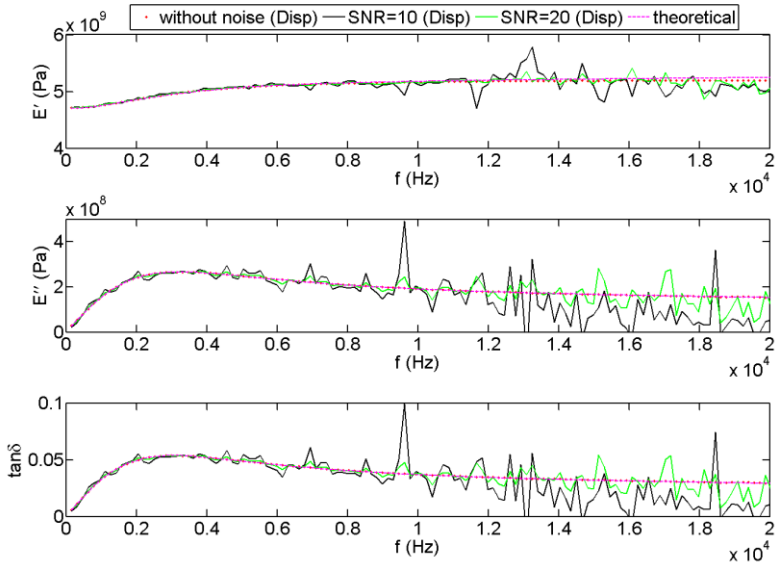
The derived material properties are shown in Fig. 5-18a. As predicted by the frequency analysis, those at relatively low frequencies (*e.g.* < 10 kHz) are not affected much by the addition of noise,

and evident fluctuations can be seen in the region above 10 kHz, with an increasing deviation with frequency. Disparities of both the clean and noisy signal-based results, with regard to their corresponding theoretical values, have been analysed quantitatively in the full *web version*. It is found that, with the appearance of noise, results deviate a lot from the theoretical and clean ones. However, as found before, Pulse2/Pulse1 gives less disparity.

For higher noise level (*e.g.* local $SNR_{dB} = 20$, global and local $SNR_{dB} = 10$), results can be found in the full *web version*. Based on Pulse 2/Pulse 1, a comparison of the results obtained by applying different global SNR_{dB} levels are presented in Fig. 5-19a (Global SNR_{dB}) and b (Local SNR_{dB}). It is seen that, generally the deviation becomes smaller with the increment of SNR_{dB}. For example, the noise generally affects the results above 10 kHz when $SNR_{dB} = 20$, while those below 10 kHz are also disturbed when $SNR_{dB} = 10$. The raw clean signal gives the closest results to the theoretical ones though dispersion correction was not included. Also obvious is, Pulse 2/Pulse 1 normally gives less deviating and thus better results than an average of Pulse 3/Pulse 1+Pulse 4/Pulse 2. This is consistent with our expectation because the first several pulses of course possess less overlapping that introduces inaccuracies in Pulse 3 and 4. However, the contrary has been showed to be true before in analysing experimental data, which is believed to be induced either by the linearity of strain gauge measurement or inaccurate locating of the strain gauges in real tests.



(a) Propagation coefficient



(b) modulus

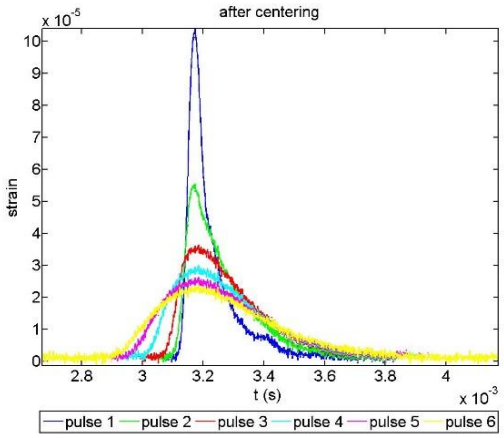
Figure. 5-19a A comparison of material properties derived at two global SNR_{dB} levels (Pulse 2/Pulse 1 without dispersion correction)

(2) Experimental noise

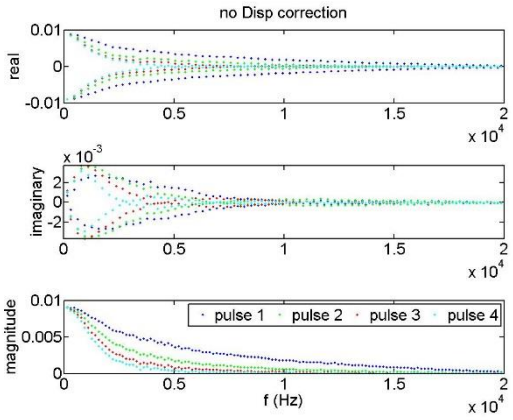
A real experimental noise profile, extracted from a PMMA single rod impact test strain gauge recording ($\emptyset 13.00 \times 1000\ mm$ PMMA rod, $T = 23.4$ ℃), was added to the clean simulation signal (Fig. 5-12(a) or Fig. 5-16(a)). Similar to Gaussian white noise investigations, two time domain noise levels, *i.e.* $SNR_{dB} = 10$ and 20, were applied in modulating the experimentally collected noise using Eq. (5.7). The individual results are presented in Fig. 5-20a and 6-22a (global $SNR_{dB} = 20$), Fig. 5-20b and 6-22b (local $SNR_{dB} = 20$), Fig. 5-20c and 5-21c (global $SNR_{dB} = 10$), Fig. 5-20d and 5-21d (local $SNR_{dB} = 10$), with a comparison shown Fig. 5-22a (global) and b (local).

Here the example of global $SNR_{dB} = 20$ was illustrated in detail, other three cases were presented in the full *web version*. Again, the same original experimental noise, as shown in Fig. 5-20a (a), was constantly employed in all modulation trials. In each case, material properties (propagation coefficient and modulus) have been derived using 2 calculation methods: an average of Pulse 3/Pulse 1+Pulse 4/Pulse 2, and Pulse 2/Pulse 1. It is again found that, Pulse 2/Pulse 1 yields less deviating results. Similar to the artificial noise case study, it is generally seen that, a relatively large SNR_{dB} of 20 mainly results in deviations for frequencies over 10 kHz, while a SNR_{dB} of 10 also affects those

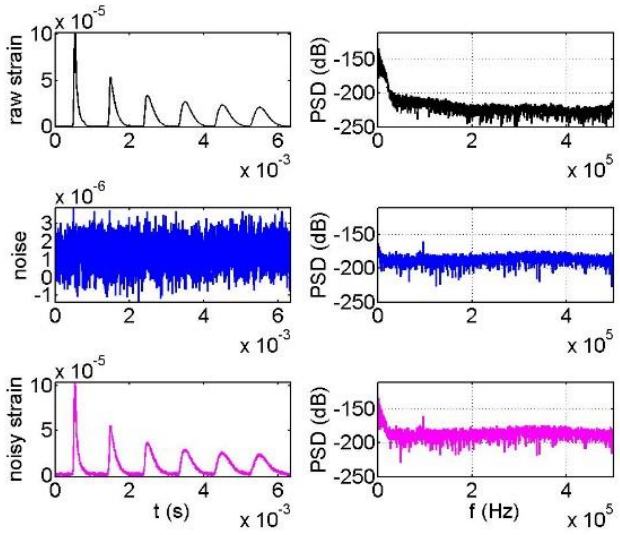
below 10 kHz. It is thus concluded that, the derived results are acceptable using this impact technique with a SNR_{dB} of 20.



(a)6 noisy pulses after centering

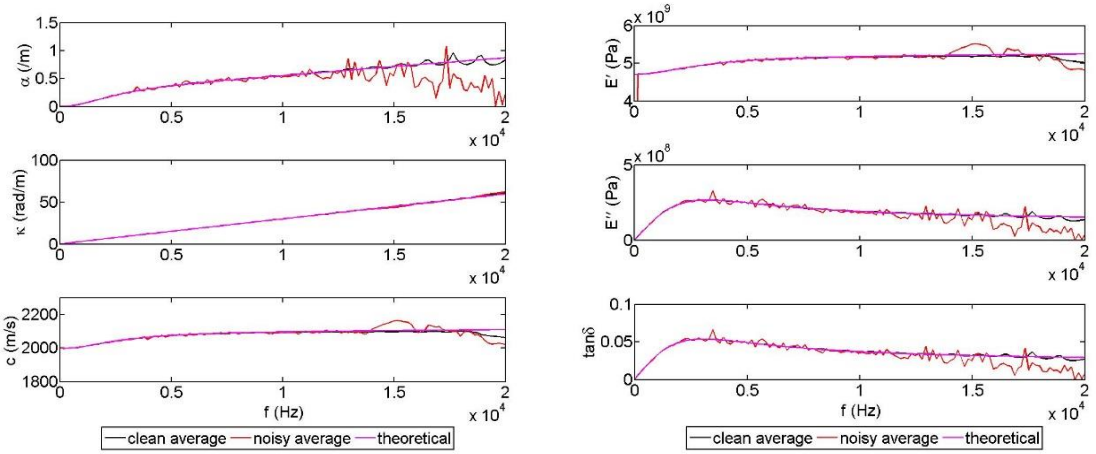


(b)FFTs of the first 4 noisy pulses

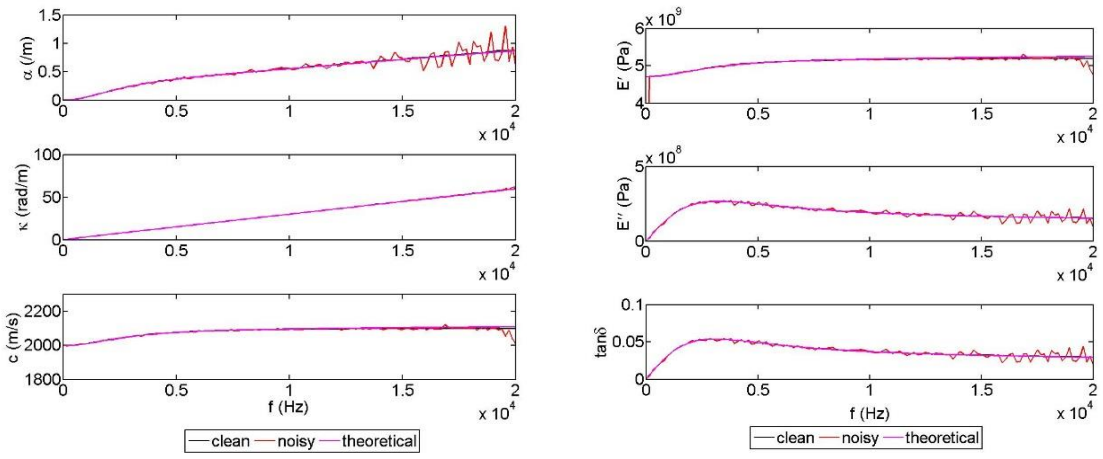


(c)Welch PSDs

Figure. 5-20a Time & frequency domain analysis of the clean and noisy signals (global $SNR_{dB} = 20$)



(a)Comparison of the results derived using (Pulse 3/Pulse 1+Pulse 4/Pulse 2)/2



(b) Comparison of the results derived using Pulse 2/Pulse 1

Figure. 5-21a Resulting material properties from the noisy signals (global $SNR_{dB} = 20$)

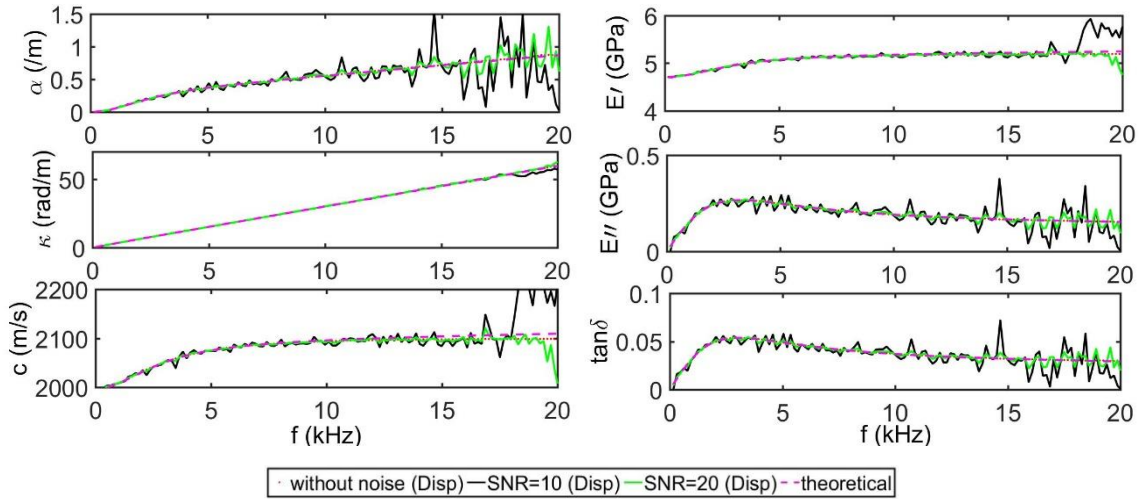


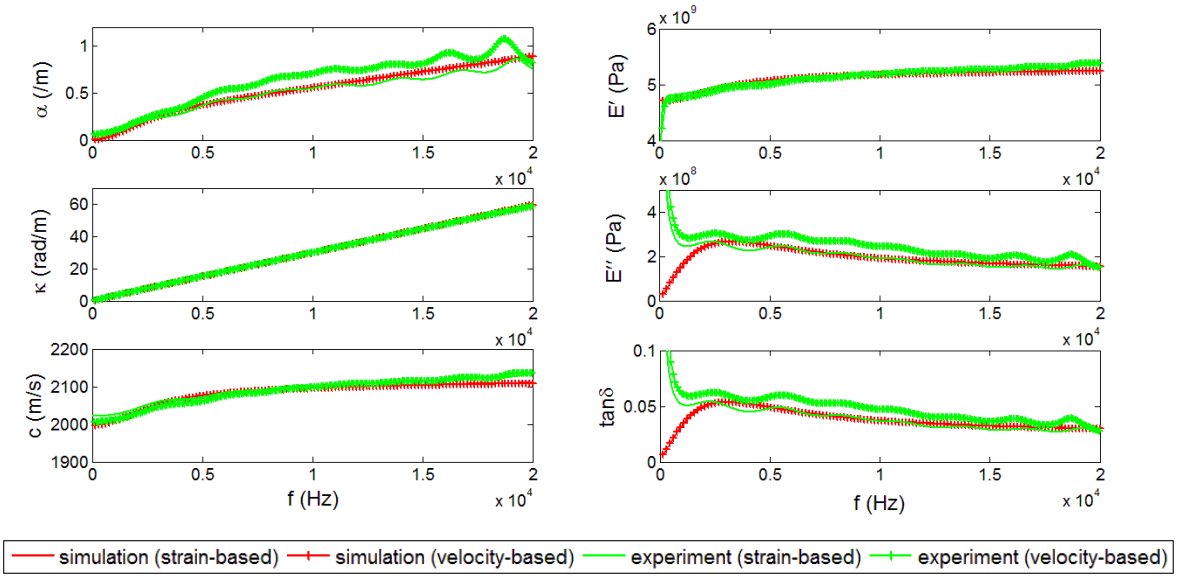
Figure. 5-22a A comparison of material properties derived at different global noise levels (Pulse 2/Pulse 1 without dispersion correction, Global SNR_{dB})

5.3.4 Comparison of the viscoelastic simulation-based and experiment-based results

A comparison of the experimental and viscoelastic simulation results is presented in Fig. 5-23. As the simulation setups (model definition and initial conditions) have been made close to a real single rod impact test (except that a longer PMMA rod was employed in the simulation), the simulation-based results may also be compared to those from the experiments. As shown in Fig 5-23, within the frequency range 2-20 *kHz*, a reasonable agreement can be seen. The strain-based and velocity-based results from simulation are almost the same while those from experiments deviate a bit from each other (this has been illustrated before in Fig. 4-16). A better agreement of the strain-based

experimental results with the simulation ones can be seen, which is due to the fact that, the strain-based experimental material properties have been employed to calibrate the simulation model.

Also, the simulation-based results are smoother due to the absence of unexpected warping (Fig. 5-12), less noise and wave superposition in the raw simulation signals. Finally, a lower useful frequency limit was observed in the experiment-based results but it is missing in the viscoelastic simulation-based ones.



Experimental: strain-based and velocity-based material properties are both averaged on the PMMA and Aluminium ball results at $T = 23.4$ °C;

Simulation: model definition see Fig. 5-10: $\emptyset 12.50$ mm PMMA ball, $h = 30$ cm, $T = 23.4$ °C, material properties derived using strain record at central edge Element 260001, velocity record at end edge Node 6.

Figure. 5-23 Comparison of the experimental and simulation results with dispersion correction

5.4 Single rod simulation summary

In general, simulations have been performed progressively to obtain material properties (with and without the presence of noise), to examine the validity of the single rod analysis method, and to test its sensitivity to noise.

Specifically, Elastic simulations confirm the validity of the single rod analysis method in deriving material properties (*i.e.* propagation coefficient, modulus and wave speed) by referencing to the known model inputs; it also confirms the necessity of performing dispersion correction: by employing different types of input profiles (*e.g.* acceleration or velocity), the degree of dispersion changes (Fig. 5-4), and proper correction is needed (Fig. 5-2 and Fig. 5-6). It is also shown that,

strain and velocity measurements both give the same results (Fig. 5-8), which is consistent with the theoretical basis of this analysis method (Eq. 3.2(a)).

Viscoelastic modelling involves issues such as defining the physical model by using numerical fitting techniques (Fig. 5-10), comparing central and edge signals (Fig. 5-12 and Fig. 5-14), investigating the effects of strain gage (Fig. 5-15), and numerically examining the effects of noise on material property derivation. By sourcing the experimental data in model definition and employing an experimental velocity input, the results derived from viscoelastic simulation are also comparable to the experimental ones (Fig. 5-23).

In viscoelastic simulations, particular emphasis has been put on noise study. Numerical analysis was performed to obtain material properties with the presence of noise, to test the sensitivity of the single rod analysis method to 2 levels (SNR=10 and 20) of noise defined both globally and locally, to study the characteristics of typical noise (AWGN) and noisy signals (*e.g.* their PSDs, amplitude distribution), to examine the relation of the time and frequency domain SNRs, and to investigate the efficiencies of three de-noising strategies. The stability of the direct impact technique has been verified: it can be reliably used to determine material properties with a noise level up to 5% of the impact strain amplitude. The presence of noise further reduces the ability of identifying material properties at high frequencies due to a low signal-to-noise ratio (SNR).

From the whole simulation timeline, we see 3 types of data processing were conducted:

Case 1 no noise, perform de-noising: The raw simulation signal itself may contain small numerical errors, wavelet-based de-noising method was applied, and material properties derived. Otherwise specified, all previous results were obtained in this way.

Case 2 add noise, perform de-noising: Consider the raw simulation signal as a ‘clean’ signal, add noise, apply 3 de-noising strategies and compare their efficiencies (Fig. 5-16).

Case 3 add noise, no de-noising: Consider the raw simulation signals as clean signals, add noise, no de-noising strategy applied, material properties were derived using the noisy signal. Noise study is a typical case of this kind.

In the first case the raw simulation signal was considered as noisy signal while in the other cases it was considered as clean enough to which extra noise was added.

Summary of the single rod impact technique (Chapter 2-5)

Chapter 2-5 investigate the classic single rod impact technique via analytical, experimental, simulation routines. Using this technique, wave propagation in a cylindrical rod was measured, frequency domain analysis was employed to derive the frequency-dependent wave propagation characteristics, based on which the material moduli have been obtained. The validity of this technique were verified by testing elastic Ti, Mg cylinders, and a viscoelastic PMMA cylinder using various projectiles and drop heights to generate different strain amplitudes in the experiments. Small spherical balls that produce non-superimposed high-frequency component pulses are preferred in the single rod impact technique, and within the linear viscoelastic region (LVR), the material behaviours are independent of strain amplitudes. Impact tests performed on a PMMA rod at 4 temperatures show that this technique is sensible to capture the thermal variations of material mechanical properties. Comparison with the DMA results further confirms the validity of the single rod impact technique.

During data processing, appropriate pulse selection of the starting and end pulse locations can help avoid oscillations in results, zero padding is essential in terms of locating each pulse while centering may optimize the Fourier transform values, the window function effect is unavoidable but can be alleviated either by appropriately choosing the window function or by proper pulse selection. The useful frequency range that can be achieved by this technique is determined by a number of experimental and numerical factors, among which sufficient excitation and high signal-to-noise are dominating. Dispersion correction is necessary in terms of extending the useful frequency range, it helps increase the wave speed and storage modulus to some extent at high frequencies.

It is shown by both experiments and simulations that, deformation across the section becomes uniform at a distance long enough from the non-uniform impact end, and the corresponding middle and edge results are shown to be the same. The size effect of a strain gauge is negligible while the non-linearity of strain gauge measurement is evident. Numerical noise study shows that, the single rod analysis method is reliable in identifying material properties with a noise level up to 5% of the impact strain amplitude. Both the strain and velocity measurements made throughout the experiments and simulations show consistency.

Chapter 6: Mechanical wave behaviours at 2-medium & 2-rod interface: Theoretical basis

This chapter provides the background to an innovative approach to derive material properties from transmission and reflection coefficients, allowing mechanical properties of one rod to be calculated if those of the other are known. This chapter builds the required theoretical basis, using time and frequency domain analysis methodologies and applying them to simple mechanical models. Subsequent simulations are presented in Chapter 8 and 9; and experiments in Chapter 10.

6.1 Introduction

In this chapter, the use of wave transmission and reflection coefficients at an interface between two rods were introduced and equations derived to calculate the mechanical behaviour of one of the rods given that the required properties of the other are known. Time domain theories are first examined before moving to the more general frequency domain analysis. In both domains, two coefficients, the transmission coefficient (TC) and the reflection coefficient (RC), were defined. The interface analysis consists of two processes: wave transmission/reflection at the interface and wave propagation in the two rods between the interface and the measurement stations. Hence, this work builds on the theory developed in Chapter 2.

6.2 Analytical description of the interface impact phenomenon

6.2.1 Time domain analysis

6.2.1.1 General time domain expressions

In general, a disturbance of any kind propagating in one medium and impinging upon an interface gives rise to reflected and refracted waves [76]. The problem of wave propagation in two rods consists of two sub-problems: propagation in two rods and behaviour at the interface. Here there is first a brief review of wave propagation in a single medium (Chapter 2). The process is governed by three equations: Newton's Second Law Eq. (2.8), the compatibility equation Eq. (2.9), and the constitutive equation. Using these relations it is possible to obtain the wave equation that governs wave propagation behaviour in that material; and the solution is the universal displacement

expression (Eq. (2.14)) and Eq. (2.19). Note in Eq. (2.14), the prefix A is a constant determined by input and boundary conditions, and the vibration frequency ω is determined by the input and it is not necessarily the natural frequency of the material.

Also note that Eq. (14) just indicates that the particle follows a harmonic movement with frequency ω; for an arbitrary input wave, the particle velocity can be expressed as a Fourier series

$$u_{real}(x,t) = \sum_j u_j(x,t) = \sum_j A_j \mathrm{e}^{\pm\gamma_j \mathrm{x}} \mathrm{e}^{\mathrm{i}\omega_j \mathrm{t}} = \sum_j A_j e^{\pm\alpha_j x} e^{i(\omega_j t \pm \kappa_j x)} \quad (6.1a)$$

where A_j is the displacement amplitude of the harmonic component ω_j at $(x = 0, t = 0)$, of course in practice all the particle displacements can only start from zero, however, this does not imply that a single frequency should have zero amplitude: what is required is that after superposition of all the Fourier components the real displacement is be zero. Extending from this, we arrive at the conclusion that for materials in which the principle of superposition holds (*e.g.* linear viscoelastic materials, the subject of this thesis), the relationships derived for a single frequency can also be applied to an arbitrary wave which is a combination of a series of Fourier components. For the remainder of this section, all relationships were derived for a single frequency.

From the displacement solution, we can derive similar wave equations expressed in strain ε, particle velocity $\dot{u}$, acceleration a, stress σ, and force F

$$\varepsilon(x,t) = \frac{\partial u(x,t)}{\partial x} = \pm\gamma \mathrm{A} \mathrm{e}^{\pm\gamma \mathrm{x}} \mathrm{e}^{\mathrm{i}\omega \mathrm{t}} = \pm\gamma u(x,t) \quad (6.1b)$$

$$\dot{u}(x,t) = \frac{\partial u(x,t)}{\partial t} = \mathrm{i}\omega \mathrm{A} \mathrm{e}^{\pm\gamma \mathrm{x}} \mathrm{e}^{\mathrm{i}\omega \mathrm{t}} = \mathrm{i}\omega u(x,t) \quad (6.1c)$$

$$a(x,t) = \frac{\partial \dot{u}(x,t)}{\partial t} = -\omega^2 \mathrm{A} \mathrm{e}^{\pm\gamma \mathrm{x}} \mathrm{e}^{\mathrm{i}\omega \mathrm{t}} = -\omega^2 u(x,t) \quad (6.1d)$$

$$\sigma(x,t) = \rho \int a(x,t)dx = \mp\frac{\rho\omega^2}{\gamma} \times \mathrm{A} \mathrm{e}^{\mathrm{i}\omega \mathrm{t}} \mathrm{e}^{\pm\gamma \mathrm{x}} = \mp\frac{\rho\omega^2}{\gamma} u(x,t) \quad (6.1e)$$

$$F(x,t) = S\sigma(x,t) = \mp\frac{S\rho\omega^2}{\gamma} u(x,t)\ . \quad (6.1f)$$

Note that, these relations are consistent with those derived in Chapter 2 (Eq. (2.20)), the difference being that, here the displacement is served as a basic expression from which other 5 quantities are obtained; whilst in Chapter 2 strain is used as a basis.

In deriving the stress (Eq. (6.1e)) and force (Eq. (6.1f)) expressions, Newton's Second Law was used, no specific mechanical model has been employed; thus they are generic relations for all materials (in

which a uniform displacement Eq. (6.1a) was assumed). Additional information about material behaviour can be incorporated; for example, for purely elastic materials we have

$$\sigma = E\varepsilon = \pm\gamma EAe^{\pm\gamma x}e^{i\omega t} = \pm\gamma Eu(x,t) \qquad (6.1e')$$

$$F = S\sigma = \pm\gamma SEAe^{\pm\gamma x}e^{i\omega t} = \pm\gamma SEu(x,t) \qquad (6.1f')$$

in which E is the elastic modulus and S the cross-section of the rod. Eq. (6.1e') and Eq. (6.1f') are in consistent with Eq. (6.1e) and Eq. (6.1f): for general materials they can be related by Eq. (2.27)

$$E^*(\omega) = -\frac{\rho\omega^2}{\gamma^2(\omega)}.$$

In practice, it is experimentally difficult to monitor the waves at the interface itself. Instead, measurements are made at other positions on the bar. Hence, the wave propagation equations (Eq. (6.1a~f)) must be used to shift the waves from the interface to arbitrary locations in the rods. For simplicity, the elastic case is used as an example to illustrate the shifting process.

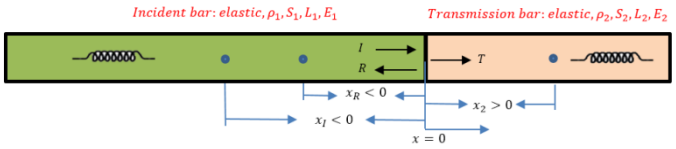


Figure. 6-1 the elastic-elastic 2-rod system

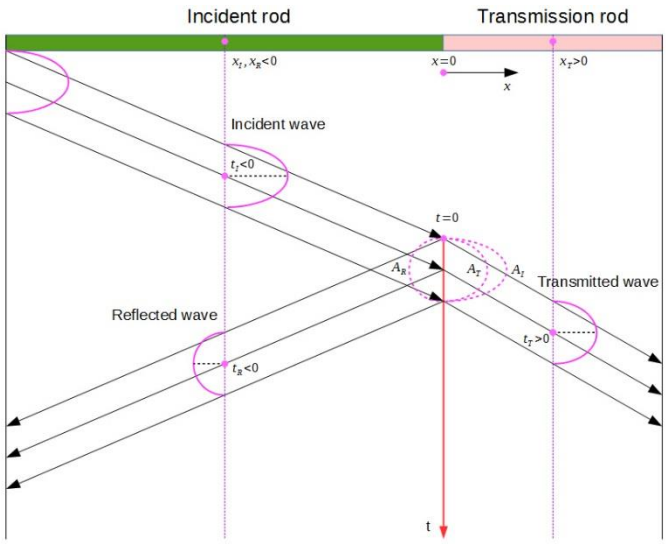


Figure. 6-2 wave propagation in 2 elastic rods in contact

Figure 6-1 shows the general set-up. It is convenient to set the origin, $x = 0$, at the interface and $t = 0$ as the moment when the incident wave arrives at this interface. Having done this, the displacement caused by the three propagating waves (*i.e.* incident, transmitted and reflected) can be shifted to the interface from the gauge locations x_I, x_R, x_T

$$u_{Ij}(x_I, t_I) = u_{Ij}\left(x = 0, t_I + \frac{|x_I|}{c_1}\right) = A_{Ij}e^{i\omega_j t_I}e^{-\gamma_{1j}x_I} = u_{Ij}(x = 0, t_I) \times e^{-\gamma_{1j}x_I} \tag{6.2a}$$

$$u_{Rj}(x_R, t_R) = u_{Rj}\left(x = 0, t_R - \frac{|x_R|}{c_1}\right) = A_{Rj}e^{i\omega_j t_R}e^{\gamma_{1j}x_R} = u_{Rj}(x = 0, t_R) \times e^{\gamma_{1j}x_R} \tag{6.2b}$$

$$u_{Tj}(x_T, t_T) = u_{Tj}\left(x = 0, t_T - \frac{|x_T|}{c_2}\right) = A_{Tj}e^{i\omega_j t_T}e^{-\gamma_{2j}x_T} = u_{Tj}(x = 0, t_T) \times e^{-\gamma_{2j}x_T} \tag{6.2c}$$

in which

$$x_I, x_R \leq 0, x_T \geq 0 \tag{6.3a}$$

$$\begin{aligned} t_I &\in \left[-\frac{|x_I|}{c_1}, -\frac{|x_I|}{c_1} + pulse\ duration\right] < 0, \\ t_R &\in \left[\frac{|x_R|}{c_1}, \frac{|x_R|}{c_1} + pulse\ duration\right] > 0, \\ t_T &\in \left[\frac{|x_T|}{c_2}, \frac{|x_T|}{c_2} + pulse\ duration\right] > 0\ ; \end{aligned} \tag{6.3b}$$

and

$$\begin{aligned} t_{Rj} - t_{Ij} &= \frac{|x_R|}{c_1} + \frac{|x_I|}{c_1}, \\ t_{Tj} - t_{Ij} &= \frac{|x_T|}{c_2} + \frac{|x_I|}{c_1}, \\ t_{Rj} - t_{Tj} &= \frac{|x_R|}{c_1} - \frac{|x_T|}{c_2}. \end{aligned} \tag{6.3c}$$

Here, A_{Ij}, A_{Rj} and A_{Tj} are constants representing the amplitudes of the j^{th} Fourier component in the incident, reflected and transmitted waves at the interface; the relationship between them is determined by boundary conditions and it is this relationship which we define as the reflection and transmission coefficients. The notations here are defined as follows: intrinsic material properties and geometries, such as the elastic wave speeds, c_1 and c_2, and the propagation coefficients γ_1 and γ_2, are denoted with arabic subscript 1 and 2, where 1 refers to the incident rod and 2 refers to the transmission rod; quantities corresponding to the three waves are denoted with subscript I, R and T. In practice, the three waves can be measured at any location, where no wave overlap occurs. For simplicity the incident and reflected waves are usually measured at the same section (*i.e.* $x_I = x_R = x_{IR}$) on the incident rod, which is equivalent to the 'one gauge' measurement method (compared to the 'multi-section' measurement method such as [32]) used in single rod tests. As the three waves are not measured at the interface, where they appear at the same time, direct division of the gauge

signals will only yield zero values unless they are first time-shifted. The usual procedure is to select the non-zero incident wave at time $t_I < 0$ $\left(t_I \in \left[-\frac{|x_1|}{c_1}, -\frac{|x_1|}{c_1} + pulse\ duration\right]\right)$ and the non-zero reflected wave at time $t_R > 0$ $\left(t_R \in \left[\frac{|x_1|}{c_1}, \frac{|x_1|}{c_1} + pulse\ duration\right]\right)$, noting that $t_R - t_I = 2\frac{|x_1|}{c_1}$. Similarly, dividing the transmission wave at $t_T > 0$ $\left(t_T \in \left[\frac{|x_2|}{c_2}, \frac{|x_2|}{c_2} + pulse\ duration\right], t_T - t_I = \frac{|x_2|}{c_2} + \frac{|x_1|}{c_1}\right)$) by the incident wave at t_I yields a non-zero ratio. Note that here no dispersion effects are included and thus the pulse durations of the three travelling pulses are assumed to remain the same.

Eq. (6.2a~c) actually reflect the relations between the displacement at the 3 arbitrary locations and that at the interface: at the same moment t_I, the displacement at x_I is the displacement at the interface multiplying by a shift factor $e^{\pm\gamma x}$.

6.2.1.2 Boundary conditions at the interface: introducing the time domain TC & RC

When the stress wave is incident at an interface, the impedance change causes some of the wave to be reflected and some to be transmitted. As long as the stress at the interface is compressive, both time and frequency domain analyses share the same boundary conditions, namely the continuity of normal force and particle velocity on both surfaces at the contact interface

$$\begin{cases} \dot{u}_I(0,t) + \dot{u}_R(0,t) = \dot{u}_T(0,t) \\ F_I(0,t) + F_R(0,t) = F_T(0,t) \end{cases} \tag{6.4a}$$

or, equivalently, summing over the Fourier components in an arbitrary wave

$$\begin{cases} \sum_j \dot{u}_{Ij}(0,t) + \sum_j \dot{u}_{Rj}(0,t) = \sum_j \dot{u}_{Tj}(0,t) \\ \sum_j F_{Ij}(0,t) + \sum_j F_{Rj}(0,t) = \sum_j F_{Tj}(0,t) \end{cases}. \tag{6.4b}$$

Note that, when investigating wave propagation at the interface between two homogeneous and isotropic elastic solid half-spaces, *i.e.* two semi-infinite elastic media in contact, the boundary conditions of stress and displacement continuity have been applied across the boundary [76]. In other particular cases, at a solid-liquid interface for example, sliding along the interface can occur and only the continuity of normal stresses and displacements is required because tangential stresses vanish as a result of the absence of rigidity [76].

The amplitudes of the reflected and transmitted waves depend on the relative mechanical impedances of the two materials (which will be shown later); the ratio of these waves to the incident wave are denoted RC and TC respectively

$$TC(x_I, t_I, x_T, t_T) = \frac{T(x_T, t_T)}{I(x_I, t_I)}$$
$$RC(x_I, t_I, x_R, t_R) = \frac{R(x_R, t_R)}{I(x_I, t_I)} \tag{6.5a}$$

in which $I(x_I, t_I)$ is the incident wave measured at t_I and x_I; $T(x_T, t_T)$ is the transmitted wave measured at t_T and x_T; and $R(x_R, t_R)$ is the reflected wave measured at t_R and x_R. Theoretically, t_I, t_T, t_R can be any time points on the corresponding signal history and thus they are relatively flexible, while x_I, x_T, x_R are the gauge coordinates and thus fixed.

The quantity (I, T and R) monitored can be strain ε ($TC_\varepsilon, RC_\varepsilon$), force F ($TC_F, RC_F$), stress σ ($TC_\sigma, RC_\sigma$), particle velocity $\dot{u}$ ($TC_{\dot{u}}, TC_{\dot{u}}$), displacement u (TC_u, RC_u), or acceleration a (TC_a, RC_a), the choice of which ratio to be used is just a matter of convenience. Using displacement as an example, for a real wave consisting of a series of Fourier components, the TC and RC measured at any time and locations can be expressed as

$$TC_u(x_I, t_I, x_T, t_T) = \frac{\sum_j u_{Tj}(x_T,t_T)}{\sum_j u_{Ij}(x_I,t_I)} = \frac{\sum_j A_{Tj} e^{i\omega_j t_T} e^{-\gamma_{2j} x_T}}{\sum_j A_{Ij} e^{i\omega_j t_I} e^{-\gamma_{1j} x_I}} \tag{6.6a}$$

$$RC_u(x_I, t_I, x_R, t_R) = \frac{\sum_j u_{Rj}(x_R,t_R)}{\sum_j u_{Ij}(x_I,t_I)} = \frac{\sum_j A_{Rj} e^{i\omega_j t_R} e^{+\gamma_{1j} x_R}}{\sum_j A_{Ij} e^{i\omega_j t_I} e^{-\gamma_{1j} x_I}} \tag{6.6b}$$

$$RT_u(x_T, t_T, x_R, t_R) = \frac{\sum_j u_{Rj}(x_R,t_R)}{\sum_j u_{Tj}(x_T,t_T)} = \frac{\sum_j A_{Rj} e^{i\omega_j t_R} e^{+\gamma_{1j} x_R}}{\sum_j A_{Tj} e^{i\omega_j t_T} e^{-\gamma_{2j} x_T}}. \tag{6.6c}$$

Eq. (6.3c) is uniform for all general materials. Using Eq. (6.3c) and the expression of the wave propagation coefficient γ (Eq. (2.19)), Eq. (6.6a~c) can be re-written:

$$TC_u(x_I, x_T) = \frac{\sum_j A_{Tj} e^{i\omega_j t_{Tj}} e^{-\gamma_{2j} x_T}}{\sum_j A_{Ij} e^{i\omega_j t_{Ij}} e^{-\gamma_{1j} x_I}} \xrightarrow{t_{Tj} = t_{Ij} + \frac{|x_I|}{c_{1j}} + \frac{|x_T|}{c_{2j}}} \frac{\sum_j A_{Tj} e^{i\omega_j \left(t_{Ij} + \frac{|x_I|}{c_{1j}} + \frac{|x_T|}{c_{2j}}\right)} e^{-\gamma_{2j} x_T}}{\sum_j A_{Ij} e^{i\omega_j t_{Ij}} e^{-\gamma_{1j} x_I}}$$
$$\xrightarrow{\gamma_{1j} = \alpha_{1j} + i\frac{\omega_j}{c_{1j}}, \gamma_{2j} = \alpha_{2j} + i\frac{\omega_j}{c_{2j}}} \frac{\sum_j A_{Tj} e^{i\omega_j (t_{Ij} + \frac{|x_I|}{c_{1j}} + \frac{|x_T|}{c_{2j}})} e^{-\alpha_{2j} x_T} e^{-i\frac{\omega}{c_{2j}} x_T}}{\sum_j A_{Ij} e^{i\omega_j t_{Ij}} e^{-\alpha_{1j} x_I} e^{-i\frac{\omega}{c_{1j}} x_I}} \rightarrow \frac{\sum_j A_{Tj} e^{-\alpha_{2j} x_T} e^{-i\omega\frac{x_I}{c_{1j}}} e^{i\omega_j t_{Ij}}}{\sum_j A_{Ij} e^{-\alpha_{1j} x_I} e^{-i\omega\frac{x_I}{c_{1j}}} e^{i\omega_j t_{Ij}}} \tag{6.6a′}$$

$$RC_u(x_I, x_R) = \frac{\sum_j A_{Rj} e^{i\omega_j t_{Rj}} e^{+\gamma_{1j} x_R}}{\sum_j A_{Ij} e^{i\omega_j t_{Ij}} e^{-\gamma_{1j} x_I}} \xrightarrow{t_{Tj} = t_{Ij} + \frac{|x_I|}{c_{1j}} + \frac{|x_R|}{c_{1j}}} \frac{\sum_j A_{Rj} e^{i\omega_j \left(t_{Ij} + \frac{|x_I|}{c_{1j}} + \frac{|x_R|}{c_{1j}}\right)} e^{+\gamma_{1j} x_R}}{\sum_j A_{Ij} e^{i\omega_j t_{Ij}} e^{-\gamma_{1j} x_I}} \tag{6.6b′}$$

$$\xrightarrow{\gamma_{1j}=\alpha_{1j}+i\frac{\omega_j}{c_{1j}},\gamma_{2j}=\alpha_{2j}+i\frac{\omega_j}{c_{2j}}} \frac{\sum_j A_{Rj}e^{i\omega_j(t_{Ij}+\frac{|x_I|}{c_{1j}}+\frac{|x_R|}{c_{1j}})}e^{+\alpha_{1j}x_R}e^{+i\frac{\omega}{c_{1j}}x_R}}{\sum_j A_{Ij}e^{i\omega_j t_{Ij}}e^{-\alpha_{1j}x_I}e^{-i\frac{\omega_j}{c_{1j}}x_I}} \rightarrow \frac{\sum_j A_{Rj}e^{+\alpha_{1j}x_R}e^{-i\omega_j\frac{x_I}{c_{1j}}}e^{i\omega_j t_{Ij}}}{\sum_j A_{Ij}e^{-\alpha_{1j}x_I}e^{-i\omega_j\frac{x_I}{c_{1j}}}e^{i\omega_j t_{Ij}}}$$

$$RT_u(x_T,x_R)=\frac{\sum_j A_{Rj}e^{i\omega_j t_R}e^{+\gamma_{1j}x_R}}{\sum_j A_{Tj}e^{i\omega_j t_T}e^{-\gamma_{2j}x_T}} \xrightarrow{t_{Rj}=t_{Tj}+\frac{|x_R|}{c_{1j}}-\frac{|x_T|}{c_{2j}}} \frac{\sum_j A_{Rj}e^{i\omega_j\left(t_{Tj}+\frac{|x_R|}{c_{1j}}-\frac{|x_T|}{c_{2j}}\right)}e^{+\gamma_{1j}x_R}}{\sum_j A_{Tj}e^{i\omega_j t_{Tj}}e^{-\gamma_{2j}x_T}} \tag{6.6c'}$$

$$\xrightarrow{\gamma_{1j}=\alpha_{1j}+i\frac{\omega_j}{c_{1j}},\gamma_{2j}=\alpha_{2j}+i\frac{\omega_j}{c_{2j}}} \frac{\sum_j A_{Rj}e^{i\omega_j(t_{Tj}+\frac{|x_R|}{c_{1j}}-\frac{|x_T|}{c_{2j}})}e^{+\alpha_{1j}x_R}e^{+i\frac{\omega}{c_{1j}}x_R}}{\sum_j A_{Tj}e^{i\omega_j t_{Tj}}e^{-\alpha_{2j}x_T}e^{-i\frac{\omega}{c_{2j}}x_T}} \rightarrow \frac{\sum_j A_{Rj}e^{+\alpha_{1j}x_R}e^{-i\omega_j\frac{x_T}{c_{2j}}}e^{i\omega_j t_{Tj}}}{\sum_j A_{Tj}e^{-\alpha_{2j}x_T}e^{-i\omega_j\frac{x_T}{c_{2j}}}e^{i\omega_j t_{Tj}}}$$

and for each individual Fourier component, we have

$$TC_{uj}(x_I,t_I,x_T,t_T)=\frac{u_{Tj}(x_T,t_T)}{u_{Ij}(x_I,t_I)}=\frac{A_{Tj}e^{i\omega_j t_T}e^{-\gamma_{2j}x_T}}{A_{Ij}e^{i\omega_j t_I}e^{-\gamma_{1j}x_I}}=\frac{A_{Tj}}{A_{Ij}}\times e^{i\omega_j\left(\frac{|x_I|}{c_1}+\frac{|x_T|}{c_2}\right)}\times \boldsymbol{e^{-(\gamma_{2j}x_T-\gamma_{1j}x_I)}}=\frac{A_{Tj}e^{-\alpha_{2j}x_T}}{A_{Ij}e^{-\alpha_{1j}x_I}} \tag{6.6a''}$$

$$RC_{uj}(x_I,t_I,x_R,t_R)=\frac{u_{Rj}(x_R,t_R)}{u_{Ij}(x_I,t_I)}=\frac{A_{Rj}e^{i\omega_j t_R}e^{+\gamma_{1j}x_R}}{A_{Ij}e^{i\omega_j t_I}e^{-\gamma_{1j}x_I}}=\frac{A_{Rj}}{A_{Ij}}\times e^{i\omega_j(\frac{|x_I|}{c_1}+\frac{|x_R|}{c_1})}\times \boldsymbol{e^{\gamma_{1j}x_I+\gamma_{1j}x_R}}=\frac{A_{Rj}e^{+\alpha_{1j}x_R}}{A_{Ij}e^{-\alpha_{1j}x_I}} \tag{6.6b''}$$

$$RT_{uj}(x_T,t_T,x_R,t_R)=\frac{u_{Rj}(x_R,t_R)}{u_{Tj}(x_T,t_T)}=\frac{A_{Rj}e^{i\omega_j t_R}e^{+\gamma_{1j}x_R}}{A_{Tj}e^{i\omega_j t_T}e^{-\gamma_{2j}x_T}}=\frac{A_{Rj}}{A_{Tj}}\times e^{i\omega_j(\frac{|x_R|}{c_1}-\frac{|x_T|}{c_2})}\times \boldsymbol{e^{\gamma_{1j}x_R+\gamma_{2j}x_T}}=\frac{A_{Rj}e^{+\alpha_{1j}x_R}}{A_{Tj}e^{-\alpha_{2j}x_T}} \tag{6.6c''}$$

It is worth checking the applicability of Eq. (6.6a'~c') in elastic and general materials. For a hybrid wave propagating in purely elastic materials, the attenuation coefficient α is zero, all wave components travel at the same speed c_1 and c_2, and thus the whole waveform remains unchanged during propagation. A uniform time set (t_I, t_R, t_T) which satisfies the relations in Eq. (6.3c) can be found for all components. As a result, the expressions of Eq. (6.6a'~c') reduce to constant ratios that are frequency-independent, location-independent, and determined by mechanical impedances. For general materials, viscoelastic materials for example, different frequency components travel at different wave speeds c_{1j} and c_{2j}, the corresponding time set valid for one frequency will not work for another. Thus it is impossible to select a group of universal time set (t_I, t_R, t_T) which satisfies the time relation in Eq. (6.3c) for all components. The frequency-dependent characteristic of Eq. (6.6a')~(6.6c') indicates it cannot be further simplified to yield a general form. Therefore, for waves propagating in general materials, the single frequency case was considered. For a single frequency component traveling between two media of different wavespeeds, the frequency remains constant while the wavelength changes. This means that a uniform time set (t_I, t_R, t_T), which satisfies the time relation in Eq. (6.3c), can still be found for a single frequency. Waves with multiple Fourier components were considered in the frequency domain analysis.

6.2.1.3 Deriving time domain TC & RC: Introduction

Now we aim to resolve the boundary equations to obtain TC and RC for general materials in the time domain. From Eq. (6.4) we see that the interaction between the two rods is described by the continuity of particle velocity and normal force on the contact surfaces. Based on the universal relations between the 6 quantities (*i.e.* $u, \dot{u}, a, \varepsilon, \sigma, F$, as reflected in Eq. (6.1b)~(6.1f)), the boundary condition can be converted (details see the full *web version*) to be represented by each quantity. These equations can be classified as displacement-based ($u, \dot{u}, a, \varepsilon$) and force-related ($\sigma, F$). As both equilibrium equations are needed to solve for the 2 unknowns TC and RC, the two boundary equations (Eq. (6.4)) have to be unified to contain the same quantity. There are two approaches to achieve this: either using Newton's Second Law (Eq. (2.8)) to rewrite the force-based equations in terms of displacement (the general method); or introducing a constitutive relation to obtain the interface force/stress (the specific method). Here, the general method is first used to derive the universal expressions of TC and RC, before moving on to four specific cases (elastic-elastic, elastic-Maxwell, elastic-Voigt, elastic-single-term Maxwell SLS).

6.2.1.4 Model-independent analysis (general material-general material)

The displacement expression Eq. (6.1a) serves as the fundamental solution in time domain; the relations between the other 5 quantities and the displacement are shown in Table. 6-1. Substituting these explicit expressions into the boundary equations (Eq. (6.4a)) yields a group of 2 equilibrium equations which contain the 2 coefficients in terms of the same quantity, as shown in Table. 6-2.

Table. 6-2 Time domain general relations between TC and RC at the general-general interface

$\dot{u}$	$TC_{\dot{u}}(0,t,0,t) - RC_{\dot{u}}(0,t,0,t) = 1,$	$\frac{\rho_2 S_2}{\rho_1 S_1}\frac{\gamma_1}{\gamma_2} TC_{\dot{u}}(0,t,0,t) + RC_{\dot{u}}(0,t,0,t) = 1$
F	$TC_F(0,t,0,t) - RC_F(0,t,0,t) = 1,$	$\frac{\rho_1 S_1}{\rho_2 S_2}\frac{\gamma_2}{\gamma_1} TC_F(0,t,0,t) + RC_F(0,t,0,t) = 1$
σ	$\frac{S_2}{S_1} TC_\sigma(0,t,0,t) - RC_\sigma(0,t,0,t) = 1,$	$\frac{\rho_1}{\rho_2}\frac{\gamma_2}{\gamma_1} TC_\sigma(0,t,0,t) + RC_\sigma(0,t,0,t) = 1$
u	$TC_u(0,t,0,t) - RC_u(0,t,0,t) = 1,$	$\frac{\rho_2 S_2}{\rho_1 S_1}\frac{\gamma_1}{\gamma_2} TC_u(0,t,0,t) + RC_u(0,t,0,t) = 1$
a	$TC_a(0,t,0,t) - RC_a(0,t,0,t) = 1,$	$\frac{\rho_2 S_2}{\rho_1 S_1}\frac{\gamma_1}{\gamma_2} TC_a(0,t,0,t) + RC_a(0,t,0,t) = 1$
ε	$\frac{\rho_2 S_2}{\rho_1 S_1}\frac{\gamma_1^2}{\gamma_2^2} TC_\varepsilon(0,t,0,t) - RC_\varepsilon(0,t,0,t) = 1,$	$\frac{\gamma_1}{\gamma_2} TC_\varepsilon(0,t,0,t) + RC_\varepsilon(0,t,0,t) = 1$

The next step is to apply the boundary conditions to obtain the specific expressions of TC and RC in terms of each quantity. This has been described in the full *web version*, here only results were presented. Based on Table. 6-1 and 6-2, the two coefficients in terms of strain, stress, force, particle velocity, and acceleration are obtained in Table. 6-3. In Table. 6-3, $\gamma(\omega)$ is again the propagation coefficient, based on the 1D wave propagation theory, it can be further linked to the material modulus via Eq. (2.27) [23], from which we have

$$\gamma(\omega) = i\omega\sqrt{\frac{\rho}{E^*(\omega)}} \tag{6.7}$$

define the characteristic impedance of a rod

$$Z(\omega) = \rho c(\omega)S = S\sqrt{E^*(\omega)\rho} = \frac{i\omega\rho S}{\gamma}. \tag{6.8}$$

The impedance is associated with material density, modulus, and sample geometry. It is frequency-independent for purely elastic materials and becomes frequency-dependent for viscoelastic materials as their moduli are functions of frequency. The characteristic impedances Z(ω) and the wave propagation coefficient γ(ω) in the incident and transmission rods play a key role in determining the wave behaviour at the interface: it is the relative magnitude of these two quantities of the incident and transmission rods that determines the reflection and transmission coefficients. The purpose of performing interface analysis is to obtain material properties as functions of these coefficients. It is now possible to invert the equations in Table. 6-2 and Table. 6-3 to obtain the propagation coefficient γ_1 and γ_2, and further the material modulus by making use of Eq. (2.27). An example of this, using the relations in Table. 6-2, is shown in Table. 6-4. Numerical methods are recommended to reverse the relations in Table. 6-3.

Table. 6-1 General expressions for general-general contact in time domain

	Incident	Reflected	Transmitted	TC, RC
$u(x,t)$	$u_{Ij}(x_I,t_I)=A_{Ij}e^{i\omega_j t_I}e^{-\gamma_{1j}x_I};$ $u_I(x_I,t_I)=\sum_j u_{Ij}(x_I,t_I)$ $=\sum_j A_{Ij}e^{i\omega_j t_I}e^{-\gamma_{1j}x_I}$	$u_{Rj}(x_R,t_R)=A_{Rj}e^{i\omega_j t_R}e^{+\gamma_{1j}x_R};$ $u_R(x_R,t_R)=\sum_j u_{Rj}(x_R,t_R)$ $=\sum_j A_{Rj}e^{i\omega_j t_R}e^{+\gamma_{1j}x_R}$	$u_{Tj}(x_T,t_T)=A_{Tj}e^{i\omega_j t_T}e^{-\gamma_{2j}x_T};$ $u_T(x_T,t_T)=\sum_j u_{Tj}(x_T,t_T)=\sum_j A_{Tj}e^{i\omega_j t_T}e^{-\gamma_{2j}x_T}$	$\begin{cases}TC_{uj}(x_I,t_I,x_T,t_T)=\frac{u_{Tj}(x_T,t_T)}{u_{Ij}(x_I,t_I)}=\frac{A_{Tj}e^{i\omega_j t_T}e^{-\gamma_{2j}x_T}}{A_{Ij}e^{i\omega_j t_I}e^{-\gamma_{1j}x_I}}=\frac{A_{Tj}e^{-\alpha_{2j}x_T}}{A_{Ij}e^{-\alpha_{1j}x_I}}\\ RC_{uj}(x_I,t_I,x_R,t_R)=\frac{u_{Rj}(x_R,t_R)}{u_{Ij}(x_I,t_I)}=\frac{A_{Rj}e^{i\omega_j t_R}e^{+\gamma_{1j}x_R}}{A_{Ij}e^{i\omega_j t_I}e^{-\gamma_{1j}x_I}}=\frac{A_{Rj}e^{\alpha_{1j}x_R}}{A_{Ij}e^{-\alpha_{1j}x_I}}\end{cases}$, $\begin{cases}TC_u(x_I,t_I,x_T,t_T)=\frac{\sum_j u_{Tj}(x_T,t_T)}{\sum_j u_{Ij}(x_I,t_I)}=\frac{\sum_j A_{Tj}e^{i\omega_j t_T}e^{-\gamma_{2j}x_T}}{\sum_j A_{Ij}e^{i\omega_j t_I}e^{-\gamma_{1j}x_I}}\\ RC_u(x_I,t_I,x_R,t_R)=\frac{\sum_j u_{Rj}(x_R,t_R)}{\sum_j u_{Ij}(x_I,t_I)}=\frac{\sum_j A_{Rj}e^{i\omega_j t_R}e^{+\gamma_{1j}x_R}}{\sum_j A_{Ij}e^{i\omega_j t_I}e^{-\gamma_{1j}x_I}}\end{cases}$
$\varepsilon(x,t)$	$\varepsilon_{Ij}(x_I,t_I)=-\gamma_{1j}u_{Ij}(x_I,t_I);$ $\varepsilon_I(x_I,t_I)=\sum_j -\gamma_{1j}u_{Ij}(x_I,t_I)$	$\varepsilon_{Rj}(x_R,t_R)=+\gamma_{1j}u_{Rj}(x_R,t_R);$ $\varepsilon_R(x_R,t_R)=\sum_j +\gamma_{1j}u_{Rj}(x_R,t_R)$	$\varepsilon_{Tj}(x_T,t_T)=-\gamma_{2j}u_{Tj}(x_T,t_T);$ $\varepsilon_T(x_T,t_T)=\sum_j -\gamma_{2j}u_{Tj}(x_T,t_T)$	$\begin{cases}TC_{\varepsilon j}(x_I,t_I,x_T,t_T)=\frac{\gamma_{2j}}{\gamma_{1j}}TC_{uj}(x_I,t_I,x_T,t_T)\\ RC_{\varepsilon j}(x_I,t_I,x_R,t_R)=-RC_{uj}(x_I,t_I,x_R,t_R)\end{cases}$, $\begin{cases}TC_\varepsilon(x_I,t_I,x_T,t_T)=\frac{\sum_j\gamma_{2j}u_{Tj}(x_T,t_T)}{\sum_j\gamma_{1j}u_{Ij}(x_I,t_I)}\\ RC_\varepsilon(x_I,t_I,x_R,t_R)=-\frac{\sum_j\gamma_{1j}u_{Rj}(x_R,t_R)}{\sum_j\gamma_{1j}u_{Ij}(x_I,t_I)}\end{cases}$
$\dot{u}(x,t)$	$\dot{u}_{Ij}(x_I,t_I)=i\omega_j u_{Ij}(x_I,t_I);$ $\dot{u}_I(x_I,t_I)=\sum_j i\omega_j u_{Ij}(x_I,t_I)$	$\dot{u}_{Rj}(x_R,t_R)=i\omega_j u_{Rj}(x_R,t_R);$ $\dot{u}_R(x_R,t_R)=\sum_j i\omega_j u_{Rj}(x_R,t_R)$	$\dot{u}_{Tj}(x_T,t_T)=i\omega_j u_{Tj}(x_T,t_T);$ $\dot{u}_T(x_T,t_T)=\sum_j i\omega_j u_{Tj}(x_T,t_T)$	$\begin{cases}TC_{\dot{u}j}(x_I,t_I,x_T,t_T)=TC_{uj}(x_I,t_I,x_T,t_T)\\ RC_{\dot{u}j}(x_I,t_I,x_R,t_R)=RC_{uj}(x_I,t_I,x_R,t_R)\end{cases}$, $\begin{cases}TC_{\dot{u}}(x_I,t_I,x_T,t_T)=\frac{\sum_j i\omega_j u_{Tj}(x_T,t_T)}{\sum_j i\omega_j u_{Ij}(x_I,t_I)}\\ RC_{\dot{u}}(x_I,t_I,x_R,t_R)=\frac{\sum_j i\omega_j u_{Rj}(x_R,t_R)}{\sum_j i\omega_j u_{Ij}(x_I,t_I)}\end{cases}$
$a(x,t)$	$a_{Ij}(x_I,t_I)=-\omega_j^2 u_{Ij}(x_I,t_I);$ $a_I(x_I,t_I)=\sum_j -\omega_j^2 u_{Ij}(x_I,t_I)$	$a_{Rj}(x_R,t_R)=-\omega_j^2 u_{Rj}(x_R,t_R);$ $a_R(x_R,t_R)=\sum_j -\omega_j^2 u_{Rj}(x_R,t_R)$	$a_{Tj}(x_T,t_T)=-\omega_j^2 u_{Tj}(x_T,t_T);$ $a_T(x_T,t_T)=\sum_j -\omega_j^2 u_{Tj}(x_T,t_T)$	$\begin{cases}TC_{aj}(x_I,t_I,x_T,t_T)=TC_{uj}(x_I,t_I,x_T,t_T)\\ RC_{aj}(x_I,t_I,x_R,t_R)=RC_{uj}(x_I,t_I,x_R,t_R)\end{cases}$, $\begin{cases}TC_a(x_I,t_I,x_T,t_T)=\frac{\sum_j\omega_j^2u_{Tj}(x_T,t_T)}{\sum_j\omega_j^2u_{Ij}(x_I,t_I)}\\ RC_a(x_I,t_I,x_R,t_R)=\frac{\sum_j\omega_j^2u_{Rj}(x_R,t_R)}{\sum_j\omega_j^2u_{Ij}(x_I,t_I)}\end{cases}$
$\sigma(x,t)$	$\sigma_{Ij}(x_I,t_I)=\frac{\rho_1\omega_j^2}{\gamma_{1j}}u_{Ij}(x_I,t_I);$ $\sigma_I(x_I,t_I)=\sum_j\frac{\rho_1\omega_j^2}{\gamma_{1j}}u_{Ij}(x_I,t_I)$	$\sigma_{Rj}(x_R,t_R)=-\frac{\rho_1\omega_j^2}{\gamma_{1j}}u_{Rj}(x_R,t_R);$ $\sigma_R(x_R,t_R)=\sum_j-\frac{\rho_1\omega_j^2}{\gamma_{1j}}u_{Rj}(x_R,t_R)$	$\sigma_{Tj}(x_T,t_T)=\frac{\rho_2\omega_j^2}{\gamma_{2j}}u_{Tj}(x_T,t_T);$ $\sigma_T(x_T,t_T)=\sum_j\frac{\rho_2\omega_j^2}{\gamma_{2j}}u_{Tj}(x_T,t_T)$	$\begin{cases}TC_{\sigma j}(x_I,t_I,x_T,t_T)=\frac{\rho_2}{\rho_1}\frac{\gamma_{1j}}{\gamma_{2j}}TC_{uj}(x_I,t_I,x_T,t_T)\\ RC_{\sigma j}(x_I,t_I,x_R,t_R)=-RC_{uj}(x_I,t_I,x_R,t_R)\end{cases}$, $\begin{cases}TC_\sigma(x_I,t_I,x_T,t_T)=\frac{\sum_j\frac{\rho_2\omega_j^2}{\gamma_{2j}}u_{Tj}(x_T,t_T)}{\sum_j\frac{\rho_1\omega_j^2}{\gamma_{1j}}u_{Ij}(x_I,t_I)}\\ RC_\sigma(x_I,t_I,x_R,t_R)=-\frac{\sum_j\frac{\rho_1\omega_j^2}{\gamma_{1j}}u_{Rj}(x_R,t_R)}{\sum_j\frac{\rho_1\omega_j^2}{\gamma_{1j}}u_{Ij}(x_I,t_I)}\end{cases}$
$F(x,t)$	$F_{Ij}(x_I,t_I)=\frac{S_1\rho_1\omega_j^2}{\gamma_{1j}}u_{Ij}(x_I,t_I);$ $F_I(x_I,t_I)=\sum_j\frac{S_1\rho_1\omega_j^2}{\gamma_{1j}}u_{Ij}(x_I,t_I)$	$F_{Rj}(x_R,t_R)=-\frac{S_1\rho_1\omega_j^2}{\gamma_{1j}}u_{Rj}(x_R,t_R);$ $F_R(x_R,t_R)$ $=\sum_j-\frac{S_1\rho_1\omega_j^2}{\gamma_{1j}}u_{Rj}(x_R,t_R)$	$F_{Tj}(x_T,t_T)=\frac{S_2\rho_2\omega_j^2}{\gamma_{2j}}u_{Tj}(x_T,t_T);$ $F_T(x_T,t_T)=\sum_j\frac{S_2\rho_2\omega_j^2}{\gamma_{2j}}u_{Tj}(x_T,t_T)$	$\begin{cases}TC_{Fj}(x_I,t_I,x_T,t_T)=\frac{S_2}{S_1}\frac{\rho_2}{\rho_1}\frac{\gamma_{1j}}{\gamma_{2j}}TC_{uj}(x_I,t_I,x_T,t_T)\\ RC_F(x_I,t_I,x_R,t_R)=-RC_{uj}(x_I,t_I,x_R,t_R)\end{cases}$, $\begin{cases}TC_F(x_I,t_I,x_T,t_T)=\frac{\sum_j\frac{S_2\rho_2\omega_j^2}{\gamma_{2j}}u_{Tj}(x_T,t_T)}{\sum_j\frac{S_1\rho_1\omega_j^2}{\gamma_{1j}}u_{Ij}(x_I,t_I)}\\ RC_F(x_I,t_I,x_T,t_T)=-\frac{\sum_j\frac{S_1\rho_1\omega_j^2}{\gamma_{1j}}u_{Rj}(x_R,t_R)}{\sum_j\frac{S_1\rho_1\omega_j^2}{\gamma_{1j}}u_{Ij}(x_I,t_I)}\end{cases}$

Table. 6-3 Time domain $TC(x_I, t_I, x_T, t_T)$, $RC(x_I, t_I, x_R, t_R)$ and $RT(x_I, t_I, x_R, t_R)$ expressions for general contact

	$TC(x_I, t_I, x_T, t_T) = \frac{T(x_T, t_T)}{I(x_I, t_I)}$ $(x_I \le 0, x_T \ge 0)$		$RC(x_I, t_I, x_R, t_R) = \frac{R(x_R, t_R)}{I(x_I, t_I)}$ $(x_I, x_R \le 0)$		$RT(x_I, t_I, x_R, t_R) = \frac{RC(x_I, t_I, x_R, t_R)}{TC(x_I, t_I, x_T, t_T)} = \frac{R(x_R, t_R)}{T(x_I, t_I)}$ $(x_R \le 0, x_T \ge 0)$	
	(γ_1, γ_2)	(Z_1, Z_2)	(γ_1, γ_2)	(Z_1, Z_2)	(γ_1, γ_2)	(Z_1, Z_2)
$\tilde{v}_{2i}$	$\frac{2\frac{\rho_1 S_1}{\gamma_1}}{\frac{\rho_1 S_1}{\gamma_1}+\frac{\rho_2 S_2}{\gamma_2}} \times \frac{\gamma_2}{\gamma_1} \times \frac{e^{-\alpha_2 x_T}}{e^{-\alpha_1 x_I}}$	$\frac{2Z_1}{Z_1+Z_2} \times \frac{\gamma_2}{\gamma_1} \times \frac{e^{-\alpha_2 x_T}}{e^{-\alpha_1 x_I}} = \frac{2Z_1^2}{(Z_1+Z_2)Z_2} \times \frac{\rho_2 S_2}{\rho_1 S_1} \times \frac{e^{-\alpha_2 x_T}}{e^{-\alpha_1 x_I}}$	$\frac{\frac{\rho_2 S_2}{\gamma_2}-\frac{\rho_1 S_1}{\gamma_1}}{\frac{\rho_2 S_2}{\gamma_2}+\frac{\rho_1 S_1}{\gamma_1}} \times \frac{e^{\alpha_1 x_R}}{e^{-\alpha_1 x_I}}$	$\frac{Z_2-Z_1}{Z_2+Z_1} \times \frac{e^{\alpha_1 x_R}}{e^{-\alpha_1 x_I}}$	$\frac{\frac{\rho_2 S_2}{\gamma_2}-\frac{\rho_1 S_1}{\gamma_1}}{2\frac{\rho_1 S_1}{\gamma_1}} \times \frac{\gamma_1}{\gamma_2} \times \frac{e^{\alpha_1 x_R}}{e^{-\alpha_2 x_T}}$	$\frac{Z_2-Z_1}{2Z_1} \times \frac{\gamma_1}{\gamma_2} \times \frac{e^{\alpha_1 x_R}}{e^{-\alpha_2 x_T}} = \frac{(Z_2-Z_1)Z_2}{2Z_1^2} \times \frac{\rho_1 S_1}{\rho_2 S_2} \times \frac{e^{\alpha_1 x_R}}{e^{-\alpha_2 x_T}}$
$\tilde{v}_{1i}$	$\frac{2\frac{\rho_2 S_2}{\gamma_2}}{\frac{\rho_2 S_2}{\gamma_2}+\frac{\rho_1 S_1}{\gamma_1}} \times \frac{e^{-\alpha_2 x_T}}{e^{-\alpha_1 x_I}}$	$\frac{2Z_2}{Z_1+Z_2} \times \frac{e^{-\alpha_2 x_T}}{e^{-\alpha_1 x_I}}$	$\frac{\frac{\rho_2 S_2}{\gamma_2}-\frac{\rho_1 S_1}{\gamma_1}}{\frac{\rho_2 S_2}{\gamma_2}+\frac{\rho_1 S_1}{\gamma_1}} \times \frac{e^{\alpha_1 x_R}}{e^{-\alpha_1 x_I}}$	$\frac{Z_2-Z_1}{Z_2+Z_1} \times \frac{e^{\alpha_1 x_R}}{e^{-\alpha_1 x_I}}$	$\frac{\frac{\rho_2 S_2}{\gamma_2}-\frac{\rho_1 S_1}{\gamma_1}}{2\frac{\rho_2 S_2}{\gamma_2}} \times \frac{e^{\alpha_1 x_R}}{e^{-\alpha_2 x_T}}$	$\frac{Z_2-Z_1}{2Z_2} \times \frac{e^{\alpha_1 x_R}}{e^{-\alpha_2 x_T}}$
$\tilde{\sigma}_{2i}$	$\frac{2\frac{\rho_2 S_2}{\gamma_2}}{\frac{\rho_1 S_1}{\gamma_1}+\frac{\rho_2 S_2}{\gamma_2}} \times \frac{S_1}{S_2} \times \frac{e^{-\alpha_2 x_T}}{e^{-\alpha_1 x_I}}$	$\frac{2Z_2}{Z_1+Z_2} \times \frac{S_1}{S_2} \times \frac{e^{-\alpha_2 x_T}}{e^{-\alpha_1 x_I}}$	$\frac{\frac{\rho_2 S_2}{\gamma_2}-\frac{\rho_1 S_1}{\gamma_1}}{\frac{\rho_1 S_1}{\gamma_1}+\frac{\rho_2 S_2}{\gamma_2}} \times \frac{e^{\alpha_1 x_R}}{e^{-\alpha_1 x_I}}$	$\frac{Z_2-Z_1}{Z_2+Z_1} \times \frac{e^{\alpha_1 x_R}}{e^{-\alpha_1 x_I}}$	$\frac{\frac{\rho_2 S_2}{\gamma_2}-\frac{\rho_1 S_1}{\gamma_1}}{2\frac{\rho_2 S_2}{\gamma_2}} \times \frac{S_2}{S_1} \times \frac{e^{\alpha_1 x_R}}{e^{-\alpha_2 x_T}}$	$\frac{Z_2-Z_1}{2Z_2} \times \frac{S_2}{S_1} \times \frac{e^{\alpha_1 x_R}}{e^{-\alpha_2 x_T}}$
$\tilde{u}$	$\frac{2\frac{\rho_1 S_1}{\gamma_1}}{\frac{\rho_1 S_1}{\gamma_1}+\frac{\rho_2 S_2}{\gamma_2}} \times \frac{e^{-\alpha_2 x_T}}{e^{-\alpha_1 x_I}}$	$\frac{2Z_1}{Z_1+Z_2} \times \frac{e^{-\alpha_2 x_T}}{e^{-\alpha_1 x_I}}$	$\frac{\frac{\rho_1 S_1}{\gamma_1}-\frac{\rho_2 S_2}{\gamma_2}}{\frac{\rho_1 S_1}{\gamma_1}+\frac{\rho_2 S_2}{\gamma_2}} \times \frac{e^{\alpha_1 x_R}}{e^{-\alpha_1 x_I}}$	$\frac{Z_1-Z_2}{Z_1+Z_2} \times \frac{e^{\alpha_1 x_R}}{e^{-\alpha_1 x_I}}$	$\frac{\frac{\rho_1 S_1}{\gamma_1}-\frac{\rho_2 S_2}{\gamma_2}}{2\frac{\rho_1 S_1}{\gamma_1}} \times \frac{e^{\alpha_1 x_R}}{e^{-\alpha_2 x_T}}$	$\frac{Z_1-Z_2}{2Z_1} \times \frac{e^{\alpha_1 x_R}}{e^{-\alpha_2 x_T}}$
$\tilde{u}$	$\frac{2\frac{\rho_1 S_1}{\gamma_1}}{\frac{\rho_1 S_1}{\gamma_1}+\frac{\rho_2 S_2}{\gamma_2}} \times \frac{e^{-\alpha_2 x_T}}{e^{-\alpha_1 x_I}}$	$\frac{2Z_1}{Z_1+Z_2} \times \frac{e^{-\alpha_2 x_T}}{e^{-\alpha_1 x_I}}$	$\frac{\frac{\rho_1 S_1}{\gamma_1}-\frac{\rho_2 S_2}{\gamma_2}}{\frac{\rho_1 S_1}{\gamma_1}+\frac{\rho_2 S_2}{\gamma_2}} \times \frac{e^{\alpha_1 x_R}}{e^{-\alpha_1 x_I}}$	$\frac{Z_1-Z_2}{Z_1+Z_2} \times \frac{e^{\alpha_1 x_R}}{e^{-\alpha_1 x_I}}$	$\frac{\frac{\rho_1 S_1}{\gamma_1}-\frac{\rho_2 S_2}{\gamma_2}}{2\frac{\rho_1 S_1}{\gamma_1}} \times \frac{e^{\alpha_1 x_R}}{e^{-\alpha_2 x_T}}$	$\frac{Z_1-Z_2}{2Z_1} \times \frac{e^{\alpha_1 x_R}}{e^{-\alpha_2 x_T}}$
$\tilde{a}$	$\frac{2\frac{\rho_1 S_1}{\gamma_1}}{\frac{\rho_1 S_1}{\gamma_1}+\frac{\rho_2 S_2}{\gamma_2}} \times \frac{e^{-\alpha_2 x_T}}{e^{-\alpha_1 x_I}}$	$\frac{2Z_1}{Z_1+Z_2} \times \frac{e^{-\alpha_2 x_T}}{e^{-\alpha_1 x_I}}$	$\frac{\frac{\rho_1 S_1}{\gamma_1}-\frac{\rho_2 S_2}{\gamma_2}}{\frac{\rho_1 S_1}{\gamma_1}+\frac{\rho_2 S_2}{\gamma_2}} \times \frac{e^{\alpha_1 x_R}}{e^{-\alpha_1 x_I}}$	$\frac{Z_1-Z_2}{Z_1+Z_2} \times \frac{e^{\alpha_1 x_R}}{e^{-\alpha_1 x_I}}$	$\frac{\frac{\rho_1 S_1}{\gamma_1}-\frac{\rho_2 S_2}{\gamma_2}}{2\frac{\rho_1 S_1}{\gamma_1}} \times \frac{e^{\alpha_1 x_R}}{e^{-\alpha_2 x_T}}$	$\frac{Z_1-Z_2}{2Z_1} \times \frac{e^{\alpha_1 x_R}}{e^{-\alpha_2 x_T}}$

Table. 6-4 Time domain relations between γ_1 and γ_2 for general-general contact (TC and RC here measured at interface, *i.e.* $x_I = x_R = x_T = 0$, $t_I = t_R = t_T = t$)

$\dot{u}$	① $TC_{\dot{u}}(0,t,0,t) - RC_{\dot{u}}(0,t,0,t) = 1$	ε	① $\gamma_2 = \sqrt{\frac{\rho_2 S_2}{\rho_1 S_1}\frac{TC_\varepsilon(0,t,0,t)}{1+RC_\varepsilon(0,t,0,t)}}\gamma_1$
	② $\gamma_2 = \frac{\rho_2 S_2}{\rho_1 S_1}\frac{TC_{\dot{u}}(0,t,0,t)}{1-RC_{\dot{u}}(0,t,0,t)}\gamma_1$		② $\gamma_2 = \frac{TC_\varepsilon(0,t,0,t)}{1-RC_\varepsilon(0,t,0,t)}\gamma_1$
	③ $\gamma_2 = \frac{\rho_2 S_2}{\rho_1 S_1}\frac{TC_{\dot{u}}(0,t,0,t)}{2-TC_{\dot{u}}(0,t,0,t)}\gamma_1$		③ $\gamma_2 = \frac{\rho_1 S_1 TC_\varepsilon(0,t,0,t) \pm \sqrt{\rho_1 S_1 TC_\varepsilon(0,t,0,t)[\rho_1 S_1 TC_\varepsilon(0,t,0,t)+8\rho_2 S_2]}}{4\rho_1 S_1}\gamma_1$
	④ $\gamma_2 = \frac{\rho_2 S_2}{\rho_1 S_1}\frac{1+RC_{\dot{u}}(0,t,0,t)}{1-RC_{\dot{u}}(0,t,0,t)}\gamma_1$		④ $\gamma_2 = \frac{\rho_2 S_2}{\rho_1 S_1}\frac{1-RC_\varepsilon(0,t,0,t)}{1+RC_\varepsilon(0,t,0,t)}\gamma_1$
	⑤ $\gamma_2 = \frac{\rho_2 S_2}{\rho_1 S_1}\frac{1}{1-2RT_{\dot{u}}(0,t,0,t)}\gamma_1$		
F	① $TC_F(0,t,0,t) - RC_F(0,t,0,t) = 1$	u	① $TC_u(0,t,0,t) - RC_u(0,t,0,t) = 1$
	② $\gamma_2 = \frac{\rho_2 S_2}{\rho_1 S_1}\frac{1-RC_F(0,t,0,t)}{TC_F(0,t,0,t)}\gamma_1$		② $\gamma_2 = \frac{\rho_2 S_2}{\rho_1 S_1}\frac{TC_u(0,t,0,t)}{1-RC_u(0,t,0,t)}\gamma_1$
	③ $\gamma_2 = \frac{\rho_2 S_2}{\rho_1 S_1}\frac{2-TC_F(0,t,0,t)}{TC_F(0,t,0,t)}\gamma_1$		③ $\gamma_2 = \frac{\rho_2 S_2}{\rho_1 S_1}\frac{TC_u(0,t,0,t)}{2-TC_u(0,t,0,t)}\gamma_1$
	④ $\gamma_2 = \frac{\rho_2 S_2}{\rho_1 S_1}\frac{1-RC_F(0,t,0,t)}{1+RC_F(0,t,0,t)}\gamma_1$		④ $\gamma_2 = \frac{\rho_2 S_2}{\rho_1 S_1}\frac{1+RC_u(0,t,0,t)}{1-RC_u(0,t,0,t)}\gamma_1$
σ	① $\frac{S_2}{S_1}TC_\sigma(0,t,0,t) - RC_\sigma(0,t,0,t) = 1$	a	① $TC_a(0,t,0,t) - RC_a(0,t,0,t) = 1$
	②$\gamma_2 = \frac{\rho_2}{\rho_1}\frac{1-RC_\sigma(0,t,0,t)}{TC_\sigma(0,t,0,t)}\gamma_1$		② $\gamma_2 = \frac{\rho_2 S_2}{\rho_1 S_1}\frac{TC_a(0,t,0,t)}{1-RC_a(0,t,0,t)}\gamma_1$
	③ $\gamma_2 = \frac{\rho_2(2S_1 - S_2 TC_\sigma(0,t,0,t))}{\rho_1 S_1 TC_\sigma(0,t,0,t)}\gamma_1$		③ $\gamma_2 = \frac{\rho_2 S_2}{\rho_1 S_1}\frac{TC_a(0,t,0,t)}{2-TC_a(0,t,0,t)}\gamma_1$
	④ $\gamma_2 = \frac{\rho_2 S_2}{\rho_1 S_1}\frac{1-RC_\sigma(0,t,0,t)}{1+RC_\sigma(0,t,0,t)}\gamma_1$		④ $\gamma_2 = \frac{\rho_2 S_2}{\rho_1 S_1}\frac{1+RC_a(0,t,0,t)}{1-RC_a(0,t,0,t)}\gamma_1$

6.2.1.5 Model-dependent analysis

Alternatively, specific models can be introduced. The key equations characterising the problem are the boundary condition equations (Eq. (6.4a)); instead of using Newton's Second Law to generally express the stress and force, Eq. (6.1e) and (6.1f), strain from the constitutive equation can be used. This requires a specific model to represent the material and gives another way to treat the problem and an alternative approach to verify the results presented in Table. 6-3.

Four cases with different mechanical models were employed to derive TC_σ and RC_σ. Case 1 has two purely elastic rods in contact, in Cases 2~4 viscoelastic materials are introduced for the transmission

rod while the incident rod remains elastic. Material viscoelasticity can be represented by various models, starting from the basic Maxwell model and Voigt model to the widely-used Maxwell form Standard Linear Solid (S.L.S). For viscoelastic materials, the boundary condition equations may be complicated. In fact, it will be seen later that extra initial conditions are needed to determine the unknown constants in viscoelastic materials in Eq. (6.4a) before the transmission and reflection coefficients can be obtained.

1) Elastic material-elastic material

The 2-rod elastic system is shown in Fig. 6-1, and the wave propagation path in Fig. 6-2. Time domain analysis is of particular use for purely elastic materials as all the elastic quantities are frequency/strain rate-independent and the constitutive relation is straightforward. Simple relations can be obtained easily in the time domain: once the constitutive relation is introduced, the stress and force expressions in Table. 6-1 can be rewritten in Table. 6-1' by using Eq. (6.1e') and (6.1f'). Note that the displacement, strain, particle velocity, and acceleration expressions are the same as they are independent of mechanical model. Table. 6-1' can be also obtained by linking the modulus E and propagation coefficient γ via Eq. (2.27). It can be seen from Table. 6-1' that the relationship $\dot{u} = \pm c\varepsilon$ (Eq. (7.11)) no longer stands for viscoelastic materials because $c\varepsilon = \frac{\omega}{\kappa}\gamma u \neq \dot{u} = i\omega u$, as $\alpha \neq 0$.While Table. 6-2 gives universal equations for general materials, Table. 6-2' represents those for purely elastic materials. They are actually interrelated, as for elastic materials we have

$$\gamma = \alpha + i\kappa \xrightarrow{\alpha=0} i\kappa = i\frac{\omega}{c}$$

thus

$$\frac{\gamma_1}{\gamma_2} = \frac{c_2}{c_1}$$

which links Table. 6-2 with Table. 6-2'.

Solving the equation pairs in Table. 6-2' yields the two unknowns $TC(0,t,0,t)$ and $RC(0,t,0,t)$, and further $RT(0,t,0,t)$, as shown in Table. 6-3'.

Table 6-1' Rewritten stress and force expressions for elastic-elastic contact in time domain

	Incident	Reflected	Transmitted	TC, RC
$\sigma(x,t)$	$\sigma_{Ij}(x_I,t_I) = -\gamma_{1j}E_{1j}u_{Ij}(x_I,t_I);$ $\sigma_I(x_I,t_I) = \sum_j -\gamma_{1j}E_{1j}u_{Ij}(x_I,t_I)$	$\sigma_{Rj}(x_R,t_R) = +\gamma_{1j}E_{1j}u_{Rj}(x_R,t_R);$ $\sigma_R(x_R,t_R) = \sum_j +\gamma_{1j}E_{1j}u_{Rj}(x_R,t_R)$	$\sigma_{Tj}(x_T,t_T) = -\gamma_{2j}E_{2j}u_{Tj}(x_T,t_T);$ $\sigma_T(x_T,t_T) = \sum_j -\gamma_{2j}E_{2j}u_{Tj}(x_T,t_T)$	$TC_{\sigma j}(x_I,t_I,x_T,t_T) = \frac{\gamma_{2j}E_{2j}}{\gamma_{1j}E_{1j}}TC_{uj}(x_I,t_I,x_T,t_T);$ $RC_{\sigma j}(x_I,t_I,x_R,t_R) = -RC_{uj}(x_I,t_I,x_R,t_R)$ $TC_{\sigma}(x_I,t_I,x_T,t_T) = \frac{\sum_j \gamma_{2j}E_{2j}u_{Tj}(x_T,t_T)}{\sum_j \gamma_{1j}E_{1j}u_{Ij}(x_I,t_I)};$ $RC_{\sigma}(x_I,t_I,x_R,t_R) = -\frac{\sum_j \gamma_{1j}E_{1j}u_{Rj}(x_R,t_R)}{\sum_j \gamma_{1j}E_{1j}u_{Ij}(x_I,t_I)}$
$F(x,t)$	$F_{Ij}(x_I,t_I) = -\gamma_{1j}S_{1j}E_{1j}u_{Ij}(x_I,t_I);$ $F_I(x_I,t_I) = \sum_j -\gamma_{1j}S_{1j}E_{1j}u_{Ij}(x_I,t_I)$	$F_{Rj}(x_R,t_R) = +\gamma_{1j}S_{1j}E_{1j}u_{Rj}(x_R,t_R);$ $F_R(x_R,t_R) = \sum_j +\gamma_{1j}S_{1j}E_{1j}u_{Rj}(x_R,t_R)$	$F_{Tj}(x_T,t_T) = -\gamma_{2j}S_{2j}E_{2j}u_{Tj}(x_T,t_T);$ $F_T(x_T,t_T) = \sum_j -\gamma_{2j}S_{2j}E_{2j}u_{Tj}(x_T,t_T)$	$TC_{Fj}(x_I,t_I,x_T,t_T) = \frac{\gamma_{2j}S_{2j}E_{2j}}{\gamma_{1j}S_{1j}E_{1j}}TC_{uj}(x_I,t_I,x_T,t_T);$ $RC_{F}(x_I,t_I,x_R,t_R) = -RC_{uj}(x_I,t_I,x_R,t_R)$ $TC_{F}(x_I,t_I,x_T,t_T) = \frac{\sum_j \gamma_{2j}S_{2j}E_{2j}u_{Tj}(x_T,t_T)}{\sum_j \gamma_{1j}S_{1j}E_{1j}u_{Ij}(x_I,t_I)};$ $RC_{F}(x_I,t_I,x_R,t_R) = -\frac{\sum_j \gamma_{1j}S_{1j}E_{1j}u_{Rj}(x_R,t_R)}{\sum_j \gamma_{1j}S_{1j}E_{1j}u_{Ij}(x_I,t_I)}$

Table 6-2' Time domain general relations between TC and RC an elastic-elastic interface

Both rods elastic	$\dot{u}$	$TC_{\dot{u}}(0,t,0,t) - RC_{\dot{u}}(0,t,0,t) = 1, \quad \frac{\rho_2c_2S_2}{\rho_1c_1S_1}TC_{\dot{u}}(0,t,0,t) + RC_{\dot{u}}(0,t,0,t) = 1$
	F	$TC_F(0,t,0,t) - RC_F(0,t,0,t) = 1, \quad \frac{\rho_1c_1S_1}{\rho_2c_2S_2}TC_F(0,t,0,t) + RC_F(0,t,0,t) = 1$
	σ	$\frac{S_2}{S_1}TC_\sigma(0,t,0,t) - RC_\sigma(0,t,0,t) = 1, \quad \frac{\rho_1c_1}{\rho_2c_2}TC_\sigma(0,t,0,t) + RC_\sigma(0,t,0,t) = 1$
	u	$TC_u(0,t,0,t) - RC_u(0,t,0,t) = 1, \quad \frac{\rho_2c_2S_2}{\rho_1c_1S_1}TC_u(0,t,0,t) + RC_u(0,t,0,t) = 1$
	a	$TC_a(0,t,0,t) - RC_a(0,t,0,t) = 1, \quad \frac{\rho_2c_2S_2}{\rho_1c_1S_1}TC_a(0,t,0,t) + RC_a(0,t,0,t) = 1$
	ε	$\frac{S_2E_2}{S_1E_1}TC_\varepsilon(0,t,0,t) - RC_\varepsilon(0,t,0,t) = 1, \quad \frac{c_2}{c_1}TC_\varepsilon(0,t,0,t) + RC_\varepsilon(0,t,0,t) = 1$

Table 6-3' Time domain $TC(0,t,0,t)$, $RC(0,t,0,t)$ and $RT(0,t,0,t)$ expressions for elastic-elastic contact

	$TC(0,t,0,t,) = \frac{T(0,t)}{I(0,t)}$	$RC(0,t,0,t) = \frac{R(0,t)}{I(0,t)}$	$RT(0,t,0,t) = \frac{R(0,t)}{T(0,t)} = \frac{RC(0,t,0,t)}{TC(0,t,0,t)}$
ε	$\frac{2\rho_1c_1S_1}{\rho_1c_1S_1+\rho_2c_2S_2}\frac{c_1}{c_2}$	$\frac{\rho_2c_2S_2-\rho_1c_1S_1}{\rho_1c_1S_1+\rho_2c_2S_2}$	$\frac{\rho_2c_2S_2-\rho_1c_1S_1}{2\rho_1c_1S_1}\frac{c_2}{c_1}$
F	$\frac{2\rho_2c_2S_2}{\rho_1c_1S_1+\rho_2c_2S_2}$	$\frac{\rho_2c_2S_2-\rho_1c_1S_1}{\rho_1c_1S_1+\rho_2c_2S_2}$	$\frac{\rho_2c_2S_2-\rho_1c_1S_1}{2\rho_2c_2S_2}$
σ	$\frac{2\rho_2c_2S_2}{\rho_1c_1S_1+\rho_2c_2S_2}\frac{S_1}{S_2}$	$\frac{\rho_2c_2S_2-\rho_1c_1S_1}{\rho_1c_1S_1+\rho_2c_2S_2}$	$\frac{\rho_2c_2S_2-\rho_1c_1S_1}{2\rho_2c_2S_2}\frac{S_2}{S_1}$
$\dot{u}$	$\frac{2\rho_1c_1S_1}{\rho_1c_1S_1+\rho_2c_2S_2}$	$\frac{\rho_1c_1S_1-\rho_2c_2S_2}{\rho_1c_1S_1+\rho_2c_2S_2}$	$\frac{\rho_1c_1S_1-\rho_2c_2S_2}{2\rho_1c_1S_1}$
u	$\frac{2\rho_1c_1S_1}{\rho_1c_1S_1+\rho_2c_2S_2}$	$\frac{\rho_1c_1S_1-\rho_2c_2S_2}{\rho_1c_1S_1+\rho_2c_2S_2}$	$\frac{\rho_1c_1S_1-\rho_2c_2S_2}{2\rho_1c_1S_1}$
a	$\frac{2\rho_1c_1S_1}{\rho_1c_1S_1+\rho_2c_2S_2}$	$\frac{\rho_1c_1S_1-\rho_2c_2S_2}{\rho_1c_1S_1+\rho_2c_2S_2}$	$\frac{\rho_1c_1S_1-\rho_2c_2S_2}{2\rho_1c_1S_1}$

The time domain coefficients at any other monitoring locations, *i.e.* $TC(x_I, t_I, x_T, t_T)$, $RC(x_I, t_I, x_R, t_R)$ and $RC(x_I, t_I, x_T, t_T)$, can be obtained in the following way (displacement as an example)

$$TC_u(x_I, t_I, x_T, t_T) = \frac{\sum_j u_{Tj}(x_T, t_T)}{\sum_j u_{Ij}(x_I, t_I)} = \frac{\sum_j A_{Tj} e^{i\omega_j t_T} e^{-\gamma_{2j} x_T}}{\sum_j A_{Ij} e^{i\omega_j t_I} e^{-\gamma_{1j} x_I}} \xrightarrow{t_T = t_I + \frac{|x_I|}{c_1} + \frac{|x_T|}{c_2}, \gamma_{1j} = i\frac{\omega_j}{c_1}, \gamma_{2j} = i\frac{\omega_j}{c_2}} \frac{\sum_j A_{Tj} e^{-i\omega_j \frac{x_I}{c_1}} e^{i\omega_j t_I}}{\sum_j A_{Ij} e^{-i\omega_j \frac{x_I}{c_1}} e^{i\omega_j t_I}} \tag{6.9a}$$

$$RC_u(x_I, t_I, x_R, t_R) = \frac{\sum_j u_{Rj}(x_R, t_R)}{\sum_j u_{Ij}(x_I, t_I)} = \frac{\sum_j A_{Rj} e^{i\omega_j t_R} e^{+\gamma_{1j} x_R}}{\sum_j A_{Ij} e^{i\omega_j t_I} e^{-\gamma_{1j} x_I}} \xrightarrow{t_T = t_I + \frac{|x_I|}{c_1} + \frac{|x_R|}{c_1}, \gamma_{1j} = i\frac{\omega_j}{c_1}, \gamma_{2j} = i\frac{\omega_j}{c_2}} \frac{\sum_j A_{Rj} e^{-i\omega_j \frac{x_I}{c_1}} e^{i\omega_j t_I}}{\sum_j A_{Ij} e^{-i\omega_j \frac{x_I}{c_1}} e^{i\omega_j t_I}} \tag{6.9b}$$

$$RT_u(x_T, t_T, x_R, t_R) = \frac{\sum_j u_{Rj}(x_R, t_R)}{\sum_j u_{Tj}(x_T, t_T)} = \frac{\sum_j A_{Rj} e^{i\omega_j t_R} e^{+\gamma_{1j} x_R}}{\sum_j A_{Tj} e^{i\omega_j t_T} e^{-\gamma_{2j} x_T}} \xrightarrow{t_R = t_T + \frac{|x_R|}{c_1} - \frac{|x_T|}{c_2}, \gamma_{1j} = i\frac{\omega_j}{c_1}, \gamma_{2j} = i\frac{\omega_j}{c_2}} \frac{\sum_j A_{Rj} e^{-i\omega_j \frac{x_T}{c_2}} e^{i\omega_j t_T}}{\sum_j A_{Tj} e^{-i\omega_j \frac{x_T}{c_2}} e^{i\omega_j t_T}}. \tag{6.9c}$$

Note that in deriving the above equations, the attenuation coefficients α_{1j} and α_{2j} are all zero in elastic materials, and a common time set (t_I, t_R, t_T) which satisfies the time relations Eq. (6.3c) has been used for all components, as they all propagate at the same wave speeds: c_1 and c_2.

Combining Eq. (6.6a''~c'') and results in Table. 6-3, for each Fourier component at the interface

$$TC_{uj}(0, t, 0, t) = \frac{u_{Tj}(0,t)}{u_{Ij}(0,t)} = \frac{A_{Tj}}{A_{Ij}} = \frac{2\rho_1 c_1 S_1}{\rho_1 c_1 S_1 + \rho_2 c_2 S_2}$$

$$RC_{uj}(0, t, 0, t) = \frac{u_{Rj}(0,t)}{u_{Ij}(0,t)} = \frac{A_{Rj}}{A_{Ij}} = \frac{\rho_1 c_1 S_1 - \rho_2 c_2 S_2}{\rho_1 c_1 S_1 + \rho_2 c_2 S_2}$$

$$RT_{uj}(0, t, 0, t) = \frac{u_{Rj}(0,t)}{u_{Tj}(0,t)} = \frac{A_{Rj}}{A_{Tj}} = \frac{\rho_1 c_1 S_1 - \rho_2 c_2 S_2}{2\rho_1 c_1 S_1}$$

which gives

$$\begin{aligned} A_{Tj} &= \frac{2\rho_1 c_1 S_1}{\rho_1 c_1 S_1 + \rho_2 c_2 S_2} \times A_{Ij} \\ A_{Rj} &= \frac{\rho_1 c_1 S_1 - \rho_2 c_2 S_2}{\rho_1 c_1 S_1 + \rho_2 c_2 S_2} \times A_{Ij} \end{aligned}. \tag{6.10}$$

Substituting Eq. (6.10) into Eq. (6.9a~c) yields

$$TC_u(x_I, t_I, x_T, t_T) = \frac{2\rho_1 c_1 S_1}{\rho_1 c_1 S_1 + \rho_2 c_2 S_2} \tag{6.11a}$$

$$RC_u(x_I, t_I, x_R, t_R) = \frac{\rho_1 c_1 S_1 - \rho_2 c_2 S_2}{\rho_1 c_1 S_1 + \rho_2 c_2 S_2} \tag{6.11b}$$

$$RT_u(x_T, t_T, x_R, t_R) = \frac{\rho_1 c_1 S_1 - \rho_2 c_2 S_2}{2\rho_1 c_1 S_1}. \tag{6.11c}$$

It is not surprising to find that in purely elastic materials the reflection coefficients are independent of frequency, so that for any arbitrary waveform, the same proportion of the incident wave was transmitted: the interface acts as a linear amplifier and, furthermore, the coefficient is the same

wherever the measurements of x_I, x_R and x_T are performed, as long as there is no geometric dispersion. In addition, the results in Table. 6-3' can be further simplified by introducing the 'characteristic impedance' $Z(\omega)$, a function of material properties and geometry (Eq. (6.8)). Also, as the elastic relations exist between wave speed c and the elastic modulus E (Eq. (2.7)), the TC and RC, using stress as an example, can expressed in different forms in terms of ρ, c, E, Z

$$TC_\sigma = \frac{2Z_2}{Z_1+Z_2}\frac{S_1}{S_2} = \frac{2\rho_2 c_2 S_2}{\rho_1 c_1 S_1+\rho_2 c_2 S_2}\frac{S_1}{S_2} = \frac{2S_1 c_1 E_2}{S_1 c_2 E_1+S_2 c_1 E_2} = \frac{2S_1\sqrt{E_2\rho_2}}{S_1\sqrt{E_1\rho_1}+S_2\sqrt{E_2\rho_2}} \quad (6.11a')$$

$$RC_\sigma = \frac{Z_2-Z_1}{Z_1+Z_2} = \frac{\rho_2 c_2 S_2-\rho_1 c_1 S_1}{\rho_1 c_1 S_1+\rho_2 c_2 S_2} = \frac{S_2 c_1 E_2-S_1 c_2 E_1}{S_1 c_2 E_1+S_2 c_1 E_2} = \frac{S_2\sqrt{E_2\rho_2}-S_1\sqrt{E_1\rho_1}}{S_1\sqrt{E_1\rho_1}+S_2\sqrt{E_2\rho_2}}. \quad (6.11b')$$

For elastic materials these ratios are only functions of material properties (ρ, c, E, Z) and geometry (S). Therefore, once the 3 waves are measured, the ratios calculated can be inverted to obtain the mechanical properties (*e.g.* E). From the above analysis it is observed that, whatever quantity is measured, both coefficients can be expressed as functions of material modulus, *i.e.* $TC = TC\ (E_1, E_2)$ and $RC = RC\ (E_1, E_2)$, and it at first appears that the modulus of both rods can be determined. Unfortunately, the 2 coefficients (*i.e.* TC and RC) are not independent: either can be obtained once the other is known, which means that only modulus ratios can be derived. This seems reasonable because we expect that 2 imaginary interface tests, one with 2 very stiff rods in contact and the other 2 relatively low impedance rods, can result in the same TC and RC ratios. This means without knowing the properties of 1 rod, just measuring the 2 ratios is inadequate for determining the properties of either rod.

Finally, based on Table. 6-3', the mechanical impedance Z is inverted as functions of TC and RC (also RT in the velocity case, see Table. 6-4'). Once the properties of 1 rod (either incident or transmission) are known, the impedance/modulus of the other rod can be derived. Similarly, by applying constitutive equations, three cases have been analysed: Elastic-Maxwell, Elastic-Voigt, Elastic-S.L.S Maxwell/S.L.S. Voigt, detailed analysis process can be found in the full *web version*, here only results are presented (Table. 6-5).

Table. 6-4' Time domain relations between Z_1 and Z_2 for elastic-elastic contact

(TC and RC can be measured at arbitrary locations $x_1 \le 0, x_2 \ge 0$, satisfying the time relations Eq. (6.3c))

$\dot{u}$	① $TC_{\dot{u}} - RC_{\dot{u}} = 1$	σ	① $TC_\sigma \frac{S_2}{S_1} - RC_\sigma = 1$	u	① $TC_u - RC_u = 1$
	② $Z_2 = \frac{1-RC_{\dot{u}}}{TC_{\dot{u}}} Z_1$		② $Z_2 = \frac{\frac{S_2}{S_1} TC_\sigma}{1-RC_\sigma} Z_1$		② $Z_2 = \frac{1-RC_u}{TC_u} Z_1$
	③ $Z_2 = \frac{2-TC_{\dot{u}}}{TC_{\dot{u}}} Z_1$		③ $Z_2 = \frac{TC_\sigma}{2\frac{S_1}{S_2} - TC_\sigma} Z_1$		③ $Z_2 = \frac{2-TC_u}{TC_u} Z_1$
	④ $Z_2 = \frac{1-RC_{\dot{u}}}{1+RC_{\dot{u}}} Z_1$		④ $Z_2 = \frac{1+RC_\sigma}{1-RC_\sigma} Z_1$		④ $Z_2 = \frac{1-RC_u}{1+RC_u} Z_1$
	⑤ $Z_2 = (1 - 2RT_{\dot{u}}) Z_1$				
F	① $TC_F - RC_F = 1$	ε	① $E_2 = \frac{S_1}{S_2} \frac{1+RC_\varepsilon}{TC_\varepsilon} E_1$ or equivalently: $Z_2 = \sqrt{\frac{\rho_2 S_2}{\rho_1 S_1}} \sqrt{\frac{1+RC_\varepsilon}{TC_\varepsilon}} Z_1$	a	① $TC_a - RC_a = 1$
	② $Z_2 = \frac{TC_F}{1-RC_F} Z_1$		② $Z_2 = \frac{\rho_2 S_2}{\rho_1 S_1} \frac{1-RC_\varepsilon}{TC_\varepsilon} Z_1$		② $Z_2 = \frac{1-RC_a}{TC_a} Z_1$
	③ $Z_2 = \frac{TC_F}{2-TC_F} Z_1$		③ $Z_2^2 + Z_1 Z_2 - \frac{\rho_2 S_2}{\rho_1 S_1} \frac{2}{TC_\varepsilon} Z_1^2 = 0$		③ $Z_2 = \frac{2-TC_a}{TC_a} Z_1$
	④ $Z_2 = \frac{1+RC_F}{1-RC_F} Z_1$		④ $Z_2 = \frac{1+RC_\varepsilon}{1-RC_\varepsilon} Z_1$		④ $Z_2 = \frac{1-RC_a}{1+RC_a} Z_1$

Table. 6-5 Time domain TC & RC Summary

$x_I, x_R \le 0$ $x_T \ge 0$		General-general	Elastic-elastic	Elastic-Maxwell (steady response)	Elastic-Voigt	Elastic-Maxwell/ Voigt SLS (steady response)
u	TC_u	$\frac{2\rho_1 S_1 \gamma_2}{\rho_1 S_1 \gamma_2 + \rho_2 S_2 \gamma_1} \times \frac{e^{-\alpha_2 x_T}}{e^{-\alpha_1 x_I}}$	$\frac{2\rho_1 c_1 S_1}{\rho_1 c_1 S_1 + \rho_2 c_2 S_2}$	$\frac{2\rho_1 c_1 S_1}{\rho_1 c_1 S_1 + \frac{S_2\gamma_2 k\tau}{(1+i\omega\tau)}} \times e^{-\alpha_2 x_T}$	$\frac{2i\rho_1 c_1 S_1 \omega}{i\rho_1 c_1 S_1 \omega + S_2\gamma_2(k+i\eta\omega)} \times e^{-\alpha_2 x_T}$	$\frac{2i\rho_1 c_1 S_1 \omega}{i\rho_1 c_1 S_1 \omega + \frac{S_2\gamma_2}{(1+i\omega\tau)}[k_e + i\omega\tau(k_1+k_e)]} \times e^{-\alpha_2 x_T}$
	RC_u	$\frac{\rho_1 S_1 \gamma_2 - \rho_2 S_2 \gamma_1}{\rho_1 S_1 \gamma_2 + \rho_2 S_2 \gamma_1} \times \frac{e^{\alpha_1 x_R}}{e^{-\alpha_1 x_I}}$	$\frac{\rho_1 c_1 S_1 - \rho_2 c_2 S_2}{\rho_1 c_1 S_1 + \rho_2 c_2 S_2}$	$\frac{\rho_1 c_1 S_1 - \frac{S_2\gamma_2 k\tau}{(1+i\omega\tau)}}{\rho_1 c_1 S_1 + \frac{S_2\gamma_2 k\tau}{(1+i\omega\tau)}}$	$\frac{i\rho_1 c_1 S_1 \omega - S_2\gamma_2(k+i\eta\omega)}{i\rho_1 c_1 S_1 \omega + S_2\gamma_2(k+i\eta\omega)}$	$\frac{i\rho_1 c_1 S_1 \omega - \frac{S_2\gamma_2}{(1+i\omega\tau)}[k_e + i\omega\tau(k_1+k_e)]}{i\rho_1 c_1 S_1 \omega + \frac{S_2\gamma_2}{(1+i\omega\tau)}[k_e + i\omega\tau(k_1+k_e)]}$
$\dot{u}$	$TC_{\dot{u}}$	$\frac{2\rho_1 S_1 \gamma_2}{\rho_1 S_1 \gamma_2 + \rho_2 S_2 \gamma_1} \times \frac{e^{-\alpha_2 x_T}}{e^{-\alpha_1 x_I}}$	$\frac{2\rho_1 c_1 S_1}{\rho_1 c_1 S_1 + \rho_2 c_2 S_2}$	$\frac{2\rho_1 c_1 S_1}{\rho_1 c_1 S_1 + \frac{S_2\gamma_2 k\tau}{(1+i\omega\tau)}} \times e^{-\alpha_2 x_T}$	$\frac{2i\rho_1 c_1 S_1 \omega}{i\rho_1 c_1 S_1 \omega + S_2\gamma_2(k+i\eta\omega)} \times e^{-\alpha_2 x_T}$	$\frac{2i\rho_1 c_1 S_1 \omega}{i\rho_1 c_1 S_1 \omega + \frac{S_2\gamma_2}{(1+i\omega\tau)}[k_e + i\omega\tau(k_1+k_e)]} \times e^{-\alpha_2 x_T}$
	$RC_{\dot{u}}$	$\frac{\rho_1 S_1 \gamma_2 - \rho_2 S_2 \gamma_1}{\rho_1 S_1 \gamma_2 + \rho_2 S_2 \gamma_1} \times \frac{e^{\alpha_1 x_R}}{e^{-\alpha_1 x_I}}$	$\frac{\rho_1 c_1 S_1 - \rho_2 c_2 S_2}{\rho_1 c_1 S_1 + \rho_2 c_2 S_2}$	$\frac{\rho_1 c_1 S_1 - \frac{S_2\gamma_2 k\tau}{(1+i\omega\tau)}}{\rho_1 c_1 S_1 + \frac{S_2\gamma_2 k\tau}{(1+i\omega\tau)}}$	$\frac{i\rho_1 c_1 S_1 \omega - S_2\gamma_2(k+i\eta\omega)}{i\rho_1 c_1 S_1 \omega + S_2\gamma_2(k+i\eta\omega)}$	$\frac{i\rho_1 c_1 S_1 \omega - \frac{S_2\gamma_2}{(1+i\omega\tau)}[k_e + i\omega\tau(k_1+k_e)]}{i\rho_1 c_1 S_1 \omega + \frac{S_2\gamma_2}{(1+i\omega\tau)}[k_e + i\omega\tau(k_1+k_e)]}$
a	TC_a	$\frac{2\rho_1 S_1 \gamma_2}{\rho_1 S_1 \gamma_2 + \rho_2 S_2 \gamma_1} \times \frac{e^{-\alpha_2 x_T}}{e^{-\alpha_1 x_I}}$	$\frac{2\rho_1 c_1 S_1}{\rho_1 c_1 S_1 + \rho_2 c_2 S_2}$	$\frac{2\rho_1 c_1 S_1}{\rho_1 c_1 S_1 + \frac{S_2\gamma_2 k\tau}{(1+i\omega\tau)}} \times e^{-\alpha_2 x_T}$	$\frac{2i\rho_1 c_1 S_1 \omega}{i\rho_1 c_1 S_1 \omega + S_2\gamma_2(k+i\eta\omega)} \times e^{-\alpha_2 x_T}$	$\frac{2i\rho_1 c_1 S_1 \omega}{i\rho_1 c_1 S_1 \omega + \frac{S_2\gamma_2}{(1+i\omega\tau)}[k_e + i\omega\tau(k_1+k_e)]} \times e^{-\alpha_2 x_T}$
	RC_a	$\frac{\rho_1 S_1 \gamma_2 - \rho_2 S_2 \gamma_1}{\rho_1 S_1 \gamma_2 + \rho_2 S_2 \gamma_1} \times \frac{e^{\alpha_1 x_R}}{e^{-\alpha_1 x_I}}$	$\frac{\rho_1 c_1 S_1 - \rho_2 c_2 S_2}{\rho_1 c_1 S_1 + \rho_2 c_2 S_2}$	$\frac{\rho_1 c_1 S_1 - \frac{S_2\gamma_2 k\tau}{(1+i\omega\tau)}}{\rho_1 c_1 S_1 + \frac{S_2\gamma_2 k\tau}{(1+i\omega\tau)}}$	$\frac{i\rho_1 c_1 S_1 \omega - S_2\gamma_2(k+i\eta\omega)}{i\rho_1 c_1 S_1 \omega + S_2\gamma_2(k+i\eta\omega)}$	$\frac{i\rho_1 c_1 S_1 \omega - \frac{S_2\gamma_2}{(1+i\omega\tau)}[k_e + i\omega\tau(k_1+k_e)]}{i\rho_1 c_1 S_1 \omega + \frac{S_2\gamma_2}{(1+i\omega\tau)}[k_e + i\omega\tau(k_1+k_e)]}$
ε	TC_ε	$\frac{2\rho_1 S_1 \gamma_2}{\rho_1 S_1 \gamma_2 + \rho_2 S_2 \gamma_1} \times \frac{\gamma_2}{\gamma_1} \times \frac{e^{-\alpha_2 x_T}}{e^{-\alpha_1 x_I}}$	$\frac{2\rho_1 c_1 S_1}{\rho_1 c_1 S_1 + \rho_2 c_2 S_2} \frac{c_1}{c_2}$	$\frac{2\rho_1 c_1 S_1}{\rho_1 c_1 S_1 + \frac{S_2\gamma_2 k\tau}{(1+i\omega\tau)}} \times e^{-\alpha_2 x_T} \times \frac{\gamma_2}{\gamma_1}$	$\frac{2i\rho_1 c_1 S_1 \omega}{i\rho_1 c_1 S_1 \omega + S_2\gamma_2(k+i\eta\omega)} \times e^{-\alpha_2 x_T} \times \frac{\gamma_2}{\gamma_1}$	$\frac{2i\rho_1 c_1 S_1 \omega}{i\rho_1 c_1 S_1 \omega + \frac{S_2\gamma_2}{(1+i\omega\tau)}[k_e + i\omega\tau(k_1+k_e)]} \times e^{-\alpha_2 x_T} \times \frac{\gamma_2}{\gamma_1}$
	RC_ε	$\frac{\rho_2 S_2 \gamma_1 - \rho_1 S_1 \gamma_2}{\rho_1 S_1 \gamma_2 + \rho_2 S_2 \gamma_1} \times \frac{e^{\alpha_1 x_R}}{e^{-\alpha_1 x_I}}$	$\frac{\rho_2 c_2 S_2 - \rho_1 c_1 S_1}{\rho_1 c_1 S_1 + \rho_2 c_2 S_2}$	$\frac{\frac{S_2\gamma_2 k\tau}{(1+i\omega\tau)} - \rho_1 c_1 S_1}{\rho_1 c_1 S_1 + \frac{S_2\gamma_2 k\tau}{(1+i\omega\tau)}}$	$\frac{S_2\gamma_2(k+i\eta\omega) - i\rho_1 c_1 S_1 \omega}{i\rho_1 c_1 S_1 \omega + S_2\gamma_2(k+i\eta\omega)}$	$\frac{\frac{S_2\gamma_2}{(1+i\omega\tau)}[k_e + i\omega\tau(k_1+k_e)] - i\rho_1 c_1 S_1 \omega}{i\rho_1 c_1 S_1 \omega + \frac{S_2\gamma_2}{(1+i\omega\tau)}[k_e + i\omega\tau(k_1+k_e)]}$
σ	TC_σ	$\frac{2\rho_2 S_1 \gamma_1}{\rho_1 S_1 \gamma_2 + \rho_2 S_2 \gamma_1} \times \frac{e^{-\alpha_2 x_T}}{e^{-\alpha_1 x_I}}$	$\frac{2\rho_2 c_2 S_2}{\rho_1 c_1 S_1 + \rho_2 c_2 S_2} \frac{S_1}{S_2}$	$\frac{\frac{2S_1\gamma_2 k\tau}{(1+i\omega\tau)}}{\rho_1 c_1 S_1 + \frac{S_2\gamma_2 k\tau}{(1+i\omega\tau)}} \times e^{-\alpha_2 x_T}$	$\frac{2S_1\gamma_2(k+i\eta\omega)}{i\rho_1 c_1 S_1 \omega + S_2\gamma_2(k+i\eta\omega)} \times e^{-\alpha_2 x_T}$	$\frac{2\frac{S_1\gamma_2}{(1+i\omega\tau)}[k_e + i\omega\tau(k_1+k_e)]}{i\rho_1 c_1 S_1 \omega + \frac{S_2\gamma_2}{(1+i\omega\tau)}[k_e + i\omega\tau(k_1+k_e)]} \times e^{-\alpha_2 x_T}$
	RC_σ	$\frac{\rho_2 S_2 \gamma_1 - \rho_1 S_1 \gamma_2}{\rho_1 S_1 \gamma_2 + \rho_2 S_2 \gamma_1} \times \frac{e^{\alpha_1 x_R}}{e^{-\alpha_1 x_I}}$	$\frac{\rho_2 c_2 S_2 - \rho_1 c_1 S_1}{\rho_1 c_1 S_1 + \rho_2 c_2 S_2}$	$\frac{\frac{S_2\gamma_2 k\tau}{(1+i\omega\tau)} - \rho_1 c_1 S_1}{\rho_1 c_1 S_1 + \frac{S_2\gamma_2 k\tau}{(1+i\omega\tau)}}$	$\frac{S_2\gamma_2(k+i\eta\omega) - i\rho_1 c_1 S_1 \omega}{i\rho_1 c_1 S_1 \omega + S_2\gamma_2(k+i\eta\omega)}$	$\frac{\frac{S_2\gamma_2}{(1+i\omega\tau)}[k_e + i\omega\tau(k_1+k_e)] - i\rho_1 c_1 S_1 \omega}{i\rho_1 c_1 S_1 \omega + \frac{S_2\gamma_2}{(1+i\omega\tau)}[k_e + i\omega\tau(k_1+k_e)]}$
F	TC_F	$\frac{2\rho_2 S_2 \gamma_1}{\rho_1 S_1 \gamma_2 + \rho_2 S_2 \gamma_1} \times \frac{e^{-\alpha_2 x_T}}{e^{-\alpha_1 x_I}}$	$\frac{2\rho_2 c_2 S_2}{\rho_1 c_1 S_1 + \rho_2 c_2 S_2}$	$\frac{\frac{2S_2\gamma_2 k\tau}{(1+i\omega\tau)}}{\rho_1 c_1 S_1 + \frac{S_2\gamma_2 k\tau}{(1+i\omega\tau)}} \times e^{-\alpha_2 x_T}$	$\frac{2S_2\gamma_2(k+i\eta\omega)}{i\rho_1 c_1 S_1 \omega + S_2\gamma_2(k+i\eta\omega)} \times e^{-\alpha_2 x_T}$	$\frac{2\frac{S_2\gamma_2}{(1+i\omega\tau)}[k_e + i\omega\tau(k_1+k_e)]}{i\rho_1 c_1 S_1 \omega + \frac{S_2\gamma_2}{(1+i\omega\tau)}[k_e + i\omega\tau(k_1+k_e)]} \times e^{-\alpha_2 x_T}$
	RC_F	$\frac{\rho_2 S_2 \gamma_1 - \rho_1 S_1 \gamma_2}{\rho_1 S_1 \gamma_2 + \rho_2 S_2 \gamma_1} \times \frac{e^{\alpha_1 x_R}}{e^{-\alpha_1 x_I}}$	$\frac{\rho_2 c_2 S_2 - \rho_1 c_1 S_1}{\rho_1 c_1 S_1 + \rho_2 c_2 S_2}$	$\frac{\frac{S_2\gamma_2 k\tau}{(1+i\omega\tau)} - \rho_1 c_1 S_1}{\rho_1 c_1 S_1 + \frac{S_2\gamma_2 k\tau}{(1+i\omega\tau)}}$	$\frac{S_2\gamma_2(k+i\eta\omega) - i\rho_1 c_1 S_1 \omega}{i\rho_1 c_1 S_1 \omega + S_2\gamma_2(k+i\eta\omega)}$	$\frac{\frac{S_2\gamma_2}{(1+i\omega\tau)}[k_e + i\omega\tau(k_1+k_e)] - i\rho_1 c_1 S_1 \omega}{i\rho_1 c_1 S_1 \omega + \frac{S_2\gamma_2}{(1+i\omega\tau)}[k_e + i\omega\tau(k_1+k_e)]}$

6.2.2 Frequency domain analysis

All following analysis is presented within the context of 1D wave propagation, though some of the theories can be applied to the 3D case (*e.g.* the BCs) with proper modification. Therefore, all material properties of both rods, *e.g.* the propagation coefficient, dynamic modulus, TC and RC, are in the 1D context.

Time domain analysis can only deal with the elastic-elastic case, or general materials with a single frequency; it is more convenient to treat signals in frequency domain, for which there is multiple-frequency processing capability. Based on the linear property of the Fourier transform, the boundary conditions (Eq. (6.4a) and Eq. (6.4b)) can be expressed equivalently as

$$\begin{cases} \tilde{u}_I(0,\omega) + \tilde{u}_R(0,\omega) = \tilde{u}_T(0,\omega) \quad ① \\ \tilde{F}_I(0,\omega) + \tilde{F}_R(0,\omega) = \tilde{F}_T(0,\omega) \quad ② \end{cases} \tag{6.4a'}$$

$$\begin{cases} \sum_j \tilde{u}_{Ij}(0,\omega) + \sum_j \tilde{u}_{Rj}(0,\omega) = \sum_j \tilde{u}_{Tj}(0,\omega) \\ \sum_j \tilde{F}_{Ij}(0,\omega) + \sum_j \tilde{F}_{Rj}(0,\omega) = \sum_j \tilde{F}_{Tj}(0,\omega) \end{cases}. \tag{6.4b'}$$

Eq. (6.4 a') corresponds to a single frequency and Eq. (6.4b') is for a group of Fourier components. In frequency domain we just focus on the performance of each individual frequency, so only Eq. (6.4a') was used in the following analysis.

Similar to Eq. (6.5a), for each frequency, we define the frequency domain transmission coefficient $TC(x_I, x_T, \omega)$ and reflection coefficient $RC(x_I, x_R, \omega)$ as ratios of the Fourier transforms of the transmitted or refleced wave to the corresponding incident wave

$$TC(x_I, x_T, \omega) = \frac{\tilde{T}(x_T,\omega)}{\tilde{I}(x_I,\omega)},\ RC(x_I, x_R, \omega) = \frac{\tilde{R}(x_T,\omega)}{\tilde{I}(x_I,\omega)} \tag{6.5a'}$$

and a less frequently used reflection-to-transmission ratio $RT(x_T, x_R, \omega) = \frac{\tilde{R}(x_R,\omega)}{\tilde{T}(x_T,\omega)}$.

Note that one should distinguish the 2 types of definitions in Eq. (6.5a) and Eq. (6.5a') from each other; as they are defined in different spaces, they are not necessarily equal, and the frequency domain $TC(x_I, x_T, \omega)$ and $RC(x_I, x_T, \omega)$ are not a Fourier transform of the corresponding time domain counterparts $TC(x_I, t_I, x_T, t_T)$ and $RC(x_I, t_I, x_R, t_R)$: it can be seen from Eq. (6.5a') that FFTs are first performed before ratios are taken. Also note that, ideally, we expect the force and velocity continuity conditions to be satisfied across the whole cross-section, this requirement can be

applied to both 1D and 3D analysis. In a 1D analysis, the 'plane assumption' indicates that all the planes along the 2 contact rods remain plane and perpendicular to the central line during wave propagation, thus deformation across a plane is uniform. 3D analysis introduces the variation of deformation across the plane, and by employing different deformation modes, *e.g.* the most common 4 modes suggested by Simon [27], the real deformation can be simulated. In this research, in order to simplify the theories while addressing the wave propagation mechanism at interface, only 1D wave propagation theories were adopted and thereby in any case that involves 3D effect, *e.g.* when it comes to high frequencies where the radius of gyration and Poisson' ratio have a great effect on the wave propagation characteristics such as wave speed, a phase-only correction method proposed by Gorham [56] was used to convert all quantities into the 1D case.

Frequency domain analysis is more useful for looking at frequency-dependent behaviours in non-elastic materials such as viscoelastic materials. Before proceeding to further frequency domain interface analysis, it is useful to present the individual expressions of the 6 quantities in frequency domain. It is noted that, instead of employing the universal displacement expression in time domain, the general strain expression $\tilde{\varepsilon}(x,\omega) = \tilde{P}(\omega)e^{-\gamma x} + \tilde{N}(\omega)e^{\gamma x}$ (Eq. (2.20a)), which is in essence equivalent to the time domain displacement expression, was widely used in the frequency domain [18, 21, 23, 42]. Here, γ is again the wave propagation coefficient of the material. It is a function of both material properties and frequency (Eq. (2.19)). The prefix functions $\tilde{P}(\omega)$ and $\tilde{N}(\omega)$ are the Fourier transforms of the strains at $x = 0$ (interface) due to the waves traveling in the directions of increasing and decreasing x, respectively, and are determined by boundary conditions.

The relations between different quantities for general materials in the frequency domain can be found from the intrinsic relations in Eq. (6.1a)~(6.1f)

$$\varepsilon(x,t) = \frac{\partial u(x,t)}{\partial x} \rightarrow u(x,t) = \int \varepsilon(x,t)dx \rightarrow \tilde{u}(x,\omega) = \int \tilde{\varepsilon}(x,\omega)dx \tag{6.1b'}$$

$$\dot{u}(x,t) = \frac{\partial u(x,t)}{\partial t} \rightarrow \tilde{\dot{u}}(x,\omega) = i\omega\tilde{u}(x,\omega) \tag{6.1c'}$$

$$a(x,t) = \frac{\partial \dot{u}(x,t)}{\partial t} = \frac{\partial^2 u(x,t)}{\partial t^2} \rightarrow \tilde{a}(x,\omega) = i\omega\tilde{\dot{u}}(x,\omega) = -\omega^2\tilde{u}(x,\omega) \tag{6.1d'}$$

$$\frac{\partial \sigma(x,t)}{\partial x} = \rho\frac{\partial^2 u(x,t)}{\partial t^2} \rightarrow \sigma(x,t) = \rho\int\frac{\partial^2 u(x,t)}{\partial t^2}dx \rightarrow \tilde{\sigma}(x,\omega) = -\rho\omega^2\int\tilde{u}(x,\omega)dx \tag{6.1e'}$$

$$F = \sigma S \to \tilde{F} = \tilde{\sigma} S = -S\rho\omega^2 \int \tilde{u}(x,\omega)dx \qquad (6.1f')$$

where ρ is the material density and S the cross-section area. Using (6.1b'~f'), we can derive Eq. (2.20b ~ f) which give the general model-independent expressions in frequency domain. The incident, reflected and transmitted waves, measured at (x_I, x_R, x_T) in terms of the 6 quantities respectively, are expressed in Table. 6-6a. As strain serves as a basic quantity in the frequency domain, the relationships between strain and the other 5 quantities are also shown in the Table.

Substituting the general expressions of velocity (Eq. (2.20*c*)) and force (Eq. (2.20*f*)) into the BC equation pair (Eq. (6.4a')) gives

$$\begin{cases} \frac{\gamma_1}{\gamma_2}\frac{\tilde{Q}}{\tilde{P}} + \frac{\tilde{N}}{\tilde{P}} = 1 \quad ① \\ \frac{\frac{\rho_2 S_2}{\gamma_2}}{\frac{\rho_1 S_1}{\gamma_1}}\frac{\gamma_1}{\gamma_2}\frac{\tilde{Q}}{\tilde{P}} - \frac{\tilde{N}}{\tilde{P}} = 1 \quad ② \end{cases} \qquad (6.4a'')$$

which actually shows the balance of the interface strains $\tilde{P}, \tilde{N}, \tilde{Q}$.

As seen from the right column in Table. 6-6a, all the coefficients are functions of the 2 ratios $\frac{\tilde{Q}}{\tilde{P}}$ and $\frac{\tilde{N}}{\tilde{P}}$, thus to obtain the expressions of TC and RC, Eq. (6.1a'') is used to obtain the interface strain amplitude ratios $\frac{\tilde{Q}}{\tilde{P}}$ and $\frac{\tilde{N}}{\tilde{P}}$

$$\begin{cases} \frac{\tilde{Q}}{\tilde{P}} = \frac{2}{\frac{\gamma_1}{\gamma_2}(1 + \frac{\rho_2 S_2}{\rho_1 S_1}\frac{\gamma_1}{\gamma_2})} = \frac{2\frac{\rho_1 S_1}{\gamma_1}}{\frac{\rho_1 S_1}{\gamma_1} + \frac{\rho_2 S_2}{\gamma_2}} \times \frac{\gamma_2}{\gamma_1} \\ \frac{\tilde{N}}{\tilde{P}} = \frac{\frac{\rho_2 S_2}{\rho_1 S_1}\frac{\gamma_1}{\gamma_2} - 1}{\frac{\rho_2 S_2}{\rho_1 S_1}\frac{\gamma_1}{\gamma_2} + 1} = \frac{\frac{\rho_2 S_2}{\gamma_2} - \frac{\rho_1 S_1}{\gamma_1}}{\frac{\rho_2 S_2}{\gamma_2} + \frac{\rho_1 S_1}{\gamma_1}} \end{cases} \qquad (6.12a)$$

All other coefficients can be directly obtained using the relations in the right column of Table. 6-6a. An alternative, and more standard, approach is firstly to express the BCs (Eq. (6.4a')) in terms of the 6 quantities, and then solve the equilibrium equation pair individually. By reversing the relations in Table. 6-6a, $\frac{\tilde{Q}}{\tilde{P}}$ and $\frac{\tilde{N}}{\tilde{P}}$ can be expressed as functions of TC and RC of the 6 quantities (Table. 6-7a). By substituting these expressions into Eq. (6.1a''), we have an equilibrium equation pair for each quantity, shown in Table. 6-8a. And particularly at the interface they lead to the values in Table. 6-8b.

Table. 6-6a General expressions in frequency domain

(Note: the origin $X = 0$ is defined at the interface, $x_I, x_R < 0, x_T > 0$)

	Incident	Reflected	Transmitted	TC, RC
$\tilde{\varepsilon}(x,\omega)$	$\tilde{P}e^{-\gamma_1 x_I}$	$\tilde{N}e^{\gamma_1 x_R}$	$\tilde{Q}e^{-\gamma_2 x_T}$	$TC_{\tilde{\varepsilon}}(x_I, x_T, \omega) = \frac{\tilde{Q}}{\tilde{P}} e^{-(\gamma_2 x_T - \gamma_1 x_I)}$ $RC_{\tilde{\varepsilon}}(x_I, x_R, \omega) = \frac{\tilde{N}}{\tilde{P}} e^{\gamma_1 x_R + \gamma_1 x_I}$
$\tilde{F}(x,\omega)$	$-\frac{\rho_1 S_1 \omega^2}{{\gamma_1}^2}\tilde{P}e^{-\gamma_1 x_I}$ $= -\frac{\rho_1 S_1 \omega^2}{{\gamma_1}^2} \times \tilde{\varepsilon}_I(x_I,\omega)$	$-\frac{\rho_1 S_1 \omega^2}{{\gamma_1}^2}\tilde{N}e^{\gamma_1 x_R}$ $= -\frac{\rho_1 S_1 \omega^2}{{\gamma_1}^2} \times \tilde{\varepsilon}_R(x_R,\omega)$	$-\frac{\rho_2 S_2 \omega^2}{{\gamma_2}^2}\tilde{Q}e^{-\gamma_2 x_T}$ $= -\frac{\rho_2 S_2 \omega^2}{{\gamma_2}^2} \times \tilde{\varepsilon}_T(x_T,\omega)$	$TC_{\tilde{F}}(x_I, x_T, \omega) = \frac{\rho_2 S_2}{\rho_1 S_1}\frac{{\gamma_1}^2}{{\gamma_2}^2}\frac{\tilde{Q}}{\tilde{P}} e^{-(\gamma_2 x_T - \gamma_1 x_I)} = \frac{\rho_2 S_2}{\rho_1 S_1}\frac{{\gamma_1}^2}{{\gamma_2}^2} TC_{\tilde{\varepsilon}}(x_I, x_T, \omega)$ $= \frac{E_2 S_2}{E_1 S_1} TC_{\tilde{\varepsilon}}(x_I, x_T, \omega)$ $RC_{\tilde{F}}(x_I, x_R, \omega) = \frac{\tilde{N}}{\tilde{P}} e^{\gamma_1 x_R + \gamma_1 x_I} = RC_{\tilde{\varepsilon}}(x_I, x_R, \omega)$
$\tilde{\sigma}(x,\omega)$	$-\frac{\rho_1 \omega^2}{{\gamma_1}^2}\tilde{P}e^{-\gamma_1 x_I}$ $= -\frac{\rho_1 \omega^2}{{\gamma_1}^2} \times \tilde{\varepsilon}_I(x_I,\omega)$	$-\frac{\rho_1 \omega^2}{{\gamma_1}^2}\tilde{N}e^{\gamma_1 x_R}$ $= -\frac{\rho_1 \omega^2}{{\gamma_1}^2} \times \tilde{\varepsilon}_R(x_R,\omega)$	$-\frac{\rho_2 \omega^2}{{\gamma_2}^2}\tilde{Q}e^{-\gamma_2 x_T}$ $= -\frac{\rho_2 \omega^2}{{\gamma_2}^2} \times \tilde{\varepsilon}_T(x_T,\omega)$	$TC_{\tilde{\sigma}}(x_I, x_T, \omega) = \frac{\rho_2}{\rho_1}\frac{{\gamma_1}^2}{{\gamma_2}^2}\frac{\tilde{Q}}{\tilde{P}} e^{-(\gamma_2 x_T - \gamma_1 x_I)} = \frac{\rho_2}{\rho_1}\frac{{\gamma_1}^2}{{\gamma_2}^2} TC_{\tilde{\varepsilon}}(x_I, x_T, \omega)$ $RC_{\tilde{\sigma}}(x_I, x_R, \omega) = \frac{\tilde{N}}{\tilde{P}} e^{\gamma_1 x_R + \gamma_1 x_I} = RC_{\tilde{\varepsilon}}(x_I, x_R, \omega)$
$\tilde{u}(x,\omega)$	$-\frac{i\omega}{\gamma_1}\tilde{P}e^{-\gamma_1 x_I}$ $= -\frac{i\omega}{\gamma_1} \times \tilde{\varepsilon}_I(x_I,\omega)$	$\frac{i\omega}{\gamma_1}\tilde{N}e^{\gamma_1 x_R}$ $= \frac{i\omega}{\gamma_1} \times \tilde{\varepsilon}_R(x_R,\omega)$	$-\frac{i\omega}{\gamma_2}\tilde{Q}e^{-\gamma_2 x_T}$ $= -\frac{i\omega}{\gamma_2} \times \tilde{\varepsilon}_T(x_T,\omega)$	$TC_{\tilde{u}}(x_I, x_T, \omega) = \frac{\gamma_1}{\gamma_2}\frac{\tilde{Q}}{\tilde{P}} e^{-(\gamma_2 x_T - \gamma_1 x_I)} = \frac{\gamma_1}{\gamma_2} TC_{\tilde{\varepsilon}}(x_I, x_T, \omega)$ $RC_{\tilde{u}}(x_I, x_R, \omega) = -\frac{\tilde{N}}{\tilde{P}} e^{\gamma_1 x_R + \gamma_1 x_I} = -RC_{\tilde{\varepsilon}}(x_I, x_R, \omega)$
$\tilde{u}(x,\omega)$	$-\frac{1}{\gamma_1}\tilde{P}e^{-\gamma_1 x_I}$ $= -\frac{1}{\gamma_1} \times \tilde{\varepsilon}_I(x_I,\omega)$	$\frac{1}{\gamma_1}\tilde{N}e^{\gamma_1 x_R}$ $= \frac{1}{\gamma_1} \times \tilde{\varepsilon}_R(x_R,\omega)$	$-\frac{1}{\gamma_2}\tilde{Q}e^{-\gamma_2 x_T}$ $= -\frac{1}{\gamma_2} \times \tilde{\varepsilon}_T(x_T,\omega)$	$TC_{\tilde{u}}(x_I, x_T, \omega) = \frac{\gamma_1}{\gamma_2}\frac{\tilde{Q}}{\tilde{P}} e^{-(\gamma_2 x_T - \gamma_1 x_I)} = \frac{\gamma_1}{\gamma_2} TC_{\tilde{\varepsilon}}(x_I, x_T, \omega)$ $RC_{\tilde{u}}(x_I, x_R, \omega) = -\frac{\tilde{N}}{\tilde{P}} e^{\gamma_1 x_R + \gamma_1 x_I} = -RC_{\tilde{\varepsilon}}(x_I, x_R, \omega)$
$\tilde{a}(x,\omega)$	$\frac{\omega^2}{\gamma_1}\tilde{P}e^{-\gamma_1 x_I}$ $= \frac{\omega^2}{\gamma_1} \times \tilde{\varepsilon}_I(x_I,\omega)$	$-\frac{\omega^2}{\gamma_1}\tilde{N}e^{\gamma_1 x_R}$ $= -\frac{\omega^2}{\gamma_1} \times \tilde{\varepsilon}_R(x_R,\omega)$	$\frac{\omega^2}{\gamma_2}\tilde{Q}e^{-\gamma_2 x_T}$ $= \frac{\omega^2}{\gamma_2} \times \tilde{\varepsilon}_T(x_T,\omega)$	$TC_{\tilde{a}}(x_I, x_T, \omega) = \frac{\gamma_1}{\gamma_2}\frac{\tilde{Q}}{\tilde{P}} e^{-(\gamma_2 x_T - \gamma_1 x_I)} = \frac{\gamma_1}{\gamma_2} TC_{\tilde{\varepsilon}}(x_I, x_T, \omega)$ $RC_{\tilde{a}}(x_I, x_R, \omega) = -\frac{\tilde{N}}{\tilde{P}} e^{\gamma_1 x_R + \gamma_1 x_I} = -RC_{\tilde{\varepsilon}}(x_I, x_R, \omega)$

Table 6-7a Interpreting $\frac{\tilde{Q}}{\tilde{P}}$ and $\frac{\tilde{N}}{\tilde{P}}$ in terms of TCs and RCs of 6 quantities

	$\frac{\tilde{Q}}{\tilde{P}} =$	$\frac{\tilde{N}}{\tilde{P}} =$
$\tilde{\varepsilon}$	$TC_{\tilde{\varepsilon}}(x_I, x_T, \omega) \times e^{\gamma_2 x_T - \gamma_1 x_I}$	$RC_{\tilde{\varepsilon}}(x_I, x_T, \omega) \times e^{-(\gamma_1 x_R + \gamma_1 x_I)}$
$\tilde{F}$	$\frac{\rho_1 S_1}{\gamma_1} \frac{\gamma_2}{\rho_2 S_2} \frac{\gamma_2}{\gamma_1} TC_{\tilde{F}}(x_I, x_T, \omega) \times e^{\gamma_2 x_T - \gamma_1 x_I}$	$RC_{\tilde{F}}(x_I, x_R, \omega) \times e^{-(\gamma_1 x_R + \gamma_1 x_I)}$
$\tilde{\sigma}$	$\frac{\rho_1}{\gamma_1} \frac{\gamma_2}{\rho_2} \frac{\gamma_2}{\gamma_1} TC_{\tilde{\sigma}}(x_I, x_T, \omega) \times e^{\gamma_2 x_T - \gamma_1 x_I}$	$RC_{\tilde{\sigma}}(x_I, x_R, \omega) \times e^{-(\gamma_1 x_R + \gamma_1 x_I)}$
$\tilde{u}$	$\frac{\gamma_2}{\gamma_1} TC_{\tilde{u}}(x_I, x_T, \omega) \times e^{\gamma_2 x_T - \gamma_1 x_I}$	$-RC_{\tilde{u}}(x_I, x_R, \omega) \times e^{-(\gamma_1 x_R + \gamma_1 x_I)}$
$\tilde{u}$	$\frac{\gamma_2}{\gamma_1} TC_{\tilde{u}}(x_I, x_T, \omega) \times e^{\gamma_2 x_T - \gamma_1 x_I}$	$-RC_{\tilde{u}}(x_I, x_R, \omega) \times e^{-(\gamma_1 x_R + \gamma_1 x_I)}$
$\tilde{a}$	$\frac{\gamma_2}{\gamma_1} TC_{\tilde{a}}(x_I, x_T, \omega) \times e^{\gamma_2 x_T - \gamma_1 x_I}$	$-RC_{\tilde{a}}(x_I, x_R, \omega) \times e^{-(\gamma_1 x_R + \gamma_1 x_I)}$

Table 6-8a Expressing frequency domain BCs in terms of TCs and RCs of the 6 quantities ($x_I, x_R \leq 0, x_T \geq 0$)

$\tilde{u}$	$\begin{cases} TC_{\tilde{u}}(x_I, x_T, \omega) \times e^{\gamma_2 x_T - \gamma_1 x_I} - RC_{\tilde{u}}(x_I, x_R, \omega) \times e^{-(\gamma_1 x_R + \gamma_1 x_I)} = 1 \\ \frac{\rho_2 S_2}{\gamma_2} \frac{\gamma_2}{\rho_1 S_1} \frac{\gamma_2}{\gamma_1} TC_{\tilde{u}}(x_I, x_T, \omega) \times e^{\gamma_2 x_T - \gamma_1 x_I} + RC_{\tilde{u}}(x_I, x_R, \omega) \times e^{-(\gamma_1 x_R + \gamma_1 x_I)} = 1 \end{cases}$
$\tilde{F}$	$\begin{cases} \frac{\rho_1 S_1}{\gamma_1} \frac{\gamma_2}{\rho_2 S_2} \frac{\gamma_2}{\gamma_1} TC_{\tilde{F}}(x_I, x_T, \omega) \times e^{\gamma_2 x_T - \gamma_1 x_I} + RC_{\tilde{F}}(x_I, x_R, \omega) \times e^{-(\gamma_1 x_R + \gamma_1 x_I)} = 1 \\ TC_{\tilde{F}}(x_I, x_T, \omega) \times e^{\gamma_2 x_T - \gamma_1 x_I} - RC_{\tilde{F}}(x_I, x_R, \omega) \times e^{-(\gamma_1 x_R + \gamma_1 x_I)} = 1 \end{cases}$
$\tilde{\sigma}$	$\begin{cases} \frac{\rho_1}{\gamma_1} \frac{\gamma_2}{\rho_2} \frac{\gamma_2}{\gamma_1} TC_{\tilde{\sigma}}(x_I, x_T, \omega) \times e^{\gamma_2 x_T - \gamma_1 x_I} + RC_{\tilde{\sigma}}(x_I, x_R, \omega) \times e^{-(\gamma_1 x_R + \gamma_1 x_I)} = 1 \\ \frac{S_2}{S_1} TC_{\tilde{\sigma}}(x_I, x_T, \omega) \times e^{\gamma_2 x_T - \gamma_1 x_I} - RC_{\tilde{\sigma}}(x_I, x_R, \omega) \times e^{-(\gamma_1 x_R + \gamma_1 x_I)} = 1 \end{cases}$
$\tilde{u}$	$\begin{cases} TC_{\tilde{u}}(x_I, x_T, \omega) \times e^{\gamma_2 x_T - \gamma_1 x_I} - RC_{\tilde{u}}(x_I, x_R, \omega) \times e^{-(\gamma_1 x_R + \gamma_1 x_I)} = 1 \\ \frac{\rho_2 S_2}{\gamma_2} \frac{\gamma_2}{\rho_1 S_1} \frac{\gamma_2}{\gamma_1} TC_{\tilde{u}}(x_I, x_T, \omega) \times e^{\gamma_2 x_T - \gamma_1 x_I} + RC_{\tilde{u}}(x_I, x_R, \omega) \times e^{-(\gamma_1 x_R + \gamma_1 x_I)} = 1 \end{cases}$
$\tilde{a}$	$\begin{cases} TC_{\tilde{a}}(x_I, x_T, \omega) \times e^{\gamma_2 x_T - \gamma_1 x_I} - RC_{\tilde{a}}(x_I, x_R, \omega) \times e^{-(\gamma_1 x_R + \gamma_1 x_I)} = 1 \\ \frac{\rho_2 S_2}{\gamma_2} \frac{\gamma_2}{\rho_1 S_1} \frac{\gamma_2}{\gamma_1} TC_{\tilde{a}}(x_I, x_T, \omega) \times e^{\gamma_2 x_T - \gamma_1 x_I} + RC_{\tilde{a}}(x_I, x_R, \omega) \times e^{-(\gamma_1 x_R + \gamma_1 x_I)} = 1 \end{cases}$
$\tilde{\varepsilon}$	$\begin{cases} \frac{\gamma_1}{\gamma_2} TC_{\tilde{\varepsilon}}(x_I, x_T, \omega) \times e^{\gamma_2 x_T - \gamma_1 x_I} + RC_{\tilde{\varepsilon}}(x_I, x_T, \omega) \times e^{-(\gamma_1 x_R + \gamma_1 x_I)} = 1 \\ \frac{\rho_2 S_2}{\gamma_2} \frac{\gamma_1}{\rho_1 S_1} \frac{\gamma_1}{\gamma_2} TC_{\tilde{\varepsilon}}(x_I, x_T, \omega) \times e^{\gamma_2 x_T - \gamma_1 x_I} - RC_{\tilde{\varepsilon}}(x_I, x_T, \omega) \times e^{-(\gamma_1 x_R + \gamma_1 x_I)} = 1 \end{cases}$

Table. 6-8b Expressing frequency domain BCs in terms of interface TCs and RCs

$\tilde{\ddot{u}}$	$TC_{\tilde{\ddot{u}}}(0,0,\omega) - RC_{\tilde{\ddot{u}}}(0,0,\omega) = 1, \quad \frac{\rho_2 S_2}{\rho_1 S_1}\frac{\gamma_1}{\gamma_2} TC_{\tilde{\ddot{u}}}(0,0,\omega) + RC_{\tilde{\ddot{u}}}(0,0,\omega) = 1$
$\tilde{F}$	$\frac{\rho_1 S_1}{\rho_2 S_2}\frac{\gamma_2}{\gamma_1} TC_{\tilde{F}}(0,0,\omega) + RC_{\tilde{F}}(0,0,\omega) = 1, \quad TC_{\tilde{F}}(0,0,\omega) - RC_{\tilde{F}}(0,0,\omega) = 1$
$\tilde{\sigma}$	$\frac{\rho_1}{\rho_2}\frac{\gamma_2}{\gamma_1} TC_{\tilde{\sigma}}(0,0,\omega) + RC_{\tilde{\sigma}}(0,0,\omega) = 1, \quad \frac{S_2}{S_1} TC_{\tilde{\sigma}}(0,0,\omega) - RC_{\tilde{\sigma}}(0,0,\omega) = 1$
$\tilde{u}$	$TC_{\tilde{u}}(0,0,\omega) - RC_{\tilde{u}}(0,0,\omega) = 1, \quad \frac{\rho_2 S_2}{\rho_1 S_1}\frac{\gamma_1}{\gamma_2} TC_{\tilde{u}}(0,0,\omega) + RC_{\tilde{u}}(0,0,\omega) = 1$
$\tilde{a}$	$TC_{\tilde{a}}(0,0,\omega) - RC_{\tilde{a}}(0,0,\omega) = 1, \quad \frac{\rho_2 S_2}{\rho_1 S_1}\frac{\gamma_1}{\gamma_2} TC_{\tilde{a}}(0,0,\omega) + RC_{\tilde{a}}(0,0,\omega) = 1$
$\tilde{\varepsilon}$	$\frac{\gamma_1}{\gamma_2} TC_{\tilde{\varepsilon}}(0,0,\omega) + RC_{\tilde{\varepsilon}}(0,0,\omega) = 1, \quad \frac{\rho_2 S_2}{\rho_1 S_1}\frac{\gamma_1^2}{\gamma_2^2} TC_{\tilde{\varepsilon}}(0,0,\omega) - RC_{\tilde{\varepsilon}}(0,0,\omega) = 1$

Comparing Table. 6-2 and Table. 6-8b, it is found that the rewritten equilibrium equations in time and frequency domain share the same forms, thus it is not surprising to see later (Table. 6-9a) that both the general expressions of the time and frequency domain TC and RC have the same form, either expressed in terms of (γ_1, γ_2) or (Z_1, Z_2).

Solving the equation pairs in Table. 6-8a leads to the solutions of $TC(x_I, x_T, \omega)$ and $RC(x_I, x_R, \omega)$ in Table. 6-9a while solving those in Table. 6-8b yields $TC(0,0,\omega)$ and $RC(0,0,\omega)$. The relations between $[TC(x_I, x_T, \omega), RC(x_I, x_R, \omega)]$ and $[TC(0,0,\omega), RC(0,0,\omega)]$ were obtained by making use of the wave propagation theory in a single rod (strain ratios as an example)

$$TC_{\tilde{\varepsilon}}(x_I, x_T, \omega) = \frac{\tilde{\varepsilon}_T(x_T,\omega)}{\tilde{\varepsilon}_I(x_I,\omega)} = \frac{\tilde{\varepsilon}_T(0,\omega)\times e^{-\gamma_2 x_T}}{\tilde{\varepsilon}_I(0,\omega)\times e^{-\gamma_1 x_I}} = TC_{\tilde{\varepsilon}}(0,0,\omega) \times \boldsymbol{e^{-(\gamma_2 x_T - \gamma_1 x_I)}} \tag{6.13a}$$

$$RC_{\tilde{\varepsilon}}(x_I, x_R, \omega) = \frac{\tilde{\varepsilon}_R(x_R,\omega)}{\tilde{\varepsilon}_I(x_I,\omega)} = \frac{\tilde{\varepsilon}_R(0,\omega)\times e^{\gamma_1 x_R}}{\tilde{\varepsilon}_I(0,\omega)\times e^{-\gamma_1 x_I}} = RC_{\tilde{\varepsilon}}(0,0,\omega) \times \boldsymbol{e^{\gamma_1 x_R + \gamma_1 x_I}} \tag{6.13b}$$

$$RT_{\tilde{\varepsilon}}(x_T, x_R, \omega) = \frac{\tilde{\varepsilon}_R(x_R,\omega)}{\tilde{\varepsilon}_T(x_T,\omega)} = \frac{\tilde{\varepsilon}_R(0,\omega)\times e^{\gamma_1 x_R}}{\tilde{\varepsilon}_T(0,\omega)\times e^{-\gamma_2 x_T}} = RT_{\tilde{\varepsilon}}(0,0,\omega) \times \boldsymbol{e^{\gamma_1 x_R + \gamma_2 x_T}} \tag{6.13c}$$

Also presented in Table. 6-9a are the extra reflection-to-transmission FT ratios (RTs) which might be of use as well. The material impedance Z and propagation coefficient γ can be linked to material modulus E^* via Eq. (6.8) and Eq. (2.27) respectively, which reveals the significance of the research into interface wave behaviour: it provides an alternative approach to test material impedance, and leads to obtaining material stiffness/modulus in either time or frequency domain.

Table 6-9a General frequency domain $TC(x_I, x_T, \omega)$, $RC(x_I, x_R, \omega)$ and $RT(x_T, x_R, \omega)$ expressions

	$TC = \frac{\tilde{T}}{\tilde{I}}(x_I \le 0, x_T \ge 0)$		$RC = \frac{\tilde{R}}{\tilde{I}}(x_I, x_R \le 0)$		$RT = \frac{RC}{TC} = \frac{\tilde{R}}{\tilde{T}}(x_R \le 0, x_T \ge 0)$	
	(γ_1, γ_2)	(Z_1, Z_2)	(γ_1, γ_2)	(Z_1, Z_2)	(γ_1, γ_2)	(Z_1, Z_2)
$\tilde{\varepsilon}$	$\frac{2\frac{\rho_1 S_1}{\gamma_1}}{\frac{\rho_1 S_1}{\gamma_1}+\frac{\rho_2 S_2}{\gamma_2}} \times \frac{\gamma_2}{\gamma_1} \times \frac{e^{-\gamma_2 x_T}}{e^{-\gamma_1 x_I}}$	$\frac{2Z_1}{Z_1+Z_2} \times \frac{\gamma_2}{\gamma_1} \times \frac{e^{-\gamma_2 x_T}}{e^{-\gamma_1 x_I}} = \frac{2Z_1^2}{(Z_1+Z_2)Z_2} \times \frac{\rho_2 S_2}{\rho_1 S_1} \times \frac{e^{-\gamma_2 x_T}}{e^{-\gamma_1 x_I}}$	$\frac{\frac{\rho_2 S_2}{\gamma_2}-\frac{\rho_1 S_1}{\gamma_1}}{\frac{\rho_2 S_2}{\gamma_2}+\frac{\rho_1 S_1}{\gamma_1}} \times \frac{e^{\gamma_1 x_R}}{e^{-\gamma_1 x_I}}$	$\frac{Z_2-Z_1}{Z_2+Z_1} \times \frac{e^{\gamma_1 x_R}}{e^{-\gamma_1 x_I}}$	$\frac{\frac{\rho_2 S_2}{\gamma_2}-\frac{\rho_1 S_1}{\gamma_1}}{2\frac{\rho_1 S_1}{\gamma_1}} \times \frac{\gamma_1}{\gamma_2} \times \frac{e^{\gamma_1 x_R}}{e^{-\gamma_2 x_T}}$	$\frac{Z_2-Z_1}{2Z_1} \times \frac{\gamma_1}{\gamma_2} \times \frac{e^{\gamma_1 x_R}}{e^{-\gamma_2 x_T}} = \frac{(Z_2-Z_1)Z_2}{2Z_1^2} \times \frac{\rho_1 S_1}{\rho_2 S_2} \times \frac{e^{\gamma_1 x_R}}{e^{-\gamma_2 x_T}}$
$\tilde{F}$	$\frac{2\frac{\rho_2 S_2}{\gamma_2}}{\frac{\rho_2 S_2}{\gamma_2}+\frac{\rho_1 S_1}{\gamma_1}} \times \frac{e^{-\gamma_2 x_T}}{e^{-\gamma_1 x_I}}$	$\frac{2Z_2}{Z_1+Z_2} \times \frac{e^{-\gamma_2 x_T}}{e^{-\gamma_1 x_I}}$	$\frac{\frac{\rho_2 S_2}{\gamma_2}-\frac{\rho_1 S_1}{\gamma_1}}{\frac{\rho_2 S_2}{\gamma_2}+\frac{\rho_1 S_1}{\gamma_1}} \times \frac{e^{\gamma_1 x_R}}{e^{-\gamma_1 x_I}}$	$\frac{Z_2-Z_1}{Z_2+Z_1} \times \frac{e^{\gamma_1 x_R}}{e^{-\gamma_1 x_I}}$	$\frac{\frac{\rho_2 S_2}{\gamma_2}-\frac{\rho_1 S_1}{\gamma_1}}{2\frac{\rho_2 S_2}{\gamma_2}} \times \frac{e^{\gamma_1 x_R}}{e^{-\gamma_2 x_T}}$	$\frac{Z_2-Z_1}{2Z_2} \times \frac{e^{\gamma_1 x_R}}{e^{-\gamma_2 x_T}}$
$\tilde{\sigma}$	$\frac{2\frac{\rho_2 S_2}{\gamma_2}}{\frac{\rho_1 S_1}{\gamma_1}+\frac{\rho_2 S_2}{\gamma_2}} \times \frac{S_1}{S_2} \times \frac{e^{-\gamma_2 x_T}}{e^{-\gamma_1 x_I}}$	$\frac{2Z_2}{Z_1+Z_2} \times \frac{S_1}{S_2} \times \frac{e^{-\gamma_2 x_T}}{e^{-\gamma_1 x_I}}$	$\frac{\frac{\rho_2 S_2}{\gamma_2}-\frac{\rho_1 S_1}{\gamma_1}}{\frac{\rho_2 S_2}{\gamma_2}+\frac{\rho_1 S_1}{\gamma_1}} \times \frac{e^{\gamma_1 x_R}}{e^{-\gamma_1 x_I}}$	$\frac{Z_2-Z_1}{Z_2+Z_1} \times \frac{e^{\gamma_1 x_R}}{e^{-\gamma_1 x_I}}$	$\frac{\frac{\rho_2 S_2}{\gamma_2}-\frac{\rho_1 S_1}{\gamma_1}}{2\frac{\rho_2 S_2}{\gamma_2}} \times \frac{S_2}{S_1} \times \frac{e^{\gamma_1 x_R}}{e^{-\gamma_2 x_T}}$	$\frac{Z_2-Z_1}{2Z_2} \times \frac{S_2}{S_1} \times \frac{e^{\gamma_1 x_R}}{e^{-\gamma_2 x_T}}$
$\tilde{u}$	$\frac{2\frac{\rho_1 S_1}{\gamma_1}}{\frac{\rho_1 S_1}{\gamma_1}+\frac{\rho_2 S_2}{\gamma_2}} \times \frac{e^{-\gamma_2 x_T}}{e^{-\gamma_1 x_I}}$	$\frac{2Z_1}{Z_1+Z_2} \times \frac{e^{-\gamma_2 x_T}}{e^{-\gamma_1 x_I}}$	$\frac{\frac{\rho_1 S_1}{\gamma_1}-\frac{\rho_2 S_2}{\gamma_2}}{\frac{\rho_1 S_1}{\gamma_1}+\frac{\rho_2 S_2}{\gamma_2}} \times \frac{e^{\gamma_1 x_R}}{e^{-\gamma_1 x_I}}$	$\frac{Z_1-Z_2}{Z_1+Z_2} \times \frac{e^{\gamma_1 x_R}}{e^{-\gamma_1 x_I}}$	$\frac{\frac{\rho_1 S_1}{\gamma_1}-\frac{\rho_2 S_2}{\gamma_2}}{2\frac{\rho_1 S_1}{\gamma_1}} \times \frac{e^{\gamma_1 x_R}}{e^{-\gamma_2 x_T}}$	$\frac{Z_1-Z_2}{2Z_1} \times \frac{e^{\gamma_1 x_R}}{e^{-\gamma_2 x_T}}$
$\tilde{u}$	$\frac{2\frac{\rho_1 S_1}{\gamma_1}}{\frac{\rho_1 S_1}{\gamma_1}+\frac{\rho_2 S_2}{\gamma_2}} \times \frac{e^{-\gamma_2 x_T}}{e^{-\gamma_1 x_I}}$	$\frac{2Z_1}{Z_1+Z_2} \times \frac{e^{-\gamma_2 x_T}}{e^{-\gamma_1 x_I}}$	$\frac{\frac{\rho_1 S_1}{\gamma_1}-\frac{\rho_2 S_2}{\gamma_2}}{\frac{\rho_1 S_1}{\gamma_1}+\frac{\rho_2 S_2}{\gamma_2}} \times \frac{e^{\gamma_1 x_R}}{e^{-\gamma_1 x_I}}$	$\frac{Z_1-Z_2}{Z_1+Z_2} \times \frac{e^{\gamma_1 x_R}}{e^{-\gamma_1 x_I}}$	$\frac{\frac{\rho_1 S_1}{\gamma_1}-\frac{\rho_2 S_2}{\gamma_2}}{2\frac{\rho_1 S_1}{\gamma_1}} \times \frac{e^{\gamma_1 x_R}}{e^{-\gamma_2 x_T}}$	$\frac{Z_1-Z_2}{2Z_1} \times \frac{e^{\gamma_1 x_R}}{e^{-\gamma_2 x_T}}$
$\tilde{a}$	$\frac{2\frac{\rho_1 S_1}{\gamma_1}}{\frac{\rho_1 S_1}{\gamma_1}+\frac{\rho_2 S_2}{\gamma_2}} \times \frac{e^{-\gamma_2 x_T}}{e^{-\gamma_1 x_I}}$	$\frac{2Z_1}{Z_1+Z_2} \times \frac{e^{-\gamma_2 x_T}}{e^{-\gamma_1 x_I}}$	$\frac{\frac{\rho_1 S_1}{\gamma_1}-\frac{\rho_2 S_2}{\gamma_2}}{\frac{\rho_1 S_1}{\gamma_1}+\frac{\rho_2 S_2}{\gamma_2}} \times \frac{e^{\gamma_1 x_R}}{e^{-\gamma_1 x_I}}$	$\frac{Z_1-Z_2}{Z_1+Z_2} \times \frac{e^{\gamma_1 x_R}}{e^{-\gamma_1 x_I}}$	$\frac{\frac{\rho_1 S_1}{\gamma_1}-\frac{\rho_2 S_2}{\gamma_2}}{2\frac{\rho_1 S_1}{\gamma_1}} \times \frac{e^{\gamma_1 x_R}}{e^{-\gamma_2 x_T}}$	$\frac{Z_1-Z_2}{2Z_1} \times \frac{e^{\gamma_1 x_R}}{e^{-\gamma_2 x_T}}$

It is again seen from Table. 6-9a that, the characteristic impedances Z(ω) and the propagation coefficient γ(ω) of the incident and transmission rods play a key role in determining wave behaviour at interface: the relative importance of these 2 quantities of the incident and transmission rods determines the how much the incident wave will be transmitted and reflected as the incident wave arrives at the interface. It is worth looking at the wave behaviour when $Z_2 \gg Z_1$,

$$RC_{\tilde{\varepsilon}}(0,0,\omega) = RC_{\tilde{F}}(0,0,\omega) = RC_{\tilde{\sigma}}(0,0,\omega) = \frac{Z_2 - Z_1}{Z_2 + Z_1} = \frac{1-\frac{Z_1}{Z_2}}{1+\frac{Z_1}{Z_2}} \approx 1$$

$$RC_{\tilde{u}}(0,0,\omega) = RC_{\tilde{u}}(0,0,\omega) = RC_{\tilde{a}}(0,0,\omega) = \frac{Z_1 - Z_2}{Z_1 + Z_2} = \frac{\frac{Z_1}{Z_2}-1}{\frac{Z_1}{Z_2}+1} \approx -1$$

this indicates that when the impedance of transmission rod is much larger than that of the incident rod, part of the incident wave will be reflected with the same sign: the contact interface serves like a fixed end for the incident rod. When $Z_1 \gg Z_2$, the reflected strain, force and stress invert sign while the particle velocity, displacement and acceleration do not: the contact interface serves as a free end. Having the TC and RC expressions prepared in Table. 6-8a and Table. 6-9a, the next step is to derive material properties using these 2 ratios, which can be calculated from either experiments or simulations. As addressed in time domain analysis (elastic material-elastic material), the 2 equations in each equation pair, *i.e.* $TC = TC\ (E_I^*, E_T^*)$ and $RC = RC\ (E_I^*, E_T^*)$, are actually not independent and thus they are not adequate to work out E_I^* and E_T^* at the same time. As a result, one can only expect to obtain the material properties of 1 rod providing the properties of the other rod are known. Due to the long length nature of the BC equations as well as the limit of thesis page number, in following analysis, only strain representations were presented; for detailed derivation process and other 5 quantities, readers are advised to refer to the full *web version*. Combining Table. 6-8a and Table. 6-9a yields an equation system which contain TC and RC

$$\begin{cases} \frac{\gamma_1}{\gamma_2} TC_{\tilde{\varepsilon}}(x_I, x_T, \omega) \times e^{\gamma_2 x_T - \gamma_1 x_I} + RC_{\tilde{\varepsilon}}(x_I, x_T, \omega) \times e^{-(\gamma_1 x_R + \gamma_1 x_I)} = 1 \text{ ①} \\ \frac{\rho_2 S_2}{\rho_1 S_1} \frac{\gamma_1}{\gamma_2} TC_{\tilde{\varepsilon}}(x_I, x_T, \omega) \times e^{\gamma_2 x_T - \gamma_1 x_I} - RC_{\tilde{\varepsilon}}(x_I, x_T, \omega) \times e^{-(\gamma_1 x_R + \gamma_1 x_I)} = 1 \text{ ②} \end{cases}$$

$$\begin{cases} TC_{\tilde{\varepsilon}}(x_I, x_T, \omega) = \dfrac{2\dfrac{\rho_1 S_1}{\gamma_1}}{\dfrac{\rho_1 S_1}{\gamma_1} + \dfrac{\rho_2 S_2}{\gamma_2}} \times \dfrac{\gamma_2}{\gamma_1} \times \dfrac{e^{-\gamma_2 x_T}}{e^{-\gamma_1 x_I}} \ ③ \\ RC_{\tilde{\varepsilon}}(x_I, x_T, \omega) = \dfrac{\dfrac{\rho_2 S_2}{\gamma_2} - \dfrac{\rho_1 S_1}{\gamma_1}}{\dfrac{\rho_2 S_2}{\gamma_2} + \dfrac{\rho_1 S_1}{\gamma_1}} \times \dfrac{e^{\gamma_1 x_R}}{e^{-\gamma_1 x_I}} \ ④ \\ RT_{\tilde{\varepsilon}}(x_I, x_T, \omega) = \dfrac{\dfrac{\rho_2 S_2}{\gamma_2} - \dfrac{\rho_1 S_1}{\gamma_1}}{2\dfrac{\rho_1 S_1}{\gamma_1}} \dfrac{\gamma_1}{\gamma_2} \times \dfrac{e^{\gamma_1 x_R}}{e^{-\gamma_2 x_T}} \ ⑤ \end{cases}$$

Simplifying the equations yields Table. 6-10a.

Table. 6-10a Expressing $(\boldsymbol{E_1}, \boldsymbol{E_2})$ & $(\boldsymbol{\gamma_1}, \boldsymbol{\gamma_2})$ as functions of TC_ε & RC_ε

	$x_I = x_R = x_T = 0$	$x_I, x_R \le 0, x_T \ge 0$
$\tilde{\varepsilon}$	① $\sqrt{\frac{E_2}{E_1}} = \frac{1-RC_{\tilde{\varepsilon}}(0,0,\omega)}{TC_{\tilde{\varepsilon}}(0,0,\omega)} \sqrt{\frac{\rho_2}{\rho_1}}$	① $\frac{\gamma_2}{\gamma_1} = \frac{TC_{\tilde{\varepsilon}}(x_I,x_T,\omega)\times e^{\gamma_2 x_T - \gamma_1 x_I}}{1-RC_{\tilde{\varepsilon}}(x_I,x_R,\omega)\times e^{-(\gamma_1 x_R + \gamma_1 x_I)}}$
	② $\sqrt{\frac{E_2}{E_1}} = \sqrt{\frac{1+RC_{\tilde{\varepsilon}}(0,0,\omega)}{TC_{\tilde{\varepsilon}}(0,0,\omega)}} \sqrt{\frac{S_1}{S_2}}$	② $\frac{\gamma_2^2}{\gamma_1^2} = \frac{S_2}{S_1}\frac{\rho_2}{\rho_1}\frac{TC_{\tilde{\varepsilon}}(x_I,x_T,\omega)\times e^{\gamma_2 x_T - \gamma_1 x_I}}{1+RC_{\tilde{\varepsilon}}(x_I,x_R,\omega)\times e^{-(\gamma_1 x_R + \gamma_1 x_I)}}$
	③ $\sqrt{\frac{E_2}{E_1}} = \frac{-1+\sqrt{1+8\frac{S_2\rho_2}{S_1\rho_1}\frac{1}{TC_{\tilde{\varepsilon}}(0,0,\omega)}}}{2} \frac{S_1}{S_2}\sqrt{\frac{\rho_1}{\rho_2}}$	③ $\frac{\gamma_1}{\gamma_2} \times (\frac{S_2}{S_1}\frac{\rho_2}{\rho_1}\frac{\gamma_1}{\gamma_2} + 1) \times TC_{\tilde{\varepsilon}}(x_I, x_T, \omega) \times e^{\gamma_2 x_T - \gamma_1 x_I} = 2$
	④ $\sqrt{\frac{E_2}{E_1}} = \frac{1+RC_{\tilde{\varepsilon}}(0,0,\omega)}{1-RC_{\tilde{\varepsilon}}(0,0,\omega)} \frac{S_1}{S_2}\sqrt{\frac{\rho_1}{\rho_2}}$	④ $\frac{\gamma_2}{\gamma_1} = \frac{S_2}{S_1}\frac{\rho_2}{\rho_1}\frac{1-RC_{\tilde{\varepsilon}}(x_I,x_R,\omega)\times e^{-(\gamma_1 x_R + \gamma_1 x_I)}}{1+RC_{\tilde{\varepsilon}}(x_I,x_R,\omega)\times e^{-(\gamma_1 x_R + \gamma_1 x_I)}}$ Or directly: $\sqrt{\frac{E_2}{E_1}} = \frac{1+RC_{\tilde{\varepsilon}}(x_I,x_R,\omega)\times e^{-(\gamma_1 x_R + \gamma_1 x_I)}}{1-RC_{\tilde{\varepsilon}}(x_I,x_R,\omega)\times e^{-(\gamma_1 x_R + \gamma_1 x_I)}} \frac{S_1}{S_2}\sqrt{\frac{\rho_1}{\rho_2}}$
	⑤ $\sqrt{\frac{E_2}{E_1}} = \frac{\sqrt{\frac{\rho_1}{\rho_2}} + \sqrt{\frac{\rho_1}{\rho_2} + 8RT_{\tilde{\varepsilon}}(0,0,\omega)\frac{S_2}{S_1}}}{2\frac{S_2}{S_1}}$	⑤ $\frac{\rho_2 S_2}{\rho_1 S_1}(\frac{\gamma_1}{\gamma_2})^2 - \frac{\gamma_1}{\gamma_2} = 2RT_{\tilde{\varepsilon}}(x_T, x_R, \omega) \times e^{-\gamma_1 x_R - \gamma_2 x_T}$

Table. 6-10a gives the relations between the material property pair (E_1, E_2) & (γ_1, γ_2). Theoretically, knowing $\rho_1, \rho_2, S_1, S_2, TC, RC$ and any one of the material property pairs, we are then able to obtain the mechanical properties of the other rod. For example, if (γ_1, E_1) are known, γ_2 can be solved by using the equations in Table. 6-10a, and then the corresponding modulus E_2 can be calculated using the 1D relation $E^*(\omega) = \frac{-\rho\omega^2}{\gamma^2(\omega)}$ (Eq. (2.27)). Here Eq. ① was based on the velocity equilibrium equation and Eq. ② derived from the force continuity equation. Eq. ③ and Eq. ④ were obtained by eliminating one of these ratios from Eq. ① and Eq. ②. The 4 equations involve different degrees of complexity but they are expected to give the same answer for (E_1, E_2) & (γ_1, γ_2). Further, the 4 equations can be classified as 3 types: containing $TC(x_I, x_T, \omega)$ or $RC(x_I, x_R, \omega)$, or both. This provides flexibility on what can be conveniently measured from experiments or simulations.

For the first instance, verification can be done via analytical approach. For example, assuming a simple elastic-elastic case, the 2 expressions of stress and strain coefficients can be verified. For both rods made of elastic materials, we have

$$\gamma_1 = i\kappa_1 = i\frac{\omega}{c_1} = i\omega\sqrt{\frac{\rho_1}{E_1}},\ \gamma_2 = i\kappa_2 = i\omega\sqrt{\frac{\rho_2}{E_2}}$$

and Eq. (2.27) gives

$$\rho_1 = -\frac{E_1\gamma_1^2}{\omega^2}, \rho_2 = -\frac{E_2\gamma_2^2}{\omega^2}$$

on the other hand, for elastic materials we also have $\tilde{\sigma} = E\tilde{\varepsilon}$, therefore

$$TC_{\tilde{\sigma}} = \frac{E_2\tilde{\varepsilon}_T}{E_1\tilde{\varepsilon}_I} = \frac{E_2}{E_1}TC_{\tilde{\varepsilon}}, RC_{\tilde{\sigma}} = \frac{E_1\tilde{\varepsilon}_R}{E_1\tilde{\varepsilon}_I} = RC_{\tilde{\varepsilon}}\ .$$

Substituting the above expressions of ρ_1, ρ_2, $TC_{\tilde{\sigma}}$ and $RC_{\tilde{\sigma}}$ into the stress equations, we can arrive at the strain equations. Use Eq. ① as an example

$$\gamma_2 \times e^{\gamma_2 x_T} = \frac{-\frac{E_2\gamma_2^2}{\omega^2}}{-\frac{E_1\gamma_1^2}{\omega^2}} \frac{1 - RC_{\tilde{\varepsilon}}(x_I, x_R, \omega) \times e^{-(\gamma_1 x_R + \gamma_1 x_I)}}{\frac{E_2}{E_1}TC_{\tilde{\varepsilon}}(x_I, x_T, \omega)} \gamma_1 \times e^{\gamma_1 x_I}\ .$$

which further gives

$$\gamma_2 \times e^{\gamma_1 x_I - \gamma_2 x_T} = \frac{\gamma_1 \times TC_{\tilde{\varepsilon}}(x_I, x_T, \omega)}{1 - RC_{\tilde{\varepsilon}}(x_I, x_R, \omega) \times e^{-(\gamma_1 x_R + \gamma_1 x_I)}}$$

which is exactly the same as the strain equation Eq. ①.

The validity of these equations was double checked via simulations in the next chapter; after that they were applied to real interface tests in chapter 10. However, note that the relations in Table. 6-10a don't count for 3D geometry effects such as the inertia-induced dispersion effect during wave propagation, thus they can only be applied for 1D cases. The 3D correction method will be introduced later in signal processing.

In this chapter, brand-new theories for interface analysis are provided. Defined in both time and frequency domain, the coefficients (*i.e.* TC, RC and RT) sit in the centre of discussions, they can be calculated from measured signals, and used to resolve for material properties. In time domain, emphasis has been put on validating the coefficient expressions, while in frequency domain we built the theory of using the coefficients to recover the unknown material properties. This was used to analyse simulation and experimental signals in the following chapters.

Chapter 7: Simulations of mechanical wave behaviours at two-medium interfaces

In the following two chapters, simulations are used to verify the interface theories, show the data processing procedure and investigate critical issues such as the necessity of dispersion correction, the numerical complexity of the established equations and the effect of noise and misalignments. In both the simulations, the interface problem was treated in two steps: firstly, by considering wave behaviour at the interface of two media in a single rod in which two materials were defined, and a 'perfect' interface was generated; secondly, by simulating two rods of the same and different materials. A similar procedure was followed in the experiments, but the single rod was necessarily also of a single material. The first of these cases is an ideal case to examine the validity of the interface theories, which were built on the assumption of a 'perfect' interface, to standardise the numerical data processing method and to study the effect of noise. The second case tests these theories and the data processing method, and to investigate the effect of misalignments. Hence, the two form an integrated and complete frame for the interface research.

7.1 Simulation scheme

The interface theories were built on the assumption of continuous force and velocity at contact interface. In reality, if any imperfection appears unexpected reflections can result due to incomplete contact and the behaviour will not match the theoretical response. In practice, such imperfections can be faces that are not flat or parallel, or experimental misalignments induced by factors such as uneven support; these will always exist to some extent. Even in an ideally aligned two-rod system, due to Poisson's effect, a longitudinal compression wave is normally accompanied by radial expansion, which will cause a discontinuity in area if the two materials have different Poisson ratios. Another source of undesired reflection is the complex nature of a dilatation wave. During dilatation/longitudinal wave propagation, the medium is subjected to a combination of compression and shear instead of simple compression [39]. Imagine the region around the wave front of a compression wave, there is a gradual lateral deformation gradient between the compressed region and the rest of the material, which means both compression and shear stresses are present. The shear

stress, however, is not passed to the transmission rod if there is no friction across the 'perfect' contact faces. As a result, the shear waves will be reflected even when the two rods have the same characteristic impedance and Poisson's ratio.

To remove the effects of interface imperfections, a two-medium system was first designed to simulate an ideal interface before moving to the two-rod system. The two-medium system, which was accommodated in a single rod, simulates a 'perfect' interface between any 2 monitoring points, and particularly it facilitates the study of noise: it excludes the noise induced by imperfections, and thus allows artificial noise to be numerically introduced.

In total four cases were simulated, and they represent three classes of interfaces: metal-metal (Ti-Ti, Ti-Mg), metal-plastic (Ti-PMMA), plastic-metal (PMMA-Mg). Bar material constants are shown in Table. 7-1. The three bar materials were selected such that they possess the potential to test low impedance materials (*e.g.* rubber) as their impedances are relatively small. Other bar material, *e.g.* aluminium, Nylon, Delrin, and PVC, can be investigated in a similar way if needed.

Table. 7-1 Material constants adopted in 'perfect' interface simulations

Material	ρ (kg/m^3)	$E\ (GPa)$	$c\ (m/s)$	ν	$Z = \rho\sqrt{EA}$ (kg $*$ N$^{\frac{1}{2}}$/ m^3, $d = 13\ mm$)
Rubber (reference)	1200	0.003	50	0.45-0.5	2.39×10^4
Ti	4500	110	4944	0.32	17.2×10^6
Mg	1740 (20 °C)	45	5085	0.29	4.25×10^6
PMMA	1180	5.37 (Instantaneous)	2133	0.38	0.996×10^6

7.2 General model descriptions

The commercial FE software ABAQUS was employed to implement simulations. One part (a rod 1.5 m long and 13 mm in diameter) was defined and partitioned into two segments, one acting as an incident rod 1 m long and the other as a transmission rod 0.5 m long. Material properties (density, Young's modulus and Poisson's ratio) were assigned separately to these segments. As the two segments were assembled as a whole, no contact information has been defined at interface, but implicitly the force and displacement are continuous.

To avoid extra noise, no separate impactor was used; instead the impact loading process was modelled using an acceleration input. A sinusoidal profile was used, to give a velocity profile

representative of that measured in previous experiments using the Laser Doppler Vibrometer (LDV) (Fig. 4-13 and Fig. 6-3 for example). A one-period ($50\,\mu s$) sine acceleration pulse $a(t) = A\omega\sin(\omega t)$, with $A = 0.25$ and $\omega = 2\pi \times 20000\,rad/s$, was applied to the free end of the incident segment (the impact end of the rod), this results in the velocity profile $v(t) = A - Acos(\omega t)$. The acceleration was distributed uniformly across the impact cross-section and defined in the boundary conditions (BCs). The input acceleration, and its resulting velocity profile, were shown in Fig. 7-1.

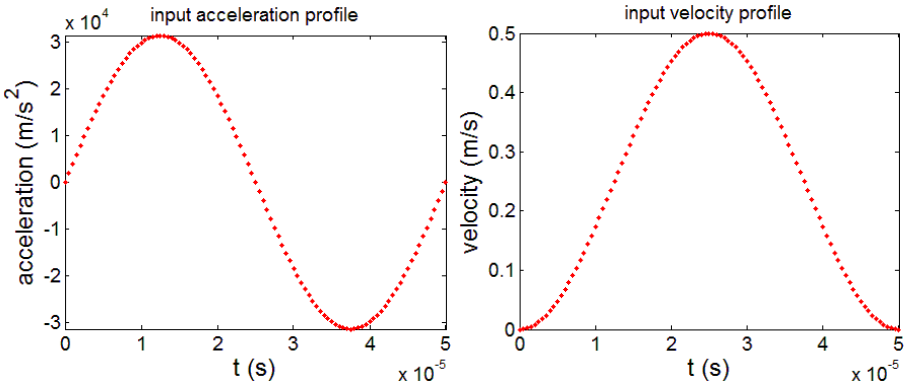


Figure. 7-1 Input acceleration and resulting velocity profiles

Two main steps were defined in the simulation: a loading step in which the acceleration is applied, lasting the same duration ($50\,\mu s$) as the input wave; and a ringing step which allows free wave propagation in the rod after the impact event. In both steps the bulk viscosity parameters, which might introduce artificial viscosity, were set to be zero. Other than the acceleration profile, no extra DOF constraints (*e.g.* rotation) were defined. The sampling rate at which output date were produced was 1 MHz (with corresponding sampling interval 1 μs).

To achieve symmetrical meshing on the cross-section, each segment was further partitioned into 4 sectors using a crisscross (Fig. 7-2). Linear hexahedral element of type C3D8R (reduced first-order 3-dimensional solid element with 8 nodes), with an element size of around4 1 mm were used, producing in total 180 elements on each section. This generates 180000 elements and 201201 nodes in the incident segment and 90000 elements and 100701 nodes in transmission. Note that the reduced element type can help save simulation time, but the results are most accurate at the integration point (for C3D8R in the middle of the element), and in later analysis all element-based data were extracted at integration points.

When analysing the signals, the origin x = 0 was set at the interface, with x increases along the transmission segment: thus $-1000\,mm \leq x_I = x_R = x_{IR} \leq 0, 0 \leq x_T \leq +500$ mm.

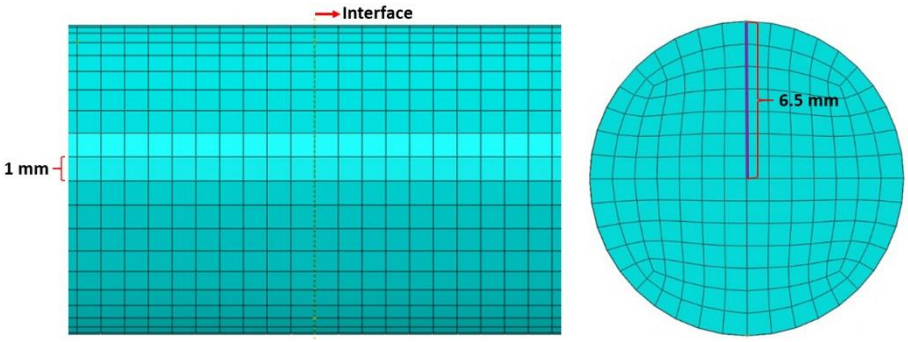


Figure. 7-2 1 Rod 2-medium Mesh scheme

7.3 Data processing procedure

The data processing routine was similar to that used in single rod analysis, *i.e.* de-noising, pulse selection, zero padding, FFT, equation solving. Specifically, the data were processed in the following steps: the raw signals were firstly de-noised using the wavelet package-based Matlab function 'wden' which keeps the original phase information but removes noise. The de-noised signals were then subjected to a zero-amplitude adjustment during which the whole signal was shifted vertically by making the baseline to be zero before the first pulse arrives; then the first 3 non-overlapped pulses were selected manually, following which a zero-padding process was conducted, so up to now, all the 3 signals have the same recording length, and each signal contains only a single pulse.

The next stage is transforming the time domain signals into the frequency domain. Unlike single rod impact signal processing, in which a centering process that aims to maximize all frequency magnitudes was performed, when dealing with interface data, no centering was conducted in order to retain the raw signal phase information. Fast Fourier Transform (FFT) was performed on the three pulses selected, and then the two frequency domain ratios, *i.e.* TC and RC, were obtained. Knowing the material properties of either rod in each contact pair, the properties of the other rod can be resolved using the equations in Table 6-10a. For verification purpose, three different comparisons between the results from signal processing and those from the prerequisite knowledge in the model definition were made: Fourier transforms, $TC_{\tilde{\varepsilon}}$ and $RC_{\tilde{\varepsilon}}$, and material properties (propagation

coefficient and modulus). In each case, these were resolved for both rods to addresses the capacity of using the interface theories to figure out material properties for either rod in a contact pair.

In this process, several issues were investigated:

(a) Pulse selection (truncation effect). Similar to single rod data processing, truncation effect can be a problem in interface studies. Welch investigated the effects of noise and truncation when identifying the complex modulus of a viscoelastic specimen using the RT coefficient measured in a SHPB setup with 2 aluminium rods, and they indicated that oscillations are induced by a truncation of the time domain signal [52]: a discontinuity in time domain results in oscillations throughout the frequency data and the oscillation intensity depends on the degree of truncation. Truncation also causes a loss of low frequency data even when the removed signal has small amplitude. The oscillations caused by truncation can be reduced by averaging results obtained using different truncation length [52]. Mousavi *et al.* [55] observed the oscillation phenomenon testing PP using an aluminium rod SHPB, the oscillations in their modulus results are induced by the truncation of the time domain signals which possess overlapping. They proposed a method for effective truncation correction, but this can only be applied to SHPB signals. They also suggested that, the truncation errors can be reduced by using longer bars or multi-point strain measurement for separation of waves.

(b) Geometric dispersion. Two approaches to correct the dispersion effect were detailed later.

(c) Numerical equation solving. Different levels of mathematical complexity, and sensitivity to noise, might be involved when solving for γ_1 and γ_2 using the equations in Table 6-10.

(d) Noise study. Two-medium studies avoid the effect of interface imperfections; different levels of artificial noises can then be introduced.

(e) Inaccuracy in distance. Sensitivity of the interface analysis method to errors in distance (x_I, x_T) was analysed in the Ti-Ti case.

(f) Comparison with single rod technique. For the Ti-Ti case, signals can also be processed using the single rod analysis method, the results were compared to those by the interface method.

This section will specifically look at (b) and (c), whilst (d), (e) and (f) were included in the Ti-Ti case.

7.3.1 Dispersion correction of interface signals

As indicated in Chapter 7, the interface theories (Table 6-10) were developed based on the 1D assumption. However, wave propagation in rods can never be perfectly 1-dimensional because finite lateral wave movement always exists. Therefore, in some non-ideal cases, *e.g.* when lateral rod size becomes comparable to the longitudinal wave length [18, 39, 56], it is necessary to correct geometric effects to yield an proper 1D wave propagation (see also 3.3.3.7 Correction of geometric dispersion). The main source of 3D effects is radial inertia, which induces multiple deformation modes of the cross-section during wave propagation [27, 34]. Even in purely elastic materials, dispersion occurs once the wavelength becomes less than 10 times the lateral dimension of the waveguide [18, 39, 56]. High frequencies propagate more slowly, which leads to high frequency oscillations (Pocchammer-Chree oscillations) in the wave profile. A detailed description of how these 3D effects may be corrected has been presented in '3.3.3.7 correction of geometric dispersion', here only the conclusions were presented.

When processing experimental or simulation data, there are two approaches to cancel the dispersion effect: either remove the 3D effects from the raw signals, or revise the interface theories to include 3D effects. The former is termed the 'pre-cancellation method' here, and the later one was called the 'revised BCs method'. For the 'pre-cancellation method', a dispersive wave speed profile, based on Love's theory [27], was employed to correct the phase errors induced by 3D effects in the frequency domain, the resulting 1D signals were then substituted into the equations in Table. 6-10 to yield the 'intrinsic' propagation coefficient, and finally the material modulus derived from the propagation coefficient using the 1D propagation coefficient-modulus relation in Eq. (2.27). In the 'revised BCs' method, the inertia effect was included in a revised expression of Newton's Second Law using the 'effective density' method (which gives the same dispersive wave speed profile as Love's theory as discussed in Chapter 3); force components obtained were then substituted into the BCs equation (Eq. (2.15b)) to yield new expressions of TC and RC, from which the 3D propagation coefficient can be obtained, and the intrinsic modulus can be obtained by using an updated 3D propagation coefficient-modulus relation Eq. (3.14a). In the research reported here, the 'pre-cancellation method' was adopted when processing both simulation and experimental data.

7.3.1.1 The pre-cancellation method

Based on Love's theory [27, 36], or equivalently the 'effective density' method by Aleyaasin [34], the dispersive wave speed profile in Eq. (3.16) or Eq. (3.17) were employed. The dispersive phase velocity tends towards the classical value $c_0 = \sqrt{\frac{E}{\rho}}$ at low frequencies [56]; it decreases as frequency increases, and the Rayleigh wave velocity (Eq. (3.18)) was used as the limiting velocity for high frequencies. Typical dispersive wave speed profiles have been shown in Fig. 3-15, the material constants used to generate these profiles were listed in Table. 7-1. Diameters used are all 6.5 mm.similar to the single rod dispersion correction, the dispersion effect was cancelled by multiplying a unity amplitude exponential term $e^{-i\omega L\left[\frac{1}{c_0}-\frac{1}{c(\omega)}\right]}$, which just corrects the dispersion-induced phase change [56], in the frequency domain owing to a propagation through distance *L*. The first implication of this, is that if the signals are measured at the interface, dispersion has no effect on the calculated ratios, since all the waves have travelled the same distance. However, in to the more practical case in which the three waves are monitored at (x_I, x_R, x_T), the measured 3D waves can be converted to 1D waves as follows:

$$\tilde{\varepsilon}_I^{1D}(x_I,\omega) = \tilde{\varepsilon}_I^{3D}(x_I,\omega) \times e^{-i\omega(L_I-|x_I|)[\frac{1}{c_{01}}-\frac{1}{c_1(\omega)}]}$$

$$\tilde{\varepsilon}_T^{1D}(x_T,\omega) = \tilde{\varepsilon}_T^{3D}(x_T,\omega) \times e^{-i\omega L_I[\frac{1}{c_{01}}-\frac{1}{c_1(\omega)}]} \times e^{-i\omega|x_T|[\frac{1}{c_{02}}-\frac{1}{c_2(\omega)}]}$$

$$\tilde{\varepsilon}_R^{1D}(x_R,\omega) = \tilde{\varepsilon}_R^{3D}(x_R,\omega) \times e^{-i\omega(L_I+|x_R|)[\frac{1}{c_{01}}-\frac{1}{c_1(\omega)}]}$$

therefore

$$TC_{\tilde{\varepsilon}}^{1D}(x_I,x_T,\omega) = TC_{\tilde{\varepsilon}}^{3D}(x_I,x_T,\omega) \times e^{-i\omega|x_T|[\frac{1}{c_{02}}-\frac{1}{c_2(\omega)}]} \times e^{-i\omega|x_I|[\frac{1}{c_{01}}-\frac{1}{c_1(\omega)}]} \quad (7.1a)$$

$$RC_{\tilde{\varepsilon}}^{1D}(x_I,x_R,\omega) = RC_{\tilde{\varepsilon}}^{3D}(x_I,x_R,\omega) \times e^{-i\omega|x_R|[\frac{1}{c_{01}}-\frac{1}{c_1(\omega)}]} \times e^{-i\omega|x_I|[\frac{1}{c_{01}}-\frac{1}{c_1(\omega)}]} \quad (7.1b)$$

$$RT_{\tilde{\varepsilon}}^{1D}(x_T,x_R,\omega) = RT_{\tilde{\varepsilon}}^{3D}(x_T,x_R,\omega) \times e^{i\omega|x_T|[\frac{1}{c_{02}}-\frac{1}{c_2(\omega)}]} \times e^{-i\omega|x_R|[\frac{1}{c_{01}}-\frac{1}{c_1(\omega)}]} \quad (7.1c)$$

Eq. (7.1) are the governing relations between 1D and 3D coefficients.

Further, we are able to derive the 1D interface coefficients from the 3D coefficients measured at any locations:

$$TC_{\tilde{\varepsilon}}^{1D}(0,0,\omega) = TC_{\tilde{\varepsilon}}^{1D}(x_I, x_T, \omega) \times \boldsymbol{e^{\gamma_2 x_T - \gamma_1 x_I}} = TC_{\tilde{\varepsilon}}^{3D}(x_I, x_T, \omega) \times e^{-i\omega|x_T|[\frac{1}{c_{02}} - \frac{1}{c_2(\omega)}]} \times e^{-i\omega|x_I|[\frac{1}{c_{01}} - \frac{1}{c_1(\omega)}]} \times \boldsymbol{e^{\gamma_2 x_T - \gamma_1 x_I}}$$

$$RC_{\tilde{\varepsilon}}^{1D}(0,0,\omega) = RC_{\tilde{\varepsilon}}^{1D}(x_I, x_R, \omega) \times \boldsymbol{e^{-(\gamma_1 x_R + \gamma_1 x_I)}} = RC_{\tilde{\varepsilon}}^{3D}(x_I, x_R, \omega) \times e^{-i\omega|x_R|[\frac{1}{c_{01}} - \frac{1}{c_1(\omega)}]} \times e^{-i\omega|x_I|[\frac{1}{c_{01}} - \frac{1}{c_1(\omega)}]} \times \boldsymbol{e^{-(\gamma_1 x_R + \gamma_1 x_I)}}$$

$$RT_{\tilde{\varepsilon}}^{1D}(0,0,\omega) = RT_{\tilde{\varepsilon}}^{1D}(x_T, x_R, \omega) \times \boldsymbol{e^{-(\gamma_1 x_R + \gamma_2 x_T)}} = RT_{\tilde{\varepsilon}}^{3D}(x_T, x_R, \omega) \times e^{i\omega|x_T|[\frac{1}{c_{02}} - \frac{1}{c_2(\omega)}]} \times e^{-i\omega|x_R|[\frac{1}{c_{01}} - \frac{1}{c_1(\omega)}]} \times \boldsymbol{e^{-(\gamma_1 x_R + \gamma_2 x_T)}}.$$

In the processing presented here, $\varepsilon_I^{3D}(x_I,\omega), \varepsilon_R^{3D}(x_R,\omega), \varepsilon_T^{3D}(x_T,\omega)$ were either measured from simulations or experiments, $\tilde{\varepsilon}_I^{3D}(x_I,\omega), \tilde{\varepsilon}_R^{3D}(x_R,\omega), \tilde{\varepsilon}_T^{3D}(x_T,\omega)$ were obtained after FFT, and the $TC_{\tilde{\varepsilon}}^{3D}(x_I, x_T, \omega)$, $RC_{\tilde{\varepsilon}}^{3D}(x_I, x_R, \omega)$ were then corrected using Eq. (7.1). The resulting 1D ratios were substituted into the strain equations in Table. 6-10a to solve for the propagation coefficient, and the corresponding moduli were obtained using the 1D relation between the propagation coefficient and modulus (Eq. (2.27)). Examples of the effect of dispersion correction were seen in later analysis.

7.3.1.2 The revised BCs method

An alternative approach to treat the dispersion problem is to revise the BCs by introducing 3D effects. As shown in Eq. (6.4a'), the 1D BCs are velocity and force continuity at interface, when it comes to the 3D case, these two equations keep the same forms but both the velocity and force components become 3 dimensional. The uniform strain expression (Eq. (2.20a)) comes in a 3D form as well

$$\tilde{\varepsilon}^{3D}(x,\omega) = \tilde{P}^{3D}(\omega)e^{-\gamma^{3D}x} + \tilde{N}^{3D}(\omega)e^{\gamma^{3D}x}. \qquad \text{Eq. (2.20a')}$$

The force expression (Eq. (6.1f')), which was previously obtained from the Newton's Second Law (Eq. (2.6e')), however, needs to be revised to reveal the inertia effect. To realise this, we firstly re-write Newton's Second Law in time domain using the 'effective density' method by Aleyaasin [34]

$$\frac{\partial \sigma^{3D}}{\partial x} = \rho \frac{\partial^2 u^{3D}}{\partial t^2} - \rho v^2 R^2 \frac{\partial^4 u^{3D}}{\partial x^2 \partial t^2}. \qquad \text{Eq. (3.13b)}$$

Similar to deriving the 1D stress $\tilde{\sigma}^{1D}$ in Eq. (6.1e'), the 3D stress $\tilde{\sigma}^{3D}$ can be obtained by performing Fourier transform of Eq. (3.13b)

$$\tilde{\sigma}^{3D}(x,\omega) = -\rho\omega^2 \int \tilde{u}^{3D}(x,\omega)dx + \rho\omega^2 v^2 R^2 \frac{\partial \tilde{u}^{3D}(x,\omega)}{\partial x}$$

and the 3D force

$$\tilde{F}^{3D} = \tilde{\sigma}^{3D} S = S\rho\omega^2[v^2 R^2 \frac{\partial \tilde{u}^{3D}(x,\omega)}{\partial x} - \int \tilde{u}^{3D}(x,\omega)dx] \,.$$

The 3D expressions of all 6 quantities are presented in the *web version*. Note that, all the geometry-related quantities, *e.g.* $[\tilde{\varepsilon}, \tilde{F}, \tilde{\sigma}, \tilde{\dot{u}}, \tilde{u}, \tilde{a}]$, $[\tilde{P}, \tilde{N}, \tilde{Q}]$ and $[\gamma_1, \gamma_2]$ are all 3-dimensional. Follow the same routine used in deriving the equations in Table. 6-10a, we have the revised version in Table 6-10b. Similar relations in terms of the other 5 quantities can be found in the *web version*.

Table 6-10b Equations used to derive the 3D propagation coefficient

	$x_I, x_R \leq 0, x_T \geq 0$
$\tilde{\varepsilon}$	① $\frac{\gamma_1}{\gamma_2} TC_{\tilde{\varepsilon}}(x_I, x_T, \omega) \times e^{\gamma_2 x_T - \gamma_1 x_I} + RC_{\tilde{\varepsilon}}(x_I, x_T, \omega) \times e^{-(\gamma_1 x_R + \gamma_1 x_I)} = 1$
	② $\frac{\frac{\rho_2 S_2}{\gamma_2}(v_2^2 R_2^2 \gamma_2^2 - 1)}{\frac{\rho_1 S_1}{\gamma_1}(v_1^2 R_1^2 \gamma_1^2 - 1)} \frac{\gamma_1}{\gamma_2} TC_{\tilde{\varepsilon}}(x_I, x_T, \omega) \times e^{\gamma_2 x_T - \gamma_1 x_I} - RC_{\tilde{\varepsilon}}(x_I, x_T, \omega) \times e^{-(\gamma_1 x_R + \gamma_1 x_I)} = 1$
	③ $TC_{\tilde{\varepsilon}}(x_I, x_T, \omega) = \frac{2\frac{\rho_1 S_1}{\gamma_1}(v_1^2 R_1^2 \gamma_1^2 - 1)}{\frac{\rho_1 S_1}{\gamma_1}(v_1^2 R_1^2 \gamma_1^2 - 1) + \frac{\rho_2 S_2}{\gamma_2}(v_2^2 R_2^2 \gamma_2^2 - 1)} \times \frac{\gamma_2}{\gamma_1} \times \frac{e^{-\gamma_2 x_T}}{e^{-\gamma_1 x_I}}$
	④ $RC_{\tilde{\varepsilon}}(x_I, x_T, \omega) = \frac{\frac{\rho_2 S_2}{\gamma_2}(v_2^2 R_2^2 \gamma_2^2 - 1) - \frac{\rho_1 S_1}{\gamma_1}(v_1^2 R_1^2 \gamma_1^2 - 1)}{\frac{\rho_2 S_2}{\gamma_2}(v_2^2 R_2^2 \gamma_2^2 - 1) + \frac{\rho_1 S_1}{\gamma_1}(v_1^2 R_1^2 \gamma_1^2 - 1)} \times \frac{e^{\gamma_1 x_R}}{e^{-\gamma_1 x_I}}$
	⑤ $RT_{\tilde{\varepsilon}}(x_I, x_T, \omega) = \frac{\frac{\rho_2 S_2}{\gamma_2}(v_2^2 R_2^2 \gamma_2^2 - 1) - \frac{\rho_1 S_1}{\gamma_1}(v_1^2 R_1^2 \gamma_1^2 - 1)}{2\frac{\rho_1 S_1}{\gamma_1}(v_1^2 R_1^2 \gamma_1^2 - 1)} \frac{\gamma_1}{\gamma_2} \times \frac{e^{\gamma_1 x_R}}{e^{-\gamma_2 x_T}}$

As the propagation coefficient derived from any equation in Table 6-10b is for a three dimensional system, the 3D relation Eq. (3.14a) should be used to further obtain the intrinsic material modulus $E^*(\omega)$. It is noted that, as required, all these 3D relations derived can be reduced to the 1D case by setting the Poisson's ratio to be zero. Furthermore, since x_1 and x_2 are axial coordinates with origins at the 2-rod interface, $\widetilde{N}$, $\widetilde{P}$ and $\widetilde{Q}$ are the amplitudes of the incident, reflected and transmitted waves at the interface. Further, while explicit analytical solutions cannot be found, numerical methods are used to derive either γ_1 or γ_2. As different degrees of complexity are involved in the 4 equations in Table 6-10b, different numerical errors, thus the results derived, may vary slightly.

7.3.2 Some mathematical issues in solving the interface equations

We first address the interrelated nature of the two BCs equations. Looking at the BCs equation (Eq. (6.4a')), Eq. ① shows the equilibrium of particle velocities on both sides of the contact interface, and Eq. ② the balance of forces. In fact, these 2 relations are interrelated because the following relation exists between force and velocity

$$F = \pm Z^* \dot{u} \tag{7.2}$$

where Z^* is the characteristic impedance of a geometry (Eq. (6.8)), Z = ρcS for elastic materials. The 2 equations can then be simplified to contain a single characteristic quantity depending on what's measured, for example, they can be expressed in terms of force

$$\begin{cases} -\frac{\tilde{F}_I(0,\omega)}{Z_1} + \frac{\tilde{F}_R(0,\omega)}{Z_1} = -\frac{\tilde{F}_T(0,\omega)}{Z_2} & ① \\ \tilde{F}_I(0,\omega) + \tilde{F}_R(0,\omega) = \tilde{F}_T(0,\omega) & ② \end{cases}$$

Though after substitution these two equations are still not the same in appearance, they are in essence physically the same, and thus they should yield the same answer to $\gamma_1$or γ_2 in any effort resorting to derive the material properties of the same rod. A numerical verification process which shows both equations give the same answer will be shown later.

As these two equations are interrelated, it is thus impossible to resolve for $\gamma_1$and γ_2 at the same time. We can also mathematically verify this. Rewrite the above force form BCs we have

$$\begin{cases} \frac{Z_2}{Z_1} = \frac{TC_{\tilde{F}|x_I=x_T=0}}{1 - RC_{\tilde{F}|x_I=x_T=0}} & ① \\ TC_{\tilde{F}|x_I=x_T=0} - RC_{\tilde{F}|x_I=x_T=0} = 1 & ② \end{cases}$$

Material property information ($Z_1$and Z_2) is only contained in Eq. ①, and it is seen from Eq. ② that, $TC_{\tilde{F}|x_I=x_T=0}$ and $RC_{\tilde{F}|x_I=x_T=0}$ are actually not independent, the other one can be told once either is measured. Substituting Eq. ② into Eq. ① only helps eliminate either $TC_{\tilde{F}|x_I=x_T=0}$ or $RC_{\tilde{F}|x_I=x_T=0}$, but won't help derive Z_1 and Z_2 simultaneously. Similar situations can be found when expressing the 2 BCs equations either in terms of particle velocity $\tilde{u}$, strain $\tilde{\varepsilon}$, stress $\tilde{\sigma}$, displacement $\tilde{u}$, or acceleration $\tilde{a}$. In some cases, Z_1 and Z_2 may be contained in both equations, but again only the impedance ratio $\frac{Z_2}{Z_1}$ can be resolved, which means only the property of 1 rod can be worked out by measuring the incident, transmitted and reflected waves. To validate the capacity of these equations, an analytical calculation was performed. Here, two simple elastic rods (Ti-Mg) were considered (Fig. 7-3).

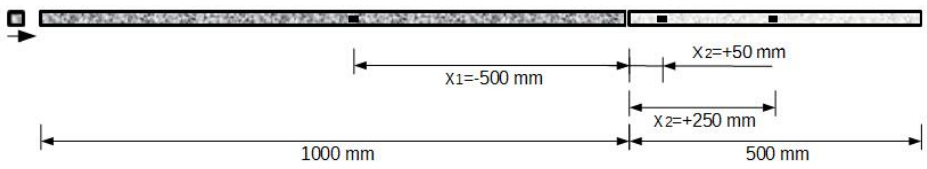


Figure. 7-3 A virtual Ti-Mg system

Incident rod: Titanium, $E_1 = 110\ GPa, \rho_1 = 4500\ kg/m^3, d_1 = 13\ mm, Z_1 = 2953\ kg/s$
Transmission rod: Magnesium, $E_2 = 45\ GPa, \rho_2 = 1740\ kg/m^3, d_2 = 13\ mm, Z_2 = 1175\ kg/s$

For purely elastic materials, the characteristic impedance is frequency-independent as its modulus is constant. Also, if no geometric dispersion is included, the attenuation coefficient is zero, only the imaginary part, *i.e.* the linearly increasing wavenumber, remains in the propagation coefficient γ

$$\gamma_1 = \alpha_1 + i\kappa_1 = i\frac{\omega}{\sqrt{E_1/\rho_1}} \xrightarrow{\alpha_1=0} i\frac{2\pi\times10000}{\sqrt{110\times10^9/4500}} = 12.708i$$

and the reference γ_2

$$\gamma_2 = \alpha_2 + i\kappa_2 = i\frac{\omega}{\sqrt{E_2/\rho_2}} \xrightarrow{\alpha_2=0} i\frac{2\pi\times10000}{\sqrt{45\times10^9/1740}} = 12.355i\ .$$

As indicated before, the origin is set at the contact interface, and x increases towards the transmission rod. The theoretical coefficients (strain coefficients at $f = 10000\,Hz$ as an example) can be calculated using the given material properties (see Table 6-9a)

$$\begin{aligned} TC_{\tilde{\varepsilon}|f=10000\,Hz}(x_I, x_T) &= \frac{2Z_1}{Z_1+Z_2}\times\frac{\gamma_2}{\gamma_1}\times\frac{e^{-\gamma_2 x_T}}{e^{-\gamma_1 x_I}} = \frac{2\times2953}{2953+1175}\times\frac{12.355i}{12.708i}\times\frac{e^{-\gamma_2 x_T}}{e^{-\gamma_1 x_I}} \\ &= 1.3911e^{\gamma_1 x_I - \gamma_2 x_T} \\ RC_{\tilde{\varepsilon}|f=10000\,Hz}(x_I, x_R) &= \frac{Z_2-Z_1}{Z_2+Z_1}\times\frac{e^{\gamma_1 x_R}}{e^{-\gamma_1 x_I}} = \frac{1175-2953}{2953+1175}\times\frac{e^{\gamma_1 x_R}}{e^{-\gamma_1 x_I}} \\ &= -0.4309e^{\gamma_1 x_I + \gamma_1 x_R} \end{aligned} .$$

For purely elastic rods, the two coefficients at the interface ($x_I = x_R = x_T = 0$) are real constants for all frequencies; the transmission coefficient is always positive, whilst the sign of the reflection coefficient depends on the difference between the transmission and incident rod impedances

$$\begin{cases} RC_{\tilde{\varepsilon}|x_I=x_T=0} > 0, & when\ Z_2 > Z_1 \\ RC_{\tilde{\varepsilon}|x_I=x_T=0} = 0, & when\ Z_1 = Z_2 \\ RC_{\tilde{\varepsilon}|x_I=x_T=0} < 0, & when\ Z_2 < Z_1 \end{cases} .$$

and, of course, as Z_2 tends to infinity, the interface behaves as a fixed end, and as it tends to zero it behaves as a free end.

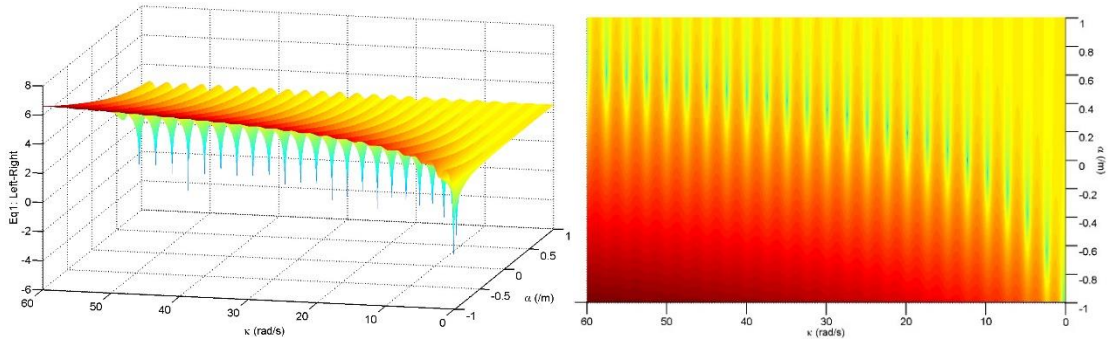
The derived TC and RC equations in Table 6-10a, were used to numerically solve for γ_1 or γ_2

$$\begin{aligned} \gamma_2 \times e^{-\gamma_2 x_T} &= \frac{\gamma_1 \times TC_{\tilde{\varepsilon}}(x_I, x_T, \omega)\times e^{-\gamma_1 x_I}}{1 - RC_{\tilde{\varepsilon}}(x_I, x_R, \omega)\times e^{-(\gamma_1 x_R + \gamma_1 x_I)}} \quad ①' \\ \gamma_2^2 \times e^{-\gamma_2 x_T} &= \gamma_1^2 \times \frac{S_2}{S_1}\frac{\rho_2}{\rho_1}\frac{TC_{\tilde{\varepsilon}}(x_I, x_T, \omega)\times e^{-\gamma_1 x_I}}{1 + RC_{\tilde{\varepsilon}}(x_I, x_R, \omega)\times e^{-(\gamma_1 x_R + \gamma_1 x_I)}} \quad ②' \end{aligned} \tag{7.3}$$

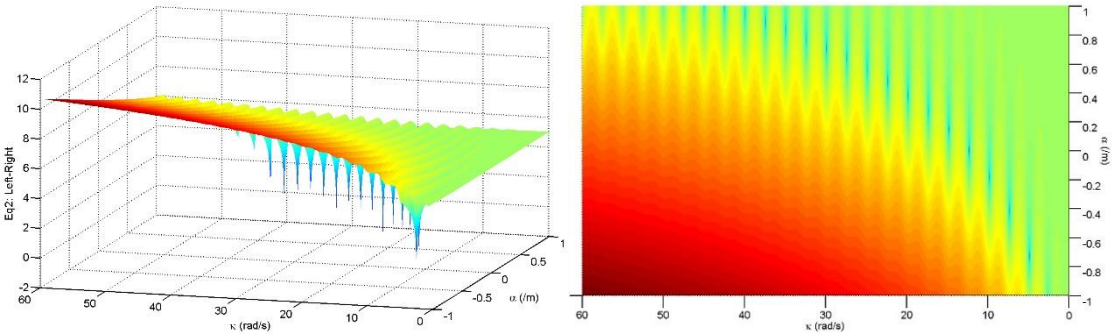
they correspond respectively to the BCs equations (Eq. (6.4a')).

If the three pulses (incident, transmitted and reflected) could be obtained separately at the contact interface, then using $x_I = x_R = x_T = 0$ gives simple equations for the relationship between γ_1 and γ_2. For example, by substituting $\omega = 2\pi \times 10000\ \mathrm{rad/s}$, $TC_{\tilde{\varepsilon}|x_I=x_T=0} = 1.3911$, $RC_{\tilde{\varepsilon}|x_I=x_T=0} = -0.4309$, $\rho_1 = 4500$, $\rho_2 = 1740\ \mathrm{kg/m^3}$, $S_1 = S_2 = 1.327 \times 10^{-4}\ \mathrm{m^2}$, $\gamma_1 = 12.708i\ /m$ into Eq. (7.3), it is found that both equations yield the unique solution $\gamma_2 = 12.355i$, as defined initially. Similarly, substituting $\gamma_2 = 12.355i$ into Eq. (7.3) gives $\gamma_1 = 12.708i$.

Actual measurement positions are normally remote from the interface, thus the situation is more complicated. The two equations are advised to be solved numerically, and multiple solutions exist due to the periodic characteristic of these equations. To address the multi-solution problem, three sets of distances are numerically tested: ($x_I = x_R = -5\ m$, $x_T = 2.5\ m$), ($x_I = x_R = -0.5\ m$, $x_T = 2.5\ m$), ($x_I = x_R = -5\ m$, $x_T = 1.25\ m$), as shown in Fig. 7-4, Fig. 7-5 and Fig. 7-6. Again, the known quantities were submitted into Eq. (7.3), and the solution for γ_2 is sought. In fact, infinite sets of solutions exist which balance the equations. To visualise these, a 3D error surface which maps the distribution of potential solution pairs, was be obtained by substituting a range of (α, κ) values into the left and right sides of each equation, using the frequency and bar information above, and a logarithm of absolute error (*i.e* log(|Left-Right|)) was calculated and plotted on the complex plane constituting $\gamma = \alpha + i\kappa$ in Fig. 7-4. From these figures, we can see that $\gamma_2 = 12.355i$ is just one of these solutions. It is also observed that in both equations, the wavenumber dominates the equilibrium between the two sides, the area where potential κ exists is narrow (*i.e.* the wavenumber band is 'slim'), and the interval between two neighbor wavenumber solutions don't overlap; the attenuation coefficient band, however, is wider, which generates a series of α values that might fit the equation even with the same value of κ. Furthermore, the α band in Eq. ①' is narrower, which indicates Eq. ①' may be more effective in identifying α. Most importantly, however wavenumber solutions appear periodically at a constant interval $(2\pi/2.5)$. Decomposing each equation using Euler transforms yields two real equations specifying the real and imaginary balance separately and confirms that the periodicity in wavenumber solutions is only determined by $2\pi/x_T$. This is confirmed by comparing Fig. 7-4, 7-5, and 7-6.

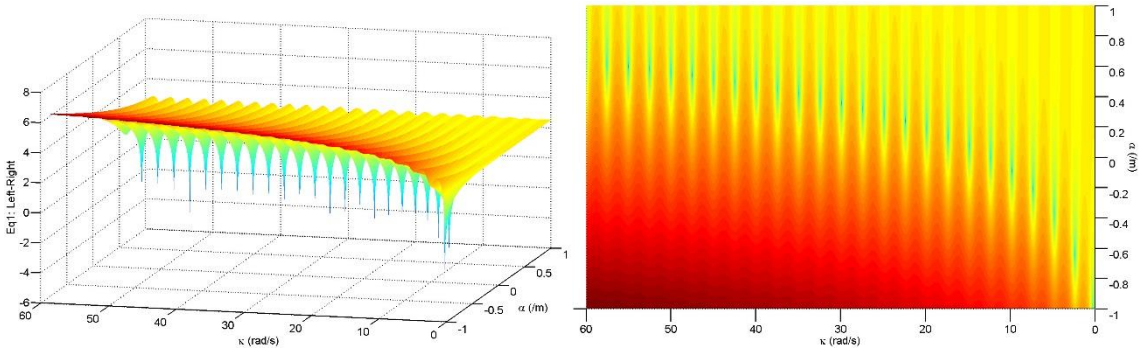


(a)Eq. ①′

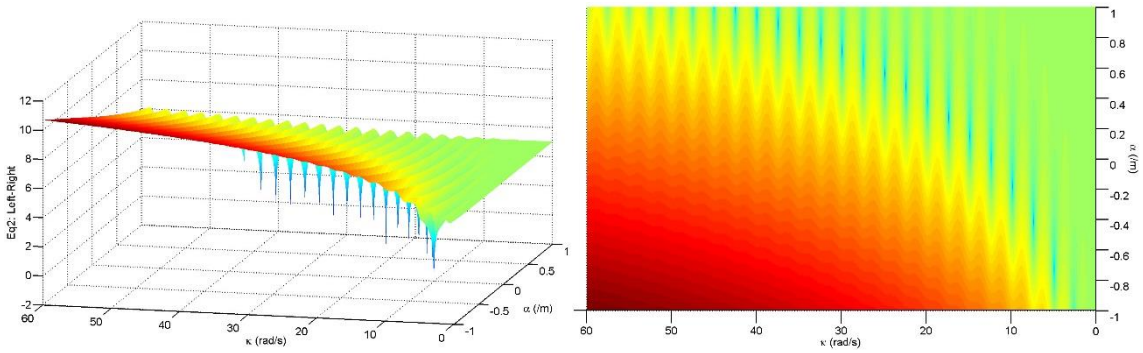


(b)Eq. ②′

Figure. 7-4 Error evaluation ($x_I = x_R = -5\ m, x_T = 2.5\ m$)

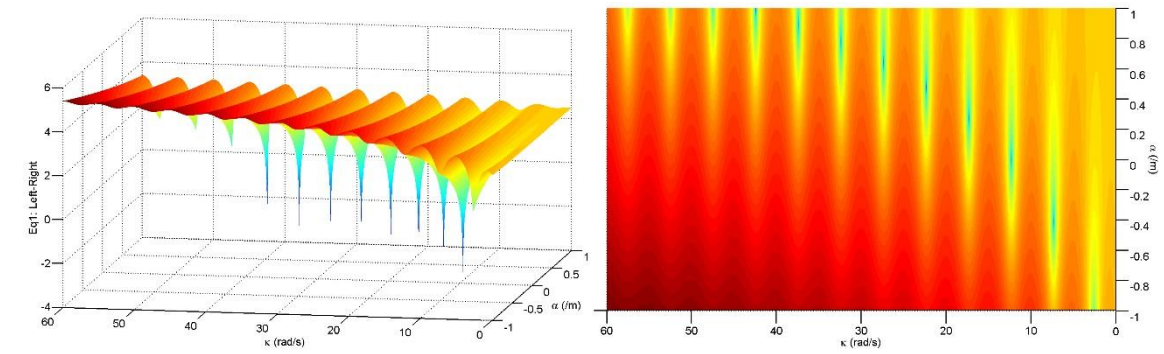


(a)Eq. ①′

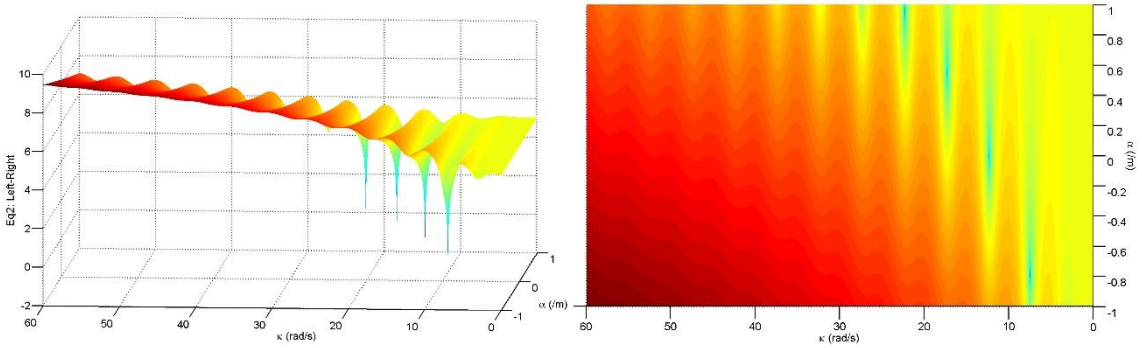


(b)Eq. ②′

Figure. 7-5 Error evaluation ($x_I = x_R = -0.5\ m, x_T = 2.5\ m$)



(a)Eq. ①′



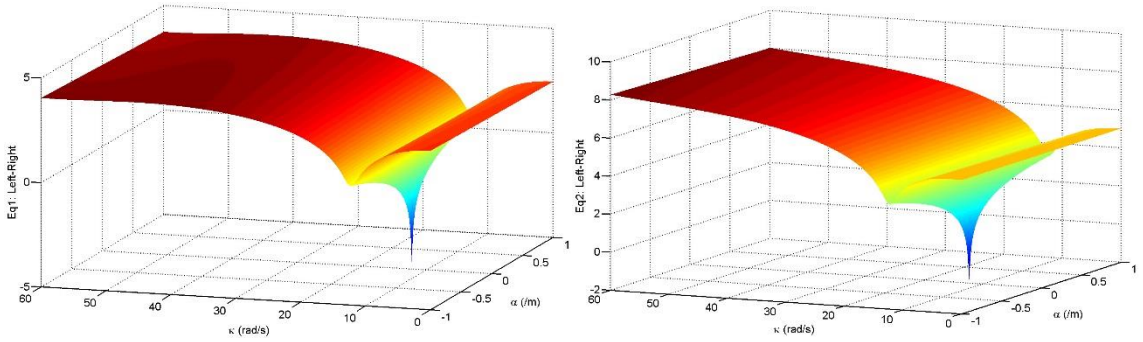
(b)Eq. ②′

Figure. 7-6 Error evaluation ($x_I = x_R = -5\ m, x_T = 1.25\ m$)

In real experiments, a SHPB setup for example, a more practical distance pair would be $x_I = x_R = -0.5\ m$ and $x_T = 0.125\ m$ (Fig. 7-7), this makes the distance between any two 'reasonable' wavenumber solutions large enough to be identified, and thus the solution becomes unique within a large area. In practice, a reasonably well constrained search area for wavenumber is needed to accurately locate the desired solution. This can be done by sitting an estimated wavenumber in the middle of the searching range and defining a search band which is smaller than the period of κ ($2\pi/x_T$). In this analytical example, knowing the elastic wave speed in the material, the desired wavenumber can be approximately estimated as (in the case of slight or medium viscoelasticity)

$$\kappa_{i0}(\omega_i) = \frac{\omega_i}{c_2} = \frac{\omega_i}{\sqrt{E_2/\rho_2}}.$$

Now, the 'Matlab' built-in numerical solver 'vpasolve' may be used to search for solutions within a rectangular searching area, with abscissa being the attenuation coefficient α and ordinate the wavenumber κ: $[-1 - \mathrm{i}\kappa_{i0}, 1 + \mathrm{i}\kappa_{i0}]$ to locate κ_i. This produces a unique solution pair (α, κ) which is exactly the same as predicted, *i.e.* $\gamma_2 = 12.355i$.



(a)Eq. ①′ (b)Eq. ②′

Figure. 7-7 Error evaluation ($x_I = x_R = -0.5\ m, x_T = 0.125\ m$)

Similar effect exists when γ_1 is sought: x_T doesn't affect the balance as $e^{-\gamma_2 x_T}$ is contained on both sides of Eq. (7.3). Periodicity occurs in wavenumber solutions of γ_1 due to the term $e^{-\gamma_1 x_I}$. Results based on the Ti-Mg case were presented in the full *web version*. It is found that now the periodicity is dominated by $2\pi/x_I$. However, the wavenumber band yielded by Eq. ②′ is narrower than that by Eq. ①′, which means optimal solution can more easily identified by Eq. ②′. In this sense, Eq②′ is preferred when solving for γ_1.

The above analytical and numerical analysis concludes that: both Eq. ①′ and Eq. ②′ can give the same and accurate solutions. However, in order to obtain the 'true' solutions, proper constrains, mainly on wavenumber, are needed. A wavenumber band with proper width covering the theoretically predicted value is recommended, the band width can be set based on an evaluation of the period of wavenumber, *i.e.* $2\pi/x_I$ (when solving for γ_1) or $2\pi/x_T$ (when solving for γ_2). In later case analysis (PMMA-Mg 2 medium), it was found that multiple wavenumber solutions can appear even in a single period, which requires more rigorous constraints, *e.g.* constrains on alpha or α and κ have certain evolution pattern (increasing, decreasing, or around certain estimated value), to be applied. Finally, Eq. ①′ is favourable when deriving γ_2 while Eq. ②′ prevails to identify γ_1.

In the rest of this chapter, we will analyse 4 cases of 2-medium interface simulations: Ti-Ti, Ti-Mg, Ti-PMMA, and PMMA-Mg. The material properties adopted (density, Poisson's ratio, Young's modulus) in simulations are the same as listed in Table. 7-1. All materials are isotropic and homogeneous; for PMMA, the instantaneous modulus is 5.37 GP, and the fitted 2-term PRONY constants (Fig. 5-11) are the same as those used in single rod simulation (Table. 5-5).

7.4 Ti-Ti 2-medium interface

7.4.1 Model descriptions

Raw signals have been monitored at various locations as shown in Fig. 7-8, and as expected, there is no reflection because there is no interface. Now, an interface location is assumed, and the equations derived in Chapter 7 are used to calculate relative material properties across it.

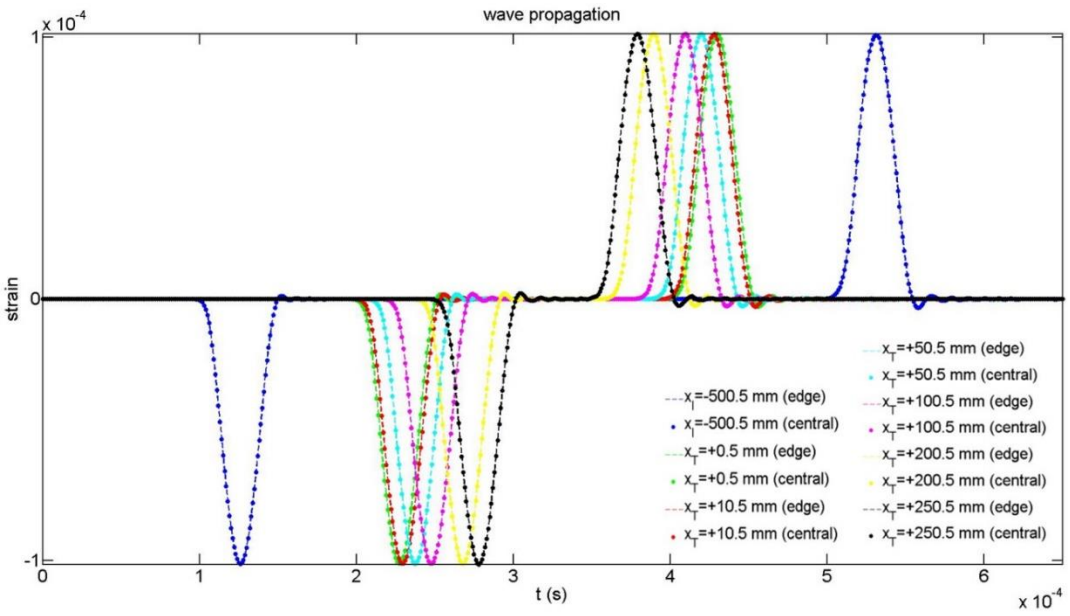


Figure. 7-8 Wave propagation in the 2 medium Ti-Ti system

7.4.2 Comparison of dispersive and dispersion corrected results

As an example an interface is chosen such that $x_{IR} = -500.5$ mm and $x_T = +250.5$ mm and the results with and without dispersion correction are compared throughout the data analysis process. The raw signals were first de-noised using the wavelet-based de-noising function 'wden' with no phase modification and then the 3 pulses were extracted and no centering performed. A comparison of the signal analysis process with and without dispersion correction is made in Fig. 7-9. After FFT, the minimum frequency resolution achieved with this simulation signal is $1536\ Hz$ (1/0.00065s, which also serves as the lower frequency limit), and the maximum frequency is $5 \times 10^5\ Hz$ ($1/10^{-6}\ s \times 0.5$); however, it is clear from from Fig. 7-9(a) that the signal carries little information above 40 kHz, this is the upper frequency limit in this case. Another factor that might pose an upper frequency limit on the analysis is the constraint on the 1D wave propagation assumption, *i.e.* to avoid appreciable dispersion effect, the wavelength should be at least 10 times as long as the rod diameter

$$f_{h-1D} = \frac{c}{10 \times rod\ diameter} \approx \frac{4944\,\frac{m}{s}}{10 \times 0.013\ mm} \approx 38\ kHz\ .$$

This applies for the case where dispersion correction was absent. Also note that, the lowest frequency waves that can be achieved in this system without overlap are

$$f_{l-incident} \approx \frac{c}{incident\ gauge\ distance} \approx \frac{4944\,\frac{m}{s}}{2 \times (1-0.5005) m} \approx 4.944\ kHz$$

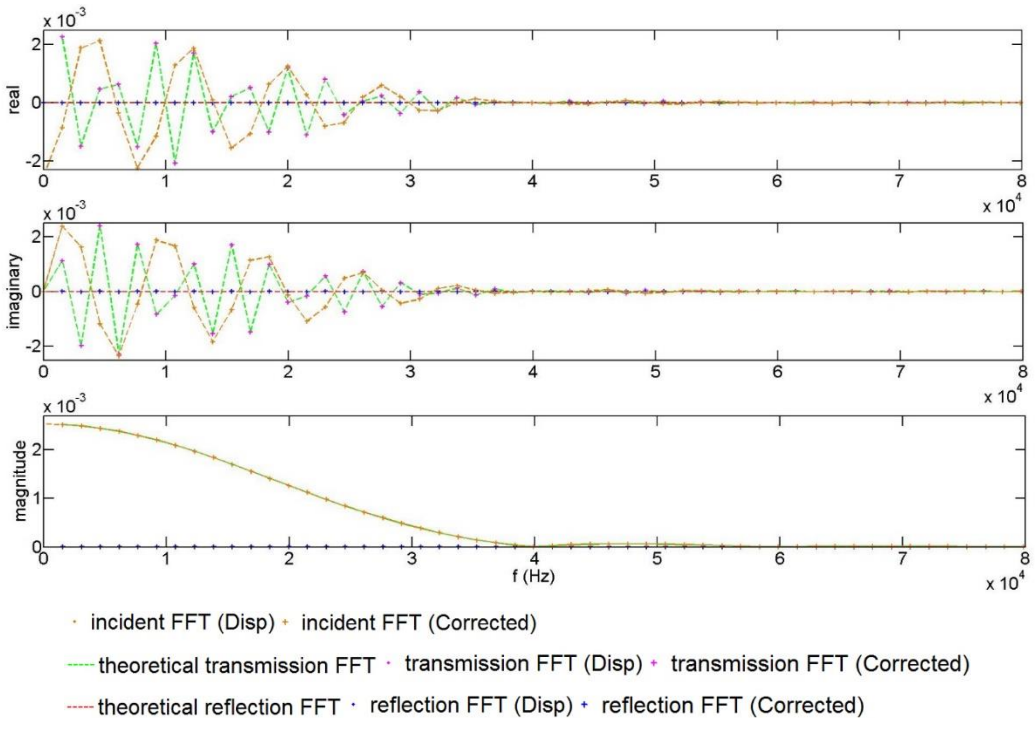
$$f_{l-transmission} \approx \frac{c}{transmission\ gauge\ distance} \approx \frac{4944\,\frac{m}{s}}{2 \times (0.5-0.2505)\ m} \approx 9.888\ kHz\ .$$

Therefore, using this configuration of the 2-medium system, a reasonable valid frequency range, within which the FFTs can be effectively identified without dispersion correction, is expected to be 9.888 kHz~40 kHz, winthin which the frequency resolution is 1536 Hz.

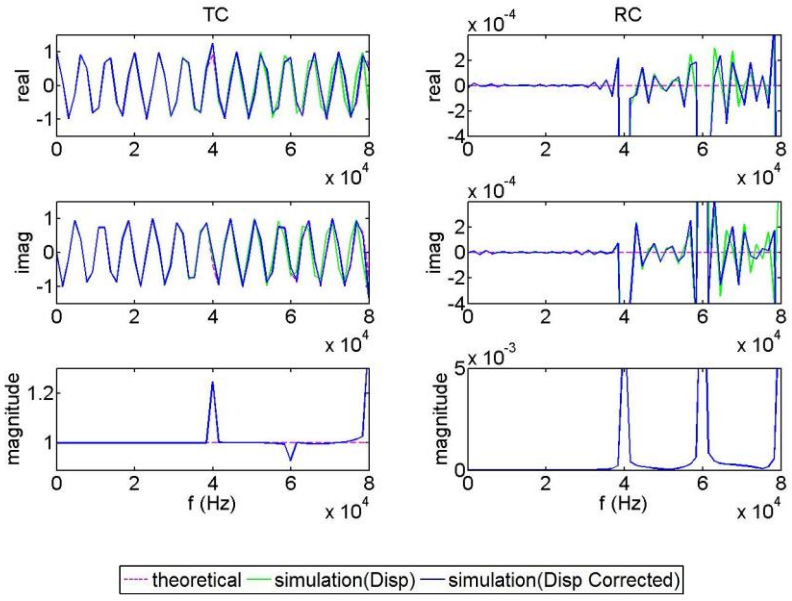
The dispersion correction strategy in Eq. (7.1) was applied to both rods using a dispersive Ti wave speed profile similar to Fig. 3-15a (only geometries are different). Theoretical FFTs used as comparison were obtained by multiplying the incident FFT and the theoretical TC and RC values

$$\tilde{R}(x_T, \omega) = RC(x_I, x_R, \omega) \times \tilde{I}(x_I, \omega), \tilde{T}(x_T, \omega) = TC(x_I, x_T, \omega) \times \tilde{I}(x_I, \omega)\ .$$

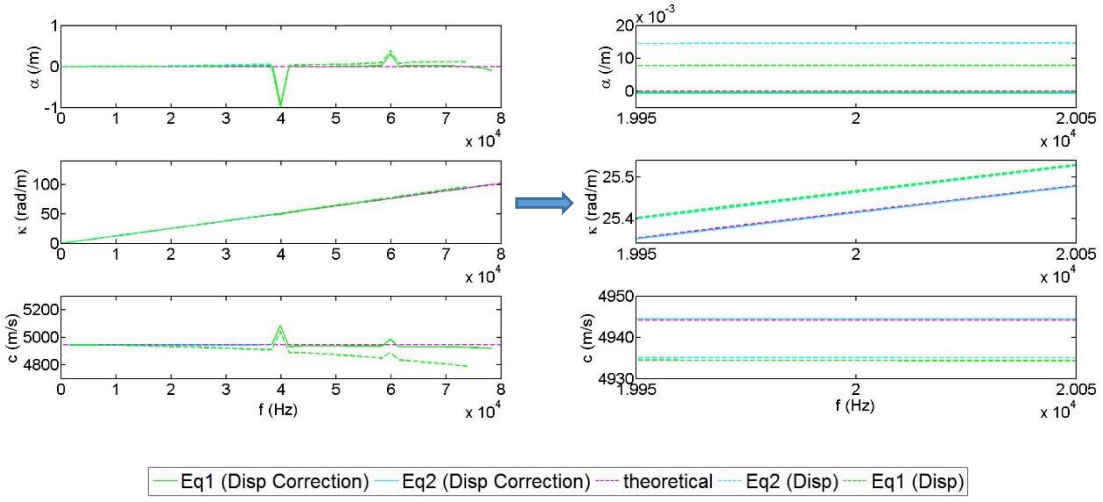
It is seen from Fig. 7-9(a) that the differences between the dispersive and dispersion corrected FFTs are insignificant within the valid frequency range (0~40 kHz).



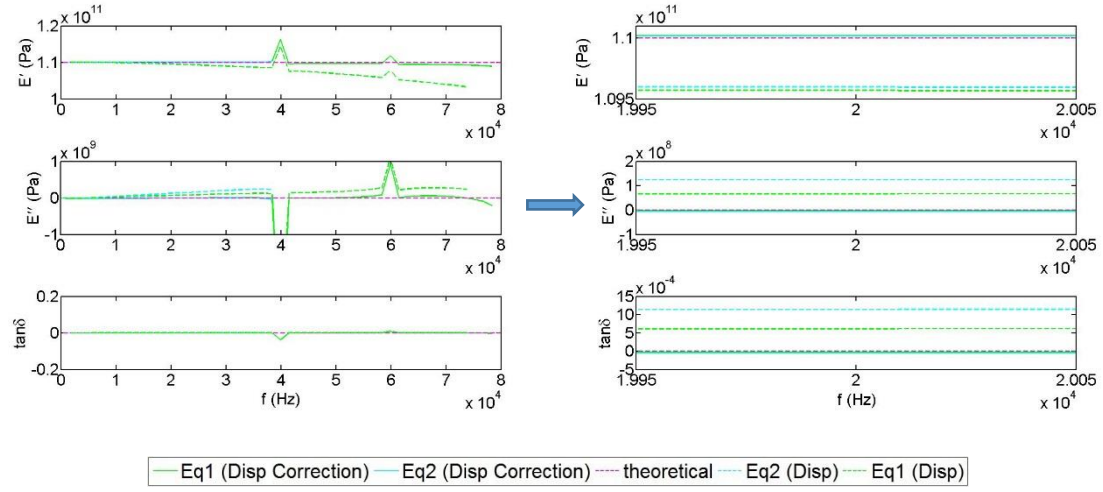
(a)Comparison of theoretical & simulation FFTs with & without dispersion correction



(b) $TC_{\tilde{\varepsilon}}$ & $RC_{\tilde{\varepsilon}}$ comparison



(c) Propagation coefficient and wave speed



(d) Modulus and loss factor

Figure. 7-9 A comparison of the dispersion and dispersion corrected results (transmission medium)

(Ti-Ti 1 Rod 2 mediums, $x_{IR} = -500.5\ mm, x_T = +250.5\ mm$)

A comparison of theoretical and simulation-based $TC_{\tilde{\varepsilon}}$ and $RC_{\tilde{\varepsilon}}$ values is made in Fig. 7-9(b). Theoretical values were calculated by submitting the material constants defined into the analytical expressions in Table 6-9. This comparison addresses the necessity of performing dispersion correction on these signals: though it doesn't modify the magnitudes, it does correct the real and imaginary parts of TC and RC in the high frequency region (*i.e.* $f > 40$ kHz). After correction, these values are quite close to the theoretical ones. The errors in the magnitudes at 40, 60 and 80 kHz are a result of the window function, which is determined by the duration of the incident pulse, this will again be reflected when deriving material properties based on these TC and RC values later.

The effect of dispersion is reflected in the disparities between the corrected and uncorrected material properties in Fig. 7-9(c) and (d). A close look at the derived material properties, those at the frequency of 20 kHz for example, reveals that, dispersion correction of the interface signals leads to a decrease of the attenuation coefficient, wavenumber, loss modulus and loss factor, and increases wave speed and storage modulus. The effect of dispersion correction becomes evident above around 10 kHz and increases with increasing frequency. After dispersion correction, the derived attenuation coefficient, α, loss modulus, E'' and loss factor, $\tan\delta$ are almost zero, while the derived storage modulus $E' \approx 110\ GPa$ and wave speed is constantly $\sqrt{\frac{E'}{\rho}} \approx 4944\ m/s$, which is consistent with those the model definitions. In deriving these results, the propagation coefficient γ_2 was first obtained by solving Eq. (7.3), and then the modulus $E^*(\omega)$ using Eq. (2.27).

An interesting phenomenon is the regularly appeared spikes in all these figures ($\alpha, \kappa, c, E', E'', tan\delta$), the period is shown to be $\frac{1}{20\ \text{kHz}} = 50\ \mu s$, which is exactly the same as the duration of the input acceleration pulse. This is thought to be induced by the window function effect (as reflected in the TC and RC values), *i.e.* when FFT is performed, a rectangular window with unity magnitude and the same length as the pulse was automatically multiplied to the time domain signal, which leads to a convolution of the Fourier transforms of the raw signal and the rectangular in frequency domain, and the synthetic FFT is in a *sinc* function shape with zero crossover points appearing periodically at $\Delta f = \frac{1}{pulse\ duration} = 20\ kHz$.

7.4.3 Error analysis

7.4.3.1 Uniformity of cross-sectional deformation

It is seen from Fig. 7-8 that waves extracted at central and edge elements have the same amplitudes, which indicates uniform deformations across the cross-section.

7.4.3.2 Sensitivity of the interface analysis technique to distance

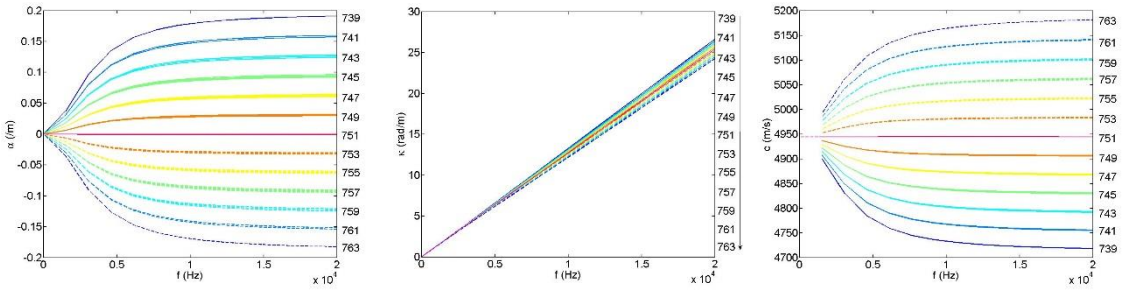
The sensitivity of the proposed analysis method to errors in distance was tested by adjusting x_{IR} and x_T. The edge data originated from the case ($x_{IR} = -500.5\ mm, x_T = +250.5\ mm$) was employed. The testing scheme was shown in Table. 7-2, in which the incident and reflection monitoring coordinate x_{IR} varies from -506.5 mm to -494.5 mm, and the transmission monitoring coordinate changes from 244.5 mm to 256.5 mm, both with increment steps of 2 mm.

Table. 7-2 distance sensitivity testing scheme

$x_T - x_{IR}$ (m)							
x_T (m) / x_{IR} (m)	244.5×10^{-3}	246.5×10^{-3}	248.5×10^{-3}	250.5×10^{-3}	252.5×10^{-3}	254.5×10^{-3}	256.5×10^{-3}
-494.5×10^{-3}	739	741	743	745	747	749	751
-496.5×10^{-3}	741	743	745	747	749	751	753
-498.5×10^{-3}	743	745	747	749	751	753	755
-500.5×10^{-3}	745	747	749	751	753	755	757
-502.5×10^{-3}	747	749	751	753	755	757	759
-504.5×10^{-3}	749	751	753	755	757	759	761
-506.5×10^{-3}	751	753	755	757	759	761	763

The corresponding results are displayed in Fig. 7-10. There are in total 13 groups of lines, in each group there are between 1 and 7 lines. It is observed that those cases with the same overall monitoring distance ($x_T - x_I$) yield almost the same results; those possessing equal distance to the real monitoring distance yield the same values but with opposite signs (symmetric distribution on both sides of the real monitoring distance). A quantitative analysis, performed at 20 kHz (Table. 7-3a), shows the effect of a gap of 2 mm in the total monitoring distance $x_T - x_I$ is small, and the analysis technique is sensitive enough to detect these variations with absence of noise. Based on the data in Table. 7-3a, it is predicted that an overall step of 10 mm can result in an accumulated error of 3.9%

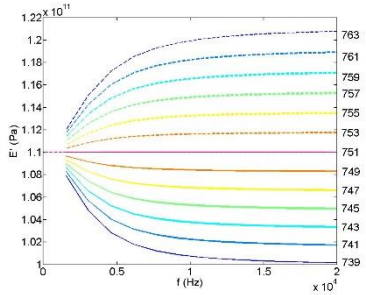
in wavenumber, 5 % in wave speed, and 8.2% in storage modulus. It thus leads to the conclusion that, without the appearance of noise, an absolute error of 10 mm may be tolerable.



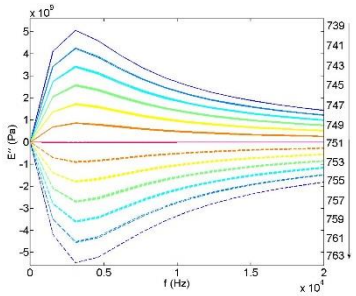
(a) alpha

(b) wavenumber

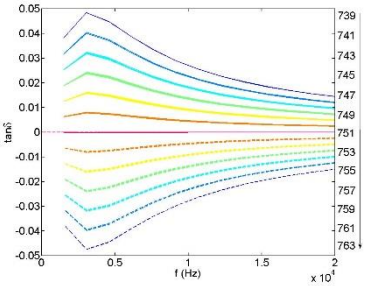
(c) phase speed



(d) storage modulus



(e) loss modulus



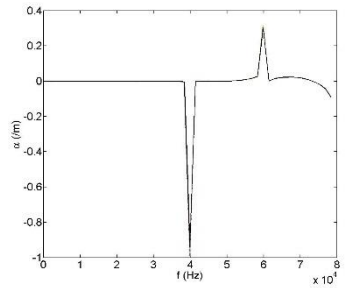
(f) $tan\delta$

Figure.7-10 Material properties yielded by the testing scheme Table. 7-2 (Results based on Eq.①′)

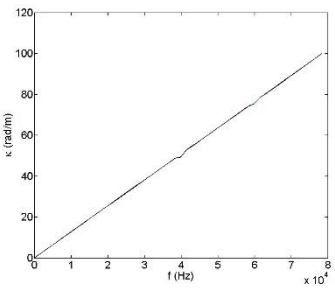
Table. 7-3a Errors at 20 kHz induced by a gap of 2 mm in $x_T - x_I$ (Results based on Eq.①′)

Error	α (/m)	κ (rad/s)	c (m/s)	E' (GPa)	E'' (GPa)	$tan\delta$
Absolute	0.03	0.2	50	1.8	0.24	0.002
Relative (w.r.t. theoretical value)	NA	0.78%	1%	1.64%	NA	NA

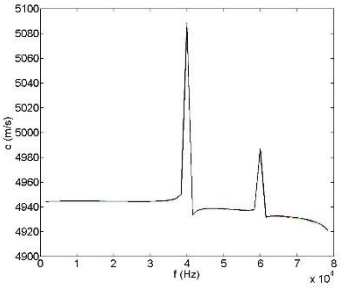
A closer examination of a particular case $x_T - x_I = 751$ (Fig. 7-11) further confirms these statements. There are 7 lines in each material property graph; they all overlap with each other, which again supports that: as wave travel in 2 media of the same material, only the relative travel distance matters. Also confirmed is the reliability and repeatability of the interface analysis technique.



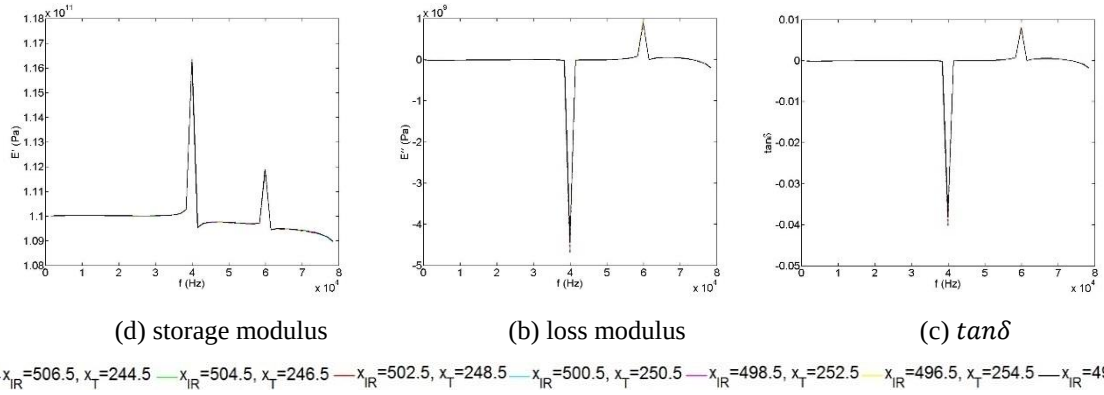
(a) alpha



(b) wavenumber



(c) phase speed



(d) storage modulus (b) loss modulus (c) $tan\delta$

Figure. 7-11 Material properties yielded with $x_T - x_I = 751$ (Results based on Eq. ①′)

Theoretical evidence can be found to clarify the aforementioned conclusions. Firstly, the prerequisites in producing the conclusions are:

(a) The incident and reflected waves are measured at the same monitoring location ($x_I = x_R = x_{IR}$);

(b) The incident and transmission rods are made of the same material ($\gamma_1 = \gamma_2$);

(c) $x_T - x_I = constant.$

The conclusion being: wherever the interface is (once it's located between x_I and x_T, and $x_T - x_I$ keeps constant), solving Eq. ①′ and ②′ will lead to the same material property γ_2. We will now theoretically verify this. The 2 equations used to derive γ_2 was shown in Eq. (7.3), here $x_I = x_R = x_{IR}$. Imagine that x_{IR} and x_T increase simultaneously by Δx

$$x'_{IR} = x_{IR} + \Delta x,\ x'_T = x_T + \Delta x$$

in which $\Delta x > 0$ means both x_{IR} and x_T shift to the right, and $\Delta x < 0$ left.

Expressing Eq. (7.3) using the updated x'_{IR}, x'_T, $TC'_{\tilde{\varepsilon}}$, $RC'_{\tilde{\varepsilon}}$

$$\begin{aligned} \gamma_2 \times e^{-\gamma_2 x'_T} &= \frac{\gamma_1 \times TC'_{\tilde{\varepsilon}}(x'_{IR}, x'_T, \omega) \times e^{-\gamma_1 x'_{IR}}}{1 - RC'_{\tilde{\varepsilon}}(x'_{IR}, \omega) \times e^{-2\gamma_1 x'_{IR}}} \quad ①' \\ \gamma_2^2 \times e^{-\gamma_2 x'_T} &= \gamma_1^2 \times \frac{S_2}{S_1}\frac{\rho_2}{\rho_1} \frac{TC'_{\tilde{\varepsilon}}(x'_{IR}, x'_T, \omega) \times e^{-\gamma_1 x'_{IR}}}{1 + RC'_{\tilde{\varepsilon}}(x'_{IR}, \omega) \times e^{-2\gamma_1 x'_{IR}}} \quad ②' \end{aligned} . \qquad (7.3')$$

We aim to use the relationship between the new (x'_{IR}, x'_T, $TC'_{\tilde{\varepsilon}}$, $RC'_{\tilde{\varepsilon}}$) and old ($x_I$, x_T, $TC_{\tilde{\varepsilon}}$, $RC_{\tilde{\varepsilon}}$) to simplify Eq. (7.3'). The relation between ($TC'_{\tilde{\varepsilon}}$, $RC'_{\tilde{\varepsilon}}$) and ($TC_{\tilde{\varepsilon}}$, $RC_{\tilde{\varepsilon}}$) can be obtained from the relationship between the shifted FFTs ($\widetilde{I'}$, $\widetilde{T'}$, $\widetilde{R'}$) and those without shift ($\tilde{I}$, $\tilde{T}$, $\tilde{R}$). The FFTs after shit can be derived either using wave propagation theory or the property of Fourier transform

$$\widetilde{I'} = I \times e^{-\alpha_1 x_{IR}} \times e^{-i\omega\frac{\Delta x}{c_1(\omega)}} = I \times e^{-\gamma_1 \Delta x}$$

$$\widetilde{T'} = T \times e^{-\alpha_2 x_T} \times e^{-i\omega\frac{\Delta x}{c_2(\omega)}} = T \times e^{-\gamma_2 \Delta x}$$

$$\widetilde{R'} = R \times e^{\alpha_1 x_{IR}} \times e^{i\omega\frac{\Delta x}{c_1(\omega)}} = R \times e^{\gamma_1 \Delta x}$$

therefore,

$$TC'_{\tilde{\varepsilon}}(x'_{IR}, x'_T, \omega) = \frac{\widetilde{T'}}{\widetilde{I'}} = \frac{T \times e^{-\gamma_2 \Delta x}}{I \times e^{-\gamma_1 \Delta x}} = TC_{\tilde{\varepsilon}} \times e^{(\gamma_1 - \gamma_2)\Delta x}$$

$$RC'_{\tilde{\varepsilon}}(x'_{IR}, \omega) = \frac{\widetilde{R'}}{\widetilde{I'}} = \frac{R \times e^{\gamma_1 \Delta x}}{I \times e^{-\gamma_1 \Delta x}} = RC_{\tilde{\varepsilon}} \times e^{2\gamma_1 \Delta x} .$$

Substituting the updated x'_{IR}, x'_T, $TC'_{\tilde{\varepsilon}}$, $RC'_{\tilde{\varepsilon}}$ into Eq. (7.3') we have

$$\gamma_2 \times e^{-\gamma_2 (x_T + \Delta x)} = \frac{\gamma_1 \times TC_{\tilde{\varepsilon}}(x_I, x_T, \omega) \times e^{(\gamma_1 - \gamma_2)\Delta x} \times e^{-\gamma_1 (x_{IR} + \Delta x)}}{1 - RC_{\tilde{\varepsilon}}(x_I, x_R, \omega) \times e^{2\gamma_1 \Delta x} \times e^{-2\gamma_1 (x_{IR} + \Delta x)}} \quad ①'$$

$$\gamma_2^2 \times e^{-\gamma_2 (x_T + \Delta x)} = \gamma_1^2 \times \frac{S_2}{S_1}\frac{\rho_2}{\rho_1}\frac{TC_{\tilde{\varepsilon}}(x_I, x_T, \omega) \times e^{(\gamma_1 - \gamma_2)\Delta x} \times e^{-\gamma_1 (x_{IR} + \Delta x)}}{1 + RC_{\tilde{\varepsilon}}(x_I, x_R, \omega) \times e^{2\gamma_1 \Delta x} \times e^{-2\gamma_1 (x_{IR} + \Delta x)}} \quad ②'$$

which further leads to

$$\gamma_2 \times e^{-\gamma_2 x_T} = \frac{\gamma_1 \times TC_{\tilde{\varepsilon}}(x_I, x_T, \omega) \times e^{-\gamma_1 x_{IR}}}{1 - RC_{\tilde{\varepsilon}}(x_I, x_R, \omega) \times e^{-2\gamma_1 x_{IR}}} \quad ①'$$

$$\gamma_2^2 \times e^{-\gamma_2 x_T} = \gamma_1^2 \times \frac{S_2}{S_1}\frac{\rho_2}{\rho_1}\frac{TC_{\tilde{\varepsilon}}(x_I, x_T, \omega) \times e^{-\gamma_1 x_{IR}}}{1 + RC_{\tilde{\varepsilon}}(x_I, x_R, \omega) \times e^{-2\gamma_1 x_{IR}}} \quad ②'$$

which are exactly the same as Eq. (7.3), which suggests that solving the updated BCs equation (Eq. (7.3')) is actually the same as solving the non-shifted ones, it is thus no surprise that they give the same answers. Till now, we have shown that: in a 2-idetical-material-medium system, if $x_I = x_R$ and $x_T - x_I = constant$, the interface location has no effect on the derivation of γ_1 or γ_2, in fact, we can assume a virtual interface anywhere between the 2 monitoring points. Results yielded by Eq. ②′ were presented in the full *web version*. They show the same trend as those in Fig. 7-10a and Table. 7-3a.

7.4.4 Applying single rod theory to analyse the 2 medium Ti-Ti signals

Though an interface was defined between the 2 mediums, as they share the same material (Ti) and the interface is 'perfect' and 'continuous', wave propagation in these 2 mediums is actually the same as that in a single rod (1.5 m in length), and we can see from Fig. 7-8 that there is no reflection in the 2-medium system. Imagine the incident and transmitted wave are actually the same wave but

monitored at 2 different gauge stations on a 1.5 m long single rod, then single rod theory applies. Use the 2 waves monitored at ($x_{IR} = -500.5\ mm, x_T = +250.5\ mm$) as an example, 2 pulses were first extracted from the incident and transmitted waves respectively (Fig. 7-12). They were then padded with zero to ensure both pulses have the same length and their original phase unchanged.

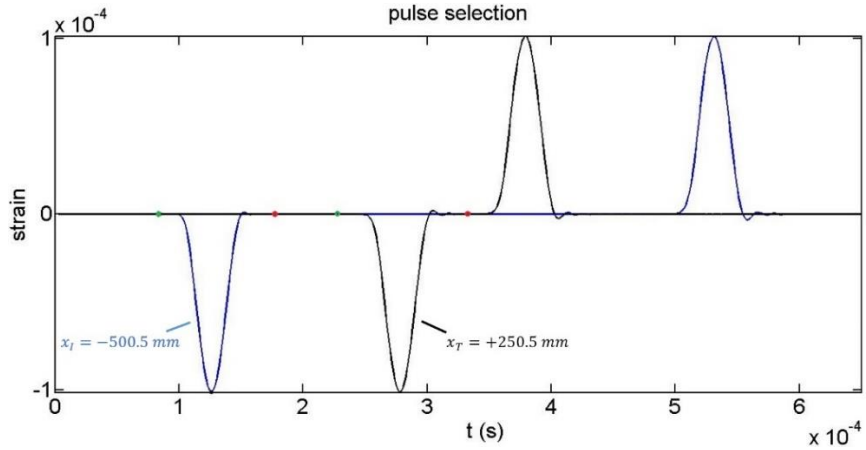
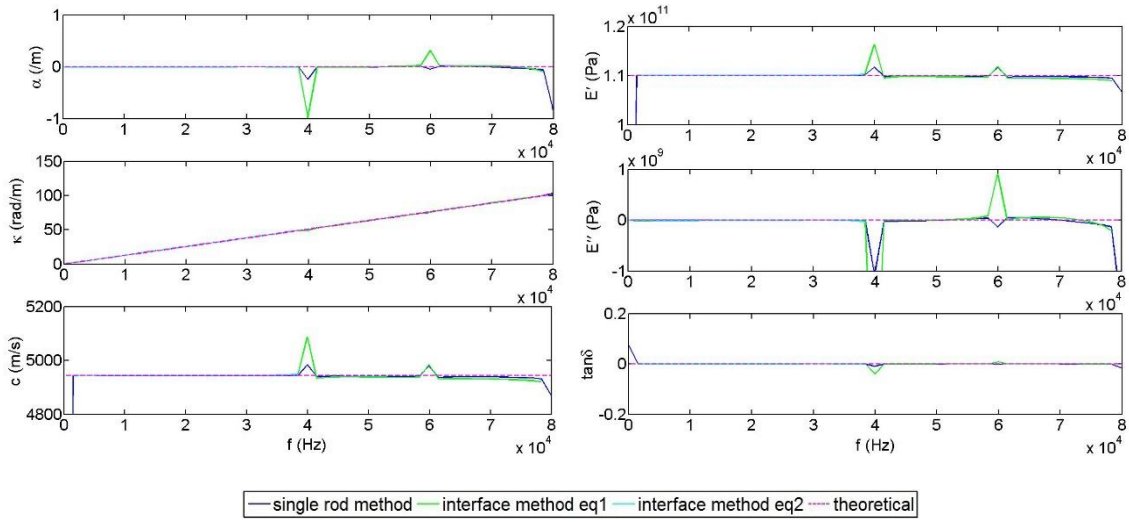


Figure. 7-12 Pulse selection (green dots: start locations; red dots: end locations)

3D dispersion effect was cancelled during FFT using Eq. (7.1). Results derived using single rod theory Eq. (3.2a), Eq. (3.2b) and Eq. (2.29), are shown in Fig. 7-13, from which we see the single rod method yields almost the same results as those by interface analysis technique.



(a) Propagation coefficient and wave speed (b)Modulus and loss factor

Figure. 7-13 Comparison of the results derived by single rod theory and interface analysis technique (Ti-Ti 1 Rod 2 mediums, $x_{IR} = -500.5\ mm, x_T = +250.5\ mm$)

7.5 Ti-Mg 2-medium interface

The second case considered is the Ti-Mg 2-medium interface. The model was defined in a similar approach as the Ti-Ti 2-medium case, *i.e.* two media (Table. 7-3) were defined in a 1.5 m rod, with the incident Ti rod being 1 m and the output Mg rod 0.5 m. The same input acceleration profile (Fig. 7-1) and the same meshing methodology (Fig. 7-2) were employed. Knowing the material properties of the input Ti rod, those of the output Mg rod were to be calculated.

The raw strain signals are shown in Fig. 7-14, and as $Z_1 > Z_2$, the transmitted wave has larger absolute amplitude than the incident wave, and the reflected wave has opposite sign to the incident.

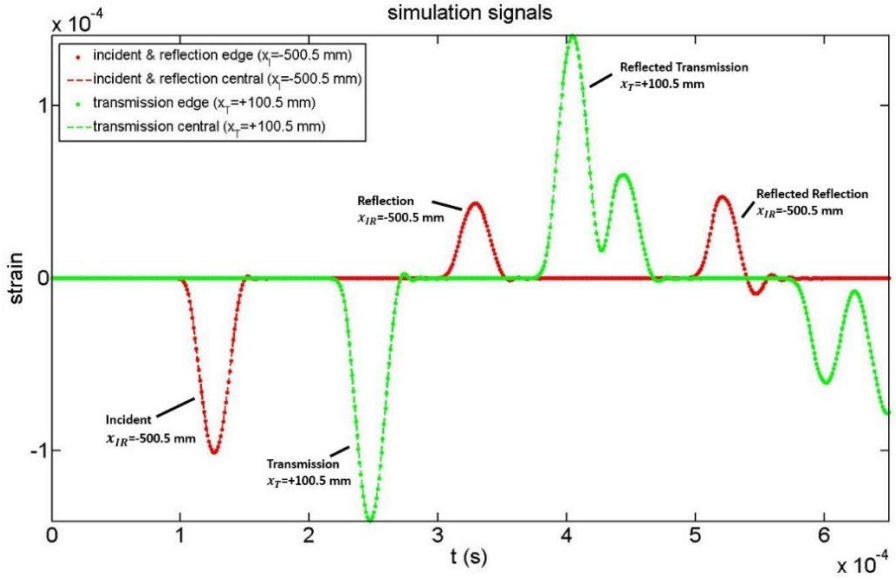
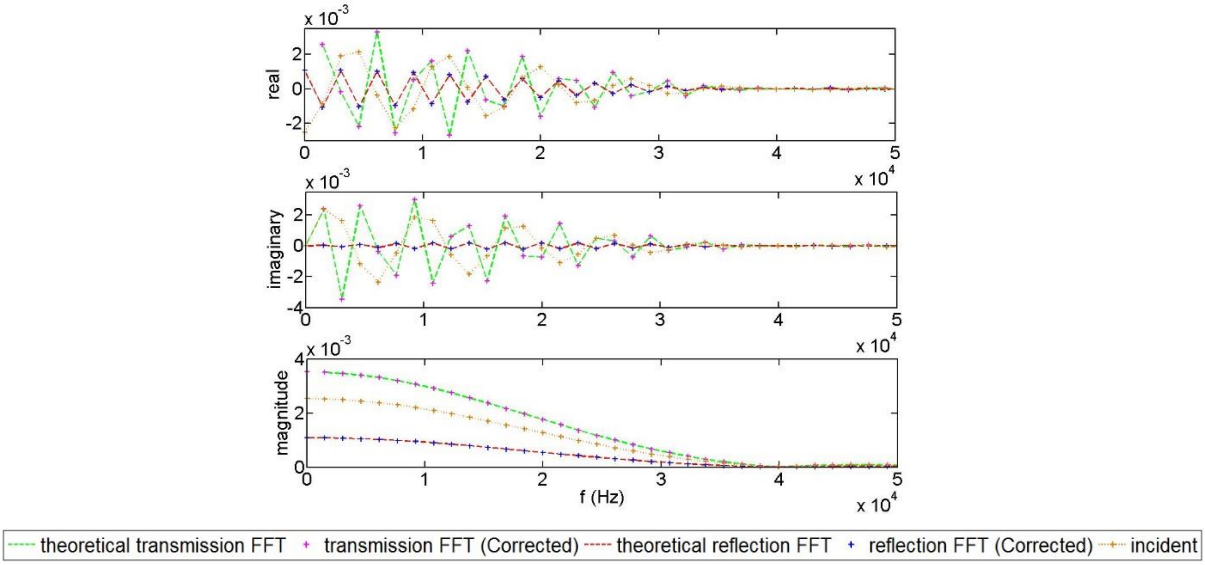


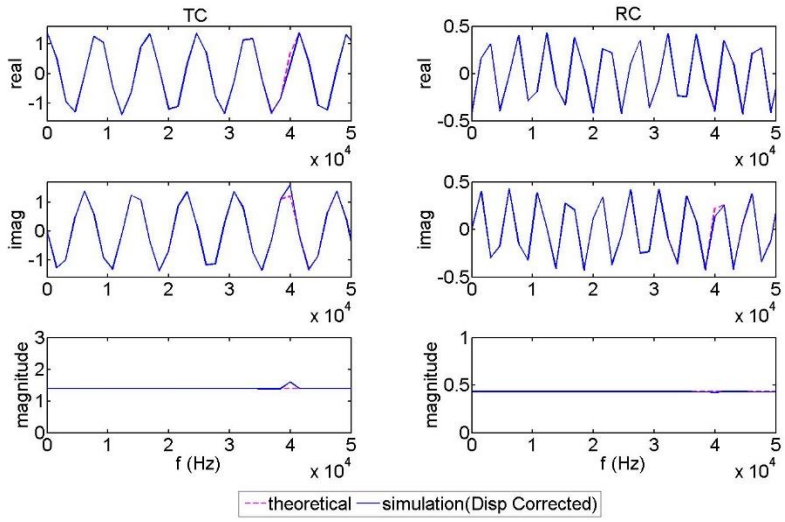
Figure. 7-14 Wave propagation in the Ti-Mg 2 medium system

The three pulses were then extracted and de-noised. FFTs were performed and corrected using the dispersive wave speed profiles shown in previous sections. The theoretical and corrected FFTs are compared in Fig. 7-15(a). In later analysis, only the corrected results were presented.

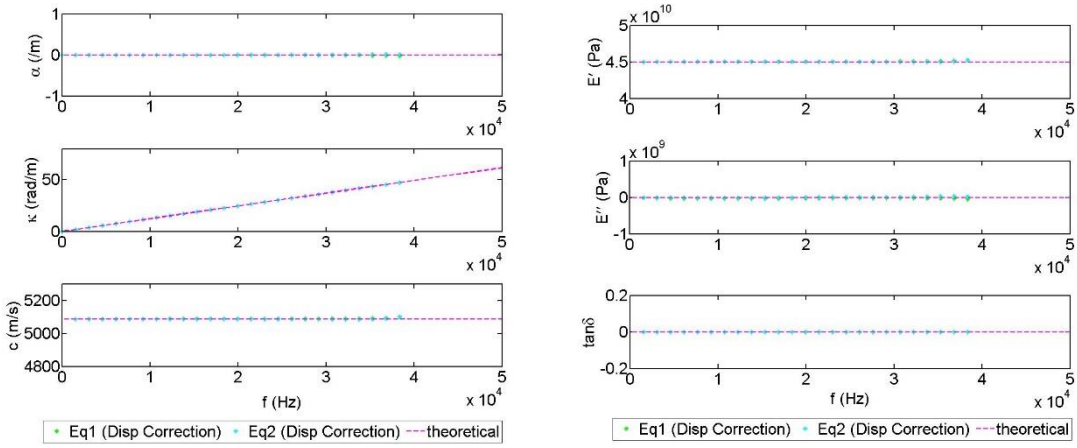
A comparison of the simulation and theoretical $TC_{\tilde{\varepsilon}}$ and $RC_{\tilde{\varepsilon}}$ is shown in Fig. 7-15(b). It is observed that the simulation-based $TC_{\tilde{\varepsilon}}$ and $RC_{\tilde{\varepsilon}}$ agree very well with the theoretical values; the upper frequency limit, is about 40 kHz; periodical critical frequencies, induced by the window function, appear again at an interval of 20 kHz. Again, solving Eq. ①' and ②' yields the material properties for the transmission rod (Fig. 7-15(c) and (d)). It is seen that, the simulation-based results agree very well with the corresponding theoretical values used to define the simulation.



(a) Comparison of theoretical & simulation FFTs with dispersion correction



(b) Comparison of the theoretical and simulation $TC_{\tilde{\varepsilon}}$ & $RC_{\tilde{\varepsilon}}$



(c) Propagation coefficient and wave speed (d)Modulus and loss factor

Figure. 7-15 Data analysis process and derived material properties

(Ti-Mg 1 Rod two media, $x_{IR} = -500.5\ mm, x_T = +100.5\ mm$)

In above analysis, three surface strains, extracted at ($x_{IR} = -500.5\ mm, x_T = +100.5\ mm$), were used; to validate the analysis, we need to make sure uniform deformation was achieved at measurement sections. The cross-sectional deformations in the transmission rod have shown to be uniform in the Ti-Ti two medium system at any location; in a system of two media with different impedances, however, as shown in Fig. 7-16, cross-sectional deformations at locations near interface ($x_T = 0.5$ mm and $x_T = 10.5$ mm) are not the same in the transmission rod: at $x_T = 0.5$ mm, the central strain is smaller than the edge/surface strain, while at $x_T = 10.5$ mm the inverse trend is seen; it becomes uniform after propagating over 50.5 mm. Thus a 'valid' measurement distance for the transmission wave is desired in every contact pair to avoid errors in obtaining the material properties.

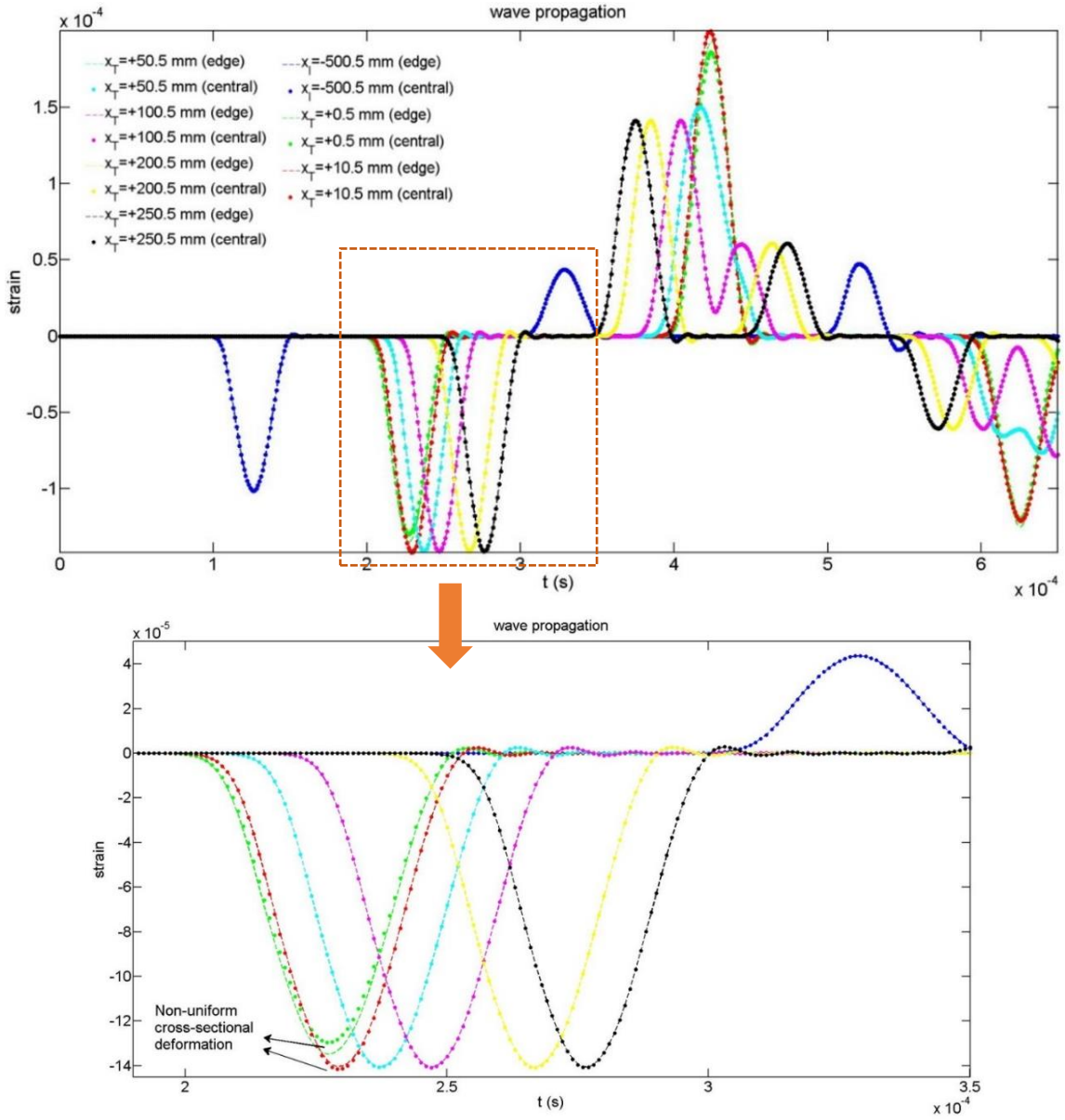


Figure. 7-16 Central & edge stain waves propagting in the Ti-Mg 2 medium system

7.6 Ti-PMMA 2-medium interface

Plastic bars were now introduced. The model was defined similarly to the previous two models (the same geometry, meshing methodology, BCs, and acceleration loading profile), except that viscoelasticity was introduced when defining the material behaviours.

Within the linear viscoelastic region (LVR), the PMMA bar was modelled using the PRONY model. The PRONY constants ($\bar{g}_i, \bar{k}_i, \tau_i$) of a 2-term PRONY model (Fig. 5-11), obtained by fitting the frequency-dependent modulus derived from single rod impact (direct impact) tests at the temperature of 23.4 ℃ within the frequency range 0-20 kHz, were listed in Table 5-3. The material properties adopted in defining the simulation model has previously been summarized in Table. 7-1.

7.6.1 Error analysis

7.6.1.1 Uniformity of cross-sectional deformation

Signals captured at different monitoring locations in the 2-medium system are shown in Fig. 7-17, in which a comparison between the central and edge signals, measured at the same location, were also made. It is found that the incident wave, which was measured at a distance of 499.5 mm from the impact end, is uniform on the Titanium cross-section; in the transmission PMMA rod, however, at locations close to the interface, the deformation across the cross-section is again not uniform, this is especially obvious in the 2 cases $x_T = +0.5\ mm$ and $x_T = +50.5\ mm$: the central transmission wave at $x_T = +0.5\ mm$ has smaller amplitude than the edge one, while at $x_T = +50.5\ mm$ the inverse is true. The largest gap between the central and edge strain amplitudes, appearing at peak values, is 1.304×10^{-4} (49.79% WRT the central strain peak value) and 0.17×10^{-4} (3.98% WRT the edge strain peak value), respectively. This phenomenon is due to the Poisson's effect and it is allieviated when the distance from interface increases as per Saint-Venant's principle. It is seen that the gap between central and edge signals in the transmission rod becomes small after wave propagates over 50.5 mm (the 'valid' transmission measurement distance in this case) from the interface. Note that Titanium has a smaller Poisson's ratio (0.32) than PMMA, and the incident wave has propagated over 499.5 mm in the Ti rod, which explains the good agreement between the incident central and edge signals.

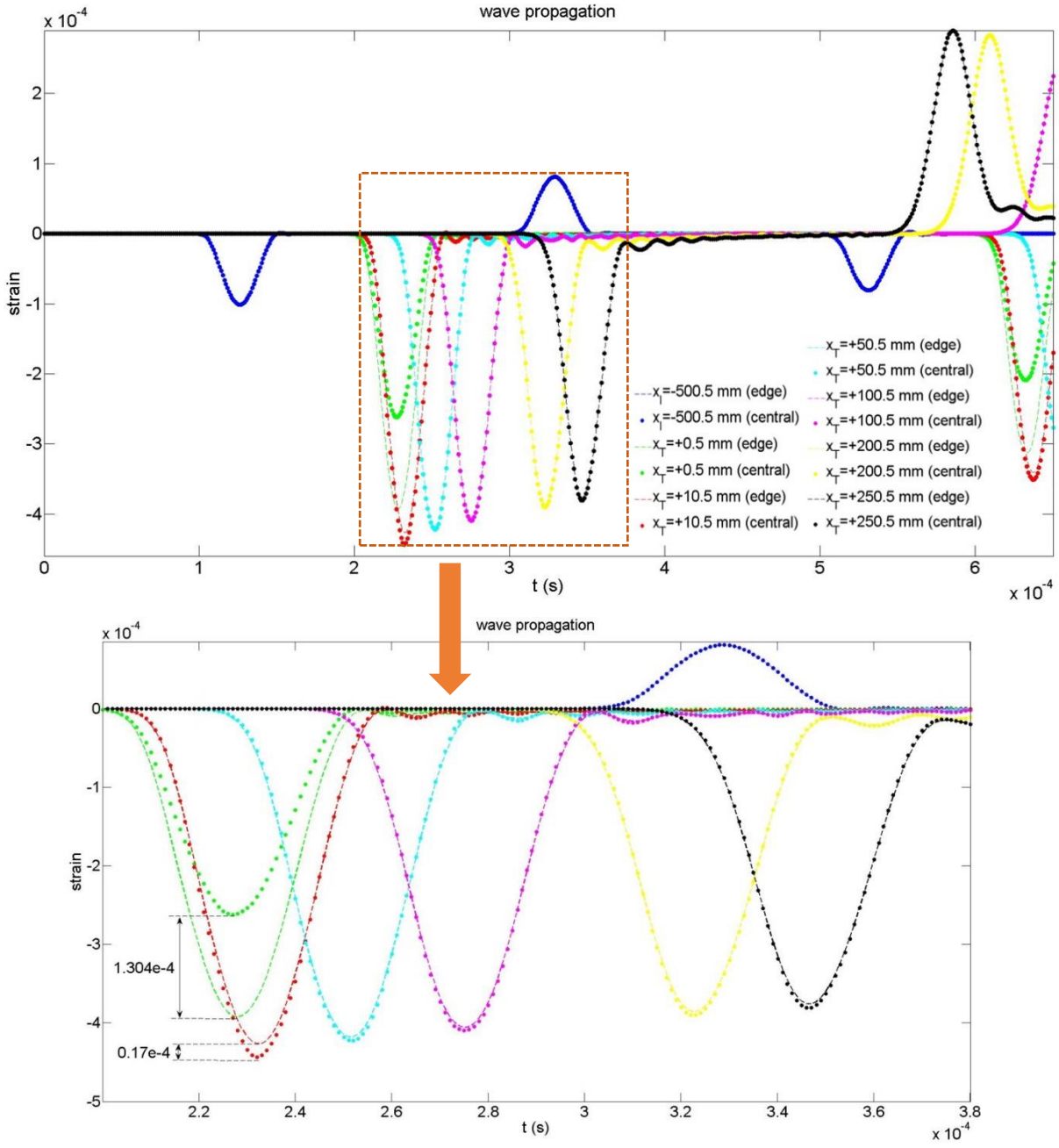
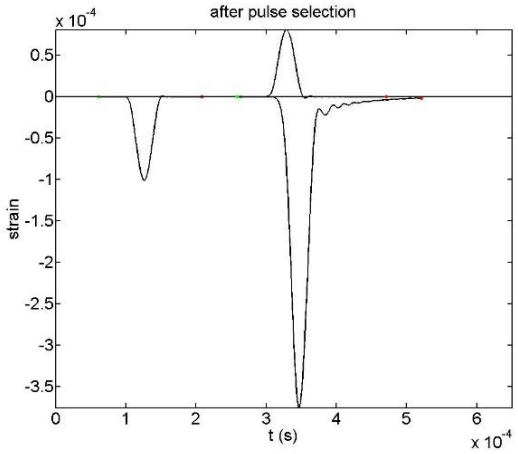
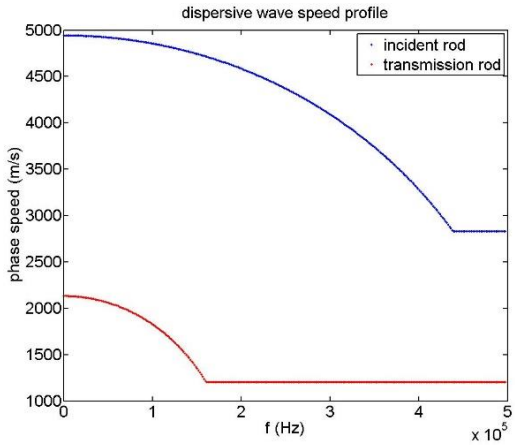


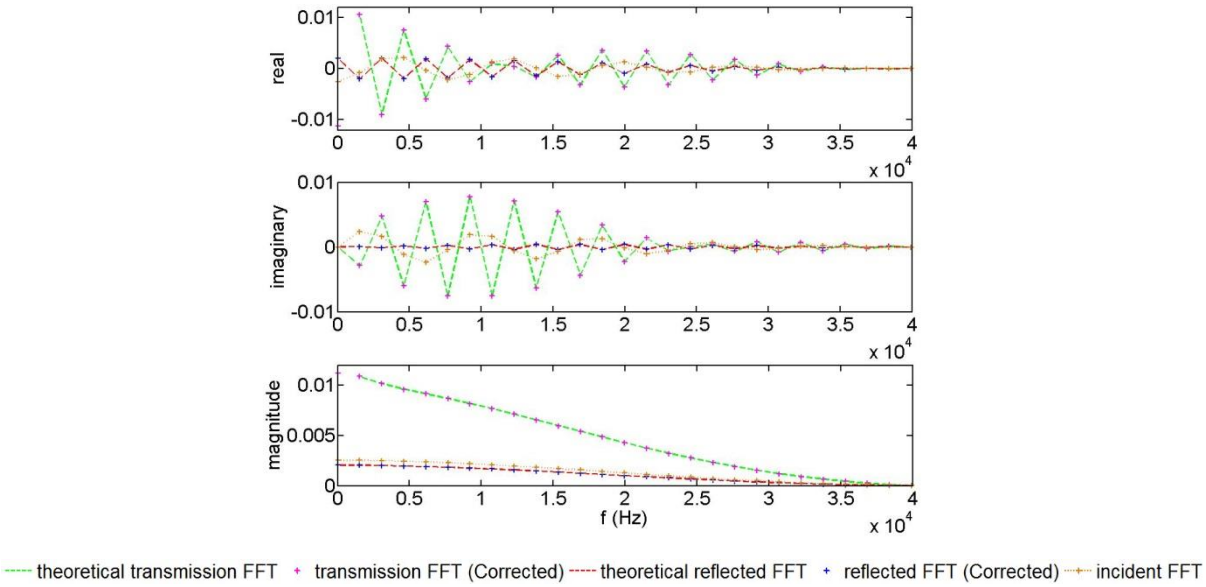
Figure. 7-17 Waves monitored at various positions

Further efforts were made to evaluate the effect of non-uniform cross-sectional deformation on material properties derivation. A typical data analysis example, using the edge signal collected at ($x_{IR} = -500.5\ mm, x_T = +250.5\ mm$), is shown in Fig. 7-18. The raw signals were first de-noised using a 2-layer wavelet-based automatic denoising method ('wden'), their amplitudes were then corrected by subtracting an average of the noise in the region before the incident wave arrives, and a re-sampling process performed with a sampling interval of 1 μs. 3 pulses were selected in Fig. 7-18(a), FFTs (Fig. 7-18(c)) were corrected using dispersive wave speed profiles shown in Fig. 7-18(b).

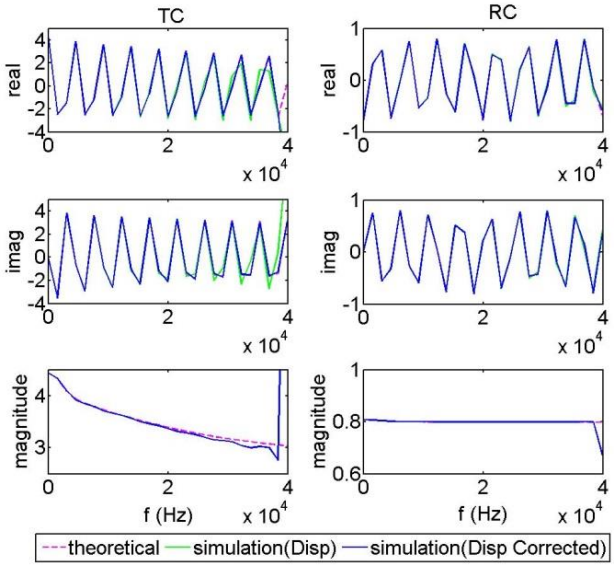




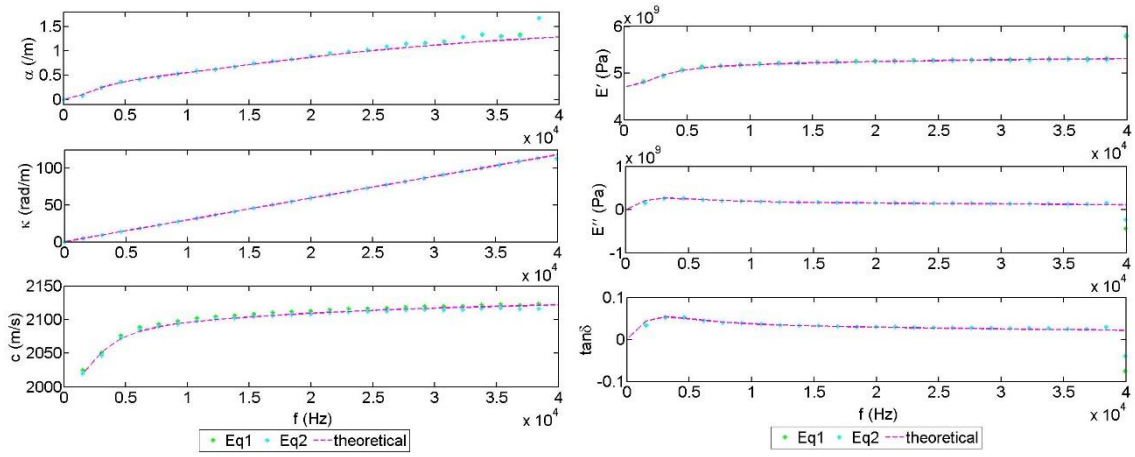
(a)Pulse selection (b)Dispersive wave speed profiles (using Table. 7-1)



(c) Comparison of theoretical & simulation FFTs with dispersion correction



(d) A comparison of the theoretical and simulation $TC_{\tilde{\varepsilon}}$ & $RC_{\tilde{\varepsilon}}$



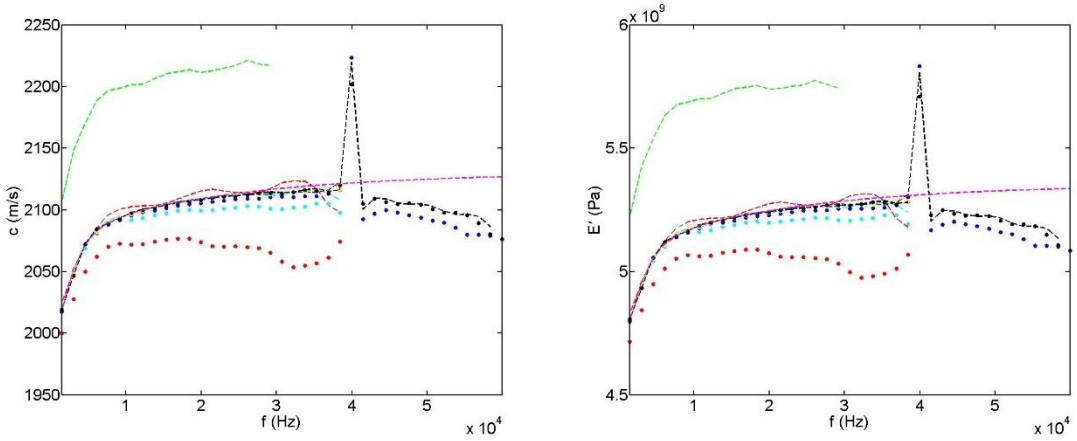
(e) Propagation coefficient and wave speed (f)Modulus and loss factor

Figure. 7-18 Data analysis process and derived material properties

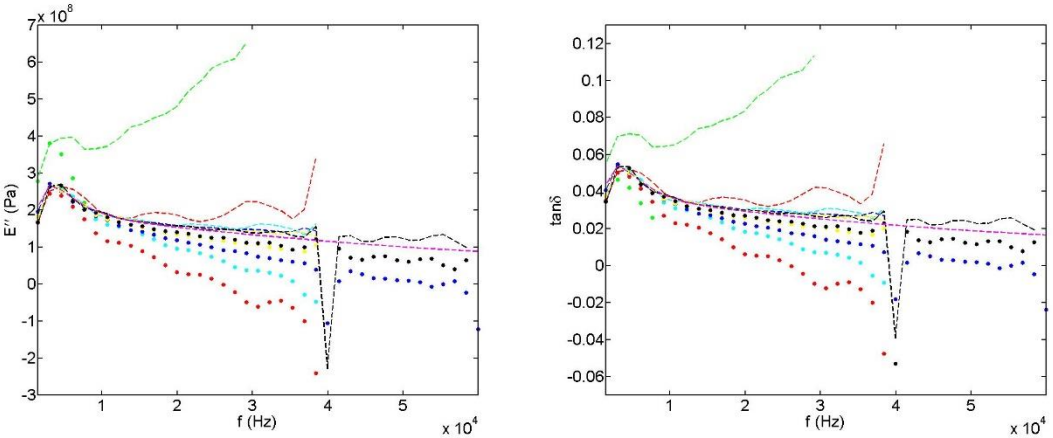
(Ti-PMMA 1 Rod 2 mediums, $x_{IR} = -500.5\ mm, x_T = +250.5\ mm$)

A comparison of the theoretical TC and RC values with the corresponding simulation corrected ones was made in Fig. 7-18(c) and (d). Finally, the corrected TC and RC were substituted into Eq. ①′ and Eq. ②′ to yield the material properties in Fig. 7-18(e) and (f). It is seen from Fig. 7-18(c) that, the reflected FFT magnitudes are quite close to the incident ones, while the transmission magnitudes are much larger. This indicates that little energy goes to the transmission wave, but it induces large deformation in the low modulus PMMA rod, this is also observed in the time domain signal in Fig. 7-17, thus the interface constraint the PMMA rod poses to the Ti rod is more like a relatively loosen constraint, according to our discussions in 7.3.2, the transmission strain possesses the same sign as incident, but larger amplitudes as well; the reflected wave has opposite sign and smaller amplitudes. Analysis was repeated on central and edge signals recorded at other 5 positions: $x_T = +0.5\ mm, +10.5\ mm, +50.5mm, +100.5\ mm, +200.5\ m$. In total, 12 cases were analysed using the same edge incident wave ($x_{IR} = -500.5\ mm$). The resulting material properties are shown in Fig. 7-19, we can conclude that: the results derived from edge signals generally show less disparity while those from center deviate more from the corresponding theoretical results. In particular, the deviation increases as the monitoring location becomes closer to interface. Further, within the 'valid' frequency range 0~30 kHz (where FFT magnitudes are identifiable), the central signal-based attenuation coefficient α, phase speed c, storage modulus E', loss modulus E'', and loss factor $tan\delta$ are generally smaller than the theoretical ones, while the wavenumber κ is slightly larger. Based on

these observations, signals measured at a distant location from the interface are encouraged; if the monitoring point is within a 'sensitive' distance (*e.g.* 50.5 mm~250.5 mm as shown in this case), then edge signals give results closer to the theoretical ones. In this case, with the configuration of a 1 m long 13 mm diameter rod, the material properties defined in Table. 7-1, and an instant strain amplitude of around 5×10^{-4}, the 'trustful' strain measurement distance without appreciable errors induced by non-uniform cross-sectional deformation shall be larger than 250.5 mm. However, the edge signals within the 'sensitive' distance 50.5 mm~250.5 mm already give very accurate results.



(a) storage modulus



(b) loss modulus

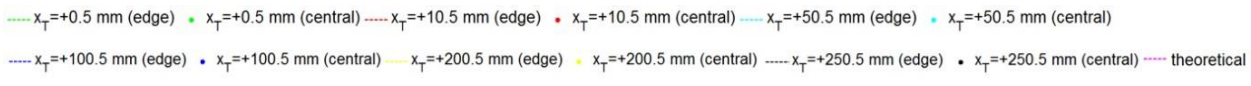


Figure. 7-19 Comparison of material properties derived using central & edge transmission signals extracted at 6 positions (Results based on Eq. ②′)

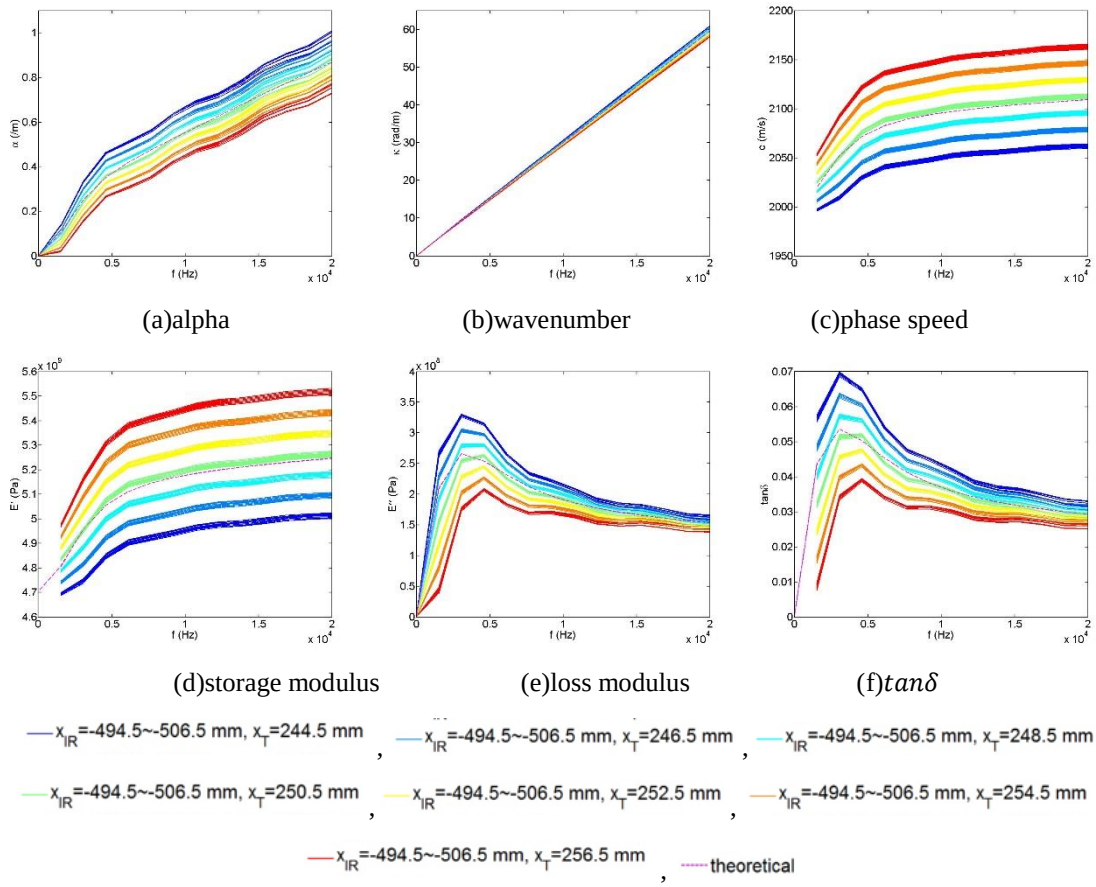
A further examination using Eq. ①′ (presented in full *web version*) draws similar conclusions: the longer the distance, the more stable and accurate the results become. The same trend is also seen in

energy dissipation components (attenuation coefficient α, loss modulus E' and loss factor $tan\delta$). The disparities and similarities of Eq. ①′ and Eq. ②′, accordingly their advantages and disadvantages (*e.g.* in which situation they are to be used), were discussed in the full *web version*.

7.6.1.2 Sensitivity of the interface analysis technique to errors in x_{IR} and x_T

Use the edge signals collected at ($x_{IR} = -500.5\ mm, x_T = 250.5\ mm$) as an example, similar to the Ti-Ti case, errors were introduced by adding variations to both values step by step, the testing scheme is the same as Table. 7-2. Note that all the cases in Table. 7-2 share the same selected pulses; only the measurement distances x_{IR} and x_T are varied. With a step of 2 mm, the incident monitoring distance x_{IR} increases from 494.5 mm to 506.5 mm, and the transmission monitoring distance x_T changes from 244.5 mm to 256.5 mm. The resulting material properties are shown in Fig. 7-20, and a quantitative error evaluation at 20 kHz in Table. 7-4 (NB: the relative error is defined WRT corresponding theoretical value). In Fig. 7-20, the results from a given x_T value are denoted by the same color, and each color group contains of 7 cases where x_{IR} varies from -244.5 mm to 256.5 mm. It is seen that, variation in x_T has the dominant influence on the resulting material properties: although at the frequency of 20 kHz, less than 5% error in all the 6 quantities was observed for a step of 2 mm variation in x_T, they are a decade larger than that induced by the same amount of variation in x_{IR}. This seems reasonable as wave propagating in the incident Ti rod does not attenuate, although the value of x_{IR} may affect the solution, the transmission rod properties primarily depend on x_T.

While the standard (real) monitoring distance group ($x_{IR} = -500.5\ mm, x_T = 250.5\ mm$) yields results closest to the given values, those with x_T larger or smaller than 250.5 mm distributes monotonously along both sides of the standard group. Specifically, a smaller x_T results in larger values in the energy dissipation components (*i.e.* the attenuation coefficient α, the loss modulus E'' and loss factor $tan\delta$) and the spatial frequency κ, but yields smaller phase speed c and storage modulus E'. This is because the energy dissipated, indicated by the magnitudes, is fixed, decreasing x_T could amplify the energy dissipation capacity (α, E'' and $tan\delta$) and the number of wave circles within the distance (κ), meanwhile, as the travel distance decreases, wave speed drops as well.



(a)alpha (b)wavenumber (c)phase speed

(d)storage modulus (e)loss modulus (f)$tan\delta$

Figure. 7-20 Material properties yielded using the testing scheme in Table. 7-2 (Results based on Eq. ①′)

Table. 7-4 Errors at 20 kHz induced by a step of 2 mm in x_{IR} or x_T (Results based on Eq. ①′)

	Error	α (/m)	κ (rad/s)	c (m/s)	E' (GPa)	E'' (GPa)	$tan\delta$
$x_{IR} = -500.5\ mm, x_T = 244.5{\sim}256.5\ mm$	Absolute	0.039	0.475	16.88	0.0844	0.00314	0.001
	Relative	4.49%	0.8%	0.8%	1.6%	2%	3.68%
$x_{IR} = -494.5{\sim} -506.5\ mm, x_T = 250.5\ mm$	Absolute	5×10^{-4}	0.023	0.811	0.00404	0.00083	6×10^{-6}
	Relative	0.057%	0.0383%	0.0384%	0.077%	0.0542%	0.02%

Sensitivity analysis here demonstrates the reliability of the interface analysis technique: it is sensible enough to detect small error contained in measurement distances, and to identify the corresponding variations in material properties. However, this also pose a challenge when this technique is to be used in real applications: the measurement distances have to be accurately measured to the order of mm. For example, comparing the results of the 2 cases ($x_{IR} = -500.5\ mm, x_T = 250.5\ mm$) and ($x_{IR} = -500.5\ mm, x_T = 244.5\ mm$) at f=20 *kHz*, in which x_{IR} stays the same while x_T is decreased by 6 mm, α increases from the theoretical 0.8686 /m to 1.007 /m (16%), κ increases from the theoretical 59.485 rad/m to 60.849 rad/m (2.3%), c drops from the theoretical 2109 m/s to 2062

m/s (2.2%), E' decreases from the theoretical 5.247 GPa to 5.013 GPa (4.5%), E'' increases from the theoretical 0.1533 GPa to 0.166 GPa (8.4%), $tan\delta$ increases from the theoretical 0.02921 to 0.03312 (13.4%). Thus, a calibration process is essential to accurately locate x_{IR} and x_T in practice. Again, the results for Eq. ②′, which somewhat diverge from Eq. ①′, are presented in the full *web version*. Both equations show the same sensible error effect, *i.e.* within the frequency range 0~20 kHz, with the increment of distance error, the derived material properties deviate further, and the desired distance group ($x_{IR} = -500.5\ mm, x_T = 250.5\ mm$) does give the most accurate results.

7.6.2 Noise study

Numerical noise seen in finite elements simulations is often induced by improper model definition such as a bad meshing methodology or lack of calculation precision. These noises can be minimized if the model has been properly set up, and thus the signals can be considered relatively 'clean' as seen in Fig. 7-17. Experimental noises, however, always exist and are unavoidable. For example, current noise is a typical background noise which can be considered as a type of additive white Gaussian noise (AWGN, an additive noise which has a constant and uniform PSD across the frequency band and its amplitudes conform to Gaussian distribution), it exists regardless of the appearance of signal. Other noises such as those induced by misalignment can also occur in an experiment. Simulations facilitate the generation of relatively 'clean' signal on which noise can be added to evaluate their effect on material properties derivation. Similar to single rod noise studies (**5.3.3**), both artificial (AWGN) and experimentally collected noises were introduced and defined both globally and locally. Artificial noises were moderated to 2 levels (10 dB and 20 dB), while the experimental noise was set on a similar level that occurs in a real experiment in which it was measured. With the interference of noises, the ability of the interface analysis technique to identify 'real' material properties was examined.

7.6.2.1 Generating of noise

(1) AWGN noise generating

The relative weight of signal to noise can be measured by the signal-to-noise ratio (SNR) which can be either defined in time or frequency domain (Eq. (5.1~5.4)). The most commonly used one, of

course, is the time domain SNR, but frequency domain SNR is of use when attentions are attracted to individual frequency components, this is especially the case considering a uniform frequency domain SNR across all frequency components can be easily achieved just by amplifying the time domain signal by $\frac{1}{\sqrt{SNR}}$ times (Eq. (5.6)). However, this is not exactly true as noises always come randomly, thus only the more practical time domain SNR was adopted in all our later trials.

It is convenient to generate a normally distributed random noise X'' ($\overline{x''} = 0, \delta_{x''} = 1$) using Matlab function 'randn', and it serves as the base noise on which the desired AWGN noise can be generated

$$X' = \sqrt{P_{noise}} X'' = \sqrt{\frac{\frac{\sum_{i=1}^{N} x_i^2}{N}}{10^{\frac{SNR_{dB}}{10}}}} X'' \qquad \text{Eq. (5.7)}$$

where x_i is the discrete amplitude, P_{noise} the power of noise, and N the length of the signal.

A time domain signal is mainly (if not uniquely) characterized by its mean and variance. However, it should be noticed that a random signal can come in different forms even with the same mean and variance values (which addresses the use of frequency domain SNR). In the following analysis, the same base noise X'', which has the same length N as the signal, has been adopted in generating noises with different SNR_{dB} levels.

(2) Extraction of experimental noise

The experimental noise was extracted from the recording of a modified SHPB interface test (Fig. 7-21), in which a 12.70 mm diameter and 25 mm long Titanium cylinder projectile, a 12.70 mm diameter and 1000 mm long Titanium incident rod, and a 13 mm diameter and 500 mm long PMMA rod were employed, no specimen was inserted. The test temperature is around 20.8 ℃. Gas pressure is around 0.15 bar, which produces a peak strain of 2.416×10^{-4} at $x_T = +50\,mm$ in the transmission PMMA rod. A noise segment was extracted in the region before the wave arrives and it can be considered as a pure additive background noise. The segment was then duplicated to have the same length as the original experimental signal, based on which the 'real' experimental SNR was calculated. The noise segment that serves as a base noise was then assembled into the simulation signal, during which it was modulated on globally and locally using the 'real' calculated experimental SNR.

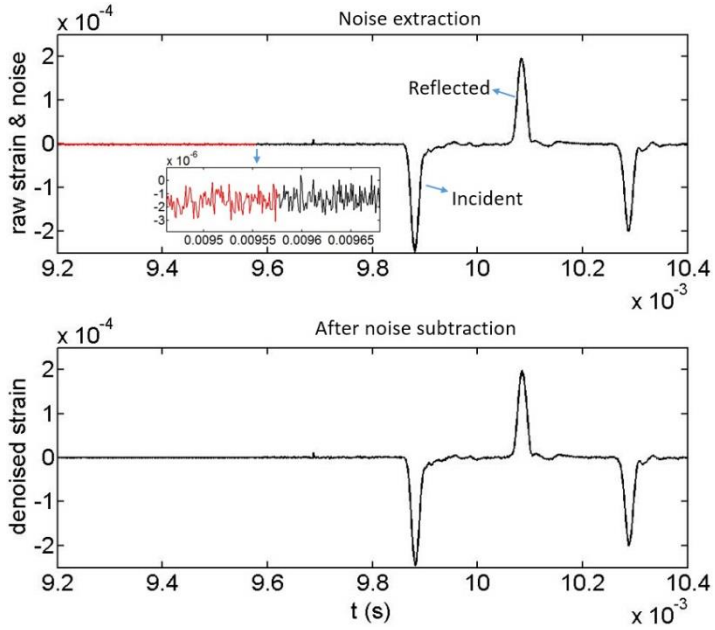


Figure. 7-21 Experimental noise extraction

7.6.2.2 Effect of noise on material property derivation

As proposed before, both artificially generated noise, *i.e.* the additive white Gaussian noise (AWGN) and the experimentally collected noise, were applied to the same 'clean' simulation strain signal extracted at edge ($x_{IR} = -500.5\,mm, x_T = 250.5\,mm$) in Fig. 7-18(a). In the AWGN noise analysis, two SNR levels, *i.e.* 10 dB and 20 dB (the signal power is 10 and 20 times that of noise according to Eq. (5.2)), were used in modulation. For each level, noises were generated in two approaches, *i.e.* the globally controlled SNR case where the three simulation pulses share the same noise which was modulated using the powers of incident and reflected waves; and the locally controlled SNR case where noises were generated separately based on the power of each individual pulse. In the experimental noise analysis, the SNR was fixed (calculated based on real experimental signals from which the noise segment was extracted), and but again used globally and locally. The global SNR is closer to real practice because in real experiments all pulses are subjected to the same background noise. The meaning of adopting local SNR is that it ensures a constant and uniform SNR for every individual pulse contained in the signal.

Here the experimental noise study was presented. For AWGN-based noise analysis, please refer to the full *web version*.

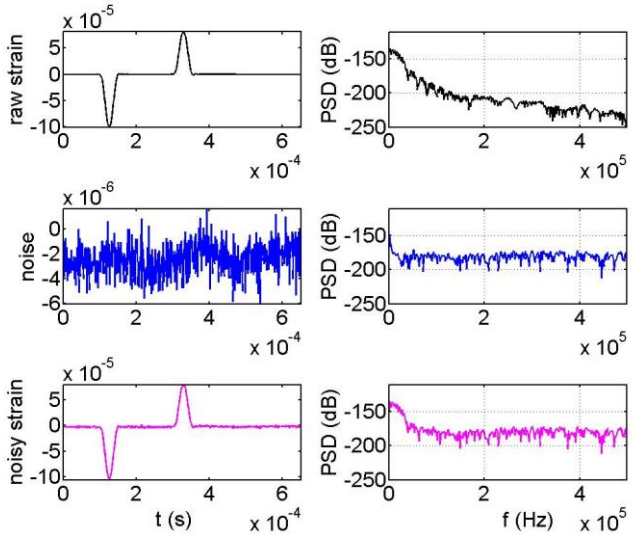
Experimental noise analysis

The experimental noise was defined in two approaches: the global method refers to control SNR_{dB} based on the overall signal energy while the local method defines SNR_{dB} based on each individual pulse.

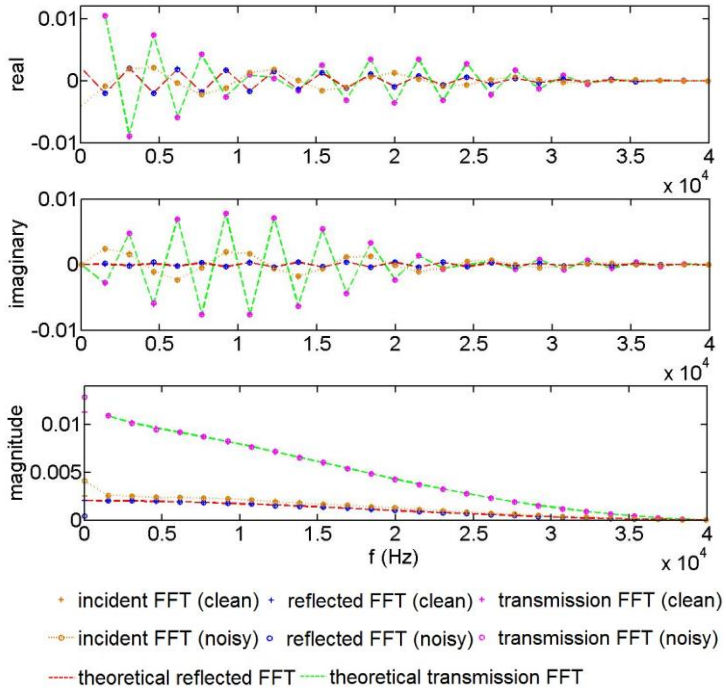
The signal being tested is the one in Fig. 7-17, in which the simulation model was defined using the PMMA single rod impact data collected at 23.4 ℃, and a sine acceleration profile with peak value of $3.14 \times 10^4\ m/s^2$ was adopted, which generated a peak strain of 4.177×10^{-4} at $x_T = +50.5\ mm$ in the transmission PMMA rod. It is thus seen that the deformation yielded in the pendulum test is of the same order as that yielded in the modified SHPB interface test. This makes sense when the noise extracted from the modified SHPB test recording was added to the simulation strain signal (although we can always use modulation to accommodate noise). We can see from Fig. 7-21 that, the experimental strain noise is in the order of 10^{-6} while the simulation stain in Fig. 7-17 is in the order of 10^{-4}. Of course, an ideal case is to concurrently collect the simulation input and noise from the same interface impact event, but we can modulate the base noise to achieve any SNR. However, an examination at the experimental interface signal can give us a clue about what the real SNR value would be in a real interface test. Using the incident measured signals (Fig. 7-21), the current noise, which is considered as pure random AWGN, was extracted in the region before the incident pulse arrives. After the 'pure noise' segment was extracted, it was duplicated to generate an 'extended' noise which has the same length as the raw noisy signal (assuming over the measurement time span the noise doesn't vary much), then the whole signal was subtracted by the noise to yield 'clean' experimental signal, and finally the time domain SNR_{dB} was calculated to be 18.13 dB using Eq. (5.2). In following analysis, only the globally assigned noise case was presented; for the local one, readers can refer to the full *web version*.

Note that, the global SNR was controlled based on incident and reflected simulation pulses, the transmission pulse was excluded when modulating the noise because the experimental SNR (18.13) was also evaluated based on a summation of the incident and reflected wave powers. This is reasonable as incident and reflected waves, from which the noise was extracted, were recorded at the

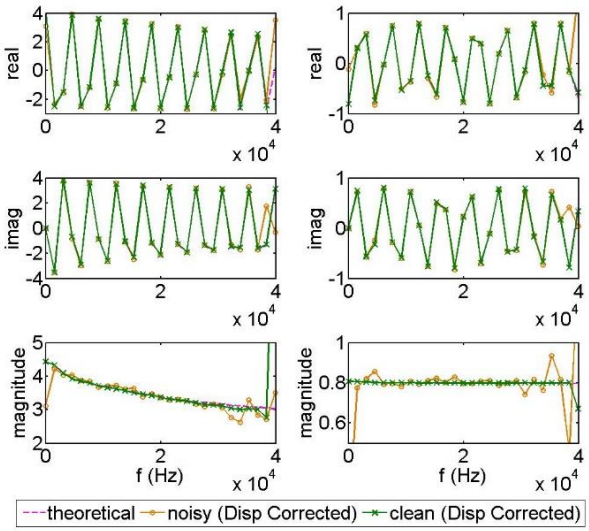
same gauge station ($x_{IR} = -500\,mm$), thus the way of generating new noise is expected to be parallel and consistent to that of noise extraction. The incident and reflected signals, before and after adding noise, were show in Fig. 7-22(a). Again, it is found that, noise doesn't weight much in the low frequency region where the signal dominates, but it improves the PSDs in high frequency area (>40 kHz). In Fig. 7-22(b), both the clean and noisy FFTs agree reasonably well with the theoretical ones within the frequency range 0~40 kHz, which guarantees a relatively good fitting between the TCs and RCs (Fig. 7-22(c)), and small disparities in material properties (Fig. 7-22(d) and (e)).



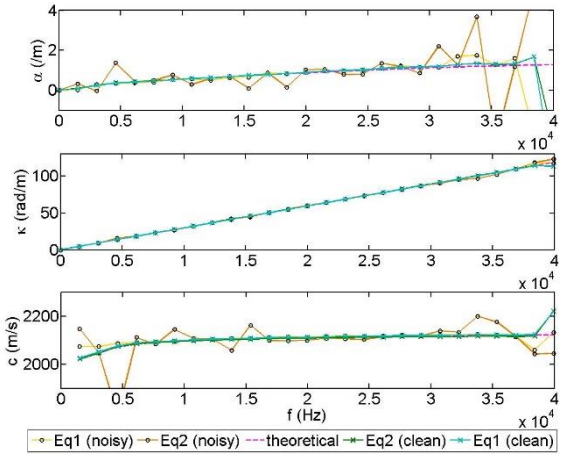
(a)Welch PSDs



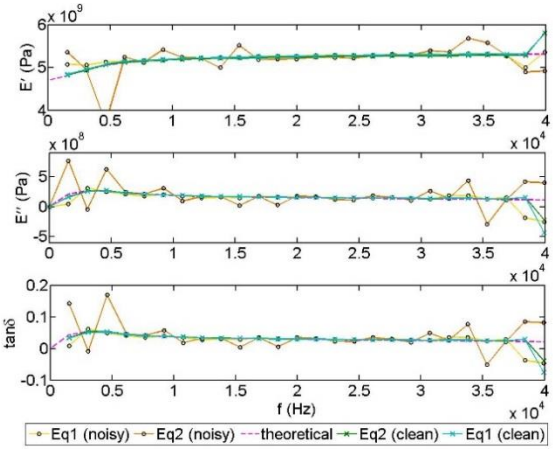
(b)Comparison of theoretical & noisy simulation FFTs with dispersion correction



(c)A comparison of the theoretical and noisy simulation $TC_{\tilde{\varepsilon}}$ & $RC_{\tilde{\varepsilon}}$



(d)Propagation coefficient and wave speed



(e)Modulus and loss factor

Figure. 7-22 Data analysis process and derived material properties

(Ti-PMMA 1 Rod 2 mediums, $x_{IR} = -500.5\ mm, x_T = +250.5\ mm,\ \ global\ experimental\ SNR_{dB} = 18.13$)

All in all, the Ti-PMMA noise analysis demonstrates that: with the interference of real experimental level noise, the interface analysis method is robust; in particular, Eq. ①′ generally yields less deviating results when resolving for γ_2, which is consistent with our previous analytical prediction.

7.7 PMMA-Mg 2-medium interface

In the previous three cases, metal incident rods were used, and Eq. ①' and Eq. ②' were used to resolve γ_2. Now a plastic PMMA is used as the incident rod and the data are solved for γ_1.

The simulation was defined similarly as previous cases (the same meshing methodology, BCs, and loading acceleration profile) except that the length of the transmission Mg rod was extended to 1 m,

as it is found that using the same input ($a(t) = A\omega\sin(\omega t)$, with $A = 0.25$ and $\omega = 2\pi \times 20000\, rad/s$) and identical configuration ($1\, m\emptyset 13\, mm$ incident rod and $0.5\, m\emptyset 13\, mm$ transmission rod), during its propagation the incident pulse was extensively elongated due to the viscoelastic dispersive nature of the PMMA incident bar, which results in severe overlapping in the transmission wave even at the contact interface. An alternative approach dealing with overlapping could be shortening the duration of incident pulse, however, this would also modify the frequency contents as well.

Simulation outputs are shown in Fig. 7-23. It is seen that: 1) both the reflected and transmitted waves are compressive, which is consistent with theoretical evidence: both $TC_{\tilde{\varepsilon}|x_I=x_T=0}$ and $RC_{\tilde{\varepsilon}|x_I=x_T=0}$ are positive, which indicates the 3 waves should have the same sign; 2) the incident and reflected deformations are almost uniform across the section, while the transmission deformation becomes uniform after propagating over 50.5 mm; 3) high frequency oscillations, as a result of dispersion in the incident bar, are observed, and the viscoelasticity generates tails that extend the wave duration.

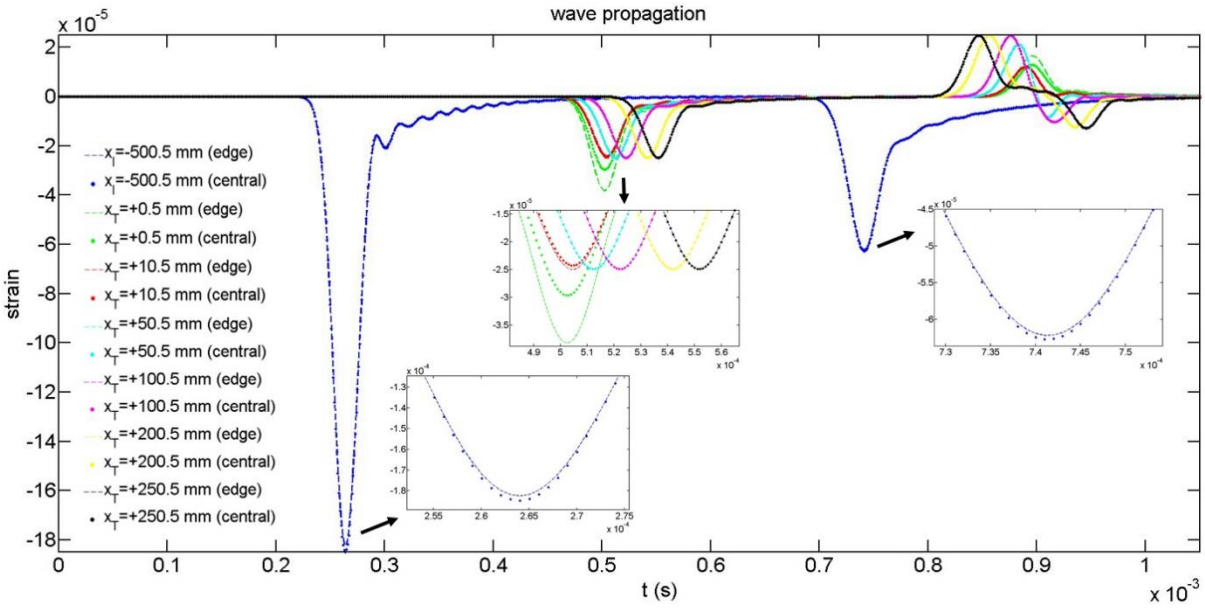
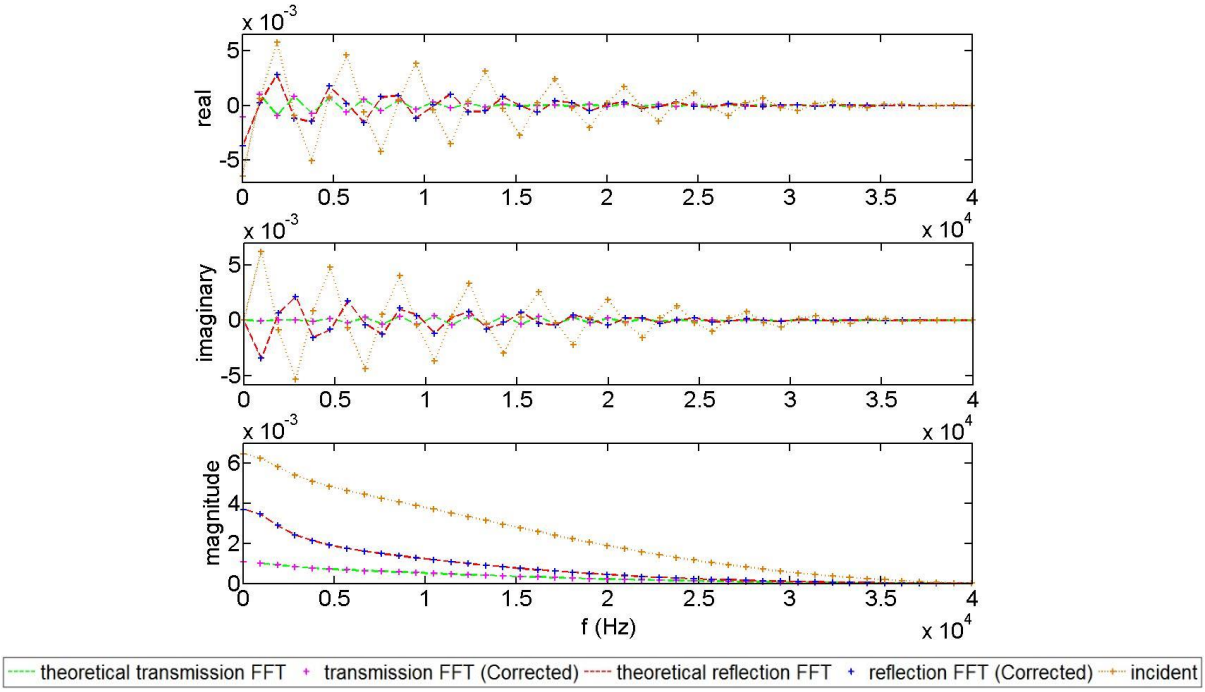


Figure. 7-23 Wave propagation in the PMMA-Mg 2 medium system

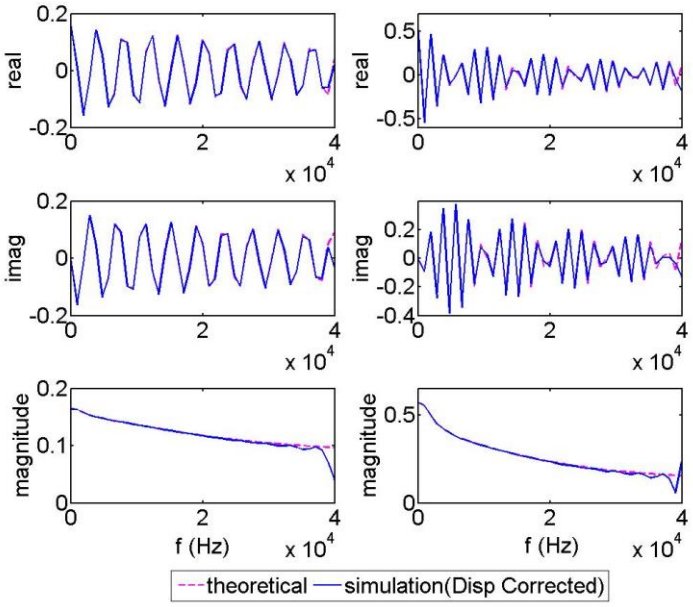
The 3 pulses, extracted at ($x_{IR} = -500.5\, mm, x_T = +50.5\, mm$), were analysed. The dispersion corrected Fourier transforms are shown in Fig. 7-24(a), and a comparison of the simulation-based and corresponding theoretical $TC_{\tilde{\varepsilon}}$ and $RC_{\tilde{\varepsilon}}$ values in Fig. 7-24(b). It is seen that all simulation-based values match well with the corresponding theoretical ones, disparities appear in relatively high

frequency region (*e.g.* >30 kHz) where the Fourier magnitudes become small and we perceive little information was carried beyond this upper frequency bound.

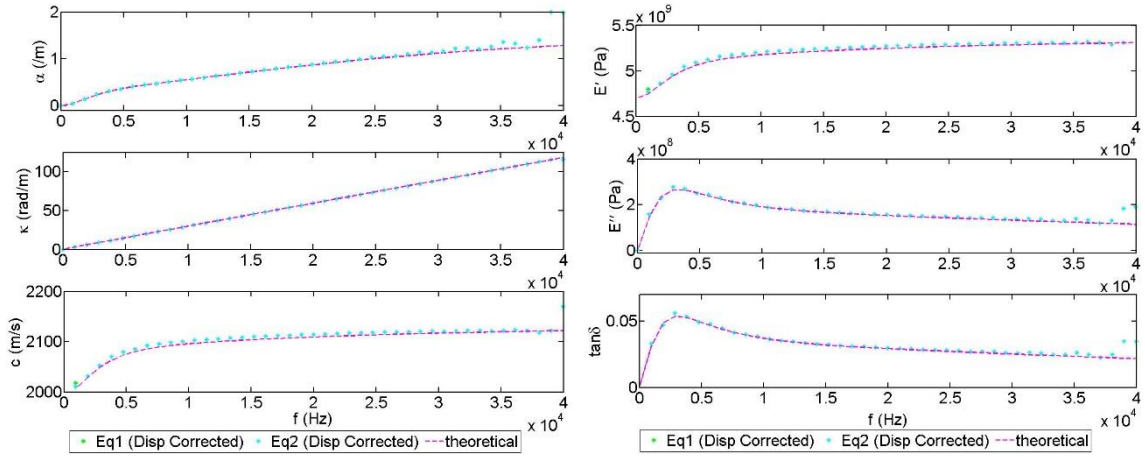
When solving Eq. ①′ and ②′, a rigorous results selection criteria was introduced. Unlike the previous cases in which only a rough search area was employed when seeking solutions for (α, κ), reinforced constrained search was used as multiple solution pairs exist even in a small searching area. Specifically, the rectangular searching area for the propagation coefficient of PMMA has first narrowed down from the previous $[-5-\left(\frac{\omega}{c_0}-5\right)i, 5-(\frac{\omega}{c_0}+5)i]$ to $[-2-\left(\frac{\omega}{c_0}-2\right)i, 2-(\frac{\omega}{c_0}+2)i]$. The updated search area was used in both the 'vpasolve' (a Matlab built-in numerical solver) method and the user-defined 'minimum error' method (in which the solution was defined as the one minimizing the errors between both sides of the target equation). The 'minimum error' was further featured by a rigorous solution selection process that helps hunt the unique desired solution: within a certain searching area, a potential solution pool was first selected, those prospective solutions were then examined with the rule that α and κ should keep increasing with frequency, finally the one that balance the equations best was chosen, as shown in Fig. 7-24(c) and (d). The solving process ensures that these results are 'mathematically' reasonable within the pre-fixed searching area, while Fig. 7-24(c) and (d) confirms that they are also theoretically correct.



(a) Comparison of theoretical & simulation FFTs after dispersion correction



(b) Comparison of the theoretical and simulation $TC_{\tilde{\varepsilon}}$ & $RC_{\tilde{\varepsilon}}$



(c) Propagation coefficient and wave speed (d)Modulus and loss factor

Figure. 7-24 Data analysis process and derived material properties

(PMMA-Mg 1 Rod 2 mediums, $x_{IR} = -500.5\ mm, x_T = +50.5\ mm$)

7.8 Summary of 2-medium interface simulations

In total four 'ideal' interface cases have been studied via simulation and numerical approaches: Ti-Ti, Ti-Mg, Ti-PMMA, PMMA-Mg. In the first three cases, efforts were resorted to solve for the material properties of the transmission rod; in the PMMA-Mg case, the incident rod properties were derived with more strict constrains. The detailed analysis procedure was presented in each case. Two types of error analysis that affect the results derivation were analysed: the non-uniformity of cross-sectional deformation and inaccurate measurement locations. Also, in the Ti-Ti case, the necessity of dispersion correction was addressed, and single rod analysis technique was applied as comparison.

The uniformity of cross-sectional deformation, especially in the transmission rod, was discussed throughout all four cases by comparing the central and edge raw signals in time domain. Generally, it is observed that the difference between central and edge signals in the transmission rod becomes insignificant after the transmission wave propagates over a 'valid' transmission measurement distance from interface (50.5 mm for metal rods and 250.5 mm for PMMA). Particularly, the Ti-PMMA case concludes that disparities increase when the x_T gets closer to interface as the cross-sectional deformation becomes more non-uniform, thus strain signals measured at a distant location from the disturbance are recommended where possible; a safe transmission measurement distance in the Ti-PMMA setup is 250.5 mm, within a 'sensitive' transmission wave measurement distance (50.5 mm~250.5 mm in this case), edge signals are suggested to be used to target more accurate results.

The sensitivity of the interface analysis technique to errors contained in x_{IR} and x_T were investigated in two cases: Ti-Ti and Ti-PMMA. With a step of 2 mm, the incident monitoring distance increases from 494.5 mm to 506.5 mm, and the transmission monitoring distance changes from 244.5 mm to 256.5 mm. In the Ti-Ti case, as both the incident and transmission rods are made of the same material, once incident and reflected waves were measured at the same location x_{IR}, only $x_T - x_{IR}$ matters in results derivation; in the Ti-PMMA case, both x_{IR} and x_T have influence. In both cases, the real monitoring distance group ($x_{IR} = -500.5\ mm, x_T = 250.5\ mm$) yields results most close to the theoretical ones, and they both show that, the interface analysis technique is quite sensitive to variations in x_{IR} and x_T, which also demonstrates the reliability of the interface analysis technique. However, Eq. ①' and Eq. ②' possess different sensitivities to these variations.

Noise analysis was performed in the Ti-PMMA case. Artificial and experimental noises, come at two levels (10 and 20 dB) and were defined on local and global scales, were applied to investigate their effects on material properties derivation. It is found that, with the appearance of noise, the resulting material properties deviate from the theoretical and clean ones: higher noise level results in larger deviations with both equations; and given the same noise level, Eq. ②' can be more easily disturbed by noise when solving for the properties of transmission rod.

Chapter 8: Simulations of mechanical wave behaviours at 2-rod interfaces

The interface theories and analysis methodologies have been tested in the previous chapter using simulations with 'perfect' interfaces. In practice, however, contact situations are more complicated than the 2-medium cases as experimental imperfections (*e.g.* non-parallel faces, misalignments, *etc.*), bending, and the Poisson's effect always exist, which challenge the assumptions of the interface theories. In this chapter, four sets of interfaces, corresponding to those in the 2-medium investigation, were simulated. Simulations were built in a similar way to the 2-medium models except that materials were defined in two separate rods; an identical signal processing procedure followed, and results are presented and discussed similarly. Typical issues include dispersion correction, upper and lower frequency limits, the uniqueness of solutions, sensitivity of the BCs equation pair to errors, and experimental misalignment effects.

8.1 Ti-Ti 2-rod interface

8.1.1 Model description

The two rods were simulated using the same material (Titanium) in ABAQUS Explicit. The incident rod is 1 m long and has a diameter for 13 mm, the transmission rod is 0.5 m in length and has the same diameter as the incident rod. The same meshing methodology was used as in the single rod two medium methodology (with ~1 mm C3D8R elements). The two parts were then aligned along their central axes and in contact at one end. The material constants used are the same as shown in Table. 7-1. Again, the origin $x = 0$ was defined at the interface, and x increases towards the free end of the transmission rod. Therefore, at any 2 monitoring locations $x_I = x_R = x_{IR} < 0, x_T > 0$.

Explicit 'Surface-to-Surface' contact type was used, with penalty contact constraint formulation defined at contact interface with finite sliding, and the contact properties are defined such that the tangential behaviour is frictionless while on the normal direction the 2 rods were made 'hard' contact and separation was allowed after contact. The "hard" contact minimizes the penetration of the slave surface into the master surface at the constraint locations and does not allow the transfer of tensile stress across the interface [77]. Default contact controls, initializations and stabilizations were

applied. It should be noted that contact stabilization introduces viscous damping to oppose incremental relative motion between 2 surfaces. This damping can be used to stabilize unconstrained rigid body motion prior to contact closure without degrading the accuracy of results; no constraints can be applied to regions that are also part of a contact surface.

In order to apply the loading, two main steps were defined: in the first step, acceleration is applied by loading the pre-defined acceleration profile via boundary conditions on the end of the input rod (50 μs step duration, which is equal to the acceleration duration); in the second step, of 400 μs, free wave propagation was allowed in the rods. The impact action was simulated using the same acceleration profile (Fig. 7-1) as in the 2-medium simulations. It was loaded uniformly across the impact end of the incident rod, and thus the resulting wave is expected to be a plane wave with uniform deformation in the plane perpendicular to the axis. Note that, no extra BC constraints have been set for other DOFs (for example, radial expansion, rotation, *etc.*) in other directions.

The same meshing methodologies as the 2-medium simulation (Fig. 7-2) were applied to both rods. When assigning meshing properties to the rods, there are some critical points to be considered [77]. For example, first-order elements, *e.g.* CPS4R, CAX4R, C3D8R, should be used for contact simulations; to achieve uniform in-plane deformation, symmetric meshing, other than random, was adopted across the cross-section; hour-glassing and shear locking could be problematic for first-order elements, and in order to minimize numerical errors, time increment has been reduced to be $1\ \mu s$ here, and data were output at nodes in full double precision when defining the job. These considerations are referred in [77] and described in the full *web version*.

8.1.2 Simulation outputs

Typical strain recordings, extracted at the integration point of elements located at 3 distinct locations ($x_{IR} = -500.5\ mm, x_T = +9.5\ mm, x_T = +250.5\ mm$), are shown in Fig. 8-1. There is evidence of a small amount of geometric dispersion (see in the small oscillations at the rear of the pulses). Although the amplitude of the transmitted waves was almost the same as the incident wave, there was a small amount of reflection, as labelled on the incident signal. This could be a result of noise or artefacts in simulation, or due to the 3-dimensional nature of real waves: the wave is accompanied

by a radial expansion, but shear stresses are not able to cross the 'real' interface so there can be a discontinuity in this expansion at interface. In experiment, bending waves can also occur, which will transmit differently across the boundary. This will lead to differences in strain across section. In these simulations the strain at the centre of the rod is the same as that at the edge.

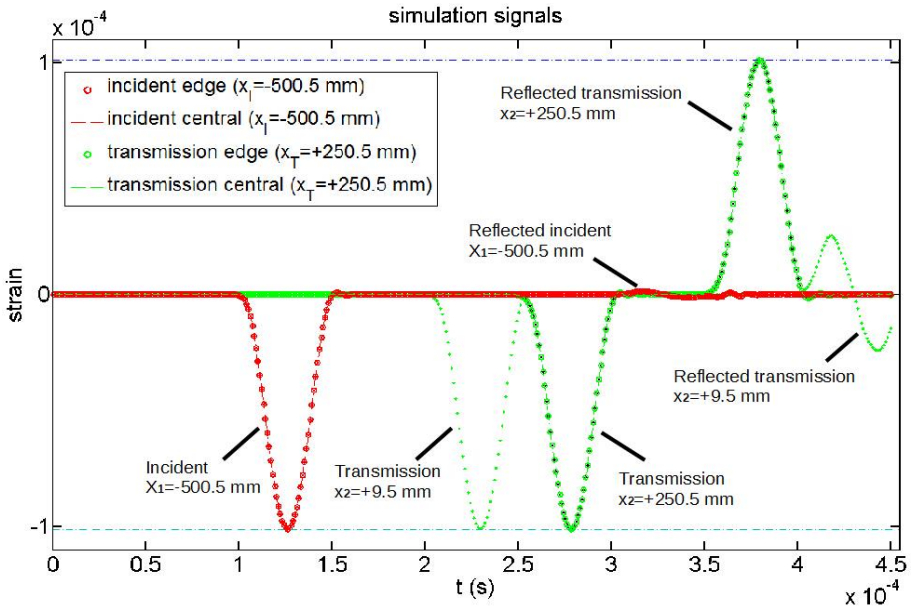
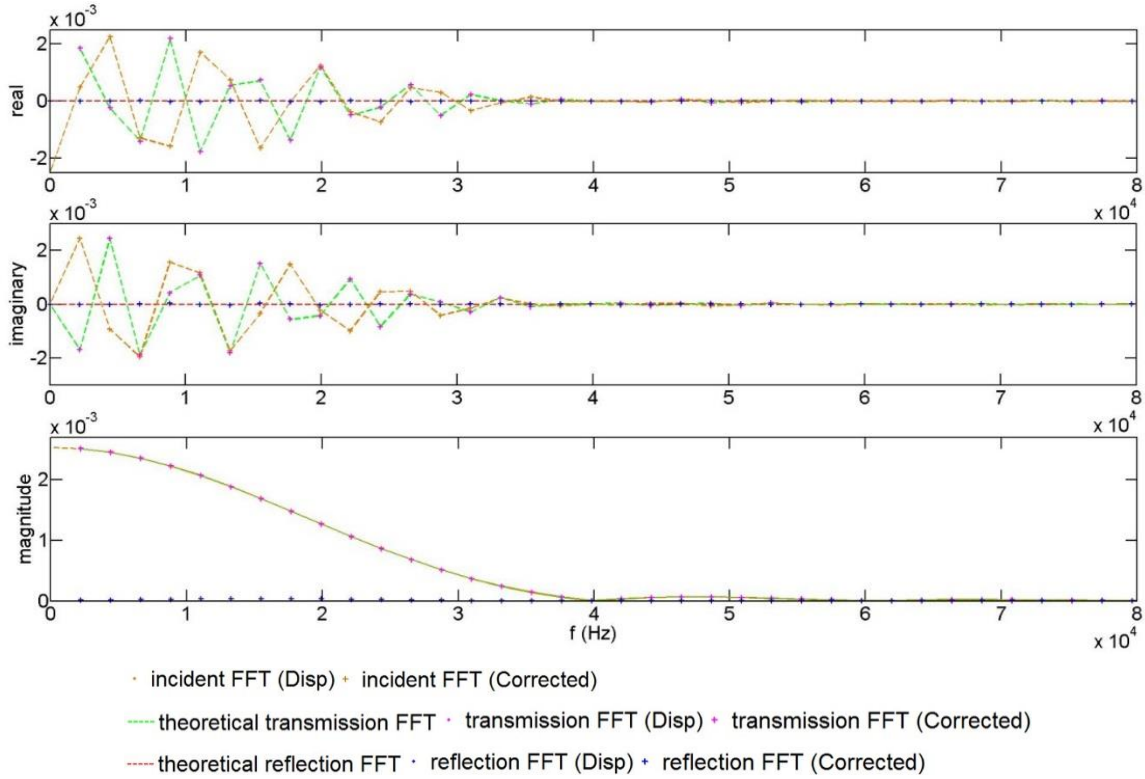


Figure. 8-1 Wave propagation in the Ti-Ti 2-rod system

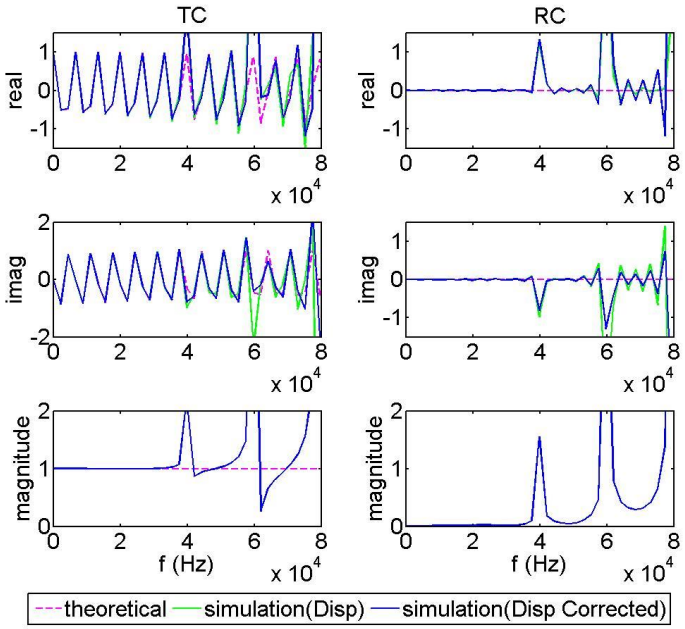
8.1.3 Data analysis

With these signals at hand, the next step is: with prerequisite knowledge of incident rod, using the 2 BC equations (Eq. ①' and Eq. ②') to calculate the material properties of the transmission rod. Here signals measured at $x_{IR} = -500.5\ mm, x_T = +250.5\ mm$ were used as an example to illustrate the data analysis process which is similar to the 2-medium simulation: Firstly, a wavelet-based non-phase-shift de-noising function '*wden*' was used to smooth the signals. Secondly, signal offsets were corrected by subtracting all amplitudes by the mean value of the background noise before any pulse arrives. Thirdly, the 3 pulses (incident, reflected, and transmitted) were selected manually to create vectors with the same length as the original signal, and the original phase information was retained; these vectors were padded with zero in regions outside the selected values and no centering has been adopted. Fourthly, Fourier transform was performed on these 3 newly-constructed vectors, with a special interest in the positive frequency range. With a signal duration of 0.00045 s and a sampling

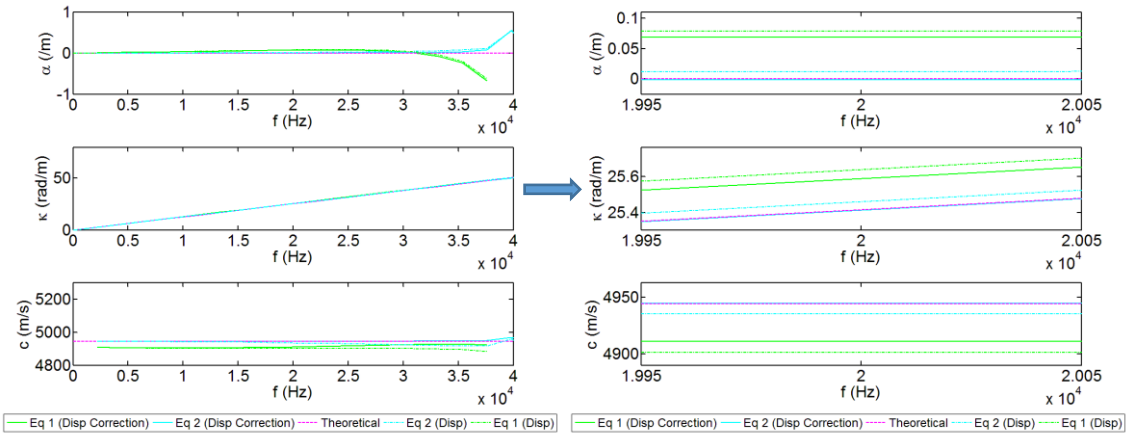
interval of 10^{-6} s, the minimum frequency resolution that can be achieved is 2222 Hz (1/0.00045s), and the maximum frequency is $5 \times 10^5\ Hz$ ($0.5 \times 1/10^{-6}\ s$). Dispersion was corrected in the FFT step. The FFT outputs are shown in Fig. 8-2 (a). As in previous simulations, the upper frequency bound for which the FFT has an identifiable magnitude is *ca.* 40 kHz, in fact the effect of the *sinc* function associated with the 50 μs pulse duration can be seen at this frequency (40 kHz corresponds to 25 μs). These FFT signals were used to produce the TC and RC values in 9-2 (b), and in both 9-2(a) and (b) they are seen to agree well with the theoretical values. In Fig 8-2 (b), spikes in the calculated TC and RC correspond to the zeros of the *sinc* function mentioned above.Inputting TCs and RCs into Eq. ①' and Eq. ②' yields solutions for γ_2 (Fig. 8-2(c)). Difference between the two equations were observed, and this was discussed later. Comparing the dispersion and corrected results, it is seen that, with this configuration of the Ti-Ti 2-rod system, it is necessary to correct for dispersion effects for frequencies above 10 kHz; after dispersion correction, the wavenumber κ and attenuation coefficient α drop (though several irregularities appear at negative α values derived from Eq. ①'), which leads to a decrease in loss modulus E'', loss factor $tan\delta$, and an increase in wave speed c and storage modulus E'.



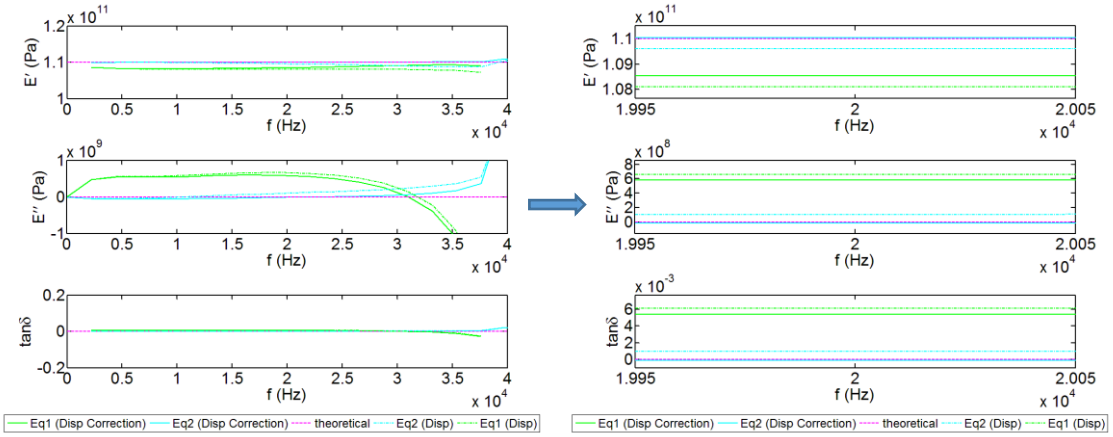
(a)Comparison of theoretical & simulation FFTs with & without dispersion correction



(b)TC & RC comparison



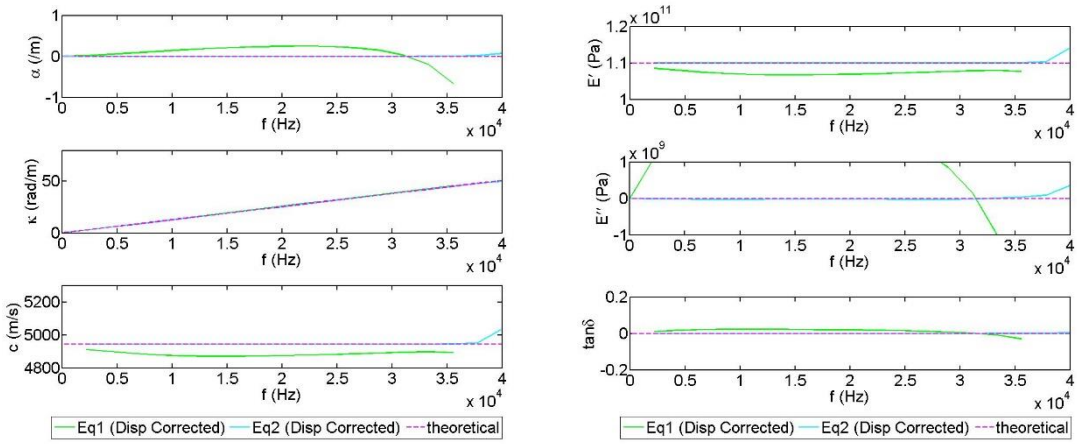
(c)Propagaiton coefficient and wave speed



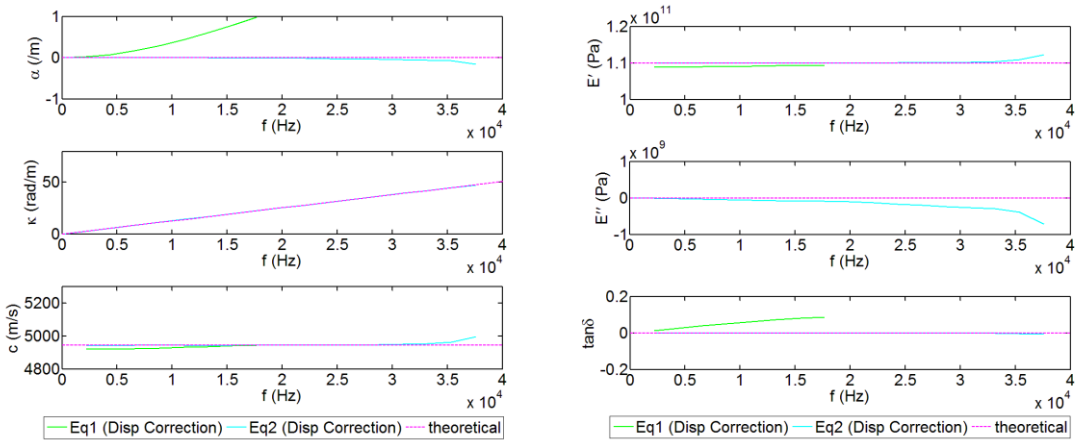
(d)Modulus and loss factor

Figure. 8-2 A comparison of the dispersion and dispersion corrected results (Ti-Ti 2 rods, $x_{IR} = -500.5\ mm, x_T = +250.5\ mm$)

Analysing another two cases where transmission signals were extracted at different distances ($x_{IR} = -500.5\ mm, x_T = +100.5\ mm$) and ($x_{IR} = -500.5\ mm, x_T = +9.5\ mm$), similar results can be found (Fig. 8-3), which further confirms the validity and reliability of the interface analysis technique, *i.e.* the material properties are unique and independent of wherever the signals are extracted.



(a) $x_{IR} = -500.5\ mm, x_T = +100.5\ mm$



(b) $x_{IR} = -500.5\ mm, x_T = +9.5\ mm$

Figure. 8-3 Propagation coefficient and modulus after dispersion correction

Some discussions about the results in Fig. 8-2 and Fig. 8-3:

(1) The lower and upper frequency bounds.

If no dispersion correction technique is to be used, the 1D wave propagation assumption also sets an upper frequency limit f_{h-1D} without yielding appreciable dispersion phenomenon

$$f_{h-1D} = \frac{c}{10 \times rod\ diameter} \approx \frac{4944\ \frac{m}{s}}{10 \times 0.013\ m} \approx 38\ kHz$$

which indicates with this rod configuration, those below 38 kHz can give accurate results even without dispersion correction. It has been seen from Fig. 8-2(a) that, the frequency region that contains identifiable magnitudes is shown to be $f_{h-3D} \approx 40\ kHz$. Furthermore, if Eq. ②' is concerned, from Fig. 8-2(c), (d) and Fig. 8-3(a), (b) we see that, within an error tolerance of 2%, with dispersion correction the highest frequency that can be achieved in this case is $f_{h-1D} \approx 35\ kHz$. The lower frequency limit is affected by several factors, *e.g.* the minimum frequency resolution which is determined by signal length

$$\Delta f_{min} = \frac{1}{signal\ duration} = \frac{1}{0.00045} = 2222\ Hz\ .$$

If no wave separation technique is to be used, the lower frequency bound is also limited by wave overlapping. For example, due to the infinite length of both rods, theoretically the lowest frequencies that can be achieved without wave overlapping, when waves are measured at ($x_{IR} = -500.5\ mm, x_T = +250.5\ mm$), are estimated to be

$$f_{l-Incident} \approx \frac{c_{Incident}}{Incident\ gauge\ distance} = \frac{4944\ m/s}{1\ m} = 4.944\ kHz$$

$$f_{l-transmission} \approx \frac{c_{Transmission}}{transmission\ gauge\ distance} = \frac{4944\ m/s}{0.5\ m} = 9.888\ kHz\ .$$

If the transmission wave is measured at other locations closer to the contact interface, $f_{l-transmission}$ can decrease. Note that, though theoretically those below 9888 Hz has a wavelength longer than the gauge distance on the transmission rod, we still gained valid information for those components as seen from the comparison of predicted and analysed FFTs (Fig. 8-3(a)), which means though with the appearance of wave overlapping, frequencies with wavelength larger than the gauge distance can still be accurately measured because not a full period is required to reflect the wave information.

All in all, using this configuration of the 2-rod system and the measurement settings, a reasonable valid frequency range is estimated to be $9.888\ kHz$~$35\ kHz$.

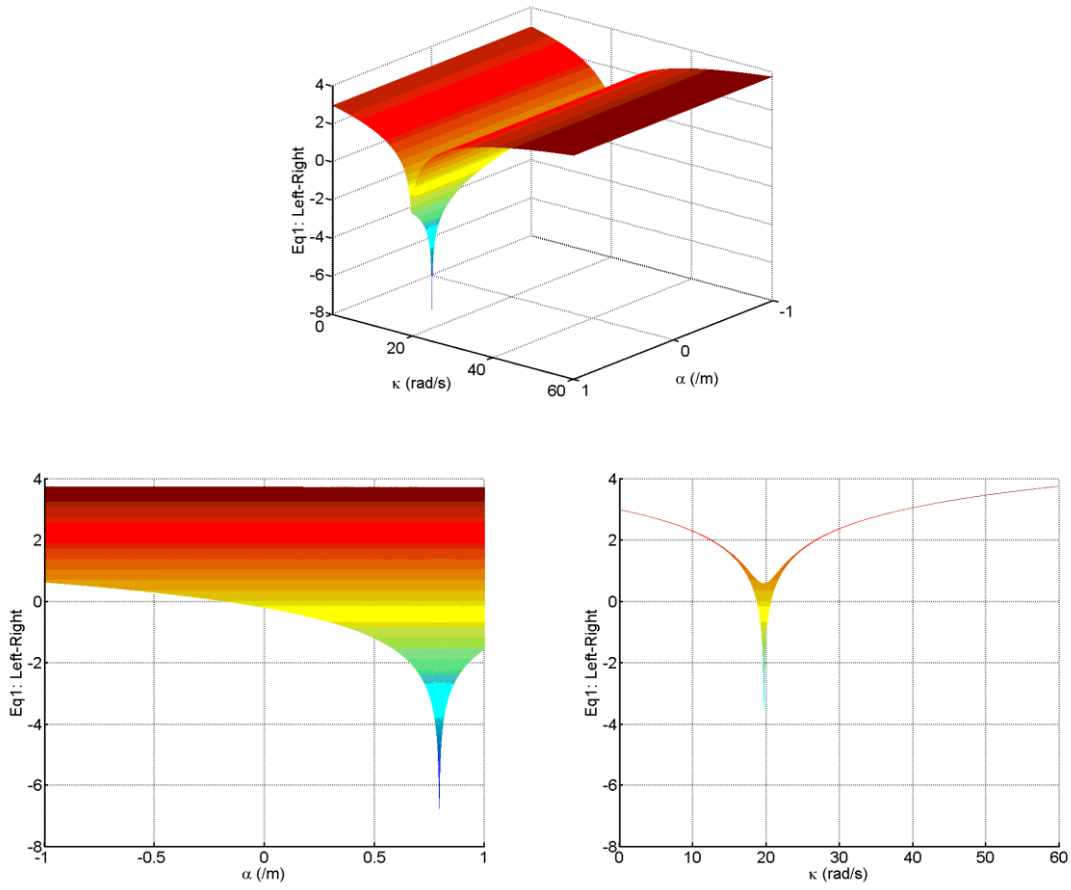
(2) Comparison of Eq. ①' and Eq. ②'

Fig. 8-3 has demonstrated the disparity when using Eq. ①' and Eq. ②' to resolve for γ_2 and E^*: Eq. ②′ gives less variable and more accurate results, which conflicts with the conclusion drawn in last chapter. This may be due to the fact that different degrees of complexity are involved in these two

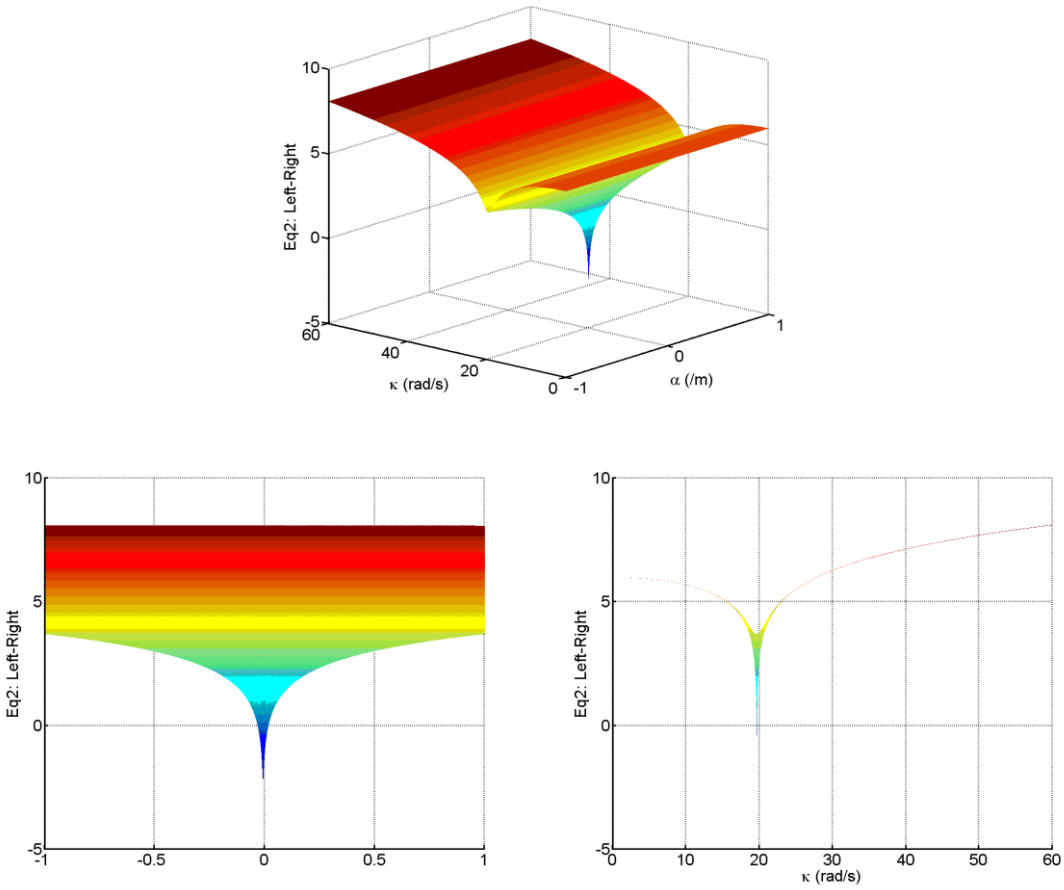
equations when solving for γ_2. As these two equations have different forms, errors such as noise in $TC_{\tilde{\varepsilon}|x_I,x_T}$ and $RC_{\tilde{\varepsilon}|x_I,x_R}$ may be treated (*e.g.* eliminated or amplified) in different ways. For example, examining a specific frequency$f = 15486.73\ Hz$, we substituted a range of γ_2 values (close to the theoretical one) into both sides of Eq. ①' and Eq. ②' and calculating the residual of imbalance between both sides

$$\alpha = [-1\colon 0.001\colon 1], \kappa = [0\colon 0.01\colon 60], \gamma_2 = \alpha + i\kappa\ .$$

The resulting error magnitude-α-κ surfaces were shown in Fig. 8-4. The minimum error between both sides was used to locate γ_2, it is found that only one potential solution exists across the whole plane. This is consistent with our previous finding: the period of solutions only depends on x_T.



(a) Eq. ①': $ln\left|\gamma_2 \times e^{-\gamma_2 x_T} - \frac{\gamma_1 \times TC_{\tilde{\varepsilon}}(x_I,x_T,\omega)\times e^{-\gamma_1 x_I}}{1-RC_{\tilde{\varepsilon}}(x_I,x_T,\omega)\times e^{-(\gamma_1 x_R+\gamma_1 x_I)}}\right|$ as a function of α and κ



(b)Eq. ②′: $ln\left|\gamma_2^2 \times e^{-\gamma_2 x_T} - \gamma_1^2 \times \frac{S_2}{S_1}\frac{\rho_2}{\rho_1}\frac{TC_{\tilde{\varepsilon}}(x_I,x_T,\omega)\times e^{-\gamma_1 x_I}}{1+RC_{\tilde{\varepsilon}}(x_I,x_R,\omega)\times e^{-(\gamma_1 x_R+\gamma_1 x_I)}}\right|$ as a function of α and κ

Figure. 8-4 The logarithm balance of Eq. ①' and Eq. ②' as functions of α and κ ($x_I = -500.5\ mm, x_T = +9.5\ mm, f = 15486.73\ Hz, TC_{\tilde{\varepsilon}} = -0.8046 + 0.5898i, RC_{\tilde{\varepsilon}} = -0.0175 - 0.0111i, \gamma_1 = 0 + 19.68i$)

Using the minimum error criterion, the following solutions were found on the planes

$$\text{Eq. ①': } \gamma_2 = 0.793 + 19.69i$$

$$\text{Eq. ②': } \gamma_2 = -0.007 + 19.69i$$

while the theoretical value is $\gamma_2 = 0 + 19.68i$, the wavenumbers resulted from both equations are very close to the theoretical one, the disparity lies in the real part, and it is believed to be induced by the different levels of sensitivity to the errors. To investigate this, a noise study was performed.

8.1.4 Error analysis: sensitivities of interface equations to noises contained in transmission and reflection coefficients

Here the sensitivities of Eq. ①' and Eq. ②' (Eq. (7.3)) to errors contained in $TC_{\tilde{\varepsilon}|x_I,x_T}$ and $RC_{\tilde{\varepsilon}|x_I,x_R}$ were numerically tested when solving for γ_2. Two steps were designed: firstly, first order derivatives,

with regards to $TC_{\tilde{\varepsilon}|x_I,x_T}$ and $RC_{\tilde{\varepsilon}|x_I,x_R}$ respectively, were analytically derived (assuming $TC_{\tilde{\varepsilon}|x_I,x_T}$ and $RC_{\tilde{\varepsilon}|x_I,x_R}$ are independent); then variations which represent noise in both coefficients were introduced and γ_2 was resolved with the appearance of noise.

The variation of γ_2 with regard to $TC_{\tilde{\varepsilon}|x_I,x_T}$ or $RC_{\tilde{\varepsilon}|x_I,x_R}$ is indicated by the first order partial derivatives $\frac{\partial\gamma_2}{\partial TC_{\tilde{\varepsilon}|x_I,x_T}}$ and $\frac{\partial\gamma_2}{\partial RC_{\tilde{\varepsilon}|x_I,x_T}}$. Use Eq. ①' as an example, to obtain these differentiations, let

$$Z = \gamma_2 \times e^{-\gamma_2 x_T} = \frac{\gamma_1 \times TC_{\tilde{\varepsilon}}(x_I,x_T,\omega)\times e^{-\gamma_1 x_I}}{1-RC_{\tilde{\varepsilon}}(x_I,x_T,\omega)\times e^{-(\gamma_1 x_R+\gamma_1 x_I)}}$$

then

$$\frac{\partial Z}{\partial TC_{\tilde{\varepsilon}|x_I,x_T}} = \frac{\partial Z}{\partial \gamma_2}\frac{\partial \gamma_2}{\partial TC_{\tilde{\varepsilon}|x_I,x_T}} = e^{-\gamma_2 x_T}(1-\gamma_2 x_T)\frac{\partial \gamma_2}{\partial TC_{\tilde{\varepsilon}|x_I,x_T}}$$

on the other hand, assuming $TC_{\tilde{\varepsilon}|x_I,x_T}$ and $RC_{\tilde{\varepsilon}|x_I,x_R}$ are independent of each other,

$$\frac{\partial Z}{\partial TC_{\tilde{\varepsilon}|x_I,x_T}} = \frac{\gamma_1 e^{-\gamma_1 x_I}}{1-RC_{\tilde{\varepsilon}}(x_I,x_T,\omega)\times e^{-(\gamma_1 x_R+\gamma_1 x_I)}}$$

combining the above 2 equations gives

$$\frac{\partial \gamma_2}{\partial TC_{\tilde{\varepsilon}|x_I,x_T}} = \frac{\gamma_1}{1-\gamma_2 x_T}\times\frac{1}{1-RC_{\tilde{\varepsilon}}(x_I,x_T,\omega)\times e^{-(\gamma_1 x_R+\gamma_1 x_I)}}\times e^{\gamma_2 x_T-\gamma_1 x_I}\ .$$

In a similar way it is possible to obtain

$$\frac{\partial \gamma_2}{\partial RC_{\tilde{\varepsilon}|x_I,x_T}} = \frac{\gamma_1}{1-\gamma_2 x_T}\times\frac{TC_{\tilde{\varepsilon}}(x_I,x_T,\omega)}{[1-RC_{\tilde{\varepsilon}}(x_I,x_T,\omega)\times e^{-(\gamma_1 x_R+\gamma_1 x_I)}]^2}\times e^{-(\gamma_1 x_R+\gamma_1 x_I)}\times e^{\gamma_2 x_T-\gamma_1 x_I}\ .$$

Similarly, for Eq. ②' we have

$$\begin{cases} \dfrac{\partial \gamma_2}{\partial TC_{\tilde{\varepsilon}|x_I,x_T}} = \dfrac{\rho_2 S_2}{\rho_1 S_1}\times\dfrac{\gamma_1}{\gamma_2}\times\dfrac{\gamma_1}{2-\gamma_2 x_T}\times\dfrac{1}{1+RC_{\tilde{\varepsilon}}(x_I,x_T,\omega)\times e^{-(\gamma_1 x_R+\gamma_1 x_I)}}\times e^{\gamma_2 x_T-\gamma_1 x_I} \\ \dfrac{\partial \gamma_2}{\partial RC_{\tilde{\varepsilon}|x_I,x_T}} = \dfrac{\rho_2 S_2}{\rho_1 S_1}\times\dfrac{\gamma_1}{\gamma_2}\times\dfrac{\gamma_1}{2-\gamma_2 x_T}\times\dfrac{-TC_{\tilde{\varepsilon}}(x_I,x_T,\omega)}{[1+RC_{\tilde{\varepsilon}}(x_I,x_T,\omega)\times e^{-(\gamma_1 x_R+\gamma_1 x_I)}]^2}\times e^{-(\gamma_1 x_R+\gamma_1 x_I)}\times e^{\gamma_2 x_T-\gamma_1 x_I} \end{cases}.$$

It is thus seen that, in deriving γ_2, these equations possess different sensitivities to $TC_{\tilde{\varepsilon}|x_I,x_T}$ or $RC_{\tilde{\varepsilon}|x_I,x_R}$ values, and if errors are contained in both values, they may be treated differently. Note that, this is an approximate estimate as $TC_{\tilde{\varepsilon}|x_I,x_T}$ and $RC_{\tilde{\varepsilon}|x_I,x_R}$ are not actually independent, but are related by $\frac{\gamma_1}{\gamma_2}TC_{\tilde{\varepsilon}}(x_I,x_T,\omega)\times e^{\gamma_2 x_T-\gamma_1 x_I}+RC_{\tilde{\varepsilon}}(x_I,x_T,\omega)\times e^{-(\gamma_1 x_R+\gamma_1 x_I)}=1$ (Table. 6-10b).

Errors can be classified into two types: random noise and those generated by the imperfections of the contact interfaces. Random noise in experiments normally come from current noise and can be represented by a Gaussian white noise. This kind of noise exists in all the 3 pulses and thus has the

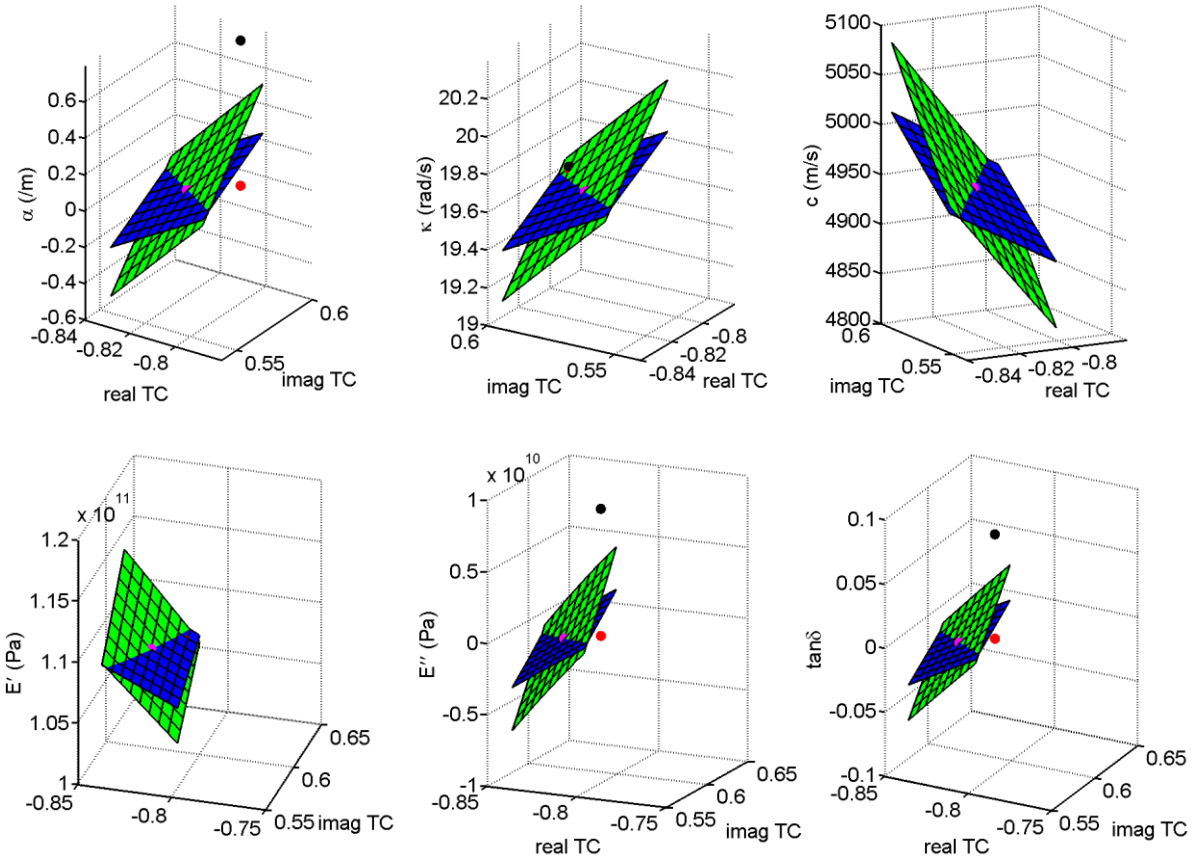
same effect on $TC_{\tilde{\varepsilon}|x_I,x_T}$ and $RC_{\tilde{\varepsilon}|x_I,x_R}$. Errors generated from imperfect contact, *e.g.* misalignments or 3D effects, are difficult to estimate, thus errors in $TC_{\tilde{\varepsilon}|x_I,x_T}$ and $RC_{\tilde{\varepsilon}|x_I,x_R}$ were treated separately. Using $f = 15486.73\,Hz$ and ($x_I = -500.5\,mm, x_T = +9.5\,mm$) as an example, with the prerequisite knowledge of the 2 rod properties, the 2 theoretical coefficients can be calculated

$$TC_{\tilde{\varepsilon}} = \frac{2Z_1}{Z_1+Z_2} \times \frac{\gamma_2}{\gamma_1} \times \frac{e^{-\gamma_2 x_T}}{e^{-\gamma_1 x_I}} = -0.8184 + 0.5751\mathrm{i},\ RC_{\tilde{\varepsilon}} = \frac{Z_2-Z_1}{Z_2+Z_1} \times \frac{e^{\gamma_1 x_R}}{e^{-\gamma_1 x_I}} = 0\ .$$

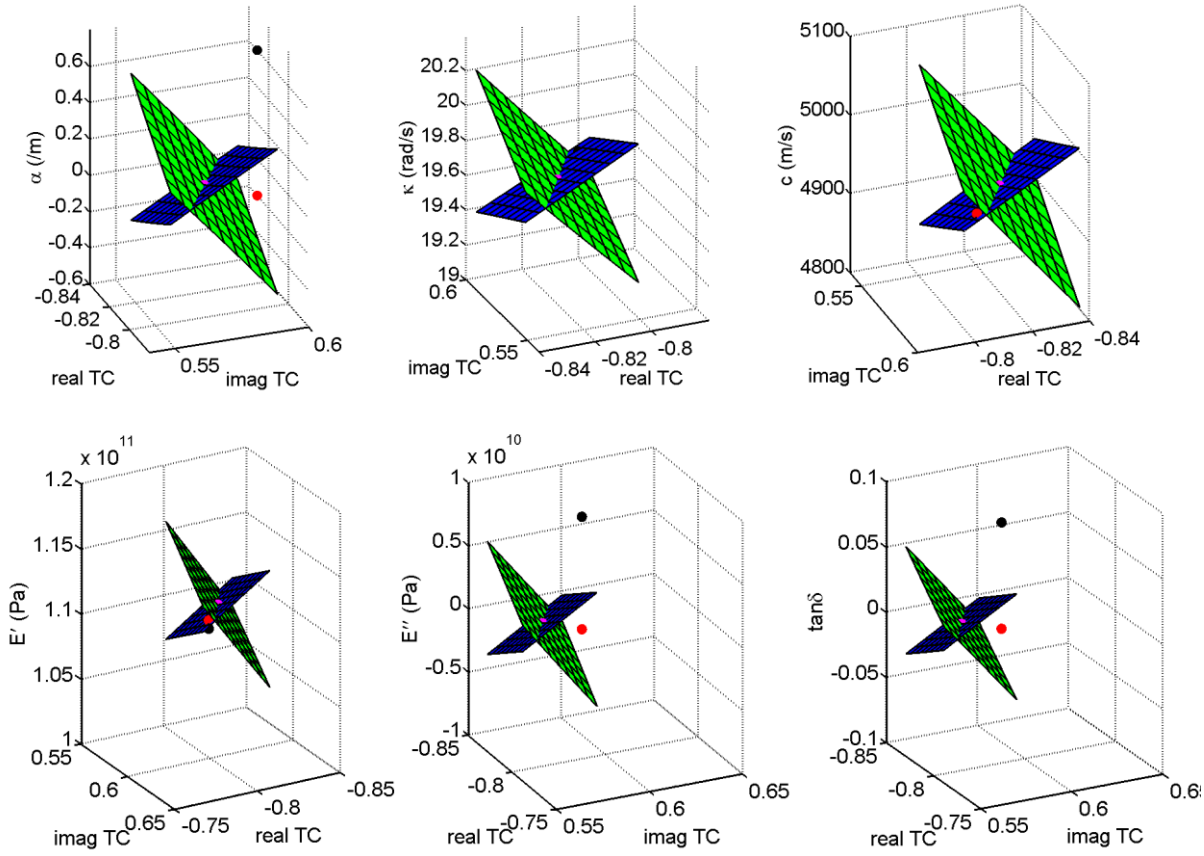
The numerical sensitivity testing scheme is show in Table. 8-1. Variations were introduced in both the real and imaginary parts of one coefficient while the other one was kept constant (equals to the corresponding theoretical value). It was designed such that the theoretical values (both real and imaginary parts) sit in the middle of the variation range. Substituting these $TC_{\tilde{\varepsilon}}$ and $RC_{\tilde{\varepsilon}}$ values into Eq. ①' and Eq. ②', various γ_2 and E_2 can be derived, as graphically shown in Fig. 8-5.

Table. 8-1 Numerical sensitivity testing scheme

$x_I = -500.5\ mm, x_T = +9.5\ mm, f = 15486.72566\ Hz$		$TC_{\tilde{\varepsilon}}$		$RC_{\tilde{\varepsilon}}$	
		real	imaginary	real	imaginary
Eq. ①' & ②'	Case 1	[-0.8284:0.005: -0.8084]	[0.5651:0.005: 0.5851]	0	
	Case 2	-0.8184 + 0.5751i		[-0.01:0.005:0.01]	[-0.01:0.005:0.01]



(a)Eq. ①' & ②': $TC_{\tilde{\varepsilon}} = (-0.838\sim0.798) + (0.555\sim0.595)i, RC_{\tilde{\varepsilon}} = 0$



(b)Eq. ①′ & ②′: $TC_{\tilde{\varepsilon}} = -0.8184 + 0.5751\mathrm{i}, RC_{\tilde{\varepsilon}} = (-0.02\sim0.02) + (-0.02\sim0.02)i$

Figure. 8-5 Sensitivities of γ_2 and E^* to the variations of $TC_{\tilde{\varepsilon}|x_I,x_T}$ and $RC_{\tilde{\varepsilon}|x_I,x_R}$

(Planes are generated by numerical tests, dots are simulation results. Green plane: Eq. ①', blue plane: Eq. ②'; black dot: Eq. ①', red dot: Eq. ②', magenta dot: theoretical) $(x_I = -500.5\ mm, x_T = +9.5\ mm, f = 15486.73\ Hz)$

Table. 8-2 Quantitative variations reflected in Fig. 8-5

	$\Delta TC_{\tilde{\varepsilon}} \neq 0, \Delta RC_{\tilde{\varepsilon}} = 0$		$\Delta TC_{\tilde{\varepsilon}} = 0, \Delta RC_{\tilde{\varepsilon}} \neq 0$	
	$\Delta real = 0.04, \Delta imag = 0.04$			
	Eq. ①′	Eq. ②′	Eq. ①′	Eq. ②′
Δα (/m)	−0.5465~0.5478	−0.2762~0.2762	−0.5249~0.5349	−0.2728~0.2743
Δκ (rad/s)	19.1378~20.2320	19.4052~19.9577	19.1679~20.2288	19.4151~19.9627
Δc (m/s)	4809.5~5084.5	4875.6~5014.4	4810.3~5076.5	4874.4~5011.9
ΔE′ (GPa)	104.0910~116.3341	106.9722~113.1498	104.1076~115.9536	106.9171~113.0332
ΔE″ (GPa)	−6.1013~6.1036	−3.0743~3.0942	−5.9895~5.8565	−3.0699~3.0461
$\Delta tan\delta$	−0.05558~0.055679	−0.02804~0.02809	−0.05377~0.05405	−0.02779~0.02782

A quantitative analysis reflecting the variations in Fig. 8-5 is presented in Table. 8-2. It is seen that, the results are very sensitive to variations in $TC_{\tilde{\varepsilon}}$ and $RC_{\tilde{\varepsilon}}$. For Eq. ①', an variation of $\pm 2.44\%$ in the real part and $\pm 3.48\%$ in the imaginary part can lead up to a variation of ± 0.54 in α, $\pm 2.8\%$ in κ and c, $\pm 5.7\%$ in E', ± 6.1GPa in E'', and ± 0.055 in $tan\delta$; For Eq. ②', these being ± 0.27 in α,

$\pm 1.4\%$ in κ and c, $\pm 2.8\%$ in E', ± 3.06GPa in E'', and ± 0.028 in $tan\delta$. And Eq. ①' has almost double sensitivity as Eq. ②', which suggests Eq. ②' be used when evaluating for transmission rod properties. This conflicts with the conclusion from noise study of 2-medium simulation.

8.1.5 Using single rod theory to analyse 2 rod signals

While the 2 rods are made of the same material and geometry, the incident and transmitted pulses can be analysed as if they were monitored at two gauge stations on a 1.5 m long single rod and using the single rod theory (Eq. (3.2)). The two signals extracted at ($x_{IR} = -500.5\ mm, x_T = +250.5\ mm$) are used an example (Fig. 8-6). After zero padding, centring, Fourier transform and dispersion correction, the results are presented in Fig. 8-7. It is seen that, the single rod theory yields almost the same results as those resulted from the interface Eq. ②', as well as the theoretical values.

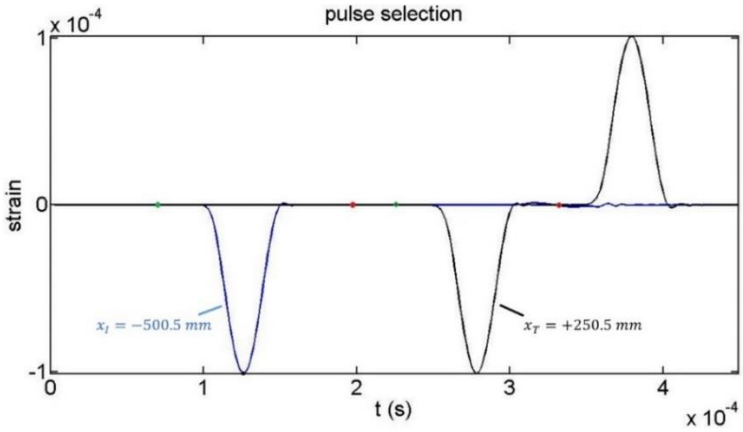
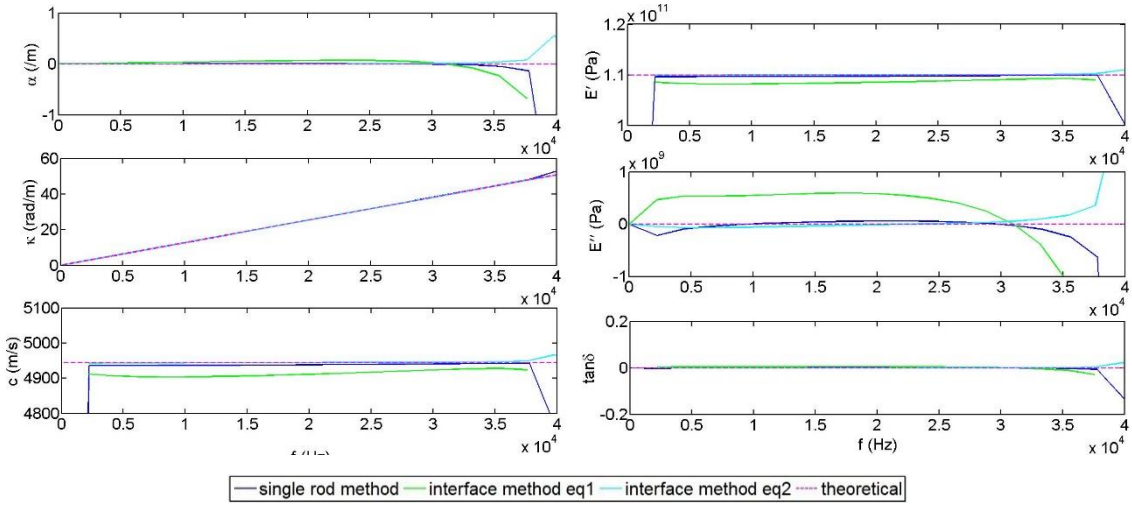


Figure. 8-6 pulse selection (green dots: start locations; red dots: end locations)



(a) Propagation coefficient and wave speed (b)Modulus and loss factor

Figure. 8-7 Comparison of the results derived by single rod theory and interface analysis technique (Ti-Ti 2 rods, $x_{IR} = -500.5\ mm, x_T = +250.5\ mm$)

8.2 Ti-Mg 2-rod interface

Second case examined is the Ti-Mg 2 rod system which hosts 2 elastic rods with distinct impedances.

8.2.1 Model description

The incident Ti rod and transmission Mg rod have the same geometries as the Ti-Ti simulation (diameter 13 mm and lengths 1 m, 0.5 m). Material properties adopted are presented in Table. 7-1. Again, the same contact settings were employed, *i.e.* frictionless explicit 'surface-to-surface' contact type with penalty contact formulation, finite sliding and separation after contact allowed when defining contact properties, default contact controls, initializations and stabilizations applied and no constraints defined in the contact surface area. When defining contact properties, the stiffer surface (Ti) should normally serve as the 'master' surface and the softer surface (Mg) as the 'slave' surface. Otherwise, the slave surface nodes will have larger mass than the nodes on the master surface, and significant contact noise can result [77]. The same acceleration input (Fig. 7-1) was defined in BCs and loaded uniformly across the cross-section at the free end of the incident rod. The same meshing methodology, *i.e.* 270000 C3D8R elements with mesh size $\sim 1\ mm$, was applied.

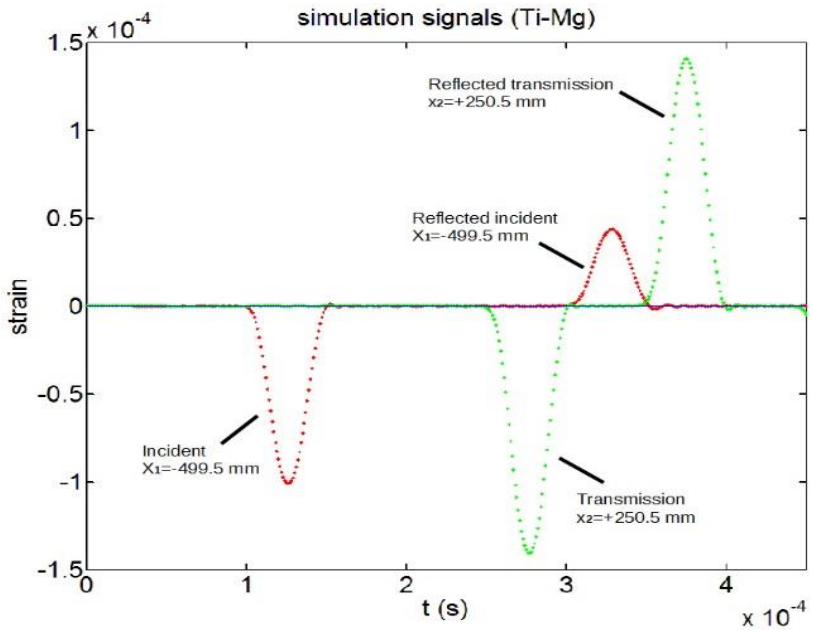
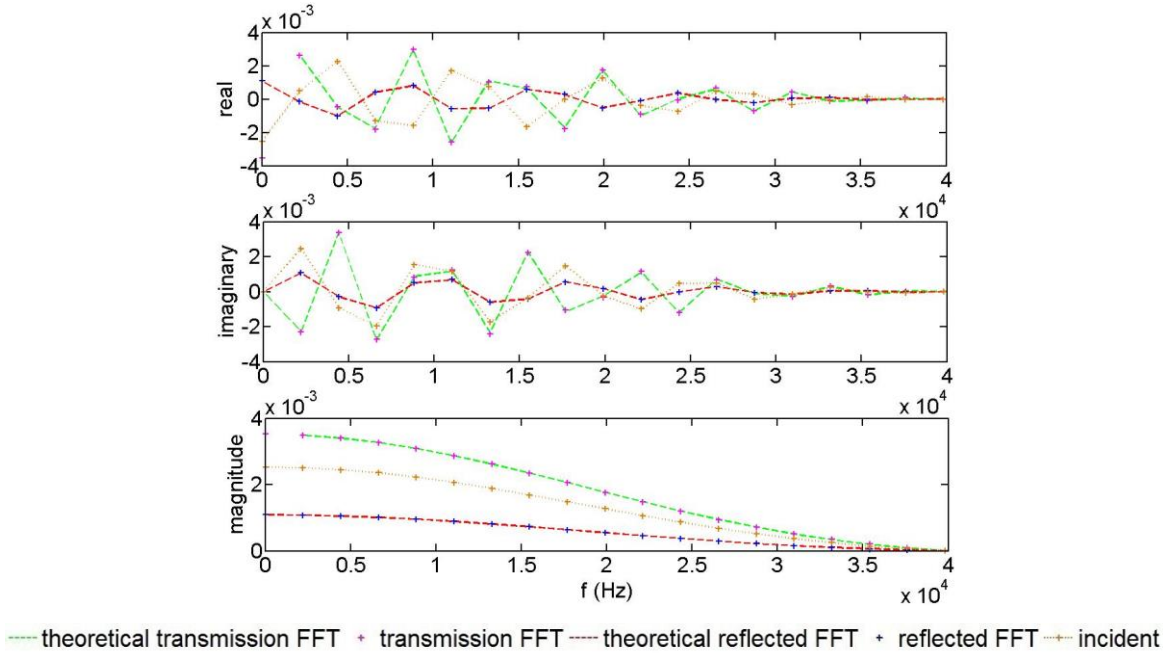


Figure. 8-8 Wave propagation in a Ti-Mg 2-rod system

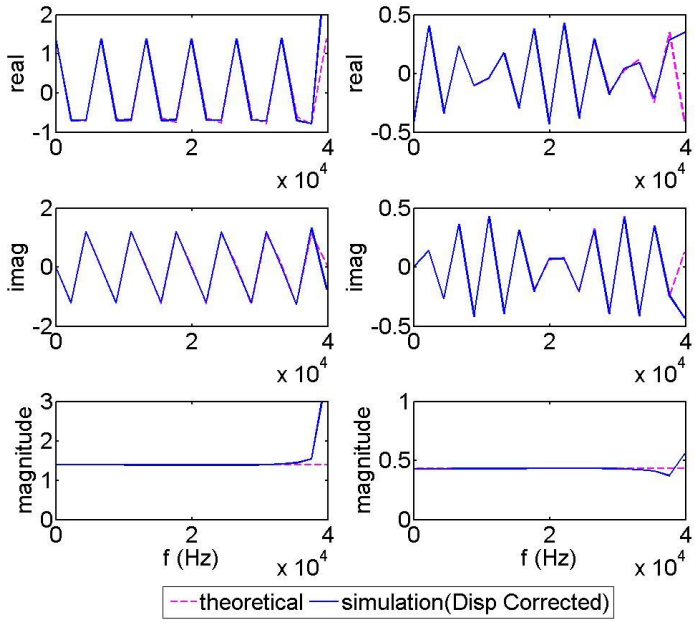
8.2.2 Simulation outputs and results

The signals captured are shown in Fig. 8-8. As can be expected from the TC and RC expressions (Table. 6-3 or Table. 6-9a), the transmitted wave has same sign as incident wave while the reflected

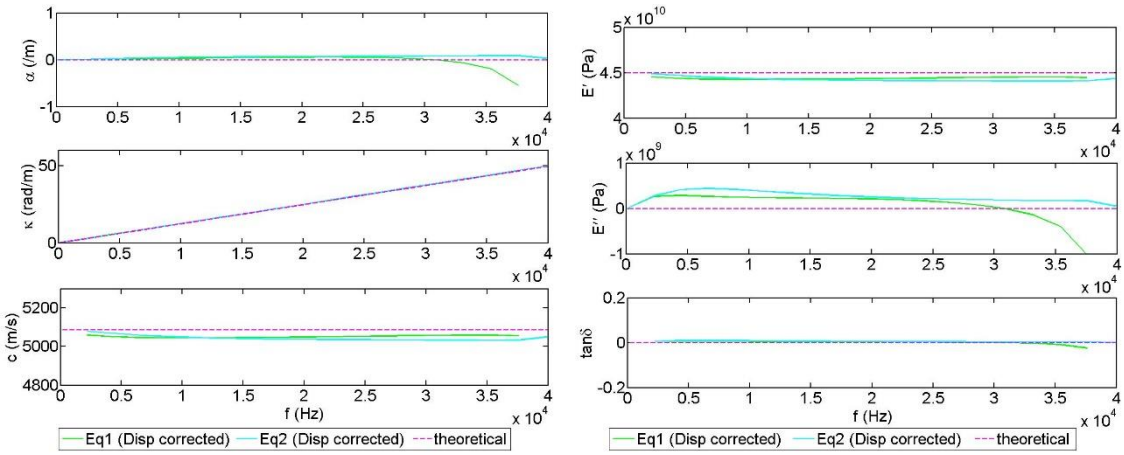
wave has a phase change because $Z_{Mg} < Z_{Ti}$. Dispersion-induced oscillations were again observed. The three pulses recorded at the middle surface ($x_{IR} = -499.5\,mm, x_T = +250.5\,mm$) were analysed, using the dispersion profiles in the previous chapter. The corrected FFTs, TCs and RCs agree well with the theoretical values (Fig. 8-9(a) and (b)). Solving Eq. ①' and Eq. ②' for the material properties of the transmission Mg rod (Fig. 8-9(c) and (d)) it was found that the two equations gave very similar results, and these were also in good agreement with theoretical values.



(a) Comparison of theoretical & simulation FFTs with dispersion correction



(b) Comparison of the theoretical and simulation $TC_{\tilde{\varepsilon}}$ & $RC_{\tilde{\varepsilon}}$



(c) Propagaiton coefficient and wave speed (d) Modulus and loss factor

Figure. 8-9 Data analysis process and derived material properties after dispersion correction

8.3 Ti-PMMA 2-rod interface

After analysing 2 examples of the elastic-elastic system (one with the same impedance and the other one sees impedance difference between the two rods), the Ti-PMMA two rod system was introduced as an example of an elastic-viscoelastic interface. All the simulation settings (rod geometries, contact, BCs, mesh scheme, *etc*) and analysis methodologies are the same as the previous two cases, except that linear viscoelasticity was introduced in material definition (Table. 7-1).

Particularly, contact settings are summarized as follows:

Surface-to-Surface contact (explicit), penalty contact method, with finite sliding
Master surface: Ti, Slave surface: PMMA
Tangential behaviour: frictionless
Normal behaviour: 'hard contact', allow separation after contact
Default contact controls, initializations, stabilizations.

Fig. 8-10 shows wave propagation in the 2-rod system. Unlike elastic rods, attenuation can be seen during wave propagation in the transmission rod due to the damping characteristic of the PMMA material. Another interesting point is the non-uniform deformation across the cross-section close to the interface end of the PMMA rod. By comparing the central and edge deformations at a series of distances ranging from $x_T = 0.5$ mm to $x_T = 249.5$ mm from the contact interface, it is found that the non-uniform strain occurs across the planes close to the contact interface (*e.g.* within a distance of 50 mm). For example, the difference between the central and edge strain recorded at $x_T = 0.5$ mm

amounts for up to 14.6 % of the edge strain. The deformation across the plane becomes uniform at larger distance, *e.g.* $x_T > 50$ mm, as per Saint-Venant's principle. In later calculations, data recorded at $x_T = 124.5$ mm was used.

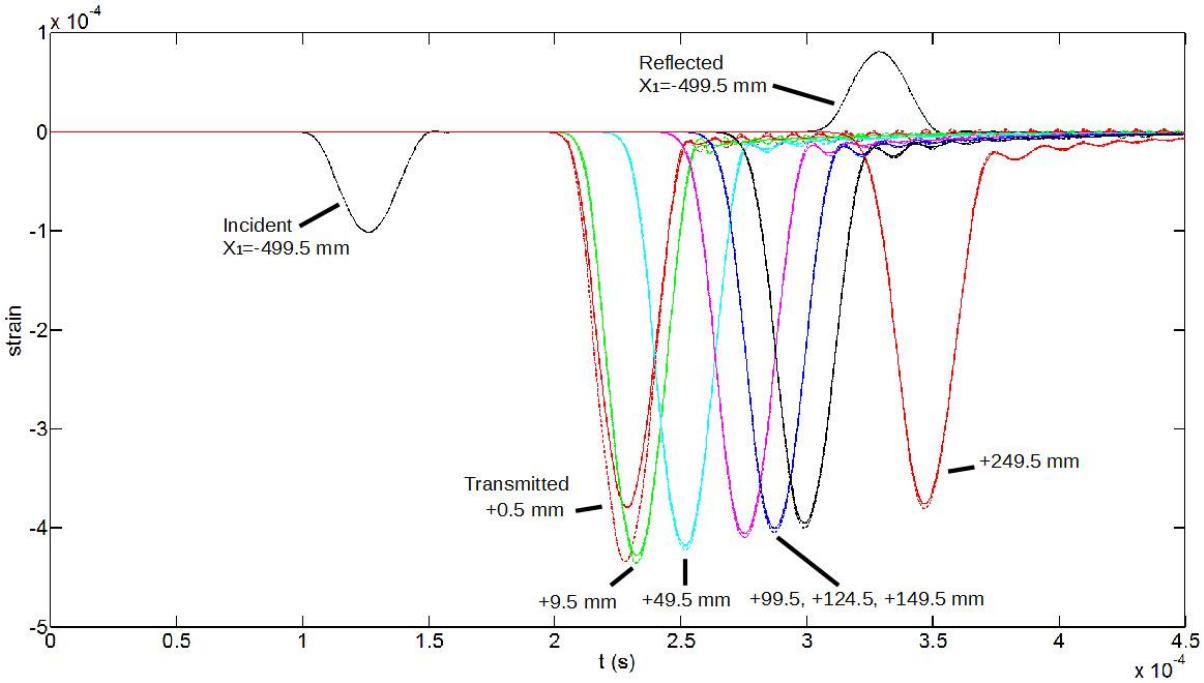
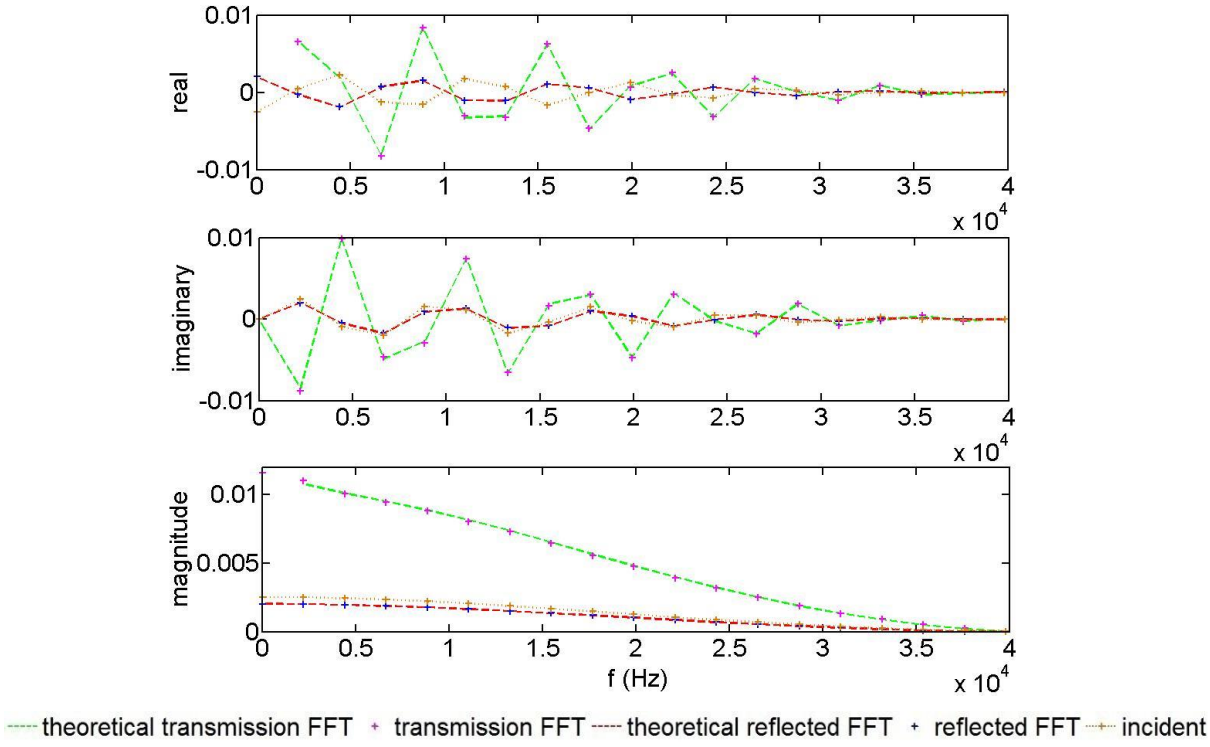


Figure. 8-10 Wave propagation in the Ti-PMMA 2 rod system (continuous line: edge strain; dash line: central strain)

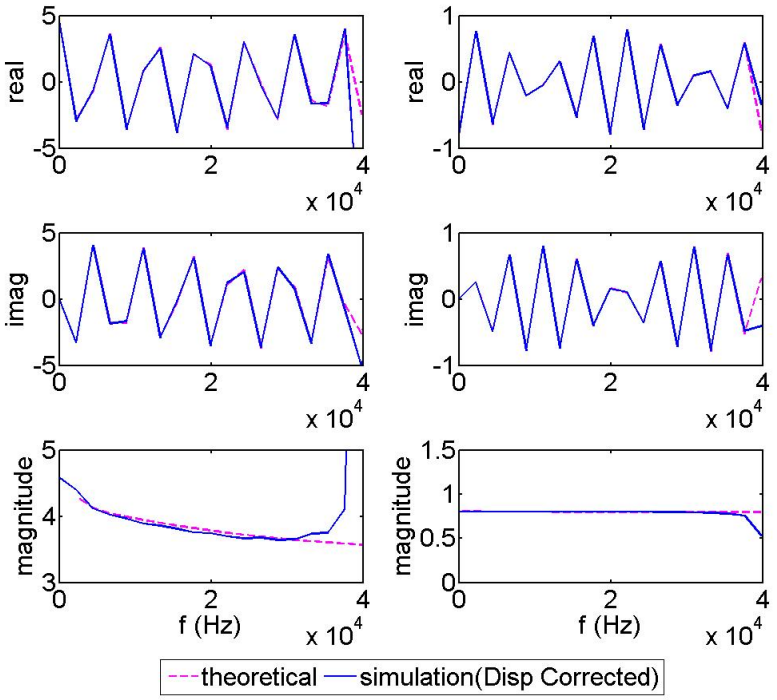
The data in Fig. 8-10 show again that the transmission strain is larger than the incident strain, as $Z_1 > Z_2$, and the reflected strain wave is of opposite sign to the incident wave. Compared to the previous elastic-elastic cases (Fig. 8-1 and Fig. 8-8), though the same input was used, wave propagating in the viscoelastic PMMA rod seems to be more dispersive, as oscillations can be seen in the tail of the transmission waves, this is consistent with the wave profile for geometric dispersion in this material, Fig. 7-18(b), and is a result of the fact that between the metals and PMMA, the decrease in modulus is by a factor of 20, whilst the decrease in density is by a factor of 2 or 3.

Fig. 8-11(a) indicates that the upper frequency limit with identifiable magnitude is around 40 kHz; however, above 30 kHz, the FFT magnitudes, and the resulting SNR (signal to noise ratio), are very small, thus it is difficult to identify the material properties. After dispersion correction the theoretical and simulation-based FFTs, TCs and RCs agree well within a 'valid frequency range' 0~30 kHz.

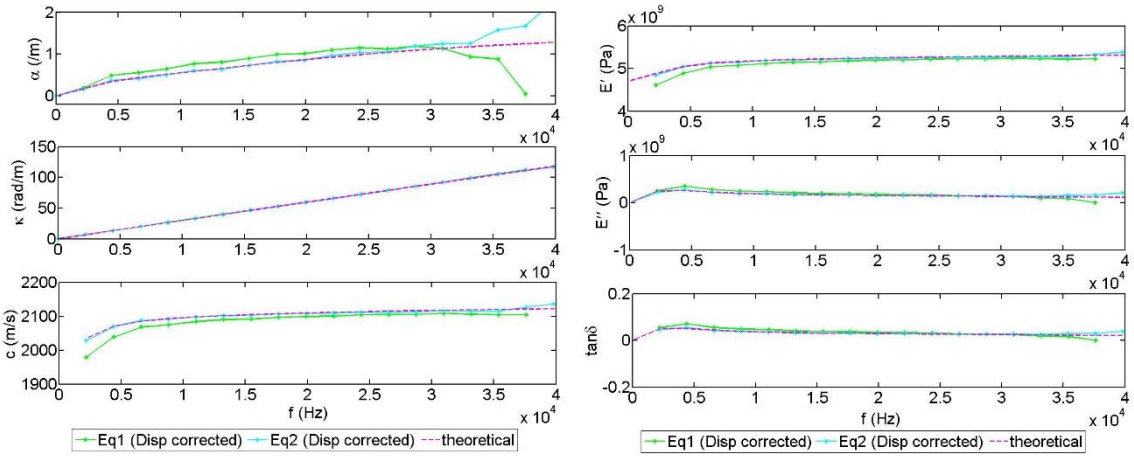
The resulting material properties (Fig. 8-11(c) and (d)) yielded by both BC equations are close to the theoretical ones, and Eq. ②' gives more reliable results in this case.



(a)Comparison of theoretical & simulation FFTs with dispersion correction



(b) Comparison of the theoretical and simulation $TC_{\tilde{\varepsilon}}$ & $RC_{\tilde{\varepsilon}}$



(c) Propagation coefficient and wave speed (d)Modulus and loss factor

Figure. 8-11 Data analysis process and derived material properties after dispersion correction (Ti-PMMA 2 rods, $x_{IR} = -500.5\ mm, x_T = +124.5\ mm$)

8.4 PMMA-Mg 2-rod interface

The last case considered is the PMMA-Mg 2-rod system, in which a viscoelastic PMMA serves as the incident rod. Unlike the previous three cases where the properties of incident rod are assumed known and efforts were made to resolve for γ_2, here the aim is to solve for γ_1. The model settings are similar to the previous two rod cases except that an extended 1 m long Mg transmission rod has been employed because of wave superposition concerns. The incident and transmission material properties are the same as those defined in the one rod two medium PMMA-Mg case (Table. 7-1).

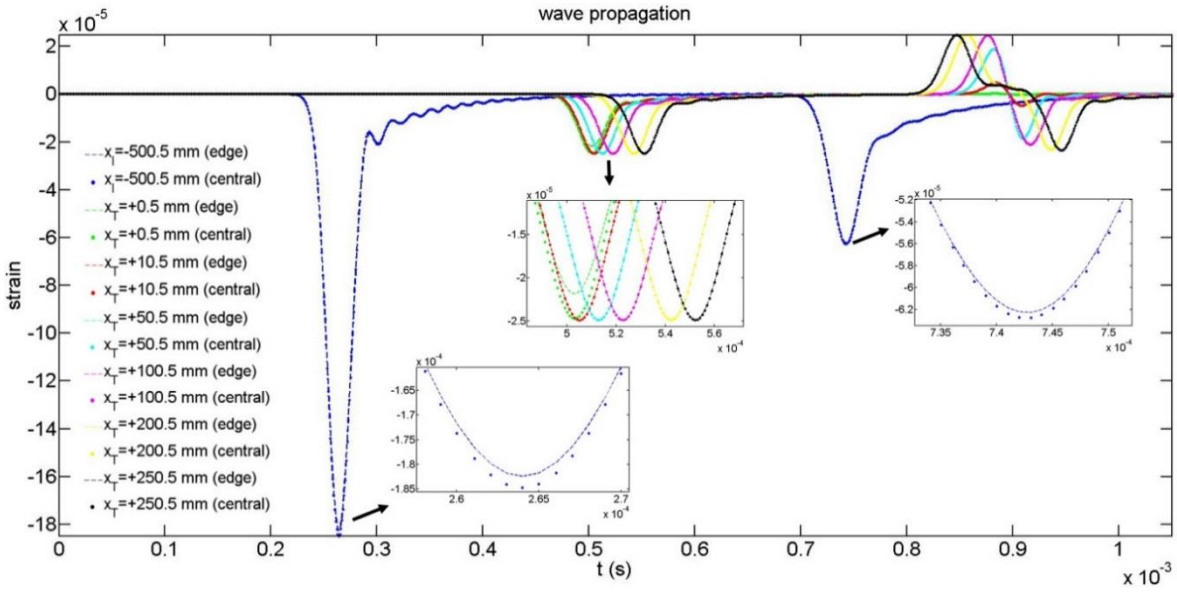
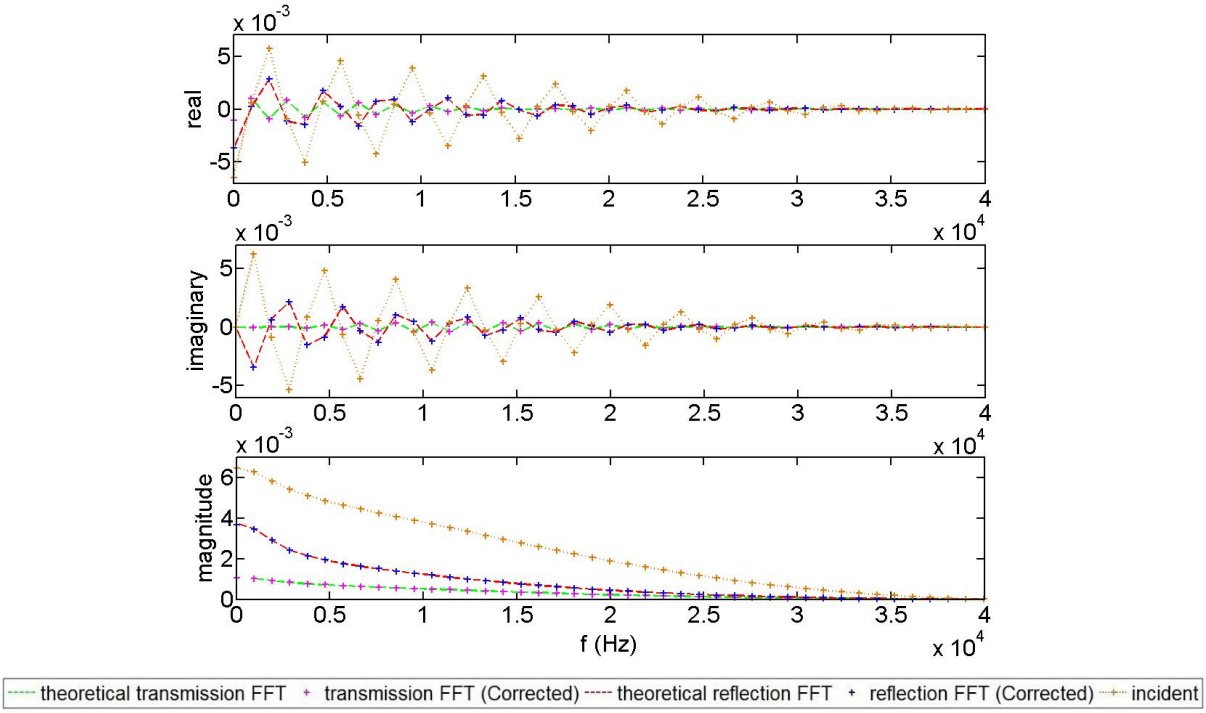


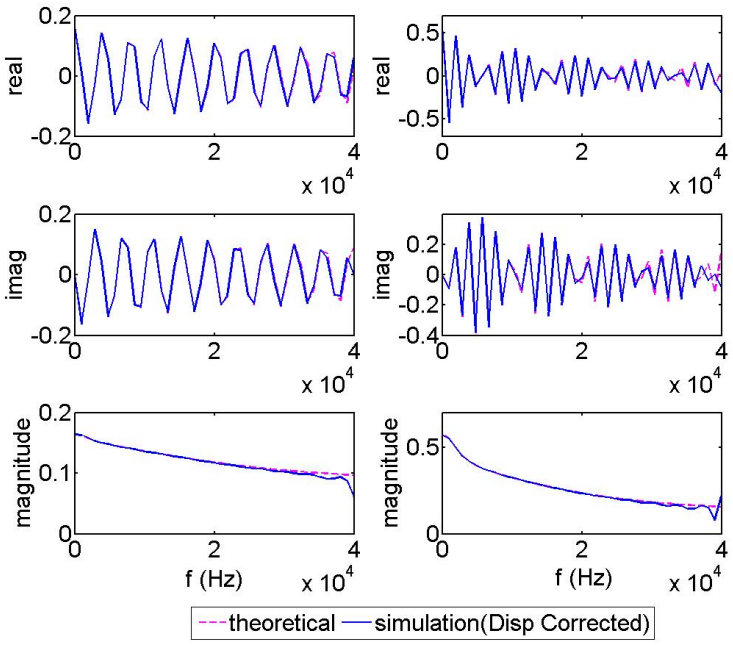
Figure. 8-12 Wave propagation in the PMMA-Mg 2 rod system

Simulation outputs are shown in Fig. 8-12. These signals are pretty much the same as 2 medium signals (Fig. 7-23). As the transmission Mg rod has a larger impedance (almost 4 times) than the incident PMMA rod, from the RC_ε expression (Table. 6-3 or Table. 6-9a) we find $RC_\varepsilon > 0$ (TC_ε is always positive, which means the transmission wave is always the same type of wave as the incident wave whatever the transmission impedance is), and the reflected wave is the same sign as the incident wave: the Mg rod acts like a relatively fixed end. As before, the incident and reflected deformations are uniform across the section, while the transmitted deformations become uniform after propagating over 50.5 mm in the Mg rod. Finally, high frequency oscillations due to dispersion effects in the PMMA can be seen in these waves, and these cause pulse durations to be elongated.

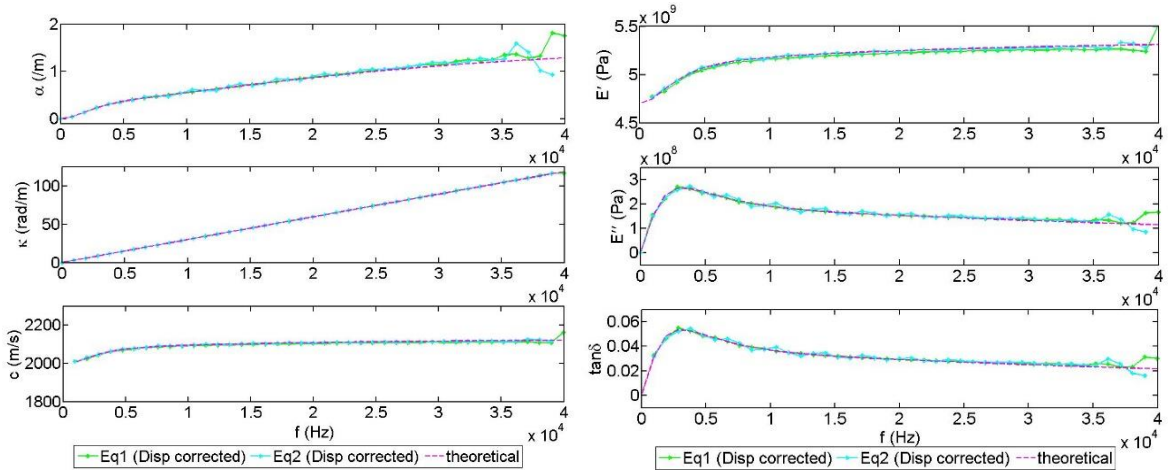
The 3 pulses extracted at ($x_{IR} = -500.5\,mm, x_T = +50.5\,mm$) were analysed. The dispersive wave speed profiles adopted are shown in previous sections. The corrected Fourier transforms, TCs and RCs are presented in Fig. 8-13(a) and (b). The '*vpasolve*' (a Matlab built-in numerical solver), with a confined square searching area $[-2 - \left(\frac{\omega}{c_0} - 2\right) i, 2 - (\frac{\omega}{c_0} + 2)i]$, was employed to find γ_1 when solving Eq. ①' and Eq. ②'. It is seen that, except for the disparities at high frequencies, the simulation-based values agree very well with the corresponding theoretical ones.



(a) Comparison of theoretical & simulation FFTs after dispersion correction



(b) Comparison of the theoretical and simulation $TC_{\tilde{\varepsilon}}$ & $RC_{\tilde{\varepsilon}}$



(c) Propagation coefficient and wave speed (d) Modulus and loss factor

Figure. 8-13 Data analysis process and derived material properties (PMMA-Mg 2 rods, $x_{IR} = -500.5\ mm, x_T = +50.5\ mm$)

It is worth checking the theoretical lower and upper frequency bounds that can be achieved in this case. The minimum frequency resolution is determined by signal duration

$$\Delta f_{min} = \frac{1}{signal\ duration} = \frac{1}{0.00105} \approx 952\ Hz\ .$$

The lowest frequency with no wave overlapping, which is limited by the shortest distance between 2 gauge stations on both rods, is

$$f_{l-PMMA} \approx \frac{c_{PMMA}}{incident\ gauge\ distance} \approx \frac{2100\frac{m}{s}}{2\times(1-0.4995)\ m} \approx 2.10\ kHz$$

$$f_{l-Mg} \approx \frac{c_{Mg}}{transmission\ gauge\ distance} \approx \frac{5085\,\frac{m}{s}}{2\times(1-0.0505)m} \approx 5.353\ kHz\ .$$

The upper frequency limit f_{h-3D} with identifiable FFT magnitudes for the 3 pulses in Fig. 8-13(a) is shown to be $f_{h-3D} \approx 35\ kHz$. If no dispersion correction is to be used, the 1D wave propagation assumption also sets an upper frequency limit without yielding appreciable dispersion phenomenon

$$f_{h-1D} = \frac{c_{PMMA}}{10\times incident\ rod\ diameter} \approx \frac{2100\,\frac{m}{s}}{10\times 0.013\ mm} \approx 16\ kHz\ (PMMA\ rod)$$

$$f_{h-1D} = \frac{c_{Mg}}{10\times transmission\ rod\ diameter} \approx \frac{5085\,\frac{m}{s}}{10\times 0.013\ mm} \approx 39\ kHz\ (PMMA\ rod)\ .$$

However, this won't be a problem as dispersion was corrected in our analysis. All in all, using this configuration of the 2-rod system and this input, the valid frequency range, within which the FFTs can be effectively identified without dispersion correction, is expected to be $5.353\ kHz$~$35\ kHz$.

8.5 Error analysis

8.5.1 Effect of non-normal incidence

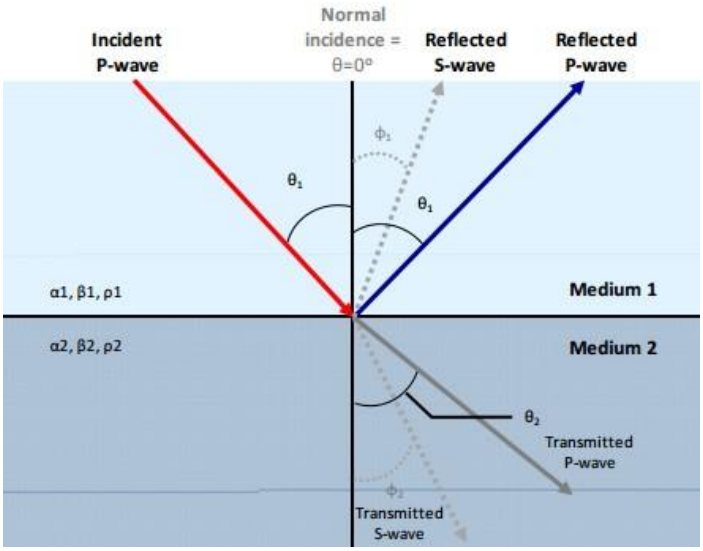


Figure. 8-14 Wave reflection and transmission at interface [81]

The interface theories were built on the assumptions of 'perfect' interface condition and interaction. However, in practice the incident wave may arrive at the interface with an angle. In the case of non-normal incidence upon the interface, mode conversion may result [78]. For example, a P-wave striking an interface can lead to 4 wave modes (Fig. 8-14): reflected and transmitted P, and reflected and transmitted SV. These 4 modes occur in different proportions and their proportions depends on

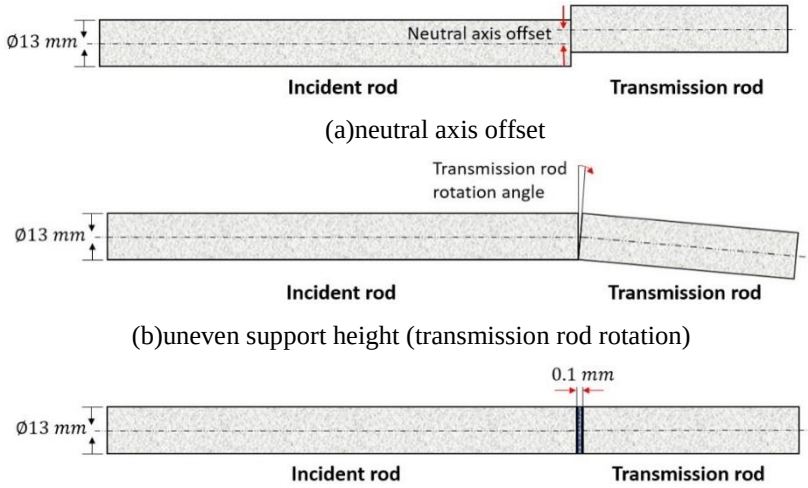
the contrast of acoustic impedances [79] and incidence angle. The exact amplitudes generated at non-normal interface incidence are dominated by the Zoeppritz equations [79, 80] which have been widely used in geophysics and seismology. More details are included in the full *web version*.

8.5.2 Misalignment investigations

Misalignments, *e.g.* imperfect interfaces (non-parallelism, separation) and non-uniform impact over the interface (which induces bending) are commonly encountered in experiments. It is found by Kariem *et al* [82] that interface parallelism caused by misalignment is the main cause of inaccuracies in analysing SHPB signals. They numerically investigated six types of commonly experienced bar misalignments in a conventional SHPB test: neutral axis offset, uneven support height, non-parallel impact face, bar straightness, dome and cone shape impact faces. Except for the first case, all other five cases have non-parallel contact surfaces (in the offset case the deformed faces are non-parallel as well). It is concluded from their investigations that, non-parallelism of contact faces, which generates flexural vibration mode, is the main cause that introduces noise in the otherwise clean signals. Mousavi *et al* [55] observed that, imperfect contact surfaces may cause errors in storage modulus when low particle velocity and short wave duration, and thus small displacements, are present in an SHPB experiment.

In this section, the six types of misalignments were investigated, and an 'effective' impedance was defined. Impedance plays an important role in determining wave behaviours at interface. The nature of all misalignment problems, essentially, is due to the change of 'effective' impedance, which is induced by bar misalignments, and is the acoustic impedance multiplied by the real contact area between the bars, rather than the bar area (Eq. (6.8)). For example, if a neutral axis offset exists, the effective area is the common area shared by the two rods, in the case of a dome shape surface, the effective contact area increases as the gap between the rods decreases. Realising the nature of the misalignment problem, it is thus reasonable to modify the impedance at the interface to simulate this phenomenon; this can be implemented by inserting a 3rd medium layer with variable impedance between the two rods.

Here simulations are described which were performed to gain some general insights into the misalignment problems, by testing a Ti-Ti 2-rod model assembled with imperfections. Three types of bar misalignment were investigated (Fig. 8-15): a neutral axis offset, an uneven support height (rotation of transmission rod), and a general non-parallel faces type. The first 2 types are commonly encountered in experiments, while the third, with a thin layer medium inserted between the two rods, was designed to generally represent all kinds of non-parallelisms (dome, cone, non-flat surfaces, *etc*).



(a)neutral axis offset

(b)uneven support height (transmission rod rotation)

(c)general non-parallel faces

Figure. 8-15 3 types of bar misalignment

The simulation scheme is shown in Table. 8-3. This was designed with evidence from previous work by Kariem *et al*. [82], in which they suggested that, with an SHPB configuration of 1 m long 12.7 mm diameter rods, an offset of 0.125 mm can generate a stress-strain curve with an error of 1.8 %; and if the rotation angle is within 0.03 °, the resulting error would be less than 0.4 %. In this work, larger misalignment errors were introduced in the first two cases (neutral axis offset and rotation of transmission rod), while in the third case, a thin layer (0.1 mm) of virtual elastic material was inserted between the two rods. There are two ways to modulate the impedance of the thin layer: either by adjusting its density or modulus. In density modulation, the layer has the same diameter, modulus and Poisson' ratio as the output rod material, which enables them to expand synchronously along the lateral direction. The density of the layer material, however, is ¼ of the transmission rod density, which makes its impedance to be half of the transmission impedance; in the other case, modulus was adjusted to be one fourth of Ti, which again gives half impedance of the rod materials.

Table. 8-3 Misalignment simulation scheme

	Neutral axis offset	Transmission rod rotation	General non-parallel faces	
Ti-Ti	0.2 mm 1 mm	0.03° 0.5°	0.1 mmØ13 mm Inserted layer	Density modulation: $S_L = S_{Ti}, \rho_L = \rho_{Ti}/4, E_L = E_{Ti}, \upsilon_L = \upsilon_{Ti}$
				Modulus modulation: $S_L = S_{Ti}, \rho_L = \rho_{Ti}, E_L = E_{Ti}/4, \upsilon_L = \upsilon_{Ti}$

8.5.2.1 *Neutral axis offset (NA. Offset)*

The offset model is graphically shown in Fig. 8-16. Three offset cases were examined: no offset, 0.2 mm and 1 mm. In each case, we first looked at the time domain signals, and then analyzed them to obtain material properties. Due to max page number limit, only the case of no offset and offset = 0.2 mm are detailed, and a comparison of all 3 cases are presented; further details can be found in the full *web version*.

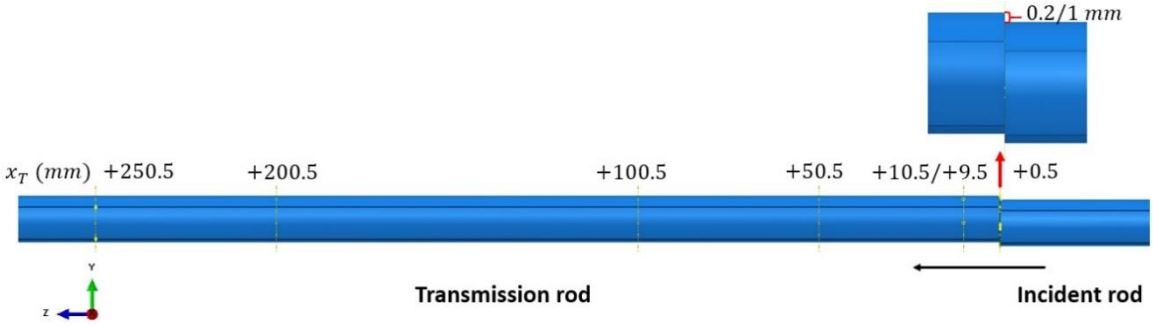
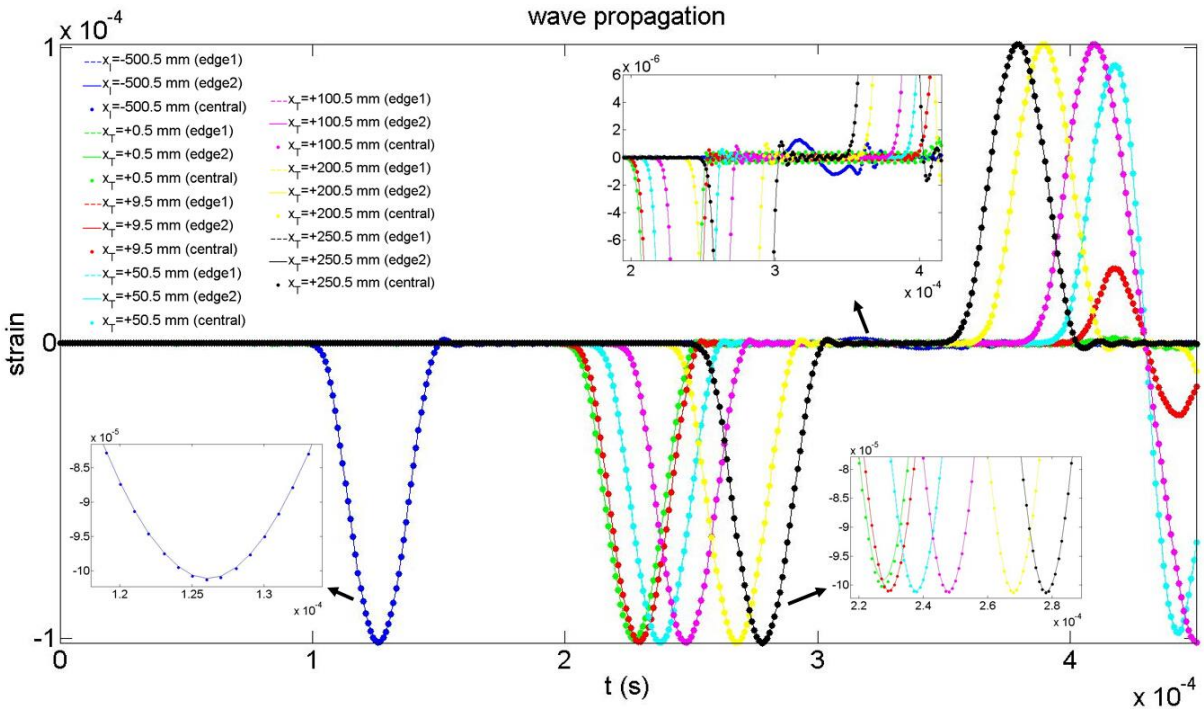


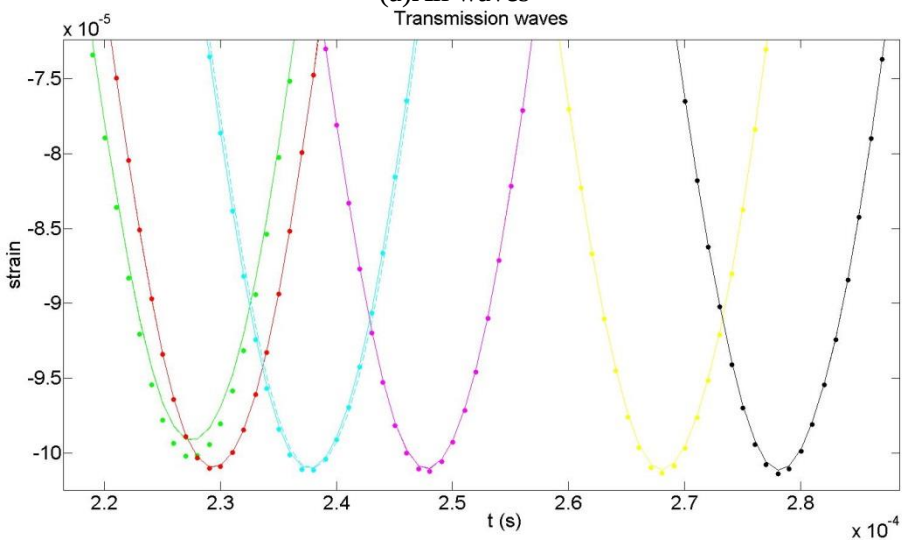
Figure. 8-16 the offset model

(1) No offset

The results without offset are shown in Fig. 8-17, which was extracted from the 2-rod Ti-Ti case simulated before (*e.g.* Fig. 8-1). On each cross-section, 3 signals were extracted: 1 from the central element, 2 from 2 axisymmetric elements at edge. It is observed that although the edge and central deformations are not the same at the contact interface, after a travel distance of 9.5 mm, all three signals line up, the cross-sectional deformation becomes uniform, which means in Ti rods the distance for uniform cross-sectional deformation to be achieved is less than 10 mm. Although a small reflected disturbance can be observed, no bending wave appears (otherwise the 2 edge signals will have different magnitudes). Derived Material properties have been presented in Fig. 8-2 and 8-3.



(a)All waves



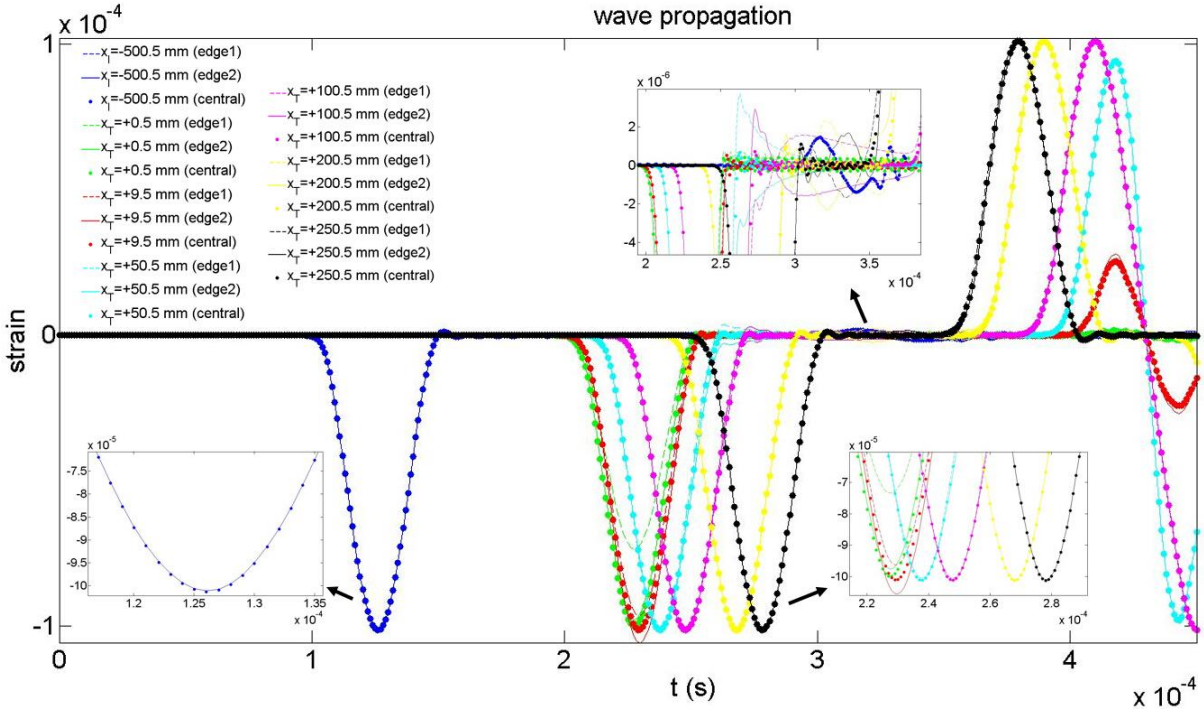
(b)Transmission waves

Figure. 8-17 Wave propagation in Ti-Ti 2 rods system *without* misalignment (a more precise copy of Fig. 8-1)

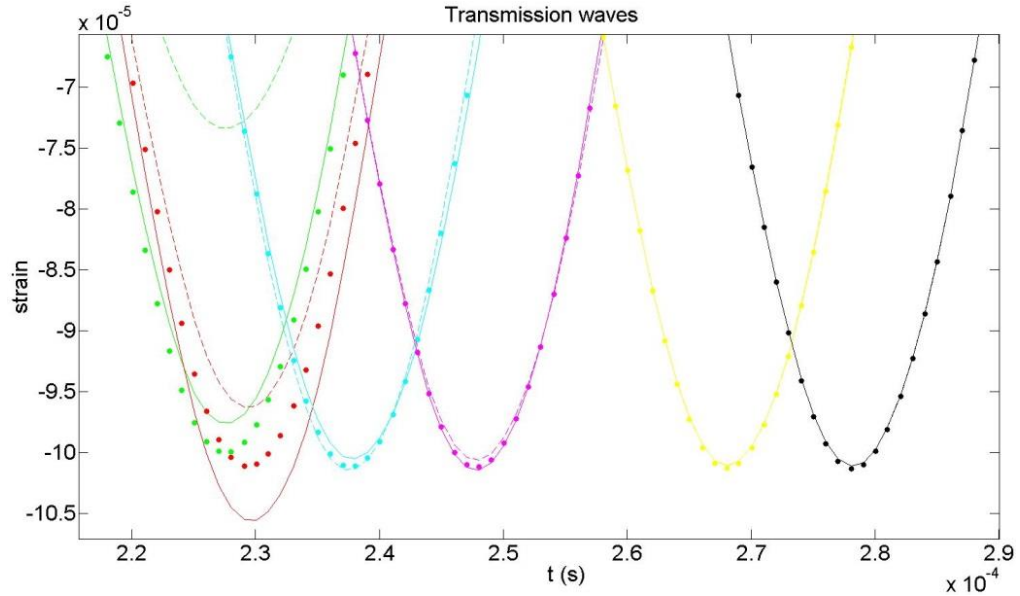
(2) offset=0.2 mm

Results from the 0.2 mm offset are shown in Fig. 8-18. Waves were captured in the middle of the incident rod and 6 monitoring locations on the transmission rod. It is observed in Fig. 8-17 that, strains on the $x_T = +0.5\ mm$ section are irregular; in fact, it is non-uniform even in a well-aligned 2 rod system. With an offset of 0.2 mm, although the strain amplitudes in all waves are similar, comparing Fig. 8-17 and Fig. 8-18, the effect of bending wave can be clearly seen in the latter case: In Fig. 8-17, after a propagation distance of 9.5 mm in the transmission rod, the 3 signals extracted

on the same cross-section tend to be the same, and no 'bending waves', characterized by opposite strain values in the tail region, was observed in the transmission waves, little reflections can be seen in the incident rod.



(a)All waves



(b)Transmission waves

Fig. 8-18 Wave propagation in Ti-Ti 2 rods system *with* NA. offset=0.2 mm

In Fig. 8-18, however, at locations close to the contact interface (*e.g.* $x_T = +9.5\ mm, +50.5\ mm, +100.5\ mm$), the differences between the edge and central strain amplitudes are obvious. This is because at these locations, the bending waves superpose with the compressive

longitudinal waves, which causes the strains at the edge elements to be larger (compression) or smaller (tension) than that of the central element, an average of both signals can yield values close to the central strain; at locations far away from the contact interface, flexural waves arrive later and are thus separated from the longitudinal waves and are instead observed in the tail of these waves. In addition, with offset the reflections are larger than those without offset.

1) Discussions of bending waves

Before we move to signal processing, bending waves attract attention. Normally, 3 types of waves are seen in a rod: quasi-longitudinal wave, shear wave, and bending wave. In a real rod impact event, both quasi-longitudinal and bending waves are involved. Bending waves in a 2-rod impact test can be generated by imperfect impact (misalignment between projectile and incident rod), rod configurations (bar straightness, non-flat faces) and contact conditions (non-parallelism, rotation, *etc.*), and they pose effect on the transmitted and reflected waves, which affects pulse selection in signal processing. It is thus worth probing into the mechanism of these flexural vibration modes, so that proper choices can be made when performing pulse selection.

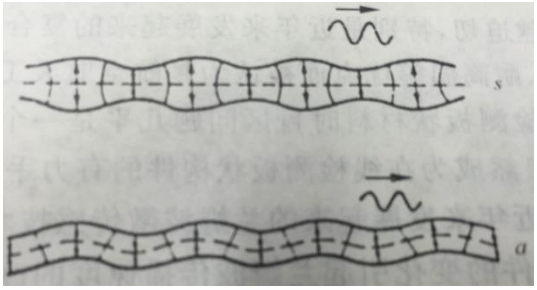


Fig. 8-19 Symmetric (up) and antisymmetric (bottom) modes of bending waves [from web]

Bending wave comes in 2 forms (Fig. 8-19): either symmetric or antisymmetric. It has been seen that, by comparing the transmission strain values extracted from the 2 axisymmetric edge elements, the antisymmetric mode appears in all our NA offset cases and transmission rod rotation cases. As shown in Fig. 8-19, if a rod is bent in the antisymmetric mode, the outer side is stretched and the inner side is compressed, while the neutral axis length remains unchanged [83].

Different beam theories, *e.g.* Euler-Bernoulli and Timoshenko beam theories, provide the basis for analytical description of bending waves. Here the simple Euler-Bernoulli beam theory (or thin beam

theory) was used to build the wave equation for a bending wave propagating in a beam [84]. Following the same path adopted before, the bending wave equation can be built (details can be found in the full *web version*); solving the wave equation using a harmonic displacement solution $u(x,t) = Ae^{i(\omega t - \kappa x)}$ yields the phase velocity c_B

$$c_B = \frac{\omega}{\kappa_B} = \sqrt{\omega\sqrt{\frac{EI}{\rho_L}}} = \sqrt{\omega c_L \sqrt{I}} \tag{8.1}$$

where EI is the flexural stiffness of a beam and I is the second moment of area of the cross-section about the neutral plane axis. $c_L = \sqrt{\frac{E}{\rho}}$ is the longitudinal wave velocity.

It is thus seen that, the bending wave velocity c_B, unlike the longitudinal wave velocity c_L, is not constant for a given material. It is proportional to the square root of frequency, which means a bending wave containing multiple frequencies was distorted during wave propagation, thus it is dispersive. From the expression of bending wave speed, it seems there is no upper limit for the speed, which violates physics. However, shear deformation sets restriction on the upper limit of the bending wave velocity [84], at higher frequencies bending waves transform into transverse waves, which has an upper limit.

Note that, bending wave velocities are generally significantly lower than longitudinal wave velocities. Using the rod properties defining the model, the frequency-dependent bending wave speed curve can be obtained based on Eq. (8.1). Here we use a $\emptyset 13\ mm$ Ti rod as an example. Generally for a circular cross-section, we have $I = \frac{\pi d^4}{32}$, therefore

$$c_B = \sqrt{\omega c_L I^{\frac{1}{2}}} = d\sqrt{1.9687 f c_L} = 1.4031 d\sqrt{f c_L}\ .$$

For this specific rod, we have material geometry $d = 0.013\ m$, and properties $E = 110\ GPa$, $\rho = 4500\ kg/m^3$, thus

$$c_L = \sqrt{\frac{110\ GPa}{4500\ kg/m^3}} = 4944\ m/s$$

and

$$c_B(f) = 1.2825\sqrt{f}\ .$$

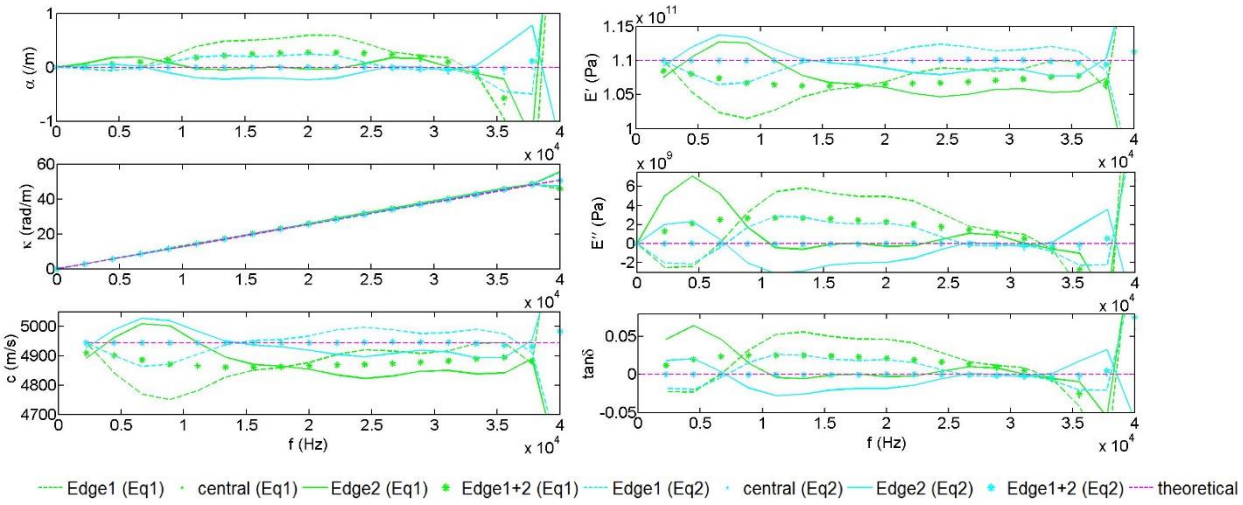
2) Pulse selection methodologies

The interface analytical work proposed previously, however, was built based on the assumption of pure quasi-longitudinal wave propagation; with the presence of bending waves, the applicability of the 2 boundary conditions (Eq. (6.4a') and (6.4b')) at the contact interface has to be re-examined. Thinking about the case where 2 rods are offset, the boundary conditions over the overlapped area and non-overlapped area at interface are different: in the overlapped area, both force and particle velocity are continuous, while in the non-overlapped area, the substances are free to move, which indicates particle velocity is not continuous over these areas. It is thus suggested that, the velocity continuity condition can only be applied in the 'overlapped' area, while the total force, with contributions from both the 'overlapped' and 'non-overlapped' areas, is equal on both surfaces regardless of the contact conditions. Another case which leads to the same conclusion is when the 2 rods have different cross-section areas, in which again we can imagine force is continuous but the velocity continuity condition can be only satisfied over the 'overlapped' area. Therefore, how to properly select these pulses, *e.g.* should we include or exclude the bending waves, becomes a problem here, as it may have effect on material property derivation. Theoretical evidence was constructed in the full *web version* to support our pulse selection.

The problem of bending waves normally appears when selecting the transmitted and reflected pulses. Assuming 2 long enough incident and transmission rods are employed, and gauge stations are mounted at positions distant enough from the contact interface (where the bending waves are generated), as bending waves travel at velocities much lower than the longitudinal waves, they will arrive later than longitudinal waves and thus can be separated. Consequently, 2 pulse selection methodologies were proposed: either including bending waves or excluding them. It seems more reasonable to include the bending wave as longitudinal components containing in both the transmitted and reflected bending waves contribute simultaneously to the balance of interface force along the longitudinal direction. However, excluding the bending effects may be a better choice in terms of obtaining more accurate results. A comparison between both methodologies was made when analysing the transmission rod rotation case (rotation angle=0.03°).

3) Results and discussions

Results based on the 3 signals (2 edge and 1 central) as well as an extra average of the 2 edge signals, all extracted on the ($x_{IR} = -500.5\ mm, x_T = +100.5\ mm$) cross-section, were presented in Fig. 8-20. Though both equations don't give exactly the same results (Eq. ②' gives closer results), they show the same trends: the results yielded by central wave sit between those by the 2 edge signals; an average of the 2 edge signals can give almost the same results as the central one, which indicates that, with the presence of bending wave, material properties can still be accurately determined using an average of the 2 diametrically opposite element strain recordings, and as indicated before, Eq. ②' gives more accurate results and thus it is preferred in analysing the misaligned signals.



(a) Propagation coefficient and wave speed (b)Modulus and loss factor

Figure. 8-20 Derived material properties of the transmission rod

(Ti-Ti 2 rods with NA. offset=0.2 mm, $x_{IR} = -500.5\ mm, x_T = +100.5\ mm$)

(3) Comparison of no offset, 0.2 mm and 1 mm

Details offset = 1 mm can be found in the full *web version*. A comparison of the results derived with no offset, offset=0.2 mm and 1 mm is made in Fig. 8-21; and a quantitative analysis, evaluated f = 20 kHz in Table. 8-4. It is seen that, within a valid frequency range 0~35 kHz, as expected, bigger offset gives more deviating results. Signals measured at a central element yield very accurate results (compared to the theoretical ones), but cannot be realised in practice. Fortunately, however, an average of the 2 diametrically opposite signals gives results of almost the same accuracy.

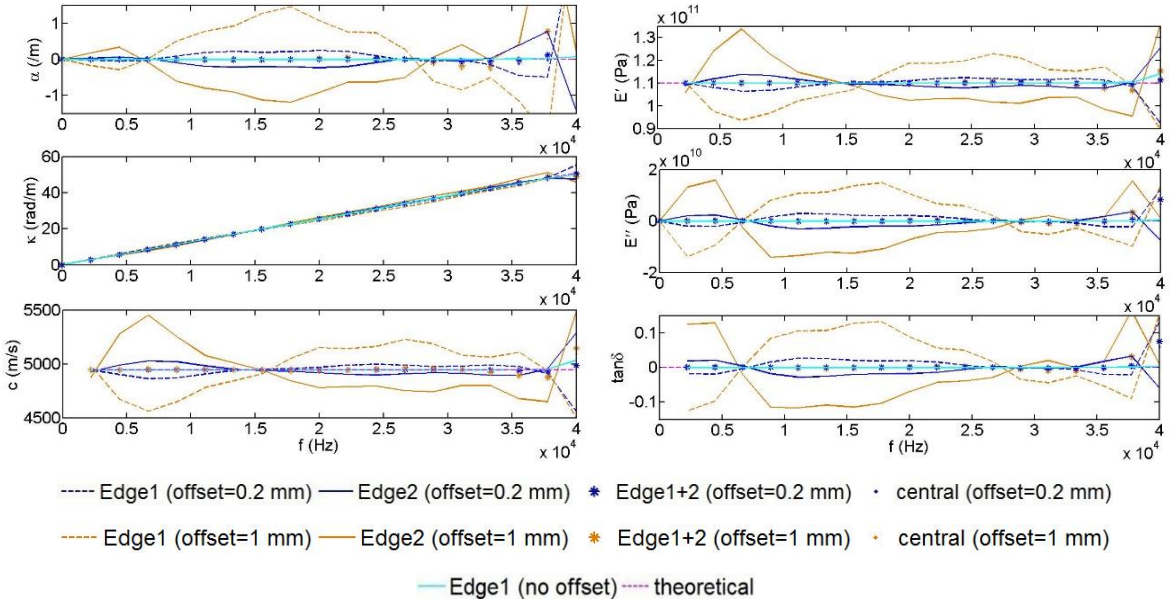


Figure. 8-21 Comparison of the material properties of the transmission rod derived from 3 cases: no offset, offset=0.2 mm and offset=1 mm (Eq. ②') (Ti-Ti 2 rods, $x_{IR} = -500.5\ mm, x_T = +100.5\ mm$)

Table. 8-4 deviations of results from 3 cases at f=20 kHz (Eq. ②' based)

		$\alpha\ (/m)$	$\kappa\ (rad/m)$	$c\ (m/s)$	$E'\ (GPa)$	$E''\ (GPa$	$tan\delta$
theoretical		0	25.4167	4944.13	110	0	0
No offset		-0.001754	25.4132 (-0.01%)	4944.13 (0%)	110.031 (+0.03%)	-0.015	-0.0001
offset=0.2 mm	edge 1	0.245	25.2967 (-0.47%)	4967.59 (+0.47%)	111.015 (+0.92%)	2.151	0.0194
	edge 2	-0.232	25.5467 (+0.51%)	4918.97 (-0.51%)	108.856 (-1.04%)	-1.977	-0.0182
	(edge 1+ edge 2)/2	0.002	25.4167 (0%)	4944.13 (0%)	110.000 (0%)	0.017	0.0002
	central	-0.015	25.4367 (+0.08%)	4940.24 (-0.08%)	109.827 (-0.16%)	0.130	-0.0012
offset=1 mm	edge 1	1.076	24.3967 (-4%)	5150.84 (+4.18%)	118.696 (+7.9%)	10.490	0.0883
	edge 2	-0.914	26.2867 (+3.42%)	4780.5 (-3.31%)	102.467 (-6.85%)	-7.134	-0.0696
	(edge 1+ edge 2)/2	0.024	25.4467 (+1.18%)	4938.3 (-0.12%)	109.740 (-0.24%)	0.207	0.0019
	central	0.027	25.4467 (+1.18%)	4938.3 (-0.12%)	109.740 (-0.24)	0.233	0.0021

8.5.2.2 *Rotation of transmission rod*

The rotation model is shown in Fig. 8-22. Consistent with the diagram in Fig. 8-16, the transmission rod rotates around the axis AB which is a tangent passing point A at the bottom edge (the 2 rods are in contact at Point A). Two rotation angles have been tested: 0.03 ° and 0.1 °. In the first case the angle is equal to the safe angle suggested by Kariem *et al* [82] while in the second case it is larger.

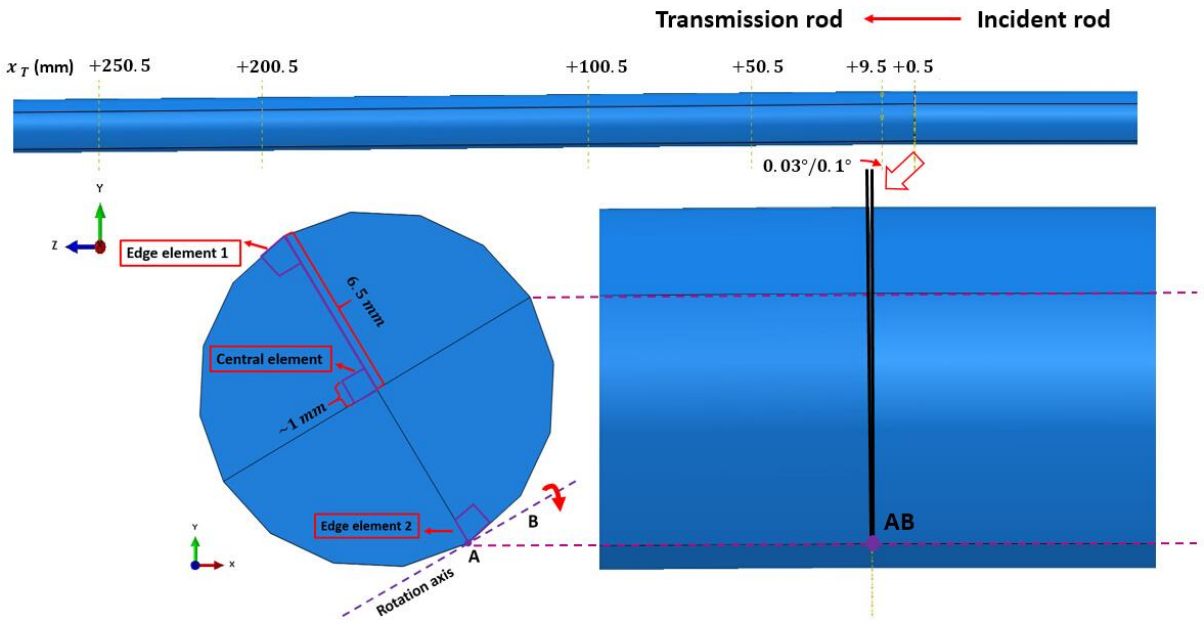


Figure. 8-22 transmission rod rotation diagram

Incident and reflected waves were measured at the same locations as in the previous section. Efforts were made to avoid involving bending waves during processing: the end points in the reflected and transmitted pulses have been selected such that the effect of bending waves is minimized. To correctly simulate the strain gauges, local coordinate systems, with an axis along the neutral axis of each rod, were defined and used to extract the strain values. Here the case of rotation angle (RA) = 0.03° was briefly presented; for greater details including the case RA=0.1 °, readers are referred to the full *web version*.

(1) Rotation angle (RA)=0.03°

Fig. 8-23 shows the longitudinal strain fields surrounding the interface when wave arrives at the interface. When the incident compressive wave arrives at contact interface, the gap gradually closes due to compressive deformations on the incident rod interface. The time domain signals are shown

in Fig. 8-24 and Fig. 8-25. Note that, in Fig. 8-24 the strain curve of the edge element 2 at $x_T = +0.5\,mm$ (where the two rods are initially in contact) has been shifted by an initial strain of -9.7×10^{-5} (which is consistent with the small compression area surrounding Point A). Incident deformations are uniform while reflections and transmissions deviate due to the appearance of bending waves. It is seen from Fig. 8-25 that, as bending waves interfere with longitudinal waves, the two edge strain signals sit each side of the central signal (neutral plane elements are not affected by the bending effect). Bending waves were gradually separated from longitudinal waves as travel distance increased; at $x_T = +250.5\,mm$, the 3 signals (Edge 1, Edge 2 and central) agree well as only longitudinal waves were contained, bending waves were again seen in the tails as they travel slower than quasi-longitudinal waves.

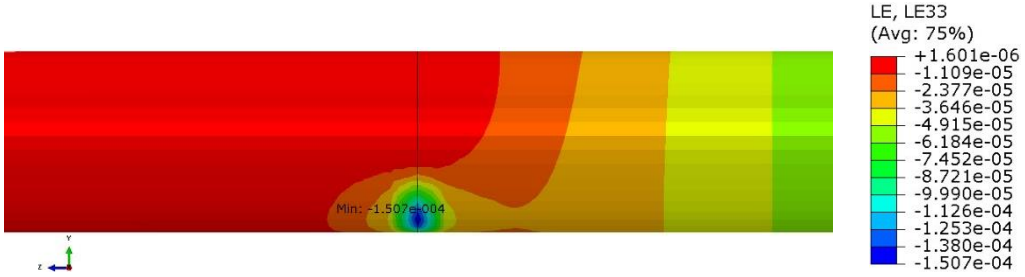


Figure. 8-23 Strain fields and clearance closure process in a transmission rod rotation simulation (RA=0.03°)

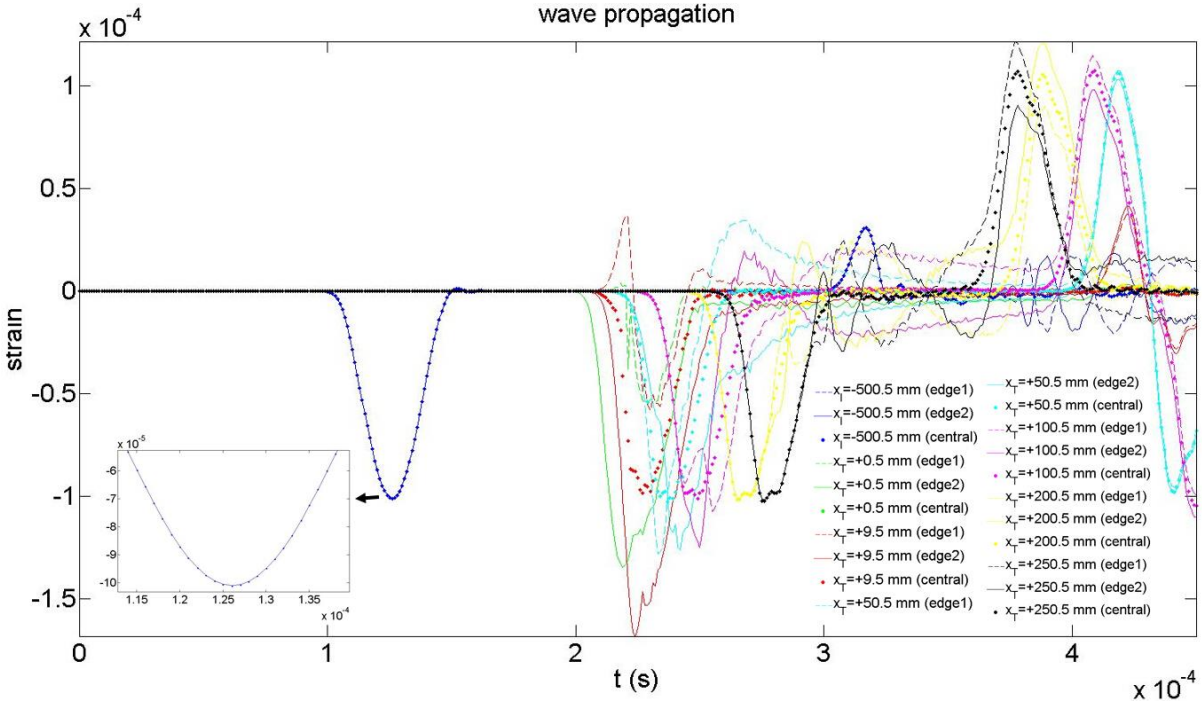


Figure. 8-24 Wave propagation in Ti-Ti 2 rods system *with* transmission rotation angle=0.03°

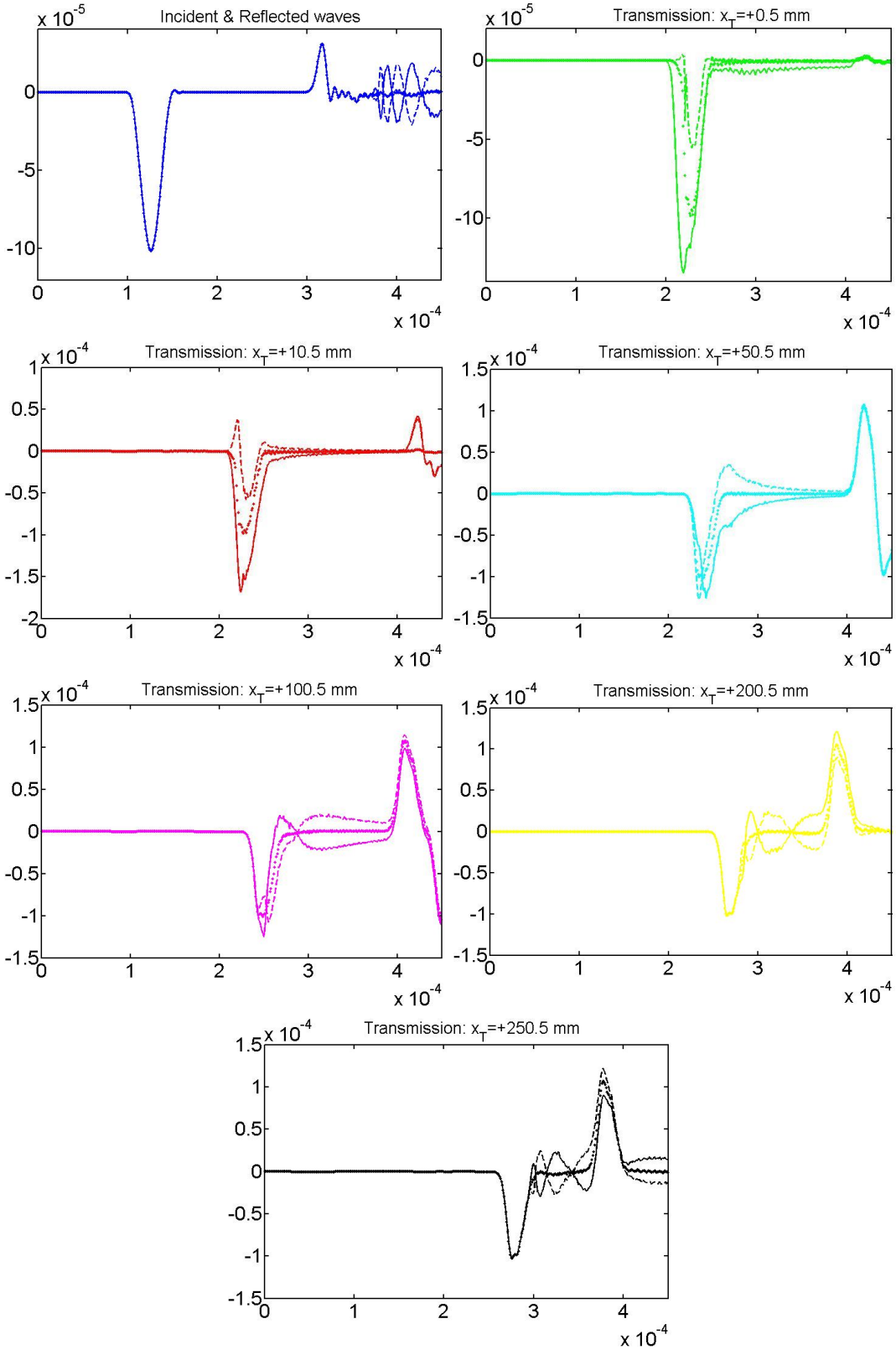


Figure. 8-25 Signals extracted at elements at various locations (dash: Edge 1; line: Edge 2; dot: Central)

Before proceeding to data processing, a rough analysis on the timing of wave propagation was performed using the signals collected at ($x_{IR} = -500.5\ mm, x_T = -250.5\ mm$) as an example (Fig. 8-26). The duration of the input acceleration pulse is 50 μs, which corresponds to a wavelength of

0.2472 m in the Ti rod. As seen from Fig. 8-26, during its propagation in the incident rod, it doesn't disperse much. The longitudinal wave speed in an elastic Ti rod is about 4944 m/s, it thus takes about 10^{-4} s for the wave to travel over a distance of 0.5 m. This estimation is consistent with the timing in Fig. 8-26: at $10^{-4}\ s$ the incident wave arrives at the middle of incident rod; at $2.5 \times 10^{-4}\ s$ it arrives at the middle of transmission rod; and at $3 \times 10^{-4}\ s$ reflection is observed at the incident monitoring station. As bending wave normally travels at the velocity $c_b = c_L/2$, they are expected to arrive the transmission gauge station ($x_T = +250.5\ mm$) at $3 \times 10^{-4}\ s$, and the incident gauge station ($x_{IR} = -500.5\ mm$) at $4 \times 10^{-4}\ s$. This can be confirmed in Fig. 8-26.

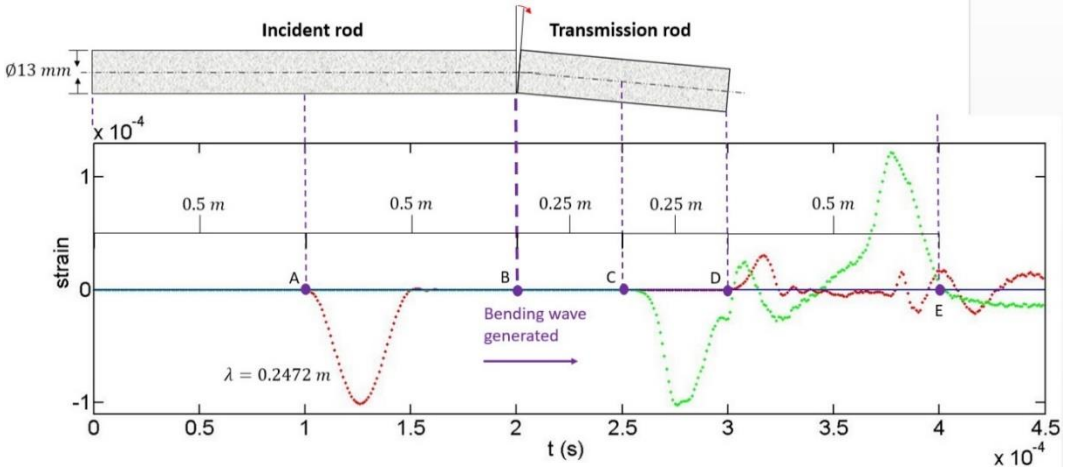
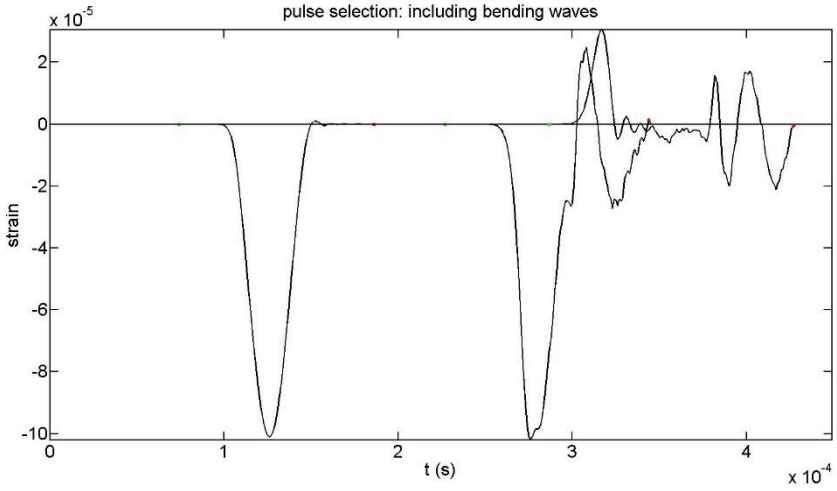


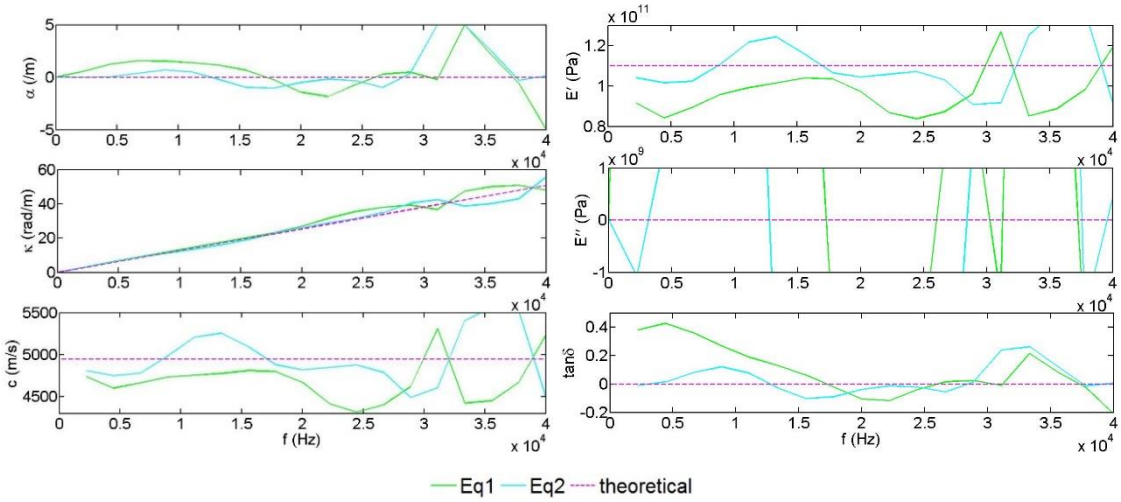
Figure. 8-26 analysis of signals collected at ($x_{IR} = -500.5\ mm, x_T = -250.5\ mm$)

In the data analysis stage, the two pulse selection methodologies, *i.e.* one includes the bending wave while the other one excludes, were tried. Using data collected at Edge 1 as an example, the pulses selected and results derived using the 2 pulse selection methods were shown in Fig. 8-27 and 8-28. The dispersive wave speed profiles used were the same as those used in Ti-Ti 2-rod simulation before. Looking at the material properties derived by Eq. ②', it is found that, excluding bending effects gives very accurate results (Fig. 8-28(b) and (c)), while oscillations appear if bending waves are to be included (Fig. 8-27(b) and (c)). Further, by excluding bending waves, 3 pulses extracted at 3 elements (Edge 1, Edge 2, and Central) on the same cross-section at ($x_{IR} = -500.5\ mm, x_T = +250.5\ mm$) were analysed. Material properties were obtained using 4 methodologies: Edge 1, Edge 2, (Edge 1+ Edge 2)/2, and the central one. A comparison was made in Fig. 8-29. It is seen that: 1)

results yielded by Eq. ②' show less deviations; 2) both edge signals give more or less oscillating results, an average of the 2 edge signals can give accurate results closer to theoretical ones.

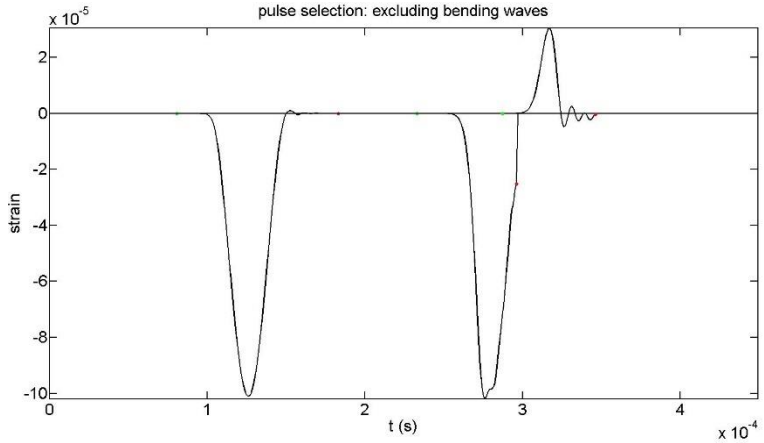


(a)Pulse selection (green dots: start locations, red dots: end locations)

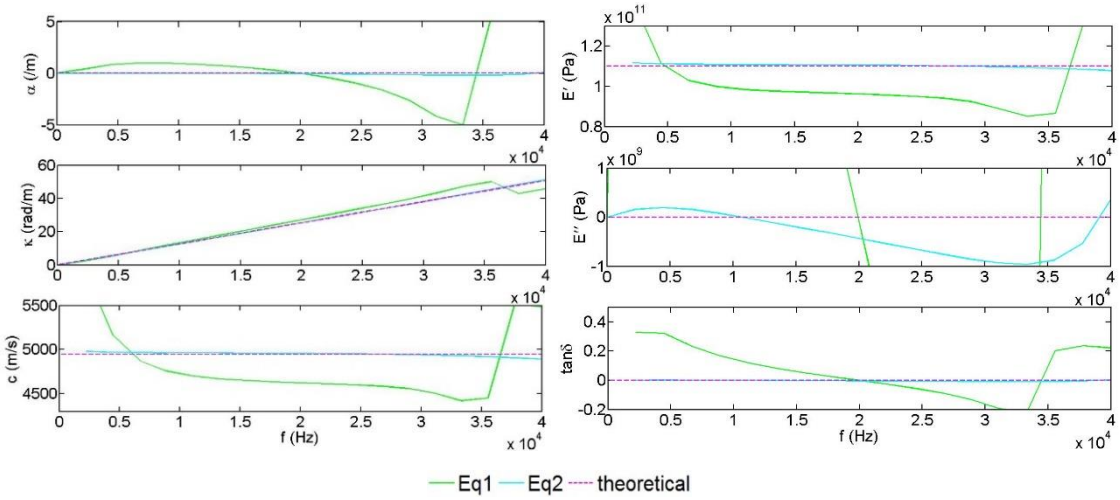


(b) Propagation coefficient and wave speed (c)Modulus and loss factor

Figure. 8-27 Inclusion of bending waves to obtain transmission rod material properties (Ti-Ti 2 rods with transmission rotation angle=0.03°, $x_{IR} = -500.5\ mm, x_T = +250.5\ mm$)

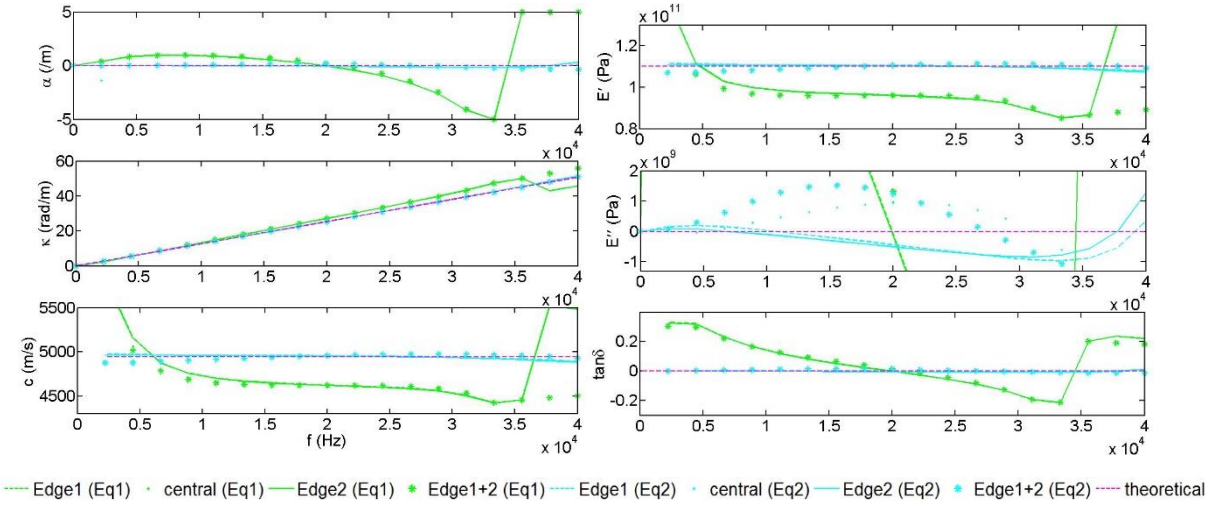


(a) Pulse selection (green dots: start locations, red dots: end locations)



(b) Propagation coefficient and wave speed (c)Modulus and loss factor

Figure. 8-28 Exclusion of bending waves to obtain transmission rod material properties (Ti-Ti 2 rods with transmission rotation angle=0.03°, $x_{IR} = -500.5\ mm, x_T = +250.5\ mm$)



(a) Propagation coefficient and wave speed (b)Modulus and loss factor

Figure. 8-29 A comparison of derived material properties by excluding bending effects

(Ti-Ti 2 rods with transmission rotation angle=0.03°, $x_{IR} = -500.5\ mm, x_T = +250.5\ mm$)

(2) Comparison of the 2 rotation cases

A graphical comparison of the Eq. ②' based material properties from the three cases (*i.e.* no RA, RA=0.03°, RA=0.1°) is made in Fig. 8-30. A quantitative analysis was presented in Table. 8-5. It is seen that, larger rotation angle leads to more deviating results; the central signal or an average of the 2 edge signals (which cancels the bending effect) can give more accurate results; within the frequency range of 0~40 kHz, a rotation angle of 0.03° gives small deviations across this frequency band, however, this is not the case for 0.1 °, where there are large deviations across the band. Hence, it is seen that minimizing rotation is more important than minimizing axial misalignment.

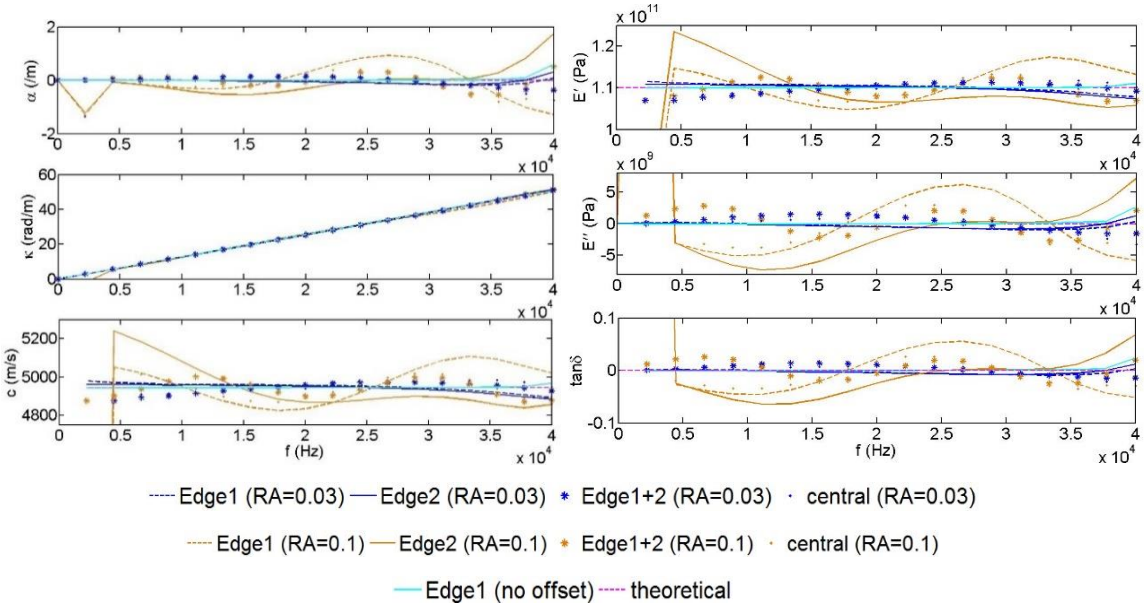


Figure. 8-30 Comparison of the transmission rod material properties derived in 3 cases (Eq. ②'): no rotation, RA=0.03° and RA=0.1° (Ti-Ti 2 rods, $x_{IR} = -500.5\ mm, x_T = +250.5\ mm$)

Table. 8-5 Deviations of the results of the 3 cases at f=20 kHz (Eq. ②' based)

		$\alpha\ (/m)$	$\kappa\ (rad/m)$	$c\ (m/s)$	$E'\ (GPa)$	$E''\ (GPa$	$tan\delta$
theoretical		0	25.4167	4944.13	110	0	0
No RA		-0.001463	25.4124 (-0.017%)	4945.0 (0.018%)	110.039 (+0.035%)	-0.0131	-0.0001
RA=0.03°	edge 1	-0.05	25.3567 (-0.236%)	4955.83 (+0.237%)	110.520 (+0.473%)	-0.436	-0.0039
	edge 2	-0.058	25.3767 (-0.157%)	4951.93 (+0.158%)	110.345 (+0.314%)	-0.504	-0.0046
	(edge 1+ edge 2)/2	0.142	25.3467 (-0.275%)	4957.79 (+0.276%)	110.598 (+0.544%)	1.239	0.0112
	central	0.109	25.4367 (+0.079%)	4940.24 (-0.079%)	109.821 (-0.163%)	0.941	0.0086
RA=0.1°	edge 1	0.292	25.9967 (+2.282%)	4833.83 (-2.231%)	105.107 (-4.448%)	-2.584	0.0225
	edge 2	-0.313	25.8167 (+1.574%)	4867.53 (-1.549%)	106.571 (-3.117%)	2.361	-0.0242
	(edge 1+ edge 2)/2	-0.058	25.6467 (+0.905%)	4899.79 (-0.897%)	108.034 (-1.788%)	-0.556	-0.0051
	central	0.228	25.7067 (+1.141%)	4888.36 (-1.128%)	107.507 (-2.267%)	1.907	-0.0177

8.5.2.3 General non-parallel faces

As discussed before, the nature of the misalignment problem may be the change of the 'effective' contact impedances. Imagine that in a well-aligned 2-rod system, the 2 contact faces remain parallel and thus their impedances keep constant during wave propagation at interface. In a badly aligned 2-rod system, a dome shape transmission face for example, the 'effective' impedance of the transmission rod increases as the gap closes when transmission rod face undergoes deformation. As modulus and density are always constant, the 'effective' impedance here is defined as

$Z_{effective}(\omega) = S_{effective}\sqrt{E^*(\omega)\rho}$ where $S_{effective}$ is the real contact area. It is thus our intention here that the misalignment phenomenon can be generally approximated by introducing a certain amount of impedance variation at the contact interface, this can be implemented by inserting a 3rd medium layer between the 2 rods, and it is expected to generally represent most types of non-parallelisms (dome, cone, non-flat surfaces, *etc*.). Besides, the insertion of the 3rd medium can also be used to simulate the lubricant effect.

The inserted 3rd medium layer has a geometry of 13 mm diameter and 0.1/0.5 mm long. Although only the 'effective' contact area $S_{effective}$ changes in a misalignment problem, in order to make the rod and the 3rd medium expand synchronously, the cross-section S_L, modulus E_L and Poisson's ratio υ_L may be selected to be the the same as the Ti rods ($S_L = S_{Ti}, E_L = E_{Ti}, \upsilon_L = \upsilon_{Ti}$), but its density $\rho_L = \rho_{Ti}/4$, to generate a half impedance ($Z_L = Z_{Ti}/2$): the density modulation method. An alternative approach is to keep density and cross-section area the same ($\rho_L = \rho_{Ti}, S_L = S_{Ti}, \upsilon_L = \upsilon_{Ti}$) but make the modulus a quarter of the Ti rod ($E_L = E_{Ti}/4$): the modulus modulation method. The simulation scheme is displayed in Table. 8-3. Here only the 0.1 mm thickness case was presented.

Frictionless tangential contact and 'hard' normal contact with finite sliding was defined. An approximate element size of 1 mm was adopted when meshing the cross-section of the thin medium layer symmetrically. In total 360 linear hexahedral elements of type C3D8R (reduced first-order 3 dimensional solid element with 8 nodes) and 603 nodes were resulted. The medium was meshed into 2 layers along the thickness direction with a finer mesh size of 0.5 mm compared to that of 1 mm in the incident and transmission rods. The assembly and mesh diagram is shown in Fig. 8-31.

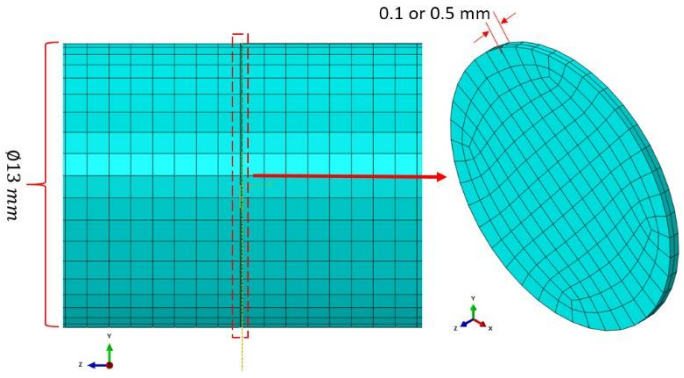


Figure. 8-31 A thin medium layer inserted between the incident and transmission Ti rods to represent general misalignment case

(1) Thickness = 0.1 mm

1) Modulus modulation

Wave propagation in the 3-medium system is shown in Fig. 8-32. Comparing with those of no misalignment in Fig. 8-17, it is seen that due to the insertion of a 3rd medium, a larger proportion of reflection wave were seen, and small amplitude bending waves observed. A closer look at the interface deformations reveals that bending waves may be induced by the sliding of the thin layer during deformation.

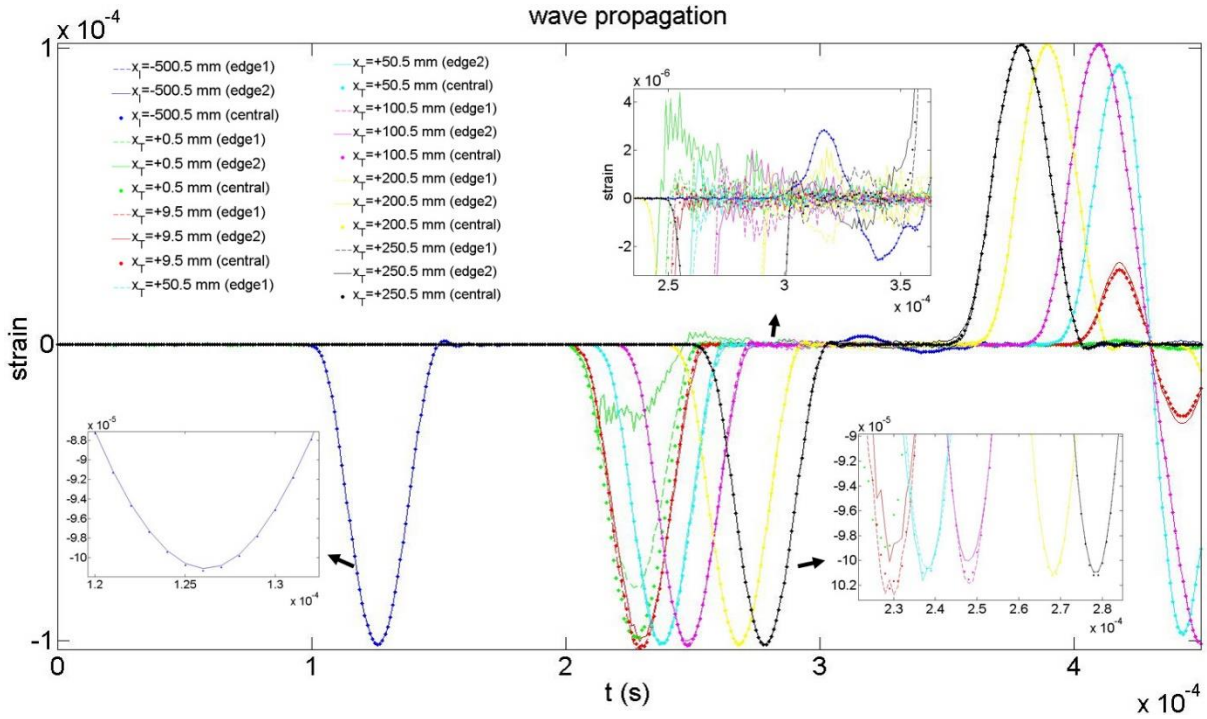
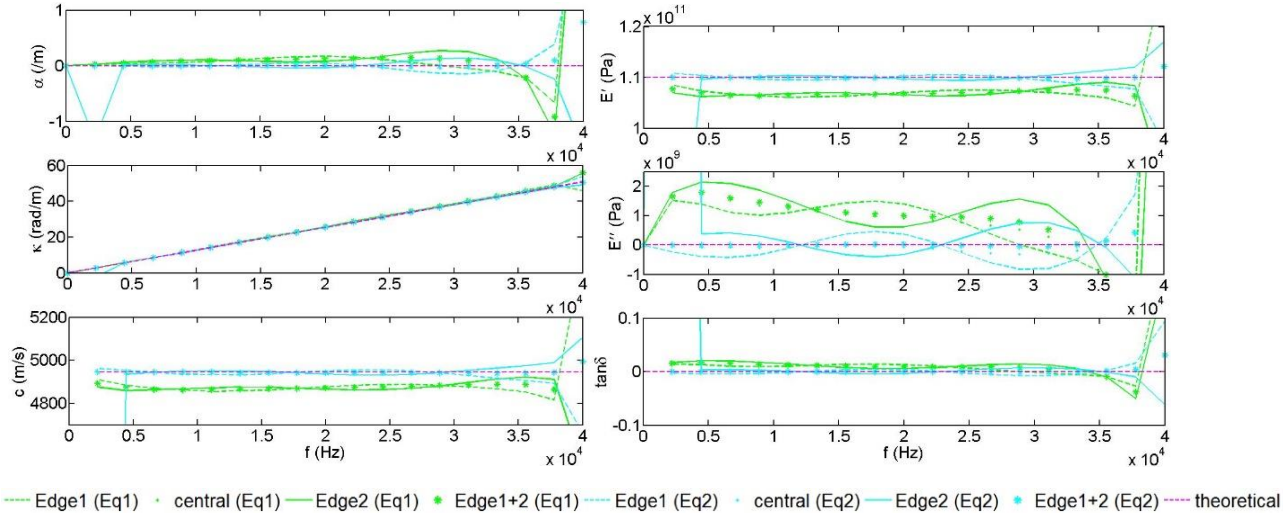


Figure. 8-32 Wave propagation in Ti-Ti 2-rod system with a 0.1 $mm\emptyset 13\ mm$ plate insertion (modulus modulation)

Signals collected at ($x_{IR} = -500.5\ mm, x_T = +250.5\ mm$) were analysed using the 2-rod interface analysis technique. As bending waves occur in the transmission and reflection signals, the 2 edge signals don't necessarily yield the same results, the results yielded by Eq. ②' are generally acceptable in Fig. 8-33. However, compared to the aligned results (Fig. 8-2 and 8-3), here the results are more deviating due to insertion of the 3rd medium. By using the central signal or an average of the 2 signals, more accurate results were obtained.



(a) Propagation coefficient and wave speed (b)Modulus and loss factor

Figure. 8-33 Derived material properties of the transmission rod (Ti-Ti 2 rods with inserted medium thickness=0.1 mm, $S_L = S_{Ti}, \rho_L = \rho_{Ti}, \upsilon_L = \upsilon_{Ti}, E_L = E_{Ti}/4$, $x_{IR} = -500.5\ mm, x_T = +250.5\ mm$)

2) Density modulation

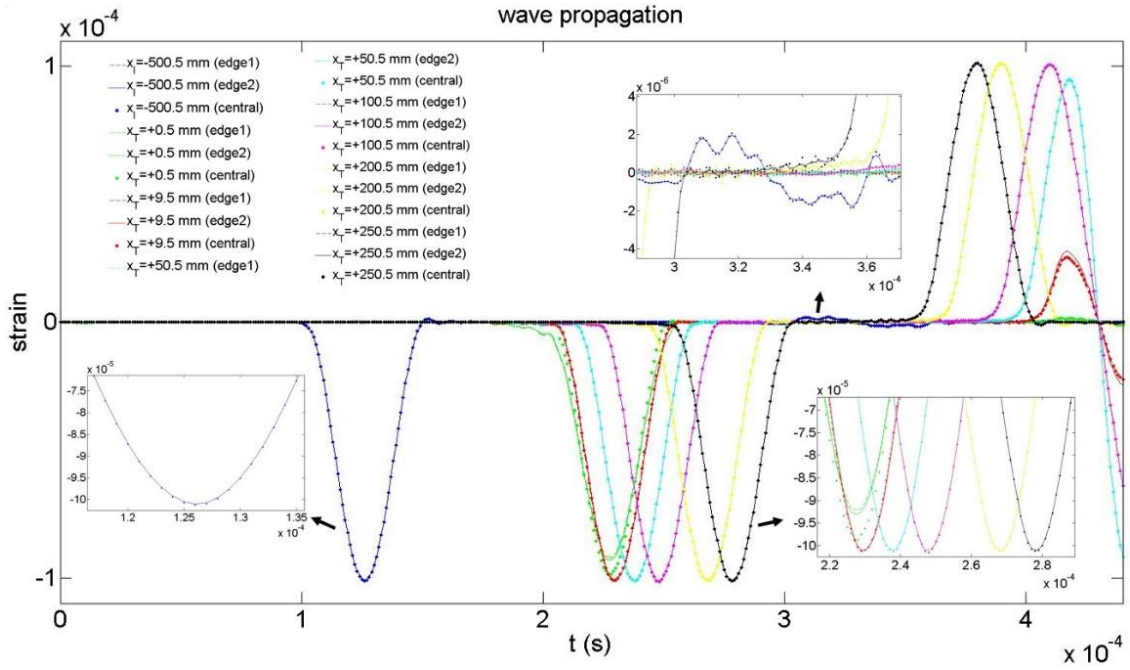
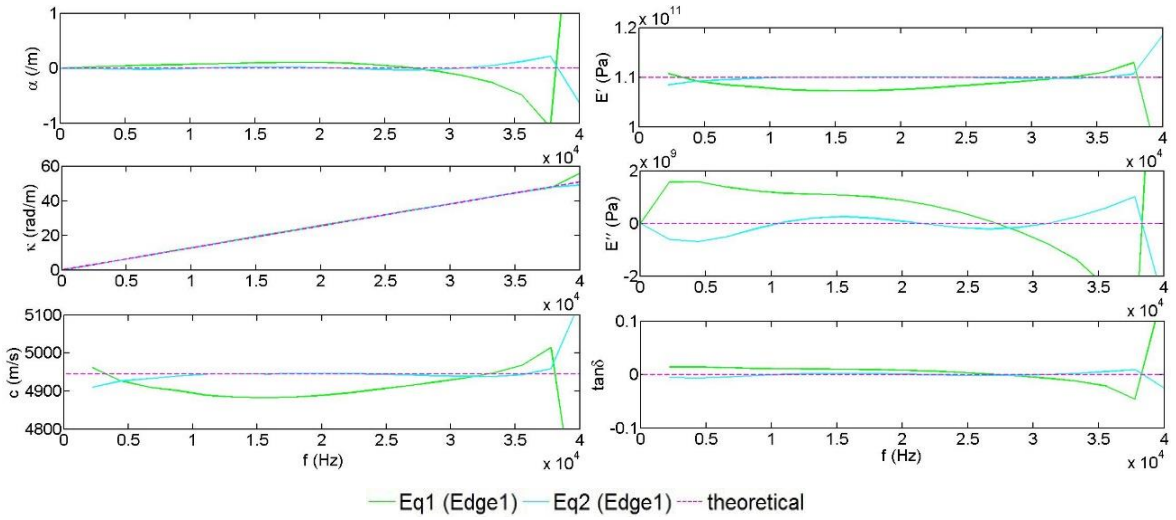


Figure. 8-34 Wave propagation in Ti-Ti 2-rod system with a 0.1 mmØ13 mm plate insertion (density modulation)

Wave propagation in the 2-rod 3 medium system is shown in Fig. 8-34. Larger reflections are seen here compared to the aligned one in Fig. 8-17. Furthermore, disturbances can be seen in the starting region of transmitted waveforms. As no apparent bending waves were observed, the cross-sectional deformation became uniform after waves propagated over a certain distance ($e.g. > +9.5\ mm$). The

resulting material properties, derived using signal collected at edge 1 element at ($x_{IR} = -500.5\ mm, x_T = +250.5\ mm$), were shown in Fig. 8-35. It is seen that, results yielded by Eq. ②' don't deviate much from theoretical ones.



(a) Propagation coefficient and wave speed (b)Modulus and loss factor

Figure. 8-35 Derived material properties of the transmission rod

(Ti-Ti 2 rods with inserted medium thickness=0.1 mm, $S_L = S_{Ti}, E_L = E_{Ti}, \upsilon_L = \upsilon_{Ti}, \rho_L = \rho_{Ti}/4$, $x_{IR} = -500.5\ mm, x_T = +250.5\ mm$)

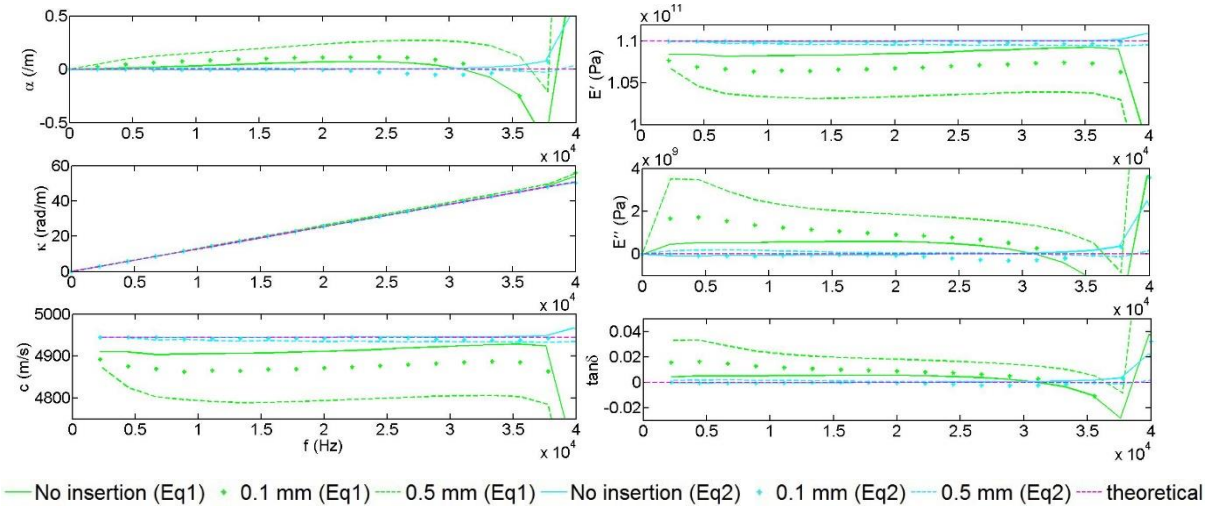
(2) Comparison of thickness = 0.1 and 0.5 mm

A quantitative summary of the reflected strain amplitudes was presented in Table. 8-6. Again, it is seen that, larger reflection amplitudes occur as a result of increasing insertion thickness. With the same impedance change, a modification of modulus of the inserted layer could induce more disturbance in reflection than the change in density.

Table. 8-6 Comparison of reflected strain amplitudes with & without inserted layer

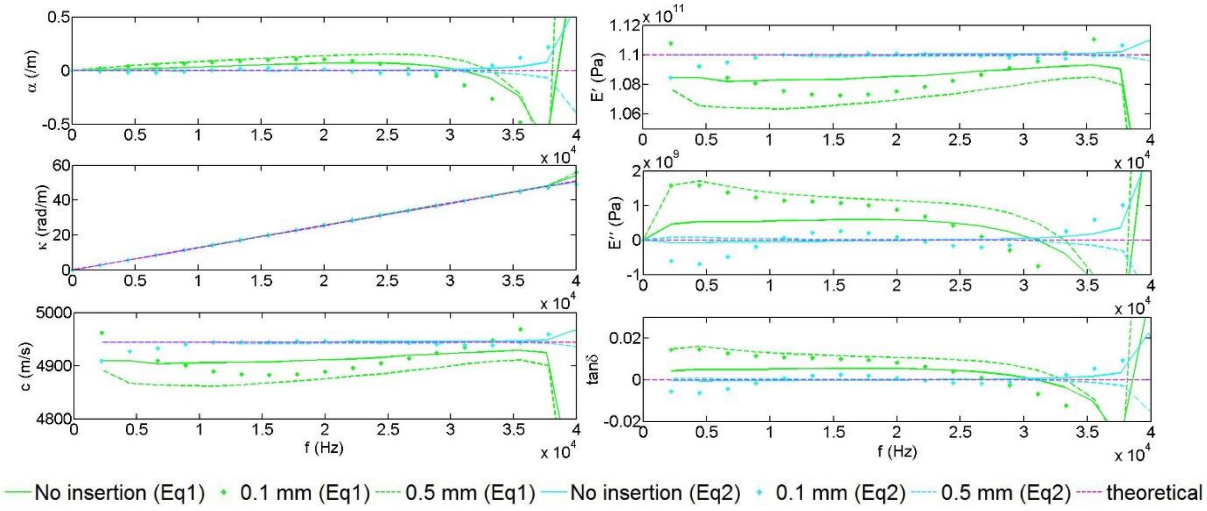
	Modulus modulation	Density modulation
No insertion	1.29×10^{-6}	
Insertion thickness=0.1 mm	2.81×10^{-6}	2×10^{-6}
Insertion thickness=0.5 mm	5.4×10^{-6}	2.73×10^{-6}

A comparison of the derived material properties of the transmission rod from the 3 cases (aligned, thickness=0.1 & 0.5 mm) were shown in Fig. 8-36 and 8-37. It is seen that: 1) force equilibrium BC (Eq. ②') yields less deviations in deriving the transmission rod material properties; 2) generally, an increment in layer thickness leads to larger deviations in both equations; 3) density modulation gives less deviating results.



(a) Propagation coefficient and wave speed (b)Modulus and loss factor

Figure. 8-36 Comparison of transmission rod material properties derived with & without an inserted layer (modulus modulation, $x_{IR} = -500.5\ mm, x_T = +250.5\ mm$)



(a) Propagation coefficient and wave speed (b)Modulus and loss factor

Figure. 8-37 Comparison of transmission rod material properties derived with & without an inserted layer (density modulation, $x_{IR} = -500.5\ mm, x_T = +250.5\ mm$)

The small difference between the time domain signals between the aligned (Fig. 8-17) and modified (Fig. 8-32, Fig. 8-34) 2-rod systems, as well as the Eq. ②' based results and theoretical ones, reveals that, if a thin layer of virtual grease, with half impedance of the input and output rods, is inserted between the 2 rods, it won't have much effect on wave propagation at interface and material property derivation using the 2 BCs equations which are based on an assumption of 'perfect' interface. However, an insertion of a thin layer is insufficient to represent general misalignments; the reason is, the way that the thin layer affects the wave propagation at interface is not the same as misalignments do. Based on our previous analysis, a neutral offset of 0.1 mm or a rotation angle of

0.03° could affect the Eq. ②' based results up to 1% (Table. 8-4 and 8-5) for all material properties at f=20 kHz, while an insertion of a thin layer, with a thickness of 0.5 mm for example, only affects the results by 0.36% at the maximum (Eq. ②' based storage modulus). To make the thin layer a better representation of a general type misalignment, efforts should be taken to properly choose the impedance of the thin layer.

Chapter 9: Mechanical wave behaviours at 2-medium & 2-rod interfaces: Experimental Implementations

In this chapter, wave behaviours at the interface of two rods were examined experimentally. Similar to the interface simulations, experiments were designed in two steps: firstly, a single rod with two strain gage measurement stations was tested, assuming a virtual 'perfect' interface exists somewhere between the two stations; then the same rods were cut into four shorter rods, on which a mixture of 'real' interface tests were performed. For the former category, tests have been performed on the 1200 mm Ti rod and the 1500 mm PMMA rod; for the latter, 4 types of tests, *i.e.* Ti-Ti, PMMA-PMMA, Ti-PMMA, PMMA-Ti, were conducted. The signals from the first category tests were analysed using both the single rod and interface analysis techniques, and a comparison of both results verified the validity of the interface technique; the results from the latter test help understand how wave behaviours at real interfaces deviate from the theories, and the effect of interface imperfections.

9.1 Experimental descriptions

9.1.1 Overview and experimental setup

The choice of rod materials was based on the consideration that the impedance of the material should be relatively small so that it possesses the potential to be implemented in a modified SHPB setup to test soft materials. When testing soft materials either using metallic or polymeric bars, those with low impedance are normally preferred so that the mismatch between the characteristic impedances of the specimen and bars is small enough to ensure that transmission signals are sensible. The nominal properties of some common low-impedance materials/rods candidates were listed in Table. 9-1. Generally speaking, even with the same rod geometry, the impedances of metallic rods are several times larger than polymers. The maximum impedance ratio between those shown in the table is evaluated to be about 11.156 (Ti to Delrin). Among these metallic bars, iron has the largest impedance while Magnesium the least. Aluminium is often used in testing soft materials [85]. For polymeric bars, Polycarbonate (PC) [86, 87] and acrylic [88] have been used before. Nylon has the lowest impedance among the polymers listed; however, it is susceptible to bending under impact, which leads to failure of the 1D wave propagation assumption because the plane assumption fails.

Thus the capacity of resisting to bending is another criterion considered when selecting the rod materials. We expect the rod to keep reasonably straight and axially movable during an impact event. In my tests, Titanium alloy (Ti6Al4V) and commercial PMMA rods were used. Initially, the Ti rod came with a diameter of half inch (12.7 mm) and length of 1200 mm; the PMMA rod was 13 mm in diameter and 1500 mm in length. The test scheme is presented in Table. 9-2.

Table. 9-1 Nominal material constants

Material	Steel	Ti	Aluminium	Mg	PMMA	Delrin	PVC	Nylon12 (Griehl [14])
ρ (kg/m^3)	7850	4500	2700	1740	1180	1420	1400	1010
E^* (Gpa)	210	110	70	45	5.36 (instantaneous)	2.80 (Tensile)	2.4-4.1 (3 Gpa)	1.172
υ	0.3	0.32	0.33	0.29 (0.35)	0.38	0.35	0.4	0.4
$c_L = \sqrt{\frac{E^*}{\rho}}$	5172	4944	5092	5085	2131	1404	1309~1711	1077
$Z = A\sqrt{\rho E^*}$ $(kg * m * Pa)^{\frac{1}{2}}$ $(d = 13\ mm)$	5.389×10^3	2.953×10^3	1.825×10^3	1.175×10^3	0.334×10^3	0.265×10^3	$(0.243\sim0.318) \times 10^3$	0.144×10^3

Table. 9-2 Interface test scheme

Ti-Ti	1200 mmØ12.7 mm Ti 1 Rod	600 mmØ12.7 mm Ti-600 mmØ12.7 mm Ti
PMMA-PMMA	1500 mmØ13 mm PMMA 1 Rod	1000 mmØ13mm PMMA-500 mmØ13 mm PMMA
Ti-PMMA	600 mmØ12.7 mm Ti - 500 mmØ13 mm PMMA	
PMMA-Ti	1000 mmØ13mm PMMA - 600 mmØ12.7 mm Ti	

In order to experimentally validate the interface analysis technique (both the analytical solutions Eq. ①' and Eq. ②' and the Matlab code), experiments were first performed on single rods with two gauge-station measurement: data were analysed using both the single rod analysis technique and the interface analysis technique. The one-rod tests have the advantage of perfect boundary conditions (continuity of force and velocity) at the 'virtual' interfaces between the two gage stations, avoiding interface imperfections and alignment errors. As verified before, the results are independent of interface location but depend on the distance between the two gauge stations.

Each rod was then cut into two rods (incident and output), and real interface tests were performed with the same gages. Interfaces in this case are regarded as 'imperfect' interfaces because

imperfections and misalignment may exist. This allowed comparison to better identify sources of error. Then, combinatory experiments were performed on mixed materials (one Ti and one PMMA) to further test the interface analysis capacity.

Interface experiments can be performed on a modified SHPB setup without specimen inserted between the incident and transmission rods; however, it's difficult to control projectiles (excited by gas gun) at low speeds (which is required for bar materials to remain in the linear viscoelastic regime) and to avoid noises. Hence, the pendulum apparatus (Fig. 9-1), which has been used previously in the single rod test, was employed.

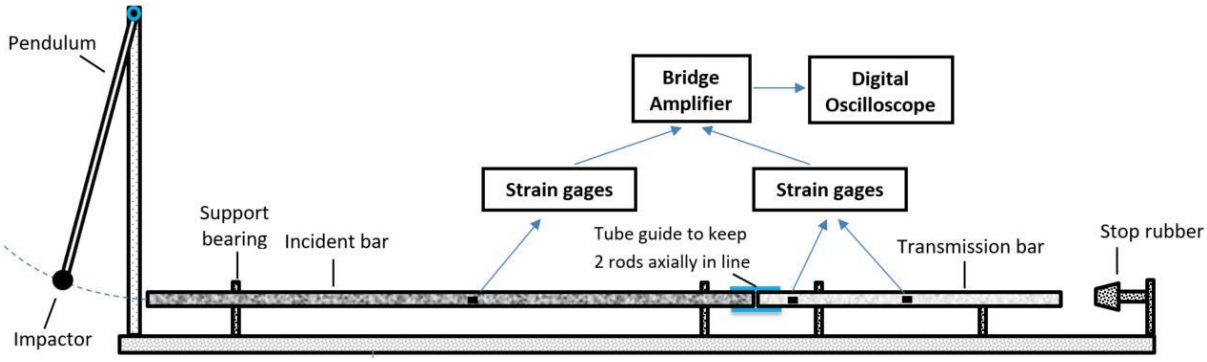


Figure. 9-1 The pendulum setup for interface testing

The rod(s) were supported using PVC bushings which allow free longitudinal movement, these are in turn supported by aluminium bearings. Interfaces were lubricated using a thin layer of grease/silicone lubricant to minimize the effects of friction and surface imperfection. In some cases, a frictionless Telflon tube guide, with diameter slightly larger than the rod diameter, was used at the contact interface to keep the two rods axially in line during the impact event. Strains were measured at three locations: incident and reflected waves were measured in the middle of the incident rod (x_{IR} = 300 mm or 500 mm), while the transmitted wave is measured both in the middle of the transmission rod (x_{T1} = 250 mm) and at a distance 50 mm from the interface (x_{T1} = 50 mm). This is based on the consideration that, ideally the three waves should be recorded separately with no overlapping. The purpose of recording transmitted wave at two locations is to compare the according results, as at a distance of 50 mm, cross-sectional deformation may not be uniform; however, as per Saint-Venant's principle, it becomes uniform at 250 mm (> 10 times of the rod diameter from the impact end).

In all the tests, four strain gauges were mounted circumferentially at each gauge station to measure the propagating wave on the same cross-section. Unlike previous experiments (*e.g.* Fig. 2-2), these gauges were not combined into the same Wheatstone bridge, but instead data were gathered from each gauge independently in an amplified *quarter* bridge. This is based on the consideration that bending waves might appear as a result of imperfect impacts and interface conditions; comparing the 4 strain recordings on the same cross-section could help detect the appearance of bending waves, while an average of the recordings from diametrically opposite gauges can help cancel the bending effects. Some other arrangements made to improve measurement sensitivity can be found in the full *web version*.

9.2 The 'perfect' interface

A 'perfect' interface cannot be made in real laboratory conditions, but can be equivalently achieved by using a single rod and assuming an interface exists somewhere (anywhere) between the two gauge stations. Two 'perfect' interface cases, Ti-Ti and PMMA-PMMA, have been tested. The Ti rod has a geometry of 1200 mm in length and 12.7 mm in diameter, the PMMA rod 1500 mm long and 13 mm diameter. Gauge locations were chosen to optimise the time before wave overlapping appears in later experiments. Waves measured at the stations can be then analysed using the interface analysis technique. Alternatively, they can also be analysed using the single rod analysis technique. A comparison between the results derived by the two techniques is therefore possible.

9.2.1 1200 mm long and 12.7 mm diameter Ti Rod

9.2.1.1 Rod geometry and 'single rod' analysis

The gauge station locations for the Ti alloy rod are shown in Fig. 9-2. Both gauge stations are 360 mm from the corresponding ends, and the distance between them is 480 mm. Stress waves were generated using pendulum impact with a 12 mm diameter aluminium ball at one end. The assumed interface is located in the middle of the 1.2 m Ti rod, *i.e.* x_{IR} = -240 mm and x_T = +240 mm.

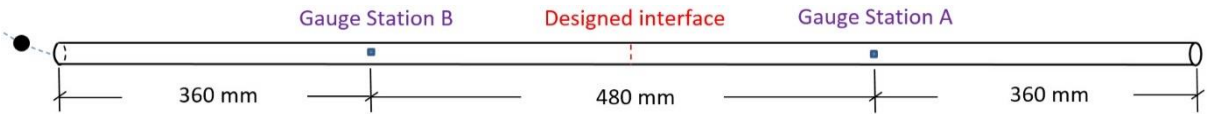
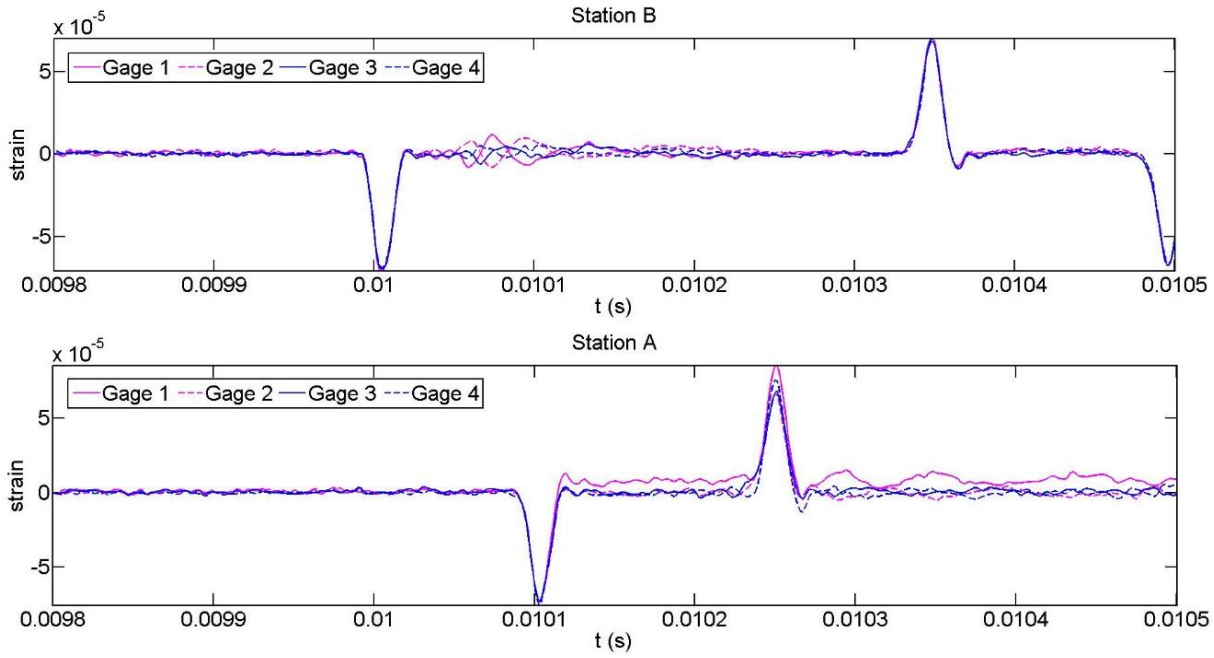
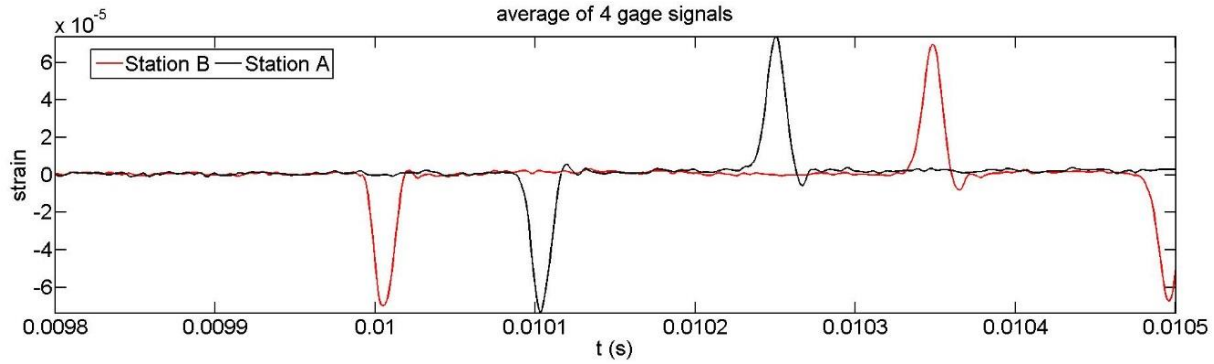


Figure. 9-2 Ti-Ti 1-rod 2 station experiment diagram

The four raw signals collected in a typical 1.2 m Ti rod impact test using a pendulum setup shown in Fig. 9-3. Dispersion, implied by the high frequency oscillations at the end of the stress pulse, was observed during wave propagation between the two stations. Wave amplitudes are almost constant, which indicates minimal energy loss during their propagation in the elastic Ti rod (though strain amplitudes at Station A is slightly larger than that at Station B due to noise interference). At station B (which is closer to the impact end), bending waves are observed following the main compression wave, as bending waves travel at about half the speed of the quasi-longitudinal wave. Bending effect can be cancelled by adding the diametrically opposite recordings together, because these gages experience opposite bending strains, as shown in Fig. 9-3(b).



(a) All 4 strain gage signals



(b) Average of 4 strain gage signals

Figure. 9-3 Denoised signals collected at 2 gage stations

When applying the single rod analysis, there are two options: to use one gauge recording together with the free boundary condition, or just two gauge recordings. The first method is the one adopted in single rod tests, and it is considered robust as signals are collected by the same set of gauges to avoid issues such as inaccurate timing interval between pulses and instrumental errors (*e.g.* errors caused by the disparity between gage sets). c It is found that, only density has appreciable effect while modulus estimate (used in dispersion correction) shows less. The frequency-independent modulus obtained ais 106.2 ± 0.3 GPa. The lower frequency bounds is 6000 Hz (by *E''*) or 1000 Hz (by *E'*), with upper being as high as 50 kHz.

Note that, as the timing between signals (incident and transmission) is very important in interface analysis (Essentially time domain shift affects the Fourier transform and thus material property derivation), considering the existence of errors, timing was calibrated by contrasting theoretical and single rod results. This adjustment equivalently compensates for inaccuracy in gauge location. This can be applied in gage location calibration in a SHPB test.

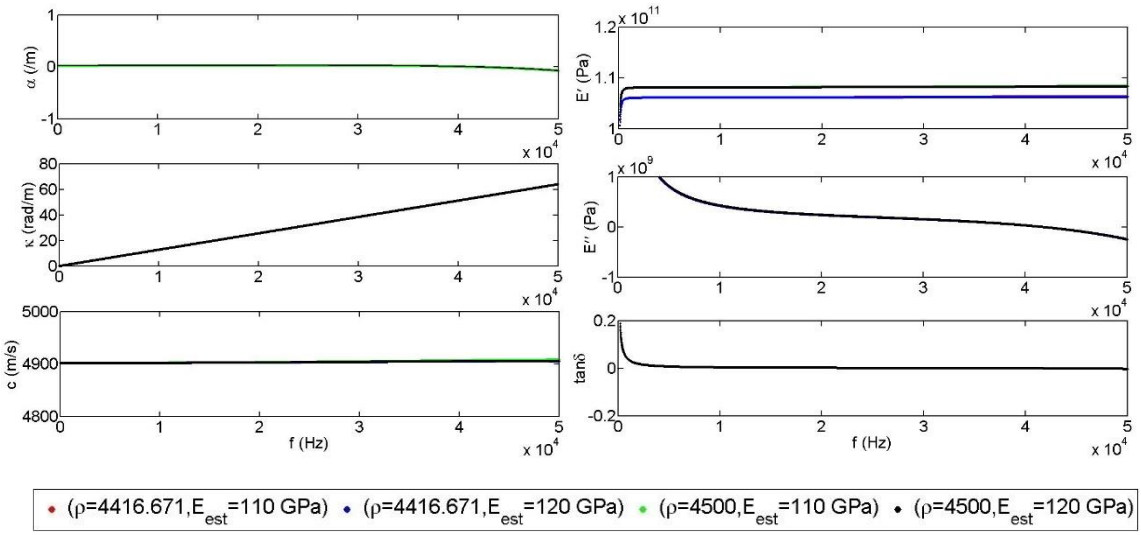


Figure. 9-4b Material properties derived by the single rod analysis technique

9.2.1.2 Interface analysis – pre-requisite data

As the 'interface' is perfect here, the particles on the 'virtual' interface strictly obey to the force and velocity continuity conditions, the reflected wave is exactly zero; and the interface analysis is expected to yield as good results as single rod analysis. However, 2 issues arose during signal processing. The first of these is proper pulse selection. As discussed in the single rod section, pulse

selection matters because errors can be generated when unwanted noise signals are included (long pulse duration) or when the dispersive waves are truncated (short pulse duration). Secondly, the calculated mechanical material properties of the target rod (transmission rod in this analysis) may be sensitive to the prerequisite knowledge of the prior rod. For example, to effectively obtain γ_2 and E_2, it is seen from eq. ①' and eq.②' that, at least material properties of incident rod γ_1 and E_1, and density of both rods ρ_1 and ρ_2 are required. Besides, as dispersion correction was applied (although dispersion is not appreciable with these rod configurations), estimates of the modulus E_2^* and Poisson's ratio ν_2 of the unknown rod were made; it is also important to precisely locate the gauges $x_{\mathrm{I}}, x_{\mathrm{R}}$ and x_{T}. To solve Eq. ②', the rod areas (S_1, S_2) and densities (ρ_1, ρ_2) are also required. All these can introduce errors, thus acquiring accurate prerequisite knowledge is very important in interface analysis to secure accurate results.

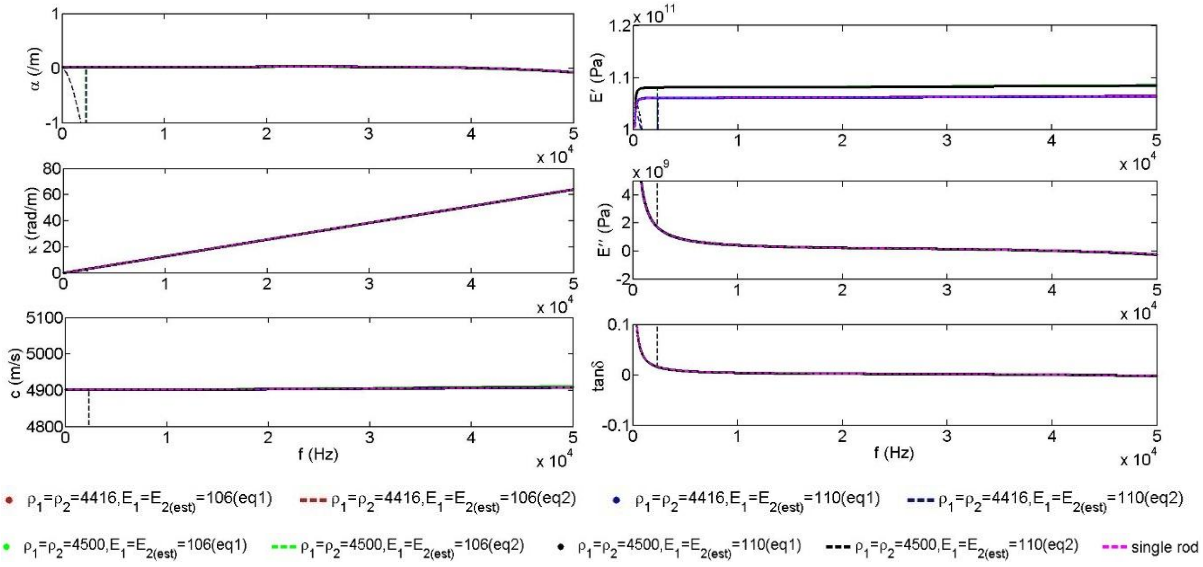


Figure. 9-5 Derivation of the transmission rod properties showing the sensitivity of the interface analysis technique to errors contained in ρ_1 and E_1^* (here, ρ is in kg m^{-3}, E in GPa; $x_{I,R}$ = -240 mm, x_T = +240 mm).

To test the sensitivity of the interface analysis technique to errors contained in the prerequisite knowledge, combinatory analysis using $\rho_{1,2}$ = 4417 or 4500 kg m^{-3}, and $E_{1,2}$ = 106.2 or 110 GPa were carried out; the first of these densities was measured for the actual rods using a set of scales and calipers, whilst the first of the moduli is the result of the single rod analysis and is used to calculate $\gamma_1 = \omega(\rho_1/E_1)^{1/2}$. In addition, an estimated $\nu_{1,2}$ = 0.32 was used in the dispersion correction. The results shown in Fig. 9-5 reveal that storage modulus is more sensitive to the inaccuracies contained in

density than in modulus. The same pulse selection methodology was adopted in all cases, and results have been derived up to 50 kHz. Consistent with the single rod results (Fig. 9-4b), the results derived by the interface analysis technique also show a lower limit of 6000 Hz (by *E''*) or 1000 Hz (by *E'*).

9.2.1.3 Interface analysis – pulse selection

Table. 9-3 pulse selection test scheme

Fixed ends	$(B_{s1,e1} - A_{s1,e1})$	$(B_{s1,e1} - A_{s4,e1})$	$(B_{s5,e1} - A_{s1,e1})$	$(B_{s5,e1} - A_{s4,e1})$
Fixed starts	$(B_{s5,e1} - A_{s4,e5})$	$(B_{s5,e7} - A_{s4,e1})$	$(B_{s5,e7} - A_{s4,e5})$	
$(B_{s1,e7} - A_{s1,e5})$				
Randomly selected start, with fixed duration=80 us for 3 pulses				

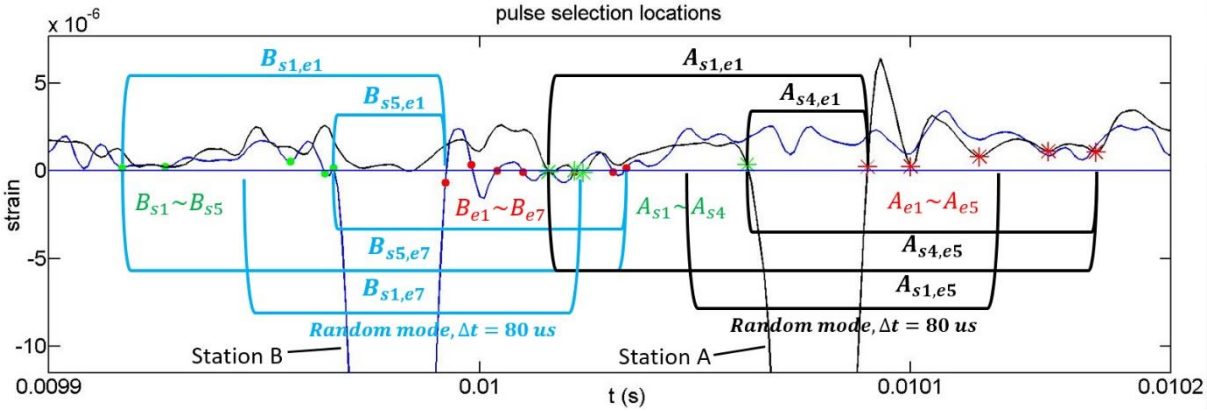
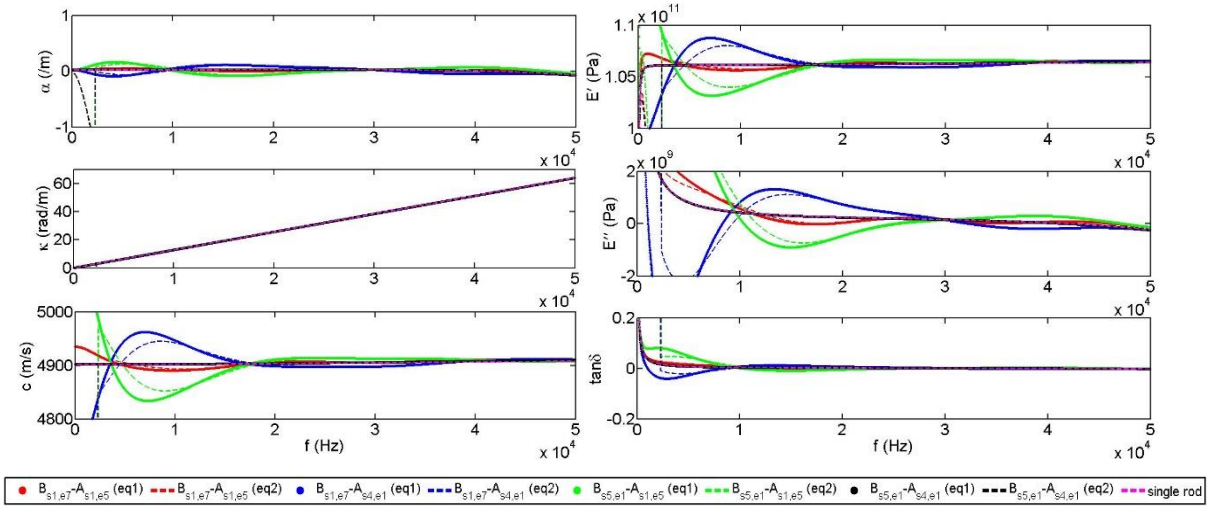


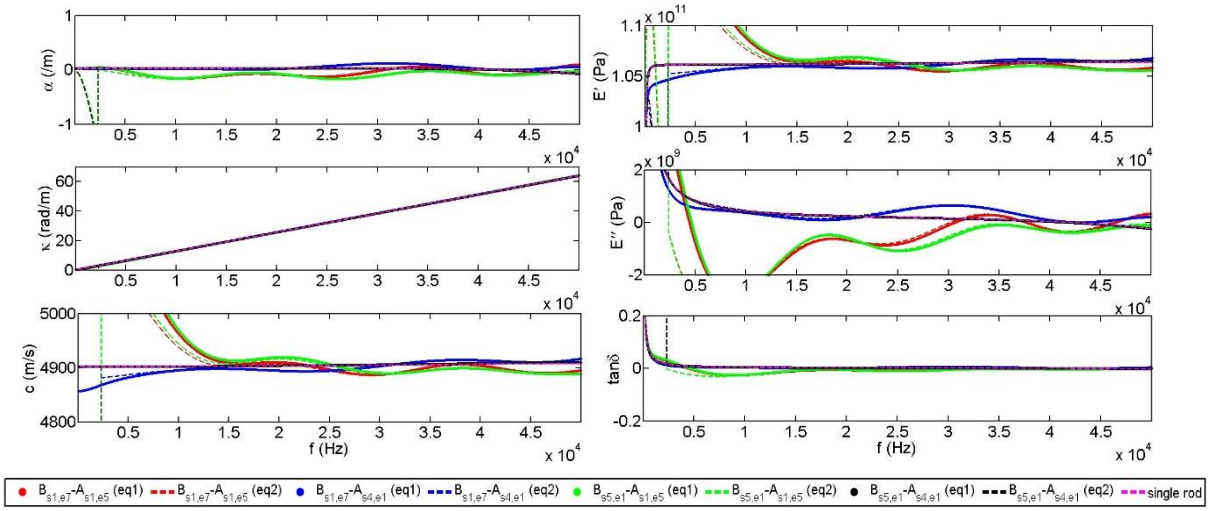
Figure. 9-6 Pulse selection scheme

With the pre-requisite properties, the effect of pulse selection can be investigated. Several combinations of start and end locations for the pulses have been tested: nine trials were performed following the test scheme in Table. 9-3 and Fig. 9-6; the results are presented in Fig. 9-7. The start and end locations were chosen as zero-strain cross-over points before or after the pulse. Using a fixed measurement duration of 80 μs from the pulse peak on both sides, in total 10 start locations and 7 end locations were obtained for the Station B pulse (incident); 6 start and 9 end locations for the Station A pulse (transmission). The superscript 's'/'e' indicates start/end location respectively. They are all located within a reasonable distance on both sides of the pulses. By fixing the start or end locations of both pulses at the same time, only the longest or shortest durations have been tried; a longest-longest mode and a random mode have also been tested. It is found that using symmetric pulse selection strategies yields results most close to the theoretical ones (*e.g.* $B_{s1,e1} - A_{s1,e1}, B_{s5,e1} - A_{s4,e1}, B_{s5,e7} - A_{s4,e5}, B_{s1,e7} - A_{s1,e5}$), otherwise oscillations can be induced. In

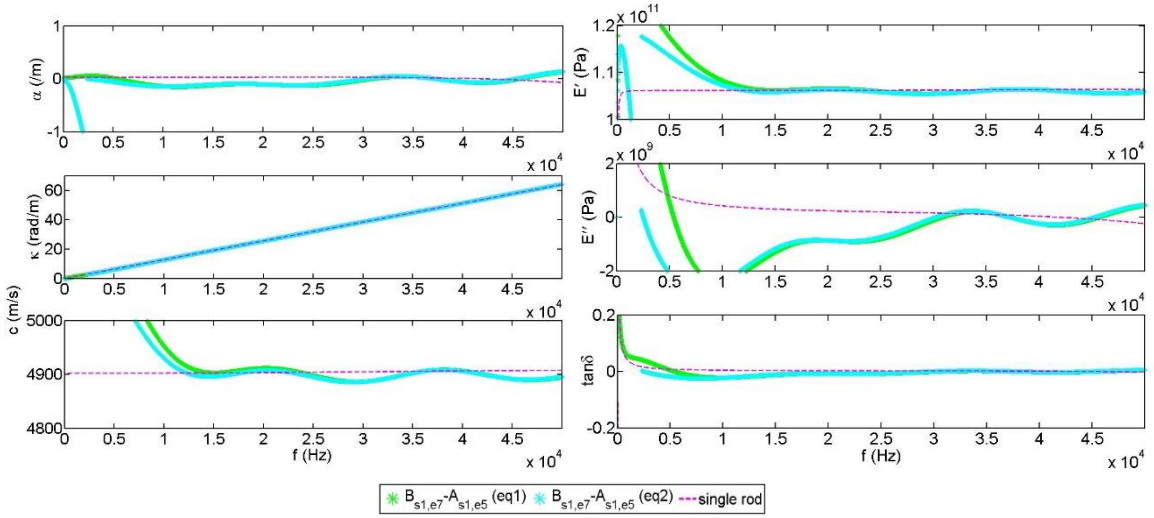
later analysis, the start and end locations of both pulses are determined using the zero strain cross-over points that give shortest pulse durations (*i.e.* $B_{s5,e1} - A_{s4,e1}$).



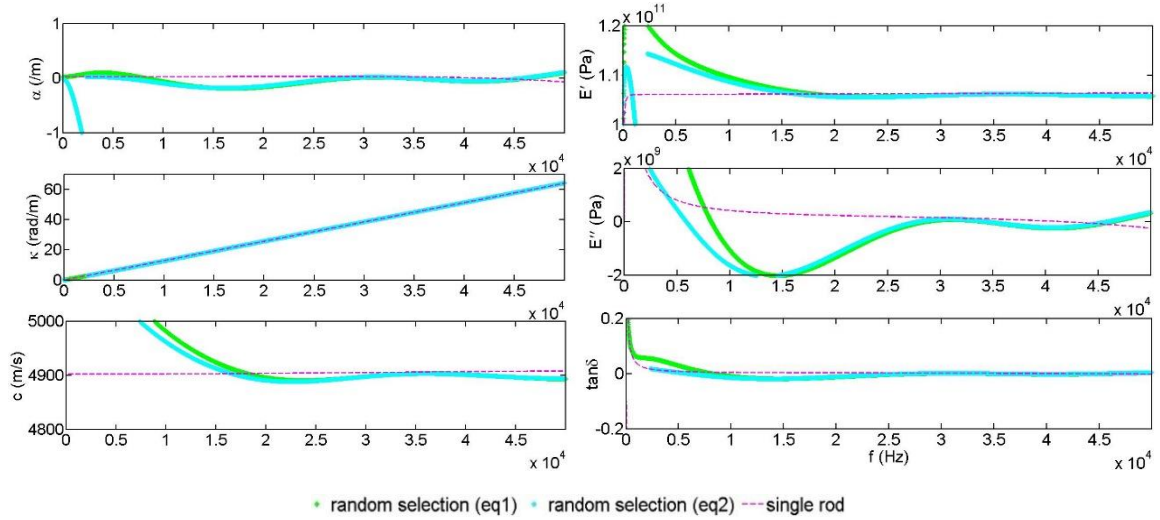
(a)fixed end



(b)fixed start



(c) Long durations ($B_{s1,e7} - A_{s1,e5}$)



(d)random mode with fixed duration=80 us for 3 pulses

Figure. 9-7 The effect of pulse selection on deriving interface results (using the single rod results as incident rod properties: ρ = 4417 kg m^{-3}, E = 106.2 GPa; $x_{I,R}$ = -240 mm, x_T = +240 mm)

9.2.1.4 Interface analysis – effect of bending waves

Distorted signal in a SHPB test is mainly due to the presence of flexural vibration mode of wave propagation which introduces 3D effects. M.A Kariem *et al*. [82] reported that a flexural vibration mode (the 'bending effect'), in which the strains recorded at opposite locations of the same section have a phase angle difference of 180°, can be observed in a SHPB experiment if the bars are not well-aligned or if the neutral axis is not straight. Non-parallelism of the two contact interfaces, i.e. bar misalignment, is the common cause and can significantly affects the result [89]: a slight fluctuation in the distorted signal could significantly influence the stress-strain curve [82]. However, bending effect can be cancelled using the averaging technique even when severe bar misalignments occur [82]. In an experiment, the effect of the flexural mode of vibration can be cancelled by taking the average values extracted from a pair of diametrically opposite mounted strain gauges. As can be seen from the raw recordings in Fig 9-3, bending waves appear as result of non-axial impact. A comparison between the results derived from a single strain recording (gauge 1) and the average of the 4 recordings was made in Fig. 9-8, from which it is observed that although efforts have been made to select the shortest pulse durations for both pulses to exclude the effect of bending waves, the single channel recording results still deviate more from the theoretical values than the averaged

one: thus using average is recommended to yield more accurate results. However, in order to detect the presence of the flexural vibration mode, single gauge measurement should be used [82].

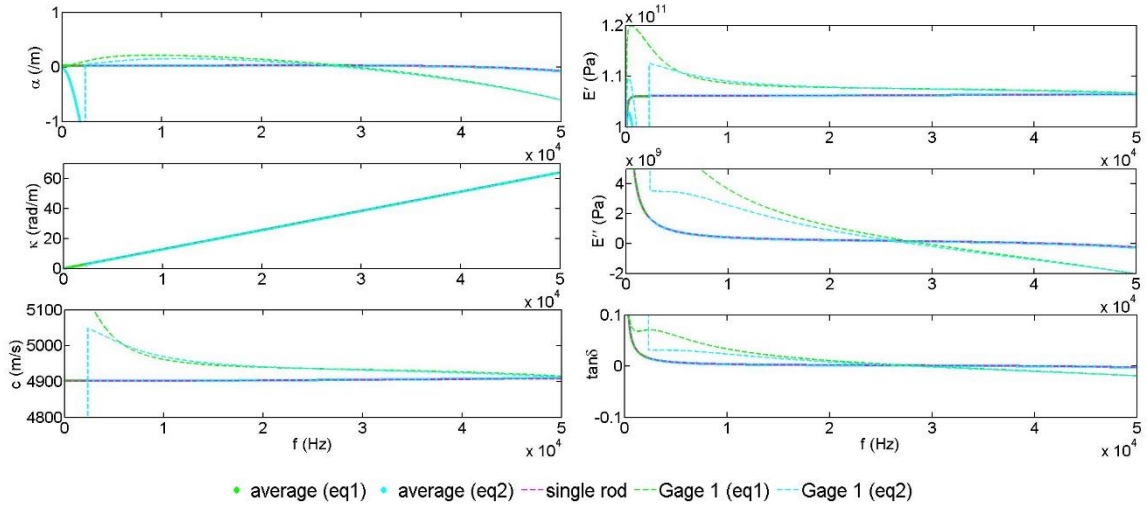
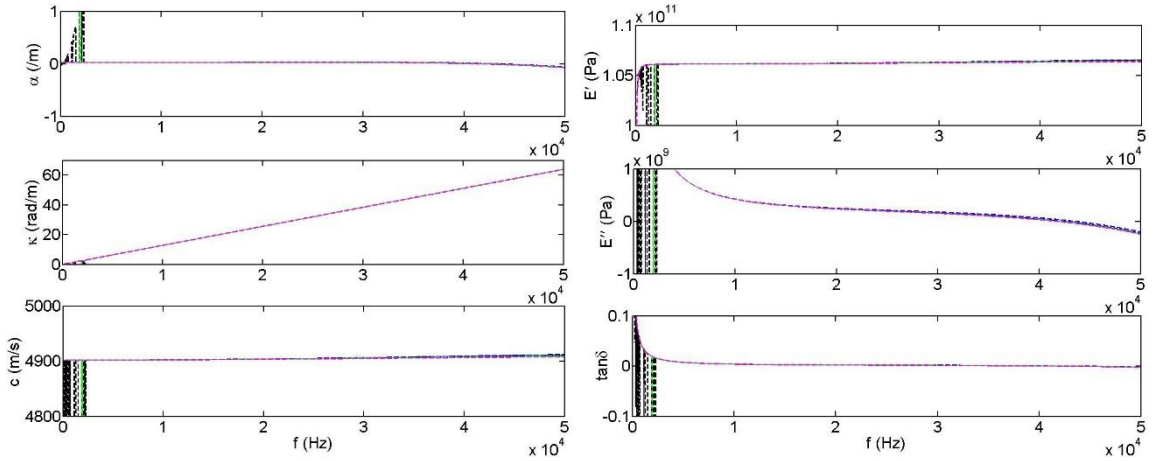


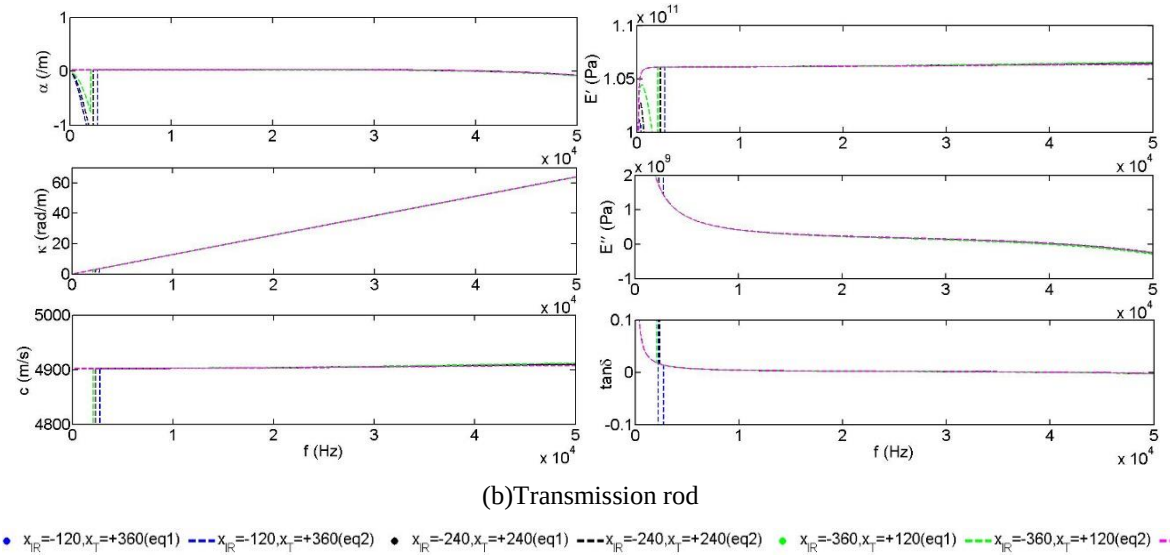
Figure. 9-8 A comparison of the results derived using a single channel signal (Gage 1) and an average of 4 channel signals (with the same single rod input $\rho_1 = \rho_2 = 4416.671\ kg/\mathrm{m}^3, E_1^* = E_2^* = 106.2$ GPa, $v = 0.32$ and pulse selection, $x_{IR} = -240$ mm, $x_T = +240$ mm)

9.2.1.5 Interface Technique – 'virtual interface' location

As verified in the Ti-Ti one rod two medium simulation, assuming a virtual interface between the gauge stations, once x_T - $x_{I,R}$ = *constant*, the results obtained using interface analysis will remain the same, this is reflected in Fig. 9-9. It gives evidence supporting the reliability of the interface analysis technique.



(a)Incident rod



(b)Transmission rod

Figure. 9-9 Comparison of the material properties derived with $|x_{IR}| + |x_T| = 480\ mm$ (Ti 1 rod 2 measurement stations)

9.2.2 1500 mm long 13 mm diameter PMMA Rod

9.2.2.1 Rod geometry and instrumentation

The second case analysed is wave propagation in a 1500 mm long, 13 mm diameter viscoelastic PMMA rod. As shown in Fig. 9-10, the two gauge stations were mounted at distances of 500 mm and 1125 mm from the impact end, respectively. This configuration was designed for later experiments where the rod was cut into two, with the interface sitting 1 m from the impact end so that the rods have lengths of 1 m and 0.5 m respectively. This is designed to optimise the time before wave overlap, whilst respecting that a distance of 125 mm gage measurement is desirable to ensure uniform deformations in the transmission rod according to Saint-Venant's principle.

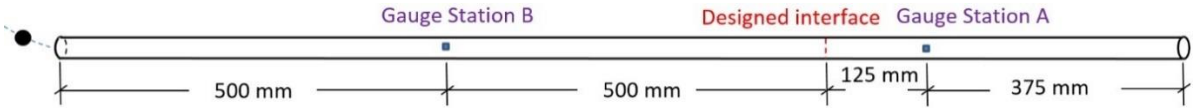


Figure. 9-10 a 1500 mm long, 13 mm diameter 1 rod 2 stations PMMA impact test diagram

The denoised signal collected from a PMMA pendulum impact event is shown in Fig. 9-11. Bending waves were again observed at both Station B and A. The first pulses of 4 signals were averaged and true strains calculated using the constants *Amplifier gain* = 2326, *GF* = 2.15 and U_{in} = 6.02 V. Both the interface analysis technique (assuming an interface sitting at a distance of 1 m from the impact

end, *i.e.* $x_{I,R}$ = -0.5 m, x_T = 0.125 m) and the single rod analysis technique (travel distance = $|x_{I,R}|+|x_T|$ = 0.625 m) were employed. They share the same pulse selection.

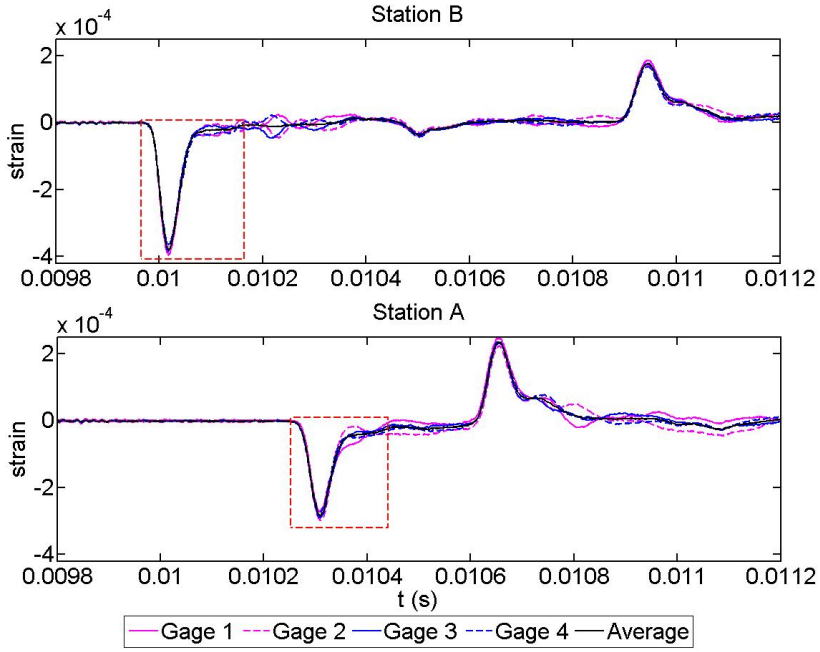


Figure. 9-11 Denoised signals collected at 2 gage stations (h=45 cm, $T = 21.5$ ℃)

9.2.2.2 The single rod method

Similar to the Ti rod case, there are two options to perform the single rod analysis: either using a combination of one gage recording and a free boundary condition, or using the two gage recordings without adoption of boundary condition. Here the two-gage method is used as an example. The selected pulses are shown in Fig. 9-12. Dispersion correction compensates for the velocity loss in high frequency components that caused by geometry dispersion. After dispersion correction, some high frequency oscillations were removed from the tails of the original signals, and they appear in wave fronts because unlike the dispersion effect, high frequency components travel faster as a result of viscoelasticity. Note that, the corrected signals shown in Fig. 9-12 are based on the assumption that $x_{I,R}$ = -0.5 m, x_T = 0.125, the corrected shapes may change a bit if different ($x_{I,R}$, x_T) values are used; however, this does not change the results as only the absolute distance between the two gages ($|x_{I,R}|+|x_T|$ = 0.625 m) matters as demonstrated before.

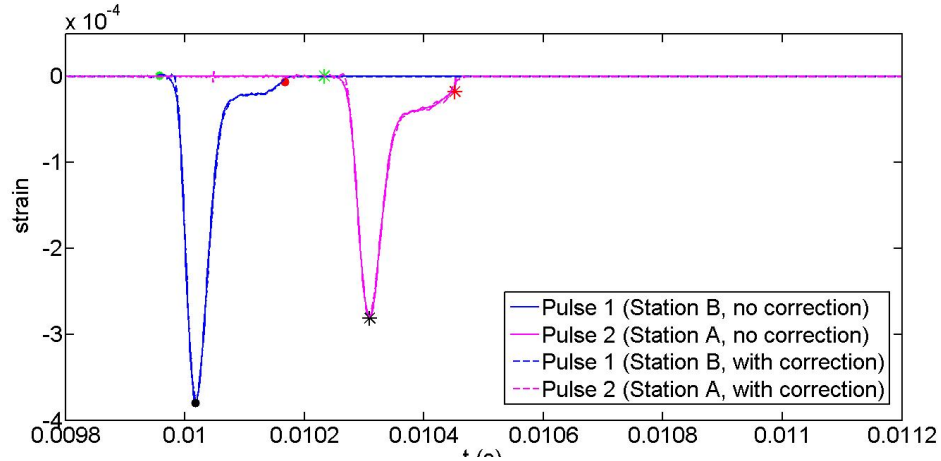


Figure. 9-12 Selected pulses and dispersion correction (strain time series)

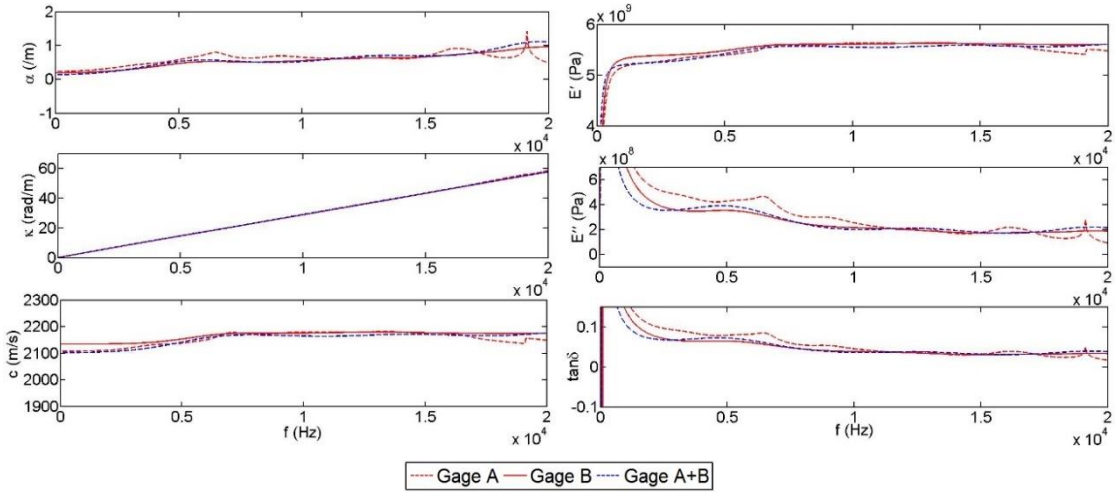


Figure. 9-13 Single rod results obtained using 1-station and 2-station recordings
(h=45 cm, T = 21.5 °C; rod properties used are ρ = 1186 kg m^{-3}, E_{inst} = 5.36 GPa, ν = 0.38).

Results from 2 single rod analysis methods, both based on the shortest pulse selection, are presented in Fig. 9-13. The consistency between these results demonstrates the reliability of the single rod analysis method. In later two rod analysis, the material properties derived using 2 gage signals were use as the input bar mechanical properties when deriving the output bar properties, and as the output bar properties when deriving the properties of the input bar.

9.2.2.3 Interface method

Imagine a virtual interface exists between the two gage stations, either the incident or transmission rod material properties can be obtained knowing the properties of the other one. Fourier transforms of the 3 pulses, in the range of 8~10 kHz as an example, are presented in Fig. 9-14, and their resulting TC and RC in Fig. 9-15, from which it is seen that dispersion correction, which modifies the phase

of each frequency component other than magnitude, becomes important for high frequency components (*e.g.* those above 20 kHz) with significant phase shift in TC and RC after correction.

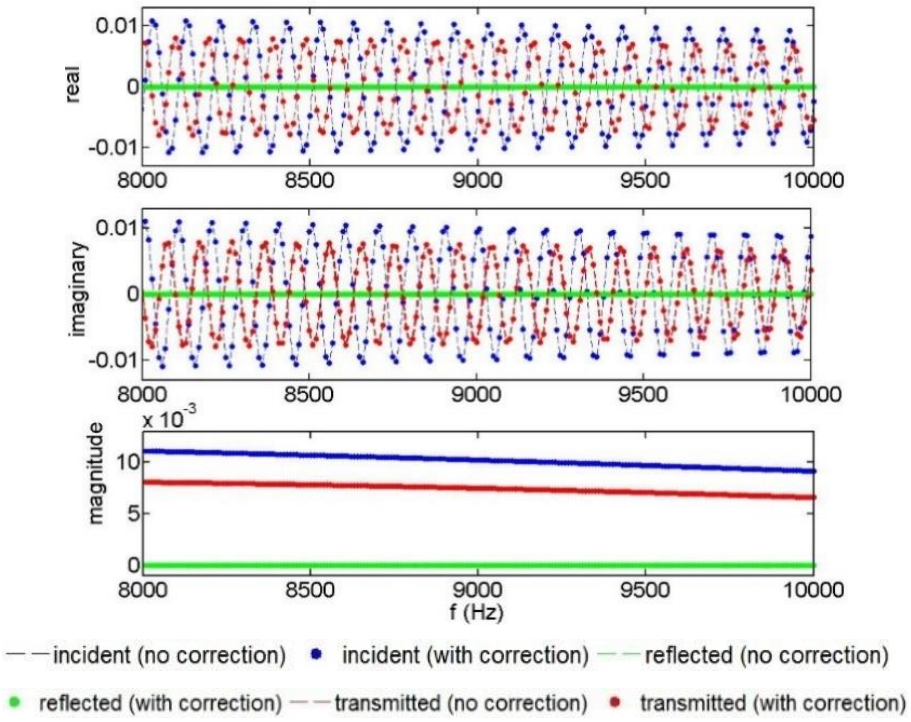


Figure. 9-14 Fourier transforms of the incident, reflected and transmitted waves in PMMA, with & without dispersion correction

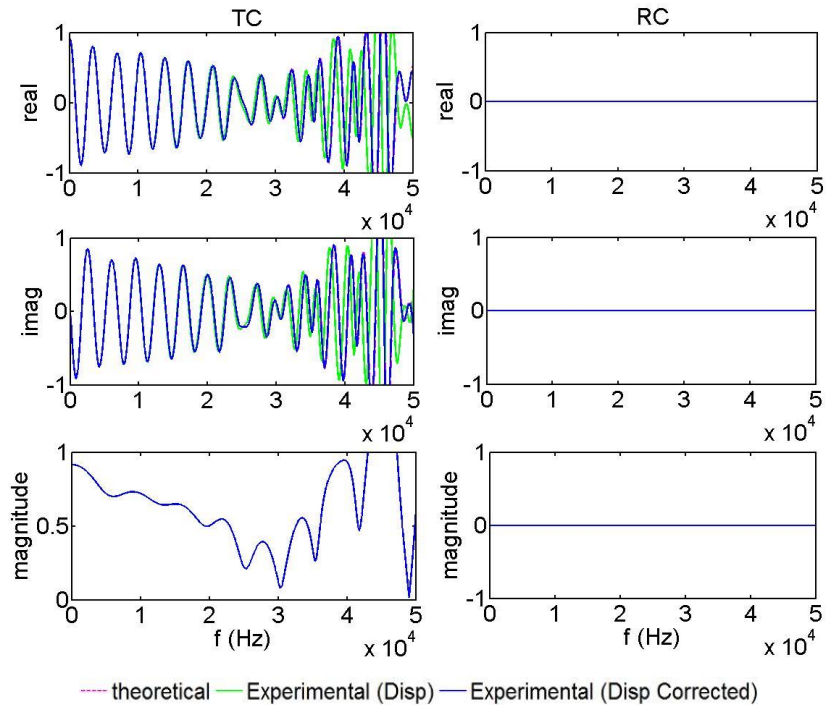
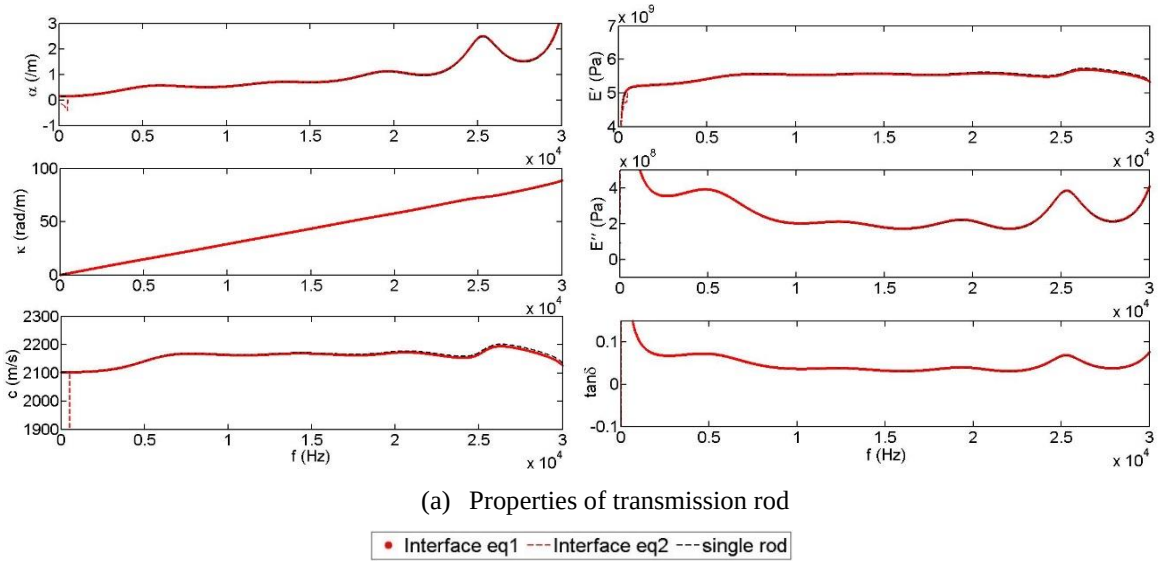


Figure. 9-15 TC (left) & RC (right) with & without dispersion correction

A comparison of the results obtained using both techniques is presented in Fig. 9-16, which shows excellent agreement in the range 0~15 kHz. Different drop heights have been tested, which lead to

different strain amplitudes and pulse lengths, but as long as the deformation remains in the linear viscoelastic region, they are all expected to give the same results. However, larger amplitude can yield larger signal-to-noise ratio (SNR) and here h=45 cm is used as an example.



(a) Properties of transmission rod

Figure. 9-16 Comparison of the transmission rod material properties derived using the single rod and interface analysis techniques (T = 21.5 °C, rod properties used for dispersion correction are ρ = 1186 kg m^{-3}, E_{inst} = 5.608 GPa, ν = 0.38).

9.2.3 Further discussion of errors in the interface analysis method (PMMA rod as an example)

Two types of errors are analyzed here: errors due to time synchronization and gage distance error.

9.2.3.1 Shift of time domain signal

The same pulse selection methodology was adopted, the incident signal was left unchanged while the transmission signal was shifted by up to 3 us forward or backward in time (the sampling rate is 1 MHz and total recording period is 0.1 s). Fig. 9-17 shows how this time shift affects material properties derivation. As time domain signal shift results in a phase change in Fourier transform, the TC and RC values shift accordingly, which generates errors when solving the balance equations (Eq. ①′ and Eq. ②′). It is seen from Fig. 9-17 that, with increase of time shift in transmission signal, the results deviate monotonically from the case of no shift, and the upper frequency bound reduces (*e.g.* the brown and blue lines which show the 2 extreme cases with largest time shifts exhibit lower upper frequency limits). Thus in practice, it is important to record the timing accurately. The timing problem is specific in this test and can be resolved by using a multiple-channel oscilloscope to

achieve instantaneous trigger and timing; alternatively a cross-measurement method, which will be introduced later when performing the real 2-rod tests, can be used. Fig. 9-17 also implies the interface analysis method is sensitive enough to detect timing errors as small as 1 us.

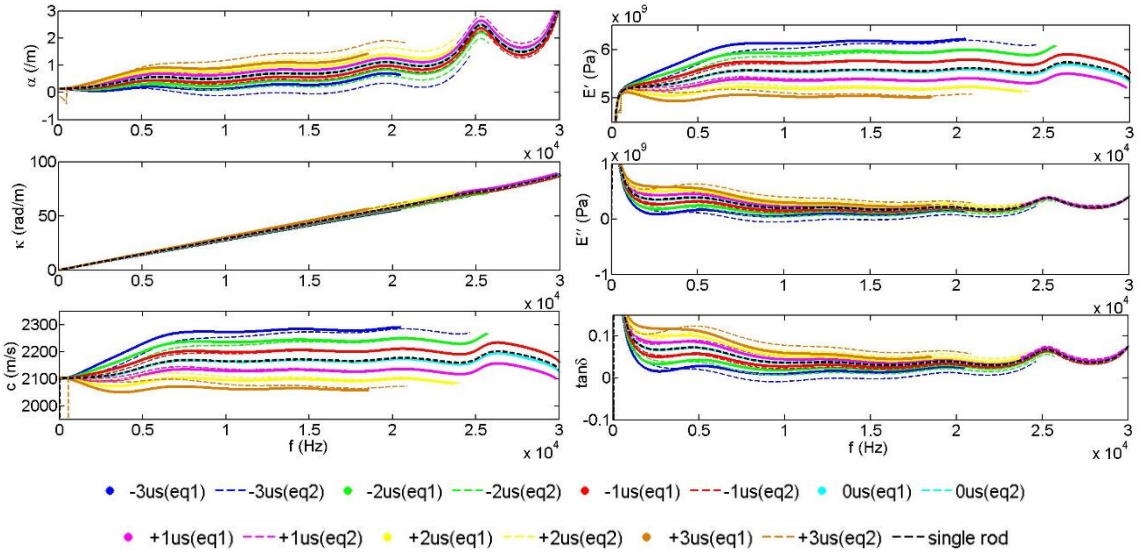


Figure. 9-17 Comparison of transmission rod material properties derived at different time shifting levels (PMMA 1 rod 2 measurement stations, h=45 cm, sampling rate: 1 μs, total recording duration: 0.1 s)

9.2.3.2 Errors in $x_{I,R}$ and x_T

There are two approaches to investigate the sensitivity of the interface analysis technique to errors contained in $x_{I,R}$ and x_T: analytical or numerical. The former one uses derivatives with regards to $x_{I,R}$ and x_T respectively based on Eq. ①' and Eq. ②'. However, these equations cannot be explicitly differentiated; more conveniently, artificial errors can be introduced to $x_{I,R}$ and x_T. With the same pulse selection methodology used before, distance is the only variable here. Comparing with the standard case of (–500, 125) mm, 4 cases were tested: ($x_{I,R}$, x_T) = (–497, 125), (–503, 125), (–500, 122), (–500, 128) mm. The error step is 3 mm, which is equal to the gage length. A comparison of the results obtained in this way is presented in Fig. 9-18. It is seen that an increase (Case 1 & 5) or decrease (Case 2 & 4) of the total travel distance $|x_{I,R}|+ |x_T|$ lead to inverse trends. For example, if the travel distance was evaluated as smaller than its 'true' value, the evaluated wavespeed, and hence storage modulus, was too small, and the evaluated energy dissipation per unit distance, and hence loss modulus, was too large.

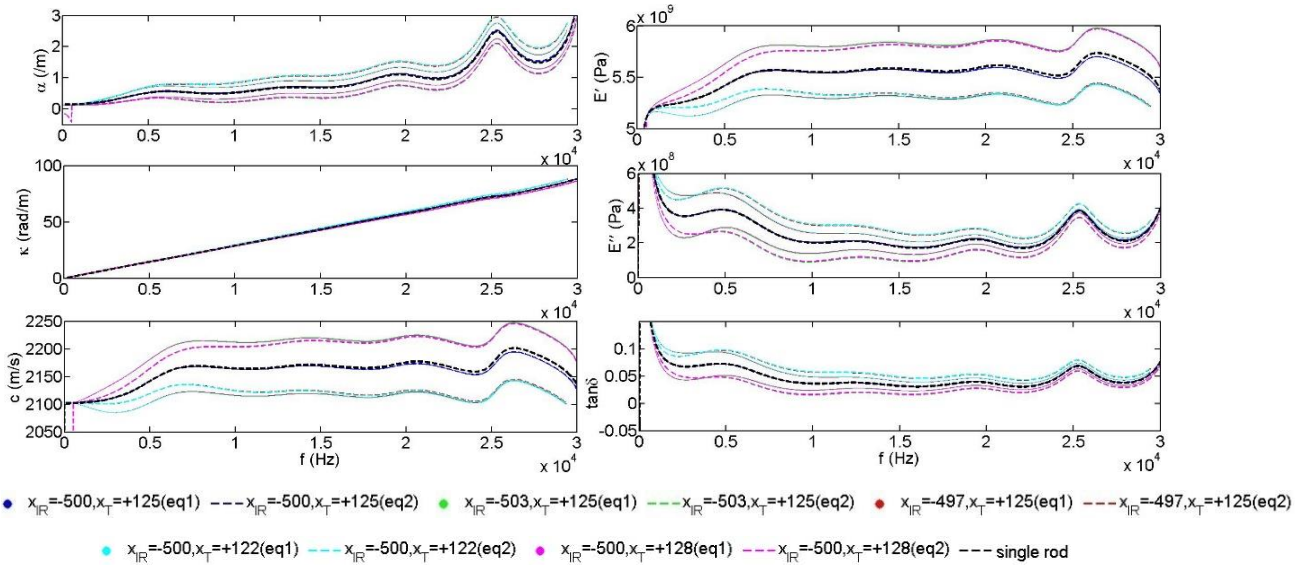


Figure. 9-18 Comparison of transmission material properties derived by introducing errors in x_{IR} or x_T (PMMA 1 rod 2 measurement stations, h=45 cm, $T = 21.5$ ℃)

Note that, Case 1 and 5 (in which the travel distance was increased by 3 mm), Case 2 and 4 (in which the travel distance was decreased by 3 mm) yield similar results, which is in agreement with previous simulation investigations that if $|x_{\mathrm{IR}}| + |x_T| = constant$, the interface location doesn't matter. By employing the same input signals, different distance groups have been tested in the data processing stage to obtain either the material properties of the incident rod (Fig. 9-19(a)) or the transmission rod (Fig. 9-19 (b)), both results agree well with this speculation.

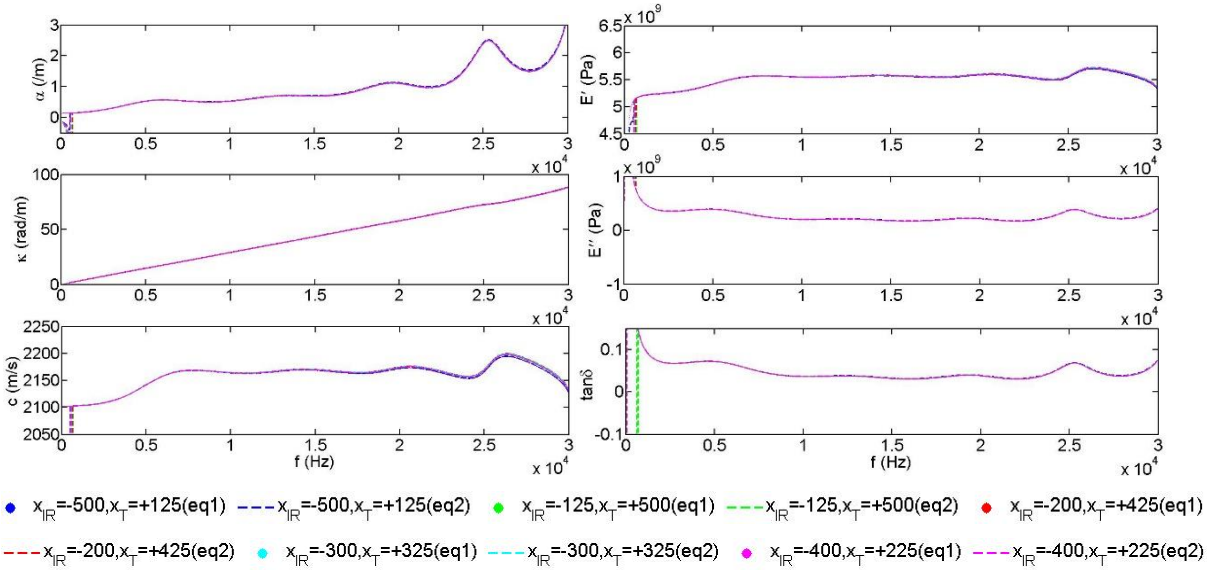


Figure. 9-19 Comparison of transmission rod material properties derived with $|x_{IR}| + |x_T| = 625\ mm$ (PMMA1 rod 2 measurement stations, h=45 cm, $T = 21.5$ ℃)

Error analysis shows that, the interface analysis technique is sensitive to the errors induced by equipment (*e.g.* trigger timing error), manufacturing (*e.g.* error with gage location) and alignment. There are some other errors brought by instruments, for example, electromagnetic interference between the lead wires, which can be resolved by effective shielding.

9.3 Real interface tests

9.3.1 Experimental scheme

The previous section demonstrates that the interface analysis technique is capable of deriving material properties using signals obtained from 'perfect' interface tests. However, more challenging is to test the wave behaviour at 'real' interfaces. While the same rods tested in the 1 rod 2 station tests and the same measurement system were employed, a relatively good interface can be achieved by cutting both rods into 2 rods at the 'designed' locations and then putting them together. As shown in Table. 9-2, 4 'imperfect' interface cases, *i.e.* Ti-Ti, PMMA-PMMA, PMMA-Ti, Ti-PMMA, have been tested. The experimental scheme was presented in Fig. 9-20.

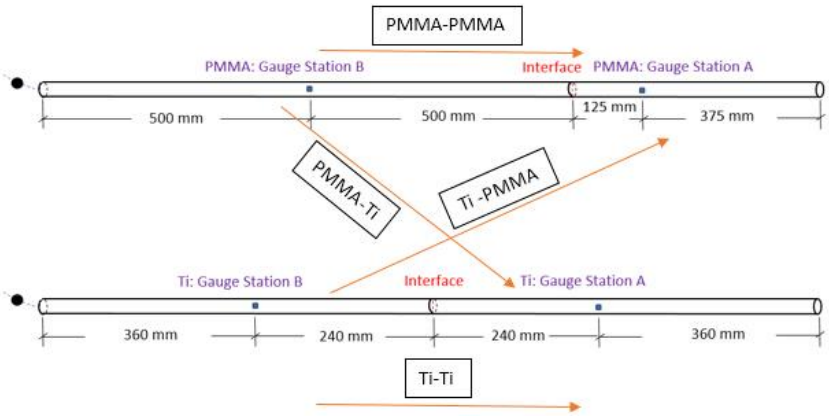


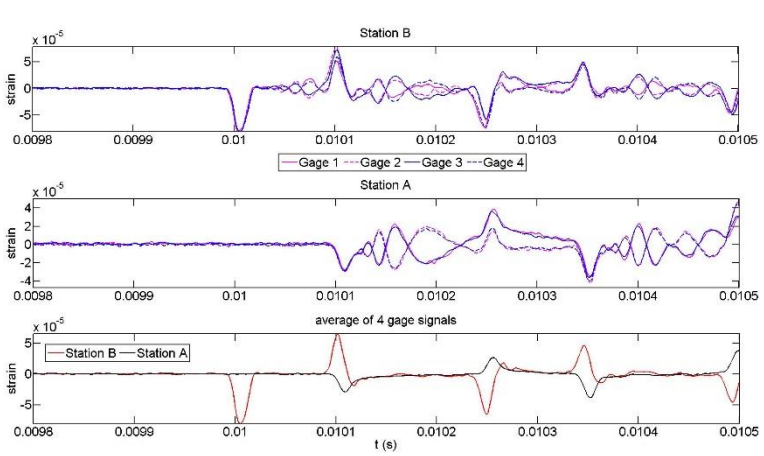
Figure. 9-20 2-rod interface experimental scheme

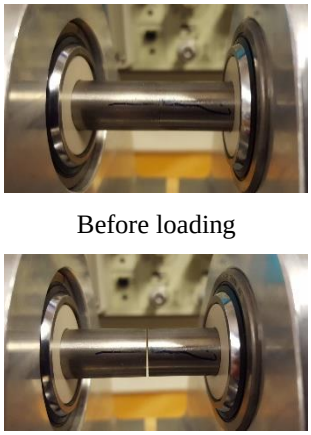
Excited by the pendulum (12 mm diameter Aluminum ball, h=45cm), impact was applied to the same end of the incident rod as employed before. Each test was repeated twice, and one of them was analyzed. Adopting a cross-over measurement system, timing was improved. Prior to the real interface tests, single rod impact tests were performed separately on each of the four rods using the single rod technique at the same temperature as the latter interface tests, from which the propagation coefficients and moduli were obtained, and these properties served as the prerequisite knowledge when solving the interface equations, and as the theoretical values when making comparisons.

9.3.2 600 mmØ12.7 mm Ti-600 mmØ12.7 mm Ti

9.3.2.1 Rod Geometry and interface contacts

As shown in Fig. 9-2, the 1200mm rod was cut off in the middle; 2 identical rods, each with length of 600mm, were generated with gage station sits 240mm away from the interface. The two cylindrical Ti rods were then placed in contact either with or without grease at the interface. The signals collected are shown in Fig. 9-21, along with photographs of the interface taken before and after loading. Significant amount of reduction can be observed in reflection and bending wave when grease is used. Without grease, the rods separate after impact; no apparent separation is observed between the lubricated rods. Also, use of grease significantly improves the transmission of signals across the interface, and higher quality data was obtained with the presence of grease.

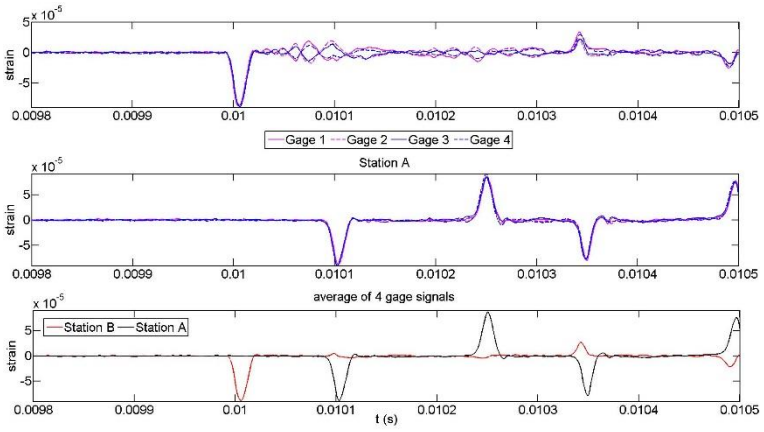


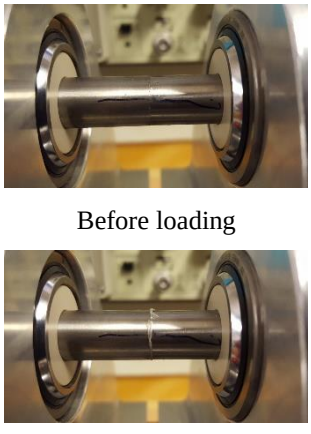


Before loading

After loading

(a)hard contact





Before loading

After loading

(b)with grease on interface

Figure. 9-21 Signals collected from a Ti-Ti 2 rod interface experiment (in each figure, upper: incident, middle: transmission, lower: average, $T = 21.7$ ℃)

9.3.2.2 'Single rod' analysis

To derive the prerequisite material properties, single rod tests were first performed separately on both rods. A typical signal collected from a single transmission rod test is shown in Fig. 9-22. It shows no wave overlapping with the 600mm Ti rod and gage configuration. Fig. 9-23 presents the material properties of Rod A obtained by analyzing the signal in Fig. 9-22 using signal rod analysis. These results were used as a reference in later interface comparison. Note that the usual dispersion correction technique has been used.

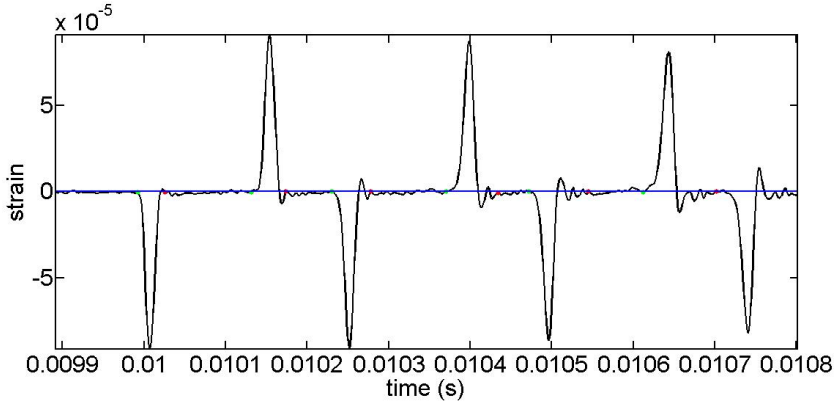


Figure. 9-22 Single rod impact signals (600 mmØ12.7 mm transmission Ti rod, $T = 22.1℃$)

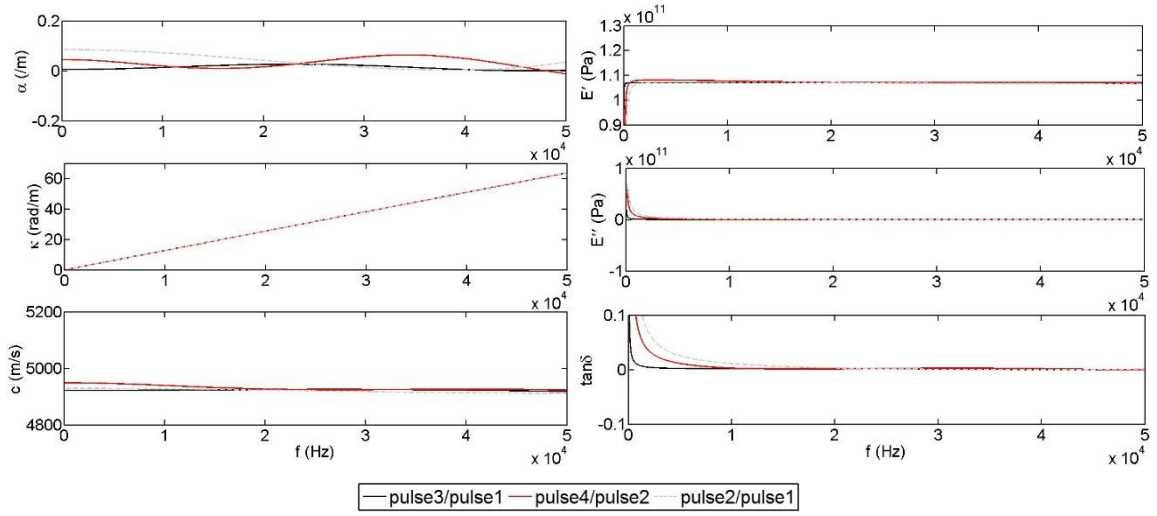


Figure. 9-23 Transmission rod material properties derived by the single rod analysis technique (600 mmØ12.7 mm Ti, $T = 22.1℃$)

9.3.2.3 Interface method

The raw signals collected from an interface test are shown in Fig. 9-24 (which is the same as that in Fig. 9-21b). The first incident, transmission and reflection pulses were selected, denoised, and

transformed into frequency domain, then material properties of either incident or transmission rods were obtained by solving the interface equations. A comparison of the theoretical and experimental FFTs, TC and RC was made in Fig. 9-25 and Fig. 9-26. The calculated values match reasonably well with those calculated from the single rod test data within the frequency range 20~50 kHz, as shown in Fig. 9-27. At frequencies 0~2 kHz, there is significant difference between the results, which is due to the limit of lower frequency bound discussed before (see also [32]). Note that there was a slight temperature difference between the single and two rod experiments (*c.* 0.4 °C).

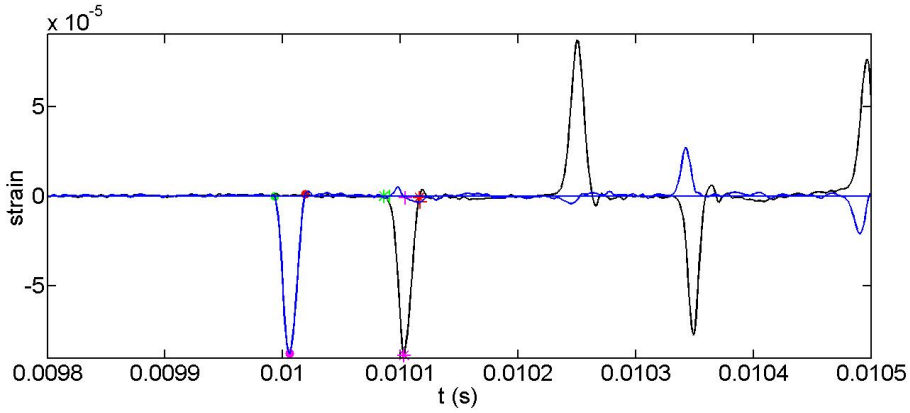


Figure. 9-24 Raw signals and pulse selection (600 mmØ12.7 mm Ti-600 mmØ12.7 mm Ti, $T = 21.7$℃)

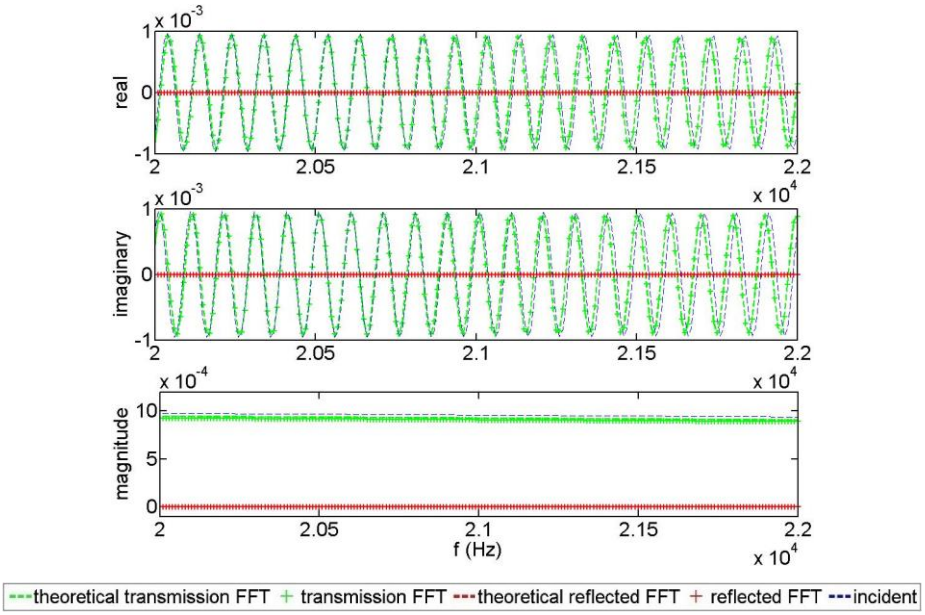


Figure. 9-25 Comparison of theoretical and experimental FFTs

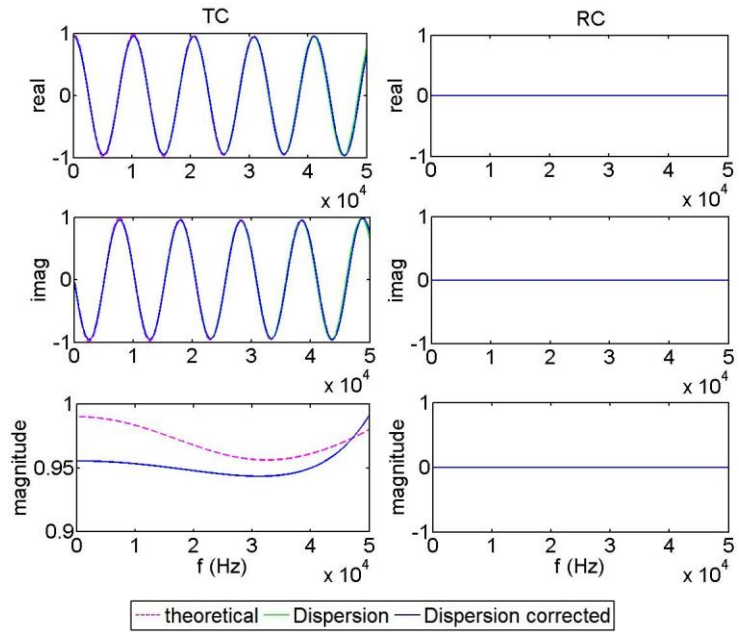
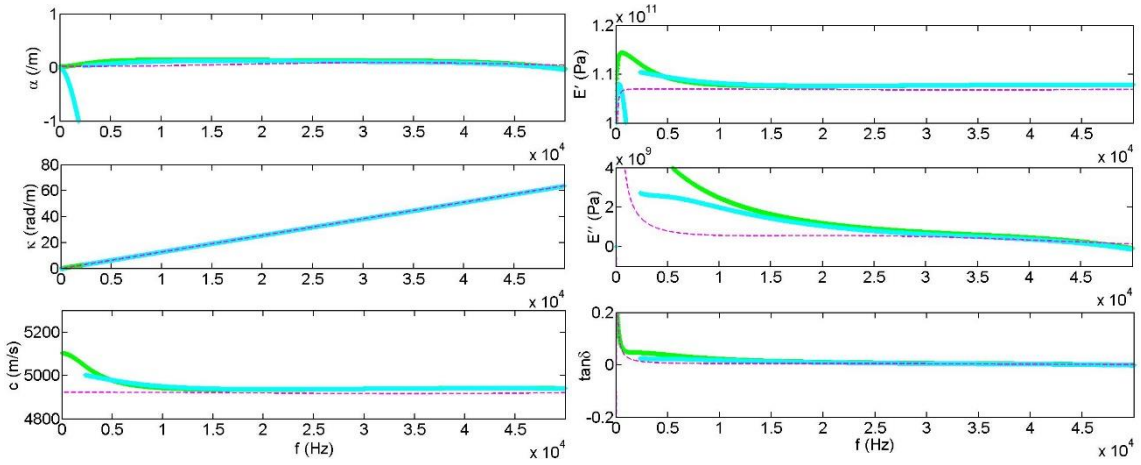
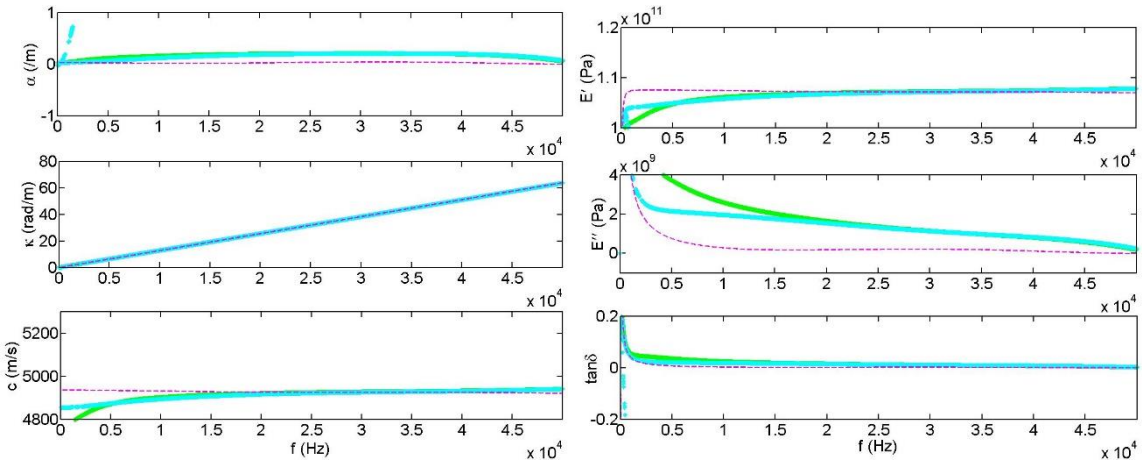


Figure. 9-26 Comparison of the theoretical and experimental TC & RC



(a) Properties of transmission rod



(b) Properties of incident rod



Figure. 9-27 Derived material properties ($T = 21.7$℃)

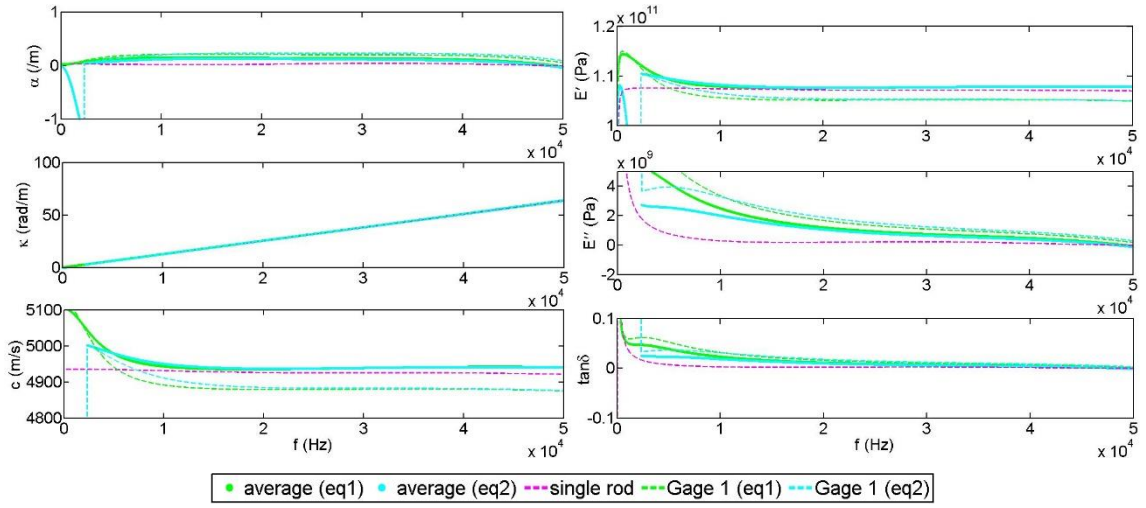


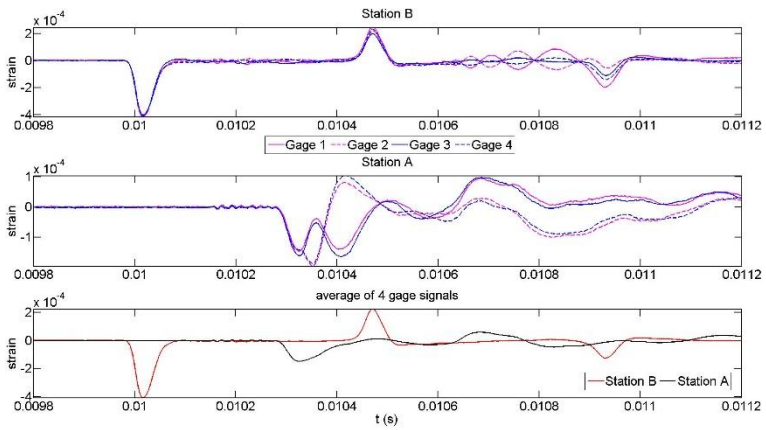
Figure. 9-28 A comparison of the results derived using a single channel signal (Gage 1) and an average of 4 channel signals (with the same prior inputs and pulse selection)

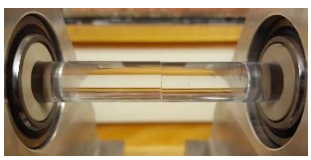
Similar to the Ti one rod two stations experiments, to investigate the effect of bending wave, results obtained using single channel and averaged signals are compared in Fig. 9-28, it is seen that, by cancelling the bending wave effect, less deviating results are yielded.

9.3.3 1000 mmØ13mm PMMA-500 mmØ13 mm PMMA

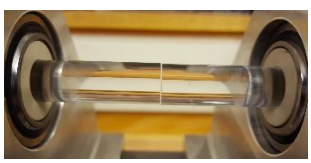
9.3.3.1 Rod Geometry and interface contacts

As shown in Fig. 9-10, after cutting, Station B is located in the middle of the incident rod while Station A sits 125 mm away from the interface end. This optimised design was made considering wave overlapping and to achieve uniform strain in the transmission rod. Again, comparison was made between the lubricated and non-lubricated cases (Fig. 9-29). The 'hard contact' case sees severe distortion of transmission wave and evident reflection wave, while the lubricated one yields almost no reflection when incident wave first arrived at interface.



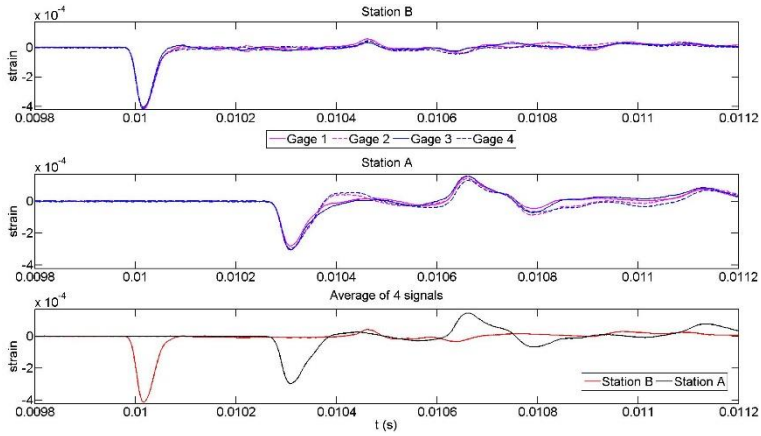


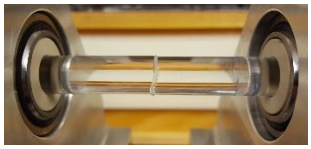
Before loading



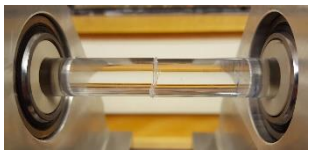
After loading

(a)hard contact





Before loading



After loading

(b)with grease on interface

Figure. 9-29 Signals collected from a PMMA-PMMA 2 rod interface experiment ($T = 22.1$ ℃)

9.3.3.2 The single rod method

Again, single rod tests (Fig. 9-30) were performed first on each PMMA rod to obtain prerequisite material properties (Fig. 9-31) which were used as reference in later interface comparison.

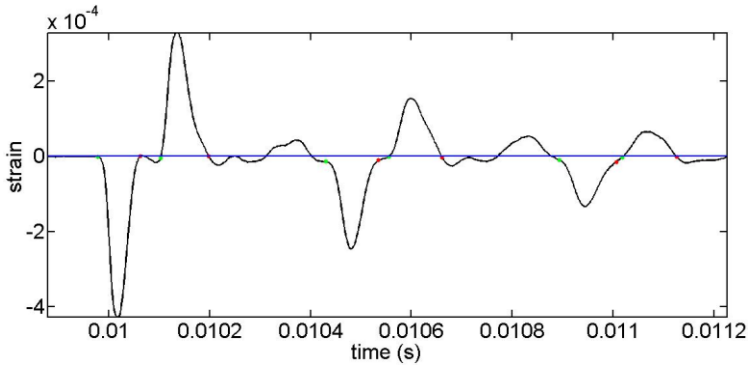


Figure. 9-30 Single rod impact signals (1000 mmØ13 mm transmission PMMA rod, $T = 22.2$℃)

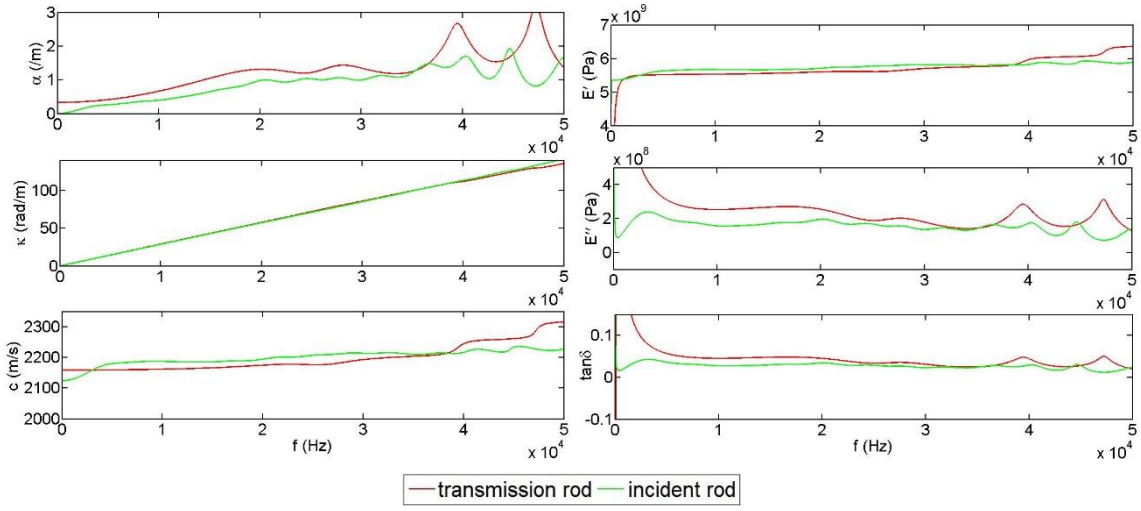
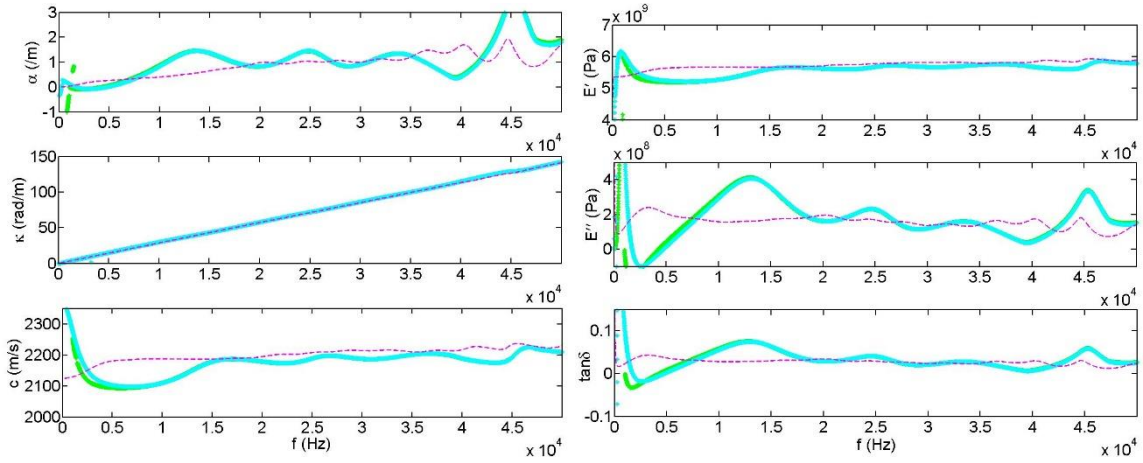


Figure. 9-31 Rod material properties derived by the single rod analysis technique ($T = 22.2$℃, prerequisite properties used for dispersion correction are ρ = 1186 kg m^{-3}, E_{inst} = 5.36 GPa, ν = 0.38).

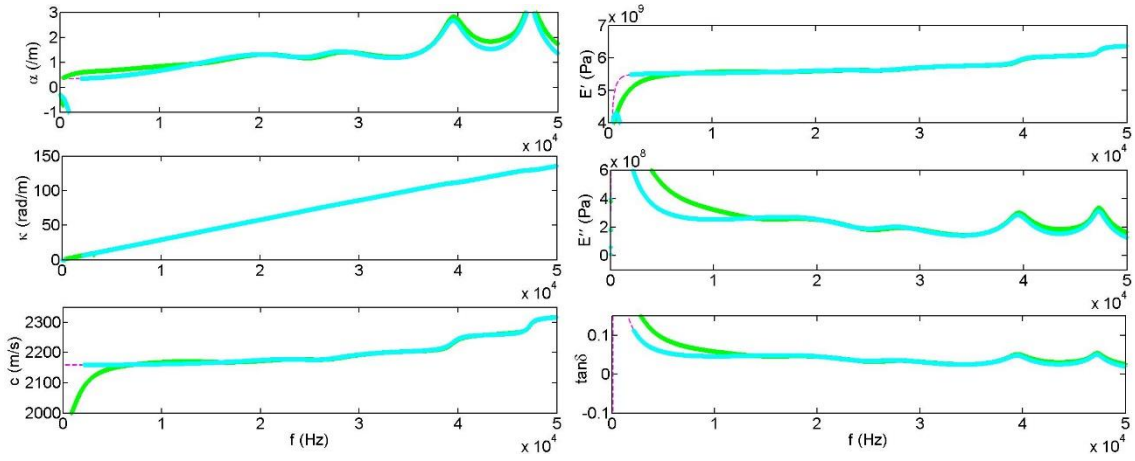
9.3.3.3 The interface method

(1) Interface results

Analysing the interface signals (with grease, Fig. 9-29b), using the same methodology adopted in simulations and in the PMMA 1 rod 2 stations tests, yields the material properties of either incident or transmission rod (Fig 9-32). Here, difference in the derived material properties of the two rods was observed, this is believed to be caused by the different degrees of complexity involved to obtain γ_1 and γ_2. The properties of the incident rod can be reliably derived by implementing the prerequisite material properties of transmission rod, obtained from transmission single rod analysis, into the two interface equations; however, this is not the case in deriving the transmission rod properties.



(a) Properties of incident rod



(b) Properties of transmission rod

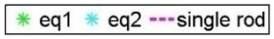


Figure. 9-32 Derived material properties ($T = 22.1$℃, rod properties used for dispersion correction are ρ = 1186 kg m^{-3}, E_{inst} = 5.7 GPa, ν = 0.38)

The discrepancy in deriving γ_1 and γ_2 is believed to be induced by 3 sources of errors: firstly, the qualities of prerequisite material properties γ_1 and γ_2 are different, as can be observed in Fig. 9-31; secondly, different levels of complexity were involved in resolving for γ_1 and γ_2, as reflected by the boundary equilibrium equations (Eq. ①' and Eq. ②'), they are not symmetric in these equations. This will be investigated using the same prerequisite inputs to derive γ_1 and γ_2 later; thirdly, γ_1 and γ_2 have different degrees of dependency on TC and RC, thus even using the same signals (*i.e.* the same TC, RC, and errors), the resulting γ_1 and γ_2 could be different, this was seen later when analysing the Ti-PMMA and PMMA-Ti cases. Also note, a tiny temperature difference exists between the single rod tests and interface tests, which can further introduces errors for both propagation coefficients when implementing the single rod results into the interface equations.

(2) Unsymmetrical derivation of the incident and transmission rod material properties

As discussed before, γ_1 and γ_2 sit in unsymmetrical positions in the 2 boundary equilibrium equations. They may have different degrees of dependences on TC and RC, and different levels of tolerance for errors contained in TC & RC. To investigate how results vary in this case, the same signal and prerequisite material properties (obtained from the 1.5 m PMMA 1 rod 2 stations test) were implemented into the 2 boundary conditions, efforts were made to solve for γ_1 and γ_2 separately, and the results are shown in Fig. 9-33. It is seen that, γ_1 results are more reliable in this case.

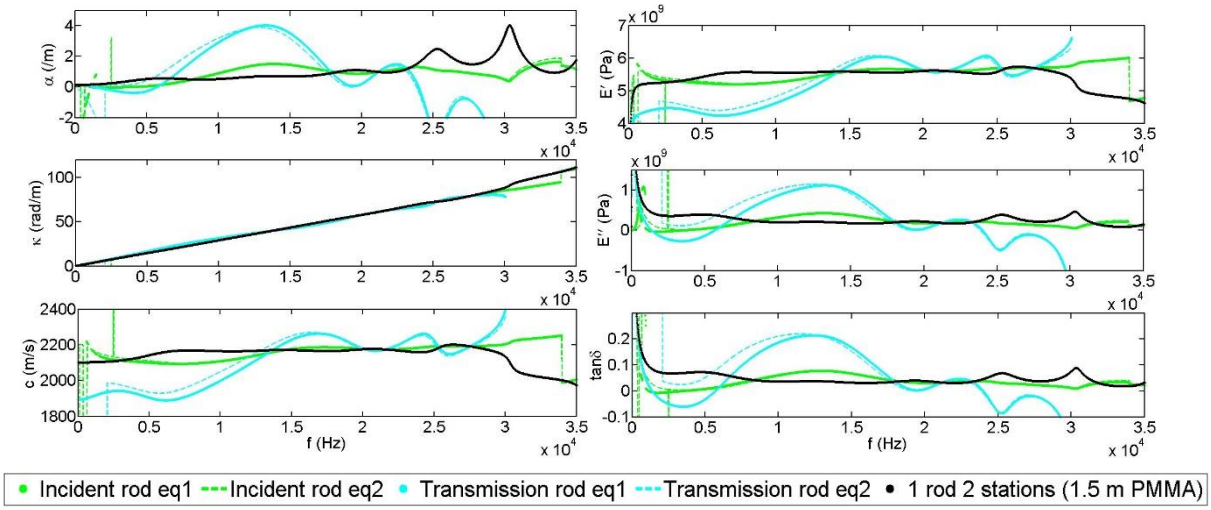
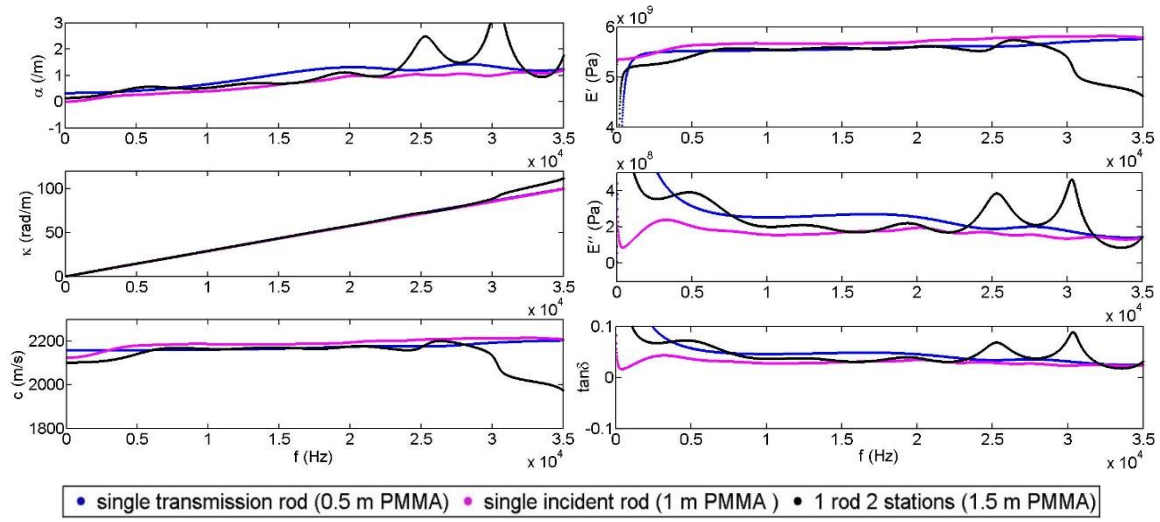


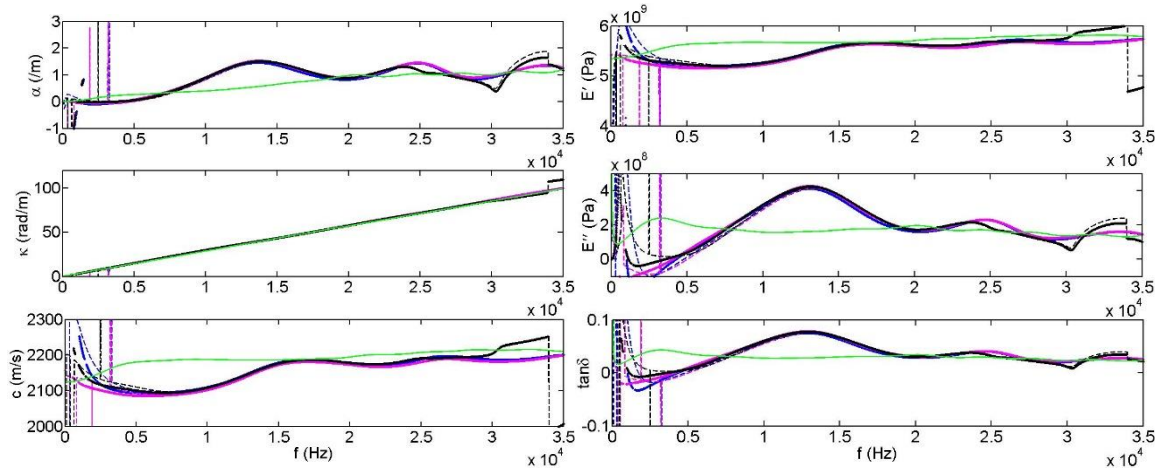
Figure. 9-33 Comparison of γ_1 and γ_2 using the same input signal and prerequisite knowledge ($T = 22.1$℃)

(3) Effect of prerequisite material properties

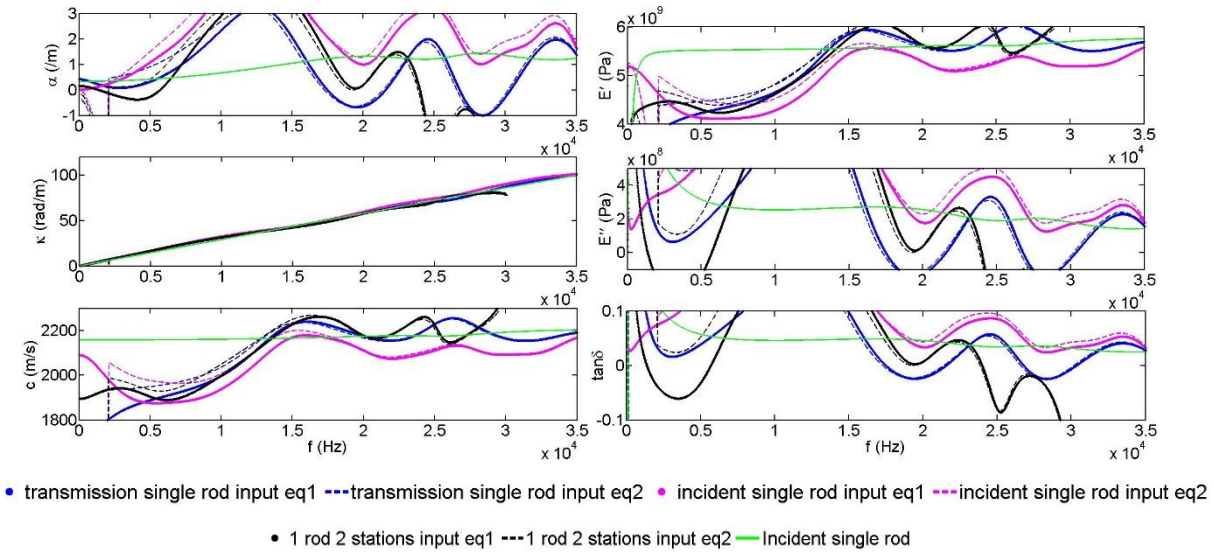
To investigate to what extent the prerequisite material properties affect the derivation of γ_1 and γ_2, material properties from three sources were employed: those derived from separate single rod tests on each rod, which is a common approach when testing an unknown material; and those obtained from one rod two stations tests. Using the same set of signals, material properties of incident (Fig. 9-34(b)) and transmission (Fig. 9-34(c)) rod were derived. Whilst there may be small differences owing to temperature changes and pulse selection, these comparisons still provide useful insight. As tiny variations were observed among the three sources, it is seen that, γ_1 is not that sensitive to errors contained in the prerequisite knowledge of γ_2, while γ_2 is more sensitive to that of γ_1. Also, however, it is noted that this dependence is not enough to explain the full variability of the γ_2 calculations compared to the expected result.



(a) Comparison of prerequisite inputs



(b) Derived incident rod material properties

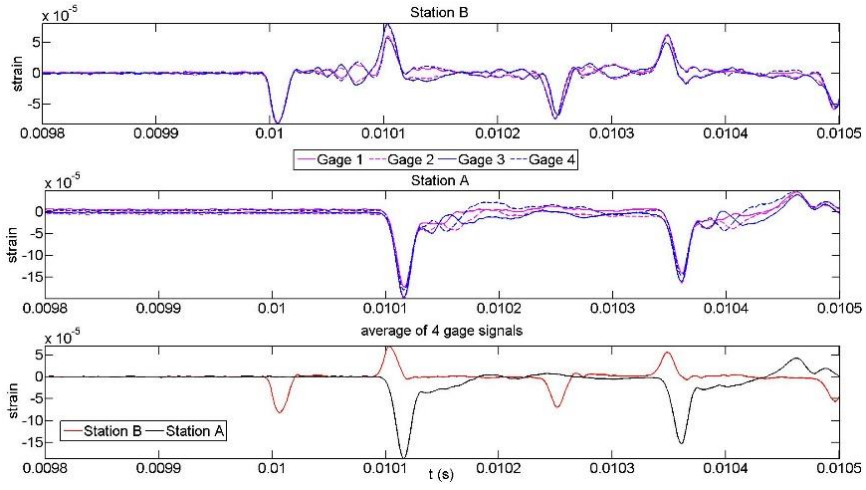


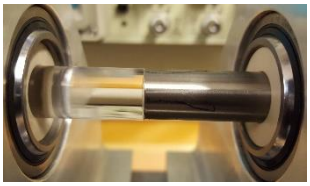
(c) Derived transmission rod material properties

Figure. 9-34 Comparison of rod material properties derived using prerequisite inputs using 3 sources of prerequisite inputs (all around $T = 22.1$℃)

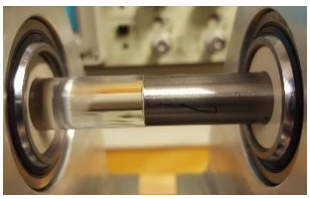
9.3.4 600 mmØ12.7 mm Ti-500 mmØ13 mm PMMA

9.3.4.1 Rod geometry and instrumentation





Before loading



After loading

Figure. 9-35 Signals collected from a Ti-PMMA 2 rod interface experiment ($T = 22.3$ ℃)

The third case tested is the Ti-PMMA two rod system. The experimental diagram was shown in Fig. 9-20. The incident gage (Station B) is located 360 mm away on the incident Ti rod from the impact end while the transmission gage (Station A) sits 125 mm away from the interface end. Wave propagating in the Ti-PMMA system is shown in Fig. 9-35. Again, bending waves can be seen in both the incident and transmission records. The viscoelasticity nature of the PMMA rod results in

pulse distortion and extension (the tail seen in the transmission wave) during its propagation in the transmission rod. A comparison of the mechanical impedance helps explain the pulse amplitudes: as PMMA is much softer than Ti (Table. 9-1), the transmitted strain has greater amplitude than incident wave, and TC is larger than unity. This was reflected in later interface analysis.

9.3.4.2 The interface method

Fig. 9-36 and Fig. 9-37 present key data in the derivation of the transmission PMMA rod properties. FFTs are consistent with the original signals in Fig. 9-35: incident and reflected pulses have similar amplitudes, while the transmitted pulse is much larger. The TC and RC values also agree with expectation: the absolute values of the strain-based TC is bigger than 1, while RC is smaller than 1. Whilst there are some deviations between the theoretical FFTs, TCs and RCs and the experimental values, the derived transmission rod material properties (Fig. 9-38) are pleasingly close to the single rod data. The incident rod properties are very well derived, but only by Eq. ②'. The difference results from the fact that TC and RC have different weights in solving for γ_1 and γ_2.

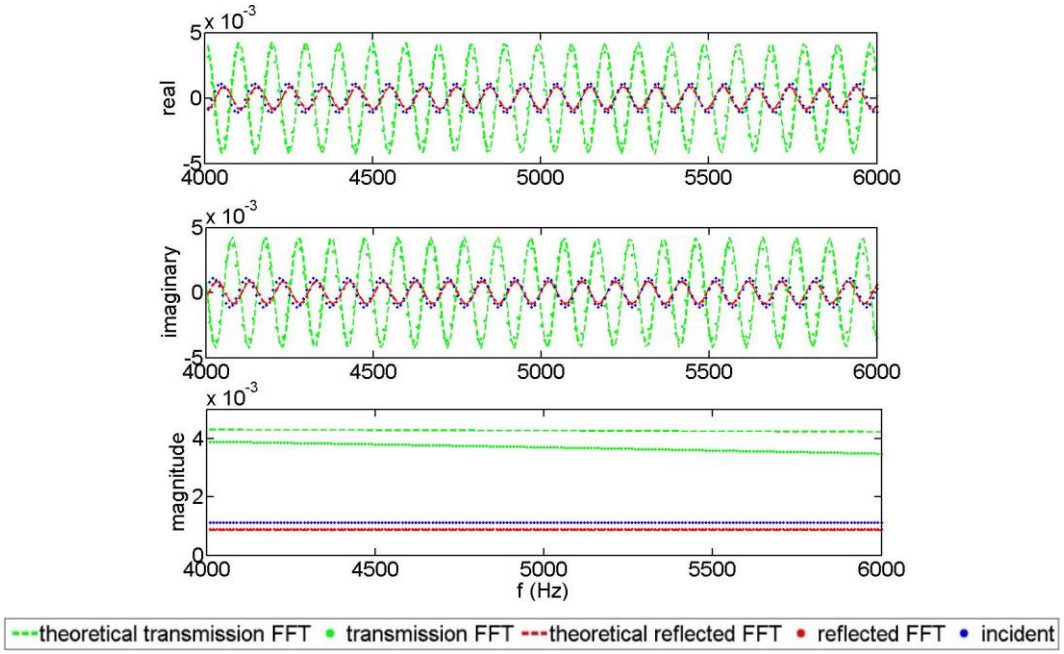


Figure. 9-36 Comparison of the theoretical and experimental FFTs

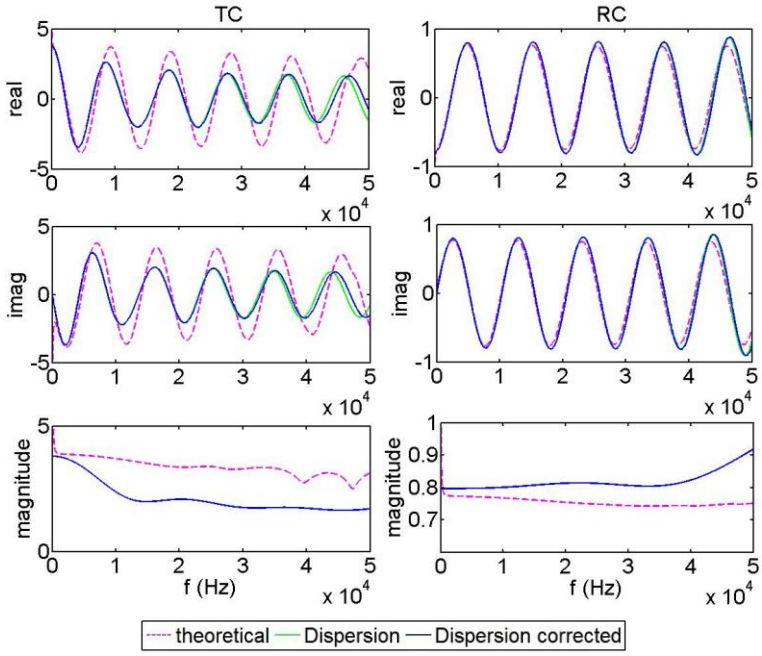
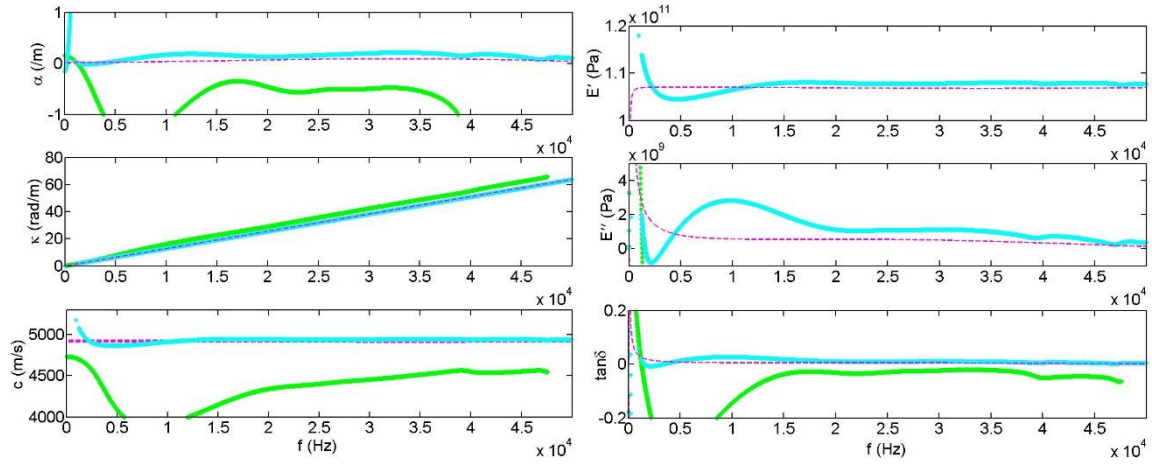
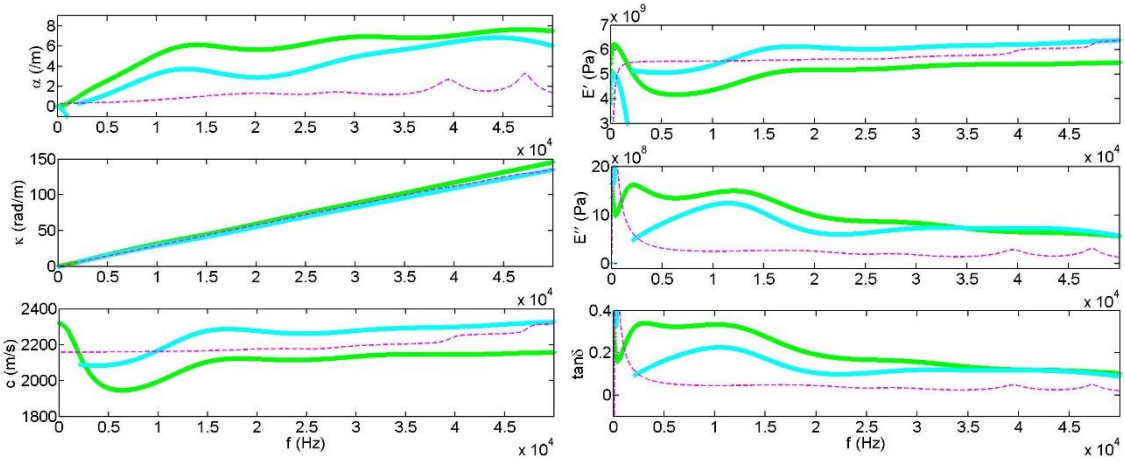


Figure. 9-37 Comparison of the theoretical and experimental TC & RC



(a) Properties of incident rod (Ti)



(b) Properties of transmission rod (PMMA)

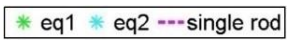


Figure. 9-38 Derived material properties (600 mm Ø12.7 mm Ti-500 mmØ13 mm PMMA, $T = 22.3℃$)

9.3.5 1000 mmØ13mm PMMA-600 mmØ12.7 mm Ti

9.3.5.1 Rod geometry and instrumentation

The last case tested is PMMA-Ti. As shown in Fig. 9-20, the incident Gage (Station B) locates in the middle of the incident rod while the transmission gage (Station A) sits 240 mm away from the interface end. The signals captured are shown in Fig. 9-39. The impedance mismatch between PMMA and Ti yields a transmission signal with amplitude smaller than the incident one.

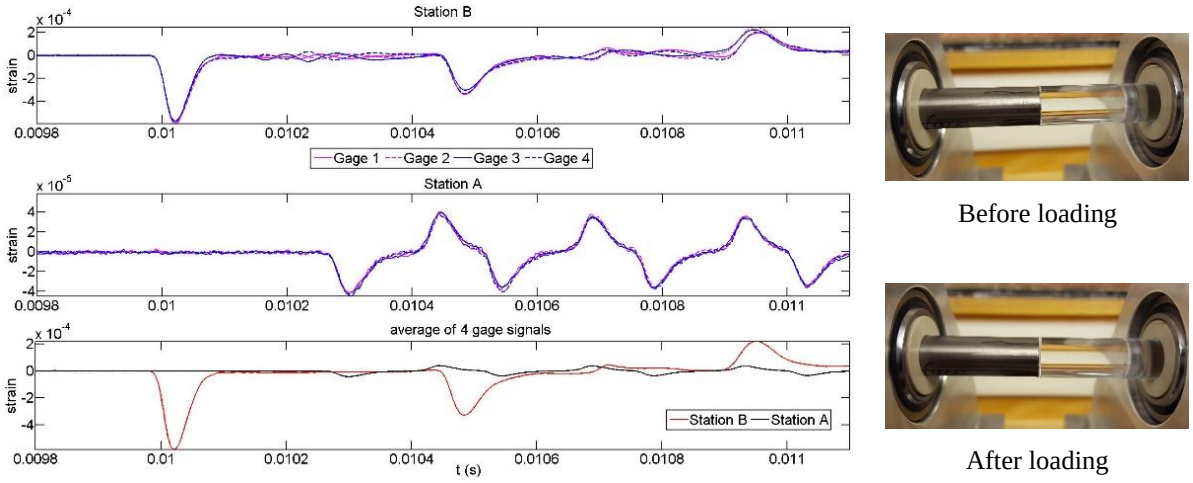


Figure. 9-39 Signals collected from a PMMA-Ti 2 rod interface experiment ($T = 22.3$ ℃)

9.3.5.2 The interface method

Comparisons were made between the theoretical and experimental curves (Fig. 9-40 and Fig. 9-41). It is seen that they agree reasonably well in the frequency range 0~20 kHz. However, deviations can be seen: for example, the transmission Ti rod material properties yielded by and Eq. ②' is reasonable but those given by Eq. ①' deviate significantly (Fig. 9-42); and the incident PMMA rod material properties cannot be resolved satisfactorily. This is due to the fact that weak transmission signal results in small TC magnitudes, and γ_1 and γ_2 exhibit different levels of dependence on TC and RC. It should also be noted that errors can result from travel distances. Similar to the unsymmetrical positions of γ_1 and γ_2 in the 2 boundary equations, x_{I}, x_R, x_T (reduced to x_1 and x_2 when $x_{\mathrm{I}} = x_R$) have different weights in deriving γ_1 and γ_2. For example, travel distance sensitivity analysis (Fig. 7-20) reveals that, in a Ti-PMMA impact system, the value of x_2 dominates the accuracy of transmission material property derivation. The situation becomes complicated when errors are involved in TC and RC, prerequisite knowledge, and travel distances.

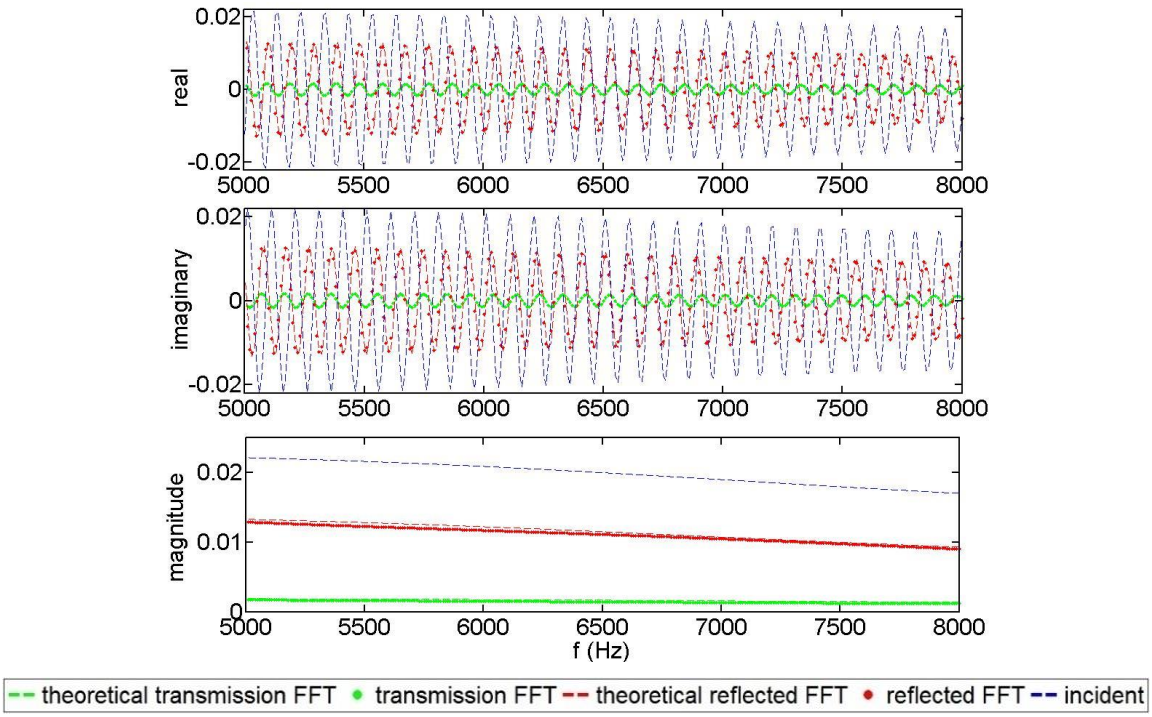


Figure. 9-40 Comparison of the theoretical and experimental FFTs

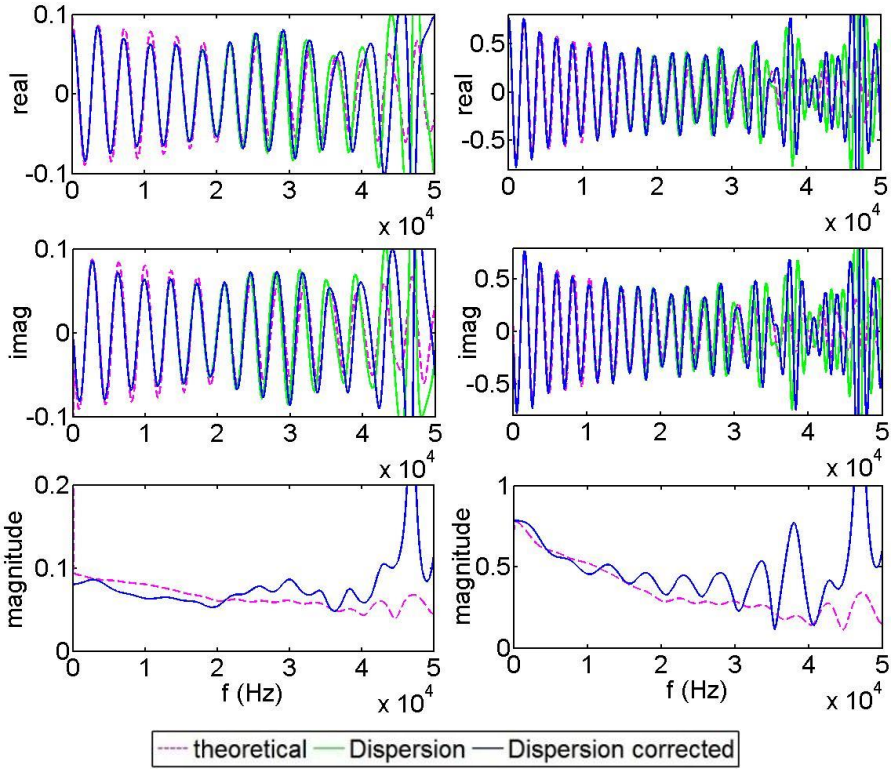


Figure. 9-41 Comparison of the theoretical and experimental TC & RC

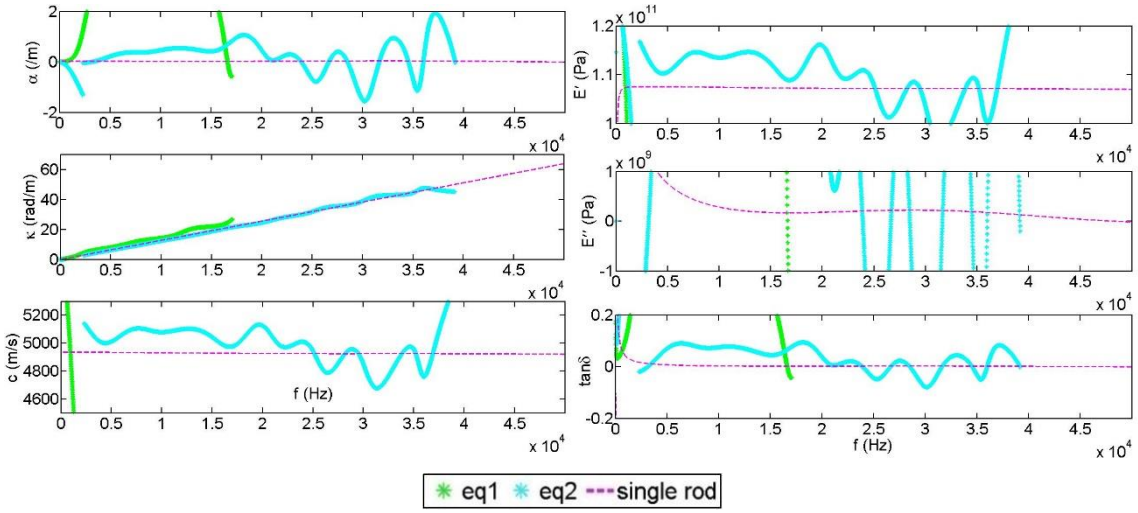


Figure. 9-42 Derived transmission Ti rod material properties ($T = 22.3$℃)

9.4 Summary of interface experiments

In this chapter, two classes of tests, *i.e.* 1-rod tests and 2-rod tests, were carried out and analysed using the interface analysis technique. For the former ones, a 1200 mm Ti rod and a 1500 mm PMMA rod were tested; for the latter ones, 4 cases were examined: Ti-Ti, Ti-PMMA, PMMA-PMMA, PMMA-Ti. While the 2-rod test materials were originated from 1-rod tests, they represent different purposes of use: the 1-rod tests assume a 'perfect' interface between the 2 measurement stations, and aim at examining the validity of the interface wave theories; the 2-rod configurations represent real but 'imperfect' interfaces, analysing the 2-rod tests helps us understand the real interface wave behaviours and error effects. Besides, single rod tests have been performed separately on all these rods, and the results either served as the prerequisite knowledge for solving interface equations, or as comparisons in interface analysis.

In the 1-rod tests, as both the 'two' rods were made of the same material, signals have been analysed using both the single rod and interface techniques. In single rod analysis of the 1200 mm Ti rod, the effect of some prerequisite information (density and initial modulus estimate) on material property derivation was investigated (Fig. 9-4b), which ensured the single rod results were robust enough for latter interface analysis, either as inputs or comparisons. Interface analysis of the 1200 mm Ti rod includes 4 sub-issues, each separately addresses the significance of accurate prior knowledge, proper

pulse selection methodology, proper treatment of bending effect, and the applicability of interface theories in 1 rod analysis. Specifically, deviance of density plays a more significant role over modulus when solving for unknown material properties (Fig. 9-5); using various pulse selection methods leads to the recommendation that, symmetric pulse selection to be used in interface analysis to avoid oscillations in results (Fig. 9-6 and Fig. 9-7); research into the effect of bending waves on results derivation (Fig. 9-8) suggests that, using an average of the diametrically opposite signals can help reduce bending effects and give more accurate results; the constant travel distance trials (Fig. 9-9) again confirmed the reliability of the interface analysis technique—in a case of 'perfect' interface, once the '2' mediums are made of the same material, the incident and reflection waves are measured at the same location x_{IR}, then where the interface locates doesn't matter—only the total travel distance has effect on the interface results, as expected.

Single rod analysis of the 1500 mm PMMA rod test sees the necessity of dispersion correction (Fig. 9-16). Error effects attracted emphasis in the 1 rod interface analysis. Firstly, the interface analysis technique is sensitive to tiny errors in the timing, a shift of the time domain signals, to the order of 1 us, can generate visible errors in the interface results (Fig. 9-17). Secondly, the effect of errors in the locations on interface results derivation was numerically investigated, which concludes that 3 mm in either $x_{I,R}$ or x_T can generate visible errors in results (Fig. 9-18). Also investigated here was the consistence of the effect of the constant travel distance.

The 4 real interface cases, *i.e.* Ti-Ti, PMMA-PMMA, PMMA-Ti, Ti-PMMA, were investigated similarly: single rod approach was applied in the homogeneous cases (Ti-Ti and PMMA-PMMA), while interface analysis was carried out through all cases. The first 2 real interface cases, *i.e.* Ti-Ti and PMMA-PMMA, both confirmed that it is necessary to use grease at interface to minimize the effect of interface imperfections, otherwise undesired reflections can generate.

Compared to the single rod results before cut (1-rod Ti, Fig. 9-4b), though some deviations can be seen, single rod results yielded from the 2-rod Ti-Ti case (Fig. 9-23) are still accurate; the interface analysis technique in this case also gave satisfying results (Fig. 9-27). Bending effect investigation (Fig. 9-28) again confirms that the averaging technique can give less deviating interface results.

In the PMMA-PMMA case, when implementing the 2 BCs equations (Eq. ①' and Eq. ②') to derive the material properties of the 2 rods separately, we see the different degrees of accuracy: while the properties of the incident rod can be reliably derived (Fig. 9-32), deviations were observed in those of the transmission rod. This is supposed to be mainly caused by the non-symmetric positions that γ_1 and γ_2 sit in the 2 interface equations, which results in different sensitivities to potential errors contained in TC and RC. Sensitivity analysis (Fig. 9-34) states that, in this PMMA-PMMA case, γ_1 is not that sensitive to errors contained in the prerequisite knowledge of γ_2, while γ_2 is more sensitive to that of γ_1.

The two real interface tests that involves two materials, *i.e.* Ti-PMMA and PMMA-Ti, yielded more deviating results: in the Ti-PMMA case, when deriving the properties of incident rod (Ti), Eq. ②' gives less deviating results (Fig. 9-38(a)), while both equations yielded deviating results when solving for those of the transmission rod (PMMA). This is not only associated with the asymmetric positions of γ_1 and γ_2, but also affected by the impedance mismatch. The PMMA-Ti case sees more deviations (Fig. 9-42), which further confirms this effect.

9.5 Summary of the interface impact technique

Investigations of interface wave behaviours spans from Chapter 6 to Chapter 9. Efforts were tried to answer the basic question: if 2 rods are made in contact, by impacting 1 rod at the free end, and measuring the 3 propagating waves in the 2 rods, is it possible to derive the material properties of at least 1 rod? The answer is yes, and only the properties of one rod can be obtained with the prerequisite knowledge of the other rod. Generally, 4 types of interface could be encountered in a SHPB experiment suited to test low-impedance materials using low-impedance metal and polymer bars: elastic-elastic, elastic-viscoelastic, viscoelastic-elastic, viscoelastic-viscoelastic interfaces. All the 4 types of interface were analysed via both simulation and experimental routes.

Chapter 7 introduces the theoretical frame work. The time and frequency domain theories were built based on the force and velocity continuity boundary conditions (*BCs*). Various forms of *BCs* have been derived, although only the 2 equations involving both *TC* and *RC* (mainly in the form of strain) were used in our simulation and experiment analysis. 4 model-dependent cases, *i.e.* the elastic-elastic,

elastic-Maxwell, elastic-Voigt, elastic-S.L.S Maxwell, were analysed in time domain; however, frequency domain analysis enjoyed popularity in later analysis.

Chapter 7 and Chapter 8 feature the 2-medium and 2-rod simulations respectively, in which 4 typical cases, *i.e.* Ti-Ti, Ti-Mg, Ti-PMMA, PMMA-Mg, have been investigated. Chapter 9 focused on experimental verification and application of the interface theories, it consists of two 1-rod tests (1200 mm Ti, 1500 mm PMMA), and four 2-rod experiments (Ti-Ti, Ti-PMMA, PMMA-PMMA, PMMA-Ti). By performing the simulations and experiments, wave behaviour at the interface of 2 cylindrical rods was examined, and the validity of the interface analysis method was verified.

There are some issues, either analytical, numerical or experimental, were encountered in the procedure. For example, to model real interface situation, the simulation model should be properly defined (inputs, meshing, *etc.*); data processing is of great importance to transfer the interface theories into real applications, the signal processing procedure has been illustrated in detail in Chapter 8. Critical issues in this process include pulse selection, dispersion correction, numerical equation solving (constrains, and unsymmetrical positions of the 2 propagation coefficients γ_1 and γ_2 in boundary equations), sensitivity to prerequisite knowledge, noise, errors contained in travel distances, timing, and those generated from misalignments.

The 1-rod 'virtual' interface case (1-rod 2 medium simulations and 1-rod experiments) has the characteristics of an 'ideal' interface: force and velocity equilibriums are strictly met on the 'interface'—it has thus been first used to verify the interface theories, and it also facilitates the introduction of artificial errors (gage location and timing) as the original signals were deemed 'clean'; real interface is always accompanied by imperfections (*e.g.* non-parallelism, misalignments, friction), which poses challenges on the interface analysis technique: although the 2-rod simulations still gave quite accurate results, the 2-rod experiments (particularly those with impedance mismatch) yielded results with certain deviations.

The 1-rod 'virtual' interface case and the after-cut 2-rod case (where 2 rods are made of the same materials) have the advantage of accommodating both single rod and interface analysis techniques. While the single rod method has been tested solidly in Chapters 3 to 5, it was considered a very reliable technique, and thus the results from the single rod analysis served as prerequisite knowledge

for interface computing, and they also acted as comparisons for checking the interface results. However, should note that, its accuracy may also subject to prerequisite knowledge (especially density of the tested rod) and pulse selection. Besides, the single rod method also helped calibrate the sensor locations and precise timing in 2-rod tests.

The two BCs equations sit in the centre of interface analysis, all prerequisite knowledge and experimental data is fed into them, and the output accuracy mainly depends on the precision of prerequisite material properties, that of the input signals, as well as the numerical methodologies used to resolve the BC equations. Error analysis plays an important role in evaluating the accuracy of the derived results. Various potential error sources have been identified and tested using both simulation and experimental methodologies, these include errors contained in travel distance (induced by misalignment, non-flat surface, manufacturing, equipment, *etc.*), signal noise, errors in prerequisite knowledge, numerical errors, and those by interface imperfections (*e.g.* friction, non-normal incidence). After they are implemented into the boundary equations, these errors can be either reduced or amplified, and as a result undesired results occur.

The unsymmetrical positions of the two propagation coefficients γ_1 and γ_2 in boundary equations bring in complexity as well. Observing these two equations, we can see the efforts to solve for the incident or transmission rod material properties, however, are not treated equivalently, which means the accuracies of the derived γ_1 and γ_2 vary even when the same set of input data was employed—the PMMA-PMMA case for example, with the same inputs obtained from the 1.5m PMMA 1 rod 2 stations test, larger variations can be seen in γ_2 (Fig. 9-33). A more complicated situation is when comparing the Ti-PMMA and the PMMA-Ti cases, in which both the asymmetricity and impedance mismatch come into effect together. In the Ti-PMMA case, impact on the incident Ti rod generates relatively large TC magnitudes (RC magnitudes are always smaller than 1), with which the incident and transmission rod material properties can be yielded within reasonable error tolerance (Fig. 9-38); for the PMMA-Ti case, however, as PMMA serves as the impact end, it generates rather small TC magnitudes (<0.1 in Fig. 9-41), which makes derivation of both coefficients unstable and difficult (Fig. 9-42). To improve this, larger excitation pressure is suggested to produce more identifiable TC values.

Errors contained in x_1 and x_2 can be induced by a number of sources, among them interface imperfections (*e.g.* the gap induced by 2 unparalleled faces) and equipment (*e.g.* finite gage length) are the main ones. Gauges used in real tests have a length of about 2-3 mm, and they were mounted such that the gauge centre was lined up diametrically at the desired location. However, what the gages measure is actually an average of the strains over the gauge length, which makes it difficult to accurately locate x_2. Also, as discussed before, even if the two gauge stations are accurately located, there still might be some undesired factors such as non-flat surface(s) which affect x_2.

Errors can be partially compensated by adjusting x_1 and x_2. It is suggested that, before experimental data can be assessed, a process called 'calibration' should be conducted on the 2-rod system to determine the 'effective' length of x_1 and x_2. By adjusting these values, for example, increasing or decreasing them a bit surrounding the designed ones, the propagation coefficient, and the resulting modulus, will change accordingly. However, it seems impossible to make both the attenuation coefficient and wavenumber meet their corresponding theoretical/referenced values at the same time, and it is recommended that, when calibrating the 2-rod system, special attention should be put on the accuracy of wavenumber, as even though there is unexpected reflection due to interface imperfection (misalignment, non-flat surface, friction, *etc*), once a wave component travels through the interface, the wavenumber (also called 'spatial velocity') as well as the wave speed is an accurate measurement of the timing, while the attenuation coefficient may not be close enough to referenced one. The agreement between wavenumbers should therefore possess priority in assessing the quality of derived results, as well as when calibrating a 2-rod system. Note that, although interface imperfections such as non-flat plane contact can also induce phase change in the signals (which results in errors in wavenumber), but these gaps are expected to be rather small to induce an apparent variation in wavenumber. The variations in attenuation coefficient, induced by the energy loss as a result of interface imperfection, however, are sensitive enough. Another evidence supporting putting more emphasis on wavenumber is, as discussed in the single rod part, storage modulus is dominated by wavenumber while loss modulus by attenuation coefficient, which explains how modulus behave coherently with the corresponding changes in the propagation coefficient. While loss modulus is

always smaller than storage modulus, and in reality, the ‘stiffness’ is of greater engineering interest, thus those dominating the storage modulus deserves more considerations.

In designing 2-rod experiments, interfaces were well machined to approximate a perfect ‘hard contact’ type. However, experimental errors such as misalignments could introduce bending waves, and averaging the diametrically collected signals can help cancel the bending effects; it is also necessary to lubricate both contact surfaces to achieve a relatively ‘perfect’ interface—it enhances energy transfer and removes errors to some extents.

The interface itself actually works in a way like a linear funnel filter does. The parameters of the filter depend on the difference of the impedances of the two rods in contact. In the case where the two rods are made of the same material, all components of the incident wave can be transmitted (no wave component filtration); and in the case where impedance mismatch exists, the incident wave is partially filtered (which results in reflections). The frequency spectrum of the reflected and transmitted waves is the same as that of incident wave, their amplitudes, however, depend on the relative ‘stiffness’ of the 2 materials: after being filtered, the reflected amplitudes are generally equal or smaller than those of incident wave as energy is partially transferred into the transmission rod.

Chapter 10: Preliminary work on wave propagation in a 3-rod system

This chapter presents the frame work for analysing 1D wave propagation in a linear 3-rod (2 interface) system, they have been summarized and extended from previous work: the general approach which counts for wave superposition in specimen was examined, validated, and translated into rigorous forms; the long-specimen approach was newly developed as a simplified approach. Using a SHPB setup, preliminary tests were carried out: phenomenal experimental results were displayed, experimental details discussed, and suggestions proposed for future work. As data processing hasn't been carried out, only theoretical framework was presented here; for accessing descriptive experimental work, readers are suggested to refer to the full *web version*.

10.1 Introduction

To sense the weak transmitted signal when testing soft materials, low impedance polymeric and metallic bars have been used to test soft materials [85]. Polymeric bars made of Polycarbonate (*PC*) [86, 87] and acrylic [88] have low impedance but also generates uncertainties when they are used to test soft materials [85]. Low-impedance metallic bars such as aluminium, magnesium and hollow bars [4] are also common in soft material testing. Among them Aluminium bar is most commonly used for testing medium soft materials [85]. It is reported three times more sensitive than steel bars due to its reduced Young's modulus [4, 85]. A hollow aluminium bar, which further lowers the impedance and increase the transmitted signal amplitude, was employed by Chen *et al* [4] to test elastomers at high strain rates.

Still, few currently available literatures see the application of spectral analysis in analysing SHPB signals to identify the complex modulus of low-impedance materials [52, 55]. S. Mousavi *et al* [55] developed a non-equilibrium Hokinson pressure bar procedure to identify complex modulus, in their research, by measuring any two of the three waves, *i.e.* incident, transmitted and reflected, material modulus can be recovered; others either focused on the experimental and simulation side [90], or dealt with part of the technical problems such as dispersion and loading conditions when using a viscoelastic split Hopkinson pressure bar [22], no systematic frame work or full description of the theoretical basis for wave propagation in multiple-rod system has been constructed in current open

source publications. Moreover, spectral analysis method has the advantage of identifying the constitutive properties (*e.g.* modulus) of soft materials in a frequency range that is difficult to achieve using other methods [52]. However, current available research on spectral analysis of wave propagation in a 3-rod system is yet not complete. They seem to be coarse and less intuitive without prior knowledge of interface wave behaviour.

This chapter aims to tackle these challenges: based on the theories of wave propagation in a single rod and at interface, I tried to build the complete frame work for describing wave behaviour in a multiple-interface system: wave propagation in a rod system can be characterized by the transmission and reflection coefficients, they are analytically linked with the material properties of all bars constituting the 'black box'—a box that combining a number of rods in contact. By measuring the input and output signals of the box, we are able to inversely retrieve the material properties of one rod—typically termed 'specimen' in the rod chain system. The simplest system consists of three rods, and the theories developed here are based on the 3-rod system; however, it is expected that they can be extended to more complex rod systems—they can be tackled following similar approach. The downside is, more potential error sources might be introduced and accuracy needs to be calibrated as complexity gains.

10.2 Theoretical basis

Theoretical frame work has been built for two cases: the first one assumes one-way wave propagation in the long specimen, and no contributions from the between-interface reflections has been counted; the second case represents a general type which poses no requirement on specimen length and considers wave propagation in both directions in the specimen.

10.2.1 Long specimen assembly

The diagram of wave propagation in a long-specimen 3-rod system is shown in Fig. 10-1. The bar and specimen density, cross-sectional area, length, propagation coefficient, and modulus are represented by ρ, S, L, γ, E respectively (differentiated by subscripts). For the convenience of expressing waves in consistent with the interface theories, the origin for incident and reflected waves is set at the input bar-specimen interface, and for transmitted wave it is at the specimen-output bar

interface: they both increase in the right direction. Wave propagating in the specimen can be expressed from these three waves. Monitoring stations are denoted by black dots in the figure.

Use strain as an example. Incident strain monitored at x_I is denoted $\tilde{\varepsilon}_I$, when it arrives at the input bar-specimen interface (the first interface), it transfers into $\tilde{P}_1$ (which is the interface strain amplitude as described in previous interface chapters), and part of it transmits through the interface and part reflected: the reflected wave $\tilde{N}_1$ arriving at x_R is denoted $\tilde{\varepsilon}_R$, and the transmitted one $\tilde{\varepsilon}_{s1}$ propagates through the specimen, reaches the second interface and transformed into $\tilde{\varepsilon}_{s2}$. The same transmission-refection process happens at the specimen-output bar interface, which generates a transmitted wave $\tilde{P}_2$, it continues to propagate through the output bar till arrives at x_T where it is denoted $\tilde{\varepsilon}_T$.

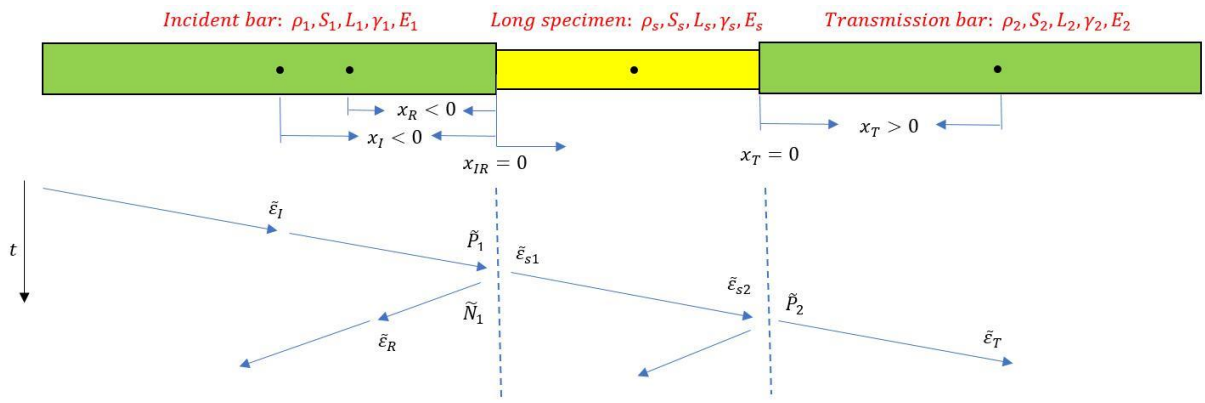


Figure. 10-1 Schematic of wave propagation in a long-specimen 3-rod system

In this case, no stress equilibrium is required; ideally, the specimen should be long enough to avoid inferences from multiple reflections between the two interfaces, as the theories here were built on the assumption that $\tilde{\varepsilon}_{s1}$ and $\tilde{\varepsilon}_R$ are generated uniquely from $\tilde{\varepsilon}_I$, and $\tilde{\varepsilon}_T$ from $\tilde{\varepsilon}_{s2}$, no afterwards reflected wave contributions were counted. Based on this assumption, the strain components can be expressed as

$$\tilde{\varepsilon}_I = \tilde{P}_1 e^{-\gamma_1 x_I},\ \tilde{\varepsilon}_R = \tilde{N}_1 e^{\gamma_1 x_R}$$

$$\tilde{\varepsilon}_{s1} = \tilde{P}_1 TC_{I-S} = \tilde{\varepsilon}_I e^{\gamma_1 x_I} TC_{I-S},\ \tilde{\varepsilon}_{s2} = \tilde{\varepsilon}_{s1} e^{-\gamma_s L_s} = \tilde{\varepsilon}_I e^{\gamma_1 x_I} TC_{I-S} e^{-\gamma_s L_s}$$

$$\tilde{P}_2 = \tilde{\varepsilon}_{s2} TC_{S-T} = \tilde{\varepsilon}_I e^{\gamma_1 x_I} TC_{I-S} e^{-\gamma_s L_s} TC_{S-T},\ \tilde{\varepsilon}_T = \tilde{P}_2 e^{-\gamma_2 x_T} = \tilde{\varepsilon}_I e^{\gamma_1 x_I} TC_{I-S} e^{-\gamma_s L_s} TC_{S-T} e^{-\gamma_2 x_T}$$

In which TC_{I-S} and TC_{S-T} denote the transmission coefficient (in terms of strain) at the input bar-specimen and specimen-output bar interface respectively.

In practice, it is more convenient to measure $\tilde{\varepsilon}_I$, $\tilde{\varepsilon}_R$ and $\tilde{\varepsilon}_T$ on the input and output bars, it is thus sensible to define a transmission coefficient $TC_{\tilde{\varepsilon}|x_I,x_T}$, reflection coefficient $RC_{\tilde{\varepsilon}|x_I,x_R}$ and reflection-transmission coefficient $RT_{\tilde{\varepsilon}|x_R,x_T}$ for the whole system

$$TC_{\tilde{\varepsilon}|x_I,x_T} = \frac{\tilde{\varepsilon}_T}{\tilde{\varepsilon}_I} = \frac{\tilde{P}_2 e^{-\gamma_2 x_T}}{\tilde{P}_1 e^{-\gamma_1 x_I}} = e^{\gamma_1 x_I} \times e^{-\gamma_s L_s} \times e^{-\gamma_2 x_T} \times \frac{\gamma_2}{\gamma_1} \times \frac{4Z_1 Z_s}{(Z_1+Z_s)(Z_2+Z_s)} = e^{\gamma_1 x_I} \times e^{-\gamma_s L_s} \times e^{-\gamma_2 x_T} \times \frac{\gamma_2}{\gamma_1} \times \frac{4\frac{\rho_1 S_1}{\gamma_1}\frac{\rho_s S_s}{\gamma_s}}{\left(\frac{\rho_1 S_1}{\gamma_1}+\frac{\rho_s S_s}{\gamma_s}\right)\left(\frac{\rho_2 S_2}{\gamma_2}+\frac{\rho_s S_s}{\gamma_s}\right)} \tag{10.1a}$$

$$RC_{\tilde{\varepsilon}|x_I,x_R} = \frac{\tilde{\varepsilon}_R}{\tilde{\varepsilon}_I} = \frac{\tilde{N}_1 e^{\gamma_1 x_R}}{\tilde{P}_1 e^{-\gamma_1 x_I}} = e^{\gamma_1 x_I} \times e^{\gamma_1 x_R} \times \frac{Z_s - Z_1}{Z_s + Z_1} = e^{\gamma_1 x_I} \times e^{\gamma_1 x_R} \times \frac{\frac{\rho_s S_s}{\gamma_s} - \frac{\rho_1 S_1}{\gamma_1}}{\frac{\rho_s S_s}{\gamma_s} + \frac{\rho_1 S_1}{\gamma_1}} \tag{10.1b}$$

$$RT_{\tilde{\varepsilon}|x_R,x_T} = \frac{\tilde{\varepsilon}_R}{\tilde{\varepsilon}_T} = \frac{\tilde{N}_1 e^{\gamma_1 x_R}}{\tilde{P}_2 e^{-\gamma_2 x_T}} = e^{\gamma_1 x_R} \times e^{\gamma_s L_s} \times e^{\gamma_2 x_T} \times \frac{2Z_s}{Z_s+Z_2} \times \frac{\gamma_2}{\gamma_s} \times \frac{Z_s - Z_1}{2Z_1} \times \frac{\gamma_1}{\gamma_s} = e^{\gamma_1 x_R} \times e^{\gamma_s L_s} \times e^{\gamma_2 x_T} \times \frac{2\frac{\rho_s S_s}{\gamma_s}}{\frac{\rho_s S_s}{\gamma_s}+\frac{\rho_2 S_2}{\gamma_2}} \times \frac{\gamma_2}{\gamma_s} \times \frac{\frac{\rho_s S_s}{\gamma_s} - \frac{\rho_1 S_1}{\gamma_1}}{2\frac{\rho_1 S_1}{\gamma_1}} \times \frac{\gamma_1}{\gamma_s}. \tag{10.1c}$$

Note that, these coefficients were written as functions of measurement locations (x_I, x_R, x_T), material constants (ρ, S, γ, Z) and frequency (γ is frequency-dependent). The flexibility of the measurement locations facilitates its use in practice. In deriving the above expressions, the relation between the characteristic impedance of a rod $Z(\omega)$ and the propagation coefficient $\gamma(\omega)$ has been applied

$$Z(\omega) = \rho c(\omega) S = S\sqrt{E^*(\omega)\rho} = \frac{i\omega\rho S}{\gamma} \qquad \text{(Eq. (6.8))}$$

also, the transmission and reflection coefficients at the input bar-specimen and the specimen-output bar interfaces have been cited from Table. 6-9a, which is derived based on the velocity and force equilibrium on each interface.

It is thus seen from Eq. (10.1) that, the three coefficients ($TC_{\tilde{\varepsilon}}$, $RC_{\tilde{\varepsilon}}$ and $RT_{\tilde{\varepsilon}}$) have all been expressed as functions of specimen material constants ($\rho_s, S_s, \gamma_s, Z_s$). Particularly, γ_s and Z_s are linked to material modulus via Eq. (6.8) or Eq. (2.27). As a result, by measuring any one of these coefficients

(which requires any two of $\tilde{\varepsilon}_I$, $\tilde{\varepsilon}_R$ and $\tilde{\varepsilon}_T$ to be measured), theoretically we should be able to inversely obtain the material modulus.

10.2.2 General treatment

The diagram was presented in Fig. 10-2. Three sets of local coordinate system were defined: for input and output bars, the origins are the same as those defined in the long-specimen case; an extra set of coordinate was defined for specimen (actually in the long-specimen case, the specimen coordinate origin was defined at the input-specimen interface), the origin of which was set in the middle of specimen. All coordinates increase in the right direction.

The difference between the long-specimen case and the general case lies in the way dealing with wave propagating in specimen. The former one only considers the first wave travelling through the specimen and assumes it's not affected by reflections between interfaces, which requires a long specimen to be used; the latter case takes into account the reflections in the specimen, which allows short specimen to be used and is more generic. As a result, any wave propagating in specimen in the general type should consist of two components: one propagating in the increasing *x* direction and one in the decreasing *x* direction.

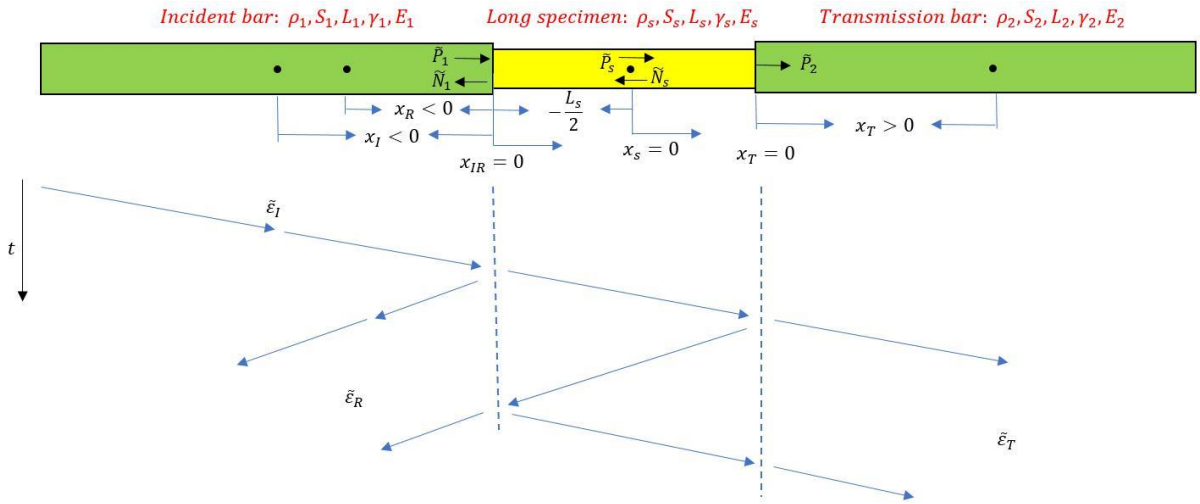


Figure. 10-2 Schematic of wave propagation in a long-specimen 3-rod system

In the figure, $\tilde{P}_1$ and $\tilde{N}_1$ denote the wave propagating in the increasing and decreasing *x* direction at the input bar-specimen interface respectively; $\tilde{P}_s$ and $\tilde{N}_s$ denote the wave propagating in the middle of specimen; $\tilde{P}_2$ is the wave propagating in the increasing *x* direction at the specimen-output bar

interface. All these quantities, plus the reflected wave in input bar $\tilde{\varepsilon}_R$, wave in specimen $\tilde{\varepsilon}_s$ and transmitted wave in output bar $\tilde{\varepsilon}_T$, take into account the effect of multiple wave reflections in the specimen. As the interface theories established in previous chapters assume two infinite rods, it is impossible to directly apply the TC_{I-S} and TC_{S-T} from Table. 6-9a, we have to re-build the velocity and force equilibrium equations at interfaces. Firstly, by making use of Eq. (2.20), the strain, velocity and force expressions can be written as

$$\tilde{\varepsilon}_I = \tilde{P}_1 e^{-\gamma_1 x_I},\ \tilde{\varepsilon}_R = \tilde{N}_1 e^{\gamma_1 x_R},\ \tilde{\varepsilon}_s = \tilde{P}_s e^{-\gamma_s x_s} + \tilde{N}_s e^{\gamma_s x_s},\ \tilde{\varepsilon}_T = \tilde{P}_2 e^{-\gamma_2 x_T}$$

$$\tilde{v}_I = -\frac{i\omega}{\gamma_1}\tilde{P}_1 e^{-\gamma_1 x_I} = -\frac{i\omega}{\gamma_1}\tilde{\varepsilon}_I,\ \tilde{v}_R = \frac{i\omega}{\gamma_1}\tilde{N}_1 e^{\gamma_1 x_R} = \frac{i\omega}{\gamma_1}\tilde{\varepsilon}_R$$

$$\tilde{v}_s = -\frac{i\omega}{\gamma_s}\tilde{P}_s e^{-\gamma_s x_s} + \frac{i\omega}{\gamma_s}\tilde{N}_s e^{\gamma_s x_s},\ \tilde{v}_T = -\frac{i\omega}{\gamma_2}\tilde{P}_2 e^{-\gamma_2 x_T} = -\frac{i\omega}{\gamma_2}\tilde{\varepsilon}_T$$

$$\tilde{F}_I = -\frac{\rho_1 S_1 \omega^2}{\gamma_1^2}\tilde{P}_1 e^{-\gamma_1 x_I} = -\frac{\rho_1 S_1 \omega^2}{\gamma_1^2}\tilde{\varepsilon}_I,\ \tilde{F}_R = -\frac{\rho_1 S_1 \omega^2}{\gamma_1^2}\tilde{N}_1 e^{\gamma_1 x_R} = -\frac{\rho_1 S_1 \omega^2}{\gamma_1^2}\tilde{\varepsilon}_R$$

$$\tilde{F}_s = -\frac{\rho_s S_s \omega^2}{\gamma_s^2}\tilde{P}_s e^{-\gamma_s x_s} - \frac{\rho_s S_s \omega^2}{\gamma_s^2}\tilde{N}_s e^{\gamma_s x_s} = -\frac{\rho_s S_s \omega^2}{\gamma_s^2}\tilde{\varepsilon}_s,\ \tilde{F}_T = -\frac{\rho_2 S_2 \omega^2}{\gamma_2^2}\tilde{P}_2 e^{-\gamma_2 x_T} = -\frac{\rho_2 S_2 \omega^2}{\gamma_2^2}\tilde{\varepsilon}_T$$

then apply boundary conditions at the two interfaces. At the input bar-specimen interface: $x_I = x_R = 0$ and $x_s = -\frac{L_s}{2}$. We have

$$\begin{cases} \tilde{v}_I + \tilde{v}_R = \tilde{v}_s \\ \tilde{F}_I + \tilde{F}_R = \tilde{F}_s \end{cases}$$

which gives

$$\begin{cases} -\dfrac{i\omega}{\gamma_1}\tilde{P}_1 + \dfrac{i\omega}{\gamma_1}\tilde{N}_1 = -\dfrac{i\omega}{\gamma_s}\tilde{P}_s e^{-\gamma_s(-\frac{L_s}{2})} + \dfrac{i\omega}{\gamma_s}\tilde{N}_s e^{\gamma_s(-\frac{L_s}{2})} \\ -\dfrac{\rho_1 S_1 \omega^2}{\gamma_1^2}\tilde{P}_1 - \dfrac{\rho_1 S_1 \omega^2}{\gamma_1^2}\tilde{N}_1 = -\dfrac{\rho_s S_s \omega^2}{\gamma_s^2}\tilde{P}_s e^{-\gamma_s(-\frac{L_s}{2})} - \dfrac{\rho_s S_s \omega^2}{\gamma_s^2}\tilde{N}_s e^{\gamma_s(-\frac{L_s}{2})} \end{cases}$$

after simplification

$$\begin{cases} \frac{1}{\gamma_1}\left(\tilde{P}_1 - \tilde{N}_1\right) = \frac{1}{\gamma_s}\left(\tilde{P}_s e^{\frac{\gamma_s L_s}{2}} - \tilde{N}_s e^{-\frac{\gamma_s L_s}{2}}\right) \\ \frac{\rho_1 S_1}{\gamma_1^2}\left(\tilde{P}_1 + \tilde{N}_1\right) = \frac{\rho_s S_s}{\gamma_s^2}\left(\tilde{P}_s e^{\frac{\gamma_s L_s}{2}} + \tilde{N}_s e^{-\frac{\gamma_s L_s}{2}}\right) \end{cases}. \tag{10.2a}$$

At the specimen-output bar interface: $x_T = 0$ and $x_s = \frac{L_s}{2}$. Similarly, we have

$$\begin{cases} \tilde{v}_s = \tilde{v}_T \\ \tilde{F}_s = \tilde{F}_T \end{cases}$$

which gives

$$\begin{cases} -\frac{i\omega}{\gamma_s}\tilde{P}_s e^{-\gamma_s\frac{L_S}{2}} + \frac{i\omega}{\gamma_s}\tilde{N}_s e^{\gamma_s\frac{L_S}{2}} = -\frac{i\omega}{\gamma_2}\tilde{P}_2 \\ -\frac{\rho_s S_s\omega^2}{\gamma_s^2}\tilde{P}_s e^{-\gamma_s\frac{L_S}{2}} - \frac{\rho_s S_s\omega^2}{\gamma_s^2}\tilde{N}_s e^{\gamma_s\frac{L_S}{2}} = -\frac{\rho_2 S_2\omega^2}{\gamma_2^2}\tilde{P}_2 \end{cases}$$

after simplification

$$\begin{cases} \frac{1}{\gamma_s}(\tilde{P}_s e^{-\gamma_s\frac{L_S}{2}} - \tilde{N}_s e^{\gamma_s\frac{L_S}{2}}) = \frac{1}{\gamma_2}\tilde{P}_2 \\ \frac{\rho_s S_s}{\gamma_s^2}(\tilde{P}_s e^{-\gamma_s\frac{L_S}{2}} + \tilde{N}_s e^{\gamma_s\frac{L_S}{2}}) = \frac{\rho_2 S_2}{\gamma_2^2}\tilde{P}_2 \end{cases}. \quad (10.2b)$$

Here comes the mathematical thinking: we have four equations and five unknowns ($\tilde{P}_1$, $\tilde{N}_1$, $\tilde{P}_s$, $\tilde{N}_s$, $\tilde{P}_2$) in Eq. (10.2), if we divide ($\tilde{N}_1$, $\tilde{P}_s$, $\tilde{N}_s$, $\tilde{P}_2$) by $\tilde{P}_1$, we are able to solve the 4 ratios—and they do possess physical meanings, for example, $TC_{\tilde{\varepsilon}} = \tilde{P}_2/\tilde{P}_1$ and $RC_{\tilde{\varepsilon}} = \tilde{N}_1/\tilde{P}_1$are the transmission and reflection coefficients of the whole system. The resulting coefficients are presented in Eq. (10.3). Note that, they were all derived at interfaces where the equilibrium BCs are satisfied.

$$TC_{\tilde{\varepsilon}|x_I=0,x_T=0} = \frac{\tilde{P}_2}{\tilde{P}_1} = \frac{4Z_1Z_s\frac{\gamma_2}{\gamma_1}}{(Z_s+Z_1)(Z_s+Z_2)e^{\gamma_s L_s}-(Z_s-Z_1)(Z_s-Z_2)e^{-\gamma_s L_s}} =$$

$$\frac{4\frac{Z_1\gamma_2}{Z_s\gamma_1}}{(1+\frac{Z_1}{Z_s})(1+\frac{Z_2}{Z_s})e^{\gamma_s L_s}-(1-\frac{Z_1}{Z_s})(1-\frac{Z_2}{Z_s})e^{-\gamma_s L_s}} = \frac{2Z_1Z_s\frac{\gamma_2}{\gamma_1}}{(Z_s^2+Z_1Z_2)\sinh(\gamma_s L_s)+Z_s(Z_2+Z_1)\cosh(\gamma_s L_s)} = \quad (10.3a)$$

$$\frac{2\frac{\gamma_2}{\gamma_1}}{\left(\frac{Z_s}{Z_1}+\frac{Z_2}{Z_s}\right)\sinh(\gamma_s L_s)+(\frac{Z_2}{Z_1}+1)\cosh(\gamma_s L_s)}$$

$$RC_{\tilde{\varepsilon}|x_I=0,x_R=0} = \frac{\tilde{N}_1}{\tilde{P}_1} = \frac{(Z_s-Z_1)(Z_s+Z_2)e^{\gamma_s L_s}-(Z_s+Z_1)(Z_s-Z_2)e^{-\gamma_s L_s}}{(Z_s+Z_1)(Z_s+Z_2)e^{\gamma_s L_s}-(Z_s-Z_1)(Z_s-Z_2)e^{-\gamma_s L_s}} =$$

$$\frac{(1-\frac{Z_1}{Z_s})(1+\frac{Z_2}{Z_s})e^{\gamma_s L_s}-(1+\frac{Z_1}{Z_s})(1-\frac{Z_2}{Z_s})e^{-\gamma_s L_s}}{(1+\frac{Z_1}{Z_s})(1+\frac{Z_2}{Z_s})e^{\gamma_s L_s}-(1-\frac{Z_1}{Z_s})(1-\frac{Z_2}{Z_s})e^{-\gamma_s L_s}} = \frac{(Z_s^2-Z_1Z_2)\sinh(\gamma_s L_s)+Z_s(Z_2-Z_1)\cosh(\gamma_s L_s)}{(Z_s^2+Z_1Z_2)\sinh(\gamma_s L_s)+Z_s(Z_2+Z_1)\cosh(\gamma_s L_s)} = \quad (10.3b)$$

$$\frac{\left(\frac{Z_s}{Z_1}-\frac{Z_2}{Z_s}\right)\sinh(\gamma_s L_s)+(\frac{Z_2}{Z_1}-1)\cosh(\gamma_s L_s)}{\left(\frac{Z_s}{Z_1}+\frac{Z_2}{Z_s}\right)\sinh(\gamma_s L_s)+(\frac{Z_2}{Z_1}+1)\cosh(\gamma_s L_s)}.$$

Based on $TC_{\tilde{\varepsilon}|x_I=0,x_T=0}$ and $RC_{\tilde{\varepsilon}|x_I=0,x_R=0}$, we derive $RT_{\tilde{\varepsilon}} = \tilde{N}_1/\tilde{P}_2 = RC_{\tilde{\varepsilon}|x_I=0,x_R=0}/TC_{\tilde{\varepsilon}|x_I=0,x_T=0}$:

$$RT_{\tilde{\varepsilon}|x_R=0,x_T=0} = \frac{\tilde{N}_1}{\tilde{P}_2} = \frac{(Z_s-Z_1)(Z_s+Z_2)e^{\gamma_s L_s}-(Z_s+Z_1)(Z_s-Z_2)e^{-\gamma_s L_s}}{4Z_1 Z_s\frac{\gamma_2}{\gamma_1}} =$$

$$\frac{(1-\frac{Z_1}{Z_s})(1+\frac{Z_2}{Z_s})e^{\gamma_s L_s}-(1+\frac{Z_1}{Z_s})(1-\frac{Z_2}{Z_s})e^{-\gamma_s L_s}}{4\frac{Z_1\gamma_2}{Z_s\gamma_1}} = \frac{\left(Z_s^2-Z_1Z_2\right)\sinh(\gamma_s L_s)+Z_s(Z_2-Z_1)\cosh(\gamma_s L_s)}{2Z_1Z_s\frac{\gamma_2}{\gamma_1}} = \tag{10.3c}$$

$$\frac{\left(\frac{Z_s}{Z_1}-\frac{Z_2}{Z_s}\right)\sinh(\gamma_s L_s)+(\frac{Z_2}{Z_1}-1)\cosh(\gamma_s L_s)}{2\frac{\gamma_2}{\gamma_1}}.$$

In the particular case where $Z_1 = Z_2 = Z_b$ (for example, when the two bars are made of the same materials and have the same cross-sectional geometry), Eqs. (10.3) can be simplified as

$$TC_{\tilde{\varepsilon}|x_I=0,x_T=0} = \frac{\tilde{P}_2}{\tilde{P}_1} = \frac{4Z_bZ_s\frac{\gamma_2}{\gamma_1}}{(Z_s+Z_b)^2e^{\gamma_s L_s}-(Z_s-Z_b)^2e^{-\gamma_s L_s}} = \frac{4\frac{Z_b\gamma_2}{Z_s\gamma_1}}{(1+\frac{Z_b}{Z_s})^2e^{\gamma_s L_s}-(1-\frac{Z_b}{Z_s})^2e^{-\gamma_s L_s}} =$$

$$\frac{2Z_bZ_s\frac{\gamma_2}{\gamma_1}}{\left(Z_s^2+Z_b^2\right)\sinh(\gamma_s L_s)+2Z_bZ_s\cosh(\gamma_s L_s)} = \frac{2\frac{\gamma_2}{\gamma_1}}{\left(\frac{Z_s}{Z_b}+\frac{Z_b}{Z_s}\right)\sinh(\gamma_s L_s)+2\cosh(\gamma_s L_s)} \tag{10.3a'}$$

$$RC_{\tilde{\varepsilon}|x_I=0,x_R=0} = \frac{\tilde{N}_1}{\tilde{P}_1} = \frac{(Z_s-Z_b)(Z_s+Z_b)(e^{\gamma_s L_s}-e^{-\gamma_s L_s})}{(Z_s+Z_b)^2e^{\gamma_s L_s}-(Z_s-Z_b)^2e^{-\gamma_s L_s}} = \frac{(1-\frac{Z_b}{Z_s})(1+\frac{Z_b}{Z_s})(e^{\gamma_s L_s}-e^{-\gamma_s L_s})}{(1+\frac{Z_b}{Z_s})^2e^{\gamma_s L_s}-(1-\frac{Z_b}{Z_s})^2e^{-\gamma_s L_s}} =$$

$$\frac{\left(Z_s^2-Z_b^2\right)\sinh(\gamma_s L_s)}{\left(Z_s^2+Z_b^2\right)\sinh(\gamma_s L_s)+2Z_bZ_s\cosh(\gamma_s L_s)} = \frac{\left(\frac{Z_s}{Z_b}-\frac{Z_b}{Z_s}\right)\sinh(\gamma_s L_s)}{\left(\frac{Z_s}{Z_b}+\frac{Z_b}{Z_s}\right)\sinh(\gamma_s L_s)+2\cosh(\gamma_s L_s)} \tag{10.3b'}$$

$$RT_{\tilde{\varepsilon}|x_R=0,x_T=0} = \frac{\tilde{N}_1}{\tilde{P}_2} = \frac{(Z_s-Z_b)(Z_s+Z_b)(e^{\gamma_s L_s}-e^{-\gamma_s L_s})}{4Z_bZ_s\frac{\gamma_2}{\gamma_1}} = \frac{(1-\frac{Z_b}{Z_s})(1+\frac{Z_b}{Z_s})(e^{\gamma_s L_s}-e^{-\gamma_s L_s})}{4\frac{Z_b\gamma_2}{Z_s\gamma_1}} =$$

$$\frac{\left(Z_s^2-Z_b^2\right)\sinh(\gamma_s L_s)}{2Z_bZ_s\frac{\gamma_2}{\gamma_1}} = \frac{\left(\frac{Z_s}{Z_b}-\frac{Z_b}{Z_s}\right)\sinh(\gamma_s L_s)}{2\frac{\gamma_2}{\gamma_1}}. \tag{10.3c'}$$

By applying the relations $\tilde{\varepsilon}_I = \tilde{P}_1 e^{-\gamma_1 x_I}$, $\tilde{\varepsilon}_R = \tilde{N}_1 e^{\gamma_1 x_R}$, $\tilde{\varepsilon}_T = \tilde{P}_2 e^{-\gamma_2 x_T}$, the interface coefficients derived in Eq. (10.3) can be extended to arbitrary measurement locations

$$TC_{\tilde{\varepsilon}|x_I,x_T} = \frac{\tilde{\varepsilon}_T}{\tilde{\varepsilon}_I} = \frac{\tilde{P}_2}{\tilde{P}_1}\times e^{\gamma_1 x_I}\times e^{-\gamma_2 x_T} = TC_{\tilde{\varepsilon}|x_I=0,x_T=0}\times e^{\gamma_1 x_I}\times e^{-\gamma_2 x_T} \tag{10.3a''}$$

$$RC_{\tilde{\varepsilon}|x_I,x_R} = \frac{\tilde{\varepsilon}_R}{\tilde{\varepsilon}_I} = \frac{\tilde{N}_1}{\tilde{P}_1}\times e^{\gamma_1 x_I}\times e^{\gamma_1 x_R} = RC_{\tilde{\varepsilon}|x_I=0,x_R=0}\times e^{\gamma_1 x_I}\times e^{\gamma_1 x_R} \tag{10.3b''}$$

$$RT_{\tilde{\varepsilon}|x_R,x_T} = \frac{\tilde{\varepsilon}_R}{\tilde{\varepsilon}_T} = \frac{\tilde{N}_1}{\tilde{P}_2}\times e^{\gamma_1 x_R}\times e^{\gamma_2 x_T} = RT_{\tilde{\varepsilon}|x_R=0,x_T=0}\times e^{\gamma_1 x_R}\times e^{\gamma_2 x_T}. \tag{10.3c''}$$

Again, Eqs. (10.3) express the three wave propagation characteristics (*TC*, *RC*, *RT*) as functions of specimen material constants (ρ, γ, Z) and frequency, it is thus possible to resolve for the material modulus by measuring any two of the three waves ($\tilde{\varepsilon}_I$, $\tilde{\varepsilon}_T$, $\tilde{\varepsilon}_R$) and using one of the three expressions.

However, should be noted that, different degrees of complexity may be involved by choosing different expressions, and they are expected to be solved numerically (similar topic has been discussed in interface analysis section 7.3.2).

Initial experiments have been carried out aiming to test the 3-rod theory. In total 5 cases were tested: Ti-Ti-Ti, PMMA-PMMA-PMMA, Ti-PMMA-Ti, PMMA-Ti-PMMA, Ti-Delrin-PMMA. The rods were assembled in the pendulum apparatus used previously in interface tests; specimen was sandwiched between the input and output bars. The phenomenal experimental results were not presented here due to limited page number, for details please refer to the full *web version*.

10.3 Conclusions

In this chapter, two genres of 3-rod wave propagation theories were constructed. The long-specimen theories are suitable for the situation where a long specimen is utilized and one-way wave propagation can be captured (*i.e.* incident $\tilde{\varepsilon}_I$, transmission $\tilde{\varepsilon}_T$, and reflection $\tilde{\varepsilon}_T$, can be measured accordingly without inference from later propagating waves between the two interfaces); the other genre is more general, it takes into account wave superposition in specimen. For both cases, transmission and reflection coefficients have been derived as functions of material properties at arbitrary measurement locations. Although verification needed, it is expected that both methodologies have the potential to be applied in a non-equilibrium Hopkinson setting. Future comparison of both methods might be interesting. Also of interest is expressing the transmission and reflection coefficients in other forms. For example, applying different expressions of TC_{I-S} and TC_{S-T} in Table. 6-9a, Eq. (10.1) can be re-written in terms of force, stress, acceleration, displacement, and velocity.

The expressions of $TC_{\tilde{\varepsilon}}$, $RC_{\tilde{\varepsilon}}$ and $RT_{\tilde{\varepsilon}}$ (Eqs. (10.1) and Eqs. (10.3)) are linked to material constants (particularly the modulus *E*), they can therefore be reversed to resolve for the material modulus. By calculating any one of these coefficients (which requires measurement of any two of $\tilde{\varepsilon}_I$, $\tilde{\varepsilon}_R$ and $\tilde{\varepsilon}_T$), and substituting them into Eqs. (10.1) or Eqs. (10.3), material modulus can be retrieved. As these equations cannot be explicitly solved, the reader is advised to pay particular attention to the numerical solving process, as discussed in 7.3.2, should note that, this work is built on the

assumptions that, all bars and specimen remain linearly viscoelastic during the impact event, and wave propagation is one-dimensional. If 3D effect exists, it can be either cancelled by applying the pre-cancellation method described in 7.3.1.1, otherwise the boundary condition equations need to be revised as in 7.3.1.2.

Five experimental cases, involving elastic (Ti) and viscoelastic (PMMA, Delrin) bars or specimens, have been tested: although results have not been analysed using the 3-rod theories yet, they coincide with theoretical analysis by drawing evidence from previous interface theories. Application of the 3-rod wave propagation theories needs to be tested in the future, particular attention is suggested to be paid to their accuracy and correction methodologies that can be applied either analytically or numerically. S. Mousavi *et al* [55] found the quality of the results from a polymer bar SHPB test is sensitive to truncation and to imperfect contact at the bar-specimen interfaces.

Note that S. Mousavi *et al* [55], and later D. R. Drodge *et al* [59] arrived at similar expressions of $TC_{\tilde{\varepsilon}}$ and $RC_{\tilde{\varepsilon}}$ as those in Eq. (10.3), however, in their research, no prior interface analytical basis was built, and direct jump from previous single rod work to 3-rod may seem coarse and less solid; also, here the derivation of Eq. (10.3) has been illustrated in detail, and they have been written in various convenient forms, for example, when the two rods have equivalent impedance, and when waves are monitored at arbitrary locations. In addition, the long-specimen theories have not appeared in any available literature to the author's knowledge.

Chapter 11: Conclusions and future work

Conclusions and findings have previously been summarized at the end of each chapter, they are presented again in Section 11.1; some promising work was discussed in Section 11.2.

In a nutshell, this research provides insights into the three impact approaches for testing rod materials: the single rod impact technique, 2-rod impact technique, and multiple-rod impact technique. To configure these techniques, wave propagation in elastic and viscoelastic rods, and at various contact interfaces were investigated via analytical, simulation and experimental methodologies: the theoretical frame was first built, in which time and frequency domain analysis was excised, simple mechanical models were analyzed, and typical characteristic coefficients, *i.e.* propagation coefficient γ, the interface coefficients *TC* and *RC*, have been expressed in terms of displacement u, stress σ, strain ε, acceleration a, normal force F and particle velocity v, and all the coefficients were linked to material constants. Simulations help validate the theoretical frameworks; experiments using pendulum, DMA and a modified SHPB demonstrate the applicability of these techniques. In single rod and interface analysis, material properties have been successfully identified from these coefficients with certain accuracy. Critical issues such as signal processing procedure, temperature effect, dispersion correction, noise sensitivity and experimental misalignment effects were studied. This research sequentially lays the basis for application of polymeric bars in Hopkinson test of soft materials, and the techniques developed each can serve as an independent impact test method, and together they have the potential to be extended to a broader range of dynamic soft material tests such as tensile Hopkinson and to more complicated situations where multiple interfaces is involved.

11.1 Summaries

11.1.1 All-in-one summaries

11.1.1.1 The single rod impact technique

The ability of the single rod impact technique to measure wave propagation characteristics and to identify material properties was first demonstrated. Through integrated analytical, experimental and simulation work, a complete description of wave propagation in typical elastic and viscoelastic solids

was presented. Analytical work, based on previous established theories, was introduced, developed, and extended; the relations between propagation coefficient, model constants, and material properties were coherently linked—this is for the first time complete single rod theories were assembled and the interlinks revealed. As application, experiments were then carried out using both direct and inverse analysis methods (*Fig.* 11-1). With reference to literatures, the direct method yielded the propagation coefficient γ with precision for both elastic and viscoelastic materials, while the inverse method retrieves material modulus. This demonstrates the feasibility and effectiveness of the designed pendulum setup in identifying the frequency-dependent and temperature-dependent material behaviours.

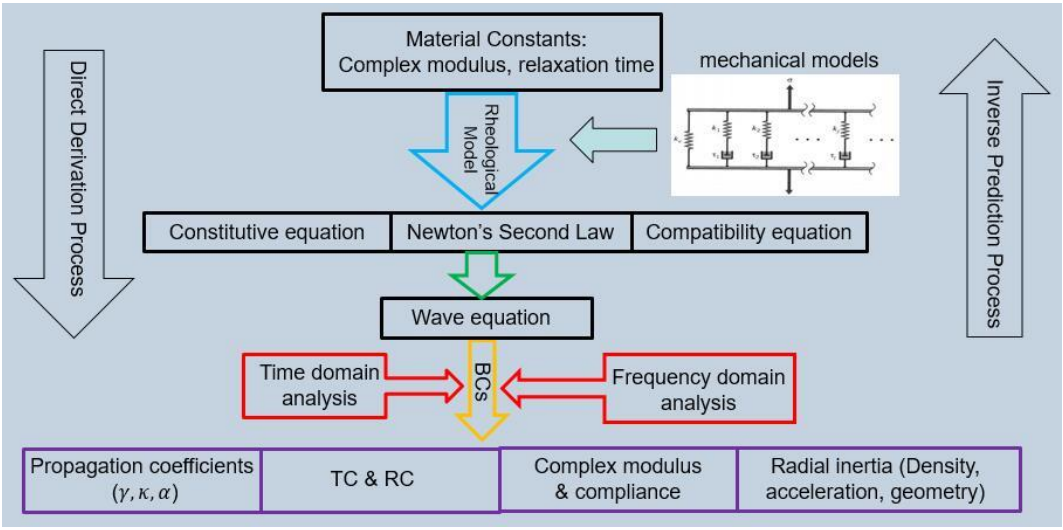


Figure. 11-1 Single rod research routine

As bar characterisation is a prior and essential step in Hopkinson tests, the single rod impact method introduces a simple but robust approach to test the low-impedance bars. In order to study the wave propagation behaviours in a single rod, theoretical basis was first built: wave propagation equations were constructed based on classical mechanics principles; constitutive equations were introduced and integrated to represent specific mechanical models (*i.e.* Maxwell, Voigt, S.L.S Maxwell and S.L.S Voigt models), these revised wave equations were then solved in time and frequency domains. The wave propagation coefficient γ plays a key role linking the physical phenomenon with intrinsic material properties, particular attention was paid to revealing this relation in frequency domain: the derived wave propagation coefficient, as a function of frequency, can be used to identify material

modulus. Evidence from simulations verified the effectiveness of this use, and confirmed the robustness of the single rod technique via noise analysis.

The technique was then applied to the pendulum-based single rod impact tests. A number of small-strain impact tests (within the linear regions of elasticity and viscoelasticity) were performed on elastic (Ti, Mg) and viscoelastic rods (PMMA). Some effects of experimental paradigms were investigated: various projectiles that are made of different materials (steel, aluminium, and PMMA) and with different shapes (balls and cylinders) were dropped from multiple heights to impact the test rod, which enables quasi-longitudinal waves with different shapes, magnitudes and durations to be generated. In the data processing stage, strain and particle velocity recordings have been analysed. The wave propagation coefficient was evaluated in a valid frequency spectrum. Some critical issues such as proper sequence of signal processing steps, the effect of window function and dispersion were discussed. Using the single rod analysis method, material moduli were successfully recovered in the 'useful' frequency range (*i.e.* 5 kHz~30k Hz for Ti and 2 kHz~20 kHz for PMMA).

Consistencies have been observed between strain and particle velocity based results, and those produced by single rod and DMA tests, which confirmed the validity of the single rod analysis technique. Thermal effect emerged as another important topic in PMMA investigations, temperature-controlled pendulum impact tests have been performed at 4 temperatures interested: *17.5 ℃, 19.5 ℃, 23.4 ℃*, and *27.5 ℃*, parallel comparisons with DMA results show that the single rod impact technique (and its associated analysis method) is sensitive enough to capture the temperature-dependent wave behaviours: it is capable of capturing small changes in material mechanical properties induced by temperature variations as small as 2°C.

11.1.1.2 The interface impact technique

Again, wave behaviours at interfaces were investigated progressively via analytical, simulation and experimental approaches: 1-rod interface analysis justified the theories and facilitated sensitivity analysis; 2-rod analysis tested their applicability and accuracy. Basically 4 types of interfaces could be encountered in a Hopkinson test involving metal and viscoelastic bars: elastic-elastic (Ti-Ti, Ti-Mg), elastic-viscoelastic (Ti-PMMA), viscoelastic-viscoelastic (PMMA-PMMA), and viscoelastic-

elastic (PMMA-Mg) interfaces. Novel complex coefficients were defined to characterize wave behaviours at interface of either two media or two rods: transmission coefficient (*TC*), reflection coefficient (*RC*) and reflection-transmission coefficient (RT). Theoretically they are functions of the mechanical impedances of the bars in contact, and experimentally they are ratios of incident pulse to corresponding transmitted or reflected pulse. Bridging the theoretical and practical gap provides an approach to derive material properties (modulus): the experimentally measured ratios could be inversed to identify material constants.

The validity, sensitivity, and accuracy of the interface theories were examined via 1-rod and 2-rod interface simulations; experimental trials were performed using a modified SHPB setup in which the two rods, *i.e.* incident and transmission, were made in direct contact, and no specimen inserted between. Again, experimental paradigm effects were investigated: several projectiles, *e.g.* 25~450 mm PMMA cylinders, were fired to generate various pulse lengths; some commonly used pulse shapers, *e.g.* paper, copper, rubber, PMMA, were employed to reduce noise. Derived results indicate that, given the properties of one rod, the unknown properties of the other one can be effectively derived with certain accuracy. Some efforts have been dedicated to understand the gap between theoretical and experimental data. This includes introducing 3D effects into the interface framework, and understanding errors brought by numerical and experimental sources.

11.1.1.3 General comments

Viscoelasticity sits in the centre of this research. Developing generic rheological models for describing viscoelasticity remains challenging, the building bricks are the Maxwell and Voigt models. The former is constructed as a combination of one spring and one dashpot in series and the latter is formed by these two acting in parallel. While the Maxwell model is able to describe the relaxation behaviour of some real materials, the Voigt model seems to be more suitable for characterizing creep behaviour. Among the common mechanical models, of particular interest is the widely used Standard Linear Solid (S.L.S) model because it possesses the flexibility of increasing and reducing terms to generically model various rheological viscoelastic materials in a range of frequencies. The S.L.S Maxwell model is formed by an auxiliary spring acting in parallel with a

Maxwell model, and the S.L.S Voigt model is formed by one spring acting in series with a Voigt model. They reduce to the elastic model with the absence of the rheological terms.

These models and their related wave behaviours have been described in detail in both single rod and interface analysis: the links between mechanical model constants (*e.g.* spring elasticity k_e, model relaxation time constant τ), wave propagation characteristics (attenuation coefficient α, wave number κ, wave speed c, transmission coefficient TC, reflection coefficient RC), and material constants (impedance *Z*, modulus E) were revealed in theoretical analysis, they were then applied in simulation and experimental data processing in both direct and inverse manners—the direct approach measures wave propagation characteristics while the inverse method retrieves material constants. Frequency domain analysis is of particular interest in this research as traditional time domain analysis shows less power when frequency dependent material behaviour dominates; although time domain method has been extended or developed in both cases, emphasis was cast on the more capable and applicable frequency domain analysis. All wave propagation characteristics and material constants were determined based on a transform of the wave propagation equations from time domain into Fourier space.

Comparisons were made constantly throughout the research to test the validity and reliability of the analysis methodologies. In simulations, derived material constants were compared to the corresponding input ones, noise-inferenced results were compared to the clean ones in both the single rod and interface cases. Comparisons have also been seen in experiments, for example, the strain-based, particle velocity-based and DMA results comparison in single rod tests.

The mathematics and logics behind signal processing are the core factor that helps secure meaningful results. For example, numerical dispersion correction technique has been adopted throughout whole single rod and interface analysis (otherwise specified). Problems such as the sequence of signal processing (*e.g.* proper pulse selection), concerns about FFT (*e.g.* the windowing effect), and the complexity (constrained root-finding) in solving mathematical Partial Differential Equations (PDEs) were discussed for the first time in similar research. Mathematical treatment of the Fourier transform (*e.g.* the construction of FFT) and the PDE related problem (*e.g.* multiple solutions) was investigated

in detail. For example, noise study finds that, the robustness of each technique, explained as the power to identify material constants with the appearance of noise, varies: the interface technique is more prone to be disturbed by noise (high sensitivity, low robustness) while the single rod analysis technique exhibits low sensitivity and high robustness; and the degree of sensitivity is linked with the complexity of the wave equation(s)—equations that are used to resolve wave propagation characteristics (attenuation, wave number, speed, transmission coefficient, *etc*), this can be improved by treating these equations with properly confined constrains.

As these techniques developed in this research are based on wave propagation theories, any measurable signals can be processed (*i.e.* either displacement u, stress σ, strain ε, acceleration a, normal force F or particle velocity v), this allows for a wide range of monitoring equipment to be used, for example, LDV (particle velocity), piezoelectrical sensors (force), and accelerometer (acceleration). Moreover, the analysis methods can be applied to more complex dynamic systems where multiple-interface wave propagation is involved.

11.1.2 Summaries by chapter

Chapters 2-6 feature the work interpreting wave propagation in a single rod. Chapter 2 provides the theoretical basis, in which wave equations were built, time and frequency domain solutions were sought. Particularly, wave propagation in a single rod was characterized by the wave propagation coefficient γ, which consists of the damping coefficient α and wavenumber κ (Eq. 2.19); the dispersion free relation (Eq. 2.27) serves as the basis for recovering material properties from the propagation coefficient. As an application of the single rod theories, three mechanical models (Maxwell, Voigt, S.L.S), together with the elastic one, were examined (Table. 2-2).

Experiments were then conducted as an application of the single rod theories. Chapter 3 first illustrates the principles for single rod data analysis. The crucial equations that were actively used were Eq. (3.2), from which the propagation coefficient γ was evaluated. Also illustrated in Chapter 3 are the motivations of the single rod experimental design, the typical data processing procedure and some critical issues (*e.g.* pulse selection and frequency limits) encountered. The effects of

geometric dispersion and methods of dispersion correction have also been treated in detail. Results from single rod tests on 3 rods (Ti, Mg and PMMA) were presented in Chapter 4. As elastic material properties were known before experiments were carried out, I started by analysing the elastic case to verify the single rod analysis method—the results from Ti and Mg showed good agreements with theoretical ones. Further application to PMMA validated the effectiveness of the pendulum-based single rod impact technique in detecting temperature-dependent viscoelastic behaviours: the proposed single rod impact method and the corresponding analysis methodology are capable of capturing the variations of mechanical material properties induced by temperature change as small as 2 ℃. Furthermore, results from other reliable techniques, such as LDV and DMA methods, provided support evidence for validating the single rod results. In addition, by employing various simulations in Chapter 6, the validity of the analysis methodology was further confirmed. Typical issues concerned in the simulation section include: numerical fitting of experimental data to build the Prony model, the strain gage effect and comparison with experimental result to check the linearity of strain gage measurements. Also presented is the noise study, in which different SNR levels have been tested on the simulation models to evaluate the sensitivity of the signal rod analysis methodology to errors—it showed perfect capacity in this use though.

Chapters 7~10 give full description of the interface impact technique. The theories and methodologies derived here are brand new (although some contents such as the boundary conditions are known). The basic problem that interface analysis aims to resolve is, given two rods in contact and the material properties of one rod, how to figure out the properties of the other one using impact methodology. The theoretical basis was provided in Chapter 7, in which the problem has been treated in both time and frequency domains: in time domain, emphasis was addressed to validate the expressions of the derived coefficients (*i.e.* TC, RC and RT), and four model-dependent cases (Elastic-Elastic, Elastic-Maxwell, Elastic-Voigt, Elastic-S.L.S Maxwell) were analysed; frequency domain analysis was featured by the capacity of using the coefficients to resolve for the unknown material properties. Simulation verifications were introduced in Chapter 8 and 9. Four cases of interfaces (Ti-Ti, Ti-Mg, Ti-PMMA and PMMA-Mg) were modelled in sequence: firstly the 2-media

case was simulated as ideal interfaces to validate the interface theories. By doing so we discussed effective dispersion strategies, the complexity of numerical computing of BCs equations, the effect of errors contained in travel distance, timing, and noise. Similar to the single rod noise analysis, 2 types of noise (artificial AGWN and experimental) were again applied at 2 levels (SNR=10 and 20) both globally and locally (though only part of results were presented), it has been seen that, the results yielded from the interface analysis can be venerably disturbed by noise, which may limit its application in future Hopkinson use if no improvement (theoretical treatment or experimental control) applied; the 'real' interfaces were modelled in Chapter 9, in which in parallel the same four cases were employed. The capacity of the two BCs equations (force and velocity equilibrium) in resolving for the unknown transmission rod properties was compared in the Ti-Ti case; error analysis was also featured in the Ti-Ti case, from which it was concluded that misalignments (central axis offset, rotation, and non-parallelism) can lead to errors in interface analysis mainly due to the occurrence of bending wave. This again supports the statement that this technique is susceptible to errors within the context of this research.

Interface experiments were presented in Chapter 10. 'Perfect' interfaces were assumed in the single rod Ti and PMMMA tests: similar to the 2-media simulations, the results were analysed using both interface and single rod methods—they generated consistent results, which gives confidence in validating the interface analysis technique. The effect of pulse selection was discussed in the Ti case; errors contained in timing and travel distance were researched in the PMMA case. Analysis of the four 'real' interface cases, *i.e.* Ti-Ti, PMMA-PMMA, Ti-PMMA, PMMA-Ti, again confirmed the high-level of sensitivity of the interface analysis technique to potential errors: the unsymmetrical positions of the wave propagation characteristics (TC, RC, and the objective wave propagation coefficients γ_1 and γ_2) in the BC equations result in different degrees of dependence on the inputs, in certain cases, rod material properties can be resolved at a satisfactory level.

Chapter 11 gives insights into the polymeric-based 3-rod SHPB system. Built on previous available work, two sets of 3-rod wave propagation theory were developed to tackle two classes of problems: a long specimen SHPB and a general type. The former one assumes that signals can be measured at

input and output rods without inference of inter-specimen reflections; the later one counts for superposed waves traveling in a short specimen. Phenomenal experimental results were obtained, with proper experimental setup (*e.g.* lubricating technique applied at interfaces), they seem to be promising and sensible; however, due to timing reason the results haven't been analysed, and the theories need to be tested via simulation and experimental approaches in the future.

11.2 Future work

11.2.1 Further investigation of multiple-interface wave propagation theories

Yet there are many aspects to be improved for these techniques and extended beyond. For example, in-depth research on wave propagation between multiple (≥3) polymeric interfaces is still in need, which calls for theoretical assembling, simulation validation, and critical error analysis. One of the final aims would be to process signals from a polymeric rod based Hopkinson system with satisfying accuracy, this ensures its revolutionary utility in testing soft materials. Optimizing a modified Hopkinson method to facilitate soft material testing calls for both configuring the hardware and developing according signal processing methodology. The theories and methodologies of single rod, 2-rod, and 3-rod impact approaches were illustrated with certain materials in this research, a wider range of soft materials (*e.g.* PVC bars) and other interfaces (*e.g.* viscoelastic-viscoelastic interface) with distinct material impedances are encouraged to be applied to test the described apparatuses and the proposed signal processing methodologies; more promisingly, the work presented can be extended to more complicated, polymeric rod involved systems, particularly for the modified Hopkinson use, preliminary work has been carried out to provide insights on wave propagation in this 3-rod system, they have been improved from methods reported in currently available literatures, and the raw experimental results seem to be sensible and promising. However, more work is required to allow its use in a modified Hopkinson analysis: the established theories need to be polished and validated in a simulation environment and tested in experiments, and potential error sources (*e.g.* numerical error induced by signal truncation, and mathematical treatise on error analysis) need to be identified as prior research shows gap between theoretical and experimental work, applications always see deviations from analytical framework and thus adjustments in theories or numerical compensation (*e.g.*

dispersion) are very important in the post-analytical stage. Errors could yield deviations as well, for example, those generated by experimental misalignments pose a big challenge in applying the theories to test soft materials, experiences indicate that wave propagation at interfaces are vulnerable to tiny disturbance induced by factors such as non-flat surfaces, non-neural alignment, bending, non-uniform impact, *etc*. Even perfect conditions have been achieved, due to the pseudo nature of longitudinal waves, it is difficult to remove undesired reflections at interface. Using grease could help to some extent, which has been demonstrated in prior chapters; however, it is more realistic to develop mathematically tractable formula to reflect the imperfect wave propagation reality; also, simulation possesses the advantage of facilitating error treatise.

Once the theories and signal processing techniques have been developed, more trials can be explored, these include utilizing a broad range of medium soft plastics (PVC, PP, Delrin) as rob materials, to test very soft samples such as rubbers. Rods can be conveniently calibrated using he single rod technique before they are used; as no stress equilibrium is required with this frequency analysis technique, long specimens can be utilized, which allows sensors to be mounted on them. Sensor size effect can affect frequency bounds, which has been investigated in single rod simulations, this hasn't been experimentally researched; also of interest is to test the theories built in this research using quantities rather than strain and velocity. On the numerical side, windowing effect is inevitable when converting all types of signals into frequency domain, depending on the purpose of signal processing (*e.g.* frequency resolution or magnitude accuracy), applying proper windows (*e.g.* a Hamming window) to the time domain signal could potentially alleviate energy leakage, this is another aspect worth investigating.

Emphasis in this research has put on developing/modifying the test apparatus other than specimen. Inspired by the use of hollow bars in testing soft materials, the author came up with the idea of using a long specimen-tube aggregate to test soft materials in a traditional metal bar Hopkinson setup. The idea can be configured as: use a hollow cylinder tube which is made of the same material and is of the same diameter as bars (the bar material is suggested to distinctly differentiate from specimen material) to accommodate the soft specimen. By analysing the arrival timing difference of the two sets of signals propagating in specimen and tube (constrained wave propagation), and knowing the

tube material properties and geometry, we might be able to characterize the specimen material. For example, the variation of wave travel time in the tube and specimen can be used to calculate the wave speed in specimen, using the known wave speed of the tube as a reference. This technique may be of particular use for extreme soft materials such as rubber, gel and biology materials, as they experience extensive deformation during a Hopkinson impact test, which generates evident non-uniform strain across the contact interface and violate the assumptions of the contact theories. The advantage of the specimen-tube aggregate configuration is, it can be simply modified from a traditional Hopkinson apparatus, and allows long specimen to be tested (actually the longer the aggregate the better, as this yields more distinct signal delay). However, the analysis may be complex, it involves contact analysis (the interaction between specimen and tube such as sliding), and mechanics of constrained wave propagation, developing the theoretical framework would be a challenge.

Further investigation in spectral analysis, *e.g.* employing an energy approach in signal processing, may be useful. For example, the power density after FFT can be an indicator of wave propagation; the area under curve (AUC) might imply potential use as well. Also, understanding bending wave would be a surplus to interface research. It is suggested pure bending test (*e.g.* transverse loading tests) to be performed for all interface test configurations to examine the existence of bending wave and evaluate their effects.

Finally, the author would like to address the emerging potential of the data science approach to treat complex data problems (particularly big data situations) in engineering. Tools and techniques are now developed to draw deep insights from data, these include machine learning (or more broadly Artificial Intelligence), computer vision (for video and image analysis), parametric and non-parametric estimation and inference methods, *etc*. Combing with our current knowledge of physical models, they could potentially improve accuracy and efficiency in signal processing, status evaluation (*e.g.* structural health monitoring), and parameter estimation. While classical physical laws are deterministic, uncertainties (*e.g.* random noise) could be introduced in experimentations, additive noise has been discussed in this work, however, and more general treatment of randomness could be performed using techniques from modern statistics. Further, when multiple transition states

are available, *e.g.* the service state of an engine component, a probabilistic approach can be fit in. This generalises to probabilistic and predictive mechanics. Mature optimisation and inference methods have been observed in engineering applications such as vibration control, seismic monitoring, wind engineering, and structural probabilistic design (where uncertainty, anomaly, and noise present). However, boundaries across disciplines still exist, and traditional engineering researchers are hesitating to embrace new techniques. The wave of Artificial Intelligence (AI) and Data Science (DS), for example, is transforming all areas, with the power of analysing large volume and complex datasets in an automated way, it creates data-centric engineering and might open a new area if some aspects of it can be integrated with material and structural engineering, and some examples could be: probabilistic finite element analysis, sensor network for non-destructive testing, fatigue prediction, network methods for defects detection, real-time in-situ monitoring using vision techniques, *etc*. Machines could be trained to do the work at satisfying level, and it possesses advantages when it comes to high-dimensional, complex, and human non-trackable problems (*e.g.* real-time state estimation considering environment factors), applying pre-defined or dynamically adopted algorithms to predict dynamic material behaviours and to identify material parameters could improve our understanding. Data deficiency becomes an issue in training algorithms, thus building a massive genetic database for material simulation and testing plays a key role (imagine ImageNet in deep learning). This network could save researchers from repeating troublesome experimentations, and share their knowledge base worldwide.

REFERENCES

1. C. J. E. Smith, M.S. Higgs and K. R. Baldwin, “Advances in Protective Coatings and their Application to Ageing Aircraft,” the RTO AVT Workshop on “New Metallic Materials for the Structure of Aging Aircraft”, Corfu, Greece, pp. 19-20 April 1999
2. Montgomery T. Shaw and William J. MacKnight, “Introduction to Polymer Viscoelasticity”, Wiley, New Jersey, 2005
3. C. M. Roland, “Mechanical Behaviuor of Rubber at High Strain Rates”, Rubber Chemistry and Technology, Vol. 79, No. 3, pp. 429-459, 2006
4. W. Chen, B. Zhang, M. J. Forrestal, “A split Hopkinson bar technique for low-impedance materials,” Experimental Mechanics, Volume 39, Issue 2, pp. 81-85, 1999
5. Capodagli, J. and Lakes, R. S., “Isothermal viscoelastic properties of PMMA and LDPE over eleven decades of frequency and time: a test of time- temperature superposition”, Rheologica Acta, 47, pp. 777-786, 2008
6. W. Chen, F. Lu, B. Zhou, “A quartz-crystal-embedded split Hopkinson pressure bar for soft materials,” Experimental Mechanics, Volume 40, Issue 1, pp. 1-6, 2000
7. Rod Lakes and John Quackenbush, “Viscoelastic behaviour in indium tin alloys over a wide range of frequency and time,” Philosophical Magazine Letters, 74, pp. 227-232, 1996
8. Dooris, A., Lakes, R. S., Myers, B. and Stephens, N., “High damping indium-tin alloys,” Mechanics of Time Dependent Materials, 3, pp. 305-318, 1999
9. Julian Vincent, Structural Biomaterials: Third Edition. Princeton University Press, 2012
10. Boyer, D. B., Papadogiannis, Y., Park, H. C., and Lakes, R. S., “Viscoelasticity and aging of dental composites,” Bio-Medical Materials and Engineering, 8, pp. 45-53, 1998
11. Amada, S. and Lakes, R. S., “Viscoelastic properties of bamboo,” Journal of Materials Science, 32, pp. 2693-2697, 1997
12. The open University, “Introduction to polymers”, online resources
13. Montgomery T. Shaw and William J. MacKnight, “Introduction to Polymer Viscoelasticity”, Wiley, New Jersey, 2005
14. G. T. Gray III, “Classic Split-Hopkinson Pressure Bar Testing”, ASM Handbook, Vol. 8: Mechanical Testing and Evaluation, pp. 462-476, ISBN 0-87170-389-0, 2007
15. J.E. Field, S.M. Walley, W.G. Proud, H.T. Goldrein, C.R. Siviour, “Review of experimental techniques for high rate deformation and shock studies,” International Journal of Impact Engineering, 30, pp.725–775, 2004
16. H. Kolsky, the propagation of stress pulses in viscoelastic solids. Phil. Mag. 1(8), pp. 693-710, 1956
17. T. Pritz, “Apparent complex Young's modulus of a longitudinally vibrating viscoelastic rod”, Journal of Sound and Vibration, 77 (1), pp. 93-100, 1981

18. C. Bacon, “An experimental method for considering dispersion and attenuation in a viscoelastic Hopkinson bar”, Experimental Mechanics, Vol. 38, No. 4, 1998
19. M. Mossberg, L. Hillström, T. Söderström, Non-parametric identification of viscoelastic materials from wave propagation experiments, Automatica, 37 (4), pp. 511-521, 2001
20. A. Benatar, A.L Yarin and D. Rittel, “Experimental measurement of the dynamic moduli of polymers using an instrumented Kolsky bar”, Proceedings 20th ICTAM, September 2000
21. B. Ahonsi, J. J. Harrigan, M. Aleyaasin, “On the propagation coefficient of longitudinal stress in viscoelastic bars,” International Journal of Impact Engineering, 45, pp. 39-51, 2012
22. H. Zhao, G. Gary, J. R. Klepaczko, On the use of a viscoelastic split Hopkinson pressure bar, International Journal of Impact Engineering, Vol. 19, No. 4, pp. 319-330, 1997
23. Lundberg, B. and Blanc, R. H., “Determination of Mechanical Material Properties from the Two-point Response of an Impacted Linearly Viscoelastic Rod Specimen,” J. Sound Vibration, 126, pp. 97-108, 1988
24. Chen R, Huang S, Xia K, Lu F, “A modified Kolsky bar system for testing ultra-soft materials under intermediate strain rates,” Rev Sci Instrum., 80(7):076108, 2009
25. T. P. M. Johnson, S. S. Sarva, S. Socrate, “Comparison of Low Impedance Split-Hopkinson Pressure Bar Techniques in the Characterization of Polyurea,” Experimental Mechanics, Volume 50, Issue 7, pp. 931-940, 2010
26. Lili Wang, K. Labibes, Z. Azari, G. Pluvinage, “Generalization of Split Hopkinson Bar technique to use viscoelastic bars,” International Journal of Impact Engineering, Vol. 15, No. 5, pp. 669-686, 1994
27. Simon P, Anderson, Higher-order rod approximations for the propagation of longitudinal stress waves in elastic bars, Journal of Sound and Vibration 290, pp. 290-30, 2006.
28. S. P. Timoshenko, J. N. Goodier, Theory of Elasticity (third edition), McGraw-Hill Singapore, 1970
29. H. Zhao, G. Gary, A three-dimensional analytical solution of the longitudinal wave propagation in an infinite linear viscoelastic cylindrical bar. Application to experimental techniques, Journal of the Mechanics and Physics of Solids 43, pp. 1335–1348, 1995
30. Welch, K., Mousavi, S., Lundberg, B. et al. Viscoelastic characterization of compacted pharmaceutical excipient materials by analysis of frequency-dependent mechanical relaxation processes, Eur. Phys. J. E Volume 18, Issue 1, pp 105–112, 2005
31. S. Mousavi, D.F. Nicolas, B. Lundberg, Identification of complex moduli and Poisson’s ratio from measured strains on an impact bar, Journal of Sound and Vibration 277, pp. 971-986, 2004
32. L. Hillstrom, M. Mossberg and B. Lundberg, Identification of complex modulus from measured strains on an axially impacted bar using least squares, Journal of Sound and Vibration 230(3), 689-707, 2000

33. A. Benatar, D. Rittel, A.L. Yarin, Theoretical and experimental analysis of longitudinal wave propagation in cylindrical viscoelastic rods, Journal of the Mechanics and Physics of Solids 51, 1413-1431, 2003
34. M. Aleyaasin, J.J. Harrigan, Wave dispersion and attenuation in viscoelastic polymeric bars: analysing the effect of lateral inertia. International Journal of Mechanical Science 52: 754-757, 2010
35. Davies, R. M., A critical study of the Hopkinson pressure bar, 1948 Phil. Trans. A, 240, 375
36. A.E.H. Love, A Treatise on the Mathematical Theory of Elasticity, fourth ed., Cambridge University Press, Cambridge, 1927
37. Pochhammer, L., Uber die Fortpflanzungsgeschwindigkeiten kleiner Schwingungen in unbe- ¨ grenzten isotropen Kreiszylinder (On the propagation velocities of small vibrations in an infinite isotropic cylinder), Zeitschrift f¨ur Reine und Angewandte Mathematik 81, pp. 324–336. (in German), 1876
38. Chree, C., The equation of an isotropic elastic solid in polar and cylindrical coordinates, their solution and applications, Transactions of the Cambridge Philosophical Society 14, pp. 250–369, 1889
39. H. Kolsky, Stress waves in Solids, Dover New-York, ISBN 0-486-49534-5, 1963
40. Gere, J.M. and Timoshenko, S.P. "Mechanics of Materials", 2nd SI Edition, Wadsworth International, California USA, 1985
41. S. C. Hunter, Progress in Solid Mechanics 1, pp. 3-56. 1960
42. Christophe Bacon, Arnaud Brun, Methodology for a Hopkinson test with a non-uniform viscoelastic bar. International Journal of Impact Engineering 24, pp. 219-230, 2000
43. David Roylance, <Engineering Viscoelasticity>, Department of materials science and engineering, MIT, October 24, 2001
44. SII NanoTechnology Inc., advantages of frequency multiplexing DMA experiments, Application Note AN44, *thass.net*
45. *http://homepages.engineering.auckland.ac.nz/~pkel015/SolidMechanicsBooks/Part_I/BookSM_Part_I/10_Viscoelasticity/10_Viscoelasticity_03_Rheological.pdf*
46. N. G. McCrum, C. P. Buckley, and C. B. Bucknall, <Principles of Polymer Engineering>, Second edition, Oxford University Press, 1997
47. *Abaqus Analysis User's Manual 22.7.2, ABAQUS 6.13*
48. *https://polymerfem.com/content.php?79-parallel-network-model*
49. Bradshaw, R. D., Brinson, L. C., A sign control method for fitting and interconverting material functions for linearly viscoelastic solids, Mechanics of Time-Dependent Materials 1, 85-108, 1997
50. Crispulo Gallegos, Francisco J., Martinez Boza, Linear Viscoelasticity, Rheology, Vol. I, 2009
51. Danton Gutierrez-Lemini, <Engineering Viscoelasticity>, Springer, ISBN 978-1-4614-8139-3

52. K. Welch, M. Strømme, Low frequency limitations of the split Hopkinson pressure bar method for identification of complex modulus, Int. J. Impact Eng., 34, pp. 1036-1046, 2007
53. <Determination of the Linear Viscoelastic Region of a Polymer using a strain sweep on the DMA 2980>, Thermal Solutions TS-61, Thermal Analysis & Rheology, TA Instruments
54. Ioannis Giannakopoulos, <The mechanical properties of polyester-based coil coatings. correlations with chemical structure>, PhD Thesis, pp. 72, June 2012
55. S. Mousavi, K. Welch, U. Valdek, B. Lundberg, Non-equilibrium split Hopkinson pressure bar procedure for non-parametric identification of complex modulus, International Journal of Impact Engineering, 31, pp. 1133-1151, 2005
56. Gorham, D.A., A numerical method for the correction of dispersion in pressure bar signals, J. Phys. E: Sci. Instrum. 16, pp. 477-479, 1983
57. Dennison Bancroft, The velocity of longitudinal waves in cylindrical bars. Physical Review, Vol. 59, pp. 588-593, 1941
58. A.V. Pichugin, Approximation of the Rayleigh wave speed, Department of civil and structural engineering, University of Sheffield, 10 January 2008
59. D. R. Drodge, D. M. Williamson and W. G. Proud, Split Hopkinson Pressure bar techniques for the estimation of a high strain-rate elastic modulus, Proceedings of the 6th International Congress and Exposition, Orlando, Florida, USA, June 2-5, 2008
60. J. Zhao, W.G. Knauss, G. Ravichandran, "Applicability of the time–temperature superposition principle in modeling dynamic response of a polyuria", Mech Time-Depend Mater 11, pp. 289–308, 2007
61. *http://www.tasupport.com/pdf/brochure/dma.pdf*, Q800 mannual, TA instruments
62. *http://en.wikipedia.org/wiki/Time%E2%80%93temperature_superposition*, Wikipedia
63. TS-236, < Dynamic Mechanical Analysis of Polymers>, TA Instruments
64. M. Gergesova, B. Zupančič, I. Saprunov, and I. Emri, "The closed form t-T-P shifting (CFS) algorithm", J. Rheol. 55(1), pp. 1-16, January/February 2011
65. S. W. Park and Y. R. Kim, fitting Prony-series viscoelastic models with power-law presmoothing, Journal of materials in civil engineering, Vol.13, No. 1, January/February 2001.
66. Tzikang Chen, Determining a Prony Series for a Viscoelastic Material From Time Strain Data, U.S. Army Research Laboratory report, NASA / TM-2000-210123, ARL-TR-2206
67. Cost, T. L., and Becker, E. B., ''A multidata method of approximate Laplace transform inversion.'' Int. J. Numerical Methods in Engineering 2, pp. 207–219, 1970.
68. Schapery, R.A., A simple collocation method for fitting viscoelastic models to experimental data. GALCIT SM 61-23A, California Institute of Technology, Pasadena, CA, 1961
69. S. W. Park and R. A. Schapery, Methods of interconversion between linear viscoelastic material functions. Part I-a numerical method based on Prony series, International Journal of Solids and Structures 36, pp. 1653-1675, 1999

70. *http://en.wikipedia.org/wiki/Noise_(signal_processing)*, Wikipedia
71. Additive noise. R.L. DobrushinV.V. Prelov (originator), Encyclopedia of Mathematics. *http://www.encyclopediaofmath.org/index.php?title=Additive_noise&oldid=18399*
72. Maria Petrou, Costas Petrou, Image Processing: The Fundamentals. John Wiley & Sons, ISBN 9780470745861, 2010
73. *http://en.wikipedia.org/wiki/Additive_white_Gaussian_noise*, Wikipedia
74. *http://en.wikipedia.org/wiki/Signal-to-noise_ratio*, Wikipedia
75. Welch, P.D, "The Use of Fast Fourier Transform for the Estimation of Power Spectra: A Method Based on Time Averaging Over Short, Modified Periodograms," IEEE Trans. Audio Electroacoustics, Vol. AU-15, pp. 70-73, June 1967
76. W. Maurice Ewing, Wenceslas S. Jardetzky and Frank Press, <Elastic waves in layered media>, McGraw-Hill Series in the geological science, Consulting editor: Robert R. Shrock, 1957
77. ABAQUS Analysis User's Manual: 30.1.2, Contact pressure-overclosure relationships
78. *https://en.wikipedia.org/wiki/S-wave*, Wikipedia
79. *https://en.wikipedia.org/wiki/Zoeppritz_equations*, Wikipedia
80. Zoeppritz, Karl. Erdbebenwellen VII. VIIb. Über Reflexion und Durchgang seismischer Wellen durch Unstetigkeitsflächen. Nachrichten von der Königlichen Gesellschaft der Wissenschaften zu Göttingen, Mathematisch-physikalische Klasse, pp. 66-84, 1919
81. Mahdi H. Almutlaq and Gary F. Margrave, Tutorial: AVO inversion, CREWS Research Report, Volume 22, 2010
82. Muhammad A. Kariem, John H. Beynon, Dong Ruan, Misalignment effect in the split Hopkinson pressure bar technique, International Journal of Impact Engineering, 47, pp. 60-70, 2012
83. Thomas D, Rossing and Daniel A,. Russell, Laboratory observation of elastic waves in solids, Am. J. Phys, 59(12), December 1990
84. M. P. Norton, and D. G. Karczub, <Fundamentals of noise and vibration analysis for engineers> second edition, Cambridge University press, 2003
85. Bo song and Weinong Chen, Split Hopkinson pressure bar techniques for characterizing soft materials, Latin American Journal of Solids and Structures (2), pp 113-152, 2005
86. D.T. Casem, W.L. Fourney and P. Chang, A Polymeric Split Hopkinson Pressure Bar Instrumented with Velocity Gages, Experimental Mechanics, Vol. 43, No. 4, pp. 420-427, Dec 2003
87. S. Rao, V. P. W. Shim, S. E. Quah, Dynamic Mechanical Properties of Polyurethane Elastomers Using a Nonmetallic Hopkinson Bar, Journal of Applied Polymer Science, Vol. 66, pp. 619–631, 1997

88. O. Sawas, N. S. Brar and R. A. Brockman, Dynamic Characterization of Compliant Materials Using an All-polymeric Split Hopkinson Bar, Experimental Mechanics, Vol. 38, No. 3, pp. 204-210, September 1998
89. Song B, Connelly K, Korellis J, Lu W-Y, Antoun BR, Improved Kosky-bar design for mechanical characterization of materials at high strain rates, Measurement Science and Technology, Vol. 20, No. 11, 2009
90. Harrigan JJ, Ahonsi B, Palamidi E, Reid SR. Experimental and numerical investigations on the use of polymer Hopkinson pressure bars. Phil. Trans. R. Soc. A 372: 20130201, 2014